THE ASYMPTOTIC RADIATION FIELD AND PROPER PROPAGATION MODE SPECTRA OF THE OPEN PLANAR WAVEGUIDE

VOLUME I

By

Jeong-Seog Lee

A DISSERTATION

Submitted to
Michigan State University
in partial fulfillment of the requirements
for the degree of

DOCTOR OF PHILOSOPHY

Department of Electrical and Computer Engineering

2002

ABSTRACT

THE ASYMPTOTIC RADIATION FIELD AND PROPER PROPAGATION MODE SPECTRA OF THE OPEN PLANAR WAVEGUIDE

By

Jeong-Seog Lee

The radiation field of the asymmetric planar dielectric waveguide is evaluated using the steepest-descent method for both TE and TM excitations.

Continuous spectrum currents/fields of integrated open waveguide structures has been until recently neither conceptualized theoretically nor quantified numerically. That spectrum can be identified as the branch cut contribution to singularity expansion of those currents/fields in the complex axial transform plane. Singularities in that plane include poles associated with the guiding structure and branch points contributed by layered background environments. The manner in which singularities in background environments manifest themselves as branch points in the complex axial transform plane is reviewed.

Based on transform domain integral equation formulation, approximate and analytical expression for spectral domain microstrip current is obtained. The delta-gap feed model is exploited. That approximation is based on Maxwellian distribution for the transverse current profile. The spectral domain current is inverted into space domain by integration contour deformation in the top sheet of the axial transform plane. This result is the representation of currents in terms of proper propagation mode spectra. That spectra

consist of bou

spectrum asso

environments.

transform plan

identified and

overall proced

continuous sp

integration in t

electric fields

bound mode is

Numerical

contribution to

mode. The ch

well-known en

point and decay

continuous spec

zone fields are

Asymptotic

achieved theore

is observed tha

transversely. T

research.

consist of bound propagation modes associated with pole singularities and continuous spectrum associated with integration around branch cuts contributed by background environments. During integration around branch cuts, singularities in the transverse transform plane migrate in a complicated manner. The trajectories of this migration are identified and suitably accommodated during the real axis integration in that plane. This overall procedure leads to a decomposition of the total currents into bound modes and continuous spectrum contributions. This representation is validated by real axis integration in the axial transform plane. Similar analysis leads to near and moderate zone electric fields of the guiding structure. The quasi TEM characteristic impedance of bound mode is calculated.

Numerical results are obtained, which compare bound mode and continuous spectrum contribution to microstrip currents. It is found that current is dominated by that of bound mode. The characteristic impedance of bound mode is validated by comparison with well-known empirical formula. The continuous spectrum current is maximal near feed point and decays rapidly with axial distant from the feed. The near field is dominated by continuous spectrum contribution. The extensive numerical results for near and moderate zone fields are obtained.

Asymptotic approximation to the field of an open integrated microstrip waveguide is achieved theoretically using the steepest-descent method (saddle point approximation). It is observed that the far zone cover field decays algebraically as $r^{-(\alpha+3/2)}\,(\alpha \neq 0)$ transversely. The algebraic decaying factor α still remains to be determined in future research.

The mo
regardful ap
I would lik
Nyquist, wh
academic tal
appreciation
guidance. I
encouraged m
Dr. Byron Dra
I also wa
Charles Macor
Finally, I a
unconditionall
three beautiful
throughout my
law who have al
in Christ who ha
Lord, Jesus Chri
man who owe Hi
ultimate appreciat

ACKNOWLEDGEMENT

The most memorable moments during my academic years remind me of sincere and regardful appreciation to those who have supported me throughout my study. First of all, I would like to extend regardful appreciation to my major professor, Dr. Dennis P. Nyquist, who has led me to true academic accomplishment with his unprecedented academic talent and thoughtful consideration. I also would like to extend sincere appreciation to Dr. Edward J. Rothwell who has supported me with his generous guidance. I would like to extend sincere appreciation to Dr. Leo C. Kempel who has encouraged me with his careful concern. I would like to extend sincere appreciation to Dr. Byron Drachman who has advised me with his mathematical talent.

I also want to share much appreciation with my colleagues; Benjamin Wilmhoff, Charles Macon, Jeffrey Meese, Jong Oh, and Michael J. Havrilla.

Finally, I always appreciate my lovely wife, Jin-Yang Park, who has supported me unconditionally with her love throughout my study. I have been truly blessed to have three beautiful daughters; Grace, Rachel, and Christine. They have been my consolation throughout my study. I also appreciate my mother, brother, father-in-law, and mother-in-law who have always cared about me. I always appreciate my sincere brothers and sisters in Christ who have been my friends. How can I extend my unlimited appreciation to my Lord, Jesus Christ, who has restored my soul and led me into His grace and peace? As a man who owe Him everything belonged to me throughout my life, I would like to extend ultimate appreciation to Him with all my heart.

LIST OF FIG

CHAPTER 1

CHAPTER 2

2.1 INT
2.2 SPE
2.2.1
2.2.2
2.2.3
2.3 IDE
2.3.1
2.3.2
2.4 THE
2.5 ALT
2.6 STE
2.7 STE
2.8 NUM
2.9 CON

CHAPTER 3

3.1 INTR
3.2 SPEC
3.2.1
3.2.2
3.2.3
3.2.4
3.2.5
3.2.6
3.3 THE E
3.4 ALTE

TABLE OF CONTENTS

LIST OF FIGURES ix

CHAPTER 1 INTRODUCTION 1

CHAPTER 2 SPECTRAL ANALYSIS AND ASYMPTOTIC RADIATION FIELD FOR TE MODES OF THE ASYMMETRIC PLANAR OPEN WAVE-GUIDE 4

2.1 INTRODUCTION AND GEOMETRICAL CONFIGURATION 4
2.2 SPECTRAL FIELD FORMULATION 7
2.2.1 COVER FIELD FORMULATION 8
2.2.2 FILM FIELD FORMULATION 9
2.2.3 SUBSTRATE FIELD FORMULATION 9
2.3 IDENTIFICATION OF THE STEEPEST-DESCENT PATH 10
2.3.1 STEEPEST-DESCENT PATH IN THE COMPLEX AXIAL TRANS-FORM PLANE *(DIRECT METHOD)* 13
2.3.2 TRANSFORMATION OF SDP FROM THE COMPLEX ϕ-PLANE TO THE COMPLEX ζ-PLANE *(INDIRECT METHOD)* 16
2.4 THE BRANCH CUT 22
2.5 ALTERNATIVE INTEGRATION PATH 26
2.6 STEEPEST-DESCENT EVALUATION OF COVER FIELD 30
2.7 STEEPEST-DESCENT EVALUATION OF SUBSTRATE FIELD 41
2.8 NUMERICAL RESULTS 47
2.9 CONCLUSION 53

CHAPTER 3 SPECTRAL ANALYSIS AND ASYMPTOTIC RADIATION FIELD FOR TM MODES OF AN ASYMMETRIC PLANAR OPEN WAVE-GUIDE 54

3.1 INTRODUCTION AND GEOMETRICAL CONFIGURATION 54
3.2 SPECTRAL FIELD FORMULATION 57
3.2.1 SPECTRAL COVER FIELD FORMULATION 59
3.2.2 SPECTRAL FILM FIELD FORMULATION 60
3.2.3 SPECTRAL SUBSTRATE FIELD FORMULATION 60
3.2.4 SPECTRAL GREEN'S DYAD REPRESENTATION 61
3.2.5 STEEPEST-DESCENT PATH IN THE COMPLEX AXIAL TRANSFORM PLANE *(DIRECT METHOD)* 65
3.2.6 TRANSFORMATION OF SDP FROM THE COMPLEX ϕ-PLANE TO THE COMPLEX ζ-PLANE *(INDIRECT METHOD)* 68
3.3 THE BRANCH CUT 70
3.4 ALTERNATIVE INTEGRATION PATH 70

3.5 STE
3.6 STE
3.7 CO

CHAPTER 4

4.1 INT
4.2 SPE
FOR
-LA
4.3 PL
.....
4.3.1
4.3.2
4.3.3
4.4 PH
RO
4.5 CO

CHAPTER 5

5.1 INT
5.2 MI
5.3 CO
5.4 DIS
5.5 MI
5.6 NU
5.7 CO

CHAPTER 6

6.1 INT
6.2 EM
6.2.1
6.2.2
6.2.3
6.3 NU
6.4 CO

CHAPTER 7

7.1 INT
7.2 IDE
7.3 THE
7.4 CO

3.5 STEEPEST-DESCENT EVALUATION OF COVER FIELD 73
3.6 STEEPEST-DESCENT EVALUATION OF SUBSTRATE FIELD 80
3.7 CONCLUSION 84

CHAPTER 4 ELECTROMAGNETICS OF INTEGRATED OPEN PLANAR LAYERED ELECTRONICS 86
4.1 INTRODUCTION AND GEOMETRICAL CONFIGURATION 86
4.2 SPECTRAL ELECTRIC FIELD INTEGRAL EQUATION FORMULATION FOR AN INTEGRATED OPEN WAVEGUIDE STRUCTURE IN A PLANAR -LAYERED BACKGROUND ENVIRONMENT 89
4.3 PLANAR-LAYERED BACKGROUND ENVIRONMENT SINGULARITIES 93
4.3.1 LOGARITHMIC-TYPE BRANCH POINT 95
4.3.2 SQUARE-ROOT TYPE BRANCH POINT 106
4.3.3 REGULAR OR ANALYTIC POINT 117
4.4 PHYSICAL INTERPRETATION OF LOGARITHMIC AND SQUARE-ROOT TYPE BRANCH POINTS 121
4.5 CONCLUSION 124

CHAPTER 5 THE PROPER CURRENT SPECTRUM OF AN OPEN INTEGRATED MICROSTRIP WAVEGUIDE 126
5.1 INTRODUCTION AND GEOMETRICAL CONFIGURATION 126
5.2 MICROSTRIP CURRENT FORMULATION 130
5.3 CONTINUOUS SPECTRUM CURRENT 139
5.4 DISCRETE SPECTRUM CURRENT 169
5.5 MICROSTRIP CURRENT SPECTRUM 178
5.6 NUMERICAL RESULTS 189
5.7 CONCLUSION 198

CHAPTER 6 THE PROPER EM FIELD SPECTRUM OF AN OPEN INTEGRATED MICROSTRIP WAVEGUIDE 199
6.1 INTRODUCTION AND GEOMETRICAL CONFIGURATION 199
6.2 EM FIELD FORMULATION 202
6.2.1 COVER FIELD FORMULATION 203
6.2.2 FILM FIELD FORMULATION 222
6.2.3 NORMAL BOUNDARY CONDITION 232
6.3 NUMERICAL RESULTS 236
6.4 CONCLUSION 307

CHAPTER 7 ASYMPTOTIC APPROXIMATION TO THE EM FIELD OF AN OPEN INTEGRATED MICROSTRIP WAVEGUIDE 308
7.1 INTRODUCTION AND GEOMETRICAL CONFIGURATION 308
7.2 IDENTIFICATION OF THE STEEPEST-DESCENT PATH 311
7.3 THE ASYMPTOTIC APPROXIMATION TO THE COVER FIELD 319
7.4 CONCLUSION 328

CHAPTER

APPENDIX

A.1 S
F
A.2 T
L

APPENDIX

APPENDIX

C.1 SP
CO
C.2 IM

APPENDIX

APPENDIX

E.1 GEO
LAY
E.2 BOU
.....
E.3 ELE
E.4 IMP

APPENDIX F

APPENDIX G

G.1 COV
G.2 FILM

BIBLIOGRAP

CHAPTER 8 CONCLUSION 329

APPENDIX A SPECTRAL TE EM FIELD FORMULATION FOR ASYMMETRIC PLANAR DIELECTRIC SLAB WAVEGUIDE USING INTEGRAL TRANSFORM TECHNIQUE 331
A.1 SPECTRAL HERTZIAN POTENTIAL REPRESENTATION OF EM FIELD 331
A.2 THE SPECTRAL EM FIELD REPRESENTATION IN THE COVER LAYER 332

APPENDIX B IDENTIFICATION OF THE STEEPEST-DESCENT PATH IN THE COMPLEX AXIAL TRANSFORM PLANE 338

APPENDIX C SPECTRAL GREEN'S DYAD REPRESENTATION OF RADIATION FIELD FOR TM MODES OF THE ASYMMETRIC PLANAR OPEN WAVEGUIDE 340
C.1 SPECTRAL GREEN'S DYAD FORMULATION WITH UNDETERMINED COEFFICIENTS 340
C.2 IMPLEMENTATION OF MATCHING BOUNDARY CONDITIONS .. 346

APPENDIX D GREEN'S DYAD INTEGRAL REPRESENTATION OF RADIATION FIELD FOR TM MODES OF THE ASYMMETRIC PLANAR OPEN WAVEGUIDE 349

APPENDIX E ELECTRIC HERTZIAN POTENTIAL FORMULATION OF THE ASYMMETRIC TRI PLANAR-LAYERED DIELECTRIC WAVEGUIDE 353
E.1 GEOMETRICAL CONFIGURATION OF ASYMMETRIC TRI PLANAR-LAYERED DIELECTRIC WAVEGUIDE 353
E.2 BOUNDARY CONDITIONS FOR ELECTRIC HERTZIAN POTENTIALS 354
E.3 ELECTRIC HERTZIAN POTENTIAL FORMULATION 356
E.4 IMPLEMENTATION OF BOUNDARY CONDITIONS 361

APPENDIX F CUT-OFF CRITERION FOR THE SURFACE-WAVE OF AN OPEN INTEGRATED MICROSTRIP WAVEGUIDE 383

APPENDIX G ELECTROMAGNETIC FIELDS FORMULATION OF AN OPEN INTEGRTED MICROSTRIP WAVEGUIDE IN THE COMPLEX λ-PLANE 388
G.1 COVER FIELD FORMULATION 388
G.2 FILM FIELD FORMULATION 394

BIBLIOGRAPHY 397

Figure 2.1.1 Geome
wavegu
are con

Figure 2.3.1 The ma

Figure 2.3.2 Polar c

Figure 2.3.3 Phase c

Figure 2.3.4 Mappin
$|\theta_i^l < \pi$

Figure 2.4.1 Hyperb
and $\pm I$

Figure 2.4.2 Branch

Figure 2.4.3 Compl

Figure 2.5.1 Singul
Riema
substra
limit ..

Figure 2.5.2 Compl
integra

Figure 2.6.1 The ste
observ
asymm
substra

Figure 2.6.2 Proper
$n_1 = 1$

LIST OF FIGURES

Figure 2.1.1 Geometrical configuration of an asymmetric planar dielectric slab waveguide with TE line-source excitation. Cover, film, and substrate layers are considered in the low loss limit 6

Figure 2.3.1 The mapping from the complex ζ -plane to the complex λ -plane 12

Figure 2.3.2 Polar coordinate transformations 13

Figure 2.3.3 Phase correction diagram in the cover layer 14

Figure 2.3.4 Mapping to the steepest-descent path in the complex $\phi = \sigma + j\eta$ plane: $|\theta| < \pi/2$ 20

Figure 2.4.1 Hyperbolic branch cut construction emanating from the branch points $\pm k_1$ and $\pm k_3$ 23

Figure 2.4.2 Branch cut construction in the low-loss limit 24

Figure 2.4.3 Complex-phasor diagram in the complex ζ -plane 25

Figure 2.5.1 Singularities and alternative integration path in the complex ζ -plane on top Riemann sheet for the complete proper propagation spectrum. Cover and substrate layers are presumably considered to be in the low-loss limit 29

Figure 2.5.2 Complex-phasor diagram with a pole singularity and $\mathrm{Re}\{\zeta\}$- axis integration path in the complex ζ -plane 30

Figure 2.6.1 The steepest-descent paths for the cover layer field calculation on various observation aspect angles in the complex axial transform plane. The asymmetric planar dielectric waveguide consists of cover, guiding and substrate layer with indices $n_1 = 1.$, $n_2 = 3.2$, and $n_3 = 3$ respectively . 36

Figure 2.6.2 Proper closure of $\mathrm{Re}\{\zeta\}$-axis inversion contour C into SDP for $\theta < \theta_t$: $n_1 = 1.$, $n_2 = 3.2$, $n_3 = 3.$, $\theta_t = 19.5^\circ$ 37

Figure 2.6

Figure 2.6.

Figure 2.6.

Figure 2.7.1

Figure 2.7.2

Figure 2.7.3

Figure 2.8.1
a

Figure 2.8.2
s

Figure 2.8.3 T
s

Figure 2.8.4 T
st

Figure 2.8.5 T
st

Figure 3.1.1 Ge
wa
la

Figure 3.2.1 Po

Figure 2.6.3 Appropriate closure of SDP into cover layer branch cut for $\theta > \theta_t$: $n_1 = 1., n_2 = 3.2, n_3 = 3., \theta_t = 19.5^\circ$ 38

Figure 2.6.4 Proper closure of $\mathrm{Re}\{\zeta\}$-axis inversion contour C into SDP and substrate branch cut for $\theta > \theta_t$: $n_1 = 1., n_2 = 3.2, n_3 = 3., \theta_t = 19.5^\circ$ 39

Figure 2.6.5 Proper closure of $\mathrm{Re}\{\zeta\}$-axis inversion contour C into SDP and partial C_{b3} for $\theta > \theta_t$: $n_1 = 1., n_2 = 3.2, n_3 = 3., \theta_t = 19.5^\circ$ 40

Figure 2.7.1 The steepest-descent paths for the substrate layer field calculation at various observation aspect angles in the complex ζ -plane. The asymmetric planar dielectric wave- guide consists of cover, guiding and substrate layers with indices $n_1 = 1.$, $n_2 = 3.2$, and $n_3 = 3.$ respectively 44

Figure 2.7.2 Closure of $\mathrm{Re}\{\zeta\}$-axis inversion contour C into SDP and full cover layer branch cut for $\theta > \theta_t$ 45

Figure 2.7.3 Proper closure of $\mathrm{Re}\{\zeta\}$-axis inversion contour C into SDP and partial cover layer branch cut for $\theta > \theta_t$ 46

Figure 2.8.1 Transverse dependence of the reflected continuous spectrum in the cover layer: the steepest-descent numerical calculation and saddle-point approximation 48

Figure 2.8.2 Transverse dependence of the continuous spectrum in the cover layer: steepest-descent numerical and saddle-point approximation 49

Figure 2.8.3 Transverse dependence of the continuous spectrum in the cover layer: steepest-descent numerical and the substrate layer branch cut 50

Figure 2.8.4 Transverse dependence of the transmitted spectrum in the substrate layer: steepest-descent numerical and the corresponding branch cut..... 51

Figure 2.8.5 Transverse dependence of the transmitted spectrum in the substrate layer: steepest-descent numerical and the partial cover layer branch cut 52

Figure 3.1.1 Geometrical configuration of an asymmetric planar dielectric slab waveguide with TM line-source excitation. Cover, film, and substrate layers are considered in the low-loss limit 56

Figure 3.2.1 Polar coordinate transformations 66

Figure 3.4.

Figure 3.5.

Figure 3.5.2

Figure 3.5.3

Figure 3.6.1

Figure 3.6.2

Figure 4.1.1

Figure 4.1.2

Figure 4.3.1

Figure 4.3.2

Figure 4.3.3

Figure 3.4.1 Singularities and alternative integration path in the complex ζ -plane on top Riemann sheet for the complete proper propagation spectrum. Cover and substrate layers are presumably considered to be in the low-loss limit 71

Figure 3.5.1 The steepest-descent paths in the complex ζ -plane for the cover layer field calculation at various observation aspect angles. The asymmetric planar dielectric waveguide consists of cover, guiding and substrate layers with indices $n_1 = 1.$, $n_2 = 3.2$ and $n_3 = 3.$ respectively 74

Figure 3.5.2 Proper closure of $\mathrm{Re}\{\zeta\}$-axis inversion contour C into SDP and substrate branch cut for $\theta > \theta_t$: $n_1 = 1.$, $n_2 = 3.2$, $n_3 = 3.$, $\theta_t = 19.5^\circ$ 78

Figure 3.5.3 Proper closure of $\mathrm{Re}\{\zeta\}$-axis inversion contour C into SDP and partial C_{b3} for $\theta > \theta_t$: $n_1 = 1.$, $n_2 = 3.2$, $n_3 = 3.$, $\theta_t = 19.5^\circ$ 79

Figure 3.6.1 The steepest-descent paths in the complex ζ -plane for the substrate layer field calculation at various observation aspect angles. The asymmetric planar dielectric waveguide consists of cover, guiding, and substrate layer with indices $n_1 = 1.$, $n_2 = 3.13$, and $n_3 = 3.$ respectively 81

Figure 3.6.2 Proper closure of $\mathrm{Re}\{\zeta\}$-axis inversion contour C into SDP and partial cover layer branch cut for $\theta > \theta_t$ 83

Figure 4.1.1 Geometrical configuration of integrated open microstrip structure immersed in layered background environment 88

Figure 4.1.2 Cross-sectional view of immersed integrated microstrip structure 88

Figure 4.3.1 Singularities in the complex ζ -plane contributed by the planar- layered background environment. The branch point $\pm k_1$ to the branch point $\pm k_1$ mapping and the pole $\pm \lambda_p$ to the branch point $\pm \lambda_p$ mapping in the low-loss limit 94

Figure 4.3.2 Complex-phasor diagram with a path in the complex ζ -plane, making one round trip about the point k_1 95

Figure 4.3.3 Path trajectory in the complex ζ -plane, encircling twice around the point $\zeta = k_1$ 100

Figure 4.3.4

Figure 4.3.5

Figure 4.3.6

Figure 4.4.1

Figure 5.1.1

Figure 5.1.2

Figure 5.3.1

Figure 5.3.2

Figure 5.3.3

Figure 5.3.4

Figure 4.3.4 Path trajectory in the complex ζ -plane, encircling twice around the point $\zeta = \lambda_{TM_0}$ 110

Figure 4.3.5 Path trajectory in the complex ζ -plane, encircling twice around the point $\zeta = \lambda_{TM_0}$ after violating the branch cut twice 113

Figure 4.3.6 Path trajectory in the complex ζ -plane, encircling once around the point $\zeta = \lambda_{TM_0}$ after violating the branch cut once 119

Figure 4.4.1 Branch cuts associated with a logarithmic type branch point k_1 and a square-root type branch point λ_{TM_0} in the complex ζ -plane and the continuous spectrum contributed by those branch cut integration 123

Figure 5.1.1 Geometrical configuration of open microstrip structure immersed in layered background environment 129

Figure 5.1.2 Cross-sectional view of immersed microstrip structure 129

Figure 5.3.1 Singularities in the complex ζ -plane contributed by the planar-layered background environment. The branch points $\lambda_s = \pm k_1$ to the branch points $\pm k_1$ mapping and the poles $\lambda_s = \pm \lambda_{TM_0}$ to the branch points $\pm \lambda_{TM_0}$ mapping in the low low-loss limit 140

Figure 5.3.2 Deformation of $\mathrm{Re}\{\zeta\}$-axis inversion contour into the *Upper Half Plane (UHP)* and the *Lower Half Plane (LHP)* in the complex ζ -plane. Branch cuts associated with branch-point singularities contributed by a background layer environment are considered to be in the low-loss limit 142

Figure 5.3.3 Branch cuts associated with a logarithmic type branch point k_1 and a square-root type branch point λ_{TM_0} in the complex ζ -plane and the proper continuous spectrum contributed by those branch cut integrations for low-loss limit 143

Figure 5.3.4 Migration of complex transverse transform plane (complex ξ -plane) branch-point singularities $\pm \xi_{k_1}$ in conjunction with changing spatial-frequency ζ along branch cuts associated with a logarithmic type branch point k_1 and a square-root type branch point λ_{TM_0} in the complex ζ -plane in the low-loss limit 144

Figure 5.3.5

Figure 5.3.6

Figure 5.3.7

Figure 5.3.8

Figure 5.3.9

Figure 5.3.10

Figure 5.3.11

Figure 5.3.12

Figure 5.3.13

Figure 5.3.5 Opposite $\mathrm{Re}\{\xi\}$-axis inversion contours corresponding to points 2 and 5 on the branch-cut contour in the complex ζ-plane as depicted in Fig. 5.3.3. 151

Figure 5.3.6 Complex-phasor diagram for branch-point singularities $\pm\xi_{k_1}$ in the complex ξ-plane for corresponding points 2 and 5 in the complex ζ-plane in Fig. 5.3.3 and evolution of C_ξ 152

Figure 5.3.7 Current amplitude longitudinal profile contributed by $\mathrm{Re}\{\xi\}$-axis inversion contour excluding surface-wave pole singularities with integrating ζ about the branch-cut contour 153

Figure 5.3.8 Current phase longitudinal profile contributed by $\mathrm{Re}\{\xi\}$-axis inversion contour excluding surface-wave pole singularities with integrating ζ about the branch-cut contour 154

Figure 5.3.9 Migration of complex transverse transform plane (complex ξ-plane) surface-wave pole singularities $\pm\xi_{TM_0}$ in conjunction with changing spatial-frequency ζ along branch cuts associated with a logarithmic type branch point k_1 and a square-root type branch point λ_{TM_0} in the complex ζ-plane in the low-loss limit 160

Figure 5.3.10 Full residue evaluation contributed by the surface-wave pole singularity $\xi_p = -\xi_{TM_0}(2) = \xi_{TM_0}(5)$ with corresponding branch point singularities $\pm\xi_{k_1}$ 161

Figure 5.3.11 Current amplitude longitudinal profile contributed by surface-wave pole singularities in the complex ξ-plane with integrating ζ about the branch-cut contour 162

Figure 5.3.12 Current phase longitudinal profile contributed by surface-wave pole singularities in the complex ξ-plane with integrating ζ about the branch-cut contour 163

Figure 5.3.13 Continuous current amplitude profile contributed by branch cut contour integration: $\mathrm{Re}\{\xi\}$-axis inversion contour integration including surface-wave pole singularities in the complex ξ- plane 166

Figure 5.3.
Figure 5.4.
Figure 5.4.
Figure 5.4.
Figure 5.4.
Figure 5.4.
Figure 5.4.
Figure 5.5.
Figure 5.5.
Figure 5.5.
Figure 5.5.

Figure 5.3.14 Continuous current phase profile contributed by branch cut contour integration: $\mathrm{Re}\{\xi\}$-axis inversion contour integration including surface-wave pole singularities in the complex ξ - plane 167

Figure 5.4.1 The discrete spectrum current contributed by a full residue evaluated about a pole-excluding contour C_{ζ_p} encircled about a bound- or guided-mode pole singularity ζ_p in the complex ζ - plane 169

Figure 5.4.2 Discrete current amplitude profile contributed by a bound- or a guided-mode pole singularity ζ_p in the complex ζ -plane 173

Figure 5.4.3 Discrete current phase profile contributed by a bound- or a guided-mode pole singularity ζ_p in the complex ζ -plane 174

Figure 5.4.4 Voltage decomposition diagram 175

Figure 5.4.5 The dispersion of the fundamental surface-wave pole singularity λ_{TM_0} and the bound or guided-mode pole singularity ζ_p through operating frequency ranges 176

Figure 5.4.6 The characteristic impedance of the microstrip waveguide calculated by the longitudinal discrete or bound-mode current spectrum through operating frequency ranges 177

Figure 5.5.1 Total microstrip current amplitude profile contributed by the continuous spectrum current and the discrete spectrum current 181

Figure 5.5.2 Total microstrip current phase profile contributed by the continuous spectrum current and the discrete spectrum current 182

Figure 5.5.3 $\mathrm{Re}\{\zeta\}$-axis inversion contour C_ζ and the half residue contribution about $\zeta = \zeta_p$ 183

Figure 5.5.4 Migration of complex transverse transform plane (complex ξ-plane) branch-point singularities $\pm\xi_{k_1}$ and surface-wave pole singularities $\pm\xi_{TM_0}$ in conjunction with changing spatial-frequency ζ on $\mathrm{Re}\{\zeta\}$-axis inversion contour in the low-loss limit 184

Figure 5.5.5 R
p
s
Figure 5.5.6 F
F
s
Figure 5.5.7 I
I
s
Figure 5.5.8
Figure 5.6.1
Figure 5.6.2
Figure 5.6.3
Figure 5.6.4
Figure 5.6.5
Figure 5.6.
Figure 5.6.
Figure 5.6
Figure 6.1
Figure 6.1

Figure 5.5.5 $\mathrm{Re}\{\zeta\}$-axis inversion contour validation of microstrip current amplitude profile contributed by the continuous spectrum current and the discrete spectrum current for near zone 185

Figure 5.5.6 $\mathrm{Re}\{\zeta\}$-axis inversion contour validation of microstrip current phase profile contributed by the continuous spectrum current and the discrete spectrum current for near zone 186

Figure 5.5.7 $\mathrm{Re}\{\zeta\}$-axis inversion contour validation of microstrip current amplitude profile contributed by the continuous spectrum current and the discrete spectrum current 187

Figure 5.5.8 $\mathrm{Re}\{\zeta\}$-axis inversion contour validation of microstrip current phase profile contributed by the continuous spectrum current and the discrete spectrum current 188

Figure 5.6.1 Near zone microstrip current amplitude profile with various electrical strip widths 190

Figure 5.6.2 Microstrip current amplitude profile with various electrical strip widths 191

Figure 5.6.3 Microstrip continuous and discrete spectrum current amplitude-ratio with various electrical strip widths 192

Figure 5.6.4 Microstrip continuous and discrete spectrum current amplitude-ratio versus electrical film thickness with various electrical strip widths 193

Figure 5.6.5 Microstrip continuous spectrum current amplitude versus electrical film thickness with various electrical strip widths 194

Figure 5.6.6 Microstrip continuous spectrum current amplitude versus electrical strip width 195

Figure 5.6.7 Microstrip current amplitude versus electrical film thickness with electrical strip widths 196

Figure 5.6.8 Microstrip current amplitude versus electrical strip widths 197

Figure 6.1.1 Geometrical configuration of open microstrip structure immersed in layered background environment 201

Figure 6.1.2 Cross-sectional view of immersed microstrip structure 201

Figure 6.2.1

Figure 6.2.2

Figure 6.2.3

Figure 6.2.4

Figure 6.2.5

Figure 6.2.6

Figure 6.2.7

Figure 6.2.8

Figure 6.2.9

Figure 6.3.1

Figure 6.3.2

Figure 6.3.3

Figure 6.2.1 Field amplitude longitudinal profile contributed by $\mathrm{Re}\{\xi\}$-axis inversion contour excluding surface-wave pole singularities with integrating ζ about the branch-cut contour 211

Figure 6.2.2 Field phase longitudinal profile contributed by $\mathrm{Re}\{\xi\}$-axis inversion contour excluding surface-wave pole singularities with integrating ζ about the branch-cut contour 212

Figure 6.2.3 Field amplitude longitudinal profile contributed by $\mathrm{Re}\{\xi\}$-axis inversion contour excluding surface-wave pole singularities with integrating ζ about the branch-cut contour 213

Figure 6.2.4 Field phase longitudinal profile contributed by $\mathrm{Re}\{\xi\}$-axis inversion contour excluding surface-wave pole singularities with integrating ζ about the branch-cut contour 214

Figure 6.2.5 Field amplitude longitudinal profile contributed by the residue evaluated at the surface-wave pole singularity with integrating ζ about the branch-cut contour 215

Figure 6.2.6 Field phase longitudinal profile contributed by the residue evaluated at the surface-wave pole singularity with integrating ζ about the branch-cut contour..... 216

Figure 6.2.7 Field amplitude longitudinal profile contributed by the residue evaluated at the surface-wave pole singularity with integrating ζ about the branch-cut contour 217

Figure 6.2.8 Field phase longitudinal profile contributed by the residue evaluated at the surface-wave pole singularity with integrating ζ about the branch-cut contour 218

Figure 6.2.9 Maxwellian transverse distribution to be matched with the normal electric field component difference at the interface $y=0$ 235

Figure 6.3.1 Transverse continuous and discrete electric cover field spectrum amplitudes profile in the low-loss limit 241

Figure 6.3.2 Transverse continuous electric cover field spectrum phase profile in the low-loss limit 242

Figure 6.3.3 Transverse discrete electric cover field spectrum phase profile in the low-

Figure 6.3.4

Figure 6.3.5

Figure 6.3.6

Figure 6.3.7

Figure 6.3.8

Figure 6.3.9

Figure 6.3.10

Figure 6.3.11

Figure 6.3.12

Figure 6.3.13

Figure 6.3.14

Figure 6.3.15

Figure 6.3.16

Figure 6.3.17

Figure 6.3.18

loss limit 243

Figure 6.3.4 Transverse total electric cover field spectrum phase profile in the low-loss limit 244

Figure 6.3.5 Transverse continuous and discrete cover electric field spectrum amplitude profiles in the low-loss limit 245

Figure 6.3.6 Transverse continuous electric cover field spectrum phase profile in the low-loss limit 246

Figure 6.3.7 Transverse discrete electric cover field spectrum phase profile in the low-loss limit 247

Figure 6.3.8 Transverse total electric cover field spectrum phase profile in the low-loss limit 248

Figure 6.3.9 Vertical continuous and discrete electric cover field spectrum amplitudes profile in the low-loss limit 249

Figure 6.3.10 Vertical continuous electric cover field spectrum phase profile in the low-loss limit 250

Figure 6.3.11 Vertical discrete electric cover field spectrum phase profile in the low-loss limit 251

Figure 6.3.12 Vertical total electric cover field spectrum phase profile in the low-loss limit 252

Figure 6.3.13 Vertical continuous and discrete electric cover field spectrum amplitudes profile in the low-loss limit 253

Figure 6.3.14 Vertical continuous electric cover field spectrum phase profile in the low-loss limit 254

Figure 6.3.15 Vertical discrete electric cover field spectrum phase profile in the low-loss limit 255

Figure 6.3.16 Vertical total electric cover field spectrum phase profile in the low-loss limit 256

Figure 6.3.17 Longitudinal continuous and discrete electric cover field spectrum amplitudes profile in the low-loss limit 257

Figure 6.3.18 Longitudinal continuous electric cover field spectrum phase profile in the low-loss limit 258

Figure 6.3.19

Figure 6.3.20

Figure 6.3.21

Figure 6.3.22

Figure 6.3.23

Figure 6.3.24

Figure 6.3.25

Figure 6.3.26

Figure 6.3.27

Figure 6.3.28

Figure 6.3.29

Figure 6.3.30

Figure 6.3.31

Figure 6.3.32

Figure 6.3.19 Longitudinal discrete electric cover field spectrum phase profile in the low-loss limit 259

Figure 6.3.20 Longitudinal total electric cover field spectrum phase profile in the low-loss limit 260

Figure 6.3.21 Longitudinal continuous and discrete electric cover field spectrum amplitudes profile in the low-loss limit 261

Figure 6.3.22 Longitudinal continuous electric cover field spectrum phase profile in the low-loss limit 262

Figure 6.3.23 Longitudinal discrete electric cover field spectrum phase profile in the low-loss limit 263

Figure 6.3.24 Longitudinal total electric cover field spectrum phase profile in the low-loss limit 264

Figure 6.3.25 $\mathrm{Re}\{\zeta\}$-axis inversion contour validation of microstrip cover field amplitude profile contributed by the continuous spectrum field and the discrete spectrum field in the near zone 265

Figure 6.3.26 $\mathrm{Re}\{\zeta\}$-axis inversion contour validation of microstrip cover field phase profile contributed by the continuous spectrum field and the discrete spectrum field in the near zone 266

Figure 6.3.27 $\mathrm{Re}\{\zeta\}$-axis inversion contour validation of microstrip cover field amplitude profile contributed by the continuous spectrum field and the discrete spectrum field 267

Figure 6.3.28 $\mathrm{Re}\{\zeta\}$-axis inversion contour validation of microstrip cover field phase profile contributed by the continuous spectrum field and the discrete spectrum field 268

Figure 6.3.29 Transverse continuous and discrete electric film field spectrum amplitudes profile in the low-loss limit 269

Figure 6.3.30 Transverse continuous electric film field spectrum phase profile in the low-loss limit 270

Figure 6.3.31 Transverse discrete electric film field spectrum phase profile in the low-loss limit 271

Figure 6.3.32 Transverse total electric film field spectrum phase profile in the low-loss

Figure 6.3.33
Figure 6.3.34
Figure 6.3.35
Figure 6.3.36
Figure 6.3.37
Figure 6.3.38
Figure 6.3.39
Figure 6.3.40
Figure 6.3.41
Figure 6.3.42
Figure 6.3.43
Figure 6.3.44
Figure 6.3.45
Figure 6.3.46
Figure 6.3.47

limit 272

Figure 6.3.33 Transverse continuous and discrete electric film field spectrum amplitudes profile in the low-loss limit 273

Figure 6.3.34 Transverse continuous electric film field spectrum phase profile in the low-loss limit 274

Figure 6.3.35 Transverse discrete electric field spectrum phase profile in the low-loss limit 275

Figure 6.3.36 Transverse total electric film field spectrum phase profile in the low-loss limit 276

Figure 6.3.37 Vertical continuous and discrete electric film field spectrum amplitudes profile in the low-loss limit 277

Figure 6.3.38 Vertical continuous electric film field spectrum phase profile in the low-loss limit 278

Figure 6.3.39 Vertical discrete electric field spectrum phase profile in the low-loss limit 279

Figure 6.3.40 Vertical total electric film field spectrum phase profile in the low-loss limit 280

Figure 6.3.41 Vertical continuous and discrete electric field spectrum amplitudes profile in the low-loss limit 281

Figure 6.3.42 Vertical continuous electric film field spectrum phase profile in the low-loss limit 282

Figure 6.3.43 Vertical discrete electric film field spectrum phase profile in the low-loss limit 283

Figure 6.3.44 Vertical total electric film field spectrum phase profile in the low-loss limit 284

Figure 6.3.45 Vertical continuous and discrete electric field spectrum amplitudes profile in the low-loss limit 285

Figure 6.3.46 Vertical continuous electric film field spectrum phase profile in the low-loss limit 286

Figure 6.3.47 Vertical discrete electric film field spectrum phase profile in the low-loss limit 287

Figure 6.3.48

Figure 6.3.49

Figure 6.3.50

Figure 6.3.51

Figure 6.3.52

Figure 6.3.53

Figure 6.3.54

Figure 6.3.55

Figure 6.3.56

Figure 6.3.57

Figure 6.3.58

Figure 6.3.59

Figure 6.3.60

Figure 6.3.61

Figure 6.3.62

Figure 6.3.48 Vertical total electric film field spectrum phase profile in the low-loss limit 288

Figure 6.3.49 $\mathrm{Re}\{\zeta\}$-axis inversion contour validation of microstrip film field amplitude profile contributed by the continuous spectrum field and the discrete spectrum field 289

Figure 6.3.50 $\mathrm{Re}\{\zeta\}$-axis inversion contour validation of microstrip cover field phase profile contributed by the continuous spectrum field and the discrete spectrum field 290

Figure 6.3.51 Longitudinal continuous and discrete electric film field spectrum amplitudes profile in the low-loss limit 291

Figure 6.3.52 Longitudinal continuous electric film field spectrum phase profile in the low-loss limit 292

Figure 6.3.53 Longitudinal discrete electric field spectrum phase profile in the low-loss limit 293

Figure 6.3.54 Longitudinal total electric film field spectrum phase profile in the low-loss limit 294

Figure 6.3.55 Longitudinal continuous and discrete electric film field spectrum amplitudes profile in the low-loss limit 295

Figure 6.3.56 Longitudinal continuous electric film field spectrum phase profile in the low-loss limit 296

Figure 6.3.57 Longitudinal discrete electric film field spectrum phase profile in the low-loss limit 297

Figure 6.3.58 Longitudinal total electric film field spectrum phase profile in the low-loss limit 298

Figure 6.3.59 Longitudinal continuous and discrete electric film field spectrum amplitudes profile in the low-loss limit 299

Figure 6.3.60 Longitudinal continuous electric film field spectrum phase profile in the low-loss limit 300

Figure 6.3.61 Longitudinal discrete electric film field spectrum phase profile in the low-loss limit 301

Figure 6.3.62 Longitudinal total electric film field spectrum phase profile in the low-loss

Figure 6.3.6

Figure 6.3.6

Figure 6.3.6

Figure 6.3.6

Figure 7.1.1

Figure 7.1.2

Figure 7.2.1

Figure 7.2.2

Figure 7.2.3

Figure 7.3.1

Figure 7.3.2

limit 302

Figure 6.3.63 $\mathrm{Re}\{\zeta\}$-axis inversion contour validation of microstrip film field amplitude profile contributed by the continuous spectrum field and the discrete spectrum field in the near zone 303

Figure 6.3.64 $\mathrm{Re}\{\zeta\}$-axis inversion contour validation of microstrip film field phase profile contributed by the continuous spectrum field and the discrete spectrum field in the near zone 304

Figure 6.3.65 $\mathrm{Re}\{\zeta\}$-axis inversion contour validation of microstrip film field amplitude profile contributed by the continuous spectrum field and the discrete spectrum field 305

Figure 6.3.66 $\mathrm{Re}\{\zeta\}$-axis inversion contour validation of microstrip film field phase profile contributed by the continuous spectrum field and the discrete spectrum field 306

Figure 7.1.1 Geometrical configuration of open microstrip structure immersed in layered background environment 310

Figure 7.1.2 Cross-sectional view of immersed microstrip structure 310

Figure 7.2.1 Branch-point singularities $\pm\xi_{k_1}$ and surface-wave pole singularities $\pm\xi_{TM_0}$ in the complex ξ-plane for a corresponding point on $\mathrm{Re}\{\zeta\}$-axis inversion contour in the complex ζ - plane 313

Figure 7.2.2 Polar coordinate transformation 315

Figure 7.2.3 Identification of the steepest-descent path in the complex ζ -plane for an observation aspect angle θ less than a threshold aspect angle θ_t and branch cuts contributed by the background layer environ-ment in the low-loss limit 318

Figure 7.3.1 Complex phasor diagram of the steepest-descent path in the complex ζ -plane with intervals I, II, III, and IV and logarithmic branch cuts in the low-loss limit 322

Figure 7.3.2 Migration of complex ξ-plane branch point singularities $\pm\xi_{k_1}$ in the low-loss limit with various ζ contouring along the steepest-descent path in the complex ζ - plane 323

Figure 7.3.3 Mig
the
com

Figure A.1.1 Geo
.....

Figure A.2.1 Pok
top

Figure A.2.2 Ider
cont

Figure E.1.1 Asy
wav
the p

Figure E.4.1 Grap
odd

Figure E.4.2 Cros
ε_3 –
curre
inter

Figure G.1.1 Tran

Figure G.1.2 Prop
bour

Figure 7.3.3 Migration of complex ξ-plane surface-wave pole singularities $\pm\xi_{TM_0}$ in the low-loss limit with various ζ along the steepest-descent path in the complex ζ - plane 324

Figure A.1.1 Geometrical configuration of asymmetric planar dielectric slab waveguide 331

Figure A.2.1 Pole singularities in the complex ξ-plane to be chosen for $p_1(\zeta)$ on the top Riemann sheet of the complex ζ -plane 333

Figure A.2.2 Identification of pole singularities by path deformation of Fourier inversion contour in the complex ξ-plane 334

Figure E.1.1 Asymmetric tri planar-layered dielectric waveguide with the z-axis as the waveguiding axis and with the x-axis tangential and the y-axis normal to the planar interfaces 353

Figure E.4.1 Graphical solution to determine the cut-off criterion for the $n'th$ even or odd surface-wave modes of the microstrip waveguide 385

Figure E.4.2 Cross-sectional view of the integrated microstrip waveguide with $\varepsilon_3 \rightarrow -j\infty$. Perpendicular TM_0 even- and parallel TE_1 odd-mode currents and their images are mirrored with respect to the $y = -t$ interface 387

Figure G.1.1 Transformation of $(x, z - z')$ into (r, θ) and (ξ, ζ) into (λ, ϕ) 389

Figure G.1.2 Proper spectrum in the complex λ-plane with the branch-point and the bound-mode pole singularities in the low-loss limit 392

A full-wave

microstrip wave

been developed

physics in electr

neither conceptu

the background

structure is rigo

integrated micr

Chapter 2

modes of an asy

be formulated

transform plan

plane ($\phi = \sigma +$

order to valida

plane). The br

diagrams. An

method to vali

descent evalua

Chapter 3

CHAPTER 1

INTRODUCTION

A full-wave integral operator formulation for electromagnetic fields in an integrated microstrip waveguide configuration in a planarly layered background environment has been developed to analyze associated EM phenomena [1]-[6]. However, the nature of the physics in electromagnetic fields of the integrated microstrip waveguide configuration is neither conceptualized nor quantified adequately. A continuous spectrum contributed by the background layer environment and a discrete spectrum contributed by the guiding structure is rigorously revealed and more physical insight into the EM behaviours of the integrated microstrip waveguide configuration is obtained.

Chapter 2 describes the steepest-descent evaluation of the radiation field for TE modes of an asymmetric planar open waveguide. The cover, film and substrate field will be formulated in the spectral domain. The steepest-descent path in the complex axial transform plane (ζ-plane) is identified as a direct method and that in the complex ϕ-plane ($\phi = \sigma + j\eta$: complex polar coordinate) is also identified as an indirect method in order to validate the steepest-descent path in the complex axial transform plane (ζ-plane). The branch cut integration will be rigorously analyzed through complex-phasor diagrams. An alternative integration path will be also identified since it is an effective method to validate the steepest-descent and branch cut integrations. Then, the steepest-descent evaluation of cover and substrate fields and numerical results will be presented.

Chapter 3 describes the steepest-descent evaluation of the radiation field for TM mo-

des of an asy

formulated ir

steepest-desc

the TE case.

2. An alterna

validate the

evaluation of

will be accon

Chapter 3

an integrated

importantly,

singularities

meaning of th

Chapter

waveguide.

conceptualize

in proper (co

Chapter

waveguide.

fields, much

surrounding

extensive nu

des of an asymmetric planar open waveguide. The cover, film and substrate field will be formulated in the spectral domain then the spectral green's dyads are represented. The steepest-descent path in the complex axial transform plane (ζ -plane) is identified as for the TE case. The branch cut integration is analyzed in a fashion similar to that in Chapter 2. An alternative integration path will be also identified since it is an effective method to validate the steepest-descent and branch cut integrations. Then, the steepest-descent evaluation of cover and substrate fields will be presented. Numerical implementation will be accommodated in the future research.

Chapter 4 discusses the spectral electric field integral equation (EFIE) formulation for an integrated open waveguide structure in a planar-layered background environment. It, importantly, introduces the concept of logarithmic- and square-root type branch-point singularities contributed by the layered background environment [7]-[9]. The physical meaning of those singularities will be interpreted.

Chapter 5 discusses the formulation for current in an open integrated microstrip waveguide. Then, the physics of currents on the microstrip waveguide configuration is conceptualized and quantified numerically. Since the microstrip currents are represented in proper (continuous and discrete) spectra, then no leaky-modes need to be considered.

Chapter 6 discusses the electromagnetic fields in an open integrated microstrip waveguide. Based upon the identity of complex analysis for the microstrip currents and fields, much of the analysis was already carried out in Chapter 5. The physics of fields surrounding the open microstrip configuration are subsequently conceptualized and extensive numerical results are presented.

Chapter

fields of ar

cover field

zone. The

is not incl

accommoda

Finally,

the numeric

Chapter 7 discusses the asymptotic approximation to the far zone electromagnetic fields of an open integrated microstrip waveguide. It is observed that the asymptotic cover field behaves algebraically like $r^{-(\alpha+3/2)}\,(\alpha \neq 0)$ when approaching to the far zone. The asymptotic form of the film field can be also obtained in a similar fashion but is not included in this chapter. The rigorous numerical implementation will be accommodated in the future research.

Finally, Chapter 8 comments on a general review of the dissertation and emphasizes the numerical implementation of Chapters 3 and 7 in future research.

SPEC
FC

21 IN

The st

to determ

to the intr

planar wa

in the com

waveguide

planar lay

branch poi

The steepe

layer maint

structure w

non-remov

For the

replaces the

natively the

remaining s

incomplete

remaining co

CHAPTER 2

SPECTRAL ANALYSIS AND ASYMPTOTIC RADIATION FIELD FOR TE MODES OF THE ASYMMETRIC PLANAR OPEN WAVEGUIDE

2.1 INTRODUCTION AND GEOMETRICAL CONFIGURATION

The steepest-descent method in the complex ϕ-plane has been extensively developed to determine the asymptotic radiation field of planar waveguide structures [10]-[13]. Due to the intrinsic nature of complexity in the complex ϕ-plane, the radiation fields of open planar waveguides are identified and classified here through the steepest-descent method in the complex axial transform plane [14], [15]. And, the spectral fields of planar open waveguide structures possess multiple branch points associated with each of the three planar layers. The branch point associated with the film layer is removable and the branch points associated with the cover layer and the substrate layers are non-removable. The steepest-descent evaluation of radiation fields in both the cover and the substrate layer maintained by TE electric sources in proximity to the simplest canonical waveguide structure will be performed when spectral representations of those fields possess multiple non-removable branch points in the complex axial transform plane.

For the cover field, the steepest-descent path in the complex axial transform plane replaces the cover layer branch cut while the substrate layer branch cut is retained. Alternatively the cover and the incomplete substrate layer branch cut are replaced while the remaining substrate layer branch cut is retained. However, in the substrate layer, the incomplete cover and the complete substrate layer branch cut are replaced while the remaining cover layer branch cut is retained.

The planar w

planar-layered b

and homogeneou

layers. A coordi

axis normal to th

extent parallel to

The planar waveguide structure consists of a dielectric guiding region immersed in a planar-layered background environment. Each planar layer is non-magnetic, isotropic, and homogeneous with complex permittivity ε_l, $l = 1, 2, 3$ for cover, film, and substrate layers. A coordinate system is chosen with the z axis as the waveguiding axis and the x axis normal to the planar interfaces as depicted in Fig. 2.1.1. The structure is of infinite extent parallel to the $y - z$ plane.

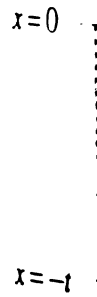

Figure

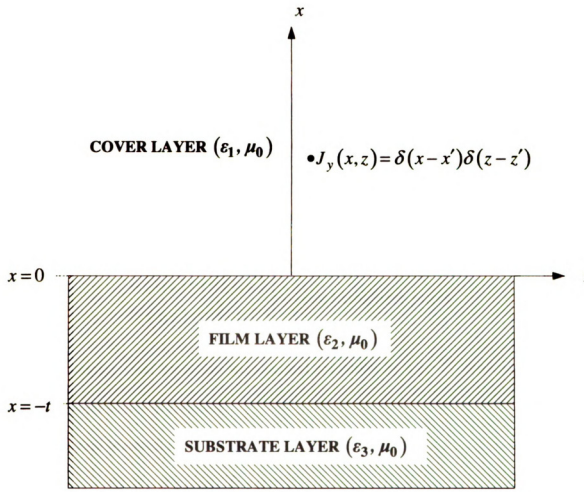

Figure 2.1.1 Geometrical configuration of an asymmetric planar dielectric slab waveguide with TE line-source excitation. Cover, film, and substrate layers are considered in the low-loss limit.

2.2 SP

The a

formulat

the wave

quantities

Since

with the p

ζ is the

unit line c

The sp

Subsequen

Helmholtz

2.2 SPECTRAL FIELD FORMULATION

The analysis of layered waveguide configurations proceed typically from a spectral formulation for currents/fields in the complex axial transform plane. Uniformity along the waveguiding axis z prompts a complex axial Fourier transformation of all field quantities with respect to the z variable.

Since the spectral fields are TE with respect to the waveguiding axis in agreement with the prescribed y-invariance, the guided wave fields are

$$\begin{aligned}
&\tilde{\boldsymbol{e}}(\boldsymbol{x},\zeta)=\hat{y}\tilde{e}_y(x,\zeta)\\
&\tilde{\boldsymbol{h}}(\boldsymbol{x},\zeta)=\hat{x}h_x(x,\zeta)+\hat{z}h_z(x,\zeta)\\
&\textit{where}\\
&\left.\begin{aligned}
&\boldsymbol{E}(\boldsymbol{x},z)\leftrightarrow\tilde{\boldsymbol{e}}(\boldsymbol{x},\zeta)\\
&\boldsymbol{H}(\boldsymbol{x},z)\leftrightarrow\tilde{\boldsymbol{h}}(\boldsymbol{x},\zeta)
\end{aligned}\right\}\cdots \textit{are transform pairs}
\end{aligned}\tag{2.2.1}$$

ζ is the complex axial transform variable and excitation by a ($e^{j\omega t}$ time dependence) unit line current source is assumed.

The spectral Maxwell equations for the *l'th* layer become

$$\begin{aligned}
&\zeta\tilde{e}_y(x,\zeta)=\omega\mu_0\tilde{h}_x(x,\zeta)\\
&\frac{\partial\tilde{e}_y(x,\zeta)}{\partial x}=-j\omega\mu_0\tilde{h}_z(x,\zeta)\\
&j\zeta\tilde{h}_x(x,\zeta)-\frac{\partial\tilde{h}_z(x,\zeta)}{\partial x}=\tilde{j}_y(x,\zeta)+j\omega\varepsilon_l\tilde{e}_y(x,\zeta)\\
&\textit{where}\\
&\tilde{j}_y(x,\zeta)=\delta(x-x')e^{-j\zeta z'}
\end{aligned}\tag{2.2.2}$$

Subsequent manipulation uncouples the spectral Maxwell equations to yield the spectral Helmholtz equation.

The in

subsequent

2.2.1 CO

Decomp

Eqn. (2.2.4)

(see Append

where $R(\zeta)$

The space-dom

$$\frac{\partial^2 \tilde{e}_y(x,\zeta)}{\partial x^2} - p_l^2(\zeta)\tilde{e}_y(x,\zeta) = j\omega\mu_0 \tilde{j}_y(x,\zeta)$$

where

$$p_l(\zeta) = \sqrt{\zeta^2 - k_l^2} \cdots l = 1, 2, 3 \tag{2.2.3}$$

$$k_l = \omega\sqrt{\mu_0\varepsilon_l} = n_l k_0 \cdots n_l = \sqrt{\varepsilon_l/\varepsilon_0}$$

The integral representation for the complete electromagnetic field is recovered by subsequent inverse transformation of the spectral fields.

2.2.1 COVER FIELD FORMULATION

Decomposition into principal and reflected spectral fields in the cover layer leads to

$$\tilde{e}_{1y}(x,\zeta) = \tilde{e}_{1y}^{p}(x,\zeta) + \tilde{e}_{1y}^{r}(x,\zeta) \tag{2.2.4}$$

Eqn. (2.2.4) superposes the primary and reflected solution in agreement with Eqn. (2.2.3) (see Appendix A)

$$\tilde{e}_{1y}^{p}(x,\zeta) = -j\omega\mu_0 \frac{e^{-p_1(\zeta)|x-x'|}}{2p_1(\zeta)} e^{-j\zeta z'}$$

$$\tilde{e}_{1y}^{r}(x,\zeta) = -j\omega\mu_0 R(\zeta) \frac{e^{-p_1(\zeta)(x+x')}}{2p_1(\zeta)} e^{-j\zeta z'} \tag{2.2.5}$$

where $R(\zeta)$ denotes the reflection coefficient given by

$$R(\zeta) = \frac{(p_1 - p_3)p_2 + (p_1 p_3 - p_2^2)\tanh(p_2 t)}{(p_1 + p_3)p_2 + (p_1 p_3 + p_2^2)\tanh(p_2 t)} \tag{2.2.6}$$

The space-domain field representation is recovered from its spectral counterpart such as

$$E_{1y}(x,z) \leftrightarrow \tilde{e}_{1y}(x,\zeta) \cdots \textit{Transform Pair}$$

E_{1y}

2.2.2 FII

The spe

fields (see

$\tilde{e}_{2y}(x,$

where $C($

Then, the sp

using the inv

$E_{2y}(x,z$

2.2.3 SUBS

The spectr

$$E_{1y}(x,z)=-j\omega\mu_0\int_{-\infty}^{\infty}\frac{e^{-p_1(\zeta)|x-x'|}+R(\zeta)e^{-p_1(\zeta)(x+x')}}{4\pi p_1(\zeta)}e^{-j\zeta(z-z')}d\zeta \quad (2.2.7)$$

2.2.2 FILM FIELD FORMULATION

The spectral field in the film layer is decomposed into the transmitted and reflected fields (see Appendix A).

$$\tilde{e}_{2y}(x,\zeta)=-j\omega\mu_0 C(\zeta)\left[e^{p_2(\zeta)x}+\bar{R}(\zeta)e^{-p_2(\zeta)(x+2t)}\right]\frac{e^{-p_1(\zeta)x'}}{2p_1(\zeta)}e^{-j\zeta z'} \quad (2.2.8)$$

where $C(\zeta)$ is the coupling and $\bar{R}(\zeta)$ is the interfacial reflection coefficient given by

$$C(\zeta)=\frac{2p_1(p_2+p_3)}{\left(1+e^{-2p_2t}\right)Z(\zeta)}$$

$$\bar{R}(\zeta)=\frac{p_2-p_3}{p_2+p_3} \quad (2.2.9)$$

where

$$Z(\zeta)=(p_1+p_3)p_2+\left(p_1p_3+p_2^2\right)\tanh(p_2t)$$

Then, the space-domain field representation is recovered from its spectral counterpart using the inverse Fourier transform.

$$E_{2y}(x,z)=-j\omega\mu_0\int_{-\infty}^{\infty}C(\zeta)\left[e^{p_2x}+\bar{R}(\zeta)e^{-p_2(x+2t)}\right]\frac{e^{-p_1x'}}{4\pi p_1}e^{-j\zeta(z-z')}d\zeta \quad (2.2.10)$$

2.2.3 SUBSTRATE FIELD FORMULATION

The spectral field in the substrate layer is the transmitted field (see Appendix A).

where $T($

Then, the s

$$E$$

2.3 IDE

The me

of the gene

where C is

If $\delta(\xi$

Eqn. (2.3.2

$$\tilde{e}_{3y}(x,\zeta)=-j\omega\mu_0 T(\zeta)e^{p_3(\zeta)(x+t)}\frac{e^{-p_1(\zeta)x'}}{2p_1(\zeta)}e^{-j\zeta z'} \tag{2.2.11}$$

where $T(\zeta)$ is the transmission coefficient defined by

$$T(\zeta)=\frac{2p_1p_2}{\cosh(p_2t)Z(\zeta)}$$

where (2.2.12)

$$Z(\zeta)=(p_1+p_3)p_2+\left(p_1p_3+p_2^2\right)\tanh(p_2t)$$

Then, the space-domain field representation is recovered as

$$E_{3y}(x,z)=-j\omega\mu_0\int_{-\infty}^{\infty}T(\zeta)e^{p_3(\zeta)(x+t)}\frac{e^{-p_1(\zeta)x'}}{4\pi p_1(\zeta)}e^{-j\zeta(z-z')}d\zeta \tag{2.2.13}$$

2.3 IDENTIFICATION OF THE STEEPEST-DESCENT PATH

The method of steepest-descents investigates the asymptotic evaluation of an integral of the generic type [16], [17]

$$I=\int_C f(\zeta)e^{r\delta(\zeta)}d\zeta \tag{2.3.1}$$

where C is an infinite contour in the complex ζ-plane.

If $\delta(\zeta)$ has a stationary point at $\zeta=\zeta_0$, then

$$\delta'(\zeta_0)=0 \tag{2.3.2}$$

Eqn. (2.3.2) implies

$$\delta(\zeta)-\delta(\zeta_0)\approx(\zeta-\zeta_0)^2\frac{\delta''(\zeta_0)}{2}+\cdots,\ \zeta\to\zeta_0 \tag{2.3.3}$$

Chew [17

since $\delta($

Eqn. (

Along the

has a cons

Furthermo

complex ζ

on the con

the imagi

$\lambda = 0$ on

function e

$\zeta = \zeta_0$ or

$e^{r\delta(\zeta)}$ des

path (SDP)

Chew [17] suggested a change of variable to λ such that

$$-\lambda^2 = \delta(\zeta) - \delta(\zeta_0) \tag{2.3.4}$$

since $\delta(\zeta) - \delta(\zeta_0)$ is quadratic around the stationary point ζ_0.

Eqn. (2.3.4) maps the complex ζ-plane to the complex λ-plane in Figure 2.3.1. Along the real axis of the λ-plane (the path P'), the function $e^{r\delta(\zeta)} = e^{-r\lambda^2 + r\delta(\zeta_0)}$ has a constant phase. According to this transformation, P also is a constant phase path. Furthermore, $e^{r\delta(\zeta)}$ is a maximum at $\lambda = 0$ on the complex λ-plane or $\zeta = \zeta_0$ on the complex ζ-plane and becomes exponentially small along the path P' away from $\lambda = 0$ on the complex λ-plane or $\zeta = \zeta_0$ on the complex ζ-plane. On the other hand, along the imaginary axis of the λ-plane (λ''), $e^{r\delta(\zeta)}$ becomes exponentially large from $\lambda = 0$ on the complex λ-plane or $\zeta = \zeta_0$ on the complex ζ-plane. Hence, the function $e^{r\delta(\zeta)}$ looks like a saddle at the point $\lambda = 0$ on the complex λ-plane or $\zeta = \zeta_0$ on the complex ζ-plane. The constant-phase path on which the function $e^{r\delta(\zeta)}$ descends steeply away from the saddle point is known as the ***steepest-descent path (SDP)***.

Figure 2

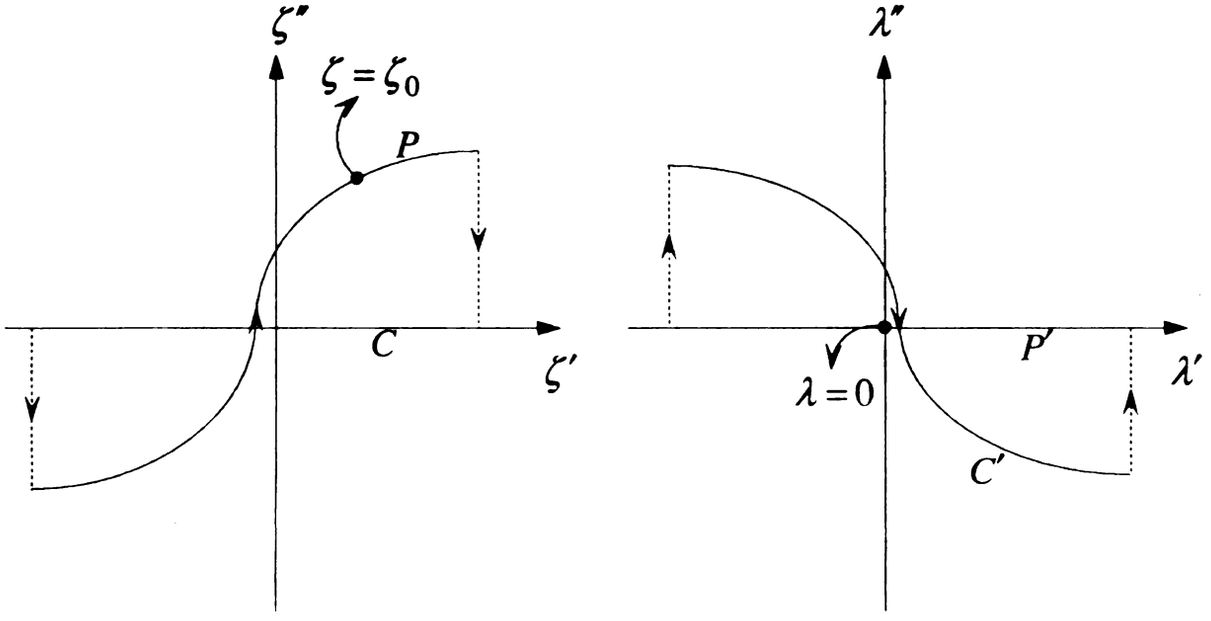

Figure 2.3.1 The mapping from the complex ζ-plane to the complex λ-plane.

2.3.1 ST
PL

Transfo

representat

As depicted

For substrate

2.3.1 STEEPEST-DESCENT PATH IN THE COMPLEX AXIAL TRANSFORM PLANE *(DIRECT METHOD)*

Transformation to spatial polar coordinates (r,θ) in both transverse and longitudinal representations is implemented as depicted in Fig. 2.3.2.

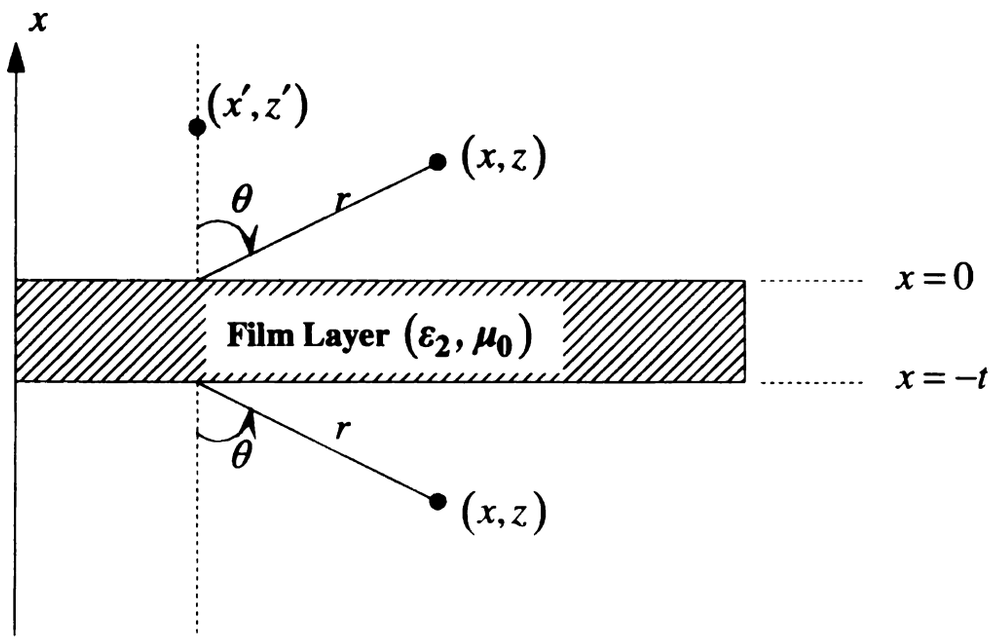

Figure 2.3.2 Polar coordinate transformations.

As depicted in Fig. 2.3.3, for the phase-corrected cover layer field,

$$\begin{aligned} |x-x'| &= r\cos\theta - x'\cos^2\theta \\ x+x' &= r\cos\theta + x'\cos^2\theta \\ z-z' &= r\sin\theta \end{aligned} \tag{2.3.5}$$

For substrate layer field,

$$\begin{aligned} x+t &= -r\cos\theta \\ z-z' &= r\sin\theta \end{aligned} \tag{2.3.6}$$

Substituting

$$E_{1y}(x,z)$$

$$= C_0 \int_{-\infty}^{\infty} \frac{e^{-}}{}$$

$$= C_0 \int_{-\infty}^{\infty} \frac{e^{-}}{}$$

$$= C_0 \int_{-\infty}^{\infty} \frac{1+}{}$$

where

$$R'(\zeta) = R($$

$$C_0 = -\frac{j\omega\mu}{4\pi}$$

and $R'(\zeta)$ is

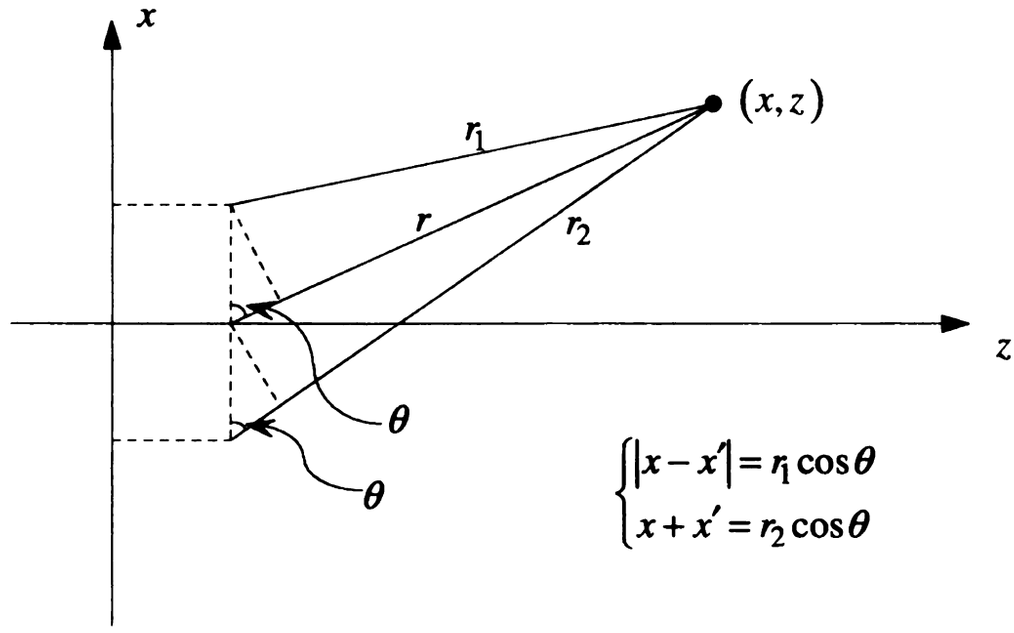

Figure 2.3.3 Phase correction diagram in the cover layer.

Substituting Eqn. (2.3.5) into Eqn. (2.2.7) yields

$$
\begin{aligned}
&E_{1y}(x,z) \\
&= C_0 \int_{-\infty}^{\infty} \frac{e^{-p_1(\zeta)|x-x'|} + R(\zeta) e^{-p_1(\zeta)(x+x')}}{p_1(\zeta)} e^{-j\zeta(z-z')} d\zeta \\
&= C_0 \int_{-\infty}^{\infty} \frac{e^{-p_1(\zeta)\left(r\cos\theta - x'\cos^2\theta\right)} + R(\zeta) e^{-p_1(\zeta)\left(r\cos\theta + x'\cos^2\theta\right)}}{p_1(\zeta)} e^{-j\zeta r\sin\theta} d\zeta \\
&= C_0 \int_{-\infty}^{\infty} \frac{1 + R'(\zeta)}{p_1(\zeta)} e^{p_1(\zeta)x'\cos^2\theta} e^{r\left[-j\zeta\sin\theta - p_1(\zeta)\cos\theta\right]} d\zeta
\end{aligned}
\tag{2.3.7}
$$

where

$$R'(\zeta) = R(\zeta) e^{-2p_1(\zeta)x'\cos^2\theta}$$

$$C_0 = -\frac{j\omega\mu_0}{4\pi}$$

and $R'(\zeta)$ is the corrected reflection coefficient.

Substitu

Eqn. (2

where l =

The station

plane. Usi

where the o

Substituting Eqn. (2.3.6) into Eqn. (2.2.13) yields

$$
\begin{aligned}
& E_{3y}(x,z) \\
&= -j\omega\mu_0 \int_{-\infty}^{\infty} T(\zeta) e^{p_3(\zeta)(x+t)} \frac{e^{-p_1(\zeta)x'}}{4\pi p_1(\zeta)} e^{-j\zeta(z-z')} d\zeta \\
&= -j\omega\mu_0 \int_{-\infty}^{\infty} T(\zeta) e^{-p_3(\zeta) r\cos\theta} \frac{e^{-p_1(\zeta)x'}}{4\pi p_1(\zeta)} e^{-j\zeta r\sin\theta} d\zeta \\
&= -j\omega\mu_0 \int_{-\infty}^{\infty} T(\zeta) \frac{e^{-p_1(\zeta)x'}}{4\pi p_1(\zeta)} e^{r\left[-j\zeta\sin\theta - p_3(\zeta)\cos\theta\right]} d\zeta
\end{aligned}
\tag{2.3.8}
$$

Eqn. (2.3.7) and Eqn. (2.3.8) lead to identification of $\delta(\zeta)$ in Eqn. (2.3.1) such that

$$
\begin{aligned}
\delta(\zeta) &= -j\zeta\sin\theta - p_l(\zeta)\cos\theta \\
p_l(\zeta) &= \sqrt{\zeta^2 - k_l^2}
\end{aligned}
\tag{2.3.9}
$$

where $l = 1$ and 3 for cover and substrate layers respectively.

The stationary point ζ_0 in the complex ζ-plane was shown to be a *saddle point* in that plane. Using Eqn. (2.3.2) yields,

$$
\begin{aligned}
& \delta'(\zeta_0) = -j\sin\theta - \frac{\zeta_0}{\sqrt{\zeta_0^2 - k_l^2}}\cos\theta = 0 \\
& \therefore \zeta_0 = k_l \sin\theta
\end{aligned}
\tag{2.3.10}
$$

where the observation aspect angle is defined by

$$
\theta = \begin{cases} l=1: \begin{cases} \tan^{-1}\left(\dfrac{z-z'}{|x-x'|}\right) \\ \tan^{-1}\left(\dfrac{z-z'}{x+x'}\right) \end{cases} \\ l=3: \tan^{-1}\left(\dfrac{z-z'}{|x+t|}\right) \end{cases}
\tag{2.3.11}
$$

Th

After s

Using th

Conseque

Eqn. (2.3

2.3.2 TR
TH

The inv

approximat

ϕ-plane de

It is noted th

by transform

The steepest-descent path in the complex ζ -plane is identified as

$$\delta(\zeta)=\delta(\zeta_0) \tag{2.3.12}$$

After some manipulation,

$$\left(\frac{\zeta}{k_l}\right)\sin\theta - j\left[\frac{p_l(\zeta)}{k_l}\right]\cos\theta = 1 \tag{2.3.13}$$

Using the complex conjugate of Eqn. (2.3.13) leads to

$$\left(\frac{\zeta}{k_l}\right)^*\sin\theta + j\left[\frac{p_l(\zeta)}{k_l}\right]^*\cos\theta = 1 \tag{2.3.14}$$

Consequently, the steepest-descent path in the complex ζ -plane is obtained by adding Eqn. (2.3.13) and Eqn. (2.3.14) as

$$\left[\frac{\zeta}{k_l}+\left(\frac{\zeta}{k_l}\right)^*\right]\frac{\sin\theta}{2} - j\left[\frac{p_l(\zeta)}{k_l}-\left\{\frac{p_l(\zeta)}{k_l}\right\}^*\right]\frac{\cos\theta}{2} = 1 \tag{2.3.15}$$

2.3.2 TRANSFORMATION OF SDP FROM THE COMPLEX ϕ-PLANE TO THE COMPLEX ζ -PLANE *(INDIRECT METHOD)*

The inversion integral for the l'th (l=1 and 3 for cover and substrate) layer can be approximated asymptotically by the steepest-descent saddle-point method in the complex ϕ-plane defined by

$$\phi = \sigma + j\eta \tag{2.3.16}$$

It is noted that the integral representation must be placed in an appropriate standard form by transforming to polar coordinates in both the (x,z) and (p_l,ζ) planes.

Due to E

identified

To determi

Therefore,

Eqn. (2.3.19

ϕ- plane su

Replacing th

$$E_{l_y}(r$$

$$= -\frac{j\omega}{4}$$

$$= -\frac{\omega\mu}{4\pi}$$

where

$$\Sigma_l(k_l s$$

Due to Eqn. (2.3.5) and Eqn. (2.3.6), the appropriate transformation in (p_l, ζ) is identified as

$$\begin{aligned} p_l &= jk_l \cos\phi \\ \zeta &= k_l \sin\phi \end{aligned} \tag{2.3.17}$$

To determine the integration limits in the complex $\phi = \sigma + j\eta$ plane,

$$\zeta = k_l \sin(\sigma + j\eta) = k_l \sin\sigma \cosh\eta + jk_l \cos\sigma \sinh\eta \tag{2.3.18}$$

Therefore,

$$\begin{aligned} \mathrm{Re}\{\zeta\} &= k_l \sin\sigma \cosh\eta \\ \mathrm{Im}\{\zeta\} &= k_l \cos\sigma \sinh\eta \end{aligned} \tag{2.3.19}$$

Eqn. (2.3.19) maps the integration limits in the complex ζ - plane to those in the complex ϕ - plane such that

$$\begin{aligned} &\mathrm{Im}\{\zeta\} = 0 \rightarrow \sigma = \pm\pi/2 \\ &\mathrm{Re}\{\zeta\} = -\infty \rightarrow \sigma = -\pi/2, \eta = -\infty \\ &\mathrm{Re}\{\zeta\} = \infty \rightarrow \sigma = \pi/2, \eta = \infty \end{aligned} \tag{2.3.20}$$

Replacing the integration limits due to the minus sign of $d\zeta = k_l \cos\phi d\phi$,

$$\begin{aligned} &E_{ly}(r,\theta) \\ &= -\frac{j\omega\mu_0}{4\pi} \int_{-\pi/2-j\infty}^{\pi/2+j\infty} \frac{\Sigma_l(k_l \sin\phi)}{jk_1 \cos\phi} e^{-r(jk_l \sin\phi \sin\theta + jk_l \cos\phi \cos\theta)} k_l \cos\phi d\phi \\ &= -\frac{\omega\mu_0}{4\pi} \left(\frac{k_l}{k_1}\right) \int_{-\pi/2-j\infty}^{\pi/2+j\infty} \Sigma_l(k_l \sin\phi) e^{-jk_l r \cos(\phi-\theta)} d\phi \end{aligned} \tag{2.3.21}$$

where

$$\Sigma_l(k_l \sin\phi) = \begin{cases} l=1: \left[1 + R'(k_1 \sin\phi)\right] e^{p_1(\zeta)x' \cos^2\theta} \\ l=3: T(k_3 \sin\phi) e^{-p_1(\zeta)x'} \end{cases}$$

The crit

$\psi(\phi) = -j$

be approxim

by $\psi'(\phi_0)$

Rewriting ψ

ψ

The steepest-

$\arg\left[\psi''(\theta)\right]$

from its value

saddle point θ

The choice of

(2.3.23) becom

The criterion for the steepest-descent method is determined by the defined factor $\psi(\phi)=-j\cos(\phi-\theta)$ for $k_l r \gg 1$. The integral representation of Eqn. (2.3.21) can be approximated based upon properties of $\psi(\phi)$ at the saddle point $\phi_0=\theta$ stipulated by $\psi'(\phi_0)=0$. Using a Taylor's expansion of $\psi(\phi)$ about $\phi=\theta$,

$$\begin{aligned}\psi(\phi)&=\psi(\theta)+\overbrace{\psi'(\theta)}^{=0}(\phi-\theta)+\frac{1}{2}\psi''(\theta)(\phi-\theta)^2+\cdots\\&\approx\psi(\theta)+\frac{1}{2}\psi''(\theta)(\phi-\theta)^2\end{aligned} \tag{2.3.22}$$

Rewriting $\psi''(\theta)=\left|\psi''(\theta)\right|e^{j\arg[\psi''(\theta)]}$ and $\phi-\theta=\mathrm{Re}^{j\delta}$,

$$\begin{aligned}\psi(\phi)&\approx\psi(\theta)+\frac{1}{2}\left|\psi''(\theta)\right|R^2e^{j\{\arg[\psi''(\theta)]+2\delta\}}\\&=\mathrm{Re}\{\psi(\theta)\}+\frac{1}{2}\left|\psi''(\theta)\right|R^2\cos\{\arg[\psi''(\theta)]+2\delta\}\\&+j\left[\mathrm{Im}\{\psi(\theta)\}+\frac{1}{2}\left|\psi''(\theta)\right|R^2\sin\{\arg[\psi''(\theta)]+2\delta\}\right]\end{aligned} \tag{2.3.23}$$

The steepest-descent path is specified by $\mathrm{Im}\{\psi(\phi)\}=\mathrm{Im}\{\psi(\theta)\}$ and the condition $\arg[\psi''(\theta)]+2\delta=\pm\pi$ is required for $\mathrm{Re}\{\psi(\phi)\}$ to decrease at a maximal rate from its value $\mathrm{Re}\{\psi(\theta)\}$. The inclination angle of the steepest-descent path at the saddle point θ is determined by

$$\delta=-\frac{\arg[\psi''(\theta)]}{2}\pm\frac{\pi}{2}=\begin{cases}\pi/4\\-3\pi/4\end{cases} \tag{2.3.24}$$

The choice of δ depends on the orientation of the inclination angle. Furthermore, Eqn. (2.3.23) becomes

Hence, t

The latte

which de

$\delta = \pi/4$

From

Assuming

original pa

$\phi = \theta$, wh

near the sad

that $\Sigma_l(k$

integral in E

$$\begin{aligned}\psi(\phi) &\approx \mathrm{Re}\{\psi(\theta)\} + j\left[\mathrm{Im}\{\psi(\theta)\}\right] - \frac{1}{2}\left|\psi''(\theta)\right|R^2 \\ &= -j - \frac{R^2}{2}\end{aligned} \tag{2.3.25}$$

Hence, the steepest-descent path in the complex $\phi = \sigma + j\eta$ plane is obtained by

$$\cos(\sigma + j\eta - \theta) = 1 \tag{2.3.26}$$

The latter expression results in

$$\cos(\sigma - \theta)\cosh(\eta) = 1 \tag{2.3.27}$$

which determines the *SDP* as depicted in Fig. (2.3.4). Since δ is in the positive sense, $\delta = \pi/4$ is chosen.

From Eqn. (2.3.21), it is observed that

$$\begin{aligned}&\int_{-\pi/2-j\infty}^{\pi/2+j\infty} \Sigma_l(k_l \sin\phi) e^{-jk_l r\cos(\phi-\theta)} d\phi \\ &\approx \int_{SDP} \Sigma_l(k_l \sin\theta) e^{k_l r\left(-j-R^2/2\right)} d\phi\end{aligned} \tag{2.3.28}$$

Assuming no poles of $\Sigma_l(k_l \sin\phi)$ are near the integration path after deformation of the original path C to *SDP* as depicted in Fig. (2.3.4), $\Sigma_l(k_l \sin\phi)$ is slowly varying near $\phi = \theta$, where the primary contribution of the steepest-descent path to the integral arises near the saddle point $\phi_0 = \theta$ in the complex ϕ-plane. Therefore, it can be approximated that $\Sigma_l(k_l \sin\phi) \approx \Sigma_l(k_l \sin\theta)$. Therefore, $\Sigma_l(k_l \sin\theta)$ can be taken out of the integral in Eqn. (2.3.28) such that

$$E_{ly}(r,\theta) \approx -\frac{\omega\mu_0}{4\pi}\left(\frac{k_l}{k_1}\right)\Sigma_l(k_l \sin\theta)\int_{SDP} e^{k_l r\left(-j-R^2/2\right)} d\phi$$

Figure

Using a

Using th

The asyn

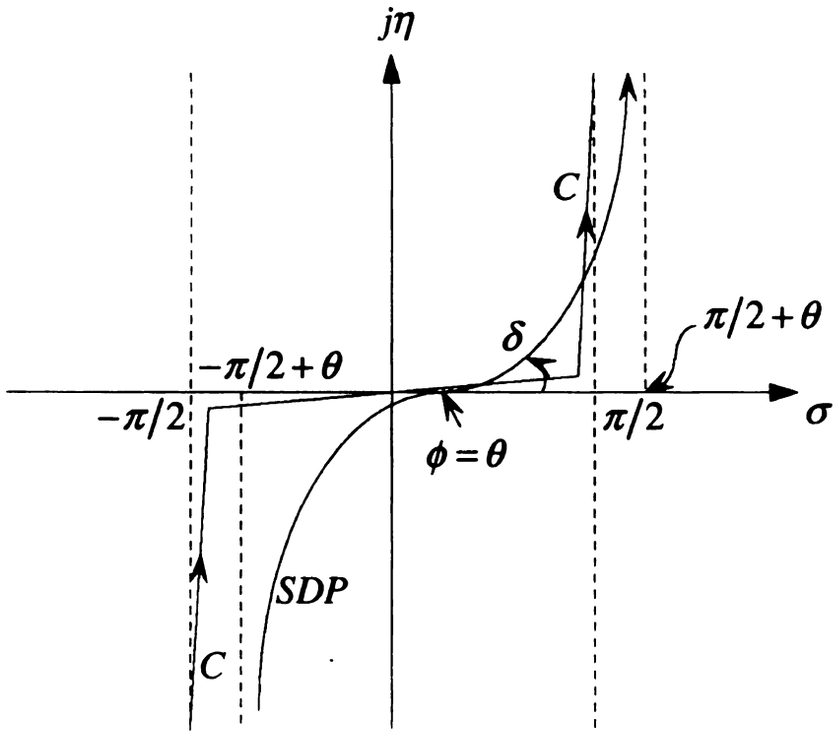

Figure 2.3.4 Mapping to the steepest-descent path in the complex $\phi = \sigma + j\eta$ plane: $|\theta| < \pi/2$.

Using $d\phi = e^{j\pi/4} dR$,

$$\begin{aligned} &\Sigma_l (k_l \sin\theta) \int_{\infty}^{0} e^{k_l r\left(-j-R^2/2\right)} e^{j(\pi/4+\pi)} dR \\ &+\Sigma_l (k_l \sin\theta) \int_{0}^{\infty} e^{k_l r\left(-j-R^2/2\right)} e^{j\pi/4} dR \\ &= \Sigma_l (k_l \sin\theta) e^{-j(k_l r-\pi/4)} \int_{-\infty}^{\infty} e^{-k_l r R^2/2} dR \end{aligned} \tag{2.3.29}$$

Using the relation [18],

$$\int_{-\infty}^{\infty} e^{-k_l r R^2/2} dR = \sqrt{\frac{2\pi}{k_l r}} \tag{2.3.30}$$

The asymptotic approximation for far zone field in the *l'th* layer becomes

Fro

Then, af

Eqn. (2.

Substitut

Hence

and Eqn.

layer field

$$E_{ly}(r,\theta) \approx -\frac{\omega\mu_0}{4}\left(\frac{k_l}{k_1}\right)\sqrt{\frac{2}{\pi}}\Sigma_l(k_l\sin\theta)\frac{e^{-j(k_l r-\pi/4)}}{\sqrt{k_l r}}$$

where (2.3.31)

$$\Sigma_l(-k_l\sin\theta)=\begin{cases} l=1:\left[1+R'(k_1\sin\theta)\right]e^{p_1(\zeta)x'\cos^2\theta} \\ l=3:T(k_3\sin\theta)e^{-p_1(\zeta)x'} \end{cases}$$

From Eqn. (2.3.17), it is observed that

$$\begin{aligned} \sin\sigma\cosh\eta + j\cos\sigma\sinh\eta &= \frac{\zeta}{k_l} \\ \sin\sigma\sinh\eta + j\cos\sigma\cosh\eta &= \frac{p_l(\zeta)}{k_l} \end{aligned} \tag{2.3.32}$$

Then, after manipulation using the complex conjugate of Eqn. (2.3.32)

$$\begin{aligned} \sin\sigma\cosh\eta &= \frac{1}{2}\left[\frac{\zeta}{k_l}+\left(\frac{\zeta}{k_l}\right)^*\right] \\ \cos\sigma\cosh\eta &= -\frac{j}{2}\left[\frac{p_l(\zeta)}{k_l}-\left\{\frac{p_l(\zeta)}{k_l}\right\}^*\right] \end{aligned} \tag{2.3.33}$$

Eqn. (2.3.27) leads to

$$\cos\theta\left[\cos\sigma\cosh\eta\right]+\sin\theta\left[\sin\sigma\cosh\eta\right]=1 \tag{2.3.34}$$

Substituting Eqn. (2.3.33) into Eqn. (2.3.34) yields

$$\left[\frac{\zeta}{k_l}+\left(\frac{\zeta}{k_l}\right)^*\right]\frac{\sin\theta}{2}-j\left[\frac{p_l(\zeta)}{k_l}-\left\{\frac{p_l(\zeta)}{k_l}\right\}^*\right]\frac{\cos\theta}{2}=1 \tag{2.3.35}$$

Hence, Eqn. (2.3.35) replicates the steepest-descent path in the complex ζ - plane and Eqn. (2.3.15) is confirmed. The steepest-descent paths for the cover and substrate layer field on various observation aspect angles are depicted in Fig. 2.6.1 and Fig. 2.7.1.

2.4 T

It is

is neces

comple

from Eq

Howeve

branch p

integral

contribu

It is r

Therefore

2.4 THE BRANCH CUT

It is observed that

$$\left.\begin{array}{l}\mathrm{Re}\{p_l(\zeta)\}>0\cdots \textit{for all } \zeta \\ \mathrm{Im}\{p_l(\zeta)\}>0\cdots \textit{for real } \zeta\end{array}\right\}\cdots p_l(\zeta)=\sqrt{\zeta^2-k_l^2}\,,\ l=1,2,3 \quad (2.4.1)$$

is necessary to satisfy the radiation condition. And $p_l(\zeta)$ is multi-valued on one of the complex Riemann sheets. It takes the opposite sign to the value on the other sheet, hence, from Eqn. (2.4.1), these sheets are separated by the branch cut defined by

$$\mathrm{Re}\{p_l(\zeta)\}=0 \quad (2.4.2)$$

However, Since the integrands of integral representations are even in $p_2(\lambda)$, then the branch points contributed by the film layer are removable [17]. But, the integrands of integral representations are not even in $p_1(\lambda)$ and $p_3(\zeta)$ therefore the branch points contributed by the cover and the substrate layer are non-removable.

It is recognized that

$$\begin{aligned}&p_l^2(\zeta)=\zeta^2-k_l^2=\left(\zeta_r^2-\zeta_i^2\right)-\left(k_{lr}^2-k_{li}^2\right)+j2(\zeta_r\zeta_i-k_{lr}k_{li})\\ &\textit{where}\\ &\zeta=\zeta_r+j\zeta_i\\ &k_l=k_{lr}+jk_{li}\\ &l=1,3\end{aligned} \quad (2.4.3)$$

Therefore, the conditions for $\mathrm{Re}\{p_l(\zeta)\}=0$ are

$$\begin{aligned}&\mathrm{Re}\{p_l^2(\zeta)\}<0\\ &\mathrm{Im}\{p_l^2(\zeta)\}=0\end{aligned} \quad (2.4.4)$$

Eqn.

Eqn.

Figure 2.4.

Eqn. (2.4.4) leads to

$$\begin{aligned} \zeta_r \zeta_i &= k_{lr} k_{li} \\ \zeta_r^2 - \zeta_i^2 &< k_{lr}^2 - k_{li}^2 \end{aligned} \tag{2.4.5}$$

Eqn. (2.4.5) constructs *hyperbolic branch cuts* emanating from $\zeta_i = k_{li}$ at $\zeta_r = k_{lr}$ with $\zeta_i \to \infty$ as $\zeta_r \to 0$ as depicted in Fig. 2.4.1.

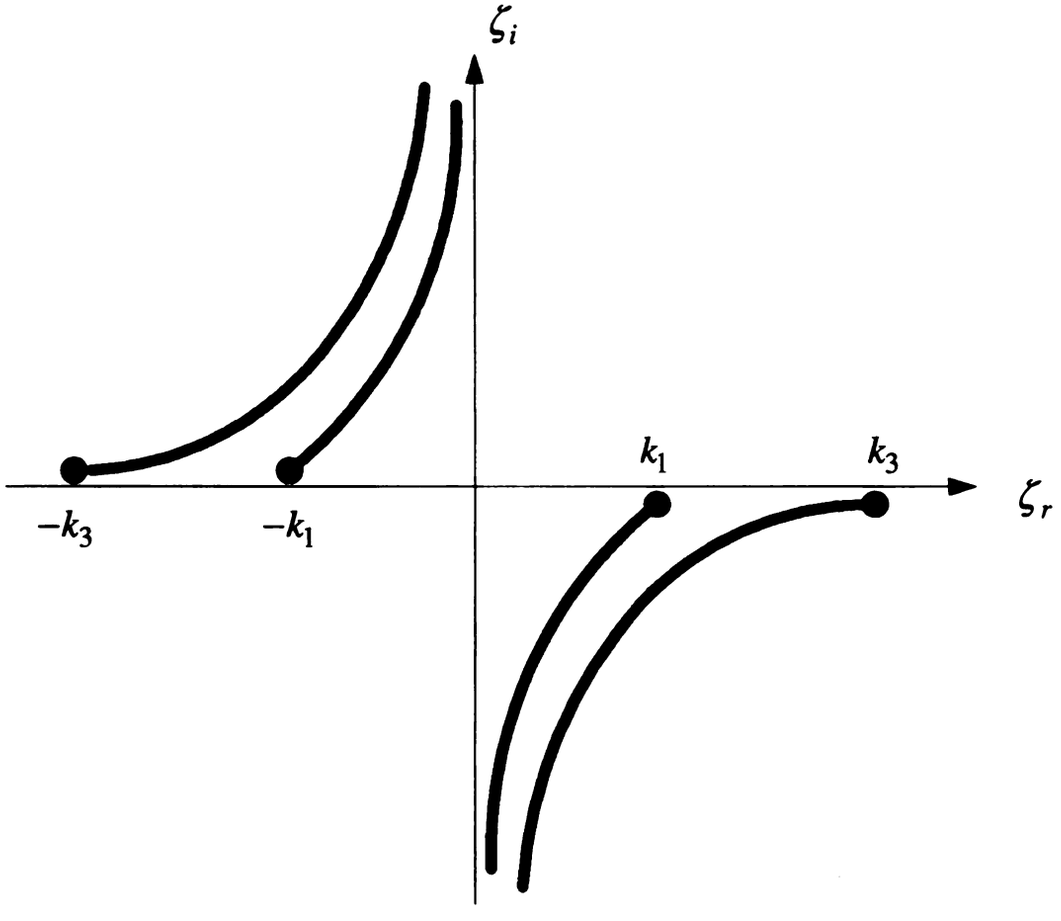

Figure 2.4.1 Hyperbolic branch cut construction emanating from the branch points $\pm k_1$ and $\pm k_3$.

As

points.

cuts for

of the

clarified

As $|\zeta_r|$ decreases from $\zeta_r = \pm k_l \ (l = 1, 3)$ moving inward from the pair of branch points, $|\zeta_i|$ must increase, hence the branch cut contour is subsequently generated. The cuts for the limiting case of low-loss are depicted in Fig. 2.4.2, i.e., $\pm k_{li} \to 0^{\mp}$. Portions of the various cuts coalesce upon one another but they are a little exaggerated to be clarified in Fig. 2.4.2

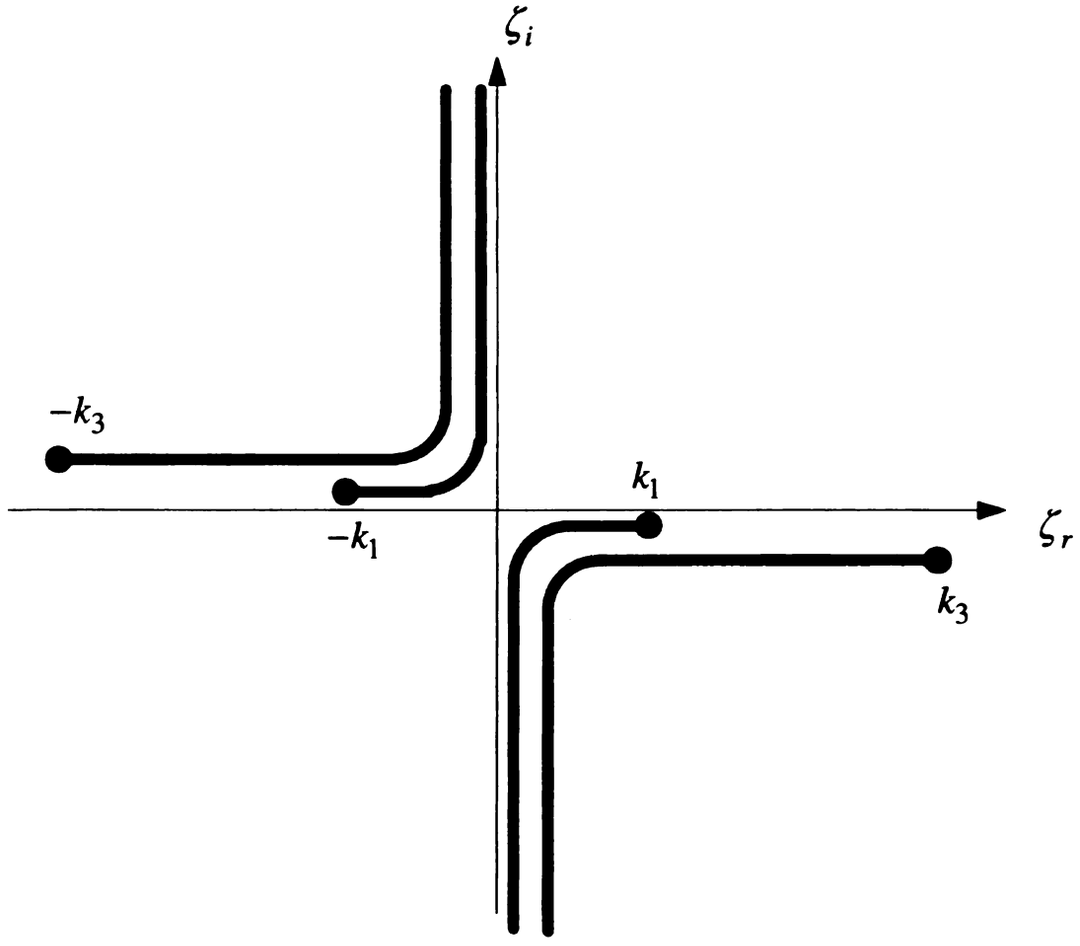

Figure 2.4.2 Branch cut construction in the low-loss limit.

It

depict

invers

the lo

approp

the cor

It is required to analyze a complex-phasor diagram in the complex ζ -plane as depicted in Fig. 2.4.3 to implement the integration along the branch cut. The real axis inversion contour can be deformed to the infinite semicircle in the upper half plane or in the lower half plane with appropriate detour about the branch cuts as shown. And also appropriate choice of branch cuts consequently leads to a 4-sheeted Riemann surface in the complex ζ -plane.

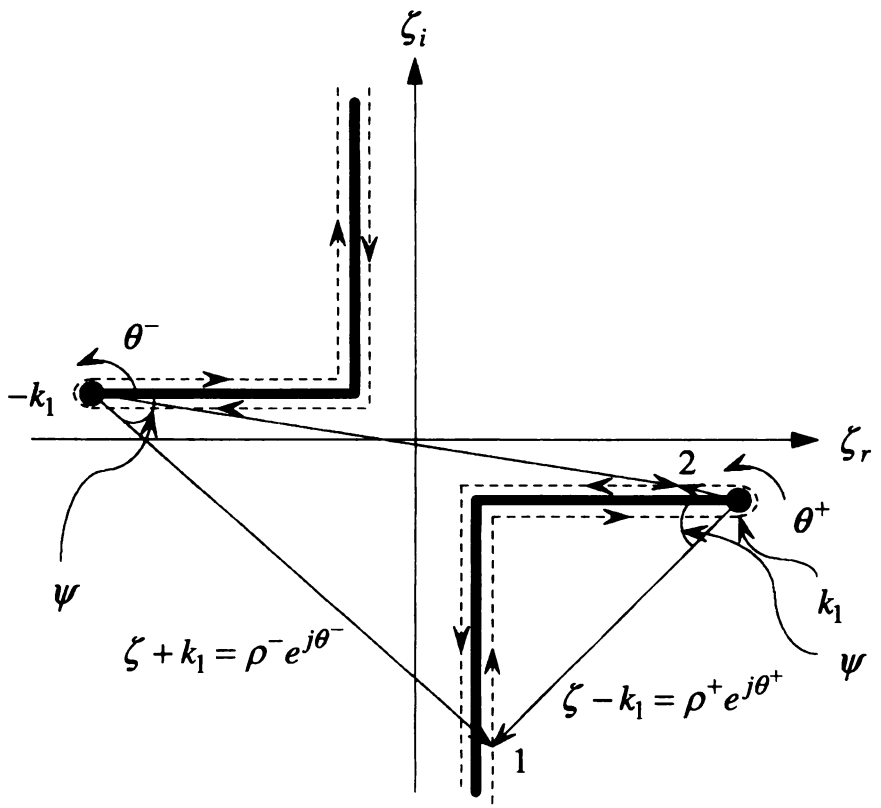

Figure 2.4.3 Complex-phasor diagram in the complex ζ -plane.

For a

Simila

And a

Simila

It is no

during

2.5 A

Def

half pla

where

in the l'

Disc

located

For a point 1 in Fig. 2.4.3,

$$p_1(\zeta)=\sqrt{\rho^+\rho^-}e^{j(-\pi+\psi-\psi)/2}=-j\left|p_1(\zeta)\right| \tag{2.4.6}$$

Similarly, for an opposite point on the left part of the negative imaginary branch cut,

$$p_1(\zeta)=\sqrt{\rho^+\rho^-}e^{j(\pi+\psi-\psi)/2}=j\left|p_1(\zeta)\right| \tag{2.4.7}$$

And also for a point 2 in Fig. 2.4.3,

$$p_1(\zeta)=\sqrt{\rho^+\rho^-}e^{j(\pi+0)/2}=j\left|p_1(\zeta)\right| \tag{2.4.8}$$

Similarly, for an opposite point on the lower part of the positive real branch cut,

$$p_1(\zeta)=\sqrt{\rho^+\rho^-}e^{j(-\pi+0)/2}=-j\left|p_1(\zeta)\right| \tag{2.4.9}$$

It is noted that the previous complex-phasor diagram analysis can be complied with that during the integration along the substrate layer branch cut and branch points $\pm k_3$.

2.5 ALTERNATIVE INTEGRATION PATH

Deforming $\mathrm{Re}\{\zeta\}$-axis inversion contour into upper $(z<z')$ or lower $(z>z')$ half plane, as depicted in Fig. 2.5.1 and applying Cauchy's integral theorem leads to

$$\oint_{C-C_{b1}-C_{b3}-C_p-C_\infty}\Psi_l(x,z:\zeta)d\zeta=0 \tag{2.5.1}$$

where $\Psi_l(x,z:\zeta)$ stands for the integrand of the inverse transform field representation in the *l'th* layer.

Discrete guided surface wave modes are associated with simple-pole singularities located at $\zeta=\pm\zeta_p$ in the complex ζ-plane. Poles $\pm\zeta_p$ are determined by

which

It is o

by the

bound

Fig. 2.

R_p (P

conseq

perform

$\mathrm{Re}\{\zeta$

Then, a

are dete

And, it

k_3 along

Since

excitation

$$(p_1 + p_3)p_2 + \left(p_1 p_3 + p_2^2\right)\tanh(p_2 t) = 0 \tag{2.5.2}$$

which is implicated in Eqn. (2.2.6), Eqn. (2.2.9), and Eqn. (2.2.12). For the far zone [19],

$$\int_{C_p} \Psi_l(x, z:\zeta)d\zeta \to 0 \tag{2.5.3}$$

It is observed that the bound mode component of the propagation spectrum is contributed by the full residue about pole-excluding contour C_p in Eqn. (2.5.3). However, for the bound mode pole singularity on the positive $\mathrm{Re}\{\zeta\}$-axis inversion contour depicted in Fig. 2.5.2, its spectrum is contributed by the half residue about pole-excluding contour R_p (Poles on the negative $\mathrm{Re}\{\zeta\}$-axis inversion contour are implicated). And it's also consequently critical to analyze the complex-phasor diagram as depicted in Fig. 2.4.3 to perform the real axis integration. Any points less than the branch point k_1 along the $\mathrm{Re}\{\zeta\}$-axis inversion contour as depicted in Fig. 2.4.3 are determined by Eqn. (2.4.8). Then, any points beyond the branch point k_1 along the $\mathrm{Re}\{\zeta\}$-axis inversion contour are determined by

$$p_1(\zeta) = \sqrt{\rho^+ \rho^-}\, e^{j(0+0)/2} = \left|p_1(\zeta)\right| \tag{2.5.4}$$

And, it can be similarly complied with any points less than or beyond the branch point k_3 along the $\mathrm{Re}\{\zeta\}$-axis inversion contour as required by Eqn. (2.4.8) and Eqn. (2.5.4).

Since the contributions from the infinite semicircles vanish for TE proper mode excitation (points on the top Riemann sheet),

$$\int_{C_\infty} \Psi_l(x, z:\zeta)d\zeta \to 0 \tag{2.5.5}$$

Finally

and Eq

The bra

the resu

were co

inversio

from the

indepen

Finally, Eqn. (2.5.1) reduces (for the radiation-zone field) in agreement with Eqn. (2.5.3) and Eqn. (2.5.5) to

$$\int_C \Psi_l(x,z:\zeta)d\zeta = \int_{C_{b1}} \Psi_l(x,z:\zeta)d\zeta + \int_{C_{b3}} \Psi_l(x,z:\zeta)d\zeta \qquad (2.5.6)$$

The branch cut contributions constitute the radiation field with a continuous spectrum and the result from direct $\mathrm{Re}\{\zeta\}$-axis inversion contour and the branch cut deformation were compared and found to be identical as depicted in Fig. 2.6.2. The $\mathrm{Re}\{\zeta\}$-axis inversion contour integration is performed in order to validate numerical results obtained from the steepest-descent method in the complex ζ -plane and has an advantage of being independent of the threshold aspect angle.

Figure 2.

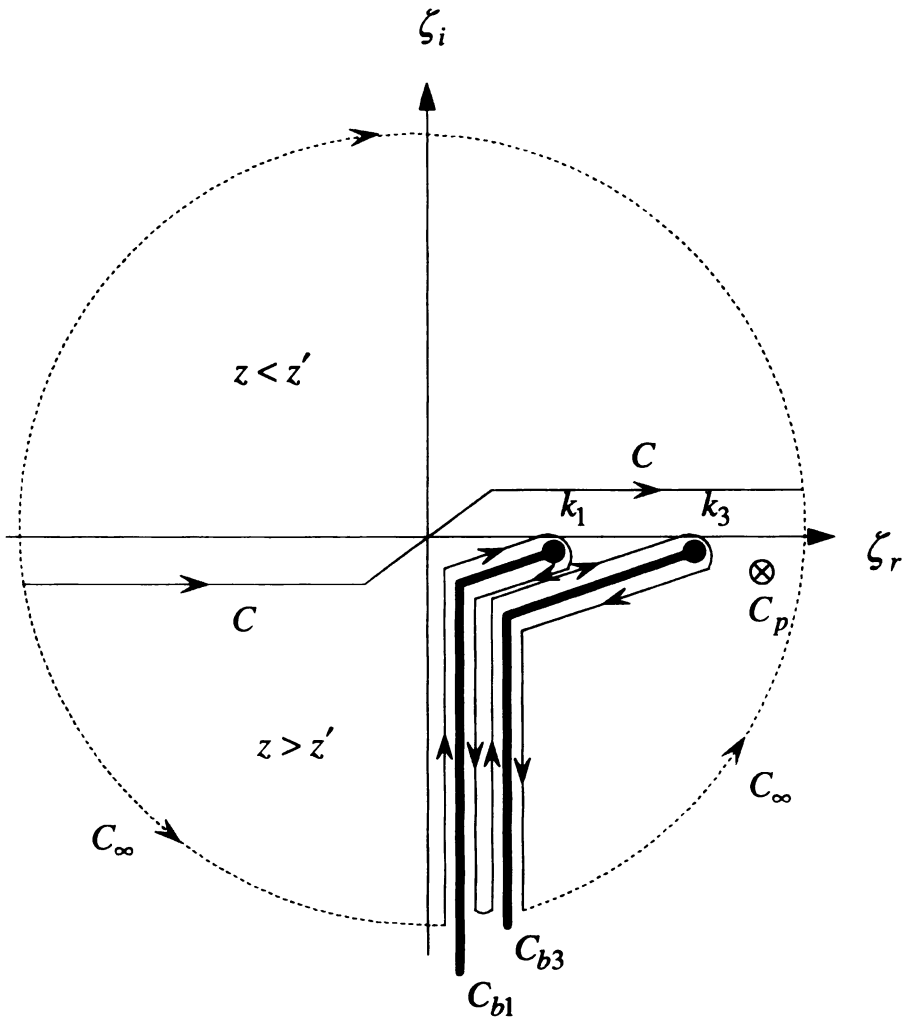

Figure 2.5.1 Singularities and alternative integration path in the complex ζ -plane on top Riemann sheet for the complete proper propagation spectrum. Cover and substrate layers are presumably considered to be in the low-loss limit.

Figur

2.6

M

simple

compr

conver

quantit

comple

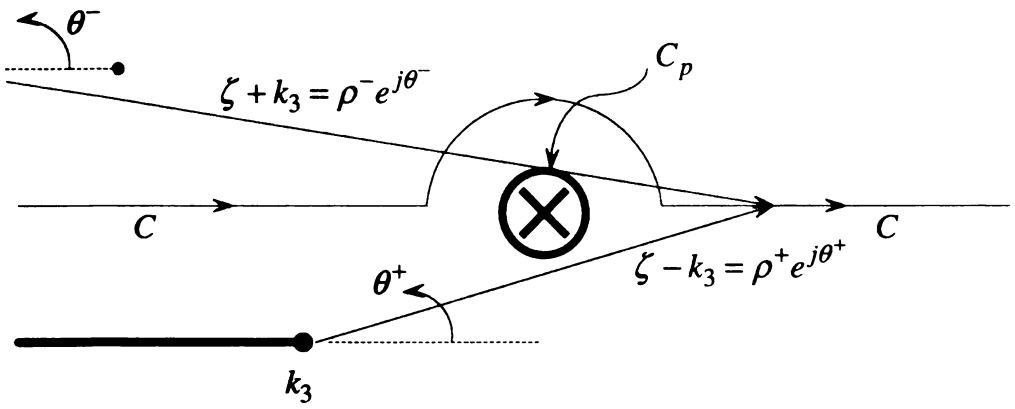

Figure 2.5.2 Complex-phasor diagram with a pole singularity and $\mathrm{Re}\{\zeta\}$- axis integration path in the complex ζ -plane.

2.6 STEEPEST-DESCENT EVALUATION OF COVER FIELD

Mapping to the complex ϕ-plane deforms the path of integration, in which case the simple representation in terms of a discrete (bound) and continuous spectrum is severely compromised due to the complicated branch cut mapping. It is consequently more convenient to use the steepest-descent path in the complex ζ -plane since all the field quantities are represented on the same spectral domain. The steepest-descent path on the complex ζ -plane is explicitly derived from Eqn. (2.3.15) such that (see Appendix B)

$$\zeta = \zeta' + j\zeta'' = (\zeta', \zeta'')$$

where (2.6.1)

$$\zeta'' = \pm \frac{|\zeta' - k_l \sin\theta||k_l - \zeta' \sin\theta|}{\cos\theta\sqrt{(\zeta'\cos\theta)^2 + (k_l - \zeta'\sin\theta)^2}}$$

Two

the sad

determi

UHP a

plane.

comple

film, a

respect

As

cut C_b

even n

intercep

it can b

Then,

In agree

Two ζ' - intercepts are found in Eqn. (2.6.1) and one of them, $\zeta' = k_l \sin\theta$ matches the saddle point obtained by Eqn. (2.3.10). The sign of the observation aspect angle θ is determined by Eqn. (2.3.11) as

$$\begin{cases} z > z'(LHP) : \theta > 0 \\ z < z'(UHP) : \theta < 0 \end{cases} \tag{2.6.2}$$

UHP and *LHP* indicate the *Upper Half Plane* and *Lower Half Plane* in the complex ζ - plane. Fig. 2.6.1 depicts the steepest-descent paths for the cover layer field in the complex ζ -plane for various observation aspect angles. The indices of the cover, the film, and the substrate layer regions are chosen to be that $n_1 = 1$, $n_2 = 3.2$, and $n_3 = 3$ respectively.

As depicted in Fig. 2.6.1, the steepest-descent path always violates the cover branch cut C_{b1} an even number of times. Similarly, the substrate branch cut C_{b3} is violated an even number of times for $\theta < \theta_t$ (θ_t = threshold aspect angle) where one of two ζ' - intercepts in Eqn. (2.6.1), $\zeta' = k_l / \sin\theta$, crosses the point $(k_3, 0)$ in Fig. 2.6.1. Then, it can be defined by

$$\frac{k_1}{\sin\theta_t} = k_3$$

Then,

$$\theta_t = \sin^{-1}\left(\frac{n_1}{n_3}\right) = \frac{\pi}{2} - \cos^{-1}\left(\frac{n_1}{n_3}\right) \tag{2.6.3}$$

In agreement with Eqn. (2.6.2),

$$\theta_t > 0 \cdots z > z'(LHP)$$

Hence

deform

inversi

2.6.2.

where

The

implies

by the c

It is also

Riemann

[20], [2

poles are

ultimate

$$\int_C$$

and the S

Since

times for

Hence both ends of the steepest-descent path lie on the top sheet and it doesn't need to be deformed about any of the branch cuts but can be directly connected to the $\mathrm{Re}\{\zeta\}$-axis inversion contour on the top sheet of the 4-sheeted Riemann surface as depicted in Fig. 2.6.2. Cauchy's integral theorem leads to

$$\oint_{C-SDP-C_p-C_\infty} \Psi_1(x,z:\zeta)d\zeta = 0 \tag{2.6.4}$$

where $\Psi_1(x,z:\zeta)$ stands for the integrand of the cover layer field representation.

The specification of a radiation condition that is most conveniently stipulated as

$$\mathrm{Re}\{p_1(\zeta)\} = \mathrm{Re}\left\{\sqrt{\zeta^2 - k_1^2}\right\} > 0 \tag{2.6.5}$$

implies that if the integration path stays on the top sheet in the complex ζ -plane, defined by the cover and the substrate branch cuts, then

$$\int_{C_\infty} \Psi_1(x,z:\zeta)d\zeta \to 0 \tag{2.6.6}$$

It is also observed that the surface wave mode arises from pole singularities on the top Riemann sheet. Conversely, the leaky wave mode poles lie on the lower Riemann sheets [20], [21]. Since the integration path does not pass to the lower sheets, the leaky wave poles are not captured and the field representation is entirely *proper*. The discrete modes ultimately vanish in the far zone as previously discussed. Then,

$$\int_C \Psi_1(x,z:\zeta)d\zeta = \int_{SDP} \Psi_1(x,z:\zeta)d\zeta = \int_{C_b=C_{b1}+C_{b3}} \Psi_1(x,z:\zeta)d\zeta \tag{2.6.7}$$

and the *SDP* contribution replicates the radiation field.

Since the steepest-descent path violates the substrate branch cut an odd number of times for $\theta \geq \theta_t$, the left side of the steepest-descent path lies on the top sheet of the

subs

it is

desc

desc

2.6.3

By th

There

and th

Th

forces

that bo

2.6.4.

sheet c

steepes

satisfie

$\Psi_1(x,$

sheeted

substrate layer Riemann surface while its right side ends on the bottom sheet. Therefore, it is necessary to deform the integration path, such that the right side of the steepest-descent path once more violates the substrate layer branch cut, which leads the steepest-descent integration path to be equivalent to the cover layer branch cut as depicted in Fig. 2.6.3. Cauchy's theorem for the complex integration contour leads to

$$\oint_{SDP-C_{b1}-C_p-C_\infty} \Psi_1(x,z:\zeta)d\zeta = 0 \tag{2.6.8}$$

By the same arguments given above,

$$\begin{aligned} \int_{C_p} \Psi_1(x,z:\zeta)d\zeta &\to 0 \\ \int_{C_\infty} \Psi_1(x,z:\zeta)d\zeta &\to 0 \end{aligned} \tag{2.6.9}$$

Therefore,

$$\int_{SDP} \Psi_1(x,z:\zeta)d\zeta = \int_{C_{b1}} \Psi_1(x,z:\zeta)d\zeta \tag{2.6.10}$$

and the *SDP* contributes the cover radiation field.

The proper closure of the steepest-descent path to the $\mathrm{Re}\{\zeta\}$-axis inversion contour forces the integration path to be deformed fully around the substrate layer branch cut so that both ends of the steepest-descent path lie on the top Riemann sheet as depicted in Fig. 2.6.4. Even if the substrate layer wavenumber, $p_3(\zeta)$, stays on the bottom Riemann sheet during the integration path deformation, the contour from the one end of the steepest-descent path to the substrate layer branch cut, C_∞, the closure condition is still satisfied. This is because the exponents in the integrand of the field representation, $\Psi_1(x,z:\zeta)$, only contains the cover layer wavenumber, $p_1(\zeta)$, on the top sheet of 4-sheeted Riemann surface so that it can still converge.

Leaky

Hence t

Eqn

contrib

the cov

cut con

from p

thresh

resolve

An

inversi

Since

cover

remain

contou

Since

$$\oint_{C-SDP-C_{b3}-C_p-C_\infty} \Psi_1(x,z:\zeta)d\zeta = 0$$
$$\int_{C_p} \Psi_1(x,z:\zeta)d\zeta \to 0 \qquad (2.6.11)$$
$$\int_{C_\infty} \Psi_1(x,z:\zeta)d\zeta \to 0$$

Leaky wave poles captured on the lower sheet do not contribute to the radiation field. Hence the cover radiation field becomes

$$\int_C \Psi_1(x,z:\zeta)d\zeta = \int_{SDP} \Psi_1(x,z:\zeta)d\zeta + \int_{C_{b3}} \Psi_1(x,z:\zeta)d\zeta \qquad (2.6.12)$$

Eqn. (2.6.12) reduces identically to Eqn. (2.6.7) when the substrate layer branch cut contribution vanishes for $\theta < \theta_t$. Moreover the substrate layer branch cut contribution to the cover layer field is annulled in the far zone but in the near zone, the substrate branch cut contribution still remains. However, in the near zone, the corresponding wave arising from path deformation around the substrate layer branch cut is negligible near the threshold aspect angle, the field discontinuity due to the branch cut contribution is resolved so that the total radiation field is continuous over that region.

Another possible proper closure of the steepest-descent path into the $\mathrm{Re}\{\zeta\}$-axis inversion contour is the partial integration path deformation as depicted in Fig. 2.6.5. Since the partial path deformation forces the steepest-descent path to violate both the cover and substrate layer branch cut an even number of times, its extremities can still remain on both the top Riemann sheets, which allows any portion of the integration contour to satisfy the closure condition.

$$\oint_{C-SDP-partial\{C_{b3}\}-C_p-C_\infty} \Psi_1(x,z:\zeta)d\zeta = 0 \qquad (2.6.13)$$

Since

Eqn.

The s

times,

it can

contou

$$\int_{C_p} \Psi_1(x,z:\zeta)d\zeta \to 0$$

$$\int_{C_\infty} \Psi_1(x,z:\zeta)d\zeta \to 0$$

Eqn. (2.6.13) reduces to

$$\int_C \Psi_1(x,z:\zeta)d\zeta = \int_{SDP} \Psi_1(x,z:\zeta)d\zeta + \int_{partial\{C_{b3}\}} \Psi_1(x,z:\zeta)d\zeta \quad (2.6.14)$$

The steepest-descent path only violates the substrate layer branch cut an odd number of times, therefore it must be deformed partially about the substrate layer branch cut so that it can still remain on the top Riemann sheet then terminate to the $\mathrm{Re}\{\zeta\}$- axis inversion contour properly.

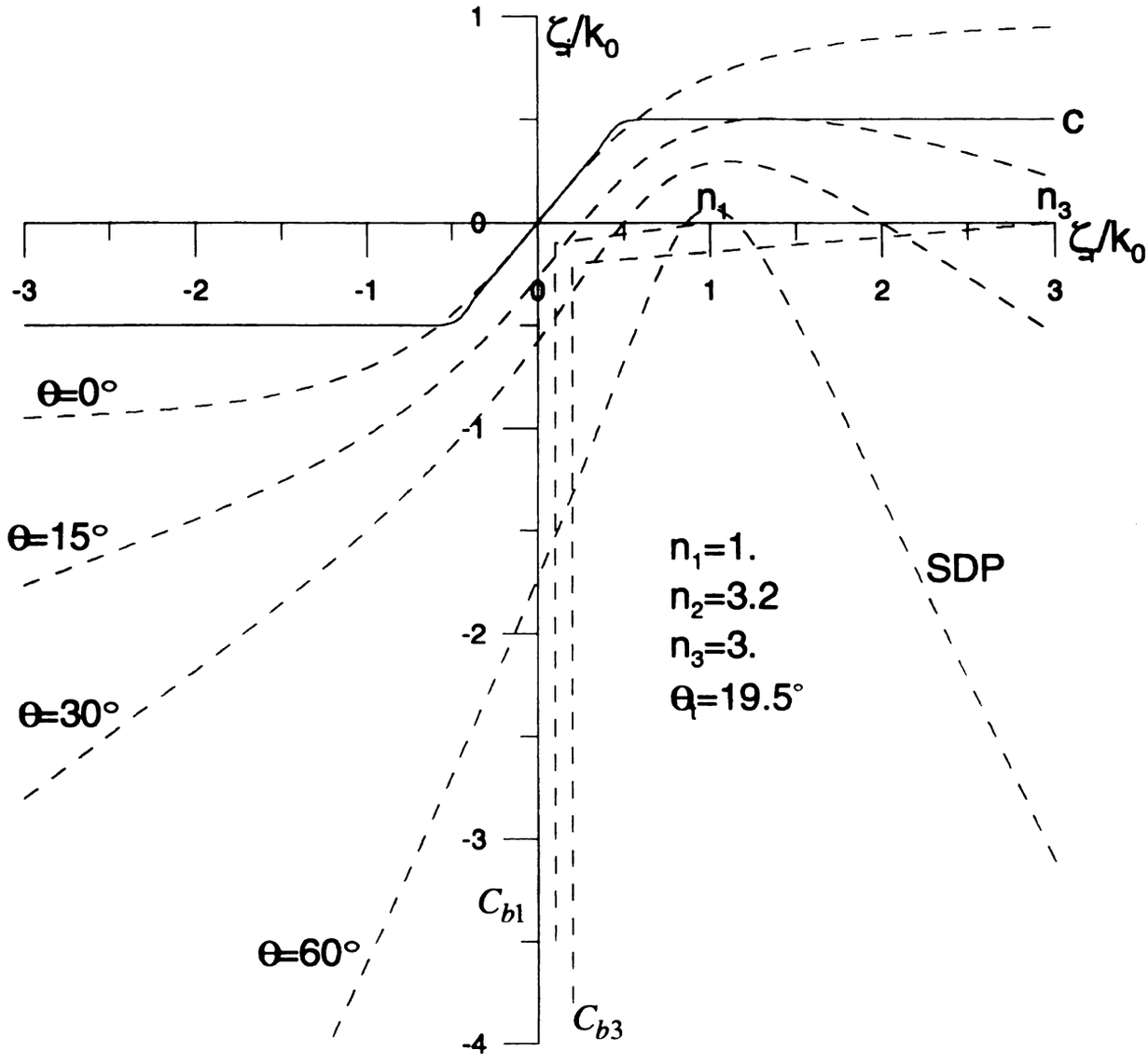

Figure 2.6.1 The steepest-descent paths for the cover layer field calculation on various observation aspect angles in the complex axial transform plane. The asymmetric planar dielectric waveguide consists of cover, guiding and substrate layer with indices $n_1 = 1$, $n_2 = 3.2$, and $n_3 = 3$ respectively.

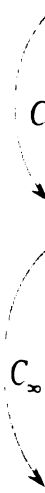

Figur

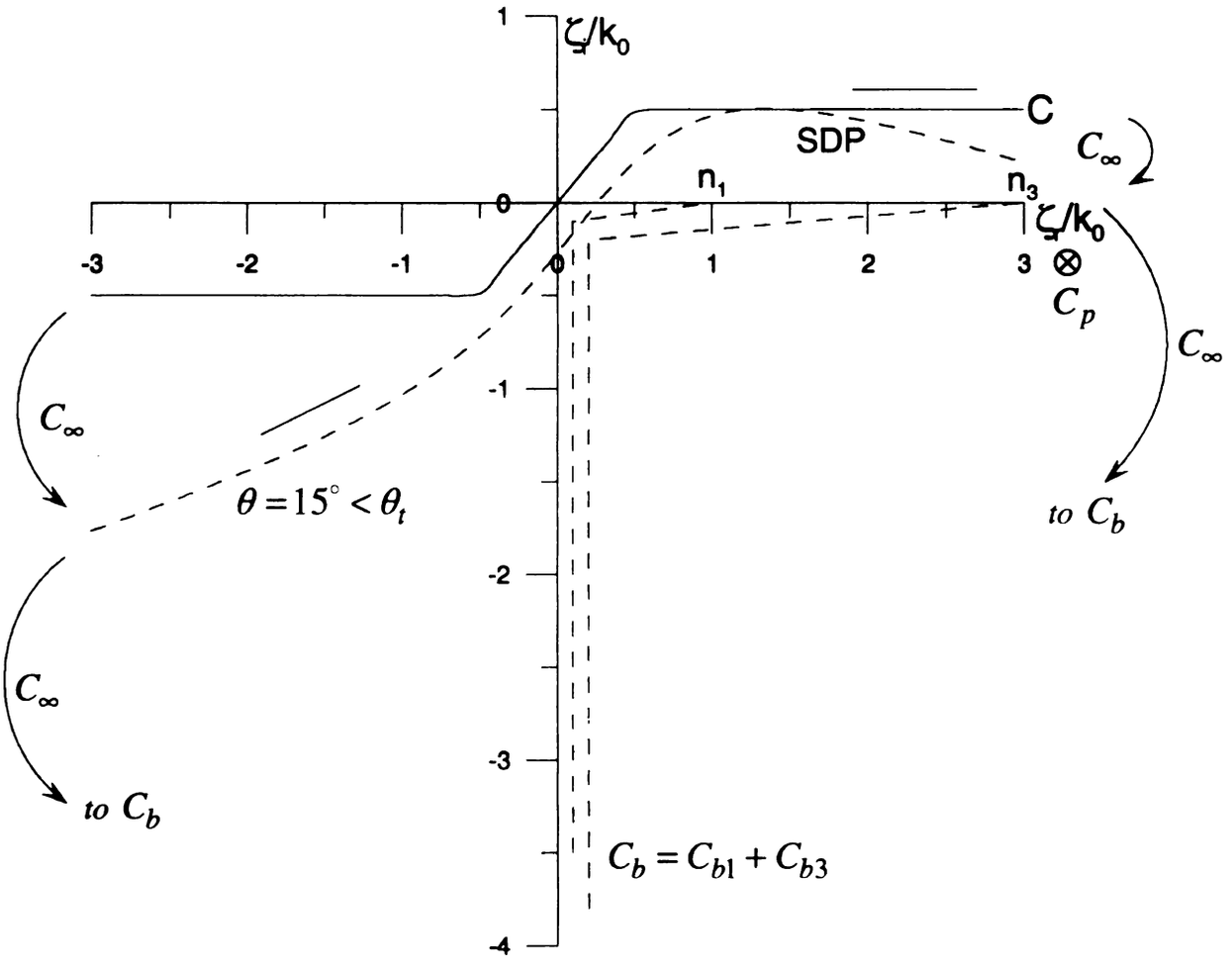

Figure 2.6.2 Proper closure of $\mathrm{Re}\{\zeta\}$-axis inversion contour C into SDP for $\theta < \theta_t$: $n_1 = 1., n_2 = 3.2, n_3 = 3., \theta_t = 19.5°$.

Figure

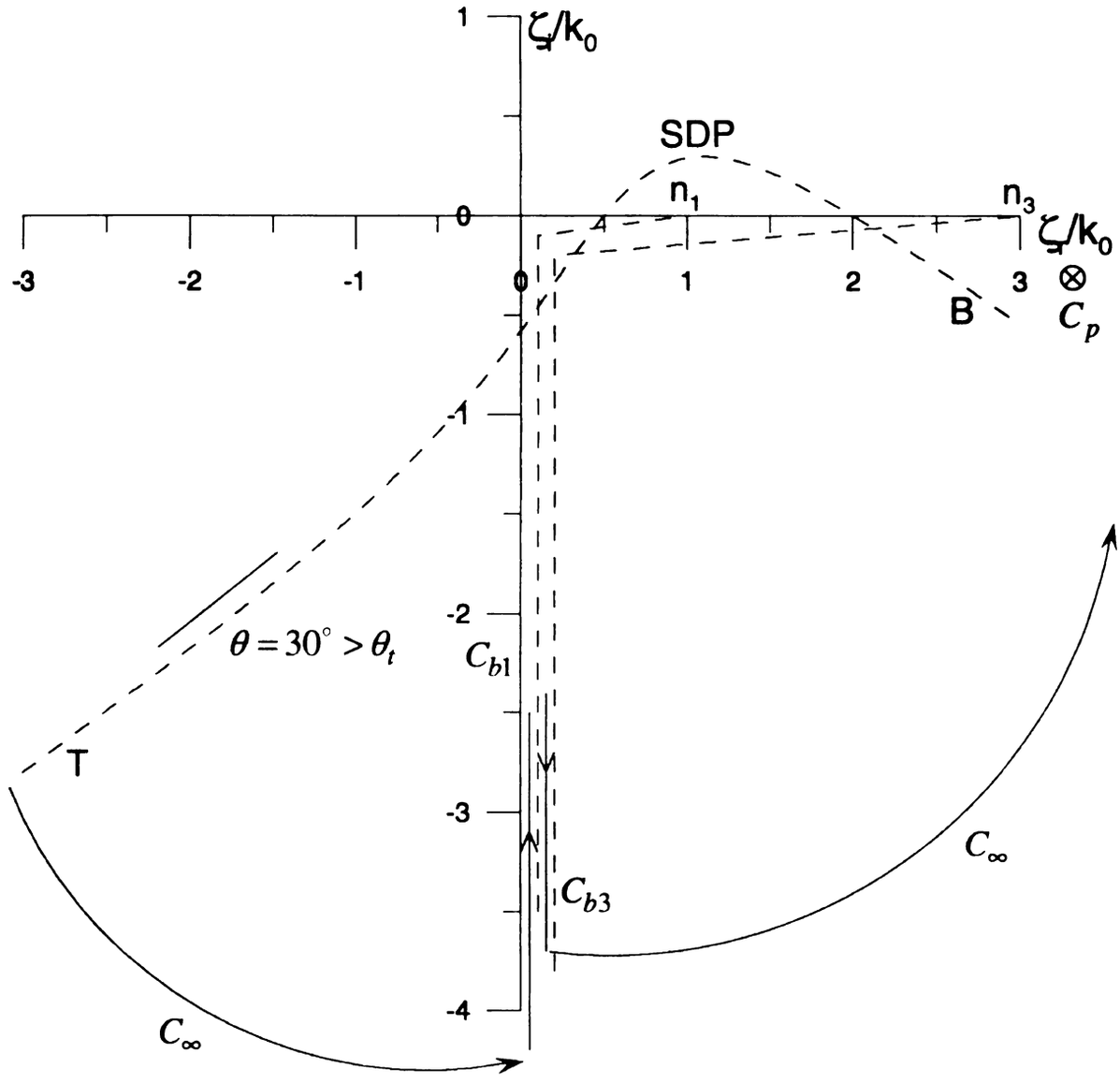

Figure 2.6.3 Appropriate closure of SDP into cover layer branch cut for $\theta > \theta_t$: $n_1 = 1., n_2 = 3.2, n_3 = 3., \theta_t = 19.5°$.

Figure

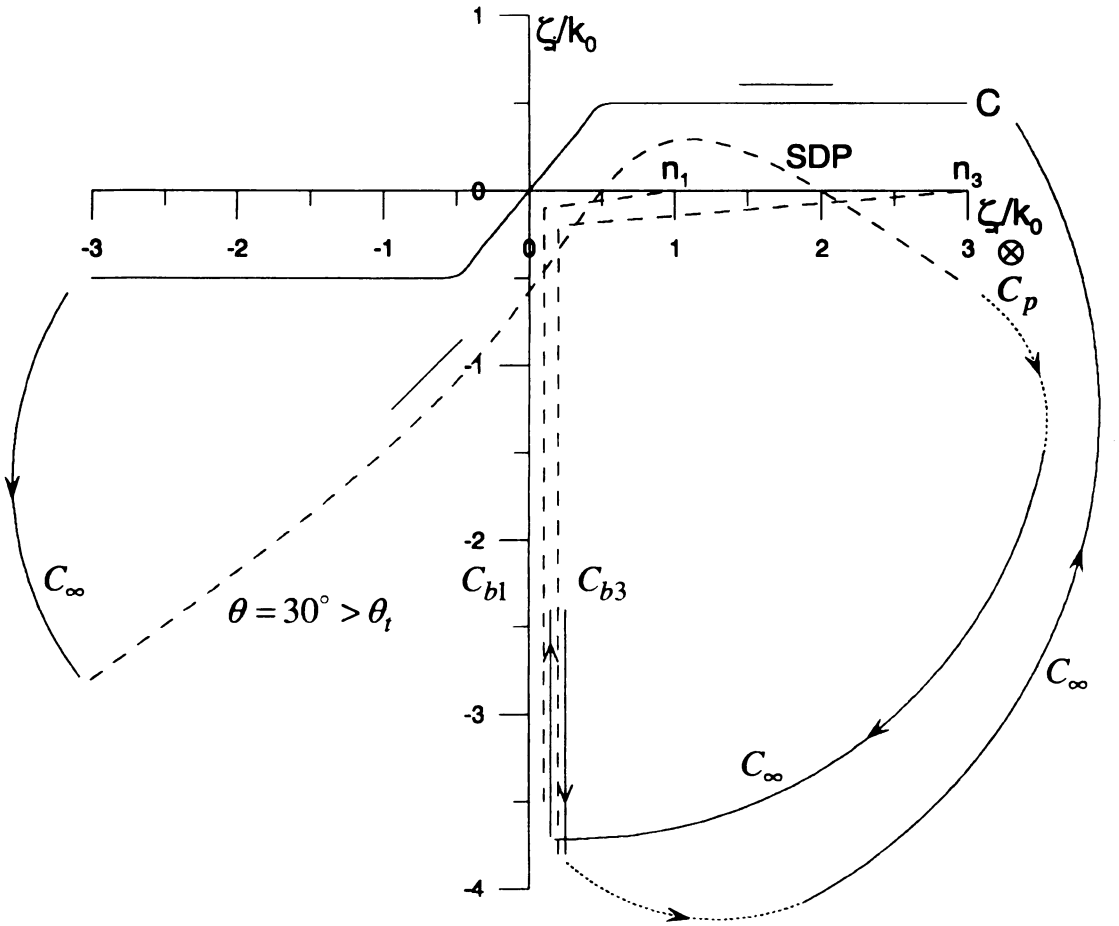

Figure 2.6.4 Proper closure of $\mathrm{Re}\{\zeta\}$-axis inversion contour C into SDP and substrate branch cut for $\theta > \theta_t$: $n_1 = 1.$, $n_2 = 3.2$, $n_3 = 3.$, $\theta_t = 19.5°$.

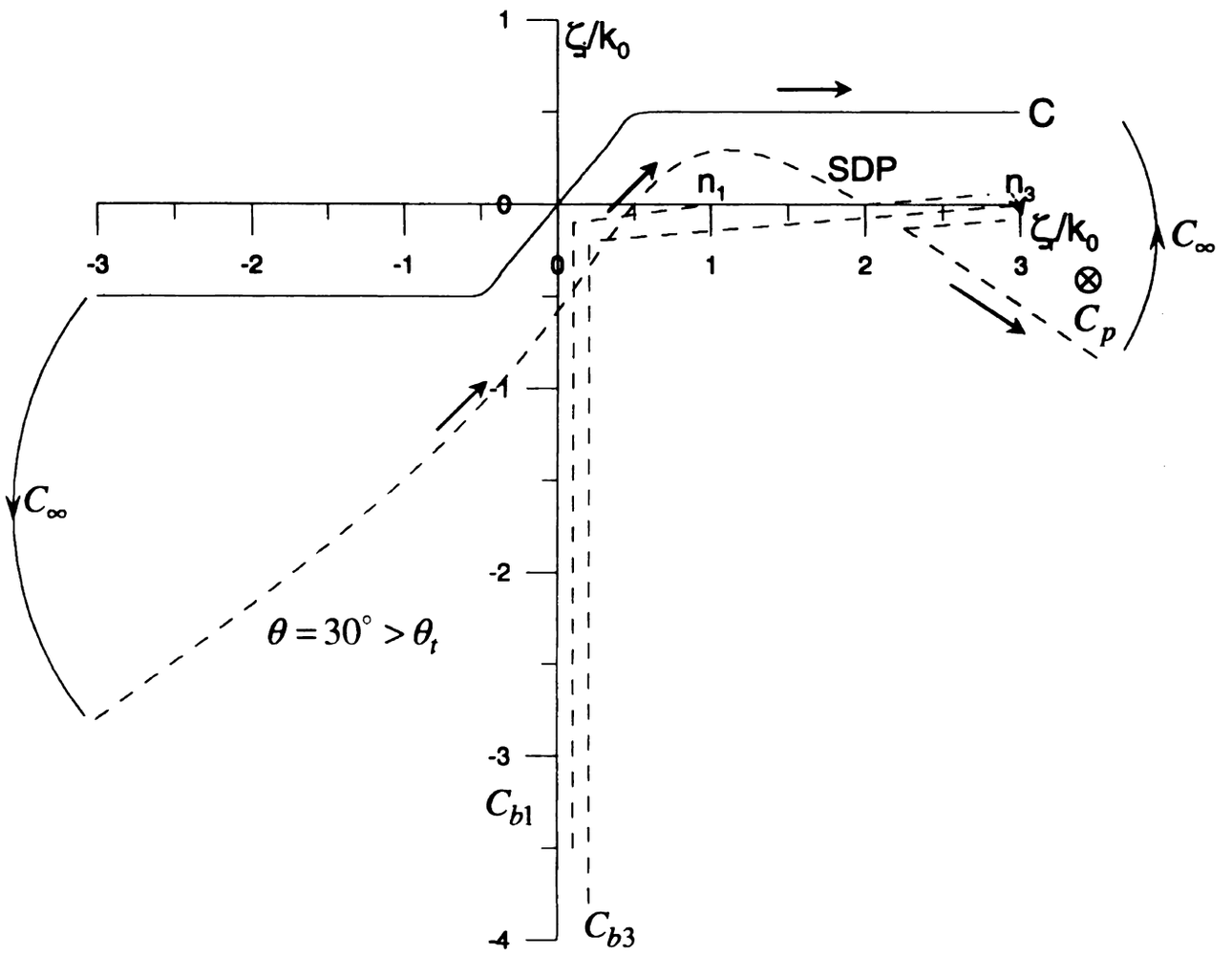

Figure 2.6.5 Proper closure of $\mathrm{Re}\{\zeta\}$-axis inversion contour C into SDP and partial C_{b3} for $\theta > \theta_t$: $n_1 = 1., n_2 = 3.2, n_3 = 3., \theta_t = 19.5^\circ$.

Th

agree

descr

singul

repres

point.

layer r

aspect

Th

for $\theta <$

be def

inversi

where a

and Eqn

for $\theta <$

2.7 STEEPEST-DESCENT EVALUATION OF SUBSTRATE FIELD

The steepest-descent path in the complex ζ -plane is obtained from Eqn. (2.3.15) in agreement with $l = 3$ for the substrate layer index. The saddle point of the steepest-descent path in the complex ζ -plane denoted by $k_3 \sin\theta$ exists near guided-mode pole singularities for certain aspect angles. Hence, the integrand of inverse transform field representation in the substrate layer, $\Psi_3(x,z:\zeta)$, doesn't vary slowly near the saddle point, which forces the saddle point approximation to fail at these angles in the substrate layer region. The steepest-descent paths in the complex ζ -plane on various observation aspect angles are depicted in Fig. 2.7.1.

The steepest-descent path (*SDP*) violates both branch cuts an even number of times for $\theta < \theta_t$ (θ_t = threshold aspect angle) hence the steepest-descent path doesn't need to be deformed about either of the branch cuts and is connected to the $\mathrm{Re}\{\zeta\}$-axis inversion contour on the top sheet as depicted in Fig. 2.7.1. Cauchy's theorem yields

$$\oint_{C-SDP-C_p-C_\infty} \Psi_3(x,z:\zeta)d\zeta = 0 \tag{2.7.1}$$

where as previously

$$\begin{aligned} \int_{C_p} \Psi_3(x,z:\zeta)d\zeta &\to 0 \\ \int_{C_\infty} \Psi_3(x,z:\zeta)d\zeta &\to 0 \end{aligned} \tag{2.7.2}$$

and Eqn. (2.7.1) leads to the radiation field.

$$\int_C \Psi_3(x,z:\zeta)d\zeta = \int_{SDP} \Psi_3(x,z:\zeta)d\zeta \tag{2.7.3}$$

for $\theta < \theta_t$.

On the

numbe

depicte

stay on

Fir

about

cannot

layer b

transfo

path d

Somm

diverg

Th

deform

condit

and ag

Sir

numbe

can sti

On the other hand, the steepest-descent path violates cover layer branch cut an odd number of times and substrate layer branch cut an even number of times for $\theta \geq \theta_t$ as depicted in Fig. 2.7.1 therefore it must be deformed about the cover layer branch cut to stay on the top Riemann sheet.

First of all, it's prompted to attempt to perform a full integration path deformation about the cover layer branch cut as depicted in Fig. 2.7.2. It seems to be logical but cannot satisfy the closure condition during the path deformation from infinity to cover layer branch cut, along C_∞. And since one of the exponents in the integrand of inverse transform field representation, $\Psi_3(x,z:\zeta)$, includes $p_1(\zeta)$ and during the specific path deformation (C_∞), cover layer wavenumber $p_1(\zeta)$ remains on the bottom sheet, Sommerfeld radiation condition is violated to cause the integrand, $\Psi_3(x,z:\zeta)$, to diverge.

Therefore, as previously discussed in Section 2.6, it is observed that a partial path deformation around the cover layer branch cut can be introduced to satisfy the closure condition as depicted in Fig. 2.7.3. Cauchy's theorem then leads to

$$\oint_{C-SDP-partial\{C_{b1}\}-C_p-C_\infty} \Psi_3(x,z:\zeta)d\zeta = 0 \qquad (2.7.4)$$

and again as in Eqn. (2.7.2), the radiation field becomes

$$\int_C \Psi_3(x,z:\zeta)d\zeta = \int_{SDP} \Psi_3(x,z:\zeta)d\zeta + \int_{partial\{C_{b1}\}} \Psi_3(x,z:\zeta)d\zeta \qquad (2.7.5)$$

Since the steepest-descent path only violates the cover layer branch cut an odd number of times, it must be deformed partially about the cover layer branch cut so that it can still remain on the top Riemann sheet then violates the substrate layer branch cut an

eve

def

whi

on t

abo

com

still

even number of times to terminate again on the top Riemann sheet. The partial path deformation allows any portion of the integration contour to satisfy the closure condition, which means both the cover and substrate layer wavenumber, $p_1(\zeta)$ and $p_3(\zeta)$, stay on the top Riemann sheet.

The field discontinuity even due to the partial deformation of the integration contour about the cover layer branch cut is considerable near a threshold aspect angle but the complex field phase compensates for the discontinuity so that the total radiation field is still continuous over that region through that angle.

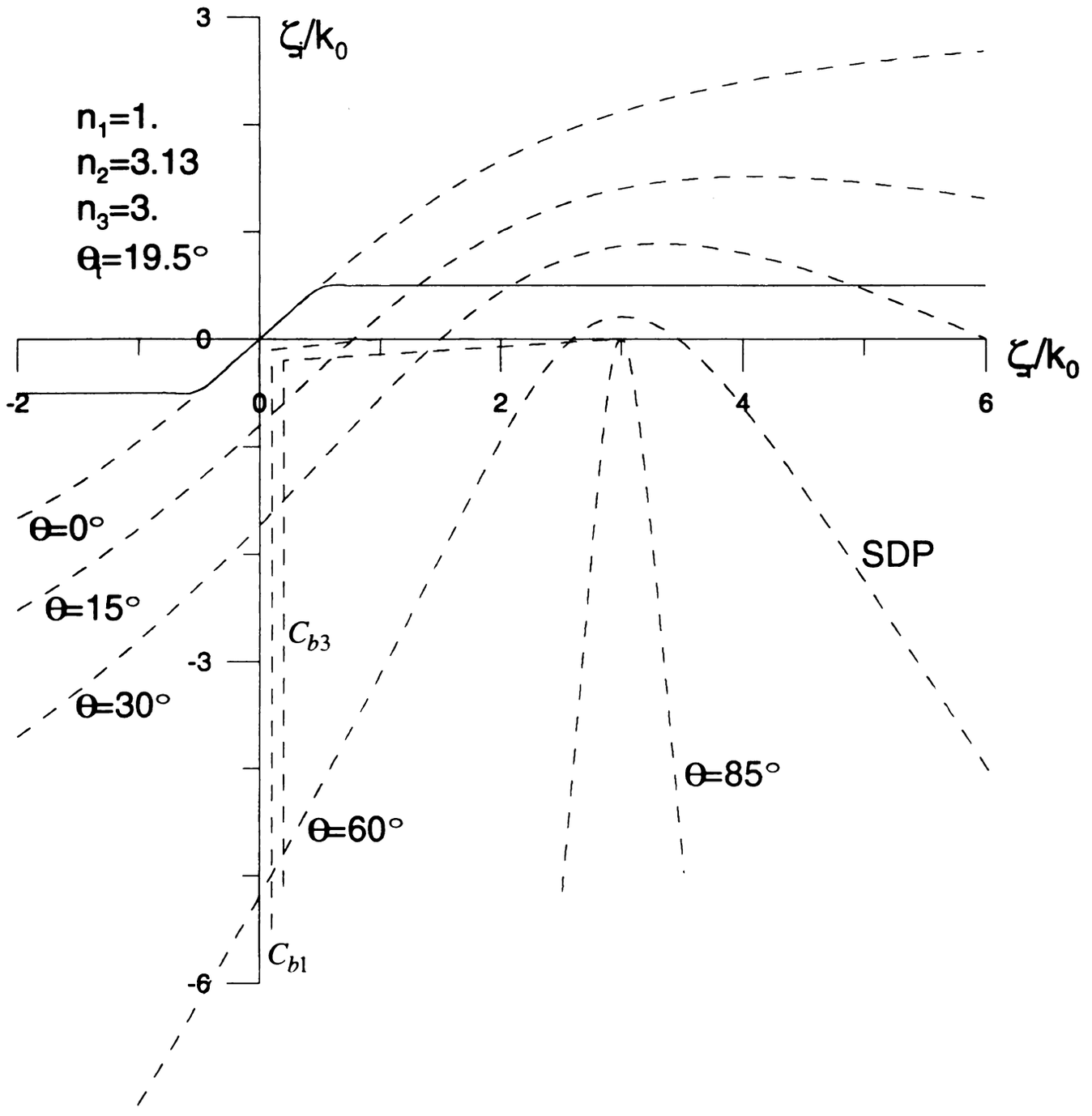

Figure 2.7.1 The steepest-descent paths for the substrate layer field calculation at various observation aspect angles in the complex ζ -plane. The asymmetric planar dielectric wave- guide consists of cover, guiding and substrate layers with indices $n_1 = 1$, $n_2 = 3.13$, and $n_3 = 3$ respectively.

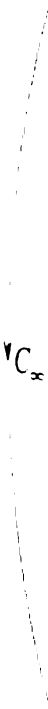

Figur

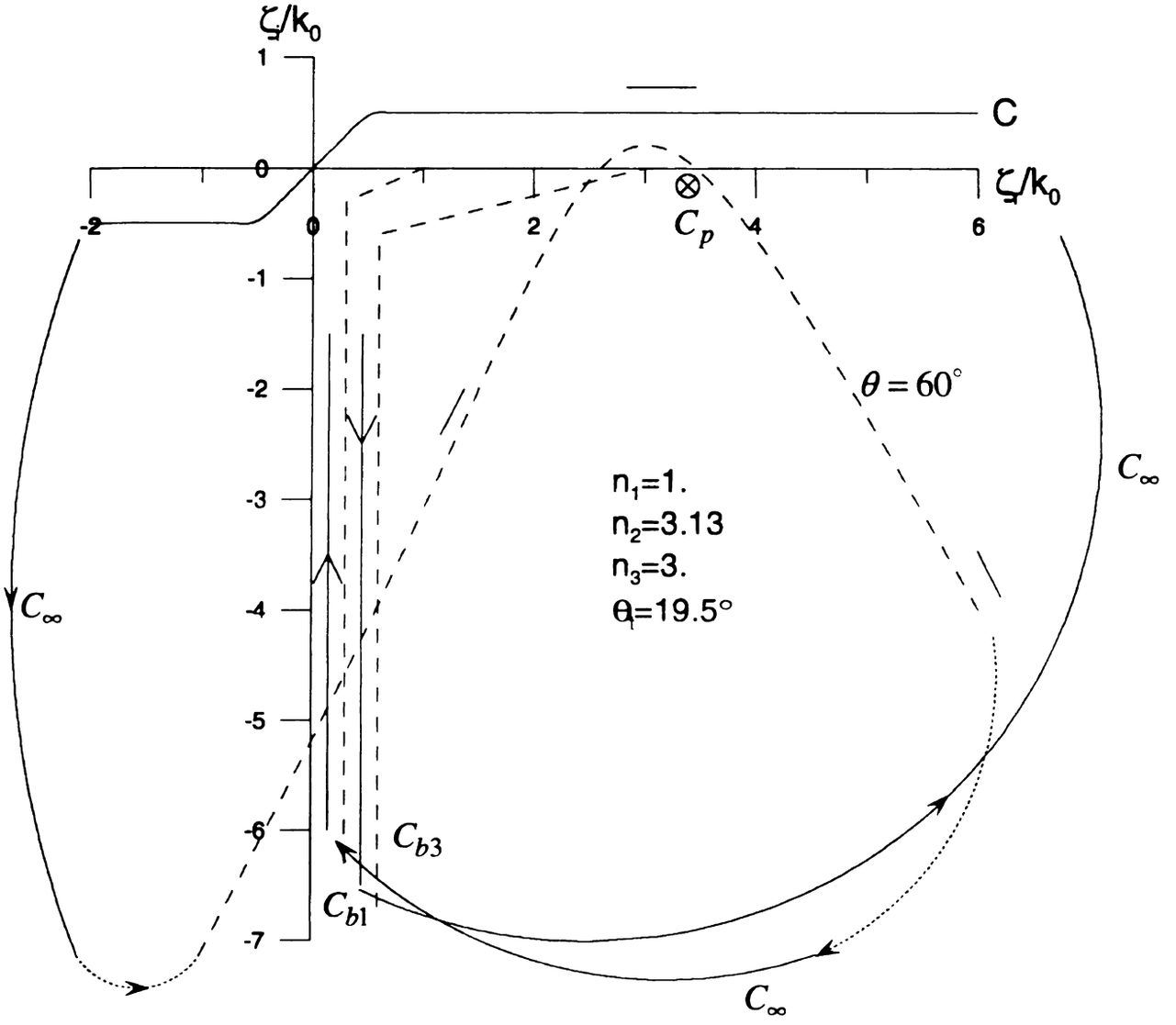

Figure 2.7.2 Closure of $\mathrm{Re}\{\zeta\}$-axis inversion contour C into SDP and full cover layer branch cut for $\theta > \theta_t$.

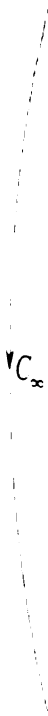

Figur

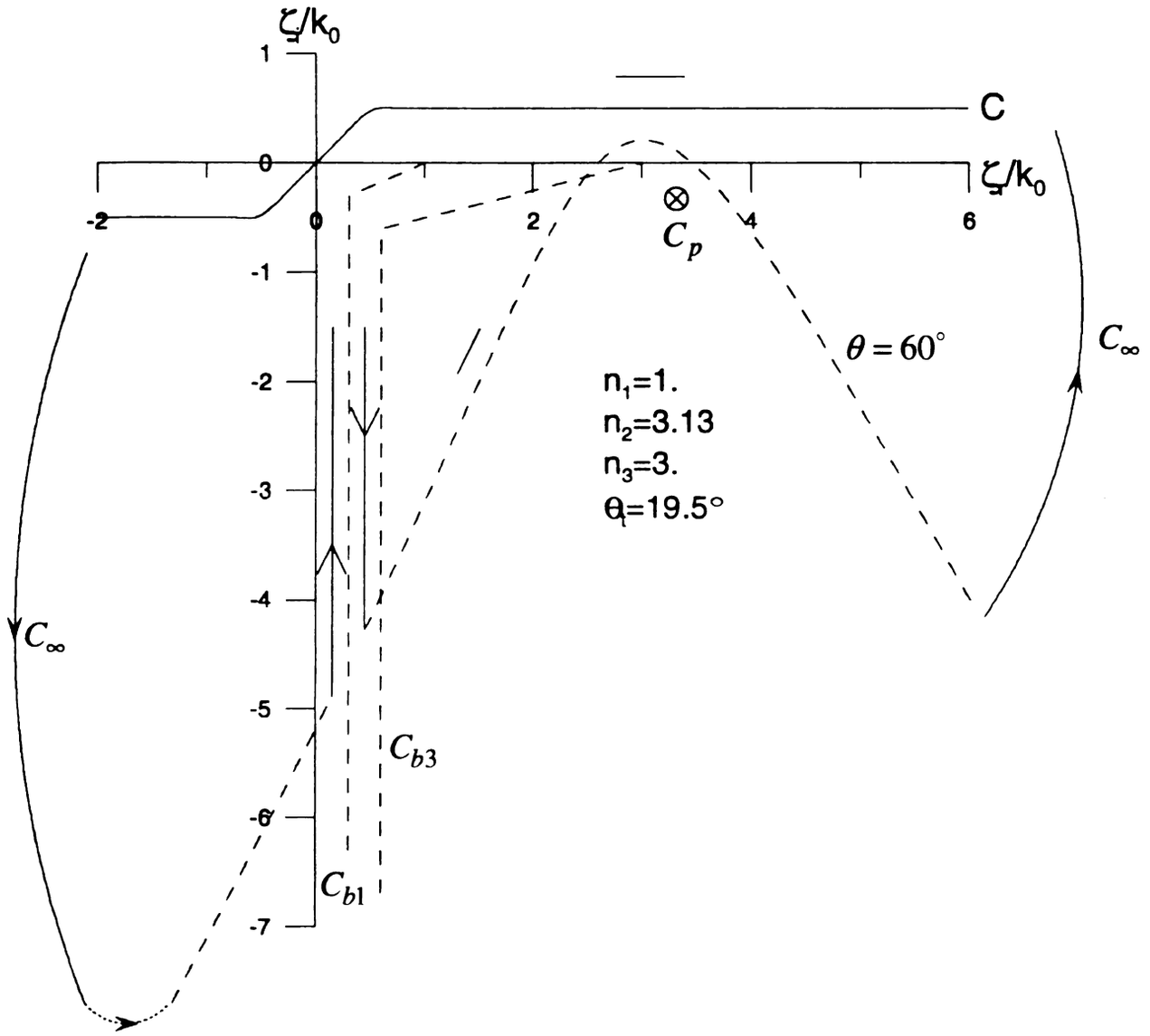

Figure 2.7.3 Proper closure of $\mathrm{Re}\{\zeta\}$-axis inversion contour C into SDP and partial cover layer branch cut for $\theta > \theta_t$.

T
point
The
field
angl
as de
steep
the n
A
cove
D
partia
the f
resol
thres
equiv
in Fig
but t
discre
Fig. 2

2.8 NUMERICAL RESULTS

The asymptotic radiation field of guiding structures is determined through the saddle-point approximation for far zone. But, in the near zone, the saddle-point method fails. The steepest-descent method in the complex ζ -plane is valid to determine the radiation field for both near and far zone. As depicted Fig. 2.3.2, the small observation aspect angle θ corresponds to the far zone and the large one does to the near zone. Therefore, as depicted in Fig. 2.8.1, it is observed that the saddle-point approximation matches to the steepest-descent method in the far zone but, deviates from the steepest-descent method in the near zone.

As depicted in Fig. 2.6.3, the steepest-descent integration path is equivalent to the cover layer branch cut for $\theta \geq \theta_t$. The numerical result is depicted in Fig. 2.8.2.

During the steepest-descent contour in the cover layer, it is observed that both the partial and the full substrate layer branch cut deformations are acceptable for $\theta \geq \theta_t$ and the field discontinuity due to the full substrate branch cut contribution over θ_t can be resolved in the cover layer since the full branch cut contribution is negligible near the threshold aspect angle θ_t. The numerical result is depicted in Fig. 2.8.3.

In the substrate layer, in agreement with Eqn. (2.7.5), the steepest-descent contour is equivalent to the remaining cover and full substrate branch-cut deformations as depicted in Fig. 2.8.4. Moreover, the partial cover branch cut contribution is considerable near θ_t but total field is still continuous over that angle since the field phase compensate the discrepancy and validated by $\mathrm{Re}\{\zeta\}$-axis inversion contour integration as depicted in Fig. 2.8.5.

Electric Field Amplitude $(E_{1y})_r$

Figu

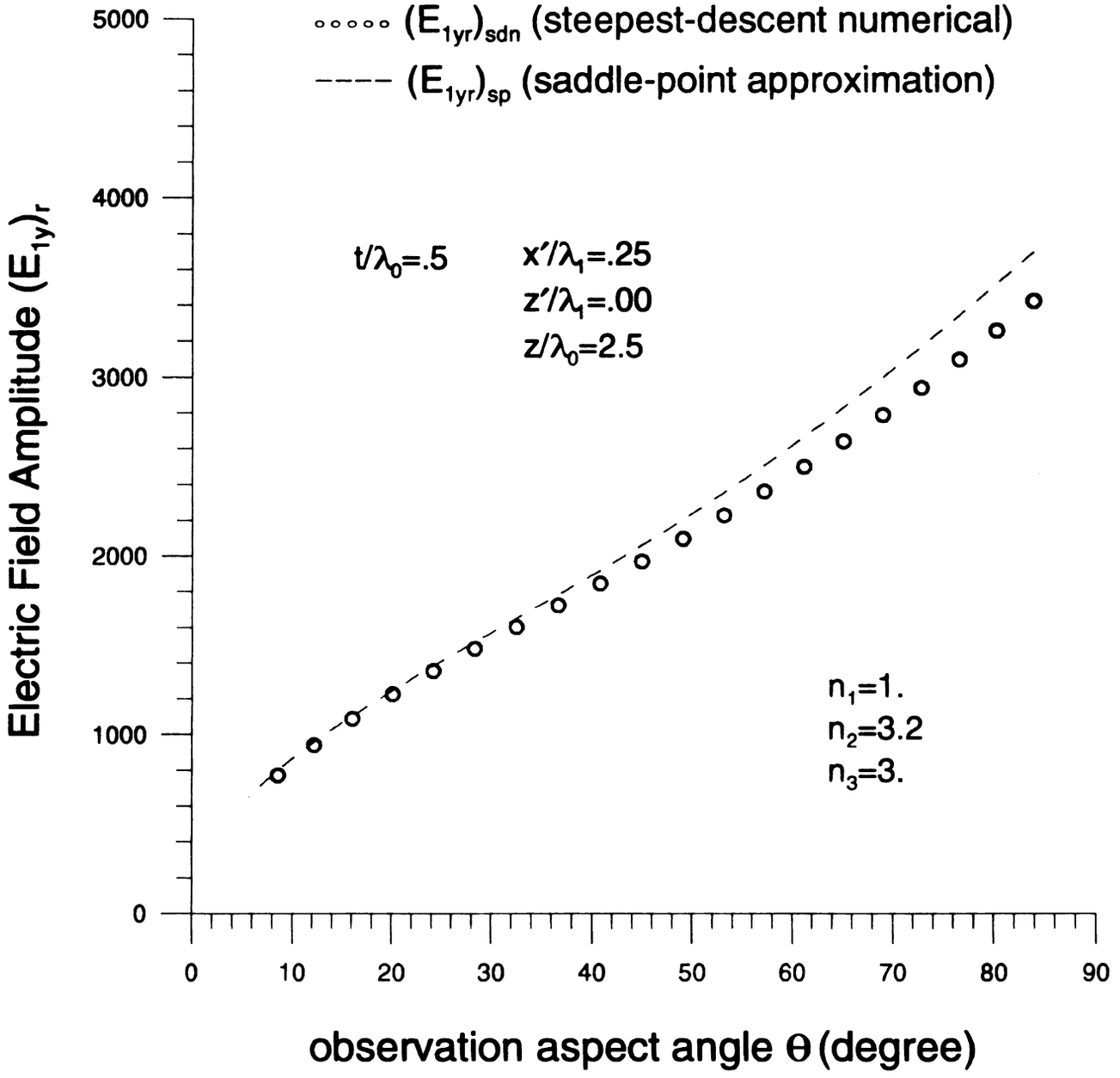

Figure 2.8.1 Transverse dependence of the reflected continuous spectrum in the cover layer: the steepest-descent numerical calculation and saddle-point approximation.

Electric Field Amplitude (E_{1y})

Figur

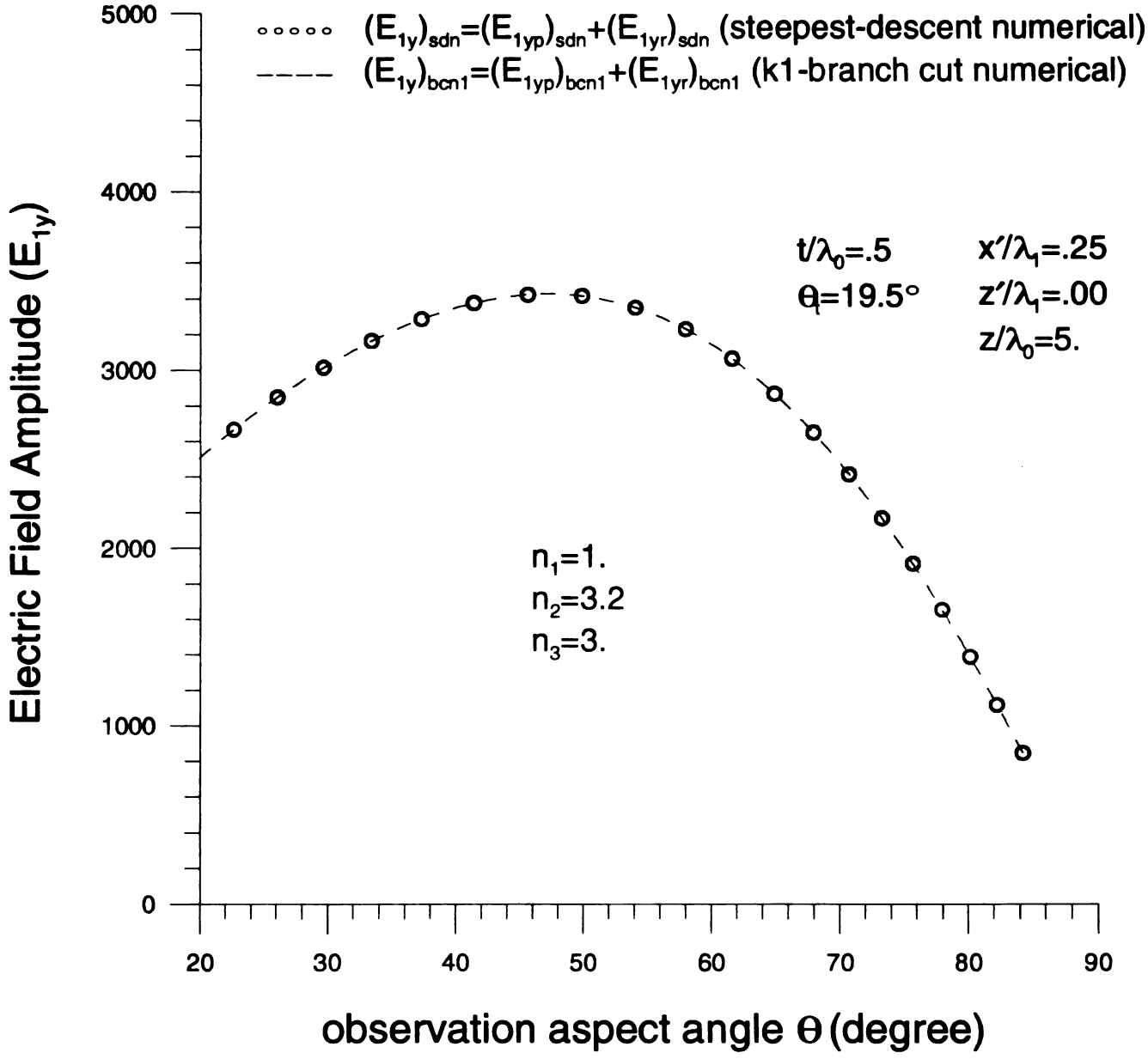

Figure 2.8.2 Transverse dependence of the continuous spectrum in the cover layer: steepest-descent numerical and saddle-point approximation.

Electric Field Amplitude (E_{1y})

Figur

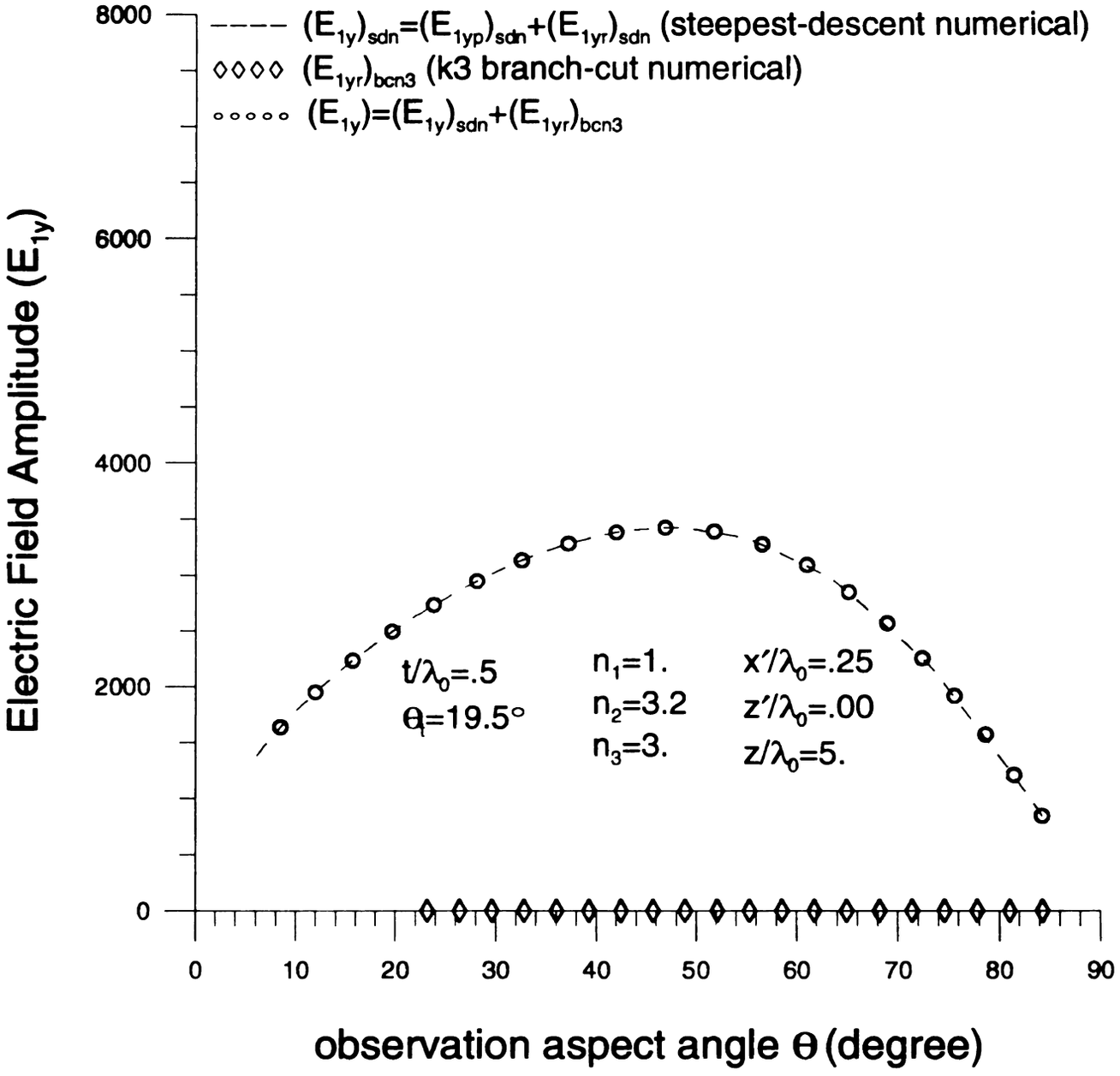

Figure 2.8.3 Transverse dependence of the continuous spectrum in the cover layer: steepest-descent numerical and the substrate layer branch cut.

Electric Field Amplitude (E_{3v})

Figu

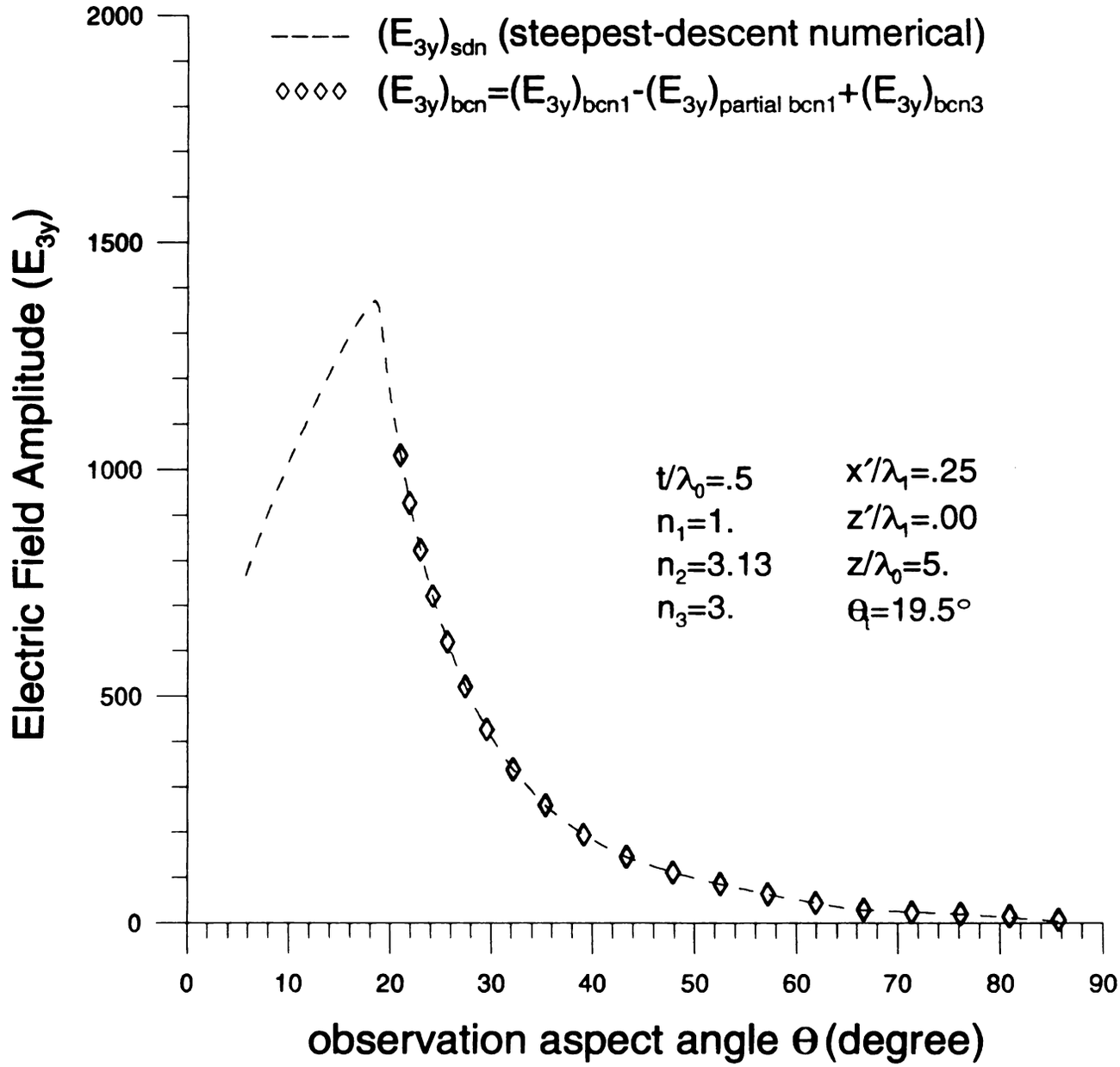

Figure 2.8.4 Transverse dependence of the transmitted spectrum in the substrate layer: steepest-descent numerical and the corresponding branch cuts.

Figure 2.8.5

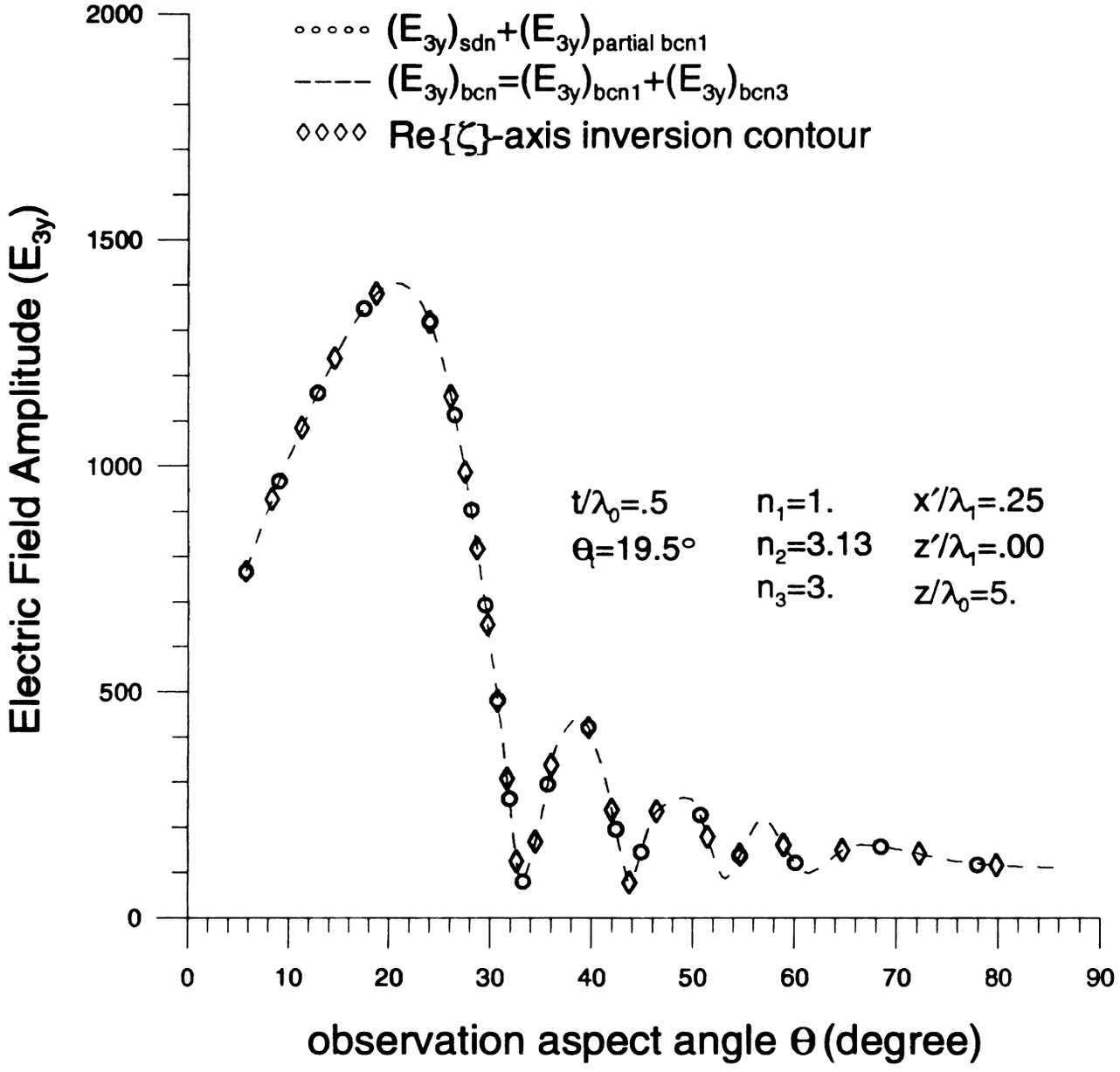

Figure 2.8.5 Transverse dependence of the transmitted spectrum in the substrate layer: steepest-descent numerical and the partial cover layer branch cut.

29 CON

The radi

$z<z'$ $(\theta <$

plane (*LHP*

steepest-des

identified as

descent path

Both me

steepest-desc

radiation fie

steepest-desc

deformed in

the $\mathrm{Re}\{\zeta\}$

radiation con

inversion con

mode spectru

2.9 CONCLUSION

The radiation field of the asymmetric planar open waveguide for $z > z'$ $(\theta > 0)$ and $z < z'$ $(\theta < 0)$ as depicted in Fig. 2.3.2 can be determined by closing the lower half plane (*LHP*) and the upper half plane (*UHP*) in the complex ζ -plane respectively. The steepest-descent path in the complex ζ -plane in both the cover and substrate layers was identified as a direct method and confirmed it using the transformation of the steepest-descent path in the complex ϕ -plane defined by $\phi = \sigma + j\eta$ as an indirect method.

Both methods yielded the identical result and reconfirmed the validity. Using the steepest-descent method in the complex ζ -plane, the numerical evaluation of the radiation field can be implemented in both the cover and the substrate layer. During the steepest-descent implementation in the complex ζ -plane, the integral path must be deformed in order to meet the closure condition so that it can be properly connected to the $\mathrm{Re}\{\zeta\}$-axis inversion contour. Then, the radiation field can satisfy Sommerfeld's radiation condition (closure condition) and can be numerically validated by $\mathrm{Re}\{\zeta\}$-axis inversion contour integration. Since the far-zone field is the main concern, the discrete-mode spectrum contributed by guided-pole singularity has been less emphasized.

CHAPTER 3

SPECTRAL ANALYSIS AND ASYMPTOTIC RADIATION FIELD FOR TM MODES OF AN ASYMMETRIC PLANAR OPEN WAVEGUIDE

3.1 INTRODUCTION AND GEOMETRICAL CONFIGURATION

Similarly as in Chapter 2, the asymptotic TM radiation field of the open planar waveguide can be identified and classified through the steepest-descent method in the complex axial transform plane. As previously discussed in Section 2.1, the spectral fields of planar open waveguide structures possess multiple branch points associated with each of the three planar layers. The branch point associated with the film layer is removable and the branch points associated with the cover layer and the substrate layer are non-removable.

Unlike in Chapter 2, where the Green's function was scalar, the steepest-descent evaluation of Green's dyad for radiation fields in both the cover and the substrate layers is performed. Those fields are maintained by TM electric sources in proximity to the simplest canonical waveguide structure. And spectral representations of Green's dyads for those fields possess multiple non-removable branch points in the complex axial transform plane.

The fundamental distinction from Chapter 2 is that due to the intrinsic nature of TM mode excitation, not only the current but also the charge contributes to the electric fields within the source region since charges is required by the continuity equation. However, the magnetic fields are not contaminated by charges within the source region since physically no real magnetic charge exists.

Like in Chapter 2, for the cover field, the steepest-descent path in the complex axial transform plane replaces the cover layer branch cut while the substrate layer branch cut is retained. Alternatively the cover and the incomplete substrate layer branch cuts are replaced while the remaining substrate layer branch cut is retained. However, in the substrate layer, the incomplete cover and the complete substrate layer branch cuts are replaced while the remaining cover layer branch cut is retained.

The planar waveguide structure consists of a dielectric guiding region immersed in a planar-layered background environment. Each planar layer is non-magnetic, isotropic, and homogeneous with complex permittivity ε_l, $l = 1,2,3$ for cover, film, and substrate layers. A coordinate system is chosen with the z axis as the waveguiding axis and the x axis normal to the planar interfaces as depicted in Fig. 3.1.1. The structure is of infinite extent parallel to the $y-z$ plane.

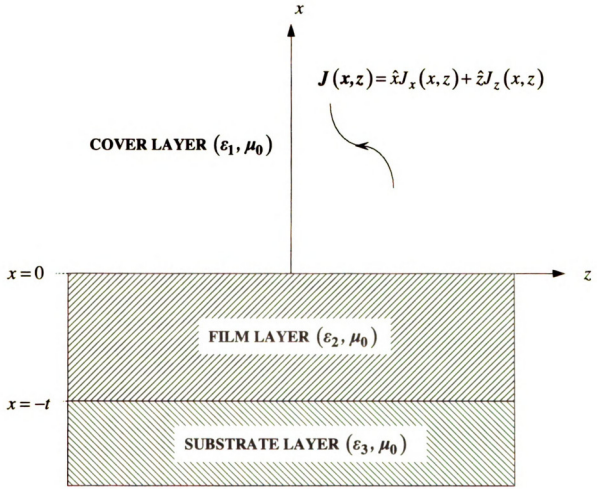

Figure 3.1.1 Geometrical configuration of an asymmetric planar dielectric slab waveguide with TM line-source excitation. Cover, film, and substrate layers are considered in the low-loss limit.

3.2 SPECTRAL FIELD FORMULATION

Since the spectral fields are TM with respect to the waveguiding axis z,

$$\begin{aligned}\tilde{\boldsymbol{e}}_l(\boldsymbol{x},\zeta) &= \hat{x}\tilde{e}_{lx}(x,\zeta)+\hat{z}\tilde{e}_{lz}(x,\zeta)\\ \tilde{\boldsymbol{h}}_l(\boldsymbol{x},\zeta) &= \hat{y}\tilde{h}_{ly}(x,\zeta)\end{aligned} \tag{3.2.1}$$

where ζ is the complex axial transform variable and excitation by a ($e^{j\omega t}$ time dependence) y-invariant current source is assumed.

The spectral Maxwell equations for the *l'th* ($l=1,2,3$ *for cover, film and substrate)* layer become

$$\begin{aligned}&(\tilde{\nabla}_t+\hat{z}j\zeta)\cdot\tilde{\boldsymbol{e}}_l(\boldsymbol{x},\zeta)=\tilde{\rho}(x,\zeta)/\varepsilon_l\\ &(\tilde{\nabla}_t+\hat{z}j\zeta)\times\tilde{\boldsymbol{e}}_l(\boldsymbol{x},\zeta)=-j\omega\mu_0\tilde{\boldsymbol{h}}_l(\boldsymbol{x},\zeta)\\ &(\tilde{\nabla}_t+\hat{z}j\zeta)\times\tilde{\boldsymbol{h}}_l(\boldsymbol{x},\zeta)=\tilde{\boldsymbol{j}}(\boldsymbol{x},\zeta)+j\omega\varepsilon_l\tilde{\boldsymbol{e}}_l(\boldsymbol{x},\zeta)\\ &(\tilde{\nabla}_t+\hat{z}j\zeta)\cdot\tilde{\boldsymbol{h}}_l(\boldsymbol{x},\zeta)=0\\ &\textit{where}\\ &\tilde{\nabla}_t=\hat{x}\frac{\partial}{\partial x}+\hat{y}\frac{\partial}{\partial y}\ \textit{and}\ \tilde{\boldsymbol{j}}(\boldsymbol{x},\zeta)=\hat{x}\tilde{j}_x(x,\zeta)+\hat{z}\tilde{j}_z(x,\zeta)\end{aligned} \tag{3.2.2}$$

The transverse/longitudinal decomposition of independent Maxwell equations yields [22]

$$\begin{aligned}\tilde{\boldsymbol{e}}_{lt}(\boldsymbol{x},\zeta) &= -\frac{1}{p_l^2(\zeta)}\left(j\zeta\tilde{\nabla}_t\tilde{e}_{lz}+j\omega\mu_0\hat{z}\times\tilde{\nabla}_t\tilde{h}_{lz}+j\omega\mu_0\tilde{\boldsymbol{j}}_t\right)\\ \tilde{\boldsymbol{h}}_{lt}(\boldsymbol{x},\zeta) &= -\frac{1}{p_l^2(\zeta)}\left(-j\omega\varepsilon_l\hat{z}\times\tilde{\nabla}_t\tilde{e}_{lz}+j\zeta\tilde{\nabla}_t\tilde{h}_{lz}-j\zeta\hat{z}\times\tilde{\boldsymbol{j}}_t\right)\\ &\textit{where}\\ p_l^2(\zeta) &= \zeta^2-k_l^2\\ k_l &= \omega\sqrt{\mu_0\varepsilon_l}\\ \tilde{\boldsymbol{j}}_t(\boldsymbol{x},\zeta) &= \hat{x}\tilde{j}_x(x,\zeta)\end{aligned} \tag{3.2.3}$$

The above becomes

$$\tilde{\boldsymbol{e}}_{lt}(\boldsymbol{x},\zeta)=-\frac{1}{p_l^2}\left(j\zeta\tilde{\nabla}_t\tilde{e}_{lz}+j\omega\mu_0\hat{z}\times\tilde{\nabla}_t\tilde{h}_{lz}+j\omega\mu_0\tilde{\boldsymbol{j}}_x\right)$$
$$\tilde{\boldsymbol{h}}_{lt}(\boldsymbol{x},\zeta)=-\frac{1}{p_l^2}\left(-j\omega\varepsilon_l\hat{z}\times\tilde{\nabla}_t\tilde{e}_{lz}+j\zeta\tilde{\nabla}_t\tilde{h}_{lz}-j\zeta\hat{z}\times\hat{x}\tilde{j}_x\right) \tag{3.2.4}$$

Then, for the *l'th* layer the transverse TM fields are

$$\tilde{e}_{lx}(x,\zeta)=-\frac{1}{p_l^2(\zeta)}\left[j\zeta\frac{\partial\tilde{e}_{lz}(x,\zeta)}{\partial x}+j\omega\mu_0\tilde{j}_x(x,\zeta)\right]$$
$$\tilde{h}_{ly}(x,\zeta)=\frac{1}{p_l^2(\zeta)}\left[j\omega\varepsilon_l\frac{\partial\tilde{e}_{lz}(x,\zeta)}{\partial x}+j\zeta\tilde{j}_x(x,\zeta)\right] \tag{3.2.5}$$

Subsequent manipulation [22] uncouples the spectral Maxwell equations to obtain the spectral Helmholtz equations.

$$\tilde{\nabla}_t^2\tilde{e}_{lz}(x,\zeta)-p_l^2(\zeta)\tilde{e}_{lz}(x,\zeta)=\frac{j\zeta}{\varepsilon_l}\tilde{\rho}(x,\zeta)+j\omega\mu_0\tilde{j}_z(x,\zeta)$$
$$\tilde{\nabla}_t^2\tilde{h}_{lz}(x,\zeta)-p_l^2(\zeta)\tilde{h}_{lz}(x,\zeta)=-\hat{z}\cdot\left\{\nabla_t\times\tilde{\boldsymbol{j}}_t(\boldsymbol{x},\zeta)\right\} \tag{3.2.6}$$

And spectral continuity equation $\tilde{\nabla}\cdot\tilde{\boldsymbol{j}}(\boldsymbol{x},\zeta)+j\omega\tilde{\rho}(x,\zeta)=0$ allows Eqn. (3.2.4) to be expressed as

$$\tilde{\nabla}_t^2\tilde{e}_{lz}-p_l^2\tilde{e}_{lz}=-\frac{\zeta}{\omega\varepsilon_l}\left(\tilde{\nabla}_t+\hat{z}j\zeta\right)\cdot\tilde{\boldsymbol{j}}+j\omega\mu_0\tilde{j}_z$$
$$\tilde{\nabla}_t^2\tilde{h}_{lz}-p_l^2\tilde{h}_{lz}=-\hat{z}\cdot\left(\tilde{\nabla}_t\times\tilde{\boldsymbol{j}}_t\right) \tag{3.2.7}$$

It is observed that $\tilde{e}_{lz}(x,\zeta)$ is the spectral-field generating function from Eqn. (3.2.5) and given by

$$\left[\frac{\partial^2}{\partial x^2}-p_l^2(\zeta)\right]\tilde{e}_{lz}(x,\zeta)=-\frac{\zeta}{\omega\varepsilon_l}\frac{\partial\tilde{j}_x(x,\zeta)}{\partial x}-\frac{jp_l^2(\zeta)}{\omega\varepsilon_l}\tilde{j}_z(x,\zeta) \tag{3.2.8}$$

3.2.1 SPECTRAL COVER FIELD FORMULATION

Decomposition into the principal and reflected spectral cover fields leads to

$$\tilde{e}_{1z}(x,\zeta)=\tilde{e}_{1z}^{p}(x,\zeta)+\tilde{e}_{1z}^{r}(x,\zeta) \tag{3.2.9}$$

Eqn. (3.2.8) yields the inhomogeneous solution for the principal spectral field and the homogeneous solution for the reflected spectral field in agreement with Eqn. (3.2.9). The spectral EM fields in the cover layer are determined through some rigorous formulation (see Appendix C) and subsequent manipulation to determine the other coefficients leads to the complete spectral EM field representation for the *l'th* layer $(l=1,2,3)$ as

$$\begin{aligned}\tilde{e}_{1z}(x,\zeta)=&-\frac{1}{j\omega\varepsilon_1}\int_0^{\infty}\left[j\zeta p_1\tilde{j}_x\operatorname{sgn}(x-x')+p_1^2\tilde{j}_z\right]\frac{e^{-p_1|x-x'|}}{2p_1}dx'\\&+\frac{1}{j\omega\varepsilon_1}2\tilde{\Lambda}\varepsilon_1\left[\varepsilon_2 p_3\cosh(p_2 t)+\varepsilon_3 p_2\sinh(p_2 t)\right]\\&\left\{\int_0^{\infty}\left(j\zeta\tilde{j}_x-p_1\tilde{j}_z\right)\frac{e^{-p_1x'}}{2p_1}dx'+\frac{j\zeta}{p_1^2}\tilde{j}_x\right\}e^{-p_1x}\\&-\frac{1}{j\omega\varepsilon_1}\int_0^{\infty}\left(j\zeta p_1\tilde{j}_x-p_1^2\tilde{j}_z\right)\frac{e^{-p_1(x+x')}}{2p_1}dx'\end{aligned}$$

$$\begin{aligned}\tilde{e}_{1x}(x,\zeta)=&\frac{1}{j\omega\varepsilon_1}\left\{\int_0^{\infty}\left[\zeta^2\tilde{j}_x-j\zeta p_1\tilde{j}_z\operatorname{sgn}(x-x')\right]\frac{e^{-p_1|x-x'|}}{2p_1}dx'+\frac{2k_1^2}{p_1^2}\tilde{j}_x\right\}\\&-\frac{1}{j\omega\varepsilon_1}2\tilde{\Lambda}\varepsilon_1\left[\varepsilon_2 p_3\cosh(p_2 t)+\varepsilon_3 p_2\sinh(p_2 t)\right]\\&\left\{\int_0^{\infty}\left(\frac{\zeta^2}{p_1}\tilde{j}_x+j\zeta\tilde{j}_z\right)\frac{e^{-p_1x'}}{2p_1}dx'+\frac{\zeta^2}{p_1^3}\tilde{j}_x\right\}e^{-p_1x}\\&+\frac{1}{j\omega\varepsilon_1}\int_0^{\infty}\left(\zeta^2\tilde{j}_x+j\zeta p_1\tilde{j}_z\right)\frac{e^{-p_1(x+x')}}{2p_1}dx'\end{aligned}$$

$$\tilde{h}_{1y}(x,\zeta)=\int_0^\infty\left[j\zeta\tilde{j}_x+p_1\tilde{j}_z\,\mathrm{sgn}(x-x')\right]\frac{e^{-p_1|x-x'|}}{2p_1}dx'+\frac{2j\zeta}{p_1^2}\tilde{j}_x$$
$$-2\tilde{\Lambda}\varepsilon_1\left[\varepsilon_2 p_3\cosh(p_2 t)+\varepsilon_3 p_2\sinh(p_2 t)\right]$$
$$\left\{\int_0^\infty\left(\frac{j\zeta}{p_1}\tilde{j}_x-\tilde{j}_z\right)\frac{e^{-p_1x'}}{2p_1}dx'+\frac{\zeta}{p_1^3}\tilde{j}_x\right\}e^{-p_1x}$$
$$+\int_0^\infty\left(j\zeta\tilde{j}_x-p_1\tilde{j}_z\right)\frac{e^{-p_1(x+x')}}{2p_1}dx'$$

3.2.2 SPECTRAL FILM FIELD FORMULATION

The spectral film fields are

$$\tilde{e}_{2z}(x,\zeta)=\frac{1}{j\omega\varepsilon_1}2\tilde{\Lambda}\varepsilon_1\left\{\int_0^\infty\left(j\zeta\tilde{j}_x-p_1\tilde{j}_z\right)\frac{e^{-p_1x'}}{2p_1}dx'+\frac{j\zeta}{p_1^2}\tilde{j}_x\right\}$$
$$\left\{\varepsilon_2 p_3\cosh\left[p_2(x+t)\right]+\varepsilon_3 p_2\sinh\left[p_2(x+t)\right]\right\}$$

$$\tilde{e}_{2x}(x,\zeta)=\frac{1}{j\omega\varepsilon_1}2\tilde{\Lambda}\varepsilon_1\left\{\int_0^\infty\left(\frac{\zeta^2}{p_2}\tilde{j}_x+\frac{j\zeta p_1}{p_2}\tilde{j}_z\right)\frac{e^{-p_1x'}}{2p_1}dx'+\frac{\zeta^2}{p_1^2p_2}\tilde{j}_x\right\}$$
$$\left\{\varepsilon_2 p_3\sinh\left[p_2(x+t)\right]+\varepsilon_3 p_2\cosh\left[p_2(x+t)\right]\right\}$$

$$\tilde{h}_{2y}(x,\zeta)=2\tilde{\Lambda}\varepsilon_2\left\{\int_0^\infty\left(\frac{j\zeta}{p_2}\tilde{j}_x-\frac{p_1}{p_2}\tilde{j}_z\right)\frac{e^{-p_1x'}}{2p_1}dx'+\frac{j\zeta}{p_1^2p_2}\tilde{j}_x\right\}$$
$$\left\{\varepsilon_2 p_3\sinh\left[p_2(x+t)\right]+\varepsilon_3 p_2\cosh\left[p_2(x+t)\right]\right\}$$

3.2.3 SPECTRAL SUBSTRATE FIELD FORMULATION

The spectral substrate fields are

$$\tilde{e}_{3z}(x,\zeta)=\frac{1}{j\omega\varepsilon_1}2\tilde{\Lambda}\varepsilon_1\varepsilon_2 p_3\left\{\int_0^{\infty}\left(j\zeta\tilde{j}_x-p_1\tilde{j}_z\right)\frac{e^{-p_1x'}}{2p_1}dx'+\frac{j\zeta}{p_1^2}\tilde{j}_x\right\}e^{p_3(x+t)}$$

$$\tilde{e}_{3x}(x,\zeta)=\frac{1}{j\omega\varepsilon_1}2\tilde{\Lambda}\varepsilon_1\varepsilon_2\left\{\int_0^{\infty}\left(\zeta^2\tilde{j}_x+j\zeta p_1\tilde{j}_z\right)\frac{e^{-p_1x'}}{2p_1}dx'+\frac{\zeta^2}{p_1^2}\tilde{j}_x\right\}e^{p_3(x+t)}$$

$$\tilde{h}_{3y}(x,\zeta)=2\tilde{\Lambda}\varepsilon_2\varepsilon_3\left\{\int_0^{\infty}\left(j\zeta\tilde{j}_x-p_1\tilde{j}_z\right)\frac{e^{-p_1x'}}{2p_1}dx'+\frac{j\zeta}{p_1^2}\tilde{j}_x\right\}e^{p_3(x+t)}$$

where

$$p_l=\sqrt{\zeta^2-k_l^2}\cdots l=1,2,3$$

$$\tilde{\Lambda}=\frac{2p_1p_2}{(\varepsilon_2p_3-\varepsilon_3p_2)(\varepsilon_1p_2-\varepsilon_2p_1)e^{-p_2t}+(\varepsilon_2p_3+\varepsilon_3p_2)(\varepsilon_1p_2+\varepsilon_2p_1)e^{p_2t}}$$

3.2.4 SPECTRAL GREEN'S DYAD REPRESENTATION

The spectral Green's dyads [23]-[25] for the spectral fields are obtained by

$$\tilde{\boldsymbol{e}}_1(x,\zeta)=\int_0^{\infty}\overline{\boldsymbol{g}}_1^{e}(x|x')\cdot\tilde{\boldsymbol{j}}(x',\zeta)dx'$$

$$\tilde{\boldsymbol{e}}_2(x,\zeta)=\int_0^{\infty}\overline{\boldsymbol{g}}_2^{e}(x|x')\cdot\tilde{\boldsymbol{j}}(x',\zeta)dx'$$

$$\tilde{\boldsymbol{e}}_3(x,\zeta)=\int_0^{\infty}\overline{\boldsymbol{g}}_3^{e}(x|x')\cdot\tilde{\boldsymbol{j}}(x',\zeta)dx'$$

$$\tilde{\boldsymbol{h}}_1(x,\zeta)=\int_0^{\infty}\overline{\boldsymbol{g}}_1^{h}(x|x')\cdot\tilde{\boldsymbol{j}}(x',\zeta)dx'$$

$$\tilde{\boldsymbol{h}}_2(x,\zeta)=\int_0^{\infty}\overline{\boldsymbol{g}}_2^{h}(x|x')\cdot\tilde{\boldsymbol{j}}(x',\zeta)dx'$$

$$\tilde{\boldsymbol{h}}_3(x,\zeta)=\int_0^{\infty}\overline{\boldsymbol{g}}_3^{h}(x|x')\cdot\tilde{\boldsymbol{j}}(x',\zeta)dx'$$

where

$$\overline{\boldsymbol{g}}_1^{e}(x|x')=\overline{\boldsymbol{g}}_{11}^{e}(x|x')+\overline{\boldsymbol{g}}_{12}^{e}(x|x')$$

$$\bar{\bar{g}}_2^e(x|x') = \bar{\bar{g}}_{21}^e(x|x')$$

$$\bar{\bar{g}}_3^e(x|x') = \bar{\bar{g}}_{31}^e(x|x')$$

$$\bar{\bar{g}}_1^h(x|x') = \bar{\bar{g}}_{11}^h(x|x') + \bar{\bar{g}}_{12}^h(x|x')$$

$$\bar{\bar{g}}_2^h(x|x') = \bar{\bar{g}}_{21}^h(x|x')$$

$$\bar{\bar{g}}_3^h(x|x') = \bar{\bar{g}}_{31}^h(x|x')$$

where $\bar{\bar{g}}_{lm}^e(x|x')$ represents the spectral Green's dyad for the spectral electric field in the *l'th* layer due to currents in or interactions with the *m'th* layer. And, the $\bar{\bar{g}}_{lm}^h(x|x')$ does for the spectral magnetic field in the *l'th* layer due to currents in or interactions with the *m'th* layer. Each spectral Green's dyad is represented by (see Appendix C)

$$g_{11xx}^e(x|x') = \frac{1}{j\omega\varepsilon_1}\left\{\frac{\zeta^2}{2p_1}\left[e^{-p_1|x-x'|} + e^{-p_1(x+x')}\right] + \frac{2k_1^2}{p_1^2}\delta(x-x')\right\}$$

$$g_{11xz}^e(x|x') = -\frac{1}{j\omega\varepsilon_1}\frac{j\zeta}{2}\left[\operatorname{sgn}(x-x')e^{-p_1|x-x'|} - e^{-p_1(x+x')}\right]$$

$$g_{11zx}^e(x|x') = -\frac{1}{j\omega\varepsilon_1}\frac{j\zeta}{2}\left[\operatorname{sgn}(x-x')e^{-p_1|x-x'|} + e^{-p_1(x+x')}\right]$$

$$g_{11zz}^e(x|x') = -\frac{1}{j\omega\varepsilon_1}\frac{p_1}{2}\left[e^{-p_1|x-x'|} - e^{-p_1(x+x')}\right]$$

$$g_{12xx}^e(x|x') = -\frac{1}{j\omega\varepsilon_1}2\tilde{\Lambda}\varepsilon_1\left[\varepsilon_2 p_3\cosh(p_2 t) + \varepsilon_3 p_2\sinh(p_2 t)\right]$$

$$\frac{\zeta^2}{p_1^2}\left[\frac{e^{-p_1 x'}}{2} + \frac{\delta(x-x')}{p_1}\right]e^{-p_1 x}$$

$$g_{12xz}^e(x|x') = \frac{1}{j\omega\varepsilon_1}j\zeta\tilde{\Lambda}\varepsilon_1\left[\varepsilon_2 p_3\cosh(p_2 t) + \varepsilon_3 p_2\sinh(p_2 t)\right]\frac{e^{-p_1(x+x')}}{p_1}$$

$$g^e_{12zx}(x|x') = \frac{1}{j\omega\varepsilon_1} 2\tilde{\Lambda}\varepsilon_1 \left[\varepsilon_2 p_3 \cosh(p_2 t) + \varepsilon_3 p_2 \sinh(p_2 t)\right] \frac{j\zeta}{p_1}\left[\frac{e^{-p_1 x'}}{2} + \frac{\delta(x-x')}{p_1}\right] e^{-p_1 x}$$

$$g^e_{12zz}(x|x') = -\frac{1}{j\omega\varepsilon_1} \tilde{\Lambda}\varepsilon_1 \left[\varepsilon_2 p_3 \cosh(p_2 t) + \varepsilon_3 p_2 \sinh(p_2 t)\right] e^{-p_1(x+x')}$$

$$g^e_{21xx}(x|x') = \frac{1}{j\omega\varepsilon_1} 2\tilde{\Lambda}\varepsilon_1 \frac{\zeta^2}{p_1 p_2}\left[\frac{e^{-p_1 x'}}{2} + \frac{\delta(x-x')}{p_1}\right] \left\{\varepsilon_2 p_3 \sinh\left[p_2(x+t)\right] + \varepsilon_3 p_2 \cosh\left[p_2(x+t)\right]\right\}$$

$$g^e_{21xz}(x|x') = \frac{1}{j\omega\varepsilon_1} j\zeta\tilde{\Lambda}\varepsilon_1 \left\{\varepsilon_2 p_3 \sinh\left[p_2(x+t)\right] + \varepsilon_3 p_2 \cosh\left[p_2(x+t)\right]\right\} \frac{e^{-p_1 x'}}{p_2}$$

$$g^e_{21zx}(x|x') = \frac{1}{j\omega\varepsilon_1} 2\tilde{\Lambda}\varepsilon_1 \frac{j\zeta}{p_1}\left[\frac{e^{-p_1 x'}}{2} + \frac{\delta(x-x')}{p_1}\right] \left\{\varepsilon_2 p_3 \cosh\left[p_2(x+t)\right] + \varepsilon_3 p_2 \sinh\left[p_2(x+t)\right]\right\}$$

$$g^e_{21zz}(x|x') = -\frac{1}{j\omega\varepsilon_1} \tilde{\Lambda}\varepsilon_1 \left\{\varepsilon_2 p_3 \cosh\left[p_2(x+t)\right] + \varepsilon_3 p_2 \sinh\left[p_2(x+t)\right]\right\} e^{-p_1 x'}$$

$$g^e_{31xx}(x|x') = \frac{1}{j\omega\varepsilon_1} 2\tilde{\Lambda}\varepsilon_1\varepsilon_2 \frac{\zeta^2}{p_1}\left[\frac{e^{-p_1 x'}}{2} + \frac{\delta(x-x')}{p_1}\right] e^{p_3(x+t)}$$

$$g^e_{31xz}(x|x') = \frac{1}{j\omega\varepsilon_1} j\zeta\tilde{\Lambda}\varepsilon_1\varepsilon_2 e^{-p_1 x'} e^{p_3(x+t)}$$

$$g^e_{31zx}(x|x') = \frac{1}{j\omega\varepsilon_1} 2\tilde{\Lambda}\varepsilon_1\varepsilon_2 p_3 \frac{j\zeta}{p_1}\left[\frac{e^{-p_1 x'}}{2} + \frac{\delta(x-x')}{p_1}\right] e^{p_3(x+t)}$$

$$g^e_{31zz}(x|x') = -\frac{1}{j\omega\varepsilon_1} \tilde{\Lambda}\varepsilon_1\varepsilon_2 p_3 e^{-p_1 x'} e^{p_3(x+t)}$$

$$g^h_{11yx}(x|x') = \frac{j\zeta}{p_1}\left[\frac{e^{-p_1|x-x'|}}{2} + \frac{e^{-p_1(x+x')}}{2} + \frac{2\delta(x-x')}{p_1}\right]$$

$$g^h_{11yz}(x|x') = \frac{1}{2}\left[\operatorname{sgn}(x-x')e^{-p_1|x-x'|} - e^{-p_1(x+x')}\right]$$

$$g^h_{12yx}(x|x') = -2\tilde{\Lambda}\varepsilon_1\left[\varepsilon_2 p_3\cosh(p_2 t) + \varepsilon_3 p_2\sinh(p_2 t)\right]$$
$$\frac{\zeta}{p_1^2}\left[j\frac{e^{-p_1 x'}}{2} + \frac{\delta(x-x')}{p_1}\right]e^{-p_1 x}$$

$$g^h_{12yz}(x|x') = \tilde{\Lambda}\varepsilon_1\left[\varepsilon_2 p_3\cosh(p_2 t) + \varepsilon_3 p_2\sinh(p_2 t)\right]\frac{e^{-p_1(x+x')}}{p_1}$$

$$g^h_{21yx}(x|x') = 2\tilde{\Lambda}\varepsilon_2\frac{j\zeta}{p_1 p_2}\left[\frac{e^{-p_1 x'}}{2} + \frac{\delta(x-x')}{p_1}\right]$$
$$\left\{\varepsilon_2 p_3\sinh\left[p_2(x+t)\right] + \varepsilon_3 p_2\cosh\left[p_2(x+t)\right]\right\}$$

$$g^h_{21yz}(x|x') = -\tilde{\Lambda}\varepsilon_2\left\{\varepsilon_2 p_3\sinh\left[p_2(x+t)\right] + \varepsilon_3 p_2\cosh\left[p_2(x+t)\right]\right\}\frac{e^{-p_1 x'}}{p_2}$$

$$g^h_{31yx}(x|x') = 2\tilde{\Lambda}\varepsilon_2\varepsilon_3\frac{j\zeta}{p_1}\left[\frac{e^{-p_1 x'}}{2} + \frac{\delta(x-x')}{p_1}\right]e^{p_3(x+t)}$$

$$g^h_{31yz}(x|x') = -\tilde{\Lambda}\varepsilon_2\varepsilon_3 e^{-p_1 x'}e^{p_3(x+t)}$$

where

$$p_l = \sqrt{\zeta^2 - k_l^2}\cdots l = 1,2,3$$

$$k_l = \omega\sqrt{\mu_0\varepsilon_l}$$

$$\tilde{\Lambda} = \frac{2p_1 p_2}{(\varepsilon_2 p_3 - \varepsilon_3 p_2)(\varepsilon_1 p_2 - \varepsilon_2 p_1)e^{-p_2 t} + (\varepsilon_2 p_3 + \varepsilon_3 p_2)(\varepsilon_1 p_2 + \varepsilon_2 p_1)e^{p_2 t}}$$

Each scalar component of the spectral EM fields is completely determined by the spectral Green's dyad above and the spectral current density $\tilde{\boldsymbol{j}}(\boldsymbol{x},\zeta) = \hat{x}\tilde{j}_x(x,\zeta) + \hat{z}\tilde{j}_z(x,\zeta)$.

3.2.5 STEEPEST-DESCENT PATH IN THE COMPLEX AXIAL TRANSFORM PLANE *(DIRECT METHOD)*

The spectral Green's dyads yield the spectral EM fields such that

$$\tilde{e}_l(x,\zeta)=\int_{-\infty}^{\infty}\bar{g}_l^e(x|x')\cdot\tilde{j}(x,\zeta)dx'$$
$$\tilde{h}_l(x,\zeta)=\int_{-\infty}^{\infty}\bar{g}_l^h(x|x')\cdot\tilde{j}(x,\zeta)dx'$$

The inverse Fourier transform of $\tilde{e}_l(x,\zeta)$ and $\tilde{h}_l(x,\zeta)$ yields

$$E_l(x,z)=\iint_{\infty}\bar{G}_l^e(x,z|x',z')\cdot J(x',z')dx'dz'$$
$$H_l(x,z)=\iint_{\infty}\bar{G}_l^h(x,z|x',z')\cdot J(x',z')dx'dz'$$

where

$$\bar{G}_l^e(x,z|x',z')=\frac{1}{2\pi}\int_{-\infty}^{\infty}\bar{g}_l^e(x|x')e^{j\zeta(z-z')}d\zeta \qquad (3.2.10)$$
$$\bar{G}_l^h(x,z|x',z')=\frac{1}{2\pi}\int_{-\infty}^{\infty}\bar{g}_l^h(x|x')e^{j\zeta(z-z')}d\zeta$$
$$\cdots l=1,2,3$$

The Green's dyads $\bar{G}_l^e(x,z|x',z')$ and $\bar{G}_l^h(x,z|x',z')$ for electric and magnetic fields are represented in Appendix D. The method of identification of the steepest-descent path in the complex ζ-plane is previously discussed in Section 2.3. From Eqn. (3.2.10), it is recognized that the steepest-descent path for the Green's dyad representation rather than for the field representation is chosen to be considered. The transformation to polar coordinate (r,θ) is depicted in Fig. 3.2.1.

For cover layer field,

$$x=r\cos\theta$$
$$z=r\sin\theta \qquad (3.2.11)$$

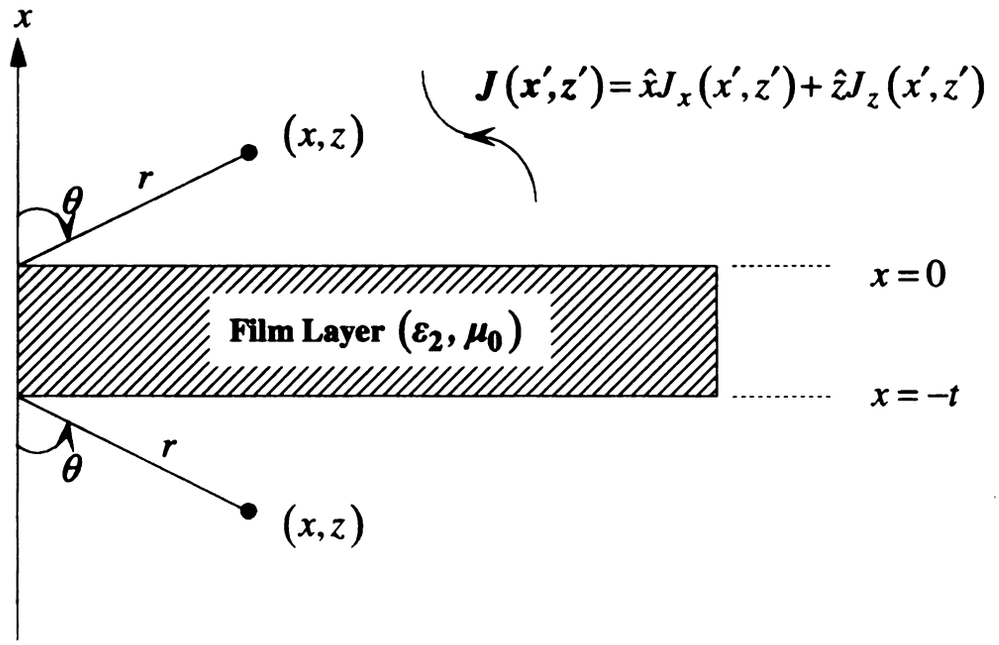

Figure 3.2.1 Polar coordinate transformations.

For substrate layer field,

$$\begin{aligned} x+t &= -r\cos\theta \\ z &= r\sin\theta \end{aligned} \tag{3.2.12}$$

Noting that the magnetic field has only a y-component, the spectral Green's dyad for the magnetic field is considered to identify the steepest-descent path.

For the far zone,

$$x \gg x' \rightarrow |x-x'| = x-x' \tag{3.2.13}$$

Therefore, the spectral magnetic Green's dyad components become

$$g^h_{11yx}(x|x') \approx \frac{j\zeta}{p_1}\cosh(p_1 x')e^{-p_1 x}$$

$$g^h_{11yz}(x|x') \approx \sinh(p_1 x')e^{-p_1 x}$$

$$g^h_{12yx}(x|x') = -j\zeta\tilde{\Lambda}\varepsilon_1\left[\varepsilon_2 p_3\cosh(p_2 t)+\varepsilon_3 p_2\sinh(p_2 t)\right]\frac{e^{-p_1 x'}}{p_1^2}e^{-p_1 x}$$

$$g^h_{12yz}(x|x') = \tilde{\Lambda}\varepsilon_1\left[\varepsilon_2 p_3\cosh(p_2 t)+\varepsilon_3 p_2\sinh(p_2 t)\right]\frac{e^{-p_1 x'}}{p_1}e^{-p_1 x}$$

$$g^h_{31yx}(x|x') \approx \tilde{\Lambda}\varepsilon_2\varepsilon_3\frac{j\zeta}{p_1}e^{-p_1 x'}e^{p_3(x+t)}$$

$$g^h_{31yz}(x|x') = -\tilde{\Lambda}\varepsilon_2\varepsilon_3 e^{-p_1 x'}e^{p_3(x+t)}$$

For simplicity, choosing $g^h_{11yx}(x|x')$ and $g^h_{31yx}(x|x')$ leads to (since the multipliers of $e^{j\zeta(z-z')}$ are odd in ζ)

$$G^h_{11yx}(x,z|x',z') = -\frac{1}{2\pi}\int_{-\infty}^{\infty}\frac{j\zeta}{p_1}\cosh(p_1 x')e^{j\zeta z'}e^{-p_1 x}e^{-j\zeta z}d\zeta \quad (3.2.14)$$

and

$$G^h_{31yx}(x,z|x',z') = -\frac{1}{2\pi}\int_{-\infty}^{\infty}\tilde{\Lambda}\varepsilon_2\varepsilon_3\frac{j\zeta}{p_1}e^{-p_1 x'}e^{j\zeta z'}e^{p_3(x+t)}e^{-j\zeta z}d\zeta \quad (3.2.15)$$

Substituting Eqn. (3.2.11) into Eqn. (3.2.14) yields

$$G^h_{12yx}(x,z|x',z') = -\frac{1}{2\pi}\int_{-\infty}^{\infty}\frac{j\zeta}{p_1}\cosh(p_1 x')e^{j\zeta z'}e^{r(-j\zeta\sin\theta-p_1\cos\theta)}d\zeta \quad (3.2.16)$$

Substituting Eqn. (3.2.12) into Eqn. (3.2.15) yields

$$G^h_{31yx}(x,z|x',z') = -\frac{1}{2\pi}\int_{-\infty}^{\infty}\tilde{\Lambda}\varepsilon_2\varepsilon_3\frac{j\zeta}{p_1}e^{-p_1 x'}e^{j\zeta z'}e^{r(-j\zeta\sin\theta-p_3\cos\theta)}d\zeta \quad (3.2.17)$$

In agreement with Eqn. (2.3.9),

$$\delta(\zeta) = -j\zeta\sin\theta - p_l\cos\theta\cdots l = 1,3 \quad (3.2.18)$$

From Eqn. (2.3.10), the saddle point in the complex ζ -plane is located by

$$\zeta_0 = k_l \sin\theta \tag{3.2.19}$$

where the observation aspect angle is defined by

$$\theta = \begin{cases} l=1: \tan^{-1}\left(\dfrac{z}{x}\right) \\ l=3: \tan^{-1}\left(\dfrac{z}{|x+t|}\right) \end{cases} \tag{3.2.20}$$

It is observed that $\theta > 0$ for $z > 0$ and $\theta < 0$ for $z < 0$. Therefore, it is necessary to close in the lower half plane (*LHP*) to determine the field for $\theta > 0$ and vice versa.

The steepest-descent path in the complex ζ -plane is identified as in Section 2.3.1.

$$\left[\frac{\zeta}{k_l} + \left(\frac{\zeta}{k_l}\right)^*\right]\frac{\sin\theta}{2} - j\left[\frac{p_l(\zeta)}{k_l} - \left\{\frac{p_l(\zeta)}{k_l}\right\}^*\right]\frac{\cos\theta}{2} = 1 \tag{3.2.21}$$

which confirms Eqn. (2.3.15).

3.2.6 TRANSFORMATION OF SDP FROM THE COMPLEX ϕ -PLANE TO THE COMPLEX ζ -PLANE *(INDIRECT METHOD)*

As previously discussed in Section 2.3.2, the steepest-descent saddle-point method can be implemented in the complex ϕ -plane defined by

$$\phi = \sigma + j\eta \tag{3.2.22}$$

The subsequent transformation in (p_l, ζ) is followed by

$$p_l = jk_l \cos\phi$$
$$\zeta = k_l \sin\phi$$

Then, the integral representation becomes

$$
\begin{aligned}
&G^h_{lmyx}(x,z|x',z') \\
&=-\frac{1}{2\pi}\int_{-\pi/2-j\infty}^{\pi/2+j\infty}\frac{\Sigma^h_{lmyx}(k_l\sin\phi)}{k_1\cos\phi}e^{r(-jk_l\sin\phi\sin\theta-jk_l\cos\phi\cos\theta)}k_l\cos\phi d\phi \\
&=-\frac{1}{2\pi}\left(\frac{k_l}{k_1}\right)\int_{-\pi/2-j\infty}^{\pi/2+j\infty}\Sigma^h_{lmyx}(k_l\sin\phi)e^{-jk_lr\cos(\phi-\theta)}d\phi \\
&\textit{where} \\
&\Sigma^h_{lmyx}(k_l\sin\phi) \\
&=\begin{cases} l=1, m=1: k_1\sin\phi\cosh(jk_1x'\cos\phi)e^{jk_1z'\sin\phi} \\ l=3, m=1: \varepsilon_2\varepsilon_3\tilde{\Lambda}(k_3\sin\phi)k_3\sin\phi e^{-jk_1x'\cos\phi}e^{jk_3z'\sin\phi} \end{cases}
\end{aligned}
\tag{3.2.23}
$$

Comparing with Eqn. (2.3.31), it is observed from Section 2.3.2 that the saddle-point asymptotic form for the far zone field in the *l'th layer* becomes,

$$
\begin{aligned}
&G^h_{lmyx}(r,\theta)\approx-\frac{1}{2\pi}\left(\frac{k_l}{k_1}\right)\sqrt{\frac{2}{\pi}}\Sigma^h_{lmyx}(k_l\sin\theta)\frac{e^{-j(k_lr-\pi/4)}}{\sqrt{k_lr}} \\
&\textit{where} \\
&\Sigma^h_{lmyx}(k_l\sin\theta) \\
&=\begin{cases} l=1, m=1: k_1\sin\theta\cosh(jk_1x'\cos\theta)e^{jk_1z'\sin\theta} \\ l=3, m=1: \varepsilon_2\varepsilon_3\tilde{\Lambda}(k_3\sin\theta)k_3\sin\theta e^{-jk_1x'\cos\theta}e^{jk_3z'\sin\theta} \end{cases}
\end{aligned}
\tag{3.2.24}
$$

where $\phi=\theta$ is the *saddle point*. In accordance with Eqns. (2.3.27) and (3.2.23),

$$
\left[\frac{\zeta}{k_l}+\left(\frac{\zeta}{k_l}\right)^*\right]\frac{\sin\theta}{2}-j\left[\frac{p_l(\zeta)}{k_l}-\left\{\frac{p_l(\zeta)}{k_l}\right\}^*\right]\frac{\cos\theta}{2}=1 \tag{3.2.25}
$$

The above identifies the steepest-descent path in the complex ζ-plane as illustrated in Eqn. (2.3.35), which also confirms Eqn. (2.3.15).

3.3 THE BRANCH CUT

The appropriate branch cuts were previously identified in Section 2.4.

3.4 ALTERNATIVE INTEGRATION PATH

As depicted in Fig. 3.4.1 and applying Cauchy's integral theorem leads to

$$\int_{C-C_{b1}-C_{b3}-C_p-C_\infty} \Psi^h_{lm\alpha\beta}\left(x,z|x',z':\zeta\right)d\zeta = 0 \tag{3.4.1}$$

and $\Psi^h_{lm\alpha\beta}\left(x,z|x',z':\zeta\right)$ represents the integrand of Green's dyad for the magnetic field $G^h_{lm\alpha\beta}\left(x,z|x',z':\zeta\right)$ for $l=1,2,3$ and $m=1,2$ (see Appendix D).

The discrete guided-mode is associated with $\zeta=\pm\zeta_p$ as previously discussed in Chapter 2.5. Those poles are determined by TM characteristic eigenvalue equation

$$\left(\frac{\varepsilon_3}{\varepsilon_1}p_1+p_3\right)p_2+\left(\frac{\varepsilon_3}{\varepsilon_2}p_2^2+\frac{\varepsilon_2}{\varepsilon_1}p_1p_3\right)\tanh\left(p_2t\right)=0 \tag{3.4.2}$$

which is implicated from zeros in the denominator of $\tilde{\Lambda}(\zeta)$. For the far zone, the pole residue contribution

$$\int_{C_p} \Psi^h_{lm\alpha\beta}\left(x,z|x',z':\zeta\right)d\zeta \to 0 \tag{3.4.3}$$

As discussed in Section 2.5, the bound mode propagation spectrum is contributed to by the full residue about C_p in Eqn. (3.4.3). However, the bound-mode spectrum on the $\mathrm{Re}\{\zeta\}$-axis inversion in Fig. 2.5.2 is contributed by half residue about R_p.

Due to the intrinsic nature of TM mode excitation, not only currents but also charges contribute to the electric field since charges are implicated by the continuity equation. So,

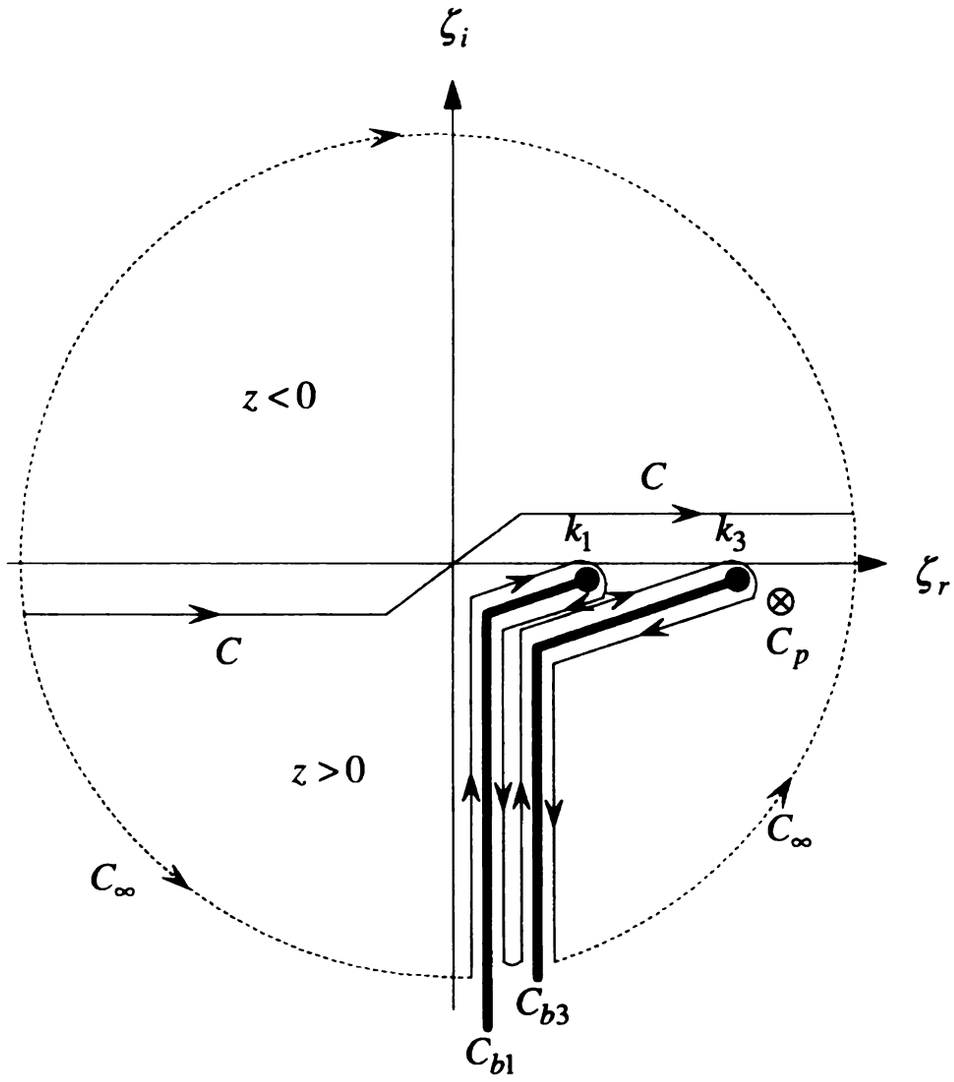

Figure 3.4.1 **Singularities and alternative integration path in the complex ζ-plane on top Riemann sheet for the complete proper propagation spectrum. Cover and substrate layers are presumably considered to be in the low-loss limit.**

since integrands of electric Green's dyads do not vanish when $|\zeta| \to \infty$ for $x = x'$ and $z = z'$. A δ-singularity is consequently needed at points in source region [26], [27] for convergence.

$$\begin{aligned}
&\int_C \Psi^e_{lm\alpha\beta}(x,z|x',z':\zeta)d\zeta \\
&= \chi\delta(x-x')\delta(z-z') + \int_{C_b=C_{b1}+C_{b3}} \Psi^e_{lm\alpha\beta}(x,z|x',z':\zeta)d\zeta \\
&+ \int_{C_p} \Psi^e_{lm\alpha\beta}(x,z|x',z':\zeta)d\zeta \qquad (3.4.4)
\end{aligned}$$

where

$l = 1,2,3$

$m = 1,2$

$\Psi^e_{lm\alpha\beta}(x,z|x',z':\zeta)$ represents the integrand of $G^e_{lm\alpha\beta}(x,z|x',z')$ for $\alpha, \beta = x$ or z (see Appendix D). To determine the unknown constant χ, integration over (x',z') in a small cross section s'_δ which contains the field point (x,z) is performed [26], [27].

$$\begin{aligned}
&\int_{S_\delta'} \chi\delta(x-x')\delta(z-z')dx'dz' \\
&= \int_{S'_\delta} \left\{ \int_C \Psi^e_{lm\alpha\beta}(x,z|x',z':\zeta)d\zeta - \int_{C_b} \Psi^e_{lm\alpha\beta}(x,z|x',z':\zeta)d\zeta \right. \qquad (3.4.5) \\
&\left. - \int_{C_p} \Psi^e_{lm\alpha\beta}(x,z|x',z':\zeta)d\zeta \right\} dx'dz'
\end{aligned}$$

Hence,

$$\begin{aligned}
\therefore \chi = \lim_{S'_\delta \to 0} \int_{S'_\delta} &\left\{ \int_C \Psi^e_{lm\alpha\beta}(x,z|x',z':\zeta)d\zeta - \int_{C_b} \Psi^e_{lm\alpha\beta}(x,z|x',z':\zeta)d\zeta \right. \\
&\left. - \int_{C_p} \Psi^e_{lm\alpha\beta}(x,z|x',z':\zeta)d\zeta \right\} dx'dz' \qquad (3.4.6)
\end{aligned}$$

and the unknown constant χ can be determined numerically.

However, the magnetic Green's dyads are never contaminated by the continuity equation then $\Psi^h_{lm\alpha\beta}(x,z|x',z':\zeta)$ still converges even if $|\zeta|\to\infty$ for $x=x'$ and $z=z'$.

$$\int_{C_\infty}\Psi^h_{lm\alpha\beta}(x,z|x',z':\zeta)d\zeta\to 0 \tag{3.4.7}$$

Finally, Eqn. (3.4.1) reduces to

$$\int_C\Psi^h_{lm\alpha\beta}(x,z|x',z':\zeta)d\zeta=\int_{C_b=C_{b1}+C_{b3}}\Psi^h_{lm\alpha\beta}(x,z|x',z':\zeta)d\zeta \tag{3.4.8}$$

Therefore, the electric field can finally be determined from the magnetic field using a Maxwell equation and convergence problems are avoided.

3.5 STEEPEST-DESCENT EVALUATION OF COVER FIELD

From Appendix B, the steepest-descent path for the *l'th layer* becomes

$$\begin{aligned}&\zeta=\zeta'+j\zeta''=(\zeta',\zeta'')\\&where\\&\zeta''=\pm\frac{|\zeta'-k_l\sin\theta||k_l-\zeta'\sin\theta|}{\cos\theta\sqrt{(\zeta'\cos\theta)^2+(k_l-\zeta'\sin\theta)^2}}\end{aligned} \tag{3.5.1}$$

where it is noted in Section 2.6 that $\zeta'=k_l\sin\theta$ is the saddle point. The sign of the observation aspect angle θ is determined by Eqn. (3.2.20) as

$$\begin{cases}z>0\,(LHP):\theta>0\\z<0\,(UHP):\theta<0\end{cases} \tag{3.5.2}$$

where *UHP* and *LHP* indicate the *Upper Half Plane* and *Lower Half Plane* in the complex ζ-plane. The steepest-descent paths in the complex ζ-plane for the cover layer field at various observation aspect angles are depicted in Fig. 3.5.1.

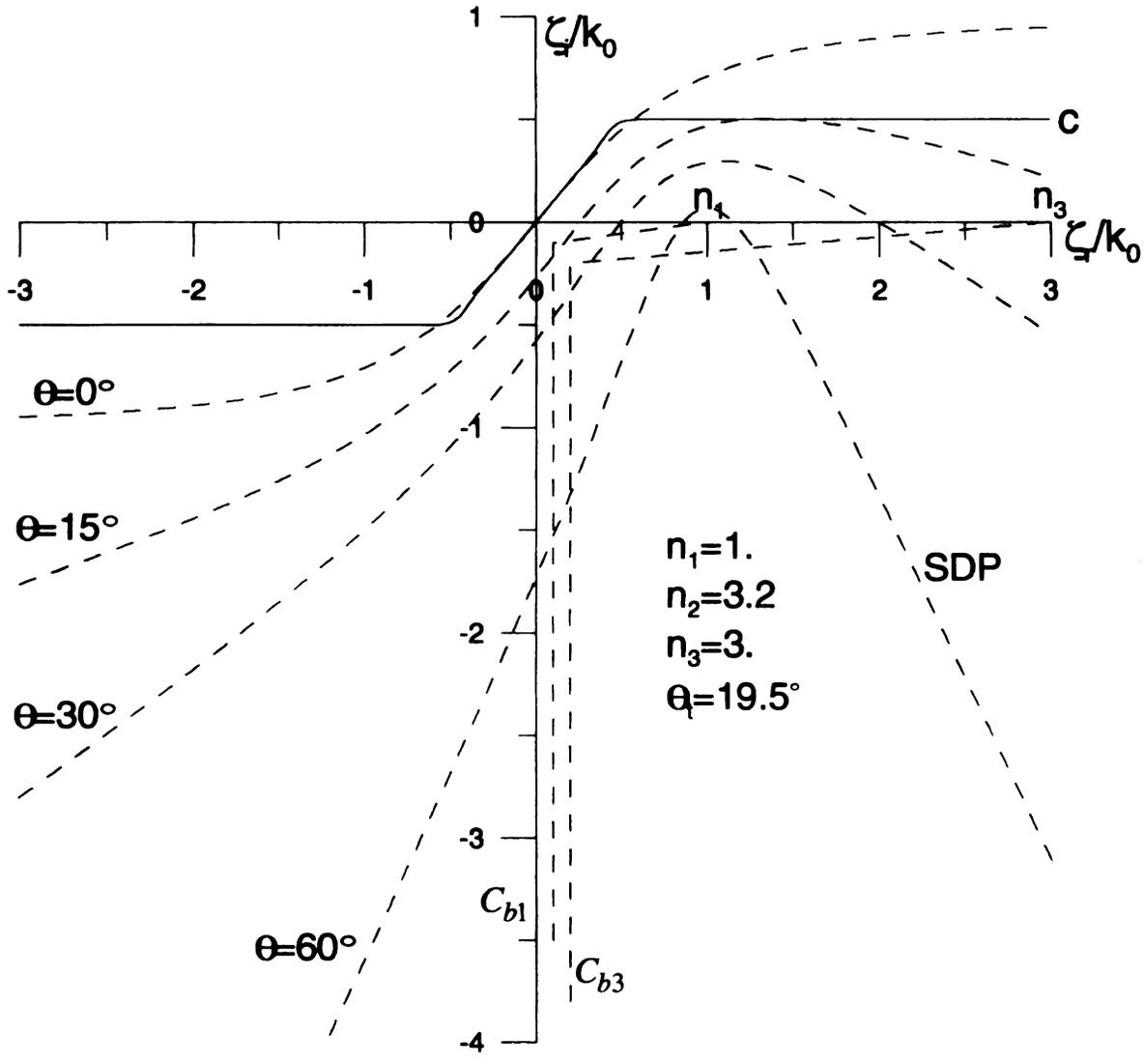

Figure 3.5.1 The steepest-descent paths in the complex ζ -plane for the cover layer field calculation at various observation aspect angles. The asymmetric planar dielectric waveguide consists of cover, guiding and substrate layers with indices $n_1 = 1$, $n_2 = 3.2$, and $n_3 = 3$ respectively.

A threshold aspect angle is defined by

$$\theta_t = \frac{\pi}{2} - \cos^{-1}\left(\frac{n_1}{n_3}\right) > 0$$

for $z > 0$ in agreement with Eqn. (2.6.3). And it is observed that $\theta_t > 0$ for $z > 0$ and $\theta_t < 0$ for $z < 0$. For $\theta < \theta_t$, the steepest-descent path can be directly connected to the real axis inversion contour on the top sheet of the 4-sheeted Riemann surface as depicted in Fig. 2.6.2.

$$\oint_{C-SDP-C_p-C_\infty} \Psi^h_{lm\alpha\beta}(x,z|x',z':\zeta)d\zeta = 0 \tag{3.5.3}$$

In agreement with Eqn. (3.4.3) and Eqn. (3.4.7),

$$\int_C \Psi^h_{lm\alpha\beta}(x,z|x',z':\zeta)d\zeta = \int_{SDP} \Psi^h_{lm\alpha\beta}(x,z|x',z':\zeta)d\zeta \tag{3.5.4}$$

Therefore, from Eqn. (3.4.8)

$$\int_{SDP} \Psi^h_{lm\alpha\beta}(x,z|x',z':\zeta)d\zeta = \int_{C_b=C_{b1}+C_{b3}} \Psi^h_{lm\alpha\beta}(x,z|x',z':\zeta)d\zeta \tag{3.5.5}$$

But, it was observed in Section 3.4 that the integrands of the electric Green's dyads are contributed to by an electric charge distribution from the continuity equation within the source region [26], [27]. Therefore, in agreement with Eqn. (3.4.4),

$$\begin{aligned}
&\int_C \Psi^e_{lm\alpha\beta}(x,z|x',z':\zeta)d\zeta \\
&= \chi\delta(x-x')\delta(z-z') + \int_{SDP} \Psi^e_{lm\alpha\beta}(x,z|x',z':\zeta)d\zeta \\
&+ \int_{C_p} \Psi^e_{lm\alpha\beta}(x,z|x',z':\zeta)d\zeta
\end{aligned} \tag{3.5.6}$$

where

$l = 1, 2, 3$ $m = 1, 2$ *and* $\alpha, \beta = x$ *or* z

Then,

$$\therefore \chi = \lim_{S'_\delta \to 0} \int_{S'_\delta} \left\{ \int_C \Psi^e_{lm\alpha\beta}(x,z|x',z':\zeta)d\zeta - \int_{SDP} \Psi^e_{lm\alpha\beta}(x,z|x',z':\zeta)d\zeta \right. \\ \left. - \int_{C_p} \Psi^e_{lm\alpha\beta}(x,z|x',z':\zeta)d\zeta \right\} dx'dz' \tag{3.5.7}$$

where s'_δ is a small cross section of source region which contains the field point (x,z) [26], [27]. Comparing with Eqn. (3.4.6) and Eqn. (3.5.7) leads to

$$\int_{SDP} \Psi^e_{lm\alpha\beta}(x,z|x',z':\zeta)d\zeta = \int_{C_b=C_{b1}+C_{b3}} \Psi^e_{lm\alpha\beta}(x,z|x',z':\zeta)d\zeta \tag{3.5.8}$$

Therefore, it is observed that the steepest-descent contributions to the integrands of the electric or magnetic Green's dyads are equivalent to the proper branch cut contributions for $\theta < \theta_t$.

As previously discussed in Section 2.6, it is observed that the exponents in both the electric and magnetic Green's dyads only contain the cover layer wavenumber, $p_1(\zeta)$, on the top Riemann sheet. Hence, the closure condition can be satisfied. Therefore, for $\theta \geq \theta_t$ as depicted in Fig. 3.5.2

$$\oint_{C-SDP-C_{b3}-C_p-C_\infty} \Psi^e_{lm\alpha\beta}(x,z|x',z':\zeta)d\zeta = 0 \\ \oint_{C-SDP-C_{b3}-C_p-C_\infty} \Psi^h_{lm\alpha\beta}(x,z|x',z':\zeta)d\zeta = 0 \tag{3.5.9}$$

For the electric Green's dyad,

$$\int_C \Psi^e_{lm\alpha\beta}(x,z|x',z':\zeta)d\zeta \\ = \chi\delta(x-x')\delta(z-z') + \int_{SDP} \Psi^e_{lm\alpha\beta}(x,z|x',z':\zeta)d\zeta \\ + \int_{C_{b3}} \Psi^e_{lm\alpha\beta}(x,z|x',z':\zeta)d\zeta + \int_{C_p} \Psi^e_{lm\alpha\beta}(x,z|x',z':\zeta)d\zeta \tag{3.5.10}$$

The pole and δ-function contributions vanish in the far zone. For the magnetic Green's

dyad,

$$\begin{aligned}&\int_C \Psi^h_{lm\alpha\beta}(x,z|x',z':\zeta)d\zeta\\&=\int_{SDP}\Psi^h_{lm\alpha\beta}(x,z|x',z':\zeta)d\zeta+\int_{C_{b3}}\Psi^h_{lm\alpha\beta}(x,z|x',z':\zeta)d\zeta\end{aligned}\tag{3.5.11}$$

Similarly as in Section 2.6, another possible proper closure of the steepest-descent path to the $\mathrm{Re}\{\zeta\}$-axis inversion contour is the partial path deformation around the substrate layer branch cut as depicted in Fig. 3.5.3. The steepest-descent path only violates the substrate layer branch cut an odd number of times therefore it must be deformed partially about the substrate layer branch cut so that it can still remain on the top Riemann sheet, which allows it terminate properly to the $\mathrm{Re}\{\zeta\}$-axis inversion contour.

$$\begin{aligned}&\oint_{C-SDP-partial\{C_{b3}\}-C_p-C_\infty}\Psi^e_{lm\alpha\beta}(x,z|x',z':\zeta)d\zeta=0\\&\oint_{C-SDP-partial\{C_{b3}\}-C_p-C_\infty}\Psi^h_{lm\alpha\beta}(x,z|x',z':\zeta)d\zeta=0\end{aligned}\tag{3.5.12}$$

For the electric Green's dyad,

$$\begin{aligned}&\int_C \Psi^e_{lm\alpha\beta}(x,z|x',z':\zeta)d\zeta\\&=\chi\delta(x-x')\delta(z-z')+\int_{SDP}\Psi^e_{lm\alpha\beta}(x,z|x',z':\zeta)d\zeta\\&+\int_{partial\{C_{b3}\}}\Psi^e_{lm\alpha\beta}(x,z|x',z':\zeta)d\zeta+\int_{C_p}\Psi^e_{lm\alpha\beta}(x,z|x',z':\zeta)d\zeta\end{aligned}\tag{3.5.13}$$

The pole and δ-function contributions vanish in the far zone. For the magnetic Green's dyad,

$$\begin{aligned}&\int_C \Psi^h_{lm\alpha\beta}(x,z|x',z':\zeta)d\zeta\\&=\int_{SDP}\Psi^h_{lm\alpha\beta}(x,z|x',z':\zeta)d\zeta+\int_{partial\{C_{b3}\}}\Psi^h_{lm\alpha\beta}(x,z|x',z':\zeta)d\zeta\end{aligned}\tag{3.5.14}$$

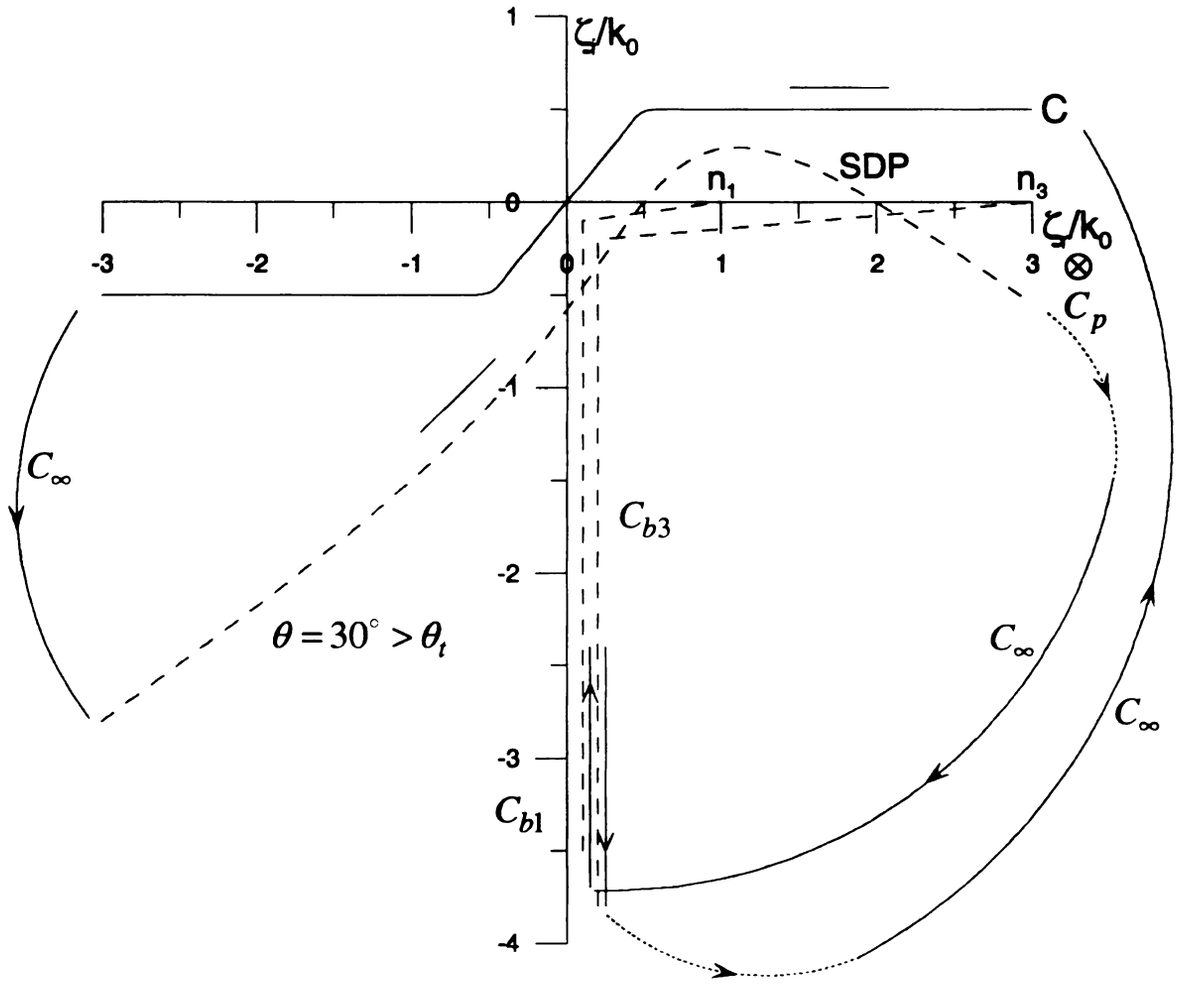

Figure 3.5.2 Proper closure of $\mathrm{Re}\{\zeta\}$-axis inversion contour C into SDP and substrate branch cut for $\theta > \theta_t$: $n_1 = 1., n_2 = 3.2, n_3 = 3., \theta_t = 19.5°$.

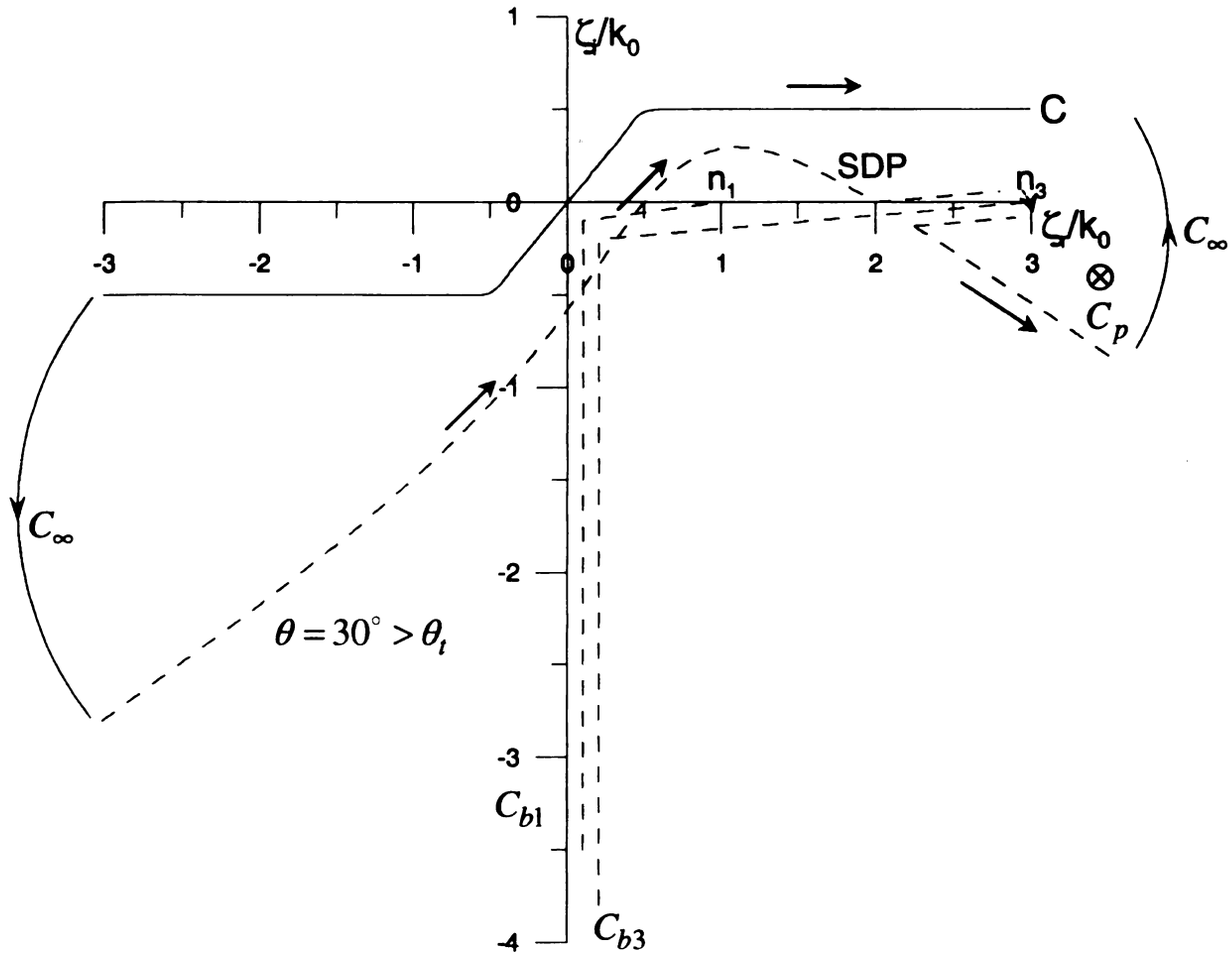

Figure 3.5.3 Proper closure of $\mathrm{Re}\{\zeta\}$-axis inversion contour C into SDP and partial C_{b3} for $\theta > \theta_t$: $n_1 = 1., n_2 = 3.2, n_3 = 3., \theta_t = 19.5^\circ$.

3.6 STEEPEST-DESCENT EVALUATION OF SUBSTRATE FIELD

The steepest-descent path in the complex ζ -plane is obtained from Eqn. (3.2.21) in agreement with $l=3$ for the substrate layer index. As previously discussed in Section 2.7, the steepest-descent saddle-point method fails if the saddle point $k_3 \sin\theta$ exists near guided-mode pole singularities, which causes the integrand of the Green's dyad in the substrate layer to vary rapidly near that point. The steepest-descent paths in the complex ζ -plane at various observation aspect angles are depicted in Fig. 3.6.1. It was observed in Section 2.7 that the steepest-descent path doesn't need to be deformed to one of the branch cuts but is connected to the $\mathrm{Re}\{\zeta\}$-axis inversion contour on the top Riemann sheet for $\theta < \theta_t$. For the magnetic Green's dyad,

$$\oint_{C-SDP-C_p-C_\infty} \Psi^h_{lm\alpha\beta}(x,z|x',z':\zeta)\,d\zeta = 0 \tag{3.6.1}$$

In agreement with Eqn. (3.4.3) and Eqn. (3.4.7),

$$\int_C \Psi^h_{lm\alpha\beta}(x,z|x',z':\zeta)\,d\zeta = \int_{SDP} \Psi^h_{lm\alpha\beta}(x,z|x',z':\zeta)\,d\zeta \tag{3.6.2}$$

It is previously observed that integrands of electric Green's dyads are contributed to by the electric charge distribution implicated by the continuity equation within a source region [26], [27]. However, since $x \neq x'$ and $z \neq z'$ in the substrate layer the substrate electric Green's dyad is not relevant to the continuity equation. Since

$$\int_C \Psi^e_{lm\alpha\beta}(x,z|x',z':\zeta)\,d\zeta = \int_{C_b=C_{b1}+C_{b3}} \Psi^e_{lm\alpha\beta}(x,z|x',z':\zeta)\,d\zeta \tag{3.6.3}$$

Then,

$$\int_{SDP} \Psi^e_{lm\alpha\beta}(x,z|x',z':\zeta)\,d\zeta = \int_{C_b=C_{b1}+C_{b3}} \Psi^e_{lm\alpha\beta}(x,z|x',z':\zeta)\,d\zeta \tag{3.6.4}$$

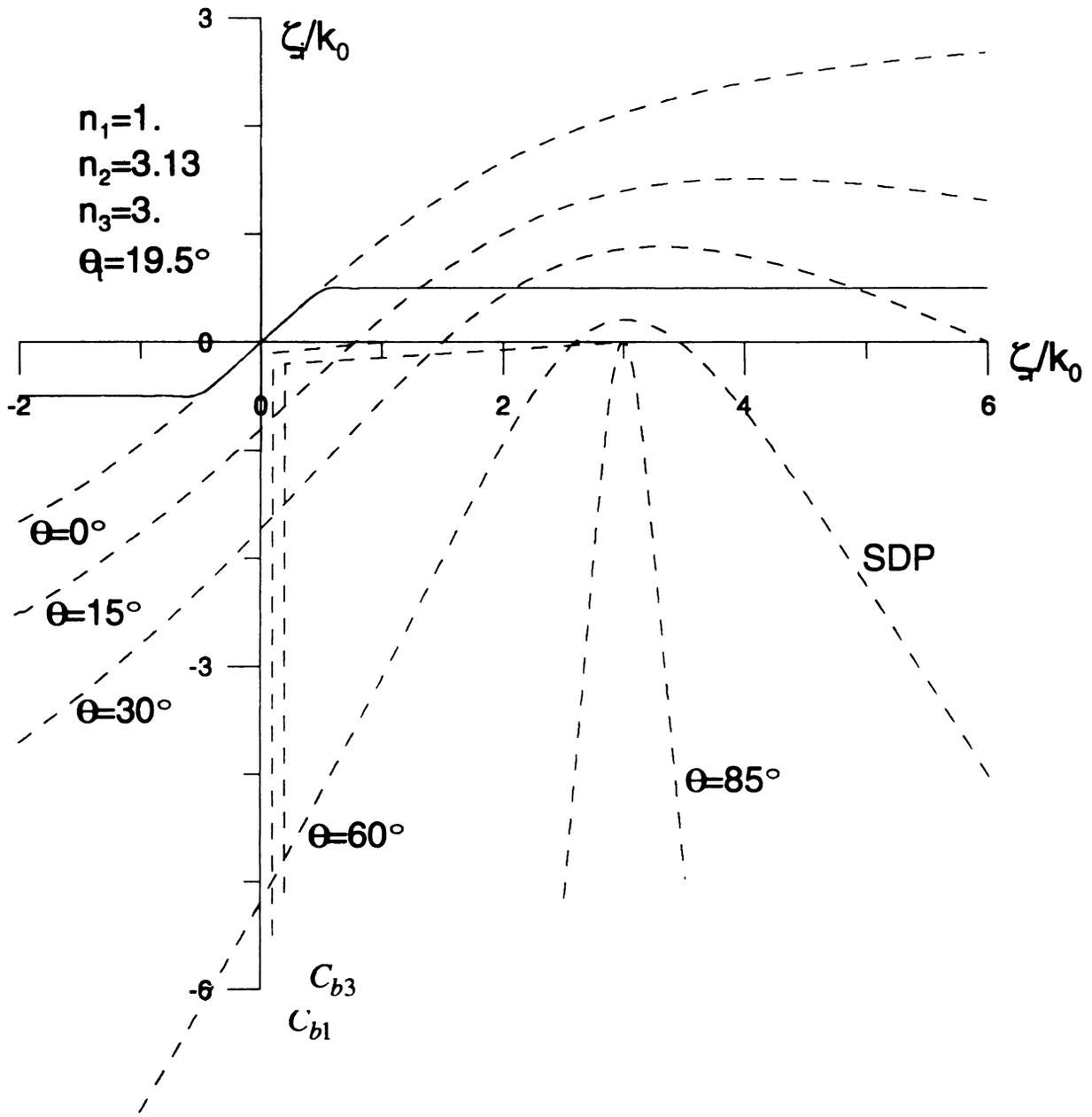

Figure 3.6.1 The steepest-descent paths in the complex ζ -plane for the substrate layer field calculation at various observation aspect angles. The asymmetric planar dielectric waveguide consists of cover, guiding, and substrate layer with indices $n_1 = 1$, $n_2 = 3.13$, and $n_3 = 3$ respectively.

Hence, it is noted that the steepest-descent contribution is equivalent to the branch cut radiation field contribution for $\theta < \theta_t$.

It is also observed in Section 2.7 that for $\theta \geq \theta_t$, only the partial integration path deformation around the cover layer branch cut can satisfy the closure condition for the substrate layer as depicted in Fig. 3.6.2 (previously depicted in Fig. 2.7.3)

$$\begin{aligned} \oint_{C-SDP-partial\{C_{b1}\}-C_p-C_\infty} \Psi^e_{lm\alpha\beta}(x,z|x',z':\zeta)d\zeta = 0 \\ \oint_{C-SDP-partial\{C_{b1}\}-C_p-C_\infty} \Psi^h_{lm\alpha\beta}(x,z|x',z':\zeta)d\zeta = 0 \end{aligned} \tag{3.6.5}$$

For the electric Green's dyad,

$$\begin{aligned} &\int_C \Psi^e_{lm\alpha\beta}(x,z|x',z':\zeta)d\zeta \\ &= \int_{SDP} \Psi^e_{lm\alpha\beta}(x,z|x',z':\zeta)d\zeta + \int_{partial\{C_{b1}\}} \Psi^e_{lm\alpha\beta}(x,z|x',z':\zeta)d\zeta \\ &+ \int_{C_p} \Psi^e_{lm\alpha\beta}(x,z|x',z':\zeta)d\zeta \end{aligned} \tag{3.6.6}$$

The pole contribution vanishes in the far zone but still remains in the near zone. For the magnetic Green's dyad,

$$\begin{aligned} &\int_C \Psi^h_{lm\alpha\beta}(x,z|x',z':\zeta)d\zeta \\ &= \int_{SDP} \Psi^h_{lm\alpha\beta}(x,z|x',z':\zeta)d\zeta + \int_{partial\{C_{b1}\}} \Psi^h_{lm\alpha\beta}(x,z|x',z':\zeta)d\zeta \end{aligned} \tag{3.6.7}$$

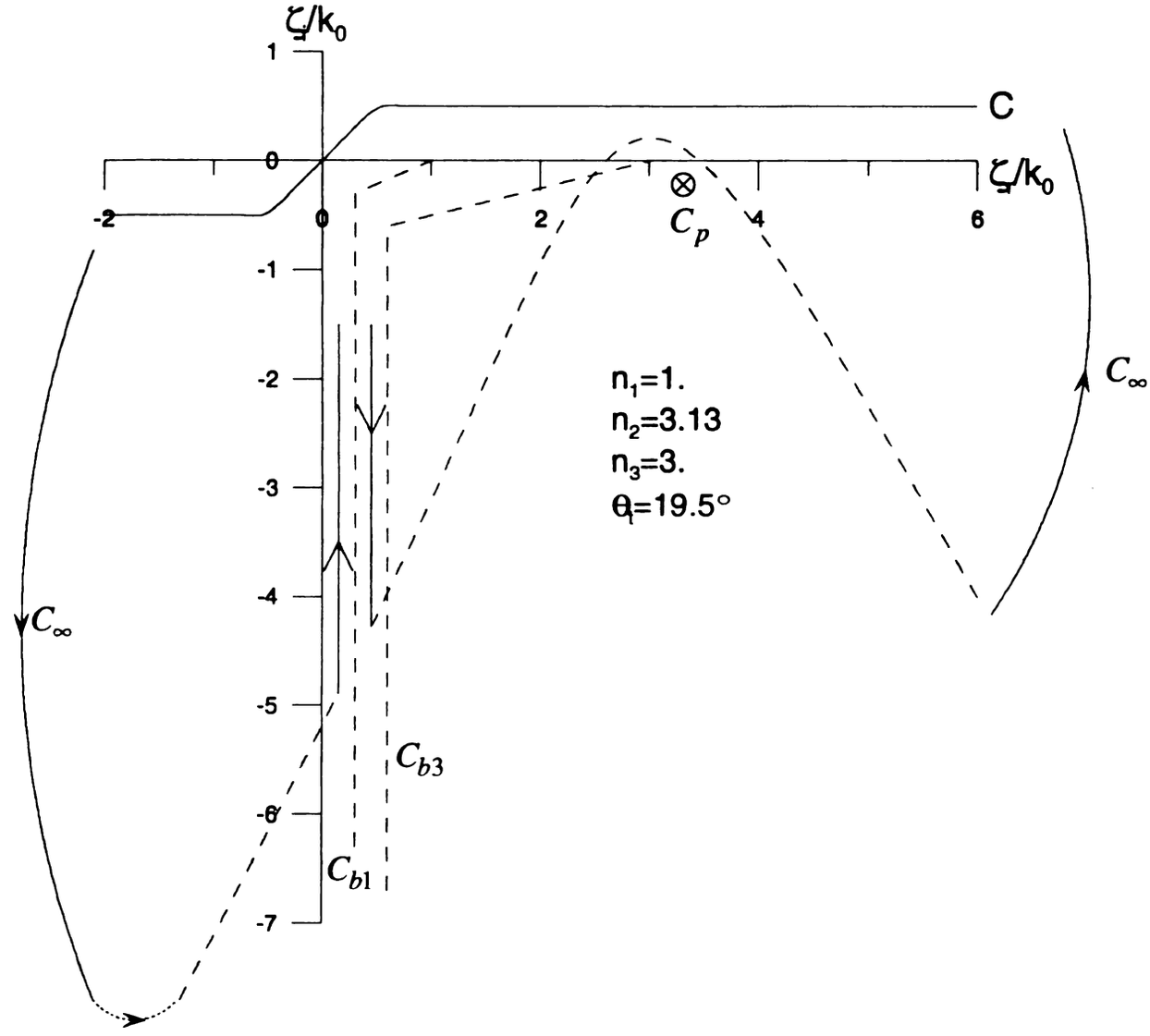

Figure 3.6.2 Proper closure of $\mathrm{Re}\{\zeta\}$-axis inversion contour C into SDP and partial cover layer branch cut for $\theta > \theta_t$.

3.7 CONCLUSION

Due to the intrinsic nature of TM mode excitation, Green's dyads for radiation fields can be formulated in both the cover and the substrate layers using the steepest-descent method in the complex ζ -plane. It is observed that the steepest-descent path in the complex ζ -plane is independent of the source excitatory mode but is dependent of the geometrical structure of the waveguide. During the steepest-descent implementation in the complex ζ -plane, the integration path must be deformed in order to meet the closure condition so that it can be properly connected to the $\mathrm{Re}\{\zeta\}$-axis inversion contour. Therefore, Green's dyad for the radiation field can satisfy Sommerfeld's radiation condition and can be numerically validated by the real axis integration. Since the far-zone field is the main concern, the discrete-mode spectrum contributed by guided-pole singularity was less emphasized (its contribution vanishes there). However, the discrete-mode spectrum for the electric Green's dyad must be considered significant within the near field and source regions. Charges contribute to the electric Green's dyad leading to a singularity term. And an important observation is that TM mode excitation cannot contribute to Green's dyad singularity for the magnetic field within the source region since no magnetic charge exists there.

During the steepest-descent contour deformation in both the cover and the substrate layers, it is observed that the corresponding branch cut deformation for each layer is identical for $\theta \geq \theta_t$ as in Section 2.6 and 2.7. The integration path deformation was reviewed in Sections 3.5 and 3.6.

Since no numerical results are presented in Chapter 3, it is observed that the apparent field discontinuity due to the branch cut contribution past the threshold aspect angle

cannot be resolved numerically. However, based upon the results in Sections 2.6 and 2.7, it can be conjectured that either the branch cut contribution is negligible or the phase compensation for Green's dyad near the threshold aspect angle can resolve the field discontinuity in both the cover and the substrate layers. The rigorous numerical implementation for Green's dyad of the radiation field in both the near and far zones and also within the source region will be accommodated in future research.

CHAPTER 4

ELECTROMAGNETICS OF INTEGRATED OPEN PLANAR LAYERED ELECTRONICS

4.1 INTRODUCTION AND GEOMETRICAL CONFIGURATION

The transform-domain integral-operator methodology for currents/fields of guiding structures contributes to the formulation of the spectral electric field integral equation (EFIE) of integrated open waveguides through a singularity expansion of fields in the complex axial transform plane (complex ζ -plane) [28], [29]. It is recognized that complex analysis in the complex ζ -plane is based upon the transform-domain integral equation formulation for currents/fields of the guiding structure. Section 2 illustrates the integral representation for the required Green's dyad kernel and identifies its singularities in that plane. Singularities in that plane are identified as poles associated with the guiding structure and branch points contributed by layered background environments.

The manner in which singularities in background environments manifest themselves as branch points in the complex ζ -plane is demonstrated. Through Section 3, those branch points are categorized as *logarithmic-type* and *square-root type* according to their complicated manner of migration in two relevant complex transform planes, i.e. complex transverse (ξ -plane) and longitudinal (ζ -plane) planes [7]-[9]. Physical significance of those logarithmic-type and square-root type of branch points will be briefly interpreted in terms of associated branch cuts [9], [30].

The geometrical configuration of integrated microstrip waveguide immersed in a planar-layered background environment is depicted in Fig. 4.1.1 and its cross-sectional

view is also depicted in Fig. 4.1.2. The waveguiding axis is chosen to be z-axis with the x-axis tangential and y-axis normal to the planar interfaces. Each of the planar layers is assumed to be non-magnetic, isotropic and homogeneous with complex permittivity ε_l, $l = 1, 2, 3$ for the cover, film, and substrate layers with $\varepsilon_3 \to -j\infty$ or $\sigma \to \infty$. The guiding structure is embedded in the cover layer adjacent to the cover/film interface.

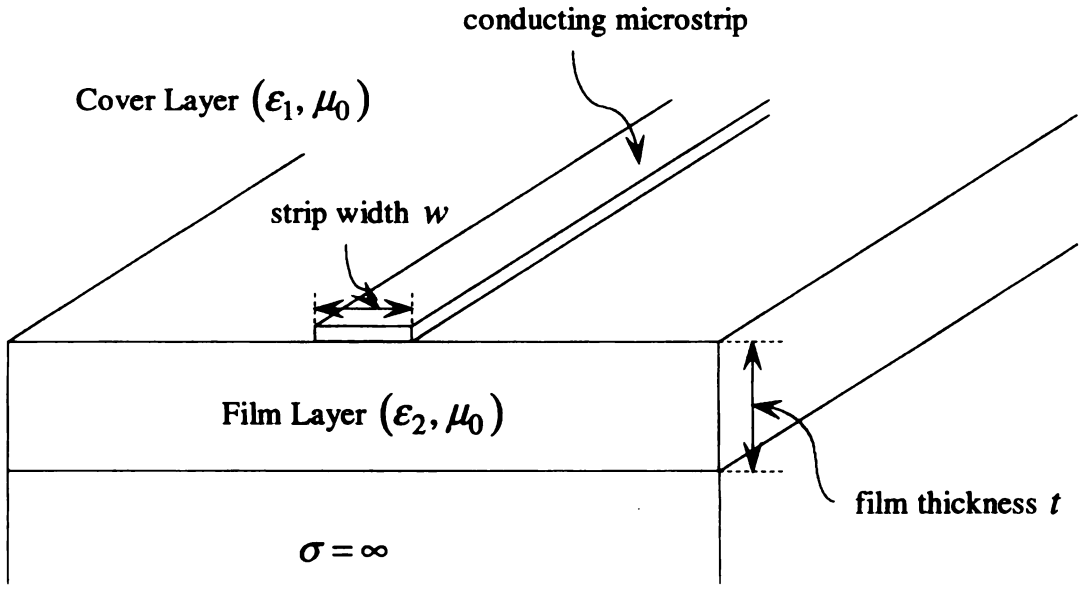

Figure 4.1.1 Geometrical configuration of integrated open microstrip structure immersed in layered background environment

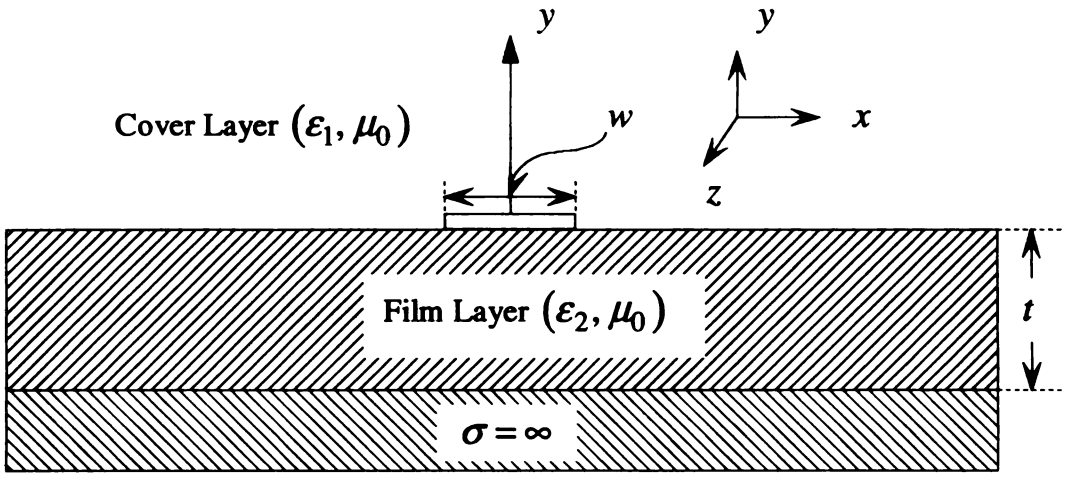

Figure 4.1.2 Cross-sectional view of immersed integrated microstrip structure.

4.2 SPECTRAL ELECTRIC FIELD INTEGRAL EQUATION FORMULATION FOR AN INTEGRATED OPEN WAVEGUIDE STRUCTURE IN A PLANAR-LAYERED BACKGROUND ENVIRONMENT

Total electric field $\boldsymbol{E}(\boldsymbol{r})$ in the cover layer less the scattered electric field $\boldsymbol{E}^s(\boldsymbol{r})$ maintained by the induced current on the conducting microstrip is equal to the impressed electric field $\boldsymbol{E}^i(\boldsymbol{r})$ maintained by an (typically a δ-gap) electric field feed model.

$$\begin{aligned} \hat{t}\bullet\boldsymbol{E}(\boldsymbol{r}) &= \hat{t}\bullet\left[\boldsymbol{E}^i(\boldsymbol{r})+\boldsymbol{E}^s(\boldsymbol{r})\right]=0\cdots\boldsymbol{r}\in S \\ \hat{t}\bullet\boldsymbol{E}^s(\boldsymbol{r}) &= -\hat{t}\bullet\boldsymbol{E}^i(\boldsymbol{r})\cdots\boldsymbol{r}\in S \end{aligned} \tag{4.2.1}$$

where $\hat{t}$ is the unit tangent vector to the surface of the conducting microstrip and S is its surface. It is noted that Eqn. (4.2.1) yields the boundary condition at the strip and the fundamental electric field integral equation (EFIE).

Electric field in the cover layer of a planar-layered conductor/film/cover environment, maintained by the induced microstrip surface current in that cover layer, becomes

$$\boldsymbol{E}_1(\boldsymbol{r})=\left(k_1^2+\nabla\nabla\bullet\right)\boldsymbol{\Pi}_1(\boldsymbol{r}) \tag{4.2.2}$$

where $k_1=n_1k_0$, $n_1=\sqrt{\varepsilon_1/\varepsilon_0}$ and subscript 1 denotes the cover layer. The electric Hertzian potential $\boldsymbol{\Pi}_1(\boldsymbol{r})$ maintained by the induced surface current $\boldsymbol{J}(\boldsymbol{r}')$ in the cover layer is obtained by (see Appendix E)

$$\boldsymbol{\Pi}_1(\boldsymbol{r})=\int_V \bar{\boldsymbol{G}}_1(\boldsymbol{r}|\boldsymbol{r}')\bullet\frac{\boldsymbol{J}(\boldsymbol{r}')}{j\omega\varepsilon_1}dV' \tag{4.2.3}$$

where $\bar{\boldsymbol{G}}_1(\boldsymbol{r}|\boldsymbol{r}')$ is the electric Hertzian potential Green's dyad in the cover layer and V is the volume of the source region immersed in the cover layer. The Green's dyad in the cover layer is represented as shown below. Thus, the Green's dyad is decomposed as

$$\bar{G}_1(r|r') = \bar{G}_1^p(r|r') + \bar{G}_1^r(r|r') \tag{4.2.4}$$

where

$$\begin{aligned} \bar{G}_1^p &= \bar{\mathbf{I}} G_1^p \\ \bar{G}_1^r &= (\hat{x}\hat{x} + \hat{z}\hat{z}) G_{1t}^r + \hat{y}\left(\frac{\partial G_{1c}^r}{\partial x}\hat{x} + G_{1n}^r \hat{y} + \frac{\partial G_{1c}^r}{\partial z}\hat{z} \right) \end{aligned} \tag{4.2.5}$$

Then, $G_1^p(r|r')$ is the principal Green's dyad (it yields the principal wave maintained by $J(r')$) and has the scalar 2-D Sommerfeld-type integral representation

$$G_1^p(r|r') = \iint_{\infty} \frac{e^{j\lambda\bullet(r-r')} e^{-p_1(\lambda)|y-y'|}}{2(2\pi)^2 p_1(\lambda)} d^2\lambda$$

where (4.2.6)

$$p_1(\lambda) = \sqrt{\lambda^2 - k_1^2} \quad (\lambda = \xi\hat{x} + \zeta\hat{z})$$

$G_{1t}^r(r|r')$ is the reflected component (which yields the reflected wave due to interaction of the principal wave with the layered media) yielding tangential components of potential maintained by tangential components of the induced current, $G_{1n}^r(r|r')$ is the reflected component yielding normal component of potential maintained by normal component of the current, and $G_{1c}^r(r|r')$ is the reflected component yielding normal component of potential maintained by coupling to tangential components of the current.

$$\begin{bmatrix} G_{1t}^r(r|r') \\ G_{1n}^r(r|r') \\ G_{1c}^r(r|r') \end{bmatrix} = \iint_{\infty} \begin{bmatrix} R_{1t}(\lambda) \\ R_{1n}(\lambda) \\ C_{1r}(\lambda) \end{bmatrix} \frac{e^{j\lambda\bullet(r-r')} e^{-p_1(\lambda)(y+y')}}{2(2\pi)^2 p_1(\lambda)} d^2\lambda \tag{4.2.7}$$

Reflection coefficients $R_{1t}(\lambda)$, $R_{1n}(\lambda)$ and coupling coefficient $C_{1r}(\lambda)$ depend on dielectric properties of the layered background environment since $\mu_l = \mu_0$ for $l = 1, 2$.

$$
\begin{aligned}
R_{1t}(\lambda) &= \frac{p_1(\lambda) - p_2(\lambda)\coth\left[p_2(\lambda)t\right]}{Z^h(\lambda)} \\
R_{1n}(\lambda) &= \frac{N_{21}^2 p_1(\lambda) - p_2(\lambda)\tanh\left[p_2(\lambda)t\right]}{Z^e(\lambda)} \\
C_{1r}(\lambda) &= \frac{2\left(N_{21}^2 - 1\right)p_1(\lambda)}{Z^h(\lambda)Z^e(\lambda)} \\
Z^h(\lambda) &= p_1(\lambda) + p_2(\lambda)\coth\left[p_2(\lambda)t\right] \\
Z^e(\lambda) &= N_{21}^2 p_1(\lambda) + p_2(\lambda)\tanh\left[p_2(\lambda)t\right] \qquad (4.2.8) \\
&\textit{where} \\
p_l(\lambda) &= \sqrt{\lambda^2 - k_l^2} \cdots l = 1, 2 \\
\lambda^2 &= \xi^2 + \zeta^2 \\
N_{21}^2 &= (n_2/n_1)^2
\end{aligned}
$$

The scattered electric field maintained by the induced strip surface current becomes

$$
\boldsymbol{E}_1^s(\boldsymbol{r}) = -\frac{j\eta_1}{k_1}\left(k_1^2 + \nabla\nabla\bullet\right)\int_S \bar{\boldsymbol{G}}_1(\boldsymbol{r}|\boldsymbol{r}')\bullet\boldsymbol{J}(\boldsymbol{r}')dS' \qquad (4.2.9)
$$

where $\eta_1 = \sqrt{\mu_1/\varepsilon_1} = \sqrt{\mu_0/\varepsilon_1}$. Therefore, substituting Eqn. (4.2.9) into Eqn. (4.2.1) yields

$$
\begin{aligned}
&\hat{t}\bullet\left(k_1^2 + \nabla\nabla\bullet\right)\int_S \bar{\boldsymbol{G}}_1(\boldsymbol{r}|\boldsymbol{r}')\bullet\boldsymbol{J}(\boldsymbol{r}')dS' = -\frac{jk_1}{\eta_1}\hat{t}\bullet\boldsymbol{E}_1^i(\boldsymbol{r}) \cdots \boldsymbol{r} \in S \\
&\hat{t}\bullet\left(k_1^2 + \nabla\nabla\bullet\right)\int_C dl'\int_{-\infty}^{\infty}\bar{\boldsymbol{G}}_1(\boldsymbol{\rho}|\boldsymbol{\rho}' : z - z')\bullet\boldsymbol{J}(\boldsymbol{\rho}', z')dz' = -\frac{jk_1}{\eta_1}\hat{t}\bullet\boldsymbol{E}_1^i(\boldsymbol{\rho}, z)
\end{aligned} \qquad (4.2.10)
$$

where $\boldsymbol{r} = \boldsymbol{\rho} + \hat{z}z$ and $\boldsymbol{\rho} = \hat{x}x + \hat{y}y$ is the 2-D position vector.

Axial uniformity of the waveguiding system prompts Fourier transformation of all field quantities with respect to the z variable. The axial integral is convolutional in the axial variable z'. Then spectral EFIE for the induced surface current $\tilde{\boldsymbol{j}}_\zeta(\boldsymbol{\rho}',\zeta)$ consequently becomes

$$\hat{t}\cdot\left(k_1^2+\tilde{\nabla}\tilde{\nabla}\cdot\right)\int_C \bar{\boldsymbol{g}}_{1\zeta}(\boldsymbol{\rho}|\boldsymbol{\rho}')\cdot\tilde{\boldsymbol{j}}_\zeta(\boldsymbol{\rho}',\zeta)dl' = -\frac{jk_1}{\eta_1}\hat{t}\cdot\tilde{\boldsymbol{e}}^i_{1\zeta}(\boldsymbol{\rho},\zeta)\cdots\boldsymbol{\rho}\in C \quad (4.2.11)$$

where $\tilde{\nabla}=\nabla_t+\hat{z}j\zeta$ is the spectral differential operator and $\bar{\boldsymbol{g}}_{1\zeta}(\boldsymbol{\rho}|\boldsymbol{\rho}')$ is a 2-D spectral Hertzian potential Green's dyad.

Thus, the spectral Green's dyad (the axial transform of the 3-D dyad) becomes

$$\bar{\boldsymbol{g}}_{1\zeta}(\boldsymbol{\rho}|\boldsymbol{\rho}')=\bar{\boldsymbol{g}}^p_{1\zeta}(\boldsymbol{\rho}|\boldsymbol{\rho}')+\bar{\boldsymbol{g}}^r_{1\zeta}(\boldsymbol{\rho}|\boldsymbol{\rho}') \quad (4.2.12)$$

where

$$\begin{aligned}
&\bar{\boldsymbol{g}}^p_{1\zeta}=\bar{\mathbf{I}}g^p_{1\zeta}\\
&\bar{\boldsymbol{g}}^r_{1\zeta}=(\hat{x}\hat{x}+\hat{z}\hat{z})g^r_{1\zeta t}+\hat{y}\left(\frac{\partial g^r_{1\zeta c}}{\partial x}\hat{x}+g^r_{1\zeta n}\hat{y}+\frac{\partial g^r_{1\zeta c}}{\partial z}\hat{z}\right)\\
&g^p_{1\zeta}(\rho|\rho')=\int_{-\infty}^{\infty}\frac{e^{j\xi(x-x')}e^{-p_1(\lambda)|y-y'|}}{4\pi p_1(\lambda)}d\xi \qquad (4.2.13)\\
&\begin{Bmatrix} g^r_{1\zeta t}(\rho|\rho')\\ g^r_{1\zeta n}(\rho|\rho')\\ g^r_{1\zeta c}(\rho|\rho')\end{Bmatrix}=\int_{-\infty}^{\infty}\begin{Bmatrix} R_{1t}(\lambda)\\ R_{1n}(\lambda)\\ C_{1r}(\lambda)\end{Bmatrix}\frac{e^{j\xi(x-x')}e^{-p_1(\lambda)(y+y')}}{4\pi p_1(\lambda)}d\xi
\end{aligned}$$

It is observed that spectral Green's dyad arguments are $(\boldsymbol{\rho}|\boldsymbol{\rho}')$ and coefficients $R_{1t}(\lambda)$, $R_{1n}(\lambda)$, and $C_{1r}(\lambda)$ are detailed in Eqn. (4.2.8).

4.3 PLANAR-LAYERED BACKGROUND ENVIRONMENT SINGULARITIES

Wavenumber parameters $p_l(\lambda)=\sqrt{\lambda^2-k_l^2}=\sqrt{\lambda-k_l}\sqrt{\lambda+k_l}$, associated with various layers of the planar background environment, yield branch point singularities at $\lambda=\pm k_l$ [31]. Since the integrands of Green's dyad integral representations are even in $p_2(\lambda)$, then the branch point contributed by the film layer is removable [17]. The integrands of Green's dyad integral representations are, however, not even in $p_1(\lambda)$ and therefore the branch point contributed by the cover layer is non-removable.

Pole singularities [31] of the reflection and coupling coefficients in Green's dyad integral representations contribute simple-pole singularities associated with the planar-layered background environment. So, $Z^h(\lambda)=0$ in Eqn. (4.2.8) leads to simple poles shared by $R_{1t}(\lambda)$ and $C_{1r}(\lambda)$ at $\lambda=\pm\lambda_p$ associated with TE-odd surface waves [31] and $Z^e(\lambda)=0$ in Eqn. (4.2.8) leads to simple poles shared by $R_{1n}(\lambda)$ and $C_{1r}(\lambda)$ at $\lambda=\pm\lambda_p$ associated with TM-even surface waves.

Hence, complex λ-plane singularities of the integrands in Green's dyad integral representations consist of branch points at $\lambda=\pm k_1$ and poles $\lambda=\pm\lambda_p$. It is observed that since $\lambda^2=\xi^2+\zeta^2$, $\lambda_s^2=\xi_s^2+\zeta^2$ for $\lambda_s=\pm k_1$, $\pm\lambda_p$. And generically, λ_s denotes λ-plane singularities and ξ_s the corresponding ξ-plane singularities for any ζ.

$$\pm\xi_s=\mp j\sqrt{\zeta-\lambda_s}\sqrt{\zeta+\lambda_s} \tag{4.2.14}$$

which clearly implicates the branch points at $\zeta=\pm\lambda_s$ in the complex ζ-plane as depicted in Fig. 4.3.1. Moreover in order to satisfy the radiation condition, it is necessary

that $\mathrm{Im}\{\xi_s\}<0$, i.e., the singularity point must not migrate across the $\mathrm{Re}\{\xi\}$-axis. As indicated in Chapter 2, this requirement is appropriately implemented by choice of the hyperbolic Sommerfeld branch cuts as depicted in the Fig. 2.4.1.

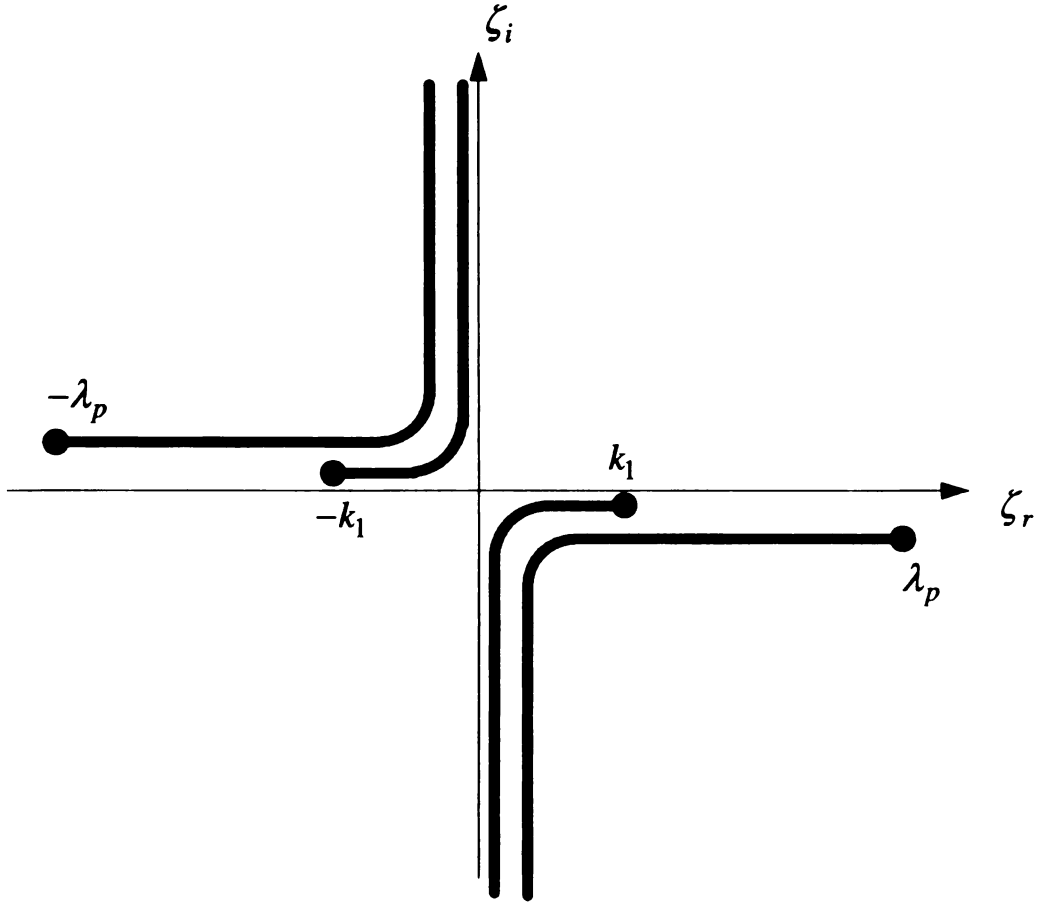

Figure 4.3.1 Singularities in the complex ζ -plane contributed by the planar-layered background environment. The branch point $\pm k_1$ to the branch point $\pm k_1$ mapping and the pole $\pm\lambda_p$ to the branch point $\pm\lambda_p$ mapping in the low-loss limit.

4.3.1 LOGARITHMIC-TYPE BRANCH POINT

To determine points $\zeta = \pm k_1$ as logarithmic type branch points in the complex ζ-plane, it is required to examine the migration of the branch points $\pm\xi_{k_1}$ in the complex ξ-plane as ζ moves around points $\zeta = \pm k_1$ in the complex ζ-plane as depicted in Fig. 4.3.2.

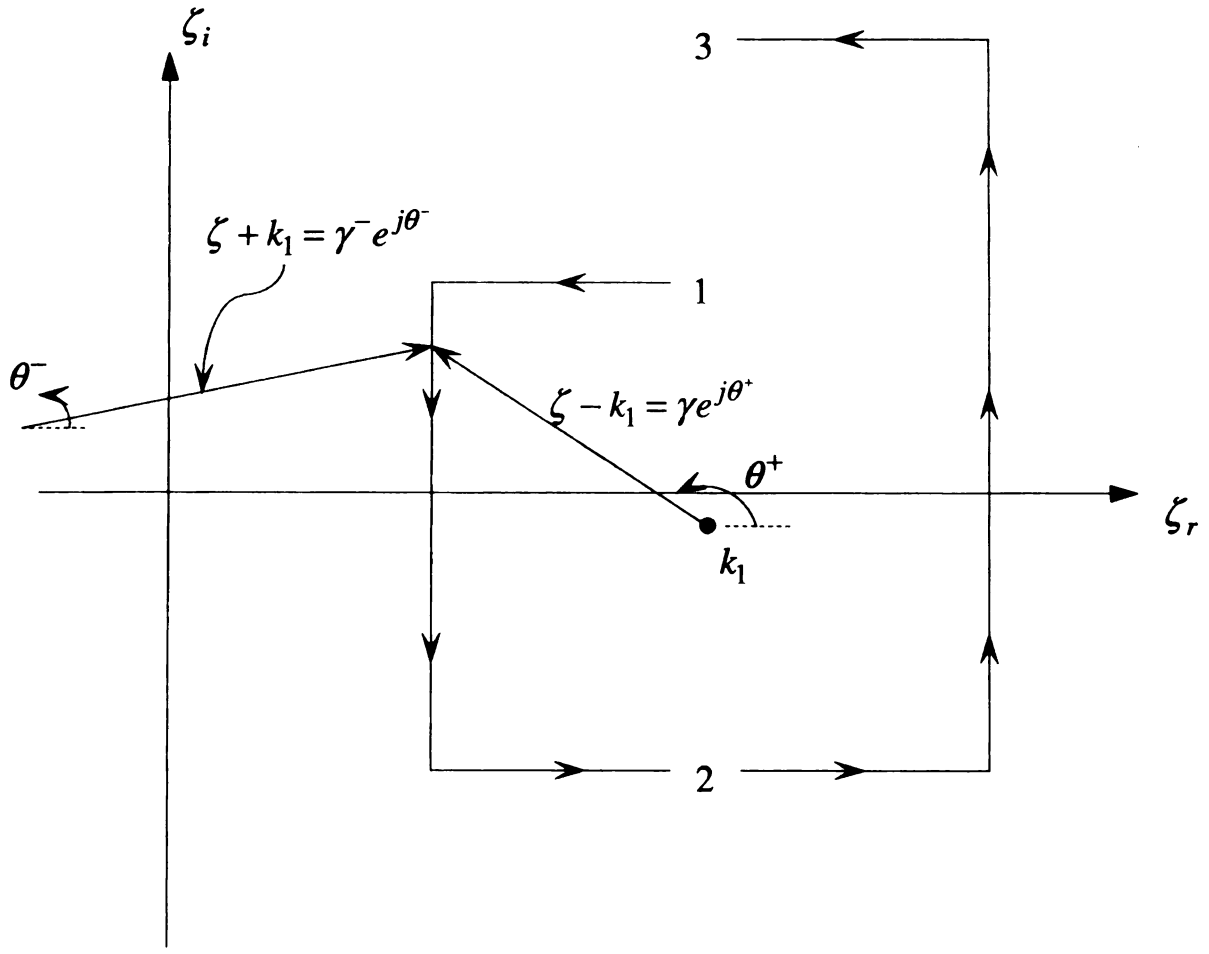

Figure 4.3.2 Complex-phasor diagram with a path in the complex ζ-plane, making one round trip about the point k_1.

Choosing $\xi_s = \xi_{k_1}$ as the fourth-quadrant singularity,

$$\xi_{k_1} = -j\sqrt{\zeta - k_1}\sqrt{\zeta + k_1} = \sqrt{\gamma^+\gamma^-}\, e^{j\left(-\pi+\theta^+ +\theta^-\right)/2} \tag{4.2.15}$$

For point 1 approaching infinitesimally close to the real axis in the complex ζ-plane as depicted in Fig. 4.3.2, $\theta^+ = \pi/2$. Therefore,

$$\xi_{k_1} = \sqrt{\gamma^+\gamma^-}\, e^{j(-\pi+\pi/2+0)/2} = \frac{1-j}{\sqrt{2}}\left|\xi_{k_1}\right| \tag{4.2.16}$$

For point 2 approaching infinitesimally close to the real axis in the complex ζ-plane, $\theta^+ = 3\pi/2$ and therefore,

$$\xi_{k_1} = \sqrt{\gamma^+\gamma^-}\, e^{j(-\pi+3\pi/2+0)/2} = \frac{1+j}{\sqrt{2}}\left|\xi_{k_1}\right| \tag{4.2.17}$$

Finally, since point 3 is reached after one complete evolution around the point $\zeta = k_1$, for point 3 infinitesimally close to the real axis, $\theta^+ = 2\pi + \pi/2 = 5\pi/2$ and therefore,

$$\xi_{k_1} = \sqrt{\gamma^+\gamma^-}\, e^{j(-\pi+5\pi/2+0)/2} = \frac{-1+j}{\sqrt{2}}\left|\xi_{k_1}\right| \tag{4.2.18}$$

Hence, it is observed that as ζ moves toward from point 1 to point 2 as depicted in Fig. 4.3.2, the branch points $\pm\xi_{k_1}$ cross the real axis in the complex ξ-plane. Therefore, the branch points $\pm\xi_{k_1}$ will cross the real axis in the complex ξ-plane whenever ζ crosses the real axis in the complex ζ-plane to the left of the point k_1. ζ moves from point 2 to point 3, the branch points $\pm\xi_{k_1}$ cross the imaginary axis in the complex ξ-plane. Therefore, it is recognized that the branch points $\pm\xi_{k_1}$ will cross the imaginary

axis in the complex ξ-plane whenever ζ crosses the real axis in the complex ζ-plane to the right of the point k_1.

It is necessary to establish the behavior of the spectral Green's dyad [9] in the complex ξ-plane as ζ moves around points $\pm k_1$ in the complex ζ-plane as depicted in Fig. 4.3.3. Much rigorous research on leaky-modes of open microstrip has led [9] to a firm understanding of this behaviour. An important reason to introduce the behaviour of the branch point is to attempt to obtain more insight into the necessary complex analysis. Chapters 5, 6, and 7 will discuss the proper continuous spectrum of open integrated microstrip waveguide, for which analyses in both the complex ξ- and ζ-planes become very complicated and are strongly influenced by the singularity migration.

It is convenient to define the spectral Green's dyad to be $\Upsilon(\zeta)$ as a general form in agreement with Eqn. (4.2.14).

$$\Upsilon(\zeta)=\int_{C_\xi}\Phi(\xi,\zeta)d\xi \tag{4.2.19}$$

where $\Phi(\xi,\zeta)$ denotes the integrands of the spectral Green's dyads and C_ξ denotes the $\mathrm{Re}\{\xi\}$-axis contour in the complex ξ-plane. Then, $\Upsilon(\zeta)$ changes smoothly as ζ encircles the point $\zeta=k_1$ in the complex ζ-plane. The required smoothness condition in changes of $\Upsilon(\zeta)$ imposes the continuous path deformation in the evolution of C_ξ.

Point 1 in Fig. 4.3.3 depicts Fig. 4.3.3a. The branch points $\pm\xi_{k_1}$ are located in the second and the fourth quadrants of the complex ξ-plane and the branch cuts have been chosen to be Sommerfeld ones, which are hyperbolas as previously discussed.

As ζ moves toward point 2 as depicted in Fig. 4.3.3, in agreement with Eqn. (4.3.3) and Eqn. (4.3.4), the branch points $\pm\xi_{k_1}$ in the complex ξ-plane cross the real axis as depicted in Fig. 4.3.3b. It is observed that the integration path goes through an improper zone denoted by I as depicted in Fig. 4.3.3b. The improper zone I is determined by

$$\mathrm{Im}\sqrt{k_1^2-\lambda^2}=\mathrm{Im}\sqrt{k_1^2-\xi^2-\zeta^2}>0 \qquad (4.2.20)$$

Therefore, Fig. 4.3.3b is equivalent to Fig. 4.3.3c by choosing the Sommerfeld branch cuts. In other words, numerical evaluation along the integral path in Fig. 4.3.3b is exactly equivalent to one in Fig. 4.3.3c. It means that changing the shape of the branch cuts does not change the value of $\Phi(\xi,\zeta)$ along the path in Fig. 4.3.3b but simply changes which Riemann sheet the points in the complex ζ-plane stay on for those points along the path in the improper zone I. The solid line in Fig. 4.3.3c stays on the top Riemann sheet and the dashed line does on the lower one.

A path on the top Riemann sheet between the branch points $\pm\xi_{k_1}$ has been added and subtracted as depicted in Fig. 4.3.3d. In Fig. 4.3.3e, the paths have been connected to a real axis on the top Riemann sheet and a round-trip path between the branch points $\pm\xi_{k_1}$, half on the top and half on the lower Riemann sheet.

As ζ moves toward point 3 as depicted in Fig. 4.3.3, in agreement with Eqn. (4.3.4) and Eqn. (4.3.5), the branch points $\pm\xi_{k_1}$ in the complex ξ-plane cross the imaginary axis as depicted in Fig. 4.3.3f. Since the paths C_ξ depicted in Fig. 4.3.3a and Fig. 4.3.3f, which correspond to points 1 and 3 depicted in Fig. 4.3.3, are different each other. Then points $\pm k_1$ are branch points in the complex ζ-plane.

As ζ moves toward point 4 as depicted in Fig. 4.3.3, the branch points $\pm\xi_{k_1}$ cross the real axis again. The integration path goes again through an improper zone I defined by Eqn. (4.3.7) as depicted in Fig. 4.3.3g.

It is observed that Fig. 4.3.3h is equivalent to Fig. 4.3.3g by choosing the Sommerfeld branch cuts. Then, the path on the top Riemann sheet in the improper zone I stays on the lower Riemann sheet and vice versa as depicted in Fig. 4.3.3h.

In Fig. 4.3.3i, another path on the top Riemann sheet between the branch points $\pm\xi_{k_1}$ has been added and subtracted. Then, the paths have been connected to the real axis on the top Riemann sheet and two round-trip paths between the branch points $\pm\xi_{k_1}$, half on the top and half on the lower Riemann sheet as depicted in Fig. 4.3.3j.

As ζ moves toward point 5 as depicted in Fig. 4.3.3, the branch points $\pm\xi_{k_1}$ cross the imaginary axis again as depicted in Fig. 4.3.3k. The paths C_ξ depicted in Fig. 4.3.3f and Fig. 4.3.3k, which correspond to points 3 and 5 depicted in Fig. 4.3.3, are different by the addition of an extra loop between the branch points $\pm\xi_{k_1}$. Therefore, each round trip around the branch points $\pm k_1$ in the complex ζ-plane will add an extra loop in the total path. Hence, the branch points $\zeta = \pm k_1$ are *logarithmic type branch points*, having an infinite number of Riemann sheets. The infinite Riemann sheets corresponding to the branch points $\pm k_1$ are denoted by $\cdots, S_{-N}, \cdots, S_{-1}, S_0, S_1, \cdots, S_N, \cdots$, where N refers to the number of loops between the branch points $\pm\xi_{k_1}$ and the sign designates the sense in which the loops are traversed. At point #2, the Riemann sheet is designated by S_{-1}.

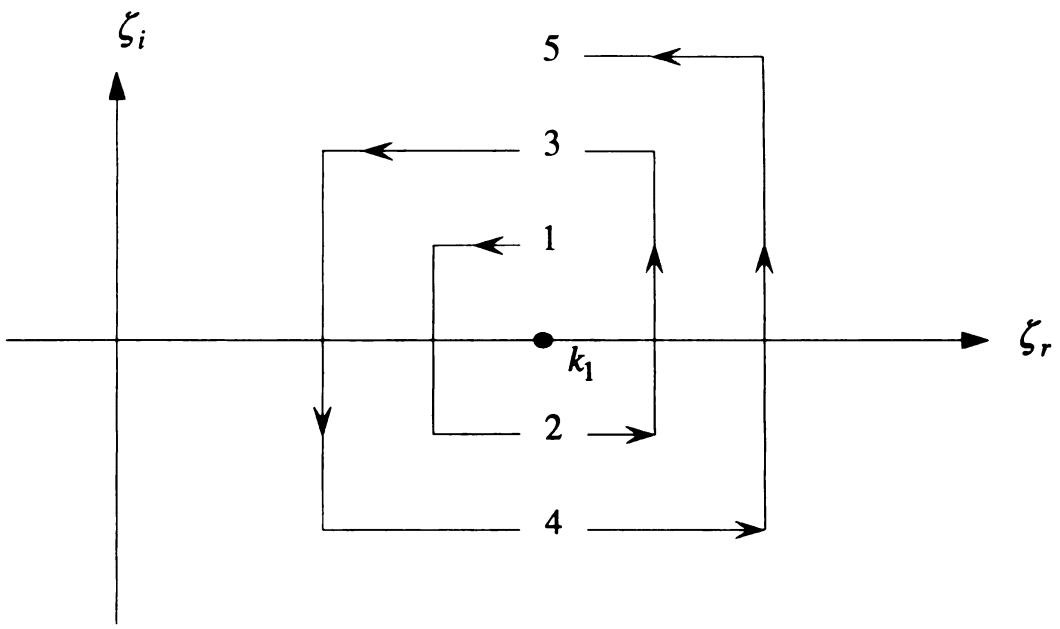

Figure 4.3.3 Path trajectory in the complex ζ -plane, encircling twice around the point $\zeta = k_1$.

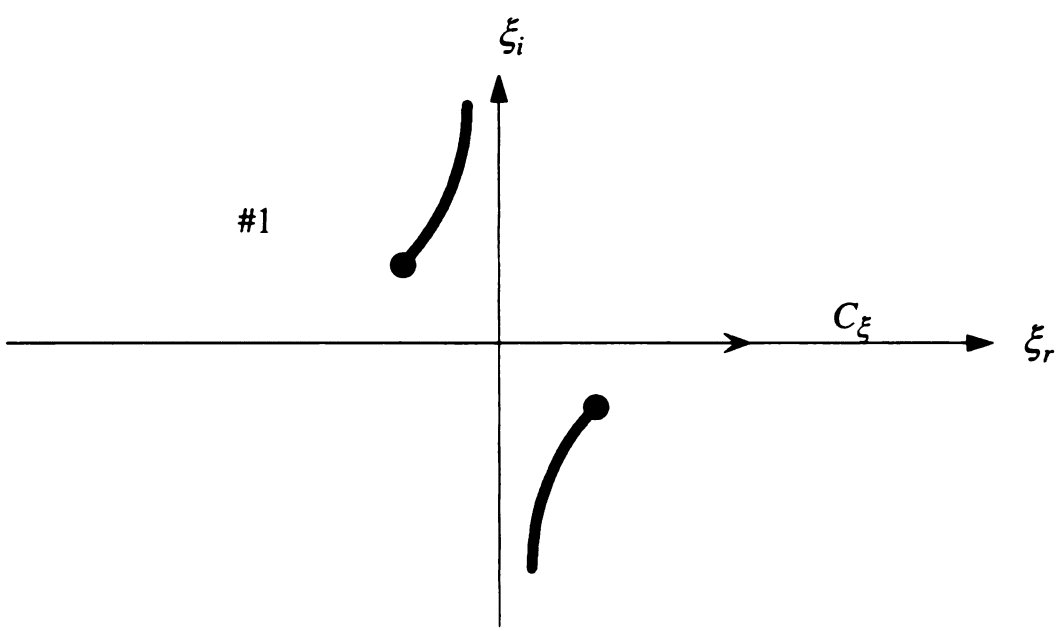

Figure 4.3.3a Evolution of C_ξ for a point 1 in Fig. 4.3.3.

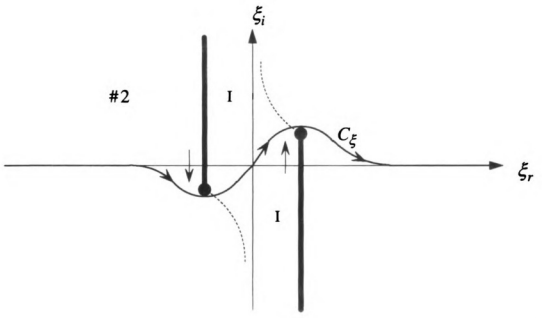

Figure 4.3.3b Evolution of C_ξ for a point 2 in Fig. 4.3.3.

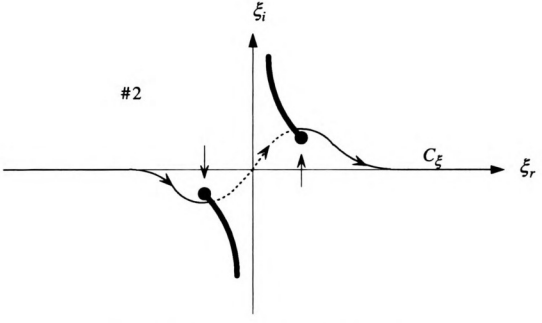

Figure 4.3.3c Evolution of C_ξ for a point 2 in Fig. 4.3.3.

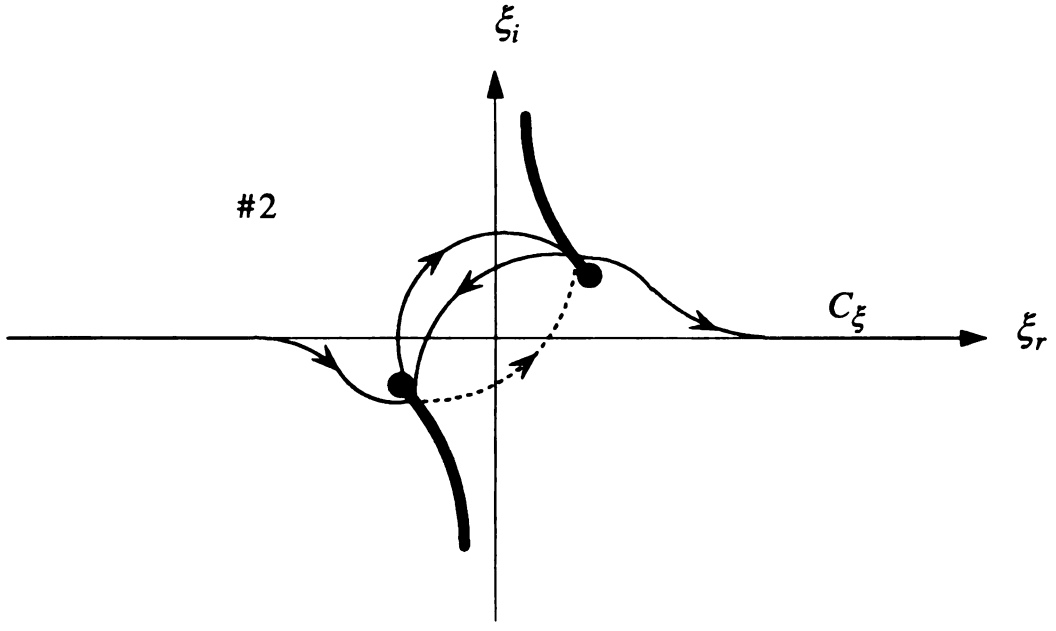

Figure 4.3.3d Evolution of C_ξ for a point 2 in Fig. 4.3.3.

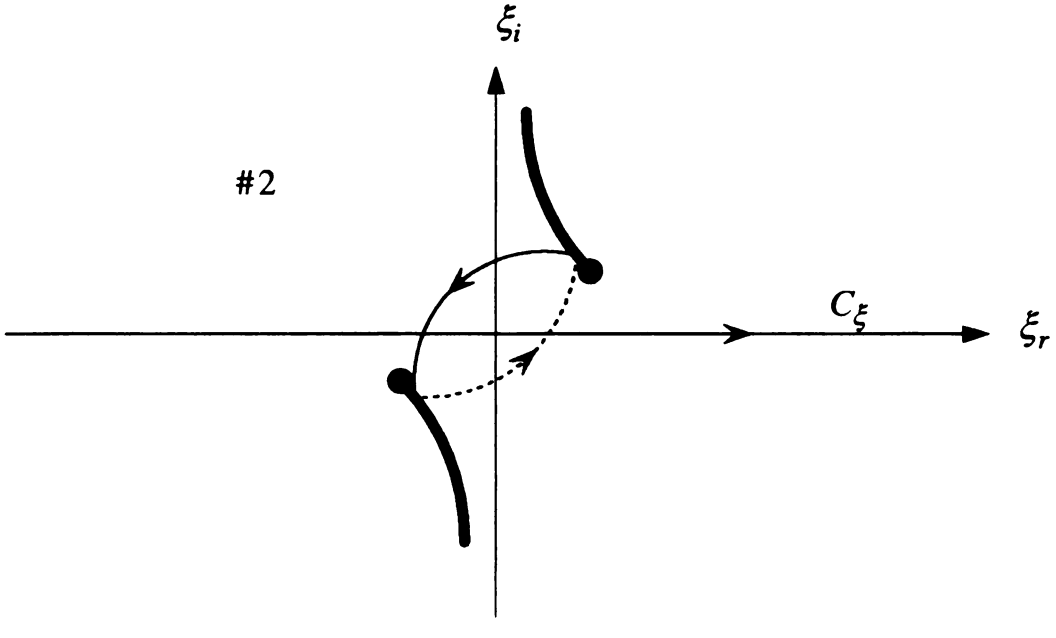

Figure 4.3.3e Evolution of C_ξ for a point 2 in Fig. 4.3.3.

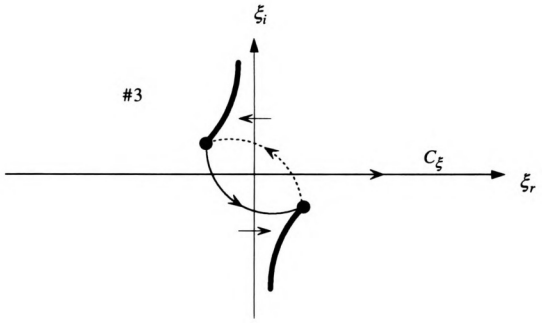

Figure 4.3.3f Evolution of C_ξ for a point 3 in Fig. 4.3.3.

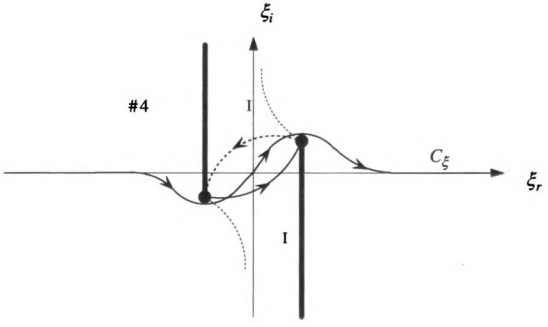

Figure 4.3.3g Evolution of C_ξ for a point 4 in Fig. 4.3.3.

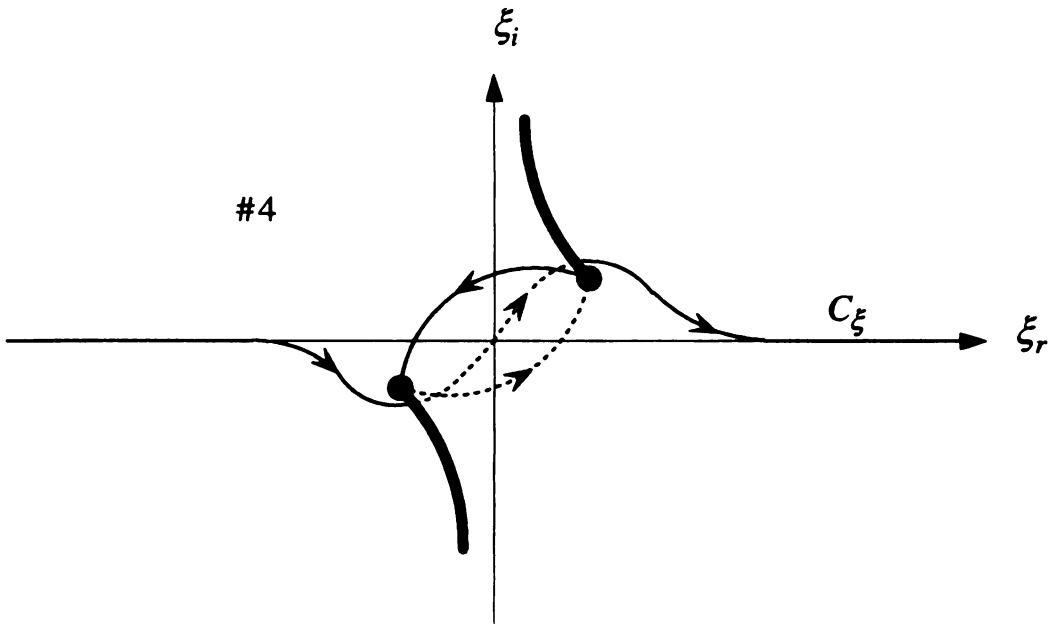

Figure 4.3.3h Evolution of C_ξ for a point 4 in Fig. 4.3.3.

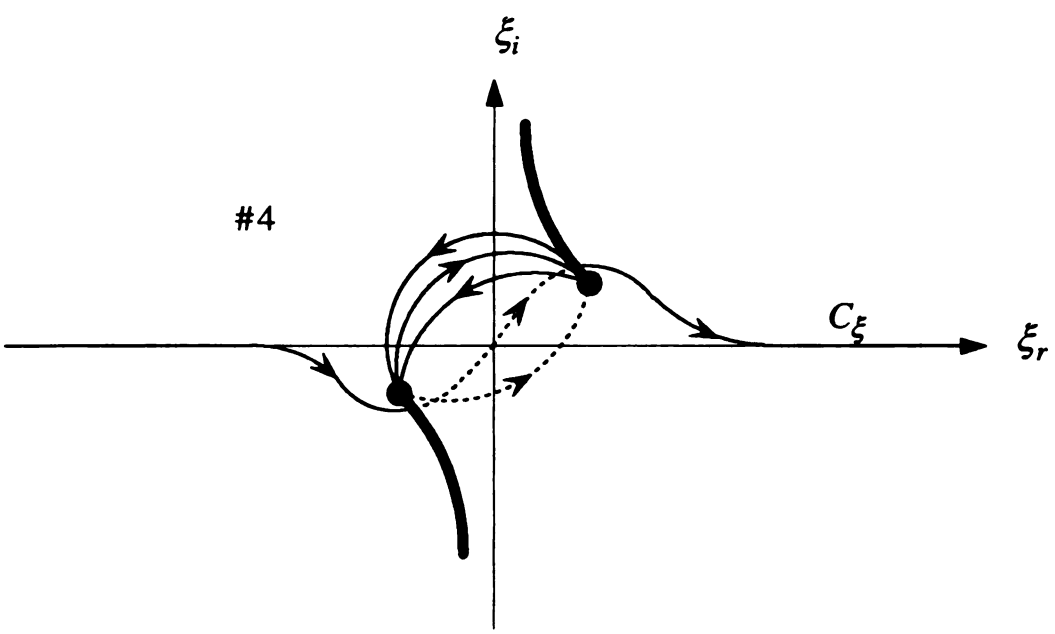

Figure 4.3.3i Evolution of C_ξ for a point 4 in Fig. 4.3.3.

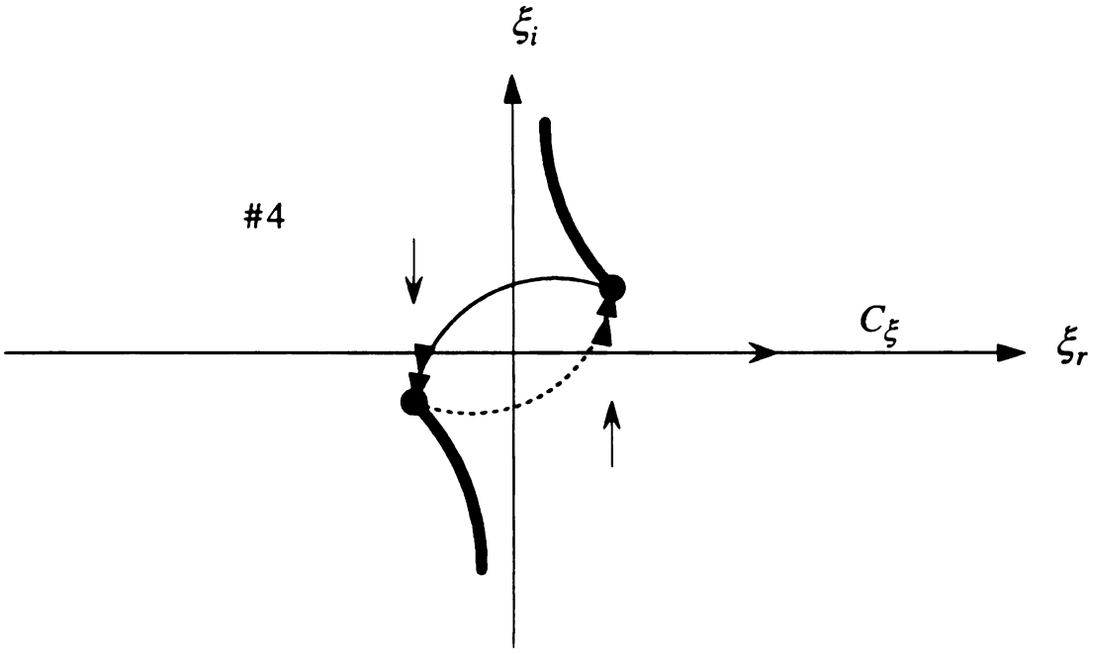

Figure 4.3.3j Evolution of C_ξ for a point 4 in Fig. 4.3.3.

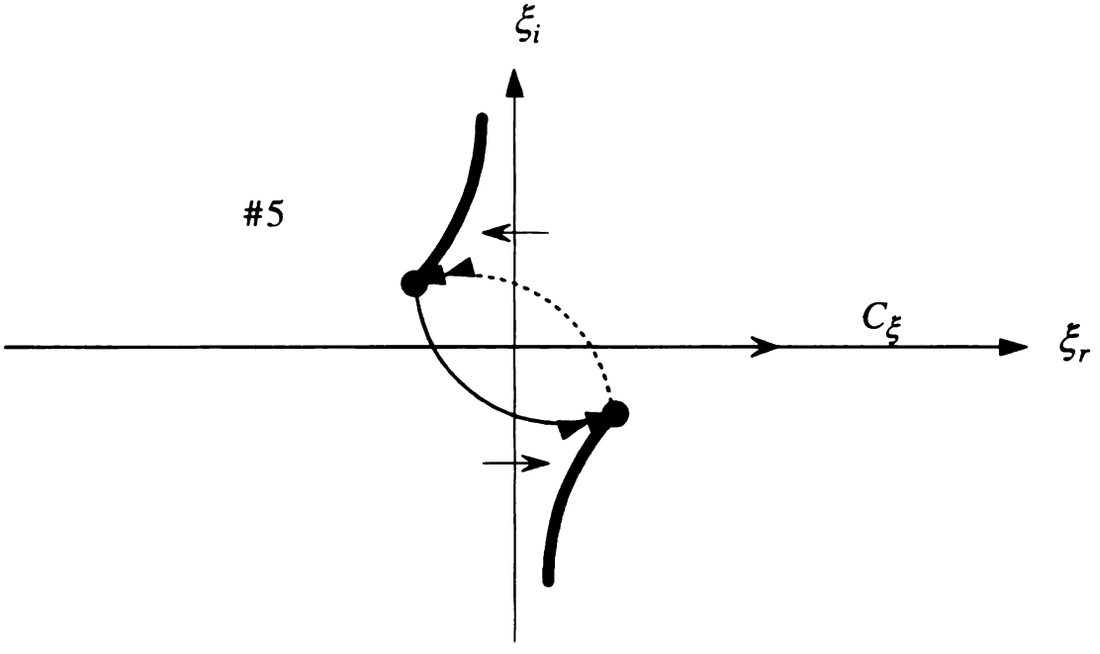

Figure 4.3.3k Evolution of C_ξ for a point 5 in Fig. 4.3.3.

4.3.2 SQUARE-ROOT TYPE BRANCH POINT

With $\lambda_p = \lambda_{TM_0}$ being the fundamental proper surface-wave mode of the grounded substrate, Fig. 4.3.4 depicts two round-trip encirclements around the point $\zeta = \lambda_{TM_0}$ in the complex ζ -plane.

At point 1 in Fig. 4.3.4, the sheet is designated by S_0 of the branch points $\pm k_1$ as depicted in Fig. 4.3.4a. The path stays on the top Riemann sheet and does not detour around the poles at $\pm\xi_{TM_0}$ in the complex ξ -plane.

As ζ moves toward point 2 as depicted in Fig. 4.3.4, the poles $\pm\xi_{TM_0}$ cross the real axis and the branch points $\pm\xi_{k_1}$ do the imaginary axis as depicted in Fig. 4.3.4b. Thus, paths around the poles are equivalent to residue contributions.

At point 3, both the poles $\pm\xi_{TM_0}$ and the branch points $\pm\xi_{k_1}$ cross the imaginary axis to return to the same quadrants at point 1. However, the total path in Fig. 4.3.4c is different than the one in Fig. 4.3.4a due to residue contributions. Therefore, the point $\zeta = \pm\lambda_{TM_0}$ is the branch point in the complex ζ -plane.

As ζ moves toward point 4 in Fig. 4.3.4, the poles $\pm\xi_{TM_0}$ cross the real axis again as depicted in Fig. 4.3.4d. But, the residue contribution is annulled since the residue-paths coalesce upon the real axis.

Finally, at point 5 in Fig. 4.3.4, again both the poles $\pm\xi_{TM_0}$ and the branch points $\pm\xi_{k_1}$ cross the imaginary axis to return to the same quadrants at point 1, which does not alter the real axis integration C_ξ in the complex ξ -plane as depicted in Fig. 4.3.4e. It is,

therefore, concluded that the points $\zeta = \pm\lambda_{TM_0}$ are *square-root type branch points* since there are only two Riemann sheets associated with those points. Since the Riemann sheet S_0 is not changed in the complex ξ-plane, the points $\zeta = \pm\lambda_{TM_0}$ are square-root type of branch points on the Riemann sheet S_0 of the branch points $\pm k_1$. Since there are infinite number of Riemann sheets associated with the branch points $\zeta = \pm k_1$, the investigation about the points $\zeta = \pm\lambda_{TM_0}$ should be completed with respect to the other Riemann sheets of those branch points. Therefore,

At point 1 in Fig. 4.3.5, the sheet is designated by S_0 of the branch points $\pm k_1$ as depicted in Fig. 4.3.5a. The path stays on the top Riemann sheet and does not detour around the poles at $\pm\xi_{TM_0}$ in the complex ξ-plane.

As ζ moves toward point 2 by violating the branch cut once as depicted in Fig. 4.3.5, both the poles $\pm\xi_{TM_0}$ and the branch points $\pm\xi_{k_1}$ cross the real axis as depicted in Fig. 4.3.5b. The poles gain residue contributions as discussed in Fig. 4.3.4b and the integral path deformation in the complex ξ-plane due to the branch points $\pm k_1$ was previously illustrated from Fig. 4.3.3b to Fig. 4.3.3e.

At point 3, the poles $\pm\xi_{TM_0}$ cross the real axis to annul residue contributions and the branch points $\pm\xi_{k_1}$ cross the imaginary axis as depicted in Fig. 4.3.5c.

As ζ moves toward point 4 after violating the branch cut twice by encircling the branch point $\zeta = k_1$ as depicted in Fig. 4.3.5, both the poles $\pm\xi_{TM_0}$ and the branch points $\pm\xi_{k_1}$ cross the real axis again as depicted in Fig. 4.3.5d. As previously discussed,

the poles gain residue contributions and the integral path deformation in the complex ξ-plane due to the branch points $\pm k_1$ was illustrated from Fig. 4.3.3f to Fig. 4.3.3j. It is observed that one extra loop was added between the branch points $\pm k_1$, which designates the Riemann sheet by S_{-2} of the branch points $\pm k_1$.

As ζ moves toward point 5 as depicted in Fig. 4.3.5, both the poles $\pm\xi_{TM_0}$ and the branch points $\pm\xi_{k_1}$ cross the imaginary axis as depicted in Fig. 4.3.5e. As the poles $\pm\xi_{TM_0}$ cross the imaginary axis, they cross loop paths between the branch points $\pm\xi_{k_1}$. Since the poles stay on the top Riemann sheet, they are not affected by the crossing the dashed loop path on the lower Riemann sheet. However, crossing the solid loop path on the top Riemann sheet affects residue contributions. Since the poles $\pm\xi_{TM_0}$ cross the double solid loop paths as depicted in Fig. 4.3.5e, they annul residue contributions when they cross the solid loop path once and regain them when they cross a second time.

As ζ moves toward point 6 as depicted in Fig. 4.3.5, the poles $\pm\xi_{TM_0}$ cross the real axis and the branch points $\pm\xi_{k_1}$ cross the imaginary axis to return to the same quadrants at point 4. However, the total path in Fig. 4.3.5f is different than the one in Fig. 4.3.5d. Then, the point $\zeta = \pm\lambda_{TM_0}$ is the branch point in the complex ζ-plane.

As ζ moves toward point 7 as depicted in Fig. 4.3.5, both the poles $\pm\xi_{TM_0}$ and the branch points $\pm\xi_{k_1}$ cross the imaginary axis as depicted in Fig. 4.3.5g. Since the poles cross the double solid loop paths again, they gain residue contributions when they cross the solid loop path once and annul them when on the second crossing.

Finally, at point 8 in Fig. 4.3.5, the poles $\pm\xi_{TM_0}$ cross the real axis to gain residue contributions and the branch points $\pm\xi_{k_1}$ cross the imaginary axis as depicted in Fig. 4.3.5h, which does not alter the real axis integration C_ξ in the complex ξ-plane as depicted in Fig. 4.3.5d. Therefore, the points $\zeta = \pm\lambda_{TM_0}$ are *square-root type branch points* on the Riemann sheet S_{-2} of the branch points $\pm k_1$. Hence, it can be explicitly deduced that the points $\zeta = \pm\lambda_{TM_0}$ are *square-root type branch points* on the even Riemann sheets S_{2N} of the branch points $\pm k_1$.

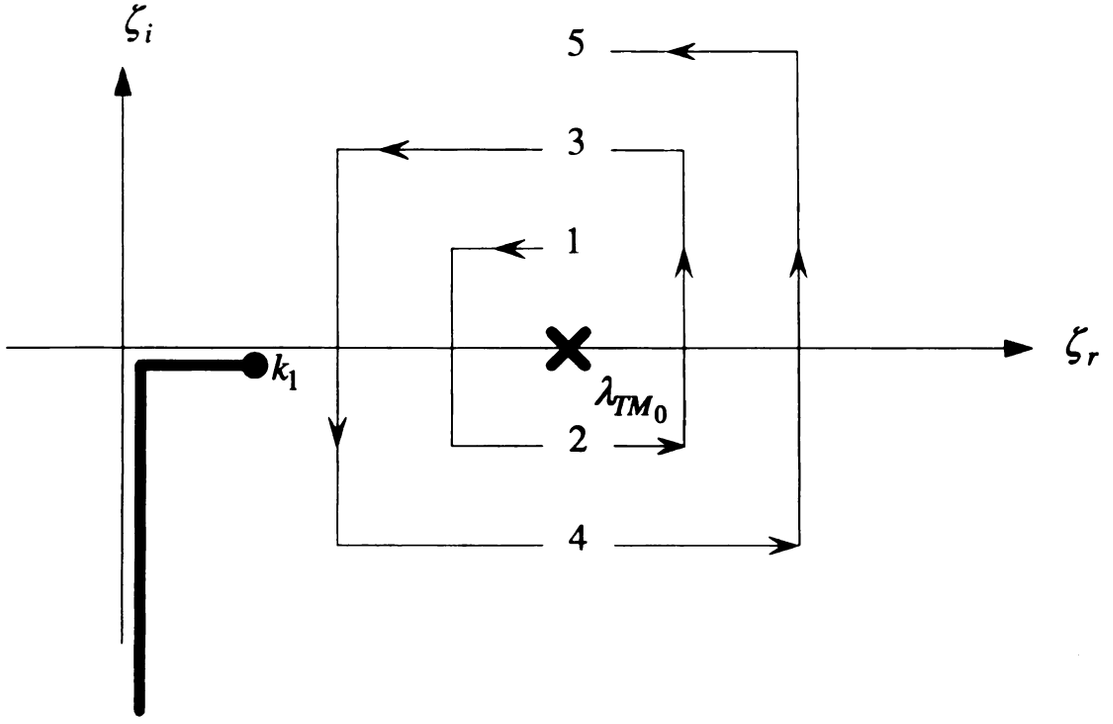

Figure 4.3.4 Path trajectory in the complex ζ -plane, encircling twice around the point $\zeta = \lambda_{TM_0}$.

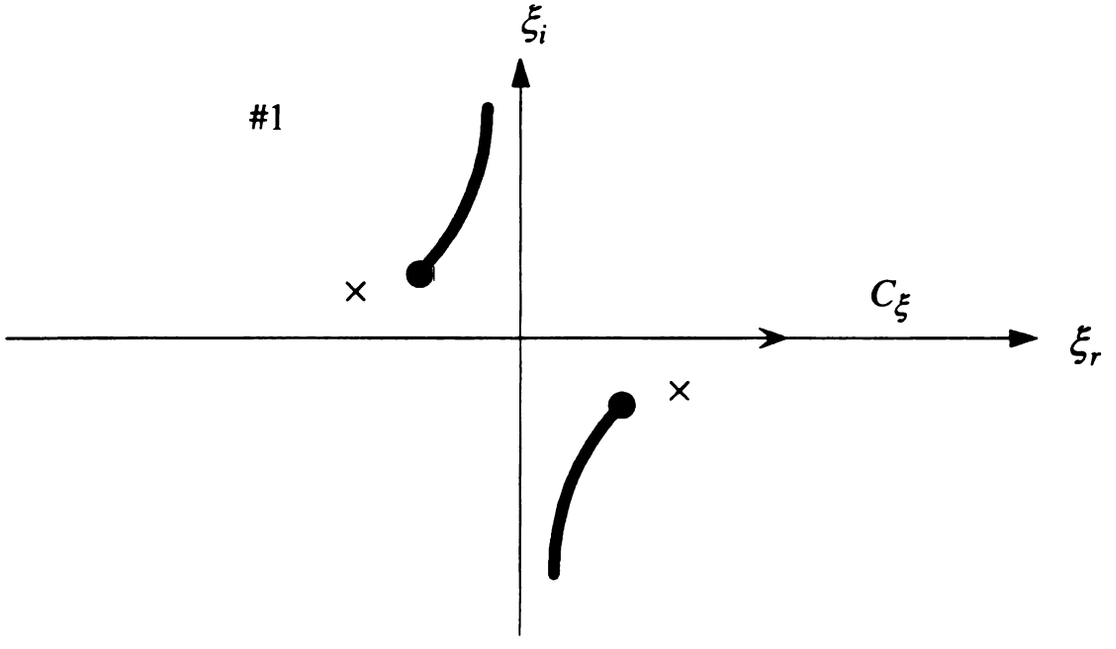

Figure 4.3.4a Evolution of C_ξ for a point 1 in Fig. 4.3.4.

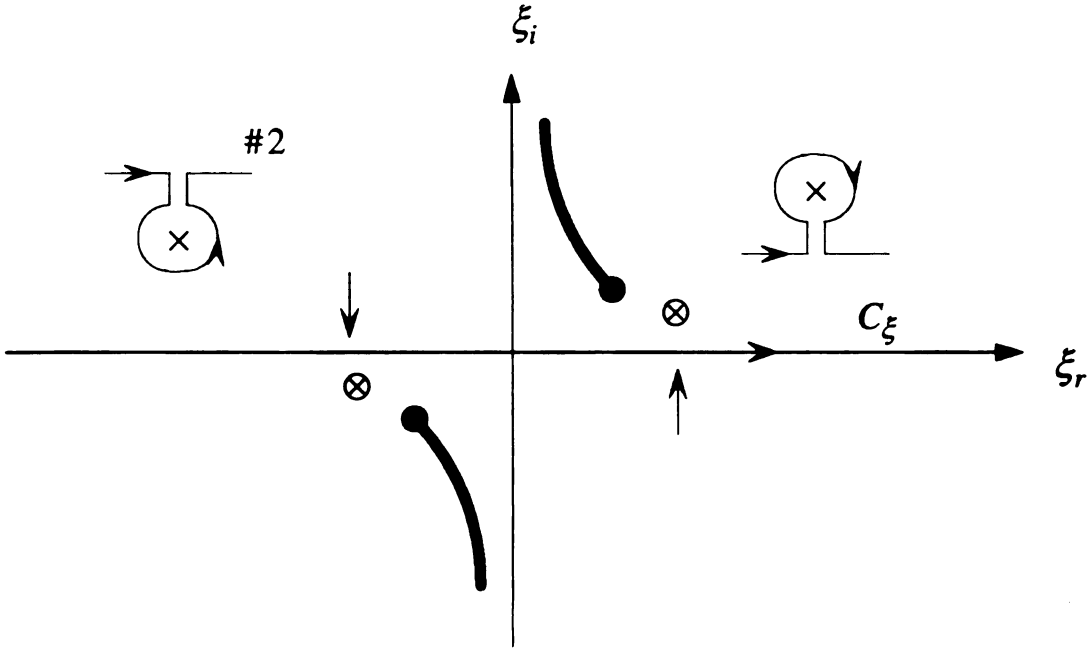

Figure 4.3.4b Evolution of C_ξ for a point 2 in Fig. 4.3.4

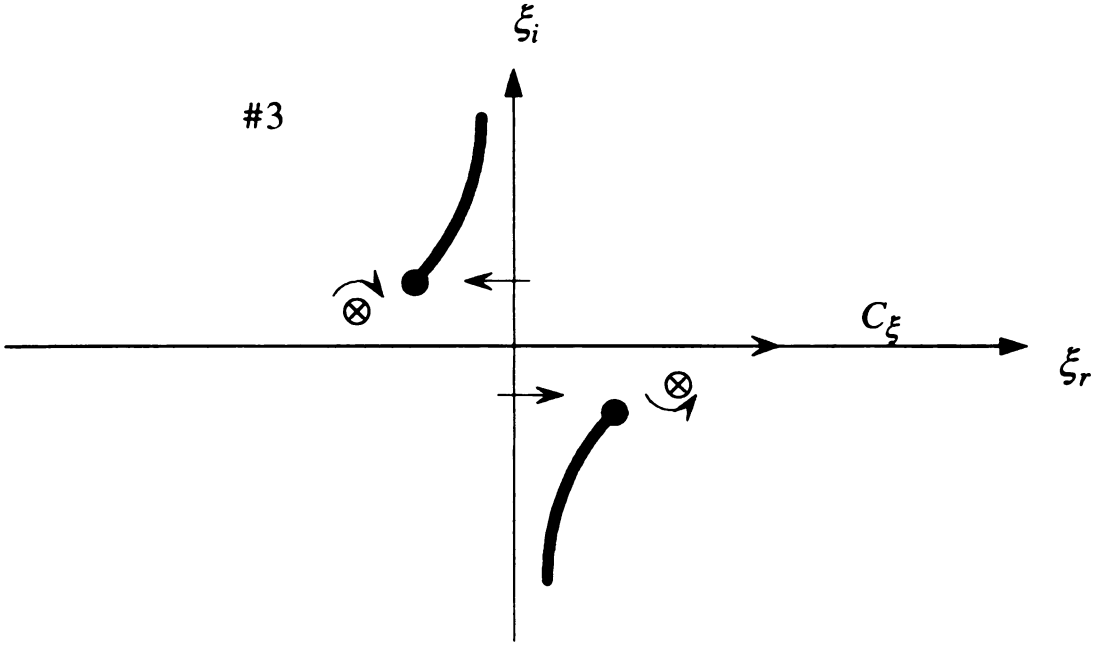

Figure 4.3.4c Evolution of C_ξ for a point 3 in Fig. 4.3.4.

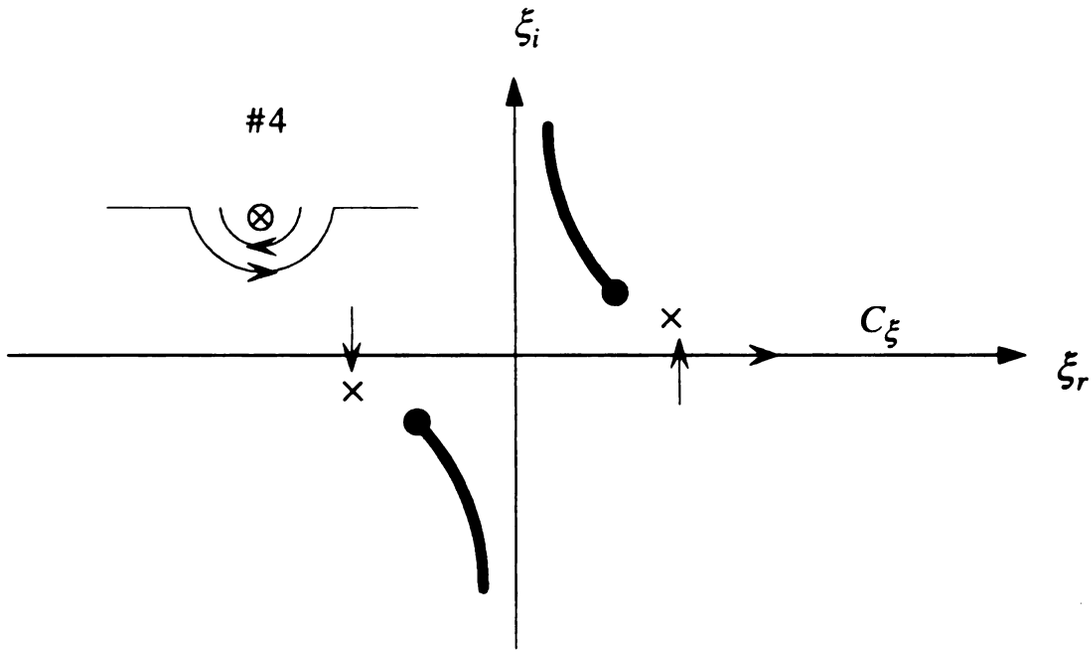

Figure 4.3.4d Evolution of C_ξ for a point 4 in Fig. 4.3.4

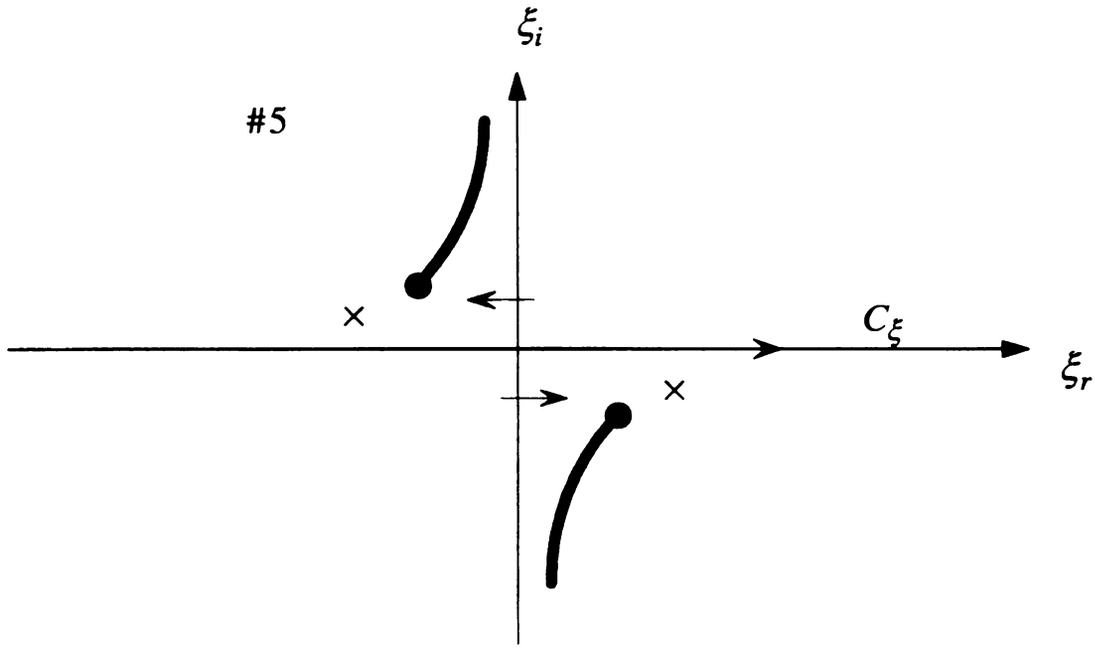

Figure 4.3.4e Evolution of C_ξ for a point 5 in Fig. 4.3.4.

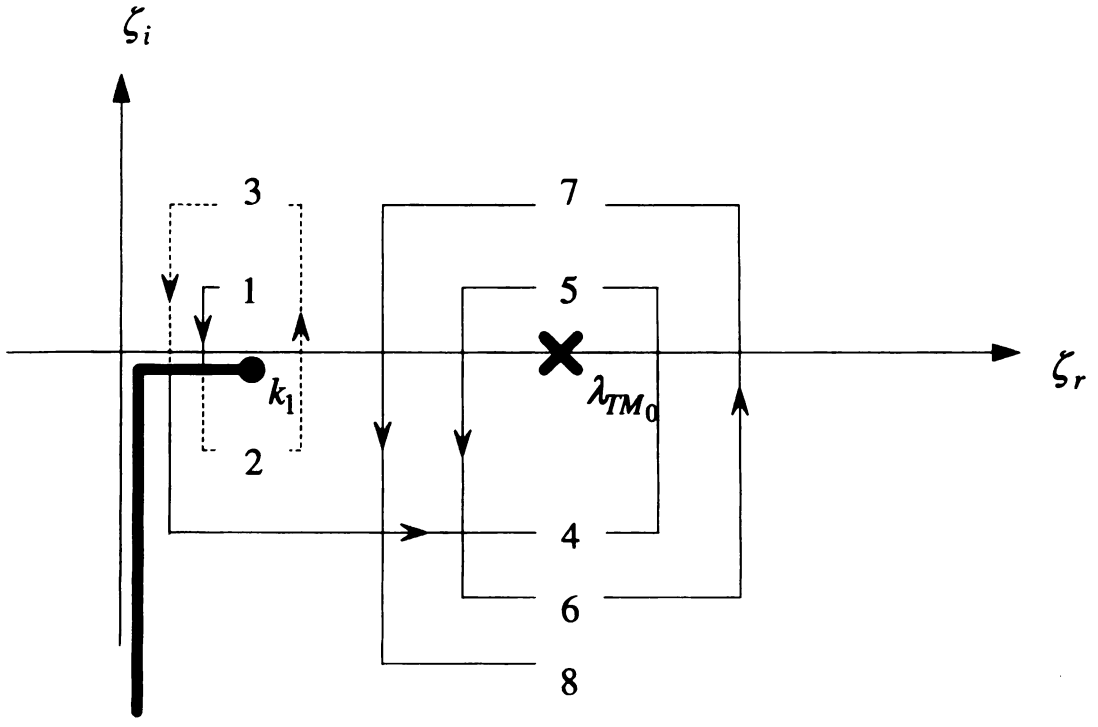

Figure 4.3.5 Path trajectory in the complex ζ -plane, encircling twice around the point $\zeta = \lambda_{TM_0}$ after violating the branch cut twice.

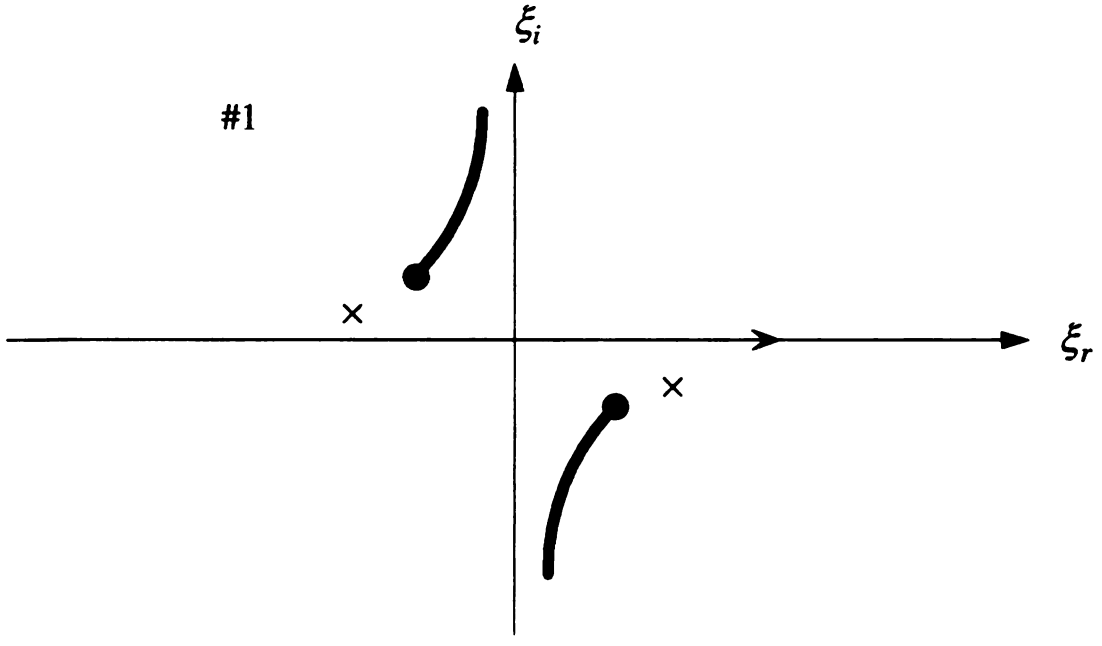

Figure 4.3.5a Evolution of C_ξ for a point 1 in Fig. 4.3.5.

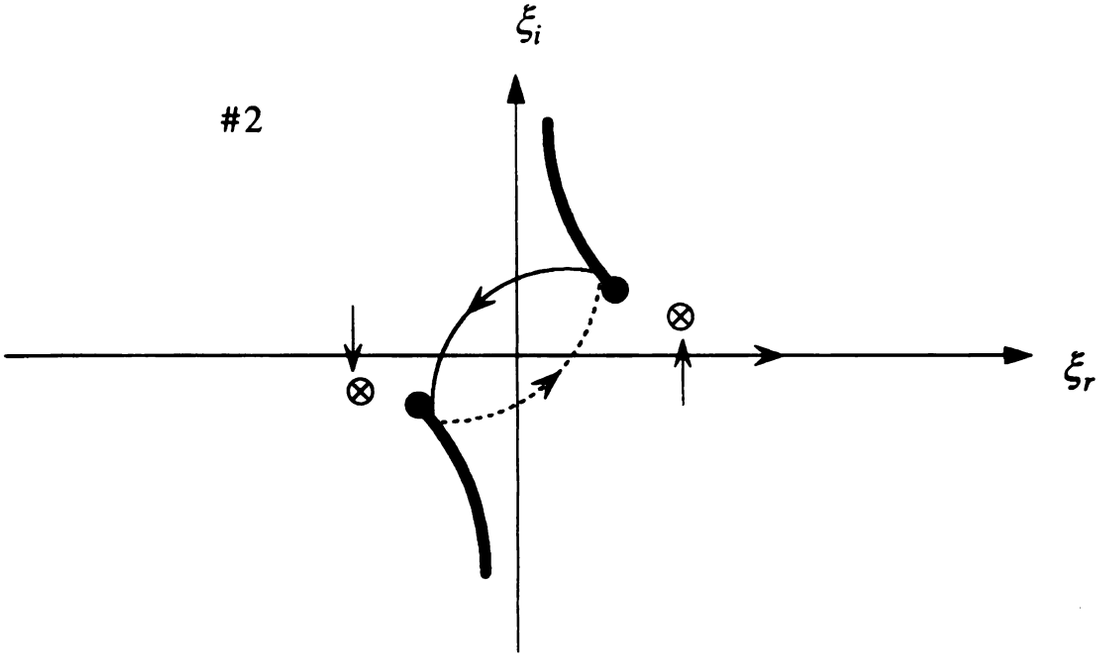

Figure 4.3.5b Evolution of C_ξ for a point 2 in Fig. 4.3.5.

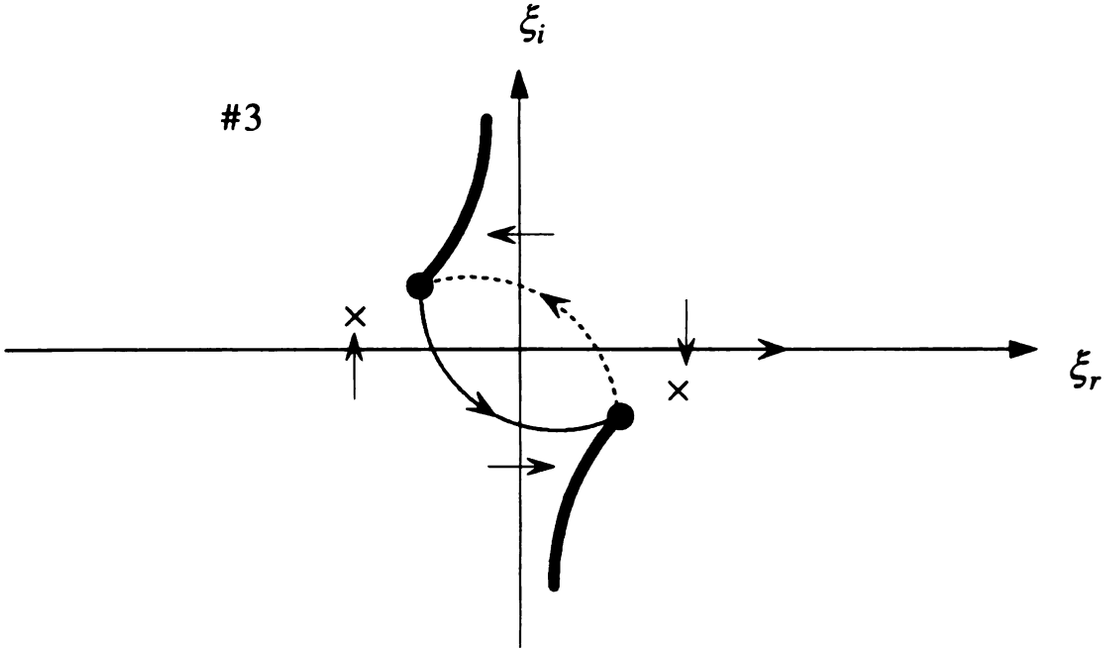

Figure 4.3.5c Evolution of C_ξ for a point 3 in Fig. 4.3.5.

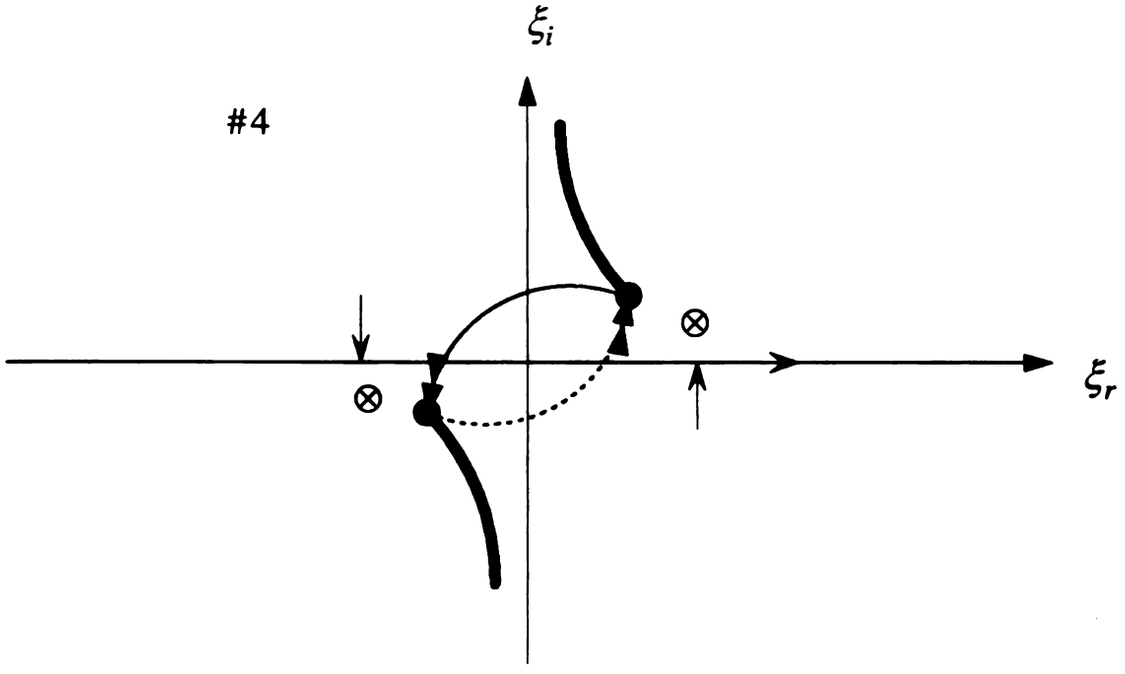

Figure 4.3.5d Evolution of C_ξ for a point 4 in Fig. 4.3.5.

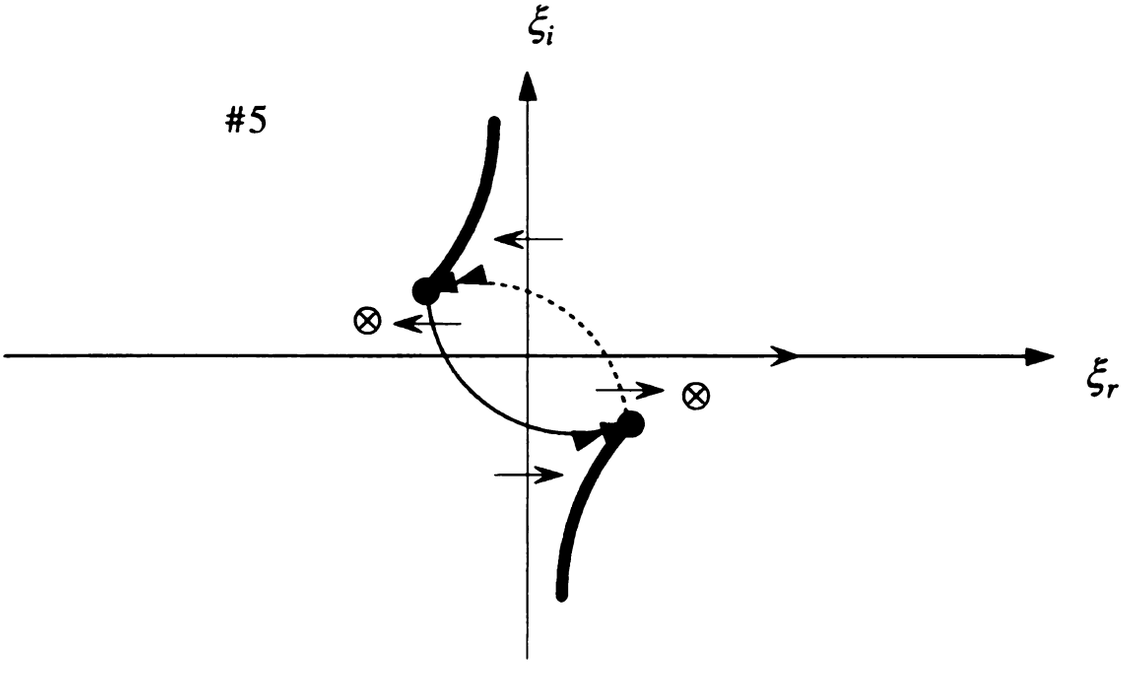

Figure 4.3.5e Evolution of C_ξ for a point 5 in Fig. 4.3.5.

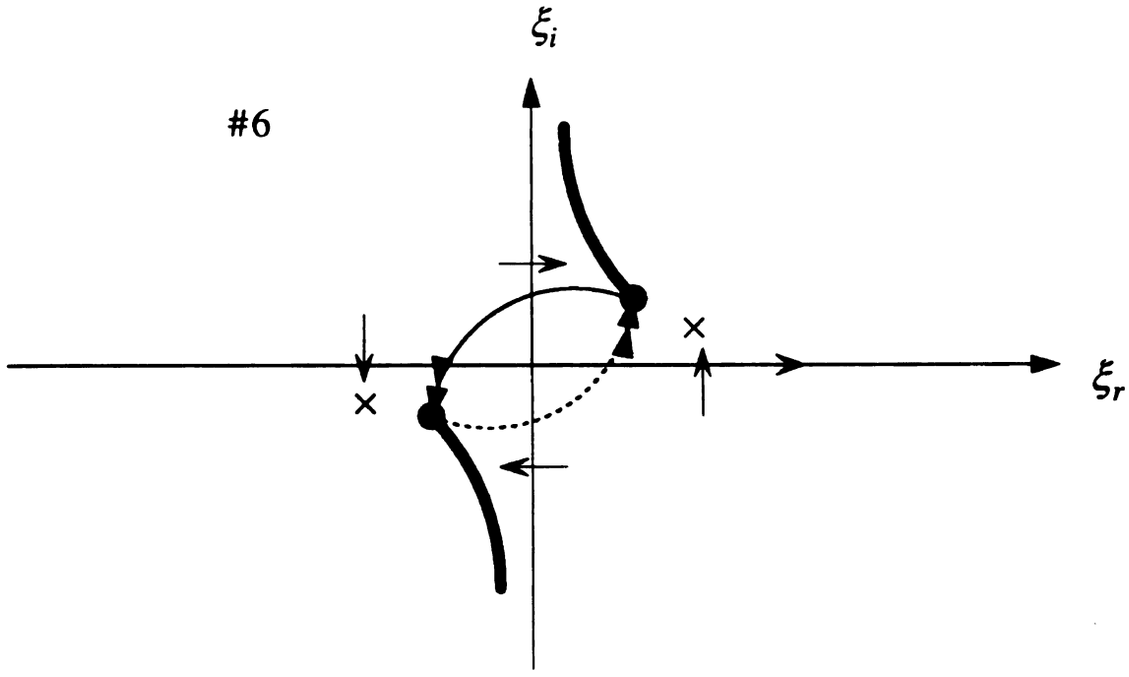

Figure 4.3.5f Evolution of C_ξ for a point 6 in Fig. 4.3.5.

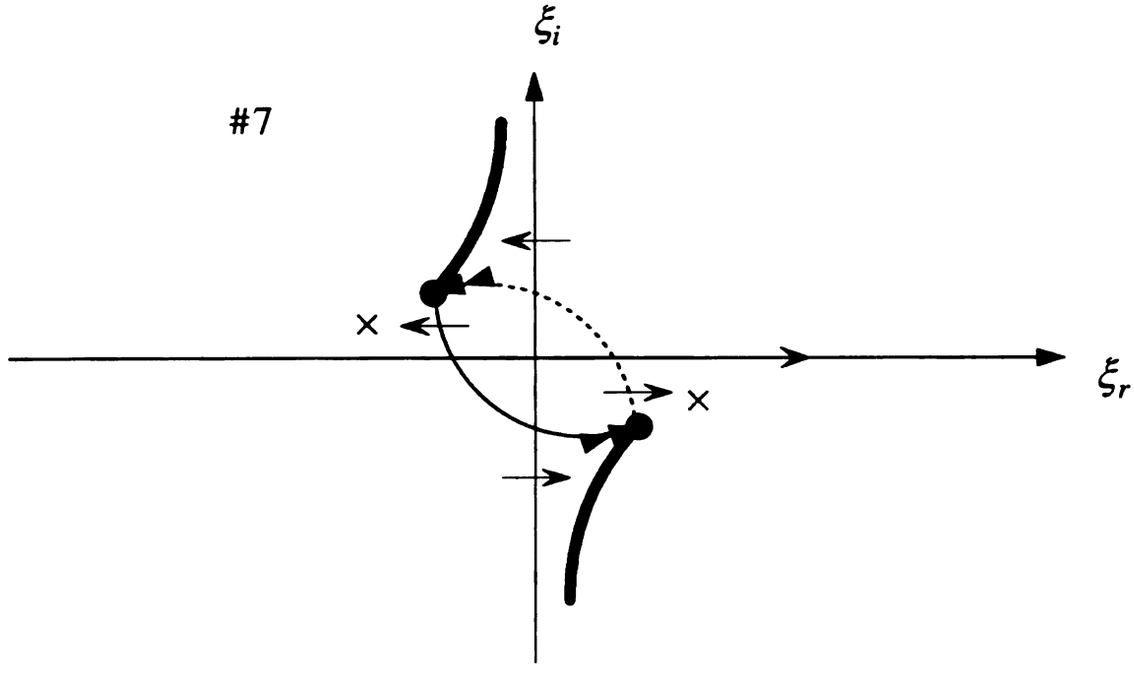

Figure 4.3.5g Evolution of C_ξ for a point 7 in Fig. 4.3.5.

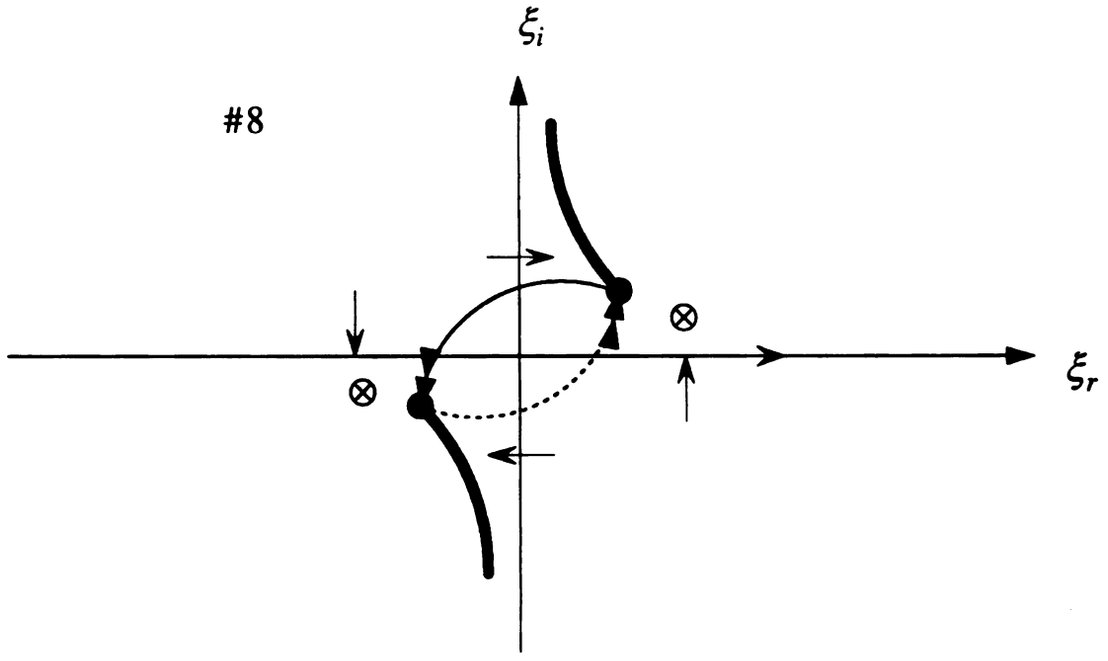

Figure 4.3.5h Evolution of C_ξ for a point 8 in Fig. 4.3.5.

4.3.3 REGULAR OR ANALYTIC POINT

The remaining investigation of the point $\zeta = \lambda_{TM_0}$ on the odd sheets S_{2N+1} of the branch points $\pm k_1$ can be also deduced from considering the S_{-1} Riemann sheet as depicted in Fig. 4.3.6.

At point 1 in Fig. 4.3.6, the sheet is designated by S_0 of the branch points $\pm k_1$ as depicted in Fig. 4.3.6a. The path stays on the top Riemann sheet and does not detour around the poles at $\pm\xi_{TM_0}$ in the complex ξ-plane.

As ζ moves toward point 2 by violating the branch cut once as depicted in Fig. 4.3.6, both the poles $\pm\xi_{TM_0}$ and the branch points $\pm\xi_{k_1}$ cross the real axis as depicted in Fig.

4.3.6b. So, the poles gain residue contributions and the integral path deformation in the complex ξ-plane was previously illustrated from Fig. 4.3.3b to Fig. 4.3.3e.

As ζ moves toward point 3 as depicted in Fig. 4.3.6, both the poles $\pm\xi_{TM_0}$ and the branch points $\pm\xi_{k_1}$ cross the imaginary axis as depicted in Fig. 4.3.6c. Since the poles cross the solid loop path on the top Riemann sheet, they annul residue contributions when they cross it.

Finally, at point 4 in Fig. 4.3.6, the poles $\pm\xi_{TM_0}$ cross the real axis to gain residue contributions and the branch points $\pm\xi_{k_1}$ cross the imaginary axis as depicted in Fig. 4.3.6d, which does not alter the real axis integration C_ξ in the complex ξ-plane as depicted in Fig. 4.3.6b. Therefore, the points $\zeta = \pm\lambda_{TM_0}$ are *regular or analytic points* on the sheet S_{-1} of the branch points $\pm k_1$. Similarly as in Fig. 4.3.5, the investigation of the points $\zeta = \pm\lambda_{TM_0}$ on the Riemann sheet S_{-3}, for example, can be implemented by violating the branch cut three times, i.e., encircling the branch point $\zeta = k_1$ three times, and the nature of the points $\zeta = \pm\lambda_{TM_0}$ is completely equivalent to that on the Riemann sheet S_{-1}. Without loss of any generality, it can be explicitly deduced that the points $\zeta = \pm\lambda_{TM_0}$ are *regular or analytic points* on the odd Riemann sheets S_{2N+1} of the branch points $\pm k_1$.

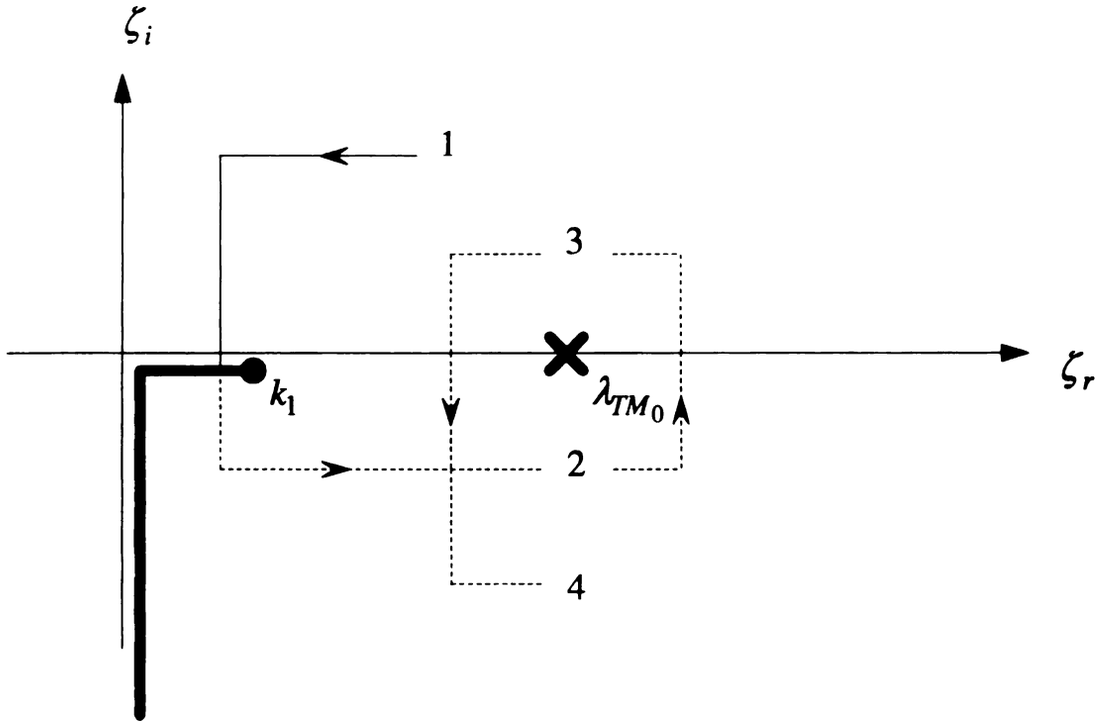

Figure 4.3.6 Path trajectory in the complex ζ -plane, encircling once around the point $\zeta = \lambda_{TM_0}$ after violating the branch cut once.

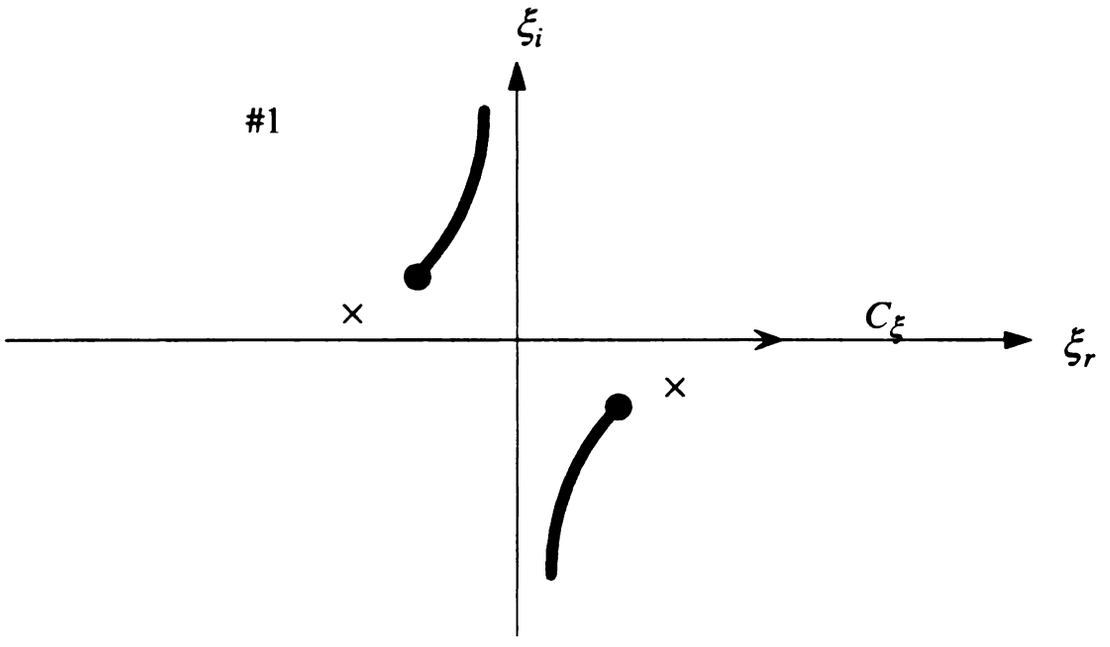

Figure 4.3.6a Evolution of C_ξ for a point 1 in Fig. 4.3.6.

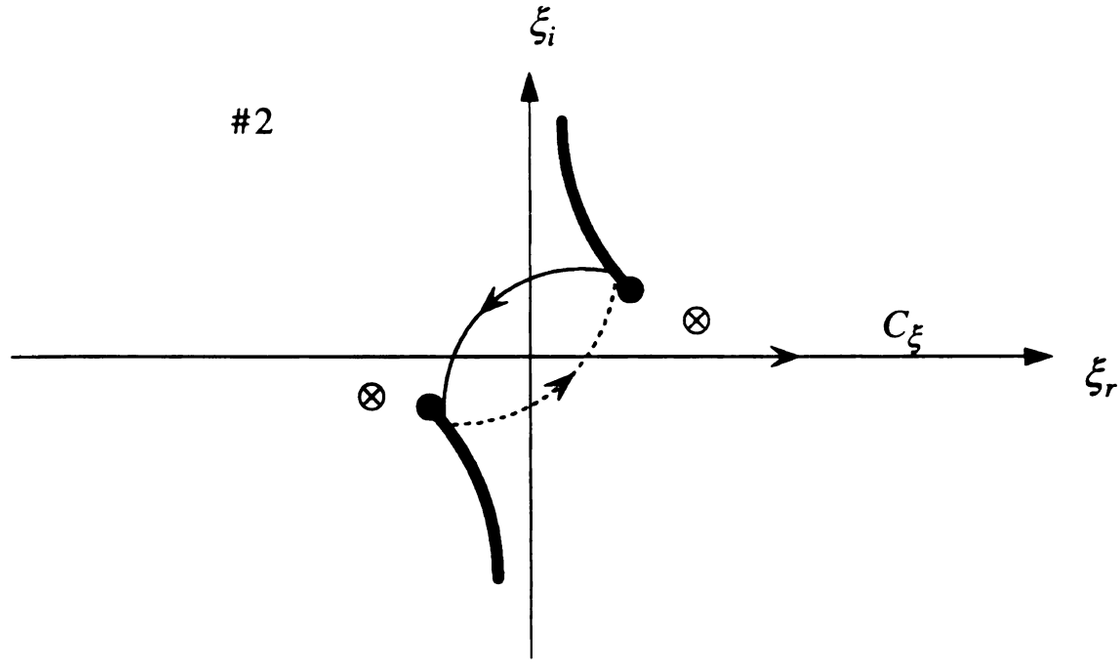

Figure 4.3.6b Evolution of C_ξ for a point 2 in Fig. 4.3.6.

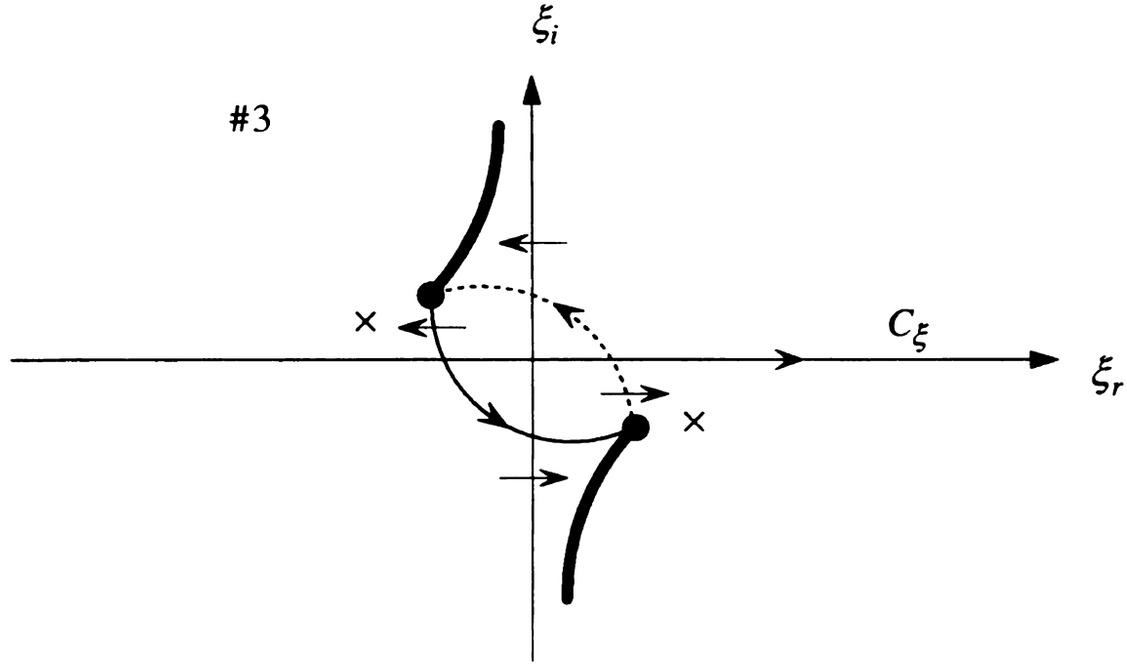

Figure 4.3.6c Evolution of C_ξ for a point 3 in Fig. 4.3.6.

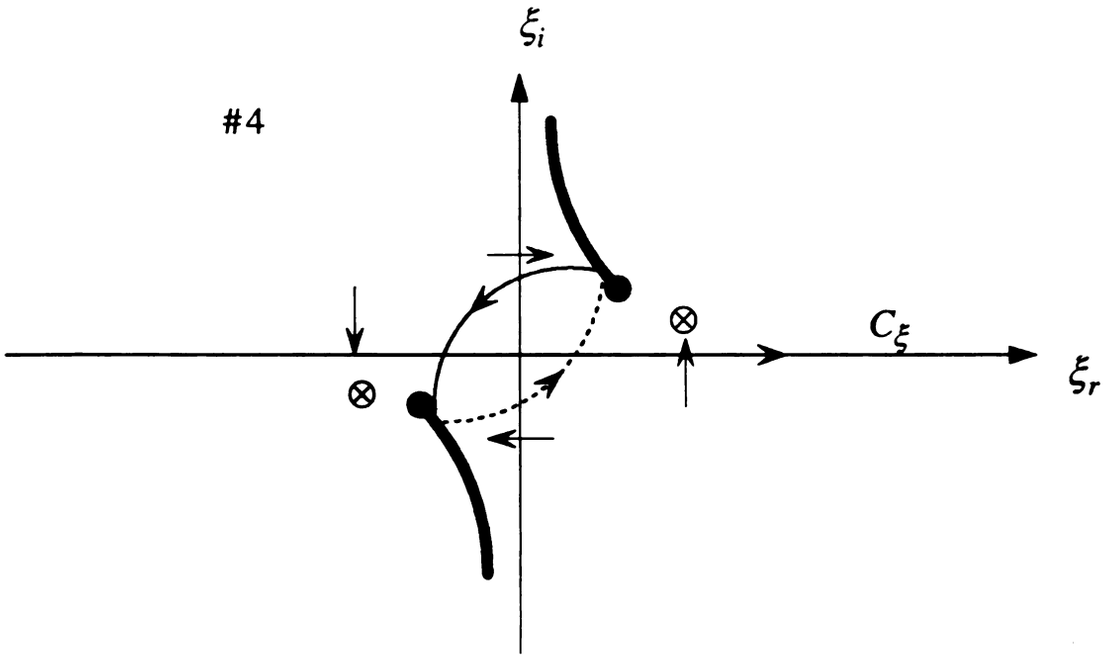

Figure 4.3.6d Evolution of C_ξ for a point 4 in Fig. 4.3.6.

4.4 PHYSICAL INTERPRETATION OF LOGARITHMIC AND SQUARE-ROOT TYPE BRANCH POINTS

It is observed that the branch points at $\zeta = \pm k_1$ are of a logarithmic type which lead to infinite number of Riemann sheets [9]. The logarithmic type branch points $\zeta = \pm k_1$ are associated with power loss due to radiation into the cover layer [30].

It is also observed that the branch points at $\zeta = \pm \lambda_{TM_0}$ are of a square-root type which lead to two Riemann sheets [9]. The square-root type branch points $\zeta = \pm \lambda_{TM_0}$ are physically associated with coupling of power into the transversely-propagating principal TM_0 surface-wave mode of that background environment. Simple- or guided-pole singularities discussed in Sec 4.3 consequently lead to surface-wave leakage into the background layer when the square-root type branch cuts are violated [30].

As depicted in Fig. 4.4.1, the branch cut path passes counter-clockwise around the logarithmic and square-root type branch cuts arising from the k_1 branch point and the proper background poles. The branch cut path in Fig. 4.4.1 defines the proper and continuous spectrum since it never violates those cuts. Proper continuous spectrum current and field will be rigorously analyzed in Chapters 5, 6, and 7.

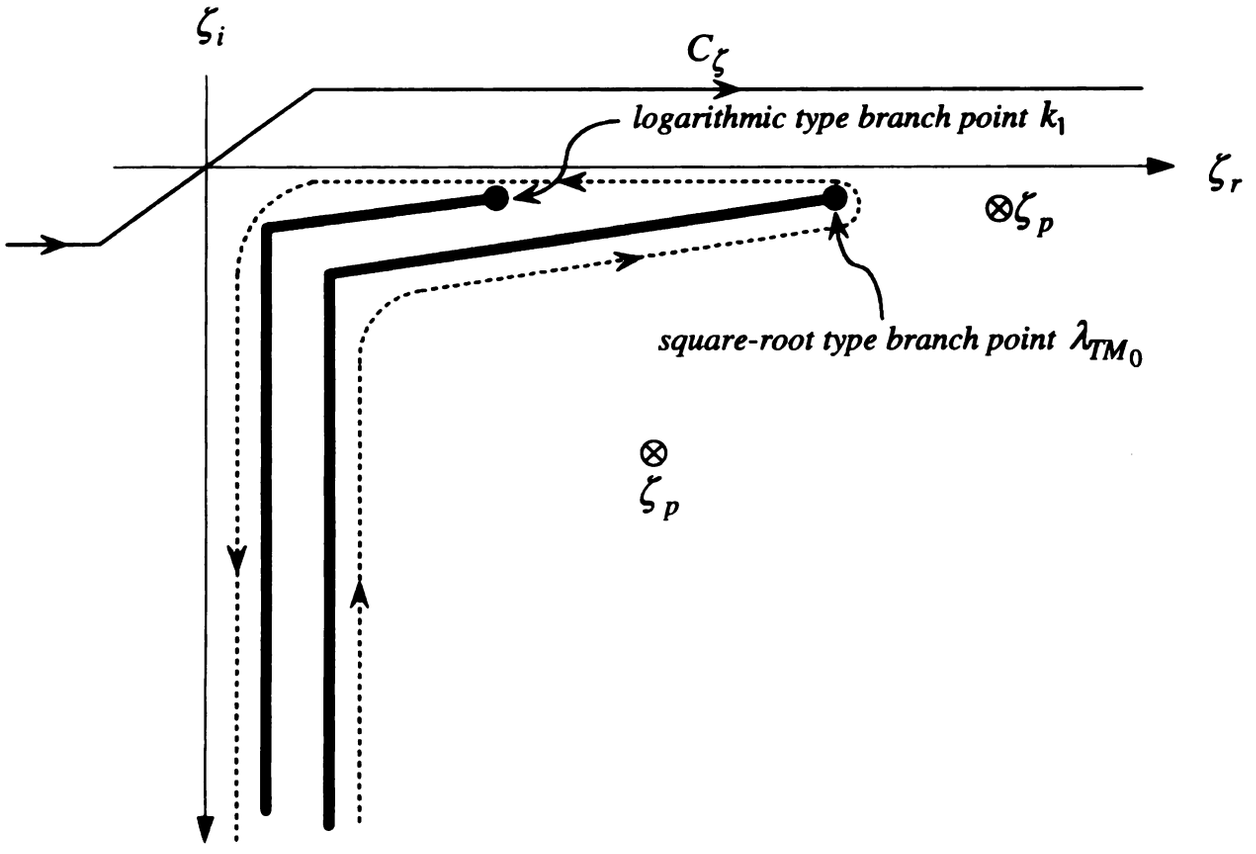

Figure 4.4.1 Branch cuts associated with a logarithmic type branch point k_1 and a square-root type branch point λ_{TM_0} in the complex ζ -plane and the continuous spectrum contributed by those branch cut integrations.

4.5 CONCLUSION

The transform-domain integral-operator methodology for currents/fields of guiding structures contributes to the formulation of the spectral electric field integral equation (EFIE) of integrated open waveguides through a singularity expansion of fields in the complex axial transform plane (complex ζ -plane). Complex analysis in the ζ -plane is based upon the transform-domain integral equation formulation for currents/fields of the guiding structure. Singularities in that plane were identified as poles associated with the guiding structure and branch points contributed by layered background environments through the integral representation for the required Green's dyad kernel.

The manner in which singularities in background environments manifest themselves as branch points in the ζ -plane [7], [8] is demonstrated. Section 3 rigorously analyzes those branch points as *logarithmic-type* and *square-root type* due to their complicated migration pattern in the ξ -plane in conjunction with points in the ζ -plane [9]. And, the logarithmic type branch points are associated with power loss due to radiation into the cover layer [30]. Meanwhile, the square-root type branch points are physically associated with coupling of power into the transversely-propagating principal TM_0 surface-wave mode of that background environment. Moreover, Simple- or guided- pole singularities ζ_p discussed in Sec 4.3 consequently lead to surface-wave leakage into the background layer when the square-root type branch cuts are violated [30].

It is observed that the branch cut path detours around, in a counter-clockwise sense, the logarithmic and square-root type branch cuts arising from the k_1 branch point and the proper background modes as depicted in Fig. 4.4.1. And, the branch cut path in Fig. 4.4.1

defines the proper and continuous spectrum since it never violates the branch cut. Proper continuous spectrum currents/fields will be rigorously analyzed in Chapters 5, 6, and 7.

CHAPTER 5

THE PROPER CURRENT SPECTRUM OF AN OPEN INTEGRATED MICROSTRIP WAVEGUIDE

5.1 INTRODUCTION AND GEOMETRICAL CONFIGURATION

The existence of leaky modes on the integrated open waveguide structure has recently received considerable attention [32]-[45]. However, the proper continuous and discrete spectrum currents of the integrated open microstrip waveguide have been until recently neither conceptualized nor quantified adequately. That spectrum can be identified as the branch cut contribution to a singularity expansion of those currents in the complex axial transform plane (ζ-plane). As discussed in Chapter 4, singularities in that plane include poles associated with the guiding structure and branch points contributed by layered background environments. The manner in which singularities in background environments manifest themselves as branch points in the complex ζ-plane is reviewed.

Based on a spectral EFIE (electric field integral equation) formulation [46]-[48], both approximate and analytical expressions for the spectral microstrip current are obtained. A δ-gap field feed model is exploited as an excitatory source [49]-[52]. It is noted that the current approximation is based on the Maxwellian distribution for the transverse current profile. Microstrip currents are recovered from the spectral representation by integration contour deformation on the top sheet of the complex ζ-plane. As a result, microstrip currents are obtained in terms of the proper propagation mode spectrum. That spectrum consists of bound propagation modes associated with pole singularities and a continuous spectrum [31], [53] which is associated with integration around branch cuts

contributed by background layer environments. During integration around the branch cuts, singularities in the complex transverse transform plane (ξ-plane) tend to migrate in a complicated manner. The trajectories of ξ-plane migration are identified and suitably accommodated during the real axis integration in the complex ξ-plane. This overall procedure leads to a decomposition of the total currents into bound mode and continuous spectrum contributions. The result is numerically validated by real axis integration in the complex ζ-plane. The quasi TEM characteristic impedance of bound modes associated with pole singularities is calculated and is validated by comparison with well-known empirical formulas [54].

Extensive numerical results are obtained, which can compare bound mode and continuous spectrum contributions to microstrip currents. It is recognized that currents are dominated by bound propagation modes. Physically, it is acceptable since the microstrip current is directly associated with the conducting microstrip rather than the background layer environment. Even if the continuous current spectrum is maximal near the feed point and decays rapidly with axial distance from the feed, it contributes negligibly to the total spectrum since the dominant contribution comes from the discrete current spectrum contributed by the bound propagation mode. However, the strengths of continuous and discrete spectrum field contributions in the background layer environment are reversed, which will be discussed in Chapter 6.

The geometrical configuration of integrated microstrip waveguide immersed in a planar-layered background environment is depicted in Fig. 5.1.1 and its cross-sectional view is also depicted in Fig. 5.1.2. The waveguiding axis is chosen to be z-axis with the x-axis tangential and y-axis normal to the planar interfaces. Each of the planar layers

is assumed to be non-magnetic, isotropic and homogeneous with complex permittivity ε_l, $l = 1, 2, 3$ for the cover, film, and substrate layers with $\varepsilon_3 \to -j\infty$ or $\sigma \to \infty$. The guiding structure is embedded in the cover layer adjacent to the cover/film interface.

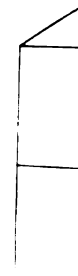

Figure 5.

Fig

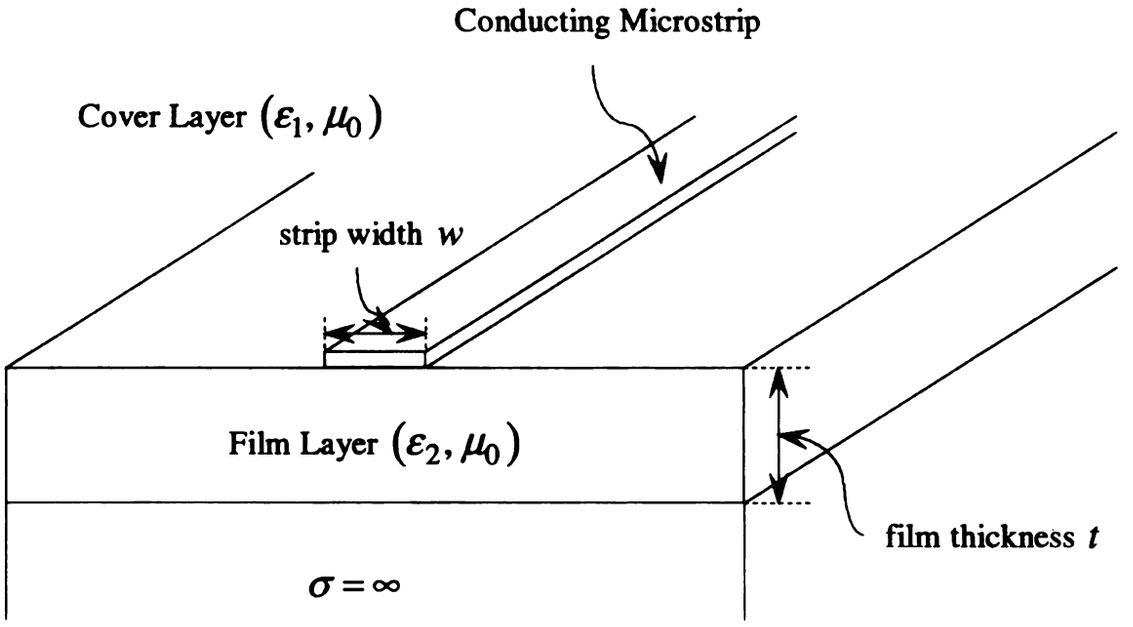

Figure 5.1.1 Geometrical configuration of open microstrip structure immersed in layered background environment.

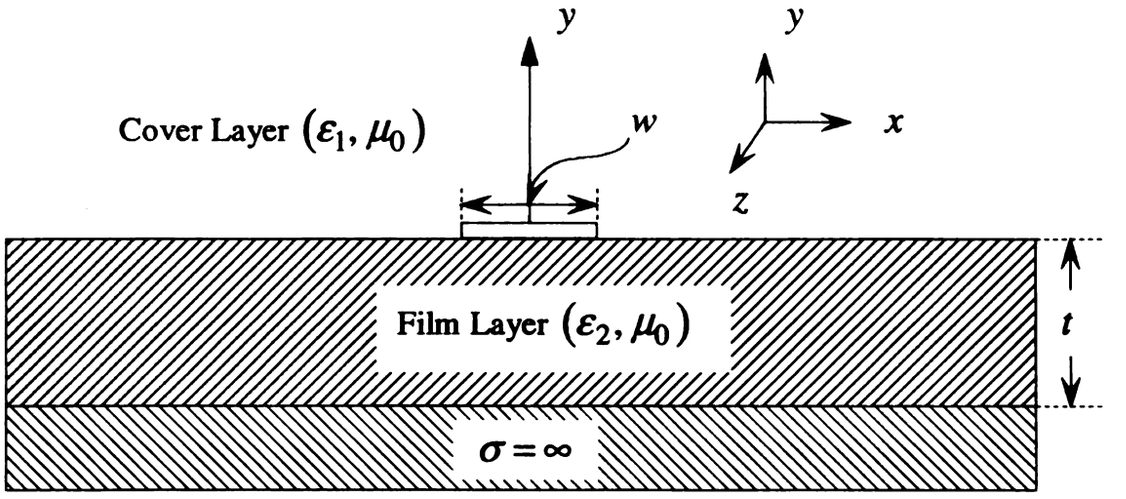

Figure 5.1.2 Cross-sectional view of immersed microstrip structure.

5.2 MIC

As disc

the microst

where $T($

takes the C

which lea

Since axia

The spe

$\hat{t}\cdot($

in agreeme

ducting stri

5.2 MICROSTRIP CURRENT FORMULATION

As discussed in Chapter 4, a δ-gap field feed is exploited as an excitation source on the microstrip. Therefore, an impressed field can be represented by

$$E_{1z}^{i}(x,z)=T(x)L_g(z) \tag{5.2.1}$$

where $T(x)$ takes unity for $|x|<w/2$ and the longitudinal δ-gap function $L_g(z)$ takes the Gaussian form [52] of

$$L_g(z)=\frac{1}{d}\frac{e^{-(z/d)^2/2}}{\sqrt{2\pi}} \tag{5.2.2}$$

which leads to faster convergence, where d is the effective gap width. Then,

$$E_{1z}^{i}(x,z)=T(x)\frac{1}{d}\frac{e^{-(z/d)^2/2}}{\sqrt{2\pi}}$$

$$\textit{where} \tag{5.2.3}$$

$$T(x)=\begin{cases}1\cdots|x|<w/2\\0\cdots|x|>w/2\end{cases}$$

Since axial uniformity of the waveguiding system prompts Fourier transformation,

$$e_{1\zeta}^{i}(x,\zeta)=T(x)\tilde{L}_g(\zeta)=T(x)e^{-(\zeta d)^2/2} \tag{5.2.4}$$

The spectral EFIE for the induced surface current $\tilde{\boldsymbol{k}}_\zeta$ on the microstrip becomes

$$\hat{t}\cdot\left(k_1^2+\tilde{\nabla}\tilde{\nabla}\cdot\right)\int_C \bar{\boldsymbol{g}}_{1\zeta}(\rho|\rho')\cdot\tilde{\boldsymbol{k}}_\zeta(\rho',\zeta)dl'=-\frac{jk_1}{\eta_1}\hat{t}\cdot\tilde{\boldsymbol{e}}_{1\zeta}^{i}(\rho,\zeta)\cdots\rho\in C \tag{5.2.5}$$

in agreement with Eqn. (4.2.11). Since C is the periphery of the infinitesimally thin conducting strip then $\tilde{\boldsymbol{k}}_\zeta(\rho',\zeta)\big|_{y'=0}=\hat{x}\tilde{k}_{\zeta x}(x',\zeta)+\hat{z}\tilde{k}_{\zeta z}(x',\zeta)$, and from Eqn. (4.2.13)

$$\int_C \bar{g}_{1\alpha}$$

$$= \int_{-w}^{w/}$$

$$= \int_{-w}^{w/}$$

$$+ \left[\hat{z} g \right.$$

$$= \int_{-w}^{w/}$$

$$+ \hat{y} \left[\begin{array}{c} \bar{c} \\ - \end{array} \right.$$

$$+ \hat{z} \left[g \right.$$

Then,

$$\tilde{\nabla} \bullet \int_{C}$$

$$= \frac{\partial}{\partial x}$$

$$+ \frac{\partial}{\partial y}$$

$$+ j\zeta$$

Defining

$$\tilde{I}_{\alpha}(x, y$$

$$\tilde{I}_{y}(x, y$$

Therefor

$$\int_C \bar{\boldsymbol{g}}_{1\zeta}(\boldsymbol{\rho}|\boldsymbol{\rho}')\cdot\tilde{\boldsymbol{k}}_\zeta(\boldsymbol{\rho}',\zeta)dl'$$

$$=\int_{-w/2}^{w/2}\left[\bar{\boldsymbol{g}}_{1\zeta}(x,y|x',0)\cdot\hat{x}\tilde{k}_{\zeta x}(x',\zeta)+\bar{\boldsymbol{g}}_{1\zeta}(x,y|x',0)\cdot\hat{z}\tilde{k}_{\zeta z}(x',\zeta)\right]dx'$$

$$=\int_{-w/2}^{w/2}\left\{\left[\hat{x}g_{1\zeta}^{p}(x,y|x',0)+\hat{x}g_{1\zeta t}^{r}(x,y|x',0)+\hat{y}\frac{\partial g_{1\zeta c}^{r}(x,y|x',0)}{\partial x}\right]\tilde{k}_{\zeta x}(x',\zeta)\right.$$

$$\left.+\left[\hat{z}g_{1\zeta}^{p}(x,y|x',0)+\hat{y}j\zeta g_{1\zeta c}^{r}(x,y|x',0)+\hat{z}g_{1\zeta t}^{r}(x,y|x',0)\right]\tilde{k}_{\zeta z}(x',\zeta)\right\}dx'$$

$$=\int_{-w/2}^{w/2}\left\{\hat{x}\left[g_{1\zeta}^{p}(x,y|x',0)+g_{1\zeta t}^{r}(x,y|x',0)\right]\tilde{k}_{\zeta x}(x',\zeta)\right.$$

$$+\hat{y}\left[\frac{\partial g_{1\zeta c}^{r}(x,y|x',0)}{\partial x}\tilde{k}_{\zeta x}(x',\zeta)+j\zeta g_{1\zeta c}^{r}(x,y|x',0)\tilde{k}_{\zeta z}(x',\zeta)\right]$$

$$\left.+\hat{z}\left[g_{1\zeta}^{p}(x,y|x',0)+g_{1\zeta t}^{r}(x,y|x',0)\right]\tilde{k}_{\zeta z}(x',\zeta)\right\}dx'$$

Then,

$$\tilde{\nabla}\cdot\int_C \bar{\boldsymbol{g}}_{1\zeta}(\boldsymbol{\rho}|\boldsymbol{\rho}')\cdot\tilde{\boldsymbol{k}}_\zeta(\boldsymbol{\rho}',\zeta)dl'$$

$$=\frac{\partial}{\partial x}\int_{-w/2}^{w/2}\left[g_{1\zeta}^{p}(x,y|x',0)+g_{1\zeta t}^{r}(x,y|x',0)\right]\tilde{k}_{\zeta x}(x',\zeta)dx'$$

$$+\frac{\partial}{\partial y}\int_{-w/2}^{w/2}\left[\frac{\partial g_{1\zeta c}^{r}(x,y|x',0)}{\partial x}\tilde{k}_{\zeta x}(x',\zeta)+j\zeta g_{1\zeta c}^{r}(x,y|x',0)\tilde{k}_{\zeta z}(x',\zeta)\right]dx'$$

$$+j\zeta\int_{-w/2}^{w/2}\left[g_{1\zeta}^{p}(x,y|x',0)+g_{1\zeta t}^{r}(x,y|x',0)\right]\tilde{k}_{\zeta z}(x',\zeta)dx'$$

Defining $\int_C \bar{\boldsymbol{g}}_{1\zeta}(\boldsymbol{\rho}|\boldsymbol{\rho}')\cdot\tilde{\boldsymbol{k}}_\zeta(\boldsymbol{\rho}',\zeta)dl'=\sum_\alpha \hat{\alpha}\tilde{I}_\alpha(x,y,\zeta)$ leads to

$$\tilde{I}_\alpha(x,y,\zeta)=\int_{-w/2}^{w/2}\left[g_{1\zeta}^{p}(x,y|x',0)+g_{1\zeta t}^{r}(x,y|x',0)\right]\tilde{k}_{\zeta\alpha}(x',\zeta)dx'\cdots\alpha=x,z$$

$$\tilde{I}_y(x,y,\zeta)=\int_{-w/2}^{w/2}\left[\frac{\partial g_{1\zeta c}^{r}(x,y|x',0)}{\partial x}\tilde{k}_{\zeta x}(x',\zeta)+j\zeta g_{1\zeta c}^{r}(x,y|x',0)\tilde{k}_{\zeta z}(x',\zeta)\right]dx'$$

Therefore,

$$\tilde{\nabla}\cdot\int_C \bar{\bar{g}}_{1\zeta}(\rho|\rho')\cdot\tilde{k}_\zeta(\rho',\zeta)dl' = \frac{\partial\tilde{I}_x(x,y,\zeta)}{\partial x}+\frac{\partial\tilde{I}_y(x,y,\zeta)}{\partial y}+j\zeta\tilde{I}_z(x,y,\zeta)$$

Eqn. (5.2.5) becomes, for $\hat{t}=\hat{x}$

$$k_1^2\tilde{I}_x(x,y,\zeta)+\frac{\partial}{\partial x}\left[\frac{\partial\tilde{I}_x(x,y,\zeta)}{\partial x}+\frac{\partial\tilde{I}_y(x,y,\zeta)}{\partial y}+j\zeta\tilde{I}_z(x,y,\zeta)\right]=-\frac{jk_1}{\eta_1}\tilde{e}^i_{1\zeta x}(x,y,\zeta)$$

For $\hat{t}=\hat{z}$,

$$k_1^2\tilde{I}_z(x,y,\zeta)+j\zeta\left[\frac{\partial\tilde{I}_x(x,y,\zeta)}{\partial x}+\frac{\partial\tilde{I}_y(x,y,\zeta)}{\partial y}+j\zeta\tilde{I}_z(x,y,\zeta)\right]=-\frac{jk_1}{\eta_1}\tilde{e}^i_{1\zeta z}(x,y,\zeta)$$

For $\hat{t}=\hat{x}$,

$$\left(k_1^2+\frac{\partial^2}{\partial x^2}\right)\int_{-w/2}^{w/2}\left[g^p_{1\zeta}(x,y|x',0)+g^r_{1\zeta t}(x,y|x',0)\right]\tilde{k}_{\zeta x}(x',\zeta)dx'$$
$$+\frac{\partial^2}{\partial x\partial y}\int_{-w/2}^{w/2}\left[\frac{\partial g^r_{1\zeta c}(x,y|x',0)}{\partial x}\tilde{k}_{\zeta x}(x',\zeta)+j\zeta g^r_{1\zeta c}(x,y|x',0)\tilde{k}_{\zeta z}(x',\zeta)\right]dx'$$
$$+j\zeta\frac{\partial}{\partial x}\int_{-w/2}^{w/2}\left[g^p_{1\zeta}(x,y|x',0)+g^r_{1\zeta t}(x,y|x',0)\right]\tilde{k}_{\zeta z}(x',\zeta)dx'=-\frac{jk_1}{\eta_1}\tilde{e}^i_{1\zeta x}(x,y,\zeta)$$

For $\hat{t}=\hat{z}$,

$$j\zeta\frac{\partial}{\partial x}\int_{-w/2}^{w/2}\left[g^p_{1\zeta}(x,y|x',0)+g^r_{1\zeta t}(x,y|x',0)\right]\tilde{k}_{\zeta x}(x',\zeta)dx'$$
$$+j\zeta\frac{\partial}{\partial y}\int_{-w/2}^{w/2}\left[\frac{\partial g^r_{1\zeta c}(x,y|x',0)}{\partial x}\tilde{k}_{\zeta x}(x',\zeta)+j\zeta g^r_{1\zeta c}(x,y|x',0)\tilde{k}_{\zeta z}(x',\zeta)\right]dx'$$
$$+\left(k_1^2-\zeta^2\right)\int_{-w/2}^{w/2}\left[g^p_{1\zeta}(x,y|x',0)+g^r_{1\zeta t}(x,y|x',0)\right]\tilde{k}_{\zeta z}(x',\zeta)dx'=-\frac{jk_1}{\eta_1}\tilde{e}^i_{1\zeta z}(x,y,\zeta)$$

Note that Green's dyad arguments are $(x,y|x',0)$ with $y\to 0$ understood subsequent to performing $\partial/\partial y$.

As defi

$$g_{1\zeta}^{p}$$

$$\frac{\partial g_{1}^{r}}{\partial x}$$

$$g_{1\zeta}^{r}$$

whe

$$Z^{h}($$

$$Z^{e}($$

$$p_{l}($$

$$N_{21}^{2}$$

Therefo

$$\int_{-\infty}^{\infty} d\xi$$

$$\left[j\xi \tilde{k}_{\zeta x}$$

leads to

$$\frac{1}{2\pi}$$

$$+\left[\frac{\xi}{Z}\right.$$

As defined in Eqn. (4.2.8),

$$g_{1\zeta}^{p}+g_{1\zeta t}^{r}=\int_{-\infty}^{\infty}\frac{\left[1+R_{1t}(\lambda)\right]e^{j\xi(x-x')}e^{-p_1 y}}{4\pi p_1}d\xi=\int_{-\infty}^{\infty}\frac{e^{j\xi(x-x')}e^{-p_1 y}}{2\pi Z^{h}(\lambda)}d\xi$$

$$\frac{\partial g_{1\zeta c}^{r}}{\partial x}=\int_{-\infty}^{\infty}\frac{j\xi C(\lambda)e^{j\xi(x-x')}e^{-p_1 y}}{4\pi p_1}d\xi=\int_{-\infty}^{\infty}\frac{j\xi\left(N_{21}^{2}-1\right)e^{j\xi(x-x')}e^{-p_1 y}}{2\pi Z^{h}(\lambda)Z^{e}(\lambda)}d\xi$$

$$g_{1\zeta c}^{r}=\int_{-\infty}^{\infty}\frac{C(\lambda)e^{j\xi(x-x')}e^{-p_1 y}}{4\pi p_1}d\xi=\int_{-\infty}^{\infty}\frac{\left(N_{21}^{2}-1\right)e^{j\xi(x-x')}e^{-p_1 y}}{2\pi Z^{h}(\lambda)Z^{e}(\lambda)}d\xi$$

where

$$Z^{h}(\lambda)=p_1(\lambda)+p_2(\lambda)\coth\left[p_2(\lambda)t\right]$$

$$Z^{e}(\lambda)=N_{21}^{2}p_1(\lambda)+p_2(\lambda)\tanh\left[p_2(\lambda)t\right]$$

$$p_l(\lambda)=\sqrt{\lambda^{2}-k_l^{2}}\cdots l=1,2\qquad\lambda^{2}=\xi^{2}+\zeta^{2}$$

$$N_{21}^{2}=\left(n_2/n_1\right)^{2}$$

Therefore, for $\hat{t}=\hat{x}$,

$$\int_{-\infty}^{\infty}d\xi e^{j\xi x}e^{-p_1 y}\int_{-w/2}^{w/2}\left\{\left(k_1^{2}-\xi^{2}\right)\frac{e^{-j\xi x'}\tilde{k}_{\zeta x}(x',\zeta)}{2\pi Z^{h}(\lambda)}-j\xi p_1\frac{\left(N_{21}^{2}-1\right)e^{-j\xi x'}}{2\pi Z^{h}(\lambda)Z^{e}(\lambda)}\right.$$

$$\left.\left[j\xi\tilde{k}_{\zeta x}(x',\zeta)+j\zeta\tilde{k}_{\zeta z}(x',\zeta)\right]-\xi\zeta\frac{e^{-j\xi x'}\tilde{k}_{\zeta z}(x',\zeta)}{2\pi Z^{h}(\lambda)}\right\}dx'=-\frac{jk_1}{\eta_1}\tilde{e}_{1\zeta x}^{i}(x,y,\zeta)$$

leads to

$$\frac{1}{2\pi}\int_{-\infty}^{\infty}d\xi e^{j\xi x}e^{-p_1 y}\int_{-w/2}^{w/2}\left\{\left[\frac{\left(k_1^{2}-\xi^{2}\right)}{Z^{h}(\lambda)}+\frac{\xi^{2}p_1\left(N_{21}^{2}-1\right)}{Z^{h}(\lambda)Z^{e}(\lambda)}\right]\tilde{k}_{\zeta x}(x',\zeta)\right.$$

$$\left.+\left[\frac{\xi\zeta p_1\left(N_{21}^{2}-1\right)}{Z^{h}(\lambda)Z^{e}(\lambda)}-\frac{\xi\zeta}{Z^{h}(\lambda)}\right]\tilde{k}_{\zeta z}(x',\zeta)\right\}e^{-j\xi x'}dx'=-\frac{jk_1}{\eta_1}\tilde{e}_{1\zeta x}^{i}(x,y,\zeta)$$

Similarly,

$$\int_{-\infty}^{\infty} d\xi e^{}$$

$$\left[j\xi \tilde{k}_{\zeta x} \right.$$

leads to

$$\frac{1}{2\pi}$$

$$+ \left\{ \begin{bmatrix} \zeta \\ - \end{bmatrix} \right.$$

Defini

lead

$$\frac{1}{2\pi}$$

$$=$$

Similarly, for $\hat{t}=\hat{z}$,

$$\int_{-\infty}^{\infty}d\xi e^{j\xi x}e^{-p_1 y}\int_{-w/2}^{w/2}\left\{-\xi\zeta\frac{e^{-j\xi x'}\tilde{k}_{\zeta x}(x',\zeta)}{2\pi Z^h(\lambda)}-j\zeta p_1\frac{\left(N_{21}^2-1\right)e^{-j\xi x'}}{2\pi Z^h(\lambda)Z^e(\lambda)}\right.$$

$$\left.\left[j\xi\tilde{k}_{\zeta x}(x',\zeta)+j\zeta\tilde{k}_{\zeta z}(x',\zeta)\right]+\left(k_1^2-\zeta^2\right)\frac{e^{-j\xi x'}\tilde{k}_{\zeta z}(x',\zeta)}{2\pi Z^h(\lambda)}\right\}dx'=-\frac{jk_1}{\eta_1}\tilde{e}^i_{1\zeta z}(x,y,\zeta)$$

leads to

$$\frac{1}{2\pi}\int_{-\infty}^{\infty}d\xi e^{j\xi x}e^{-p_1 y}\int_{-w/2}^{w/2}\left\{\left[-\frac{\xi\zeta}{Z^h(\lambda)}+\frac{\xi\zeta p_1\left(N_{21}^2-1\right)}{Z^h(\lambda)Z^e(\lambda)}\right]\tilde{k}_{\zeta x}(x',\zeta)\right.$$

$$\left.+\left[\frac{\zeta^2 p_1\left(N_{21}^2-1\right)}{Z^h(\lambda)Z^e(\lambda)}+\frac{\left(k_1^2-\zeta^2\right)}{Z^h(\lambda)}\right]\tilde{k}_{\zeta z}(x',\zeta)\right\}e^{-j\xi x'}dx'=-\frac{jk_1}{\eta_1}\tilde{e}^i_{1\zeta z}(x,y,\zeta)$$

Defining spectral coefficients as

$$\tilde{\tilde{C}}_{xx}(\xi,\zeta)=\frac{\left(k_1^2-\xi^2\right)}{Z^h(\lambda)}+\frac{\xi^2 p_1\left(N_{21}^2-1\right)}{Z^h(\lambda)Z^e(\lambda)}$$

$$\tilde{\tilde{C}}_{xz}(\xi,\zeta)=C_{zx}(\xi,\zeta)=\frac{\xi\zeta p_1\left(N_{21}^2-1\right)}{Z^h(\lambda)Z^e(\lambda)}-\frac{\xi\zeta}{Z^h(\lambda)}$$

$$\tilde{\tilde{C}}_{zz}(\xi,\zeta)=\frac{\left(k_1^2-\zeta^2\right)}{Z^h(\lambda)}+\frac{\zeta^2 p_1\left(N_{21}^2-1\right)}{Z^h(\lambda)Z^e(\lambda)}$$

leads to

$$\frac{1}{2\pi}\int_{-\infty}^{\infty}d\xi e^{j\xi x}e^{-p_1 y}\int_{-w/2}^{w/2}\left[\tilde{\tilde{C}}_{xx}(\xi,\zeta)\tilde{k}_{\zeta x}(x',\zeta)+\tilde{\tilde{C}}_{xz}(\xi,\zeta)\tilde{k}_{\zeta z}(x',\zeta)\right]e^{-j\xi x'}dx'$$

$$=-\frac{jk_1}{\eta_1}\tilde{e}^i_{1\zeta x}(x,y,\zeta)\cdots\hat{t}=\hat{x}$$

and

$$\frac{1}{2\pi}\int_{-\infty}^{\infty} d$$

$$= -\frac{jk_1}{\eta_1}\tilde{e}_1^i$$

Since E_{1z}^i

As required

An appr

assuming $\tilde{k}_{\zeta}$

represent the

approximate

where t der

width. Forw

and

$$\frac{1}{2\pi}\int_{-\infty}^{\infty} d\xi e^{j\xi x} e^{-p_1 y} \int_{-w/2}^{w/2} \left[\tilde{\tilde{C}}_{zx}(\xi,\zeta)\tilde{k}_{\zeta x}(x',\zeta) + \tilde{\tilde{C}}_{zz}(\xi,\zeta)\tilde{k}_{\zeta z}(x',\zeta) \right] e^{-j\xi x'} dx'$$
$$= -\frac{jk_1}{\eta_1}\tilde{e}^i_{1\zeta z}(x,y,\zeta)\cdots \hat{t} = \hat{z}$$

Since $\boldsymbol{E}^i_{1z}(x,z) = \hat{z}E^i_{1z}(x,z) = \hat{z}T(x)L_g(z) = \hat{z}L_g(z)$,

$$\begin{aligned} \tilde{\boldsymbol{e}}^i_{1\zeta z}(x,y,\zeta) &= \hat{z}\tilde{e}^i_{1\zeta z}(x,y,\zeta) = \hat{z}T(x)\tilde{L}_g(\zeta) = \hat{z}\tilde{L}_g(\zeta) \\ \tilde{\boldsymbol{k}}_{\zeta z}(x',\zeta) &= \hat{z}\tilde{k}_{\zeta z}(x',\zeta) \end{aligned} \tag{5.2.6}$$

As required by Eqn. (5.2.6),

$$\begin{aligned} &\frac{1}{2\pi}\int_{-\infty}^{\infty} d\xi e^{j\xi x} e^{-p_1 y} \int_{-w/2}^{w/2} \tilde{\tilde{C}}_{zz}(\xi,\zeta)\tilde{k}_{\zeta z}(x',\zeta) e^{-j\xi x'} dx' \\ &= -\frac{jk_1}{\eta_1}\tilde{L}_g(\zeta)\cdots \hat{t} = \hat{z} \end{aligned} \tag{5.2.7}$$

An approximate solution is obtained for narrow microstrip with $k_0 w \ll 1$ by assuming $\tilde{k}_{\zeta x}(x',\zeta) \approx 0$ and ignoring the x-component integral equation. In order to represent the induced surface transverse current distribution along microstrip width, the approximate Maxwellian current function [52] is exploited as

$$\eta(x) = \begin{cases} \dfrac{1}{\pi(w/2)\sqrt{1-\left[x/(w/2)\right]^2}} \cdots w/t < 2 \\ \dfrac{1}{w} \cdots w/t \geq 2 \end{cases} \tag{5.2.8}$$

where t denotes the film thickness and $\eta(x)$ integrates to unity over the microstrip width. Forward Fourier transform of $\eta(x)$ yields

Then,

Repla

Eqn.

For

The

nat

$$\tilde{\eta}(\xi)=\int_{-\infty}^{\infty}\eta(x)e^{-j\xi x}dx$$

Then, for $w/t<2$

$$\begin{aligned}\tilde{\eta}(\xi)&=\int_{-\infty}^{\infty}\frac{1}{\pi(w/2)\sqrt{1-\left[x/(w/2)\right]^2}}e^{-j\xi x}dx\\&=\int_{-w/2}^{w/2}\frac{1}{\pi(w/2)\sqrt{1-\left[x/(w/2)\right]^2}}e^{-j\xi x}dx\\&=2\int_{0}^{w/2}\frac{\cos(\xi x)}{\pi(w/2)\sqrt{1-\left[x/(w/2)\right]^2}}dx\end{aligned}\tag{5.2.9}$$

Replacing $x/(w/2)=\sin\theta$ leads to

$$\begin{aligned}x=0&\rightarrow\sin\theta=0\rightarrow\theta=0\\x=w/2&\rightarrow\sin\theta=1\rightarrow\theta=\pi/2\end{aligned}$$

Eqn. (5.2.9) becomes [18]

$$\begin{aligned}\tilde{\eta}(\xi)&=\frac{2}{\pi}\int_{0}^{\pi/2}\cos(\xi w\sin\theta/2)d\theta\\&=J_0(\xi w/2)\end{aligned}\tag{5.2.10}$$

For $w/t\geq 2$,

$$\begin{aligned}\tilde{\eta}(\xi)&=2\int_{0}^{w/2}\frac{\cos(\xi x)}{w}dx\\&=\frac{\sin(\xi w/2)}{\xi w/2}\\&=sinc(\xi w/2)\end{aligned}\tag{5.2.11}$$

The approximate Maxwellian transverse current distribution has the advantage of eliminating the need for calculation of that current on the conducting microstrip. Therefore, it

is noted

where J

Using th

Eqn. (5.

It is obse

Since by

even in

is valid.

profile is

is noted that the microstrip current profile is represented by

$$k_z(x,z)=J_z(z)\eta(x) \tag{5.2.12}$$

where $J_z(z)$ is the longitudinal current distribution. Therefore,

$$\tilde{k}_{\zeta z}(x',\zeta)=\tilde{j}_z(\zeta)\eta(x') \tag{5.2.13}$$

Using this representation in Eqn. (5.2.7),

$$\begin{aligned}&\frac{1}{2\pi}\int_{-\infty}^{\infty}d\xi e^{j\xi x}e^{-p_1 y}\int_{-w/2}^{w/2}\tilde{\tilde{C}}_{zz}(\xi,\zeta)\tilde{j}_z(\zeta)\eta(x')e^{-j\xi x'}dx'\\&=-\frac{jk_1}{\eta_1}\tilde{L}_g(\zeta)\end{aligned} \tag{5.2.14}$$

Eqn. (5.2.14) is rearranged as

$$\begin{aligned}&\frac{1}{2\pi}\tilde{j}_z(\zeta)\int_{-\infty}^{\infty}e^{-p_1 y}\tilde{\tilde{C}}_{zz}(\xi,\zeta)\left[\int_{-w/2}^{w/2}\eta(x')e^{-j\xi x'}dx'\right]e^{j\xi x}d\xi\\&=-\frac{jk_1}{\eta_1}\tilde{L}_g(\zeta)\end{aligned} \tag{5.2.15}$$

It is observed that

$$\begin{aligned}&\int_{-w/2}^{w/2}\eta(x')e^{-j\xi x'}dx'\\&=\int_{-\infty}^{\infty}\eta(x')e^{-j\xi x'}dx'\\&=\int_{-\infty}^{\infty}\eta(-x')e^{-j\xi x'}dx'\\&=\tilde{\eta}(\xi)\end{aligned} \tag{5.2.16}$$

Since by symmetry $\eta(x')=\eta(-x')$ then this leads to $J_0(\xi w/2)$ and $sinc(\xi w/2)$ even in $\xi w/2$. Hence, regardless of the microstrip dimension ratio w/t, Eqn. (5.2.16) is valid. As assumed in Eqn. (5.2.8), the total normalized Maxwellian transverse current profile is taken as unity over the microstrip width, i.e.

Substitu

Finally,

Now, t

transfo

leads

$$\int_{-w/2}^{w/2}\eta(x)dx=\int_{-\infty}^{\infty}\eta(x)dx=1 \tag{5.2.17}$$

Substitution Eqn. (5.2.16) and Eqn. (5.2.17) into Eqn. (5.2.15) yields

$$\begin{aligned}
&\frac{1}{2\pi}\tilde{j}_z(\zeta)\int_{-\infty}^{\infty}e^{-p_1 y}\tilde{\tilde{C}}_{zz}(\xi,\zeta)\left[\int_{-\infty}^{\infty}\eta(x')e^{-j\xi x'}dx'\right]e^{j\xi x}d\xi \\
&=\frac{1}{2\pi}\tilde{j}_z(\zeta)\int_{-\infty}^{\infty}e^{-p_1 y}\tilde{\tilde{C}}_{zz}(\xi,\zeta)\tilde{\eta}(\xi)e^{j\xi x}d\xi \\
&=\frac{1}{2\pi}\tilde{j}_z(\zeta)\int_{-\infty}^{\infty}e^{-p_1 y}\tilde{\tilde{C}}_{zz}(\xi,\zeta)\tilde{\eta}(\xi)\underbrace{\left[\int_{-\infty}^{\infty}\eta(x)e^{j\xi x}dx\right]}_{=\tilde{\eta}(\xi)}d\xi \\
&=-\frac{jk_1}{\eta_1}\tilde{L}_g(\zeta)
\end{aligned} \tag{5.2.18}$$

Finally, the spectral microstrip current is

$$\begin{aligned}
\tilde{j}_z(\zeta)&=\lim_{y\to 0}\frac{2\pi\tilde{L}_g(\zeta)}{\int_{-\infty}^{\infty}\tilde{\eta}^2(\xi)\left[\frac{j\eta_1}{k_1}e^{-p_1(\lambda)y}\tilde{\tilde{C}}_{zz}(\xi,\zeta)\right]d\xi} \\
\therefore\ \tilde{j}_z(\zeta)&=\frac{2\pi\tilde{L}_g(\zeta)}{\int_{-\infty}^{\infty}\tilde{\eta}^2(\xi)\left[\frac{j\eta_1}{k_1}\tilde{\tilde{C}}_{zz}(\xi,\zeta)\right]d\xi}
\end{aligned} \tag{5.2.19}$$

Now, the microstrip current is recovered from Eqn. (5.2.19) through the inverse Fourier transform. Thus,

$$J_z(z)=\frac{1}{2\pi}\int_{-\infty}^{\infty}\tilde{j}_z(\zeta)e^{j\zeta z}d\zeta \tag{5.2.20}$$

leads to

$$J_z(z)=\int_{-\infty}^{\infty}\frac{\tilde{L}_g(\zeta)}{\int_{-\infty}^{\infty}\tilde{\eta}^2(\xi)\left[\frac{j\eta_1}{k_1}\tilde{\tilde{C}}_{zz}(\xi,\zeta)\right]d\xi}e^{j\zeta z}d\zeta \tag{5.2.21}$$

5.3

yiel

in f

the i

the c

the

$\lambda =$

asso

curr

λ_s^2

wh

λ_f

It

sh

5.3 CONTINUOUS SPECTRUM CURRENT

As discussed in Section 4.3, wavenumber parameters $p_l(\lambda)=\sqrt{\lambda^2-k_l^2}\ (l=1,2)$ yield branch point singularities at $\lambda=\pm k_l$. Since the integrand in Eqn. (5.2.21) is even in $p_2(\lambda)$, then the branch point contributed by the film layer is removable [17]. But, the integrand in Eqn. (5.2.21) is not even in $p_1(\lambda)$ then the branch point contributed by the cover layer is non-removable.

Pole singularities of $\tilde{\tilde{C}}_{zz}(\xi,\zeta)$ contribute simple-pole singularities associated with the planar-layered background environment. So, $Z^h(\lambda)=0$ leads to simple poles at $\lambda=\pm\lambda_p$ associated with TE-odd surface waves and $Z^e(\lambda)=0$ leads to simple poles associated with TM-even surface waves.

Hence, complex λ-plane singularities of the integral representation for the microstrip current consist of branch points at $\lambda=\pm k_1$ and poles $\lambda=\pm\lambda_p$. Since $\lambda^2=\xi^2+\zeta^2$, $\lambda_s^2=\xi_s^2+\zeta^2$. Conventionally, λ_s and ξ_s denotes λ- and ξ-plane singularities. So,

$$\begin{aligned}\pm\xi_{k_1}&=\mp j\sqrt{\zeta-\lambda_s}\sqrt{\zeta+\lambda_s}=\mp j\sqrt{\zeta-k_1}\sqrt{\zeta+k_1}\\ \pm\xi_{TM_0}&=\mp j\sqrt{\zeta-\lambda_s}\sqrt{\zeta+\lambda_s}=\mp j\sqrt{\zeta-\lambda_{TM_0}}\sqrt{\zeta+\lambda_{TM_0}}\end{aligned}\qquad(5.2.22)$$

which clearly implicates the branch points at $\zeta=\pm\lambda_s$ in the complex ζ-plane with $\lambda_p=\lambda_{TM_0}$ being the fundamental proper surface-wave mode as depicted in Fig. 5.3.1. It is assumed that k_0t is sufficiently small that the TM_0 pole is the only one on the top sheet of the complex λ-plane.

$-\lambda_1$

Figure

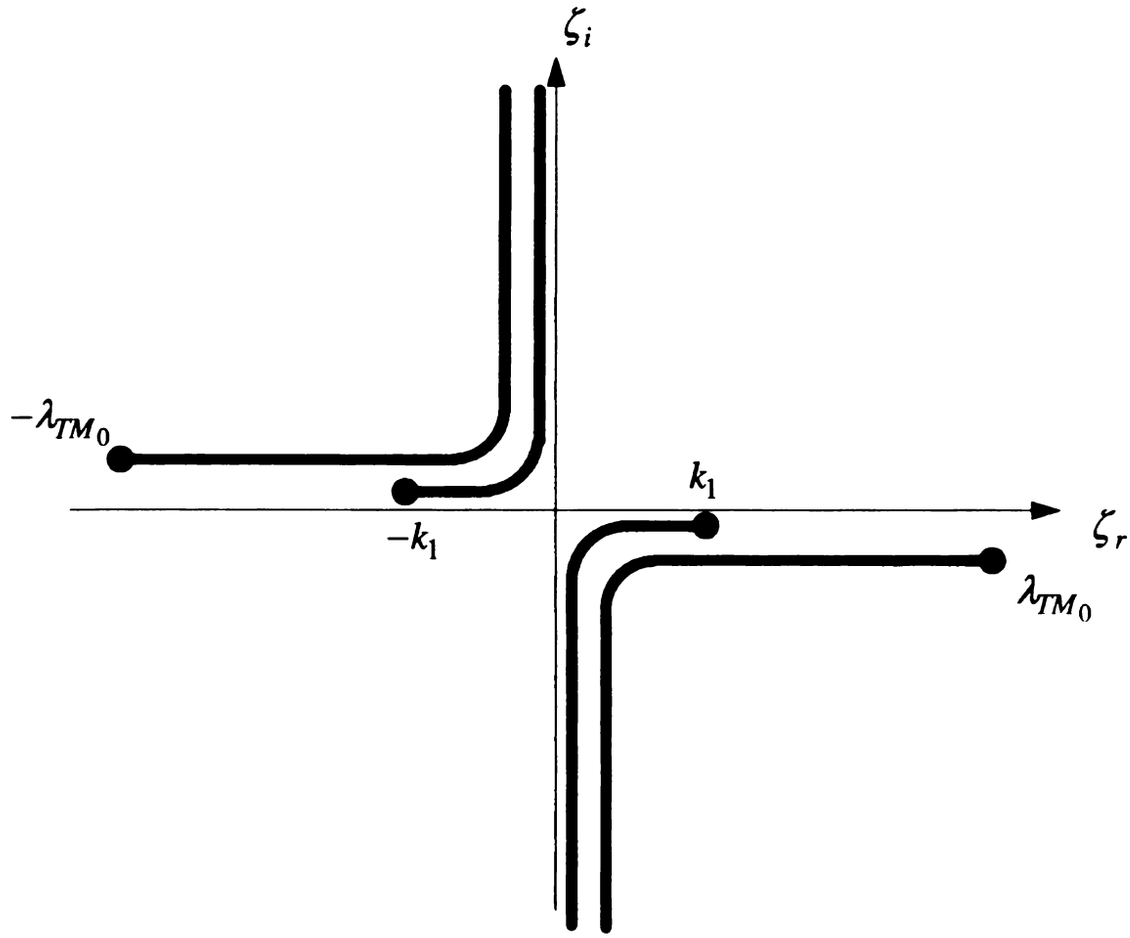

Figure 5.3.1 Singularities in the complex ζ -plane contributed by the planar-layered background environment. The branch points $\lambda_s = \pm k_1$ to the branch points $\pm k_1$ mapping and the poles $\lambda_s = \pm \lambda_{TM_0}$ to the branch points $\pm \lambda_{TM_0}$ mapping in the low low-loss limit.

Singularities associated with the background layer environment consist of branch points in the complex ζ-plane. The associated Sommerfeld branch cuts lead to $\mathrm{Im}\{\xi_s\}<0$ and the proper spectrum as shown in Chapter 4. The real axis inversion contour can be deformed into the upper $(z>0)$ half and the lower $(z<0)$ half of the complex ζ-plane as depicted in Fig. 5.3.2. Using Cauchy's integral theorem, Eqn. (5.2.21) becomes

$$\int_{-\infty}^{\infty}(\cdots)d\zeta+\int_{C_{\zeta_p}}(\cdots)d\zeta+\int_{C_b}(\cdots)d\zeta+\int_{C_\infty}(\cdots)d\zeta=0 \qquad (5.3.2)$$

$(\cdots)$ is an integrand of $d\zeta$ in Eqn. (5.2.21). Due to Sommerfeld's radiation condition,

$$\int_{C_\infty}(\cdots)d\zeta\to 0 \qquad (5.3.3)$$

So, the continuous spectrum is contributed by detouring about logarithmic and square-root type branch cuts arising from the k_1 branch point and the proper background pole λ_{TM_0} as depicted in Fig. 5.3.3. Then, as evident from Eqn. (5.3.1), singularities in the complex ξ-plane migrate in conjunction with changing spatial-frequency ζ along branch cuts associated with a logarithmic type branch point k_1 and a square-root type branch point k_{TM_0} in the complex ζ-plane as depicted in Fig. 5.3.3.

For branch-point singularities in the complex ξ-plane (see Fig. 2.4.3 in Chapter 2),

$$\begin{aligned}\zeta-k_1&=\rho^+e^{j\theta^+}\\ \zeta+k_1&=\rho^-e^{j\theta^-}\end{aligned} \qquad (5.3.4)$$

$$\pm\xi_{k_1}=\mp j\sqrt{\zeta-k_1}\sqrt{\zeta+k_1}=\begin{cases}\sqrt{\rho^+\rho^-}\,e^{j\left(-\pi+\theta^++\theta^-\right)/2}\\ \sqrt{\rho^+\rho^-}\,e^{j\left(\pi+\theta^++\theta^-\right)/2}\end{cases} \qquad (5.3.5)$$

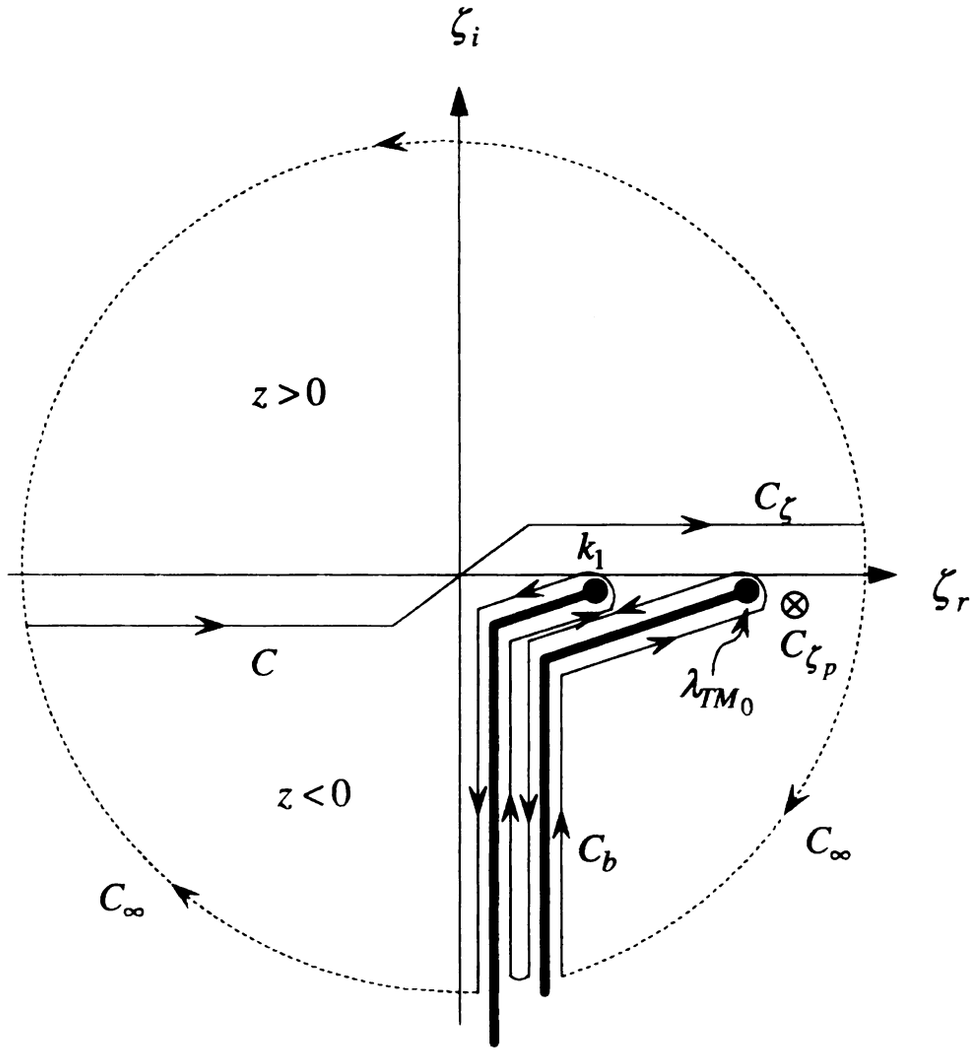

Figure 5.3.2 Deformation of $\mathrm{Re}\{\zeta\}$-axis inversion contour into the *Upper Half Plane* (*UHP*) and the *Lower Half Plane* (*LHP*) in the complex ζ -plane. Branch cuts associated with branch-point singularities contributed by a background layer environment are considered to be in the low-loss limit.

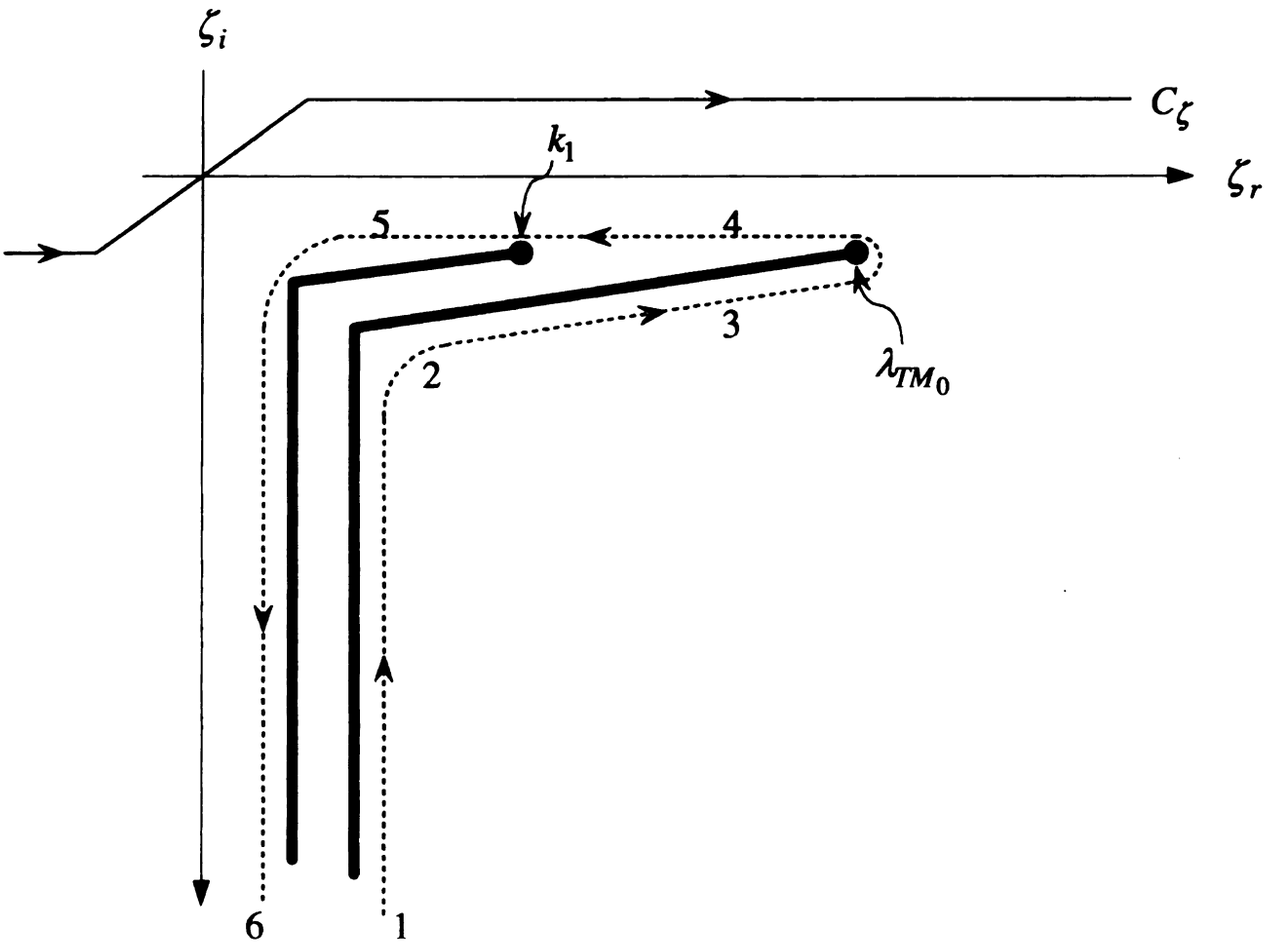

Figure 5.3.3 Branch cuts associated with a logarithmic type branch point k_1 and a square-root type branch point λ_{TM_0} in the complex ζ -plane and the proper continuous spectrum contributed by those branch cut integrations for low-loss limit.

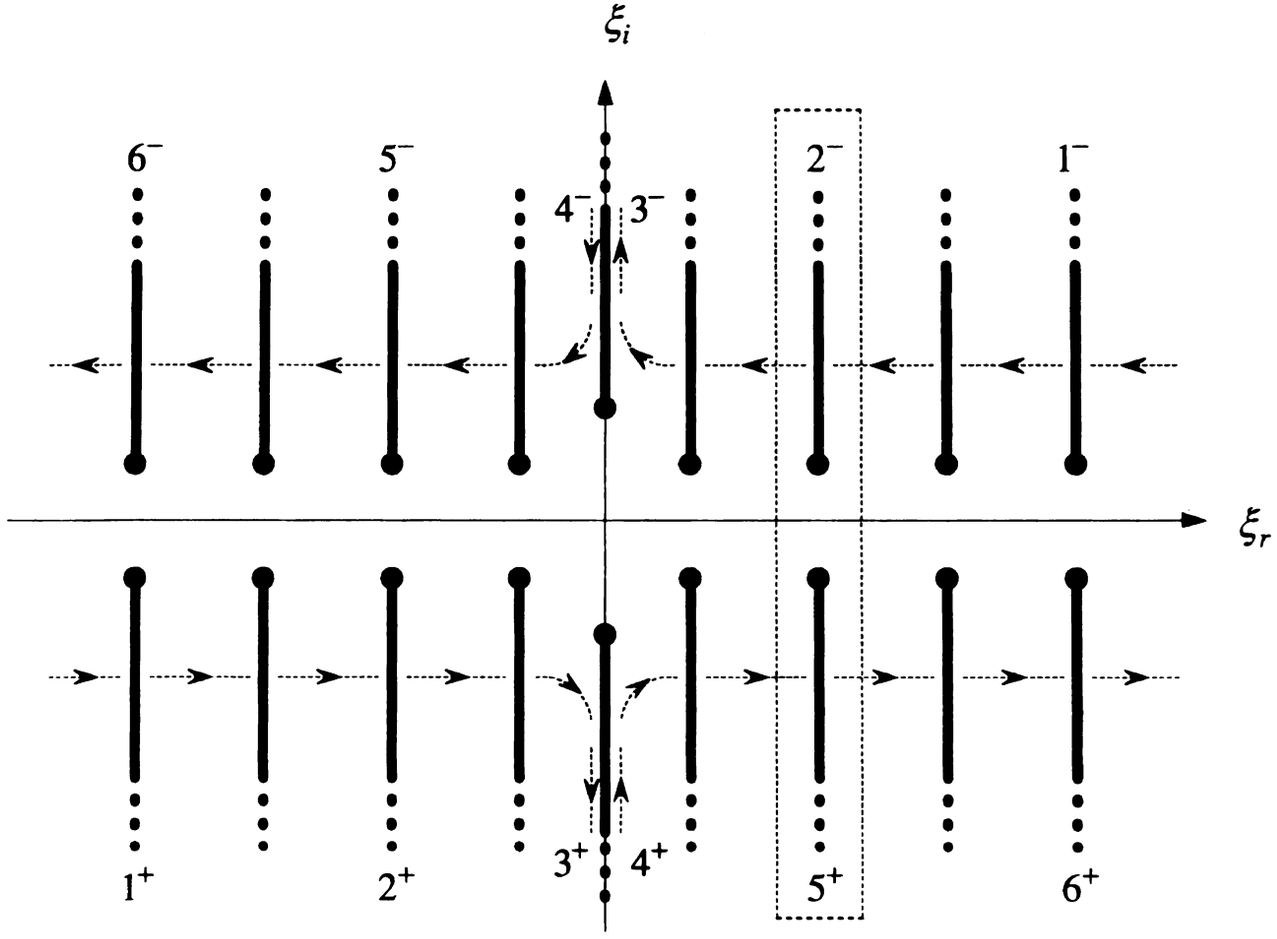

Figure 5.3.4 Migration of complex transverse transform plane (complex ξ-plane) branch-point singularities $\pm\xi_{k_1}$ in conjunction with changing spatial-frequency ζ along branch cuts associated with a logarithmic type branch point k_1 and a square-root type branch point λ_{TM_0} in the complex ζ-plane in the low-loss limit.

For a poin

For a poin

For points

For a poin

For a poin

Therefore,

in the cor

complex

from $-j\sqrt$

loss limit

singularity

in the com

as depicted

ξ-plane.

For a point 1 in Fig. 5.3.3,

$$\xi_{k_1} = \sqrt{\rho^+\rho^-}\, e^{j(-\pi-\pi+\psi-\psi)/2} = -\sqrt{\rho^+\rho^-}$$

For a point 2 in Fig. 5.3.3,

$$\xi_{k_1} = \sqrt{\rho^+\rho^-}\, e^{j(-\pi-\pi)/2} = -\sqrt{\rho^+\rho^-}$$

For points 3 and 4 in Fig. 5.3.3,

$$\xi_{k_1} = \sqrt{\rho^+\rho^-}\, e^{j(-\pi)/2} = -j\sqrt{\rho^+\rho^-}$$

For a point 5 in Fig. 5.3.3,

$$\xi_{k_1} = \sqrt{\rho^+\rho^-}\, e^{j(-\pi+\pi)/2} = \sqrt{\rho^+\rho^-}$$

For a point 6 in Fig. 5.3.3,

$$\xi_{k_1} = \sqrt{\rho^+\rho^-}\, e^{j(-\pi+\pi+\psi-\psi)/2} = \sqrt{\rho^+\rho^-}$$

Therefore, as the integration contour detours from a point 1 to a point 6 about branch cuts in the complex ζ-plane in Fig. 5.3.3, ξ_{k_1}, one of the branch-point singularities in the complex ξ-plane, migrates from $-\infty$ to 0 on $\mathrm{Re}\{\xi\}$-axis, from 0 to $-j\sqrt{\rho^+\rho^-}$ and from $-j\sqrt{\rho^+\rho^-}$ to 0 on $\mathrm{Im}\{\xi\}$-axis, and from 0 to ∞ on $\mathrm{Re}\{\xi\}$-axis in the low-loss limit as depicted in Fig. 5.3.4. The superscript + denotes the positive branch-point singularity ξ_{k_1} and the number does its corresponding position on the branch-cut contour in the complex ζ-plane. For example, 1^+ implies that a point 1 in the complex ζ-plane as depicted in Fig. 5.3.3 maps into a positive branch-point singularity ξ_{k_1} in the complex ξ-plane. Similarly, the other branch-point singularity (negative branch-point singularity),

$-\xi_{k_1}$

$j\sqrt{\rho}$

Theref

compl

plane.

Fo

invers

singul

is in a

the co

each

each

compl

singul

plane.

negati

Regard

$-\xi_{k_1}$, migrates from ∞ to 0 on $\mathrm{Re}\{\xi\}$-axis, from 0 to $j\sqrt{\rho^+\rho^-}$ and from $j\sqrt{\rho^+\rho^-}$ to 0 on $\mathrm{Im}\{\xi\}$-axis, and from 0 to $-\infty$ on $\mathrm{Re}\{\xi\}$-axis in Fig. 5.3.4. Therefore, there is a continuous migration of branch-point singularities $\pm\xi_{k_1}$ in the complex ξ-plane for corresponding points along branch-cut contour in the complex ζ-plane.

For a point along a branch cut contour in the complex ζ-plane, $\mathrm{Re}\{\xi\}$-axis inversion contour integration is implemented for its corresponding branch-point singularities $\pm\xi_{k_1}$. The integration detour about branch cuts from a point 4 to a point 6 is in an opposite sense to that from a point 1 to a point 3 as depicted in Fig. 5.3.3. Thus, the corresponding $\mathrm{Re}\{\xi\}$-axis inversion contour C_ξ's are also in an opposite sense to each other as depicted in Fig. 5.3.5, but their integral contributions are not annulled by each other since $p_1(\xi,\zeta)$ takes different values along them on the top sheet of the complex ξ-plane and must be evaluated with respect to different branch-point singularities in the complex ξ-plane for corresponding different ζ's in the complex ζ-plane. For example, $\xi_{k_1}(2)$ and $-\xi_{k_1}(2)$ in Fig. 5.3.5 and 5.3.6 imply positive and negative branch-point singularities ξ_{k_1} and $-\xi_{k_1}$ respectively for a point 2 in Fig. 5.3.3.

$$p_1(\xi,\zeta)=\sqrt{\xi^2+\zeta^2-k_1^2}=\sqrt{\xi+\xi_{k_1}}\sqrt{\xi-\xi_{k_1}} \tag{5.3.6}$$

Regarding ξ_{k_1} as a fourth-quadrant singularity leads to

$$\xi_{k_1}=-j\sqrt{\zeta-k_1}\sqrt{\zeta+k_1} \tag{5.3.7}$$

For π_1 in Fig. 5.3.6,

$$\pi_1 = \xi + \xi_{k_1}(2) = \gamma_1 e^{j\varphi^-} \tag{5.3.8}$$

For π_2 in Fig. 5.3.6,

$$\pi_2 = \xi + \xi_{k_1}(5) = \gamma_2 e^{j\varphi^-} \tag{5.3.9}$$

For π_3 in Fig. 5.3.6,

$$\pi_3 = \xi - \xi_{k_1}(2) = \gamma_3 e^{j\varphi^+} \tag{5.3.10}$$

For π_4 in Fig. 5.3.6,

$$\pi_4 = \xi - \xi_{k_1}(5) = \gamma_4 e^{j\varphi^+} \tag{5.3.11}$$

For π_1,

$$\gamma_1 = \sqrt{\left[\mathrm{Re}\left\{\xi + \xi_{k_1}(2)\right\}\right]^2 + \left[\mathrm{Im}\left\{\xi + \xi_{k_1}(2)\right\}\right]^2}$$

$$\varphi^- = -\phi = -\tan^{-1}\left(\frac{\mathrm{Im}\left\{\xi + \xi_{k_1}(2)\right\}}{\mathrm{Re}\left\{\xi + \xi_{k_1}(2)\right\}}\right) + \frac{\pi}{2}\left(\mathrm{sgn}\left[\mathrm{Re}\left\{\xi + \xi_{k_1}(2)\right\}\right] - 1\right) \tag{5.3.12}$$

where

$$\mathrm{sgn}\left[\mathrm{Re}\left\{\xi + \xi_{k_1}(2)\right\}\right] = \begin{cases} 1 \cdots \mathrm{Re}\left\{\xi + \xi_{k_1}(2)\right\} > 0 \\ -1 \cdots \mathrm{Re}\left\{\xi + \xi_{k_1}(2)\right\} < 0 \end{cases}$$

For π_2,

$$\gamma_2 = \sqrt{\left[\mathrm{Re}\left\{\xi + \xi_{k_1}(5)\right\}\right]^2 + \left[\mathrm{Im}\left\{\xi + \xi_{k_1}(5)\right\}\right]^2}$$

$$\varphi^- = -\phi = -\tan^{-1}\left(\frac{\mathrm{Im}\left\{\xi + \xi_{k_1}(5)\right\}}{\mathrm{Re}\left\{\xi + \xi_{k_1}(5)\right\}}\right) + \frac{\pi}{2}\left(\mathrm{sgn}\left[\mathrm{Re}\left\{\xi + \xi_{k_1}(5)\right\}\right] - 1\right) \tag{5.3.13}$$

For π_3,

For π_4,

Therefore

where γ_1

a point 5

where γ_2

Hence

another or

an opposit

C_ξ's are

For π_3,

$$\gamma_3 = \sqrt{\left[\mathrm{Re}\left\{\xi - \xi_{k_1}(2)\right\}\right]^2 + \left[\mathrm{Im}\left\{\xi - \xi_{k_1}(2)\right\}\right]^2}$$
$$\varphi^+ = \phi = \tan^{-1}\left(\frac{\mathrm{Im}\left\{\xi - \xi_{k_1}(2)\right\}}{\mathrm{Re}\left\{\xi - \xi_{k_1}(2)\right\}}\right) - \frac{\pi}{2}\left(\mathrm{sgn}\left[\mathrm{Re}\left\{\xi - \xi_{k_1}(2)\right\}\right] - 1\right) \tag{5.3.14}$$

For π_4,

$$\gamma_4 = \sqrt{\left[\mathrm{Re}\left\{\xi - \xi_{k_1}(5)\right\}\right]^2 + \left[\mathrm{Im}\left\{\xi - \xi_{k_1}(5)\right\}\right]^2}$$
$$\varphi^+ = \phi = \tan^{-1}\left(\frac{\mathrm{Im}\left\{\xi - \xi_{k_1}(5)\right\}}{\mathrm{Re}\left\{\xi - \xi_{k_1}(5)\right\}}\right) - \frac{\pi}{2}\left(\mathrm{sgn}\left[\mathrm{Re}\left\{\xi - \xi_{k_1}(5)\right\}\right] - 1\right) \tag{5.3.15}$$

Therefore, for a point 2 in Fig. 5.3.3, $p_1(\xi,\zeta)$ is defined by

$$p_1(\xi,\zeta) = \sqrt{\gamma_1\gamma_3}\, e^{j\left(\varphi^- + \varphi^+\right)/2} \tag{5.3.16}$$

where $\gamma_1, \gamma_3, \varphi^-, \varphi^+$ are determined by Eqn. (5.3.12) and Eqn. (5.3.14). Similarly, for a point 5 in Fig. 5.3.3,

$$p_1(\xi,\zeta) = \sqrt{\gamma_2\gamma_4}\, e^{j\left(\varphi^- + \varphi^+\right)/2} \tag{5.3.17}$$

where $\gamma_2, \gamma_4, \varphi^-, \varphi^+$ are determined by Eqn. (5.3.13) and Eqn. (5.3.15).

Hence, as depicted in Fig. 5.3.3 and Fig. 5.3.5, points 2 and 5 are adjacent to one another on the integration detour about branch cuts. However the integration paths have an opposite sense to each other so the corresponding $\mathrm{Re}\{\xi\}$-axis inversion contour C_ξ's are also oppositely directed. Since the cover wavenumber $p_1(\xi,\zeta)$ is defined

with respect to branch-point singularities in the complex ξ-plane for corresponding different ζ's in the complex ζ-plane, $\mathrm{Re}\{\xi\}$-axis inversion contour integral contributions are not annulled by each other. So, the overall procedure for $\mathrm{Re}\{\xi\}$-axis inversion contour C_ξ's for points 2 and 5 in Fig. 5.3.3 yields

$$\int_{C_\xi(2)+C_\xi(5)}(\cdots)d\xi=\int_{C_\xi(2)}(\cdots)d\xi-\int_{C_\xi(5)}(\cdots)d\xi \tag{5.3.18}$$

where $C_\xi(2)$ and $C_\xi(5)$ are $\mathrm{Re}\{\xi\}$-axis inversion contours for points 2 and 3 in Fig. 5.3.3 respectively and $(\cdots)$ is in agreement with Eqn. (5.2.21) such that

$$(\cdots)=\tilde{\eta}^2(\xi)\left[\frac{j\eta_1}{k_1}\tilde{\tilde{C}}_{zz}(\xi,\zeta)\right]$$

where

$$\tilde{\eta}(\xi)=\begin{cases}J_0(\xi w/2)\cdots \textit{for } w/t<2\\ sinc(\xi w/2)\cdots \textit{for } w/t\geq 2\end{cases}$$

$$\tilde{\tilde{C}}_{zz}(\xi,\zeta)=\frac{\left(k_1^2-\zeta^2\right)}{Z^h(\xi,\zeta)}+\frac{\zeta^2 p_1\left(N_{21}^2-1\right)}{Z^h(\xi,\zeta)Z^e(\xi,\zeta)}$$

$$Z^h(\xi,\zeta)=p_1(\xi,\zeta)+p_2(\xi,\zeta)\coth\left[p_2(\xi,\zeta)t\right]$$

$$Z^e(\xi,\zeta)=N_{21}^2 p_1(\xi,\zeta)+p_2(\xi,\zeta)\tanh\left[p_2(\xi,\zeta)t\right]$$

$$p_l(\xi,\zeta)=\sqrt{\xi^2+\zeta^2-k_l^2}\cdots l=1,2$$

$$N_{21}^2=(n_2/n_1)^2$$

Thus, throughout the integration detour about branch cuts from a point 1 to 6 in Fig. 5.3.3, the corresponding overall procedure for $\mathrm{Re}\{\xi\}$-axis inversion contour C_ξ's leads to

$$\int_{\sum_{m=1}^{6}C_\xi(m)}(\cdots)d\xi=\int_{\sum_{m=1}^{3}C_\xi(m)}(\cdots)d\xi-\int_{\sum_{m=4}^{6}C_\xi(m)}(\cdots)d\xi \tag{5.3.19}$$

where $C_\xi(m)$ indicates $\mathrm{Re}\{\xi\}$-axis inversion contour for a corresponding point m in Fig. 5.3.3. Eqn. (5.3.19) implicates $\mathrm{Re}\{\xi\}$-axis inversion contour integral contribution excluding surface-wave pole singularities on $\mathrm{Re}\{\xi\}$-axis defined by Eqn. (5.3.1). Then, Fig. 5.3.7 and Fig. 5.3.8 depict the current amplitude and phase longitudinal profiles respectively contributed by $\mathrm{Re}\{\xi\}$-axis inversion contour excluding surface-wave pole singularities in the complex ξ-plane with changing ζ about the branch-cut contour in Fig. 5.3.3. The cover and film layers are non-magnetic, isotropic and homogeneous with indices $n_1 = 1.,\ n_2 = 3.0578$ and with integrated microstrip dimensions as follows.

$$\begin{aligned}
&\textit{microstrip width}: w = .1016\ mm \ \Rightarrow w/\lambda_0 = .0051\\
&\textit{effective gap width}: d = w/10\ mm \ \Rightarrow d/\lambda_0 = (w/\lambda_0)/10\\
&\textit{film thickness}: t = 1.27\ mm \ \Rightarrow t/\lambda_0 = .06\\
&\textit{operating frequency}: f = 15\ GHz
\end{aligned}$$

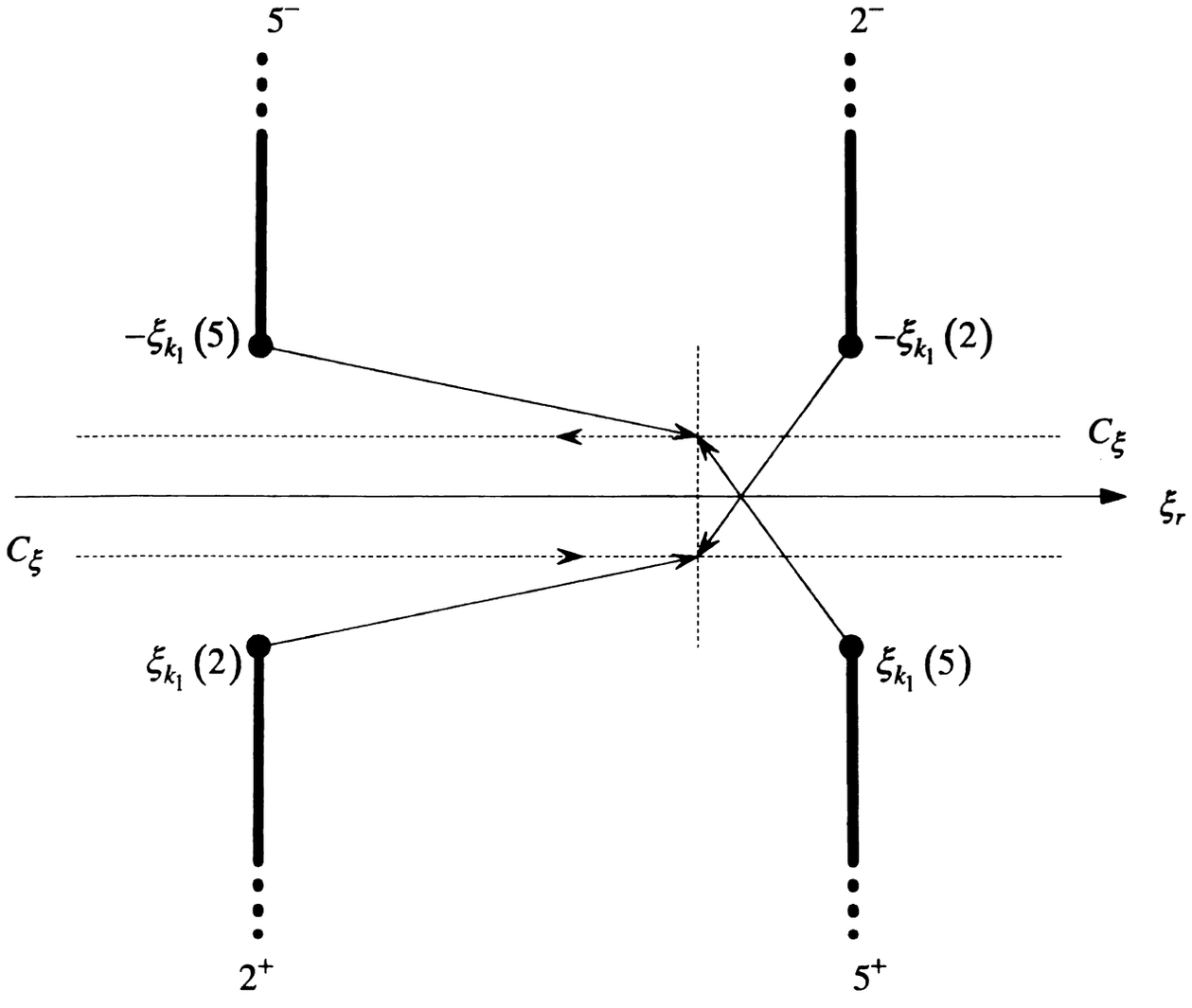

Figure 5.3.5 Opposite $\mathrm{Re}\{\xi\}$-axis inversion contours corresponding to points 2 and 5 on the branch-cut contour in the complex ζ -plane as depicted in Fig. 5.3.3.

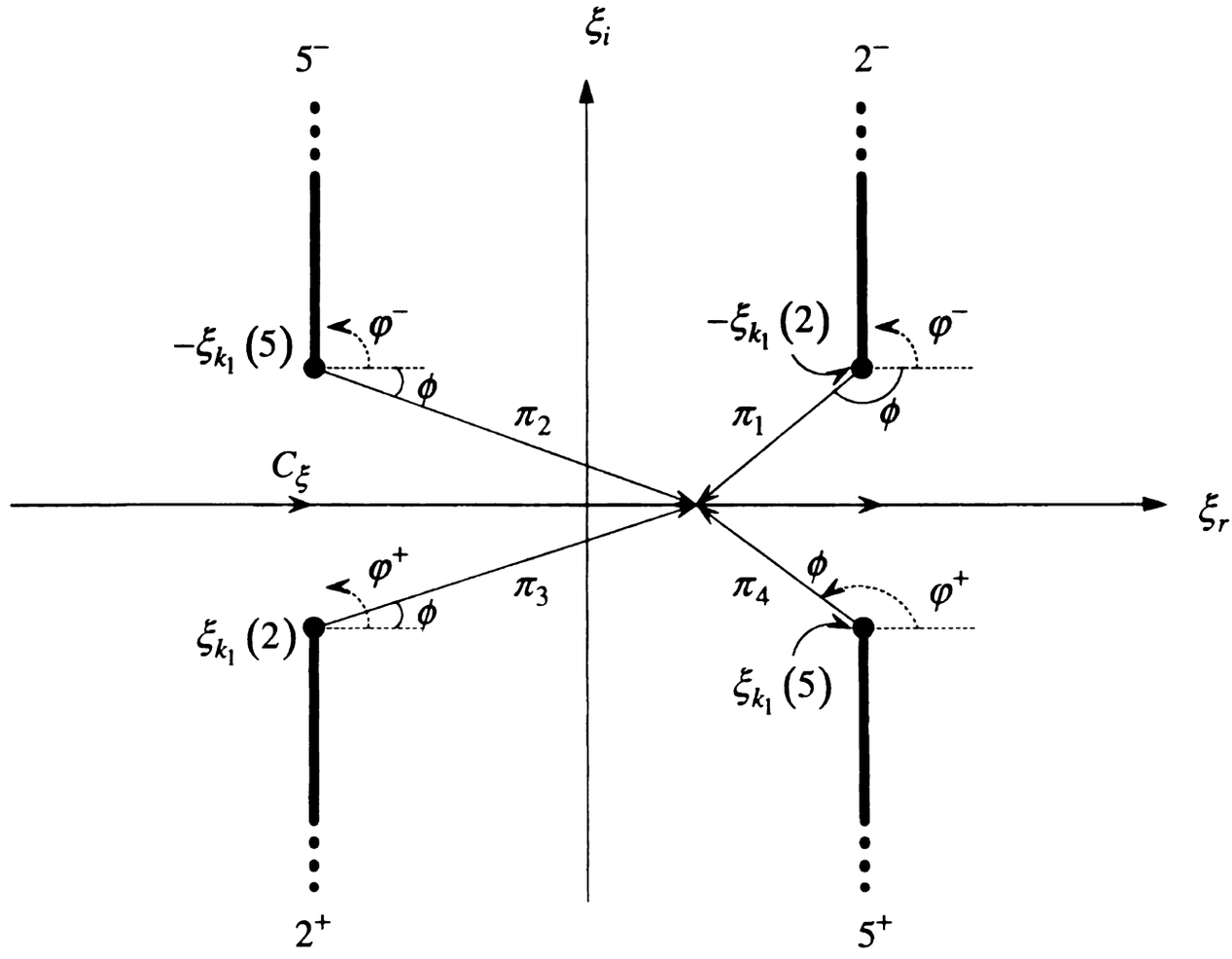

Figure 5.3.6 Complex-phasor diagram for branch-point singularities $\pm\xi_{k_1}$ in the complex ξ-plane for corresponding points 2 and 5 in the complex ζ-plane in Fig. 5.3.3 and evolution of C_ξ.

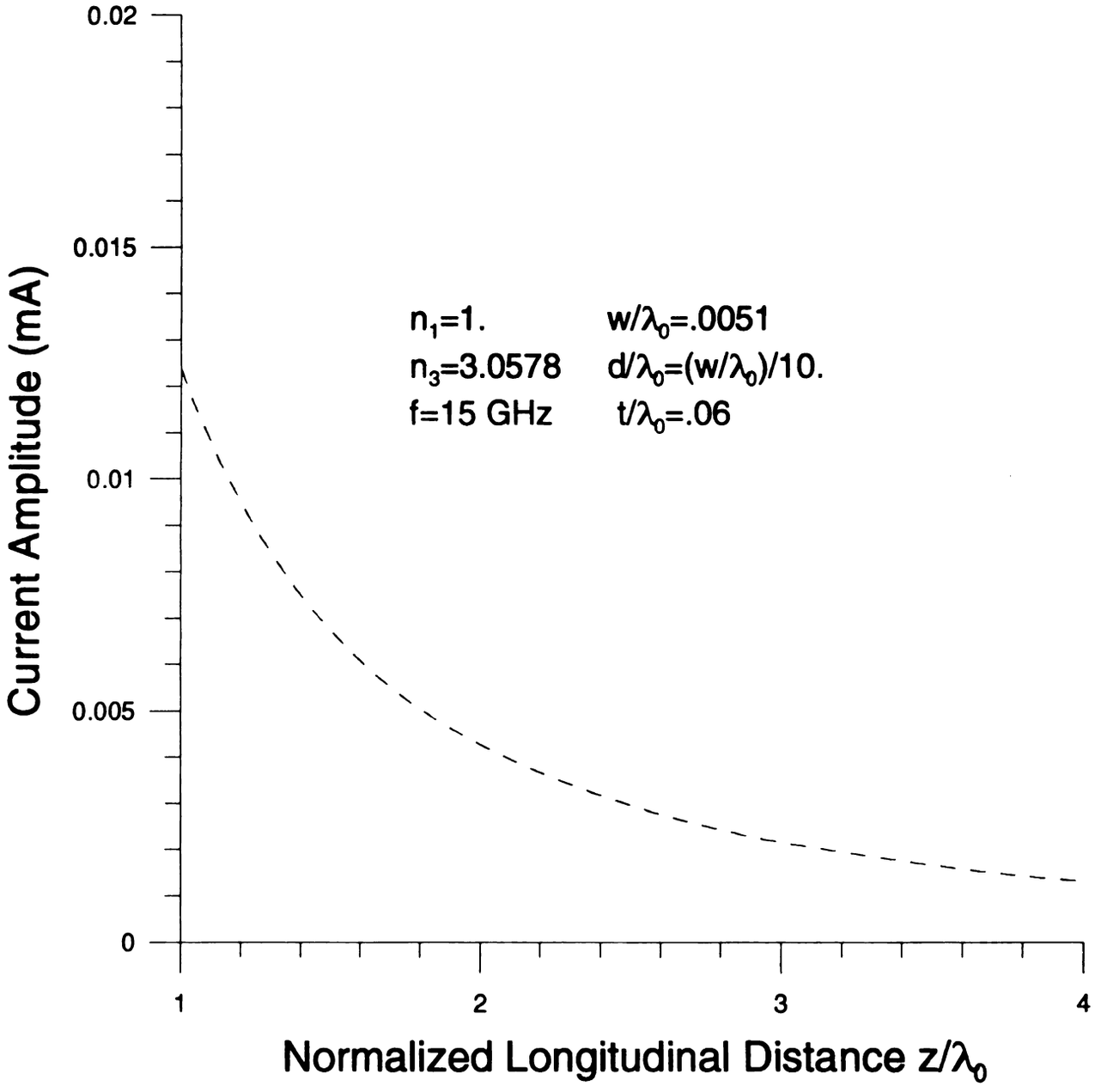

Figure 5.3.7 Current amplitude longitudinal profile contributed by $\mathrm{Re}\{\xi\}$-axis inversion contour excluding surface-wave pole singularities with integrating ζ about the branch-cut contour.

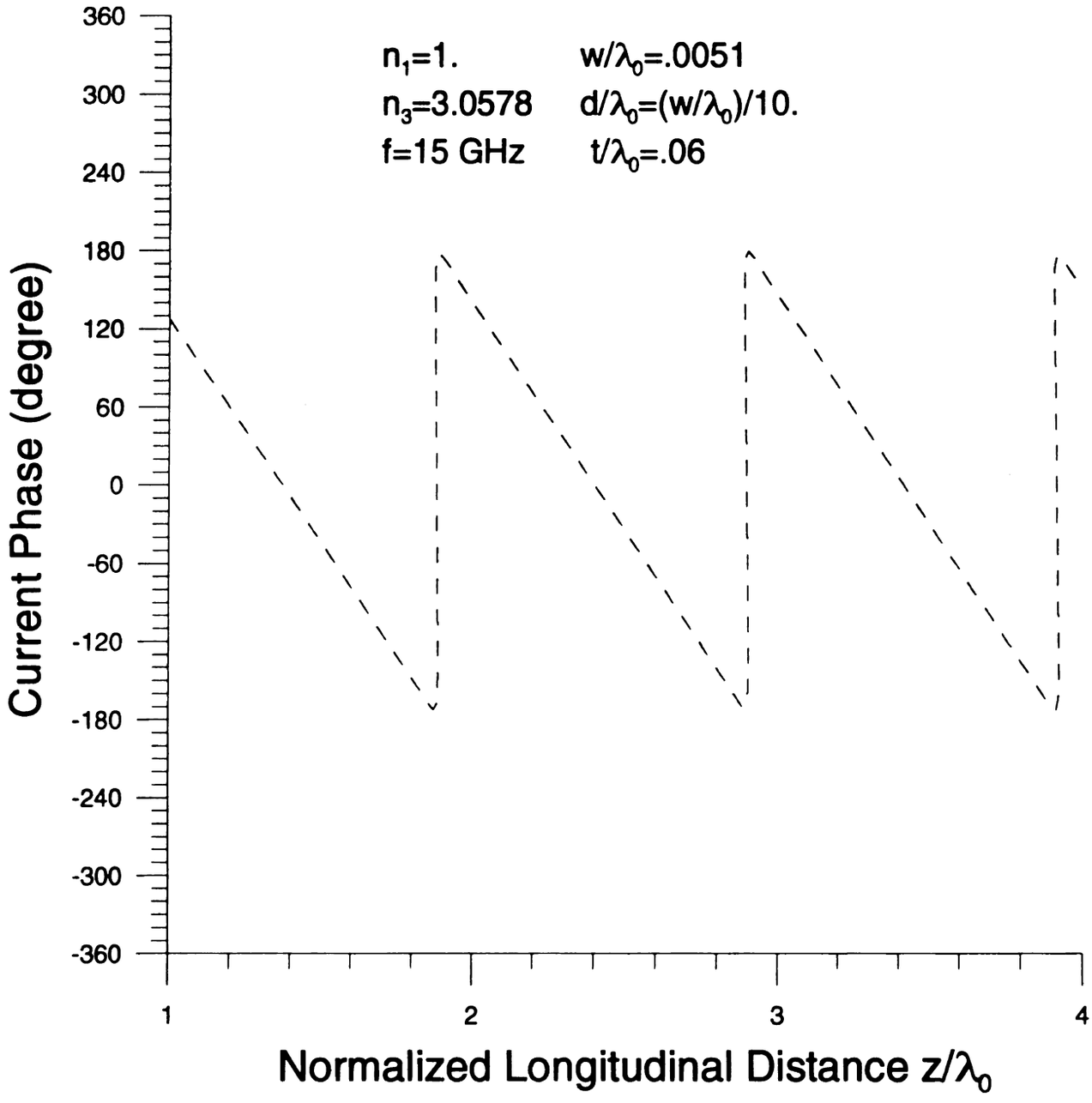

Figure 5.3.8 **Current phase longitudinal profile contributed by $\mathrm{Re}\{\xi\}$-axis inversion contour excluding surface-wave pole singularities with integrating ζ about the branch-cut contour.**

As evident from Eqn. (5.3.1), in addition to branch-point singularities $\pm\xi_{k_1}$, there exist surface-wave pole singularities $\pm\xi_{TM_0}$ in the complex ξ-plane for corresponding points on a branch-cut contour in Fig. 5.3.3. For surface-wave pole singularities in the complex ξ-plane (see Fig. 2.4.3 in Chapter 2),

$$\begin{aligned} \zeta - \lambda_{TM_0} &= \rho^+ e^{j\theta^+} \\ \zeta + \lambda_{TM_0} &= \rho^- e^{j\theta^-} \end{aligned} \tag{5.3.20}$$

Then,

$$\pm\xi_{TM_0} = \mp j\sqrt{\zeta - \lambda_{TM_0}}\sqrt{\zeta + \lambda_{TM_0}} = \begin{cases} \sqrt{\rho^+\rho^-}\, e^{j\left(-\pi+\theta^++\theta^-\right)/2} \\ \sqrt{\rho^+\rho^-}\, e^{j\left(\pi+\theta^++\theta^-\right)/2} \end{cases} \tag{5.3.21}$$

Eqn. (5.3.21) maps points as depicted in Fig. 5.3.3 into surface-wave pole singularities $\pm\xi_{TM_0}$. For a point 1 in Fig. 5.3.3,

$$\xi_{TM_0} = \sqrt{\rho^+\rho^-}\, e^{j(-\pi-\pi+\psi-\psi)/2} = -\sqrt{\rho^+\rho^-}$$

For points 2 and 3 in Fig. 5.3.3,

$$\xi_{TM_0} = \sqrt{\rho^+\rho^-}\, e^{j(-\pi-\pi)/2} = -\sqrt{\rho^+\rho^-}$$

For points 4 and 5 in Fig. 5.3.3,

$$\xi_{TM_0} = \sqrt{\rho^+\rho^-}\, e^{j(-\pi+\pi)/2} = \sqrt{\rho^+\rho^-}$$

For a point 6 in Fig. 5.3.3,

$$\xi_{TM_0} = \sqrt{\rho^+\rho^-}\, e^{j(-\pi+\pi+\psi-\psi)/2} = \sqrt{\rho^+\rho^-}$$

Therefore, as the integration contour detours from a point 1 to a point 6 about branch cuts in the complex ζ-plane as depicted in Fig. 5.3.3, one of surface-wave pole singularities, ξ_{TM_0}, in the complex ξ-plane, migrates from $-\infty$ to ∞ on $\mathrm{Re}\{\xi\}$-axis in the low-loss limit as depicted in Fig. 5.3.9. The symbol × denotes the surface-wave pole singularity in the complex ξ-plane for a corresponding point on branch cuts in the complex ζ-plane. The superscript + denotes the positive surface-wave pole singularity ξ_{TM_0} and the number does its corresponding position on the branch-cut contour in the complex ζ-plane. For example, 1^+ implies that a point 1 in the complex ζ-plane as depicted in Fig. 5.3.3 maps into a positive surface-wave pole singularity ξ_{TM_0} in the complex ξ-plane. Similarly, the other surface-wave pole singularity (negative surface-wave pole singularity), $-\xi_{TM_0}$, migrates exactly conversely from ∞ to $-\infty$ on $\mathrm{Re}\{\xi\}$-axis as depicted in Fig. 5.3.9. Therefore, there is a continuum of surface-wave pole singularities in the complex ξ-plane for corresponding points on the branch-cut contour in the complex ζ-plane.

The location of a surface-wave pole singularity is a little exaggerated for clarity in Fig. 5.3.9. In the low-loss limit, a positive surface-wave pole singularity ξ_{TM_0} approaches infinitesimally close to $\mathrm{Re}\{\xi\}$-axis from the below as depicted in Fig. 5.3.9 since it is necessary that $\mathrm{Im}\{\xi_{TM_0}\}<0$ to satisfy the radiation condition. Conversely, a negative surface- wave pole singularity $-\xi_{TM_0}$ approaches infinitesimally close to $\mathrm{Re}\{\xi\}$-axis

from the above in Fig. 5.3.9 since it is necessary that $\mathrm{Im}\{-\xi_{TM_0}\}>0$. And, if physical continuity of the surface-wave is to be maintained during $\mathrm{Re}\{\xi\}$-axis inversion contour integration, $\mathrm{Re}\{\xi\}$-axis inversion contour must remain disposed above the positive surface-wave pole singularity ξ_{TM_0}. Then, the half residue contributed by ξ_{TM_0} leads to a surface-wave contribution. From a point 1 to a point 3 about the branch cut in the complex ζ-plane as depicted in Fig. 5.3.3, the corresponding positive surface-wave pole singularities $1^+, 2^+, 3^+$ in Fig. 5.3.9 are in a clockwise sense however from a point 4 to a point 6 about the branch cut in Fig. 5.3.3, the corresponding positive surface-wave pole singularities $4^+, 5^+, 6^+$ in Fig. 5.3.9 are in a counter-clockwise sense since the branch cut integration contour from a point 4 to a point 6 in Fig. 5.3.3 is in an opposite sense to that from a point 1 to a point 3. Conversely, $\mathrm{Re}\{\xi\}$-axis inversion contour must remain disposed below the negative surface-wave pole singularity $-\xi_{TM_0}$ and the half residue contributed by $-\xi_{TM_0}$ leads to a surface-wave contribution. From a point 1 to a point 3 about the branch cut in the complex ζ-plane as depicted in Fig. 5.3.3, the corresponding negative surface-wave pole singularities $1^-, 2^-, 3^-$ as depicted in Fig. 5.3.9 are in a counter-clockwise sense however from a point 4 to a point 6 about the branch cut in Fig. 5.3.3, the corresponding negative surface-wave pole singularities $4^-, 5^-, 6^-$ as depicted in Fig. 5.3.9 are in a clockwise sense. Hence the overall procedure leads to a full residue contribution for two corresponding points on the branch cut contour in Fig. 5.3.3. For example, as depicted in Fig. 5.3.9, both a negative surface-wave pole singularity 2^- and

a positive surface-wave pole singularity 5^+ lead to a full residue contribution in the fashion discussed above. More importantly, since all the residues on a positive $\mathrm{Re}\{\xi\}$-axis are in a counter-clockwise sense and those on a negative $\mathrm{Re}\{\xi\}$-axis in a clockwise sense the overall residue contribution will not be annulled. Since

$$\tilde{\tilde{C}}_{zz}(\xi,\zeta)=\frac{\left(k_1^2-\zeta^2\right)}{Z^h(\xi,\zeta)}+\frac{\zeta^2 p_1\left(N_{21}^2-1\right)}{Z^h(\xi,\zeta)Z^e(\xi,\zeta)}$$

$$Z^h(\xi,\zeta)=p_1(\xi,\zeta)+p_2(\xi,\zeta)\coth\left[p_2(\xi,\zeta)t\right]$$

$$Z^e(\xi,\zeta)=N_{21}^2 p_1(\xi,\zeta)+p_2(\xi,\zeta)\tanh\left[p_2(\xi,\zeta)t\right]$$

TE-odd and TM-even surface-waves are supported by pole singularities associated with $Z^h(\xi,\zeta)=0$ and $Z^e(\xi,\zeta)=0$ respectively. For a surface-wave pole singularity ξ_p as depicted in Fig. 5.3.10, it is noted that $\xi_p=-\xi_{TM_0}(2)=\xi_{TM_0}(5)$ in the low-loss limit since $\mathrm{Im}\left\{-\xi_{TM_0}(2)\right\}\to 0^+$ and $\mathrm{Im}\left\{\xi_{TM_0}(5)\right\}\to 0^-$. $-\xi_{TM_0}(2)$ denotes a negative surface-wave pole singularity for a corresponding point 2 on the branch cut contour in Fig. 5.3.3. Similarly, $\xi_{TM_0}(5)$ does a positive surface-wave pole singularity for a corresponding point 5 on the branch cut contour in Fig. 5.3.3. Therefore, for a full residue evaluated at $\xi=\xi_p$

$$\oint_{C_{\xi_p}}\frac{d\xi}{Z^e(\xi,\zeta)}\approx\oint_{C_{\xi_p}}\frac{d\xi}{\underbrace{Z^e\left(\xi_p,\zeta\right)}_{=0}+Z^{e'}\left(\xi_p,\zeta\right)\left(\xi-\xi_p\right)+\cdots}$$

where (5.3.22)

$$Z^{e'}\left(\xi_p,\zeta\right)=\frac{d}{d\xi}Z^e(\xi,\zeta)\Big|_{\xi=\xi_p}$$

It is noted that C_{ξ_p} is the pole-excluding contour. Using

$$\frac{d}{d\xi}p_l(\xi,\zeta)=\frac{\xi}{p_l}\ (l=1,2)$$

$$\frac{d}{d\xi}\tanh\left[p_2(\xi,\zeta)t\right]=\frac{\xi t}{p_2(\xi,\zeta)}\operatorname{sech}^2\left[p_2(\xi,\zeta)t\right]$$

leads to

$$Z^{e'}(\xi_p,\zeta)=\frac{N_{21}^2\xi_p}{p_1(\xi_p,\zeta)}+\frac{\xi_p\tanh\left[p_2(\xi_p,\zeta)t\right]}{p_2(\xi_p,\zeta)}+\xi_p t\operatorname{sech}^2\left[p_2(\xi_p,\zeta)t\right]$$

Then, letting $\xi-\xi_p=\varepsilon e^{j\psi}$ as depicted in Fig. 5.3.10, Eqn. (5.3.22) becomes

$$\oint_{C_{\xi_p}}\frac{d\xi}{Z^{e'}(\xi_p,\zeta)(\xi-\xi_p)}=\frac{1}{Z^{e'}(\xi_p,\zeta)}\int_0^{2\pi}\frac{j\varepsilon e^{j\psi}d\psi}{\varepsilon e^{j\psi}}=\frac{j2\pi}{Z^{e'}(\xi_p,\zeta)}\quad(5.3.23)$$

Therefore, the full residue at $\xi=\xi_p$ is evaluated by

$$\oint_{C_{\xi_p}}\tilde{\tilde{C}}_{zz}(\xi,\zeta)d\xi=j2\pi\frac{\zeta^2 p_1(\xi_p,\zeta)\left(N_{21}^2-1\right)}{Z^h(\xi_p,\zeta)Z^{e'}(\xi_p,\zeta)}\quad(5.3.24)$$

It is observed that $\left|\xi_{TM_0}\right|>\left|\xi_{k_1}\right|$ for any ζ as depicted in Fig. 5.3.10. Hence, a standard square-root function is exploited in $p_1(\xi_p,\zeta)$. Then, all other residues are evaluated in a similar fashion. Using the same dimension of an integrated microstrip waveguide detailed previously, the current amplitude and phase longitudinal profiles contributed by surface-wave pole singularities with changing ζ about the branch-cut contour in Fig. 5.3.3 are depicted in Fig. 5.3.11 and Fig. 5.3.12.

Consequently, as required by Eqn. (5.3.2) and Eqn. (5.3.3)

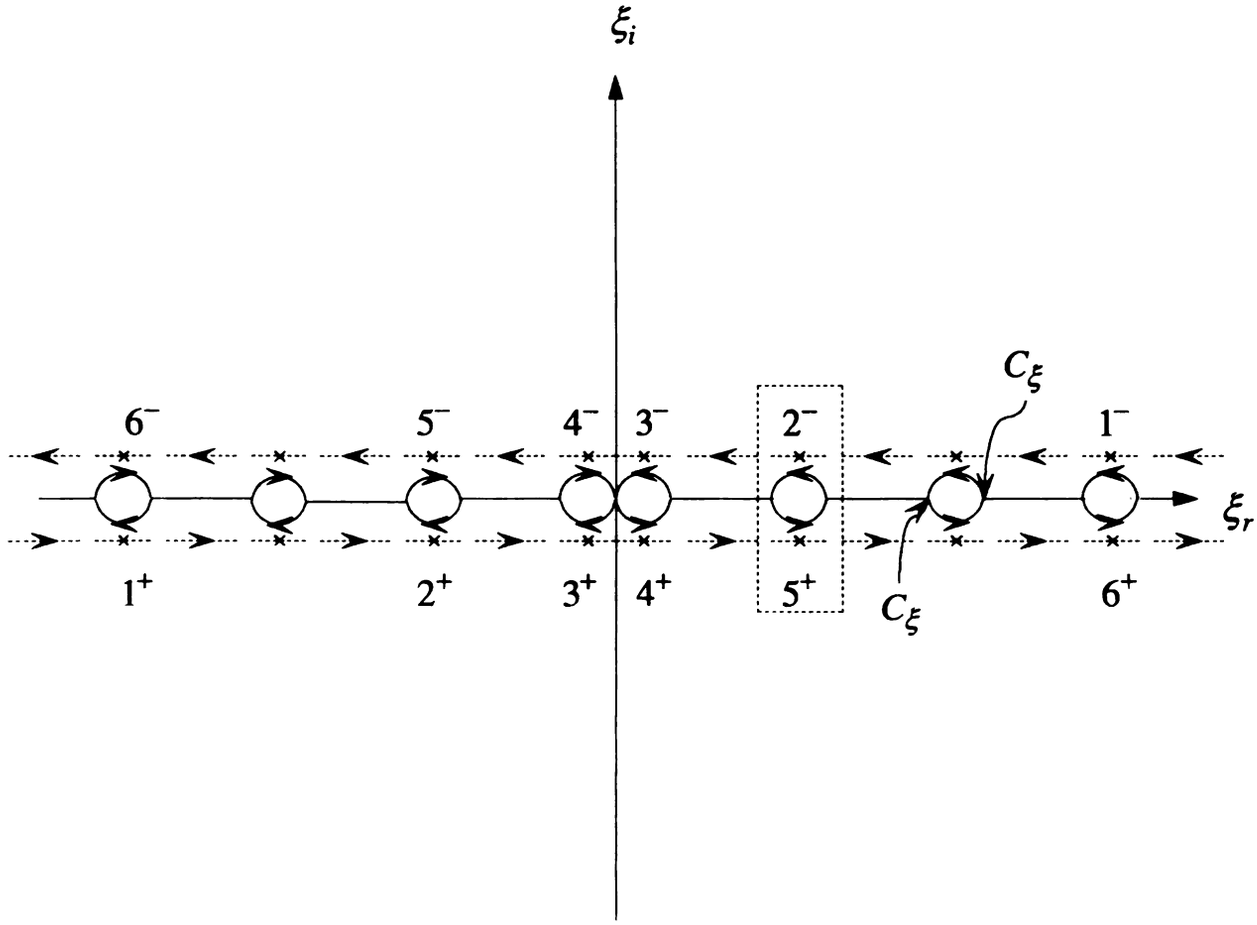

Figure 5.3.9 Migration of complex transverse transform plane (complex ξ-plane) surface-wave pole singularities $\pm\xi_{TM_0}$ in conjunction with changing spatial-frequency ζ along branch cuts associated with a logarithmic type branch point k_1 and a square-root type branch point λ_{TM_0} in the complex ζ-plane in the low-loss limit.

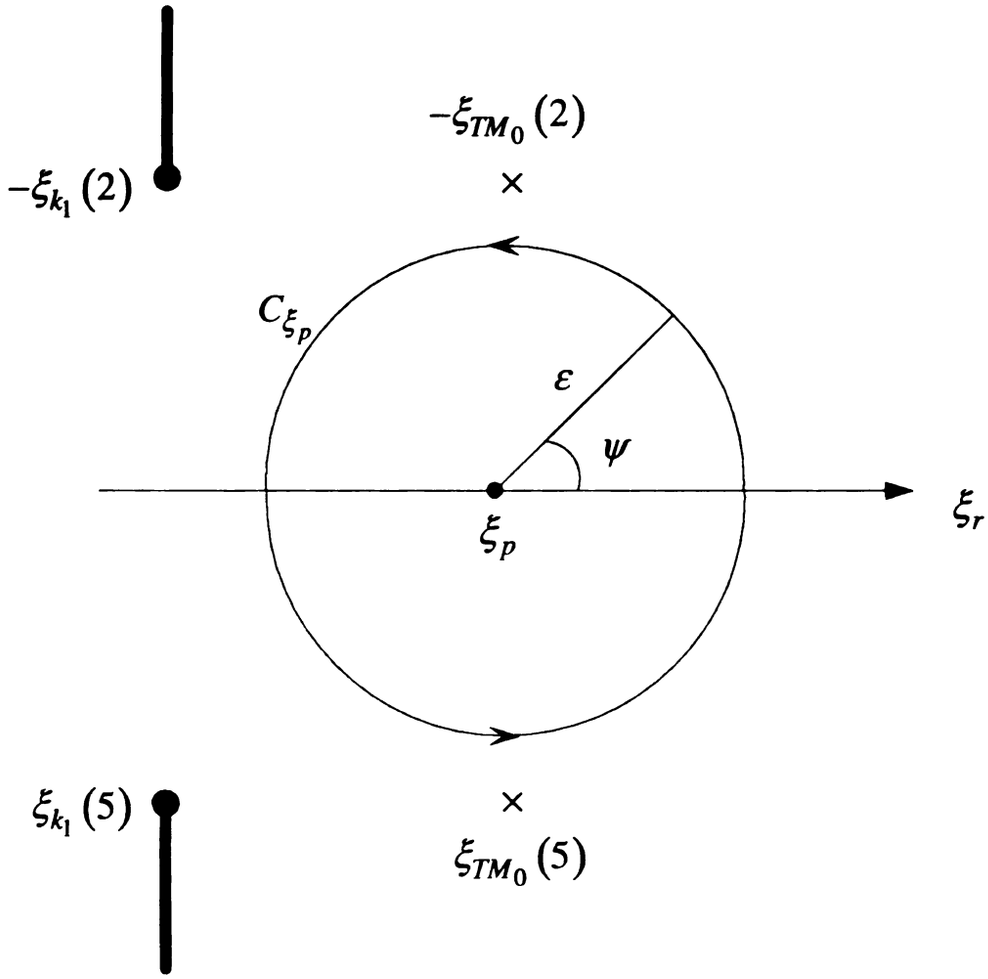

Figure 5.3.10 **Full residue evaluation contributed by the surface-wave pole singularity $\xi_p = -\xi_{TM_0}(2) = \xi_{TM_0}(5)$ with corresponding branch point singularities $\pm\xi_{k_1}$.**

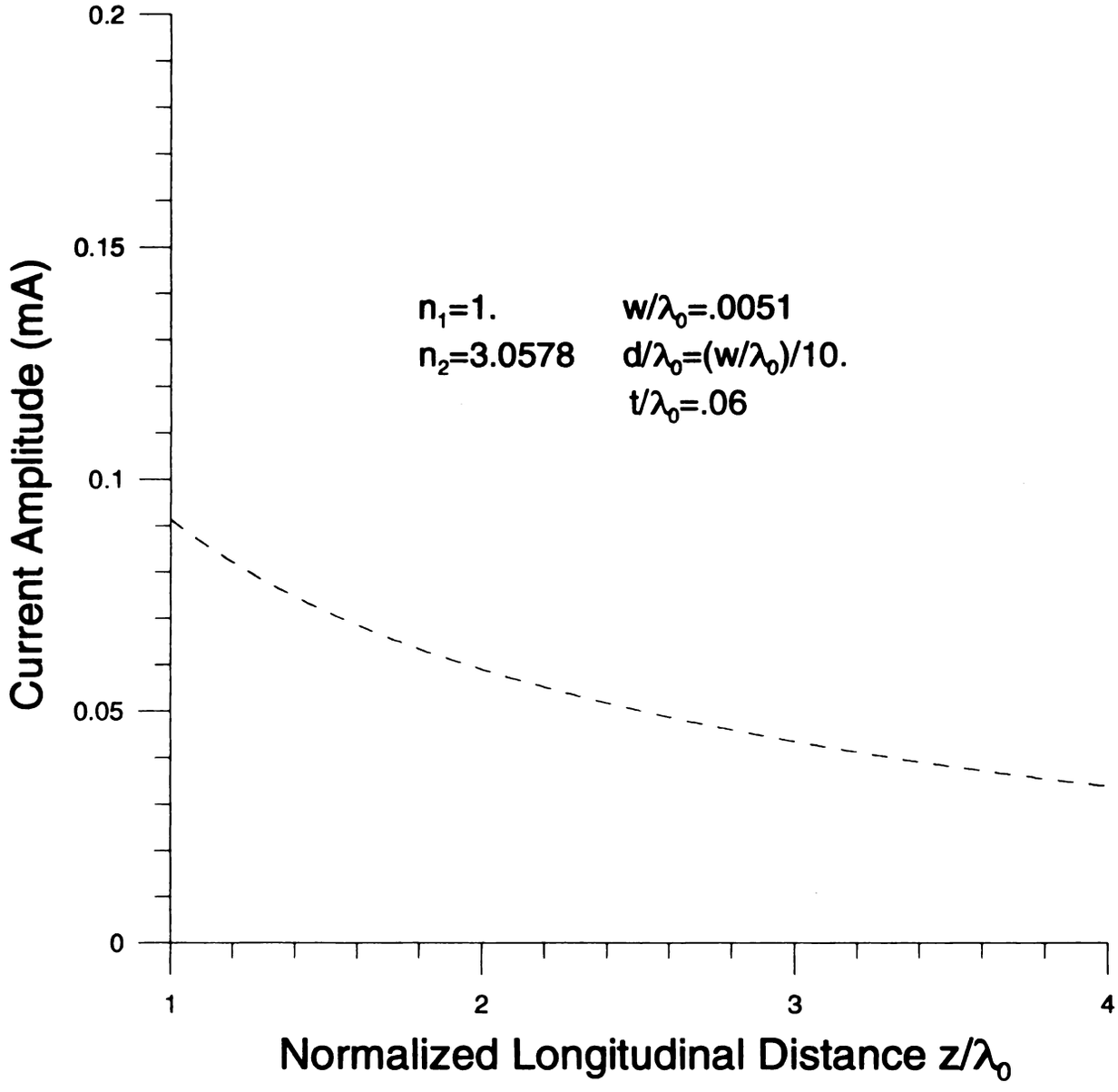

Figure 5.3.11 Current amplitude longitudinal profile contributed by surface-wave pole singularities in the complex ξ-plane with integrating ζ about the branch-cut contour.

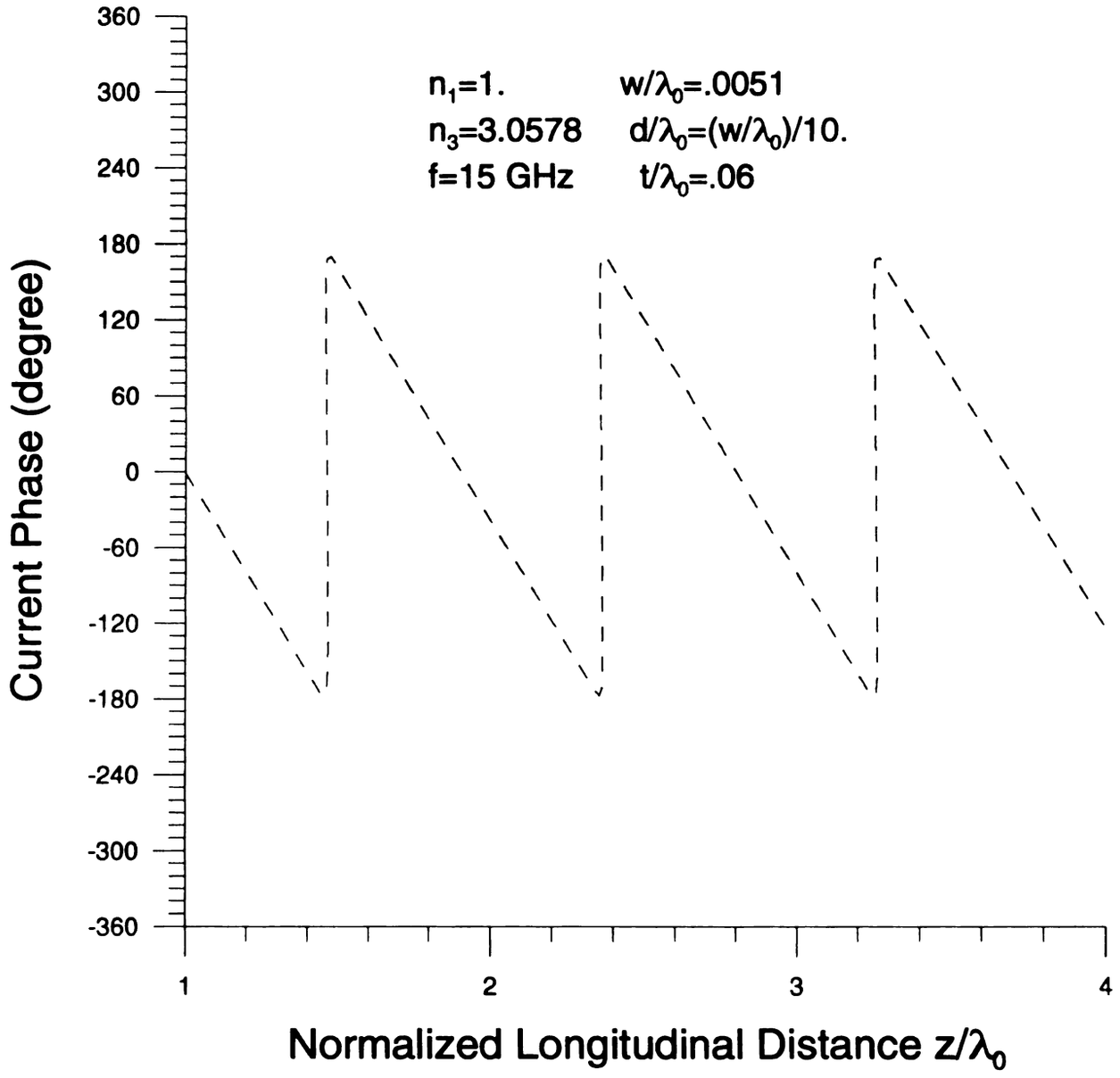

Figure 5.3.12 Current phase longitudinal profile contributed by surface-wave pole singularities in the complex ξ-plane with integrating ζ about the branch-cut contour.

$$\int_{-\infty}^{\infty}(\cdots)d\zeta = -\int_{C_b}(\cdots)d\zeta - \int_{C_{\zeta_p}}(\cdots)d\zeta \tag{5.3.25}$$

where $(\cdots)$ is an integrand of $d\zeta$ in Eqn. (5.2.21) and C_b is the branch cut contour as depicted in Figures 5.3.2 and 5.3.3. It is recognized that the continuous spectrum is contributed by an integration about the branch cut and proper if the integration path never violates the branch cut as depicted in Figures 5.3.2 and 5.3.3. The continuous spectrum is then decomposed into that contributed by $\mathrm{Re}\{\xi\}$-axis inversion contour excluding surface-wave pole singularities in the complex ξ-plane and that by surface-wave pole singularities in that plane. Therefore, the continuous spectrum is

$$\begin{aligned}
&-\int_{C_b}\frac{\tilde{L}_g(\zeta)}{\int_{-\infty}^{\infty}\tilde{\eta}^2(\xi)\left[\frac{j\eta_1}{k_1}\tilde{\tilde{C}}_{zz}(\xi,\zeta)\right]d\xi}e^{j\zeta z}d\zeta \\
&=-\int_{C_b}\frac{\tilde{L}_g(\zeta)}{\int_{C_\xi-\xi_p}\tilde{\eta}^2(\xi)\left[\frac{j\eta_1}{k_1}\tilde{\tilde{C}}_{zz}(\xi,\zeta)\right]d\xi}e^{j\zeta z}d\zeta \\
&-\int_{C_b}\frac{\tilde{L}_g(\zeta)}{\oint_{C_{\xi_p}}\tilde{\eta}^2(\xi)\left[\frac{j\eta_1}{k_1}\tilde{\tilde{C}}_{zz}(\xi,\zeta)\right]d\xi}e^{j\zeta z}d\zeta
\end{aligned} \tag{5.3.26}$$

where C_ξ denotes the $\mathrm{Re}\{\xi\}$-axis inversion contour and C_{ξ_p} the pole-excluding contour. The minus sign is retained in Eqn. (5.3.26) since the continuous spectrum will be confirmed by $\mathrm{Re}\{\zeta\}$-axis inversion contour integration along with a discrete spectrum contributed by a bound- or a guided-mode pole singularity ζ_p in agreement with Eqn. (5.3.25). Figs. 5.3.13 and 5.3.14 depict the longitudinal continuous spectrum

profile. It is noted that the same configuration of an integrated microstrip waveguide detailed previously is assumed.

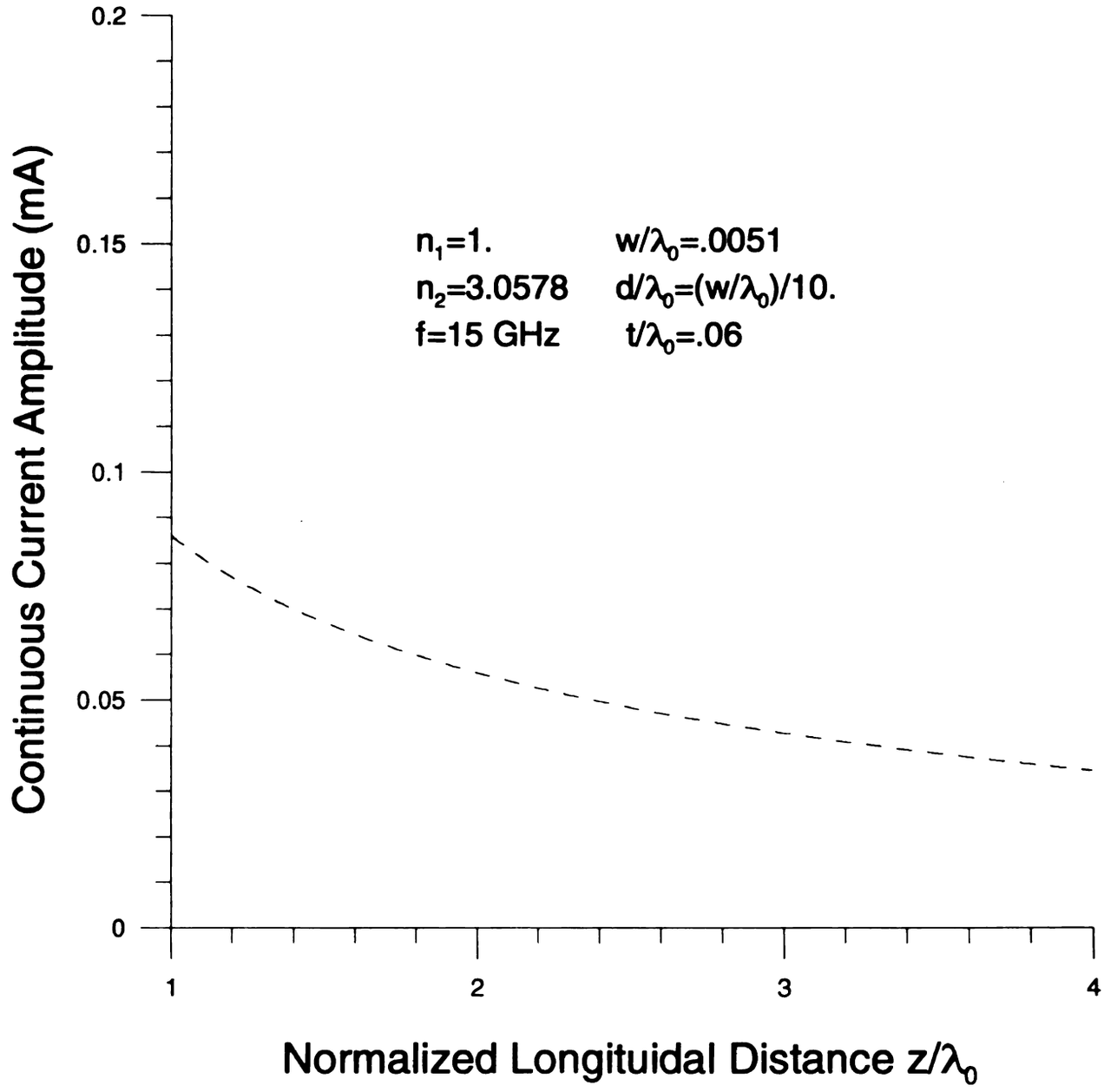

Figure 5.3.13 **Continuous current amplitude profile contributed by branch cut contour integration: $\mathrm{Re}\{\xi\}$-axis inversion contour integration including surface-wave pole singularities in the complex ξ-plane.**

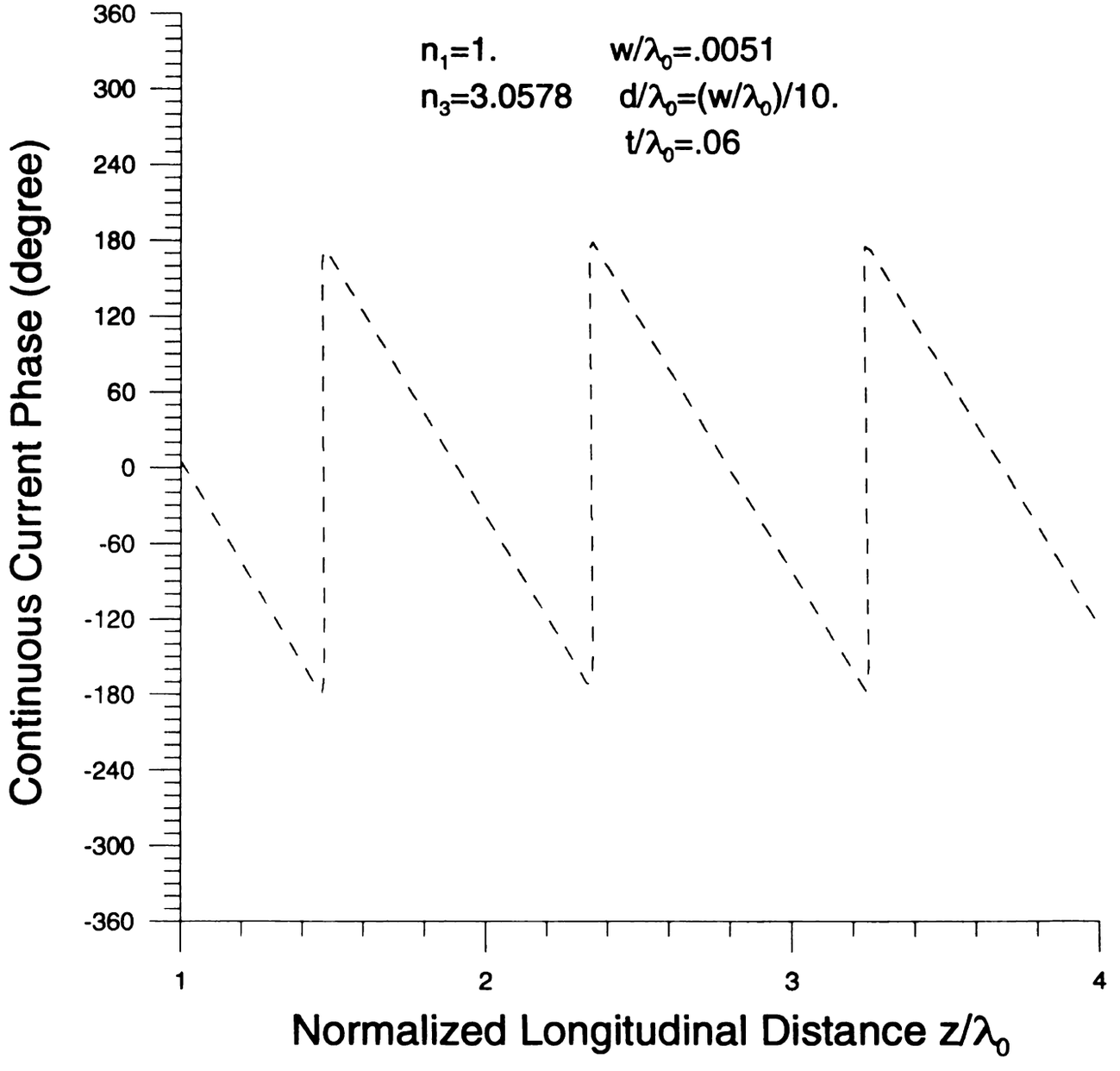

Figure 5.3.14 Continuous current phase profile contributed by branch cut contour integration: $\mathrm{Re}\{\xi\}$ -axis inversion contour integration including surface-wave pole singularities in the complex ξ -plane.

Additionally, it is necessary to consider the cut-off criterion for the surface-wave. Fig. F2 (see Appendix F) depicts the first two higher-order modes, i.e., TM_0 and TE_1. Using the same dimension of the microstrip structure detailed previously, for example, $n=0$ defines $(t/\lambda_0)_{co}=0$ and $n=1$ does $(t/\lambda_0)_{co}=.0865$. Therefore, in order to confine the TM_0 mode, the electrical film thickness t/λ_0 must be within the range of

$$0<\frac{t}{\lambda_0}\leq .0865$$

where the operating frequency is 15 GHz.

5.4 DISCRETE SPECTRUM CURRENT

As is evident from Eqn. (5.3.25), the discrete spectrum or the bound-mode spectrum is associated with bound- or guided-mode pole singularities ζ_p in the complex ζ -plane as depicted in Fig. 5.4.1.

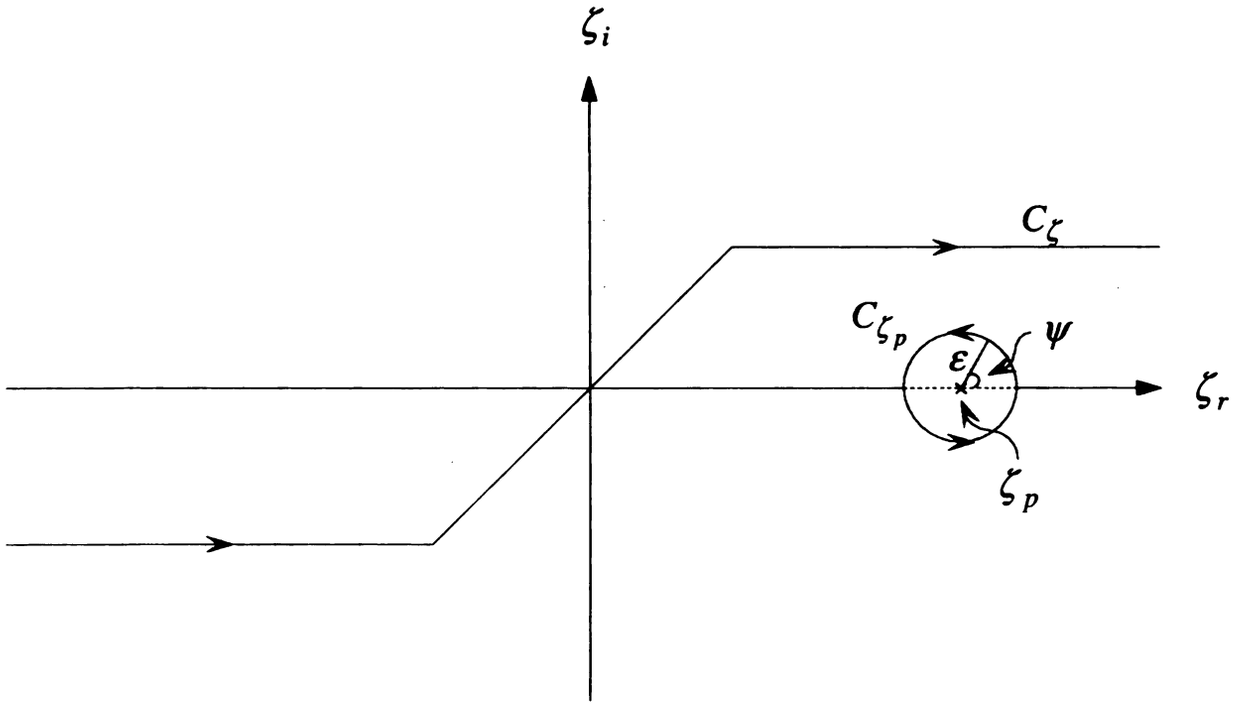

Figure 5.4.1 The discrete spectrum current contributed by a full residue evaluated about a pole-excluding contour C_{ζ_p} encircled about a bound- or guided-mode pole singularity ζ_p in the complex ζ -plane.

Fig. 5.4.1 is zoomed in Fig. 5.3.2 focusing on the pole-excluding contour C_{ζ_p}. It is observed that Fig. 5.3.2 is a little exaggerated for clarity. Since the *LHP* (*Lower Half*

Plane) is closed in the complex ζ -plane, C_{ζ_p} is in a counter-clockwise sense as depicted in Fig. 5.4.1. As evident from Eqn. (5.2.21), a characteristic eigenvalue equation for bound-mode pole singularities ζ_p is

$$\int_{-\infty}^{\infty} \tilde{\eta}^2(\xi)\left[\frac{j\eta_1}{k_1}\tilde{\tilde{C}}_{zz}(\xi,\zeta_p)\right]d\xi = 0$$

where

$$\tilde{\eta}(\xi) = \begin{cases} J_0(\xi w/2)\cdots \textit{for } w/t < 2 \\ sinc(\xi w/2)\cdots \textit{for } w/t \geq 2 \end{cases} \tag{5.4.1}$$

$$\tilde{\tilde{C}}_{zz}(\xi,\zeta_p) = \frac{\left(k_1^2-\zeta_p^2\right)}{Z^h(\xi,\zeta_p)} + \frac{\zeta_p^2 p_1\left(N_{21}^2-1\right)}{Z^h(\xi,\zeta_p)Z^e(\xi,\zeta_p)}$$

Then, for a full residue evaluation at $\zeta = \zeta_p$

$$\oint_{C_{\zeta_p}} \frac{d\zeta}{I_\xi(\xi,\zeta)} \approx \oint_{C_{\zeta_p}} \frac{d\zeta}{\underbrace{I_\xi(\xi,\zeta_p)}_{=0} + I_\xi'(\xi,\zeta_p)(\zeta-\zeta_p)+\cdots}$$

where

$$I_\xi(\xi,\zeta) = \int_{-\infty}^{\infty} \tilde{\eta}^2(\xi)\left[\frac{j\eta_1}{k_1}\tilde{\tilde{C}}_{zz}(\xi,\zeta)\right]d\xi \tag{5.4.2}$$

$$I_\xi'(\xi,\zeta_p) = \frac{d}{d\zeta} I_\xi(\xi,\zeta)\Big|_{\zeta=\zeta_p}$$

Due to complexity of $\tilde{\tilde{C}}_{zz}(\xi,\zeta)$ with respect to ζ, it is convenient to exploit a finite-difference scheme for $I_\xi'(\xi,\zeta_p)$. With a reasonable choice of $\Delta\zeta$,

$$\frac{d}{d\zeta} I_\xi(\xi,\zeta)\Big|_{\zeta=\zeta_p} \approx \frac{I_\xi(\xi,\zeta_p+\Delta\zeta)}{\Delta\zeta} \tag{5.4.3}$$

where $\Delta\zeta$ denotes an increment for ζ -differentiation. As depicted in Fig. 5.4.1, letting $\zeta - \zeta_p = \varepsilon e^{j\psi}$, Eqn. (5.4.2) becomes

$$\oint_{C_{\zeta_p}} \frac{d\zeta}{I_\xi'(\xi,\zeta_p)(\zeta-\zeta_p)} = \frac{1}{I_\xi'(\xi,\zeta_p)} \int_0^{2\pi} \frac{j\varepsilon e^{j\psi} d\psi}{\varepsilon e^{j\psi}} = \frac{j2\pi}{I_\xi'(\xi,\zeta_p)} \quad (5.4.4)$$

Exploiting Eqn. (5.4.3) leads to

$$\frac{j2\pi}{I_\xi'(\xi,\zeta_p)} \approx j2\pi \frac{\Delta\zeta}{I_\xi(\xi,\zeta_p+\Delta\zeta)} \quad (5.4.5)$$

Thus, in agreement with Eqn. (5.2.21), the full residue at $\zeta = \zeta_p$ is evaluated by

$$\oint_{C_{\zeta_p}} \frac{\tilde{L}_g(\zeta)}{I_\xi(\xi,\zeta)} e^{j\zeta z} d\zeta = j2\pi \frac{\Delta\zeta \tilde{L}_g(\zeta_p)}{I_\xi(\xi,\zeta_p+\Delta\zeta)} e^{j\zeta_p z}$$

where (5.4.6)

$$I_\xi(\xi,\zeta_p+\Delta\zeta) = \int_{-\infty}^{\infty} \tilde{\eta}^2(\xi) \left[\frac{j\eta_1}{k_1} \tilde{\tilde{C}}_{zz}(\xi,\zeta) \right] d\xi \Big|_{\zeta=\zeta_p+\Delta\zeta}$$

Eqn. (5.4.6) defines the discrete spectrum current (bound-mode spectrum current). Using the same microstrip configuration detailed previously, numerical results for the discrete current profile are depicted in Fig. 5.4.2 and Fig. 5.4.3. Eigenvalue equation (5.4.1) is solved for ζ_p by a Newton's method root search.

It is noted that the characteristic impedance of the microstrip waveguide is not unique since it supports quasi TEM-modes. However, a meaningful characteristic impedance can be calculated by exploiting the discrete (bound-mode) spectrum current. As depicted in Fig. 5.4.4a of Fig. 5.4.4, the discrete current I_D is propagating longitudinally with a voltage V. The voltage can be decomposed into half of the voltage as depicted in Fig.

5.4.4b of Fig. 5.4.4. The upward and downward discrete currents annul each other at $z=0$ but as depicted in Fig. 5.4.4c of Fig. 5.4.4, infinitesimally separated upward and downward discrete currents can flow at $z=0$. Therefore, the characteristic impedance Z_c is derived by

$$Z_c = \frac{V/2}{I_D(z=0)} = \frac{V}{2I_D(z=0)} \tag{5.4.7}$$

where $I_D(z=0)$ is the discrete (bound-mode) current at $z=0$. The fundamental proper surface-wave mode λ_{TM_0} and the bound- or guided-mode pole singularity ζ_p are dispersed through operating frequency ranges (1~38 GHz) as depicted in Fig. 5.4.5. For a δ-gap feed model, the voltage is set to be unity. Thus,

$$Z_c = \frac{1}{2I_D(z=0)} \tag{5.4.8}$$

Using the same configuration detailed previously, the characteristic impedance Z_c of the microstrip waveguide through operating frequency ranges (1~38 GHz) is, in agreement with Eqn. (5.4.8), depicted in Fig. 5.4.6 and compared with the well-known empirical formula [54].

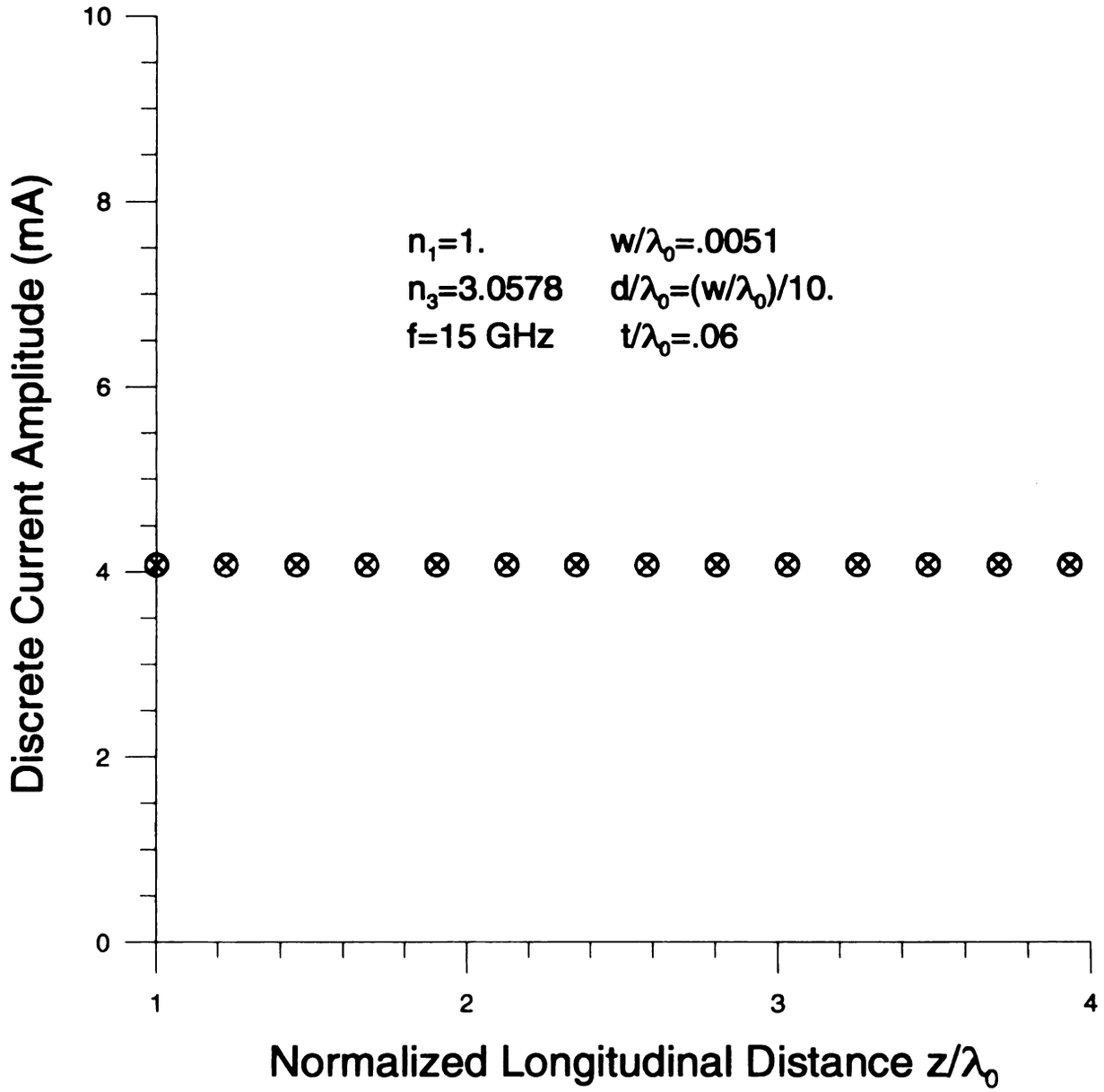

Figure 5.4.2 Discrete current amplitude profile contributed by a bound- or a guided-mode pole singularity ζ_p in the complex ζ -plane.

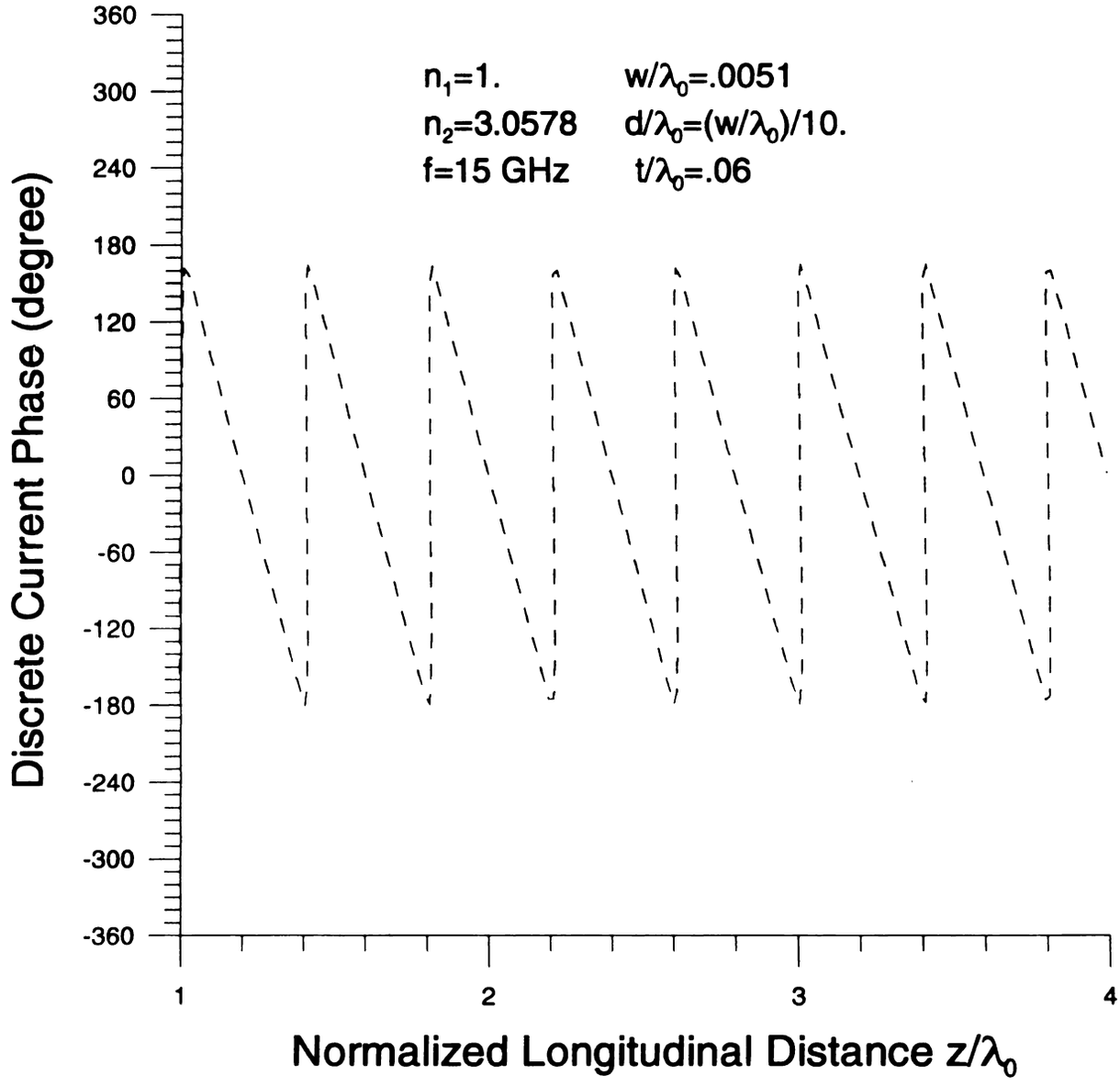

Figure 5.4.3 Discrete current phase profile contributed by a bound- or a guided-mode pole singularity ζ_p in the complex ζ -plane.

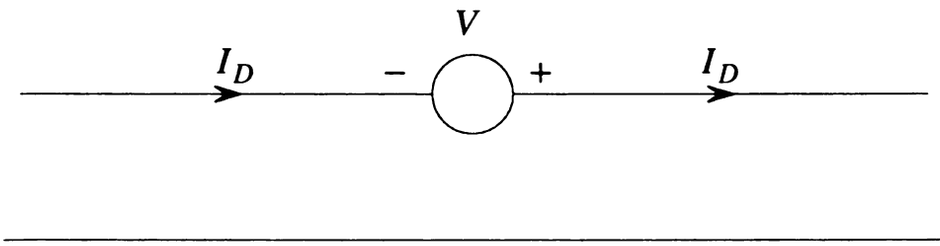

$\sigma = \infty$

Figure 5.4.4a

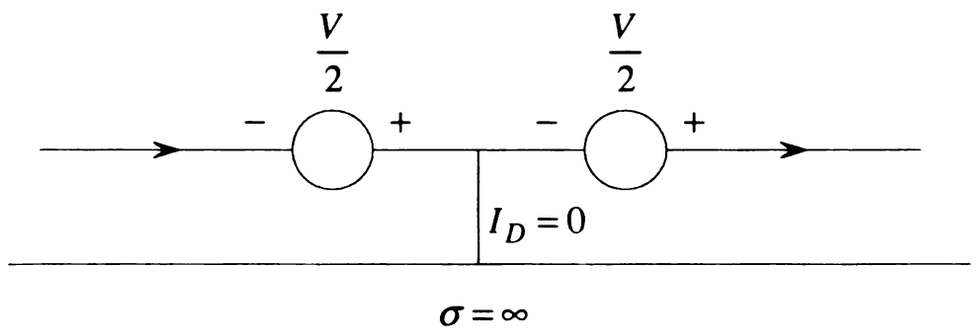

$\sigma = \infty$

Figure 5.4.4b

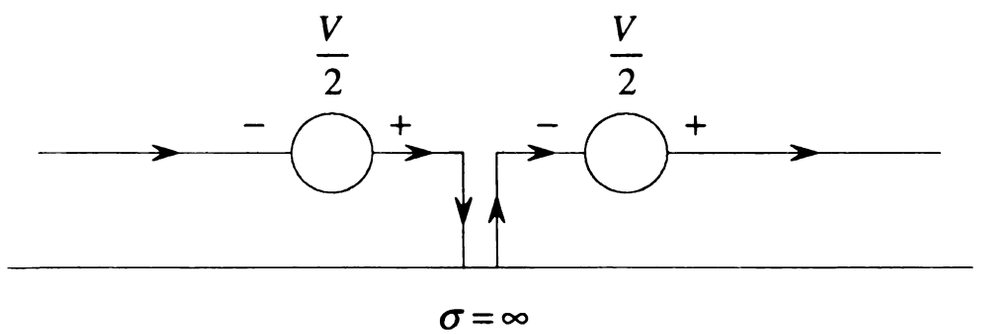

$\sigma = \infty$

Figure 5.4.4c

Figure 5.4.4 Voltage decomposition diagram.

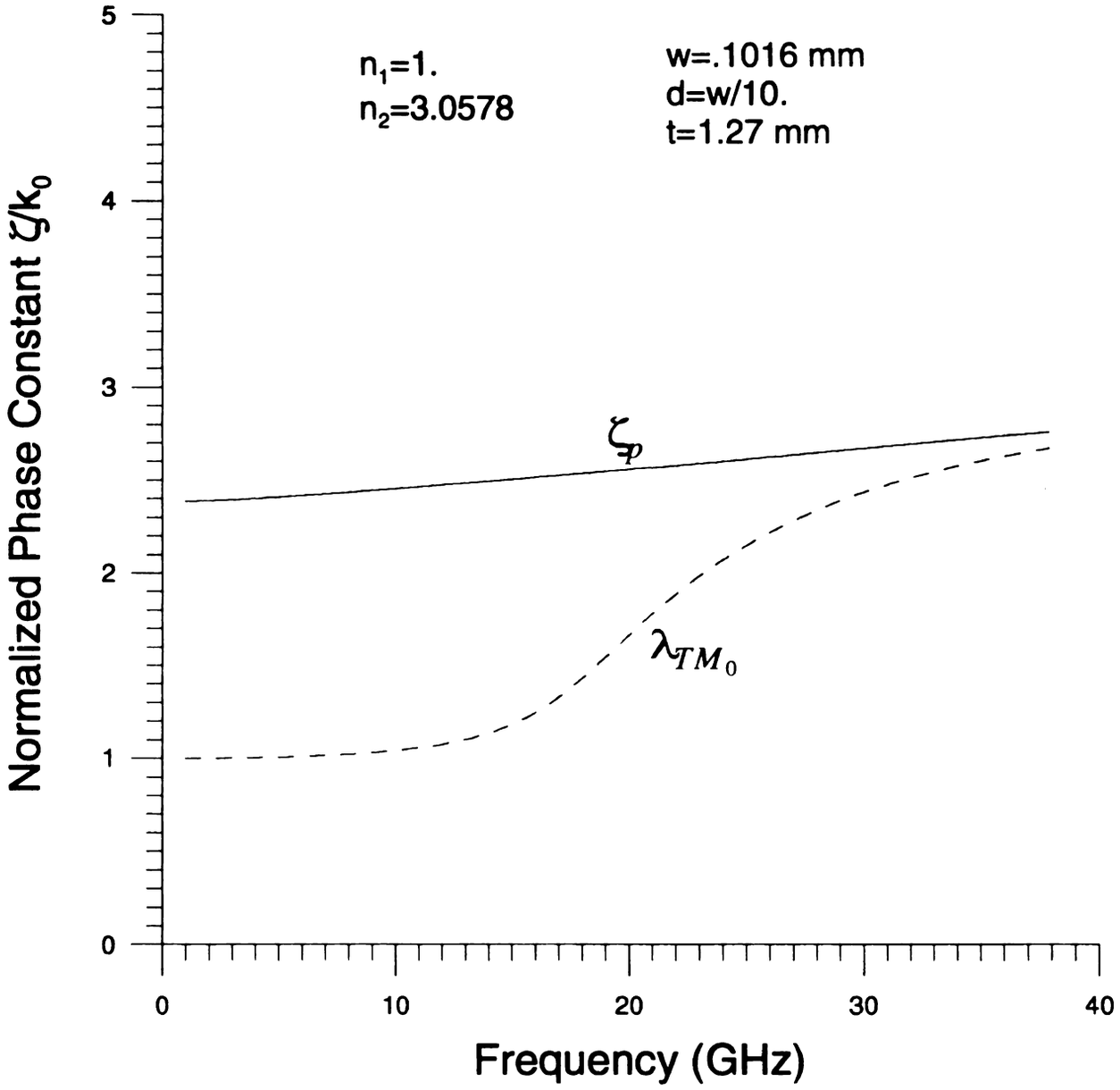

Figure 5.4.5 **The dispersion of the fundamental surface-wave pole singularity λ_{TM_0} and the bound or guided-mode pole singularity ζ_p through operating frequency ranges.**

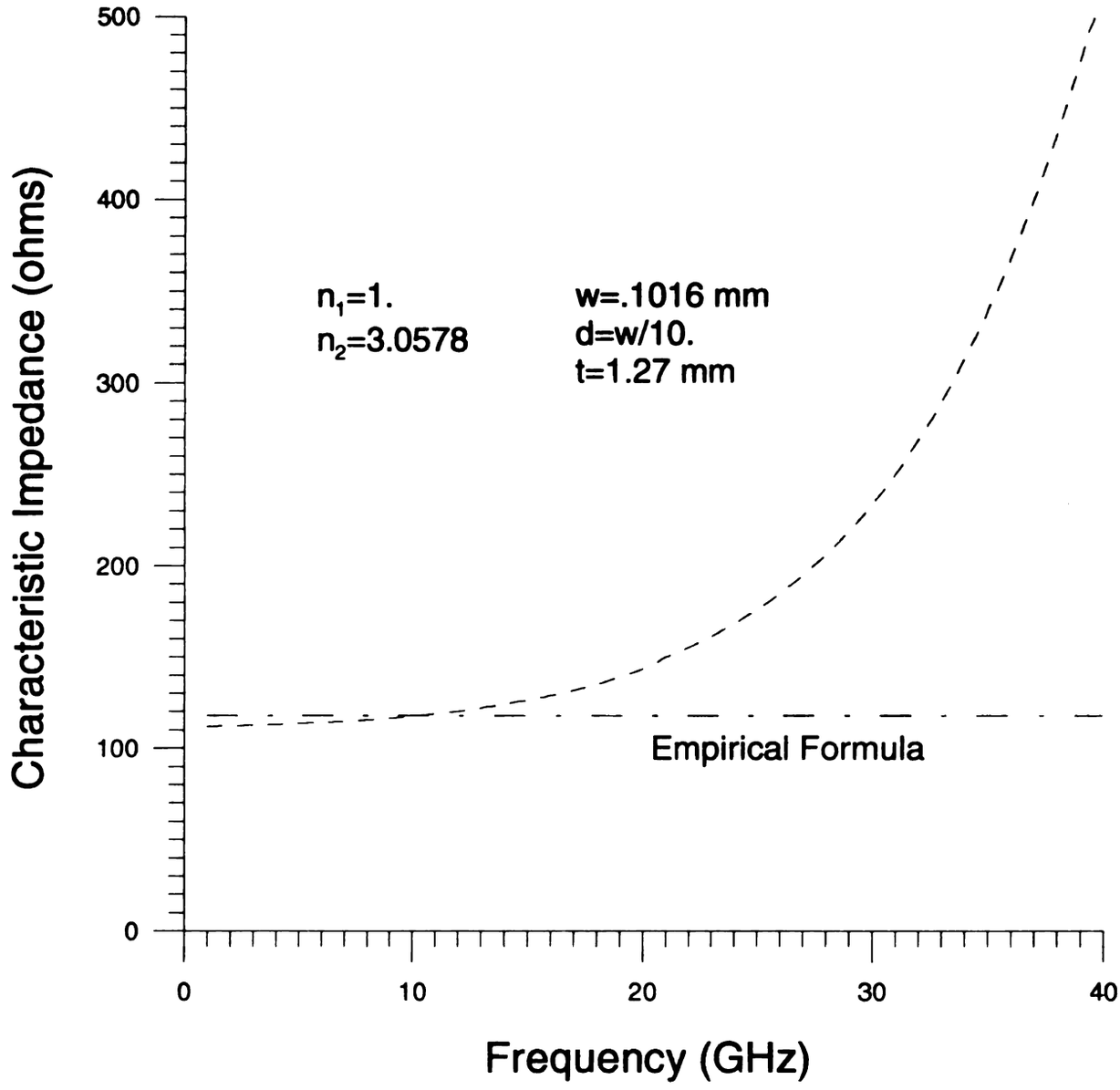

Figure 5.4.6 The characteristic impedance of the microstrip waveguide calculated by the longitudinal discrete or bound-mode current spectrum through operating frequency ranges.

5.5 MICROSTRIP CURRENT SPECTRUM

The microstrip current is composed of the continuous spectrum current contributed by the background layer environment (branch points) and the discrete spectrum current contributed by the guiding structure (poles). As depicted in Fig. 5.5.1, the microstrip current is dominated by the discrete spectrum current rather than the continuous spectrum current. It is noted that physically, the microstrip current is associated with the guiding structure rather than the background layer environment. Therefore, the microstrip current is less dominated by the continuous spectrum current contributed by the that background.

In agreement with Eqn. (5.3.25), the microstrip current spectrum can be validated by $\mathrm{Re}\{\zeta\}$-axis inversion contour integration as depicted in Fig. 5.5.3. Since the integrand of $d\zeta$ in Eqn. (5.2.21) is even in ζ,

$$J_z(z)=2\int_0^{\infty}\frac{\tilde{L}_g(\zeta)}{\int_{-\infty}^{\infty}\tilde{\eta}^2(\xi)\left[\frac{j\eta_1}{k_1}\tilde{\tilde{C}}_{zz}(\xi,\zeta)\right]d\xi}\cos(\zeta z)d\zeta \qquad (5.5.1)$$

Therefore, even though Fig. 5.5.3 depicts the entire $\mathrm{Re}\{\zeta\}$-axis integration from $-\infty$ to ∞, the migration of ξ-plane singularities with changing ζ needs to be considered only along the positive $\mathrm{Re}\{\zeta\}$-axis inversion contour as depicted in Fig. 5.5.4. More importantly, the cut-off criterion for the nth surface-wave mode must be carefully considered. In the interval 1, as discussed in Section 5.3,

$$\begin{cases}\xi_{k_1}=\left|\xi_{k_1}\right|e^{j(-\pi+\pi)/2}=\left|\xi_{k_1}\right| \\ \xi_{TM_0}=\left|\xi_{TM_0}\right|e^{j(-\pi+\pi)/2}=\left|\xi_{TM_0}\right|\end{cases}$$

In the interval 2,

$$\begin{cases} \xi_{k_1} = \left|\xi_{k_1}\right| e^{j(-\pi)/2} = -j\left|\xi_{k_1}\right| \\ \xi_{TM_0} = \left|\xi_{TM_0}\right| e^{j(-\pi+\pi)/2} = \left|\xi_{TM_0}\right| \end{cases}$$

In the interval 3,

$$\begin{cases} \xi_{k_1} = \left|\xi_{k_1}\right| e^{j(-\pi)/2} = -j\left|\xi_{k_1}\right| \\ \xi_{TM_0} = \left|\xi_{TM_0}\right| e^{j(-\pi)/2} = -j\left|\xi_{TM_0}\right| \end{cases}$$

It is observed that $\left|\xi_{TM_0}\right| > \left|\xi_{k_1}\right|$ for any ζ along the positive $\mathrm{Re}\{\zeta\}$-axis inversion contour. Hence, in the low-loss limit, a standard square-root function can be exploited in $p_1\left(\pm\xi_{TM_0}, \zeta\right)$ (no complex-phasor diagram is required). In the interval 1 in Fig. 5.5.3, ξ_{k_1}, the positive branch-point singularity in the complex ξ-plane, migrates from $\left|\xi_{k_1}\right|$ to 0 on $\mathrm{Re}\{\xi\}$-axis. In the intervals 2 and 3, ξ_{k_1} migrates from 0 to $-j\infty$ on $\mathrm{Im}\{\xi\}$-axis as depicted in Fig. 5.5.4. Similarly, in the interval 1, the negative branch-point singularity $-\xi_{k_1}$ migrates from $-\left|\xi_{k_1}\right|$ to 0 on $\mathrm{Re}\{\xi\}$-axis and in the intervals 2 and 3, migrates from 0 to $j\infty$ on $\mathrm{Im}\{\xi\}$-axis. As depicted in Fig. 5.5.4, the positive surface-wave pole singularity ξ_{TM_0} migrates from $\left|\xi_{TM_0}\right|$ to 0 on $\mathrm{Re}\{\xi\}$-axis in the intervals 1 and 2. In the interval 3, ξ_{TM_0} migrates from 0 to $-j\infty$ on $\mathrm{Im}\{\xi\}$-axis. Similarly, in the intervals 1 and 2, $-\xi_{TM_0}$ migrates from $-\left|\xi_{TM_0}\right|$ to 0 on $\mathrm{Re}\{\xi\}$-axis and in the interval 3, migrates from 0 to $j\infty$ on $\mathrm{Im}\{\xi\}$-axis. And also $\mathrm{Re}\{\xi\}$-axis inversion contour integration and the surface-wave residue contribution in the complex ξ-plane are

similarly calculated as discussed in Section 5.3. On the other hand, more carefully, in the interval 3 in Fig. 5.5.3, the bound- or guided-mode pole singularity ζ_p contributes to the half residue as depicted in the dotted box. Therefore, in agreement with Eqn. (5.4.6) and Eqn. (5.5.1), the half residue about $\zeta = \zeta_p$ is evaluated by

$$\oint_{C_{\zeta_p}} \frac{2\tilde{L}_g(\zeta)}{I_\xi(\xi,\zeta)}\cos(\zeta z)d\zeta = -j2\pi \frac{\Delta\zeta \tilde{L}_g(\zeta_p)}{I_\xi(\xi,\zeta_p+\Delta\zeta)}\cos(\zeta_p z)$$

where (5.5.2)

$$I_\xi(\xi,\zeta_p+\Delta\zeta) = \int_{-\infty}^{\infty}\tilde{\eta}^2(\xi)\left[\frac{j\eta_1}{k_1}\tilde{\tilde{C}}_{zz}(\xi,\zeta)\right]d\xi\Big|_{\zeta=\zeta_p+\Delta\zeta}$$

Unlike in Eqn. (5.4.6), the minus sign denotes that C_{ζ_p} is in a clockwise sense. Then, Eqns. (5.5.1) and (5.5.2) require,

$$J_z(z) = 2\int_0^{\infty}\frac{\tilde{L}_g(\zeta)}{I_\xi(\xi,\zeta)}\cos(\zeta z)d\zeta + 2\oint_{C_{\zeta_p}}\frac{\tilde{L}_g(\zeta)}{I_\xi(\xi,\zeta)}\cos(\zeta z)d\zeta$$

where (5.5.3)

$$I_\xi(\xi,\zeta) = \int_{-\infty}^{\infty}\tilde{\eta}^2(\xi)\left[\frac{j\eta_1}{k_1}\tilde{\tilde{C}}_{zz}(\xi,\zeta)\right]d\xi$$

Using the same microstrip waveguide configuration detailed previously, Eqn. (5.3.25) can be validated numerically as depicted in Figs. 5.5.5, 5.5.6, 5.5.7 and 5.5.8 for and away from near zones.

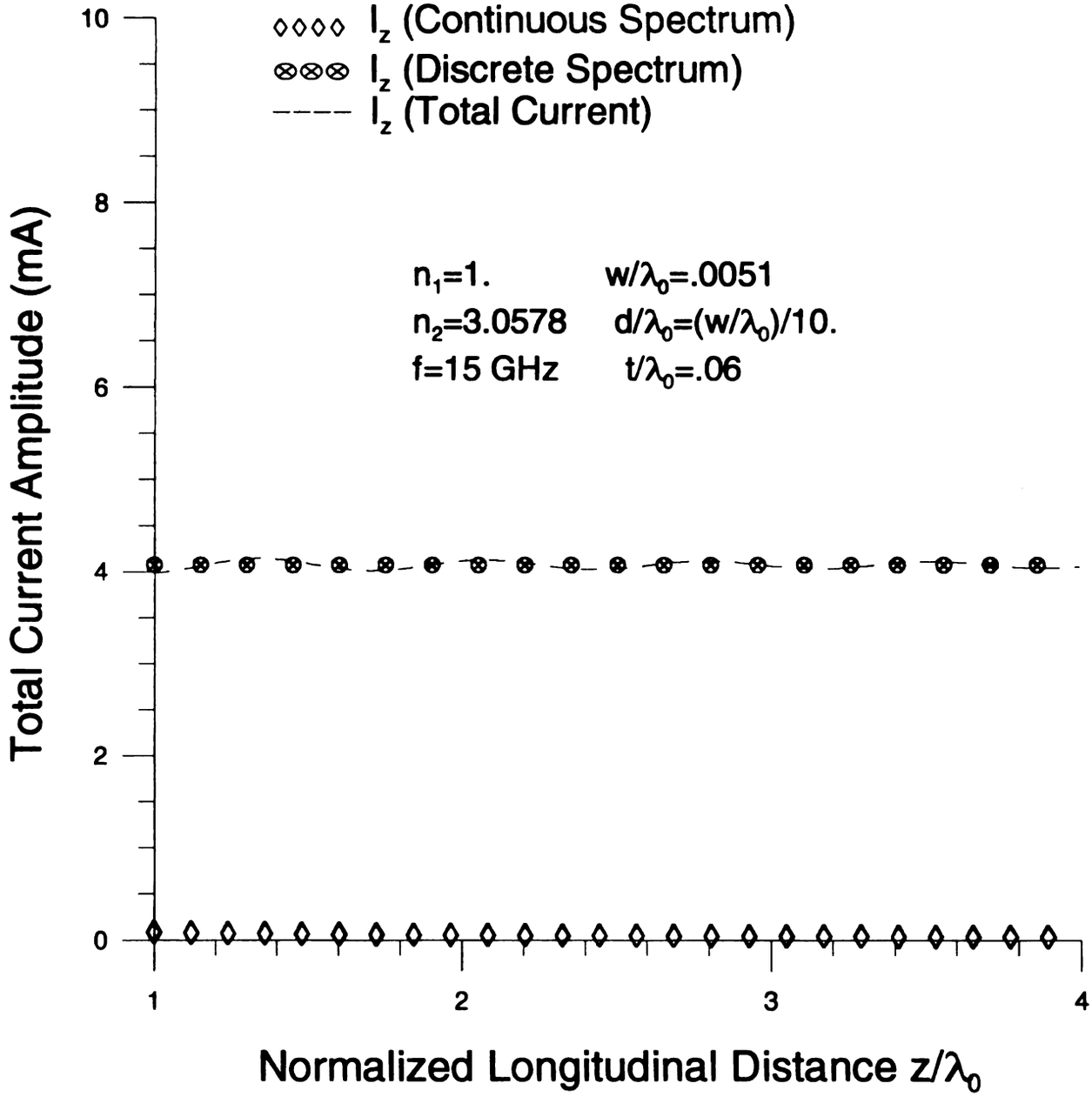

Figure 5.5.1 Total microstrip current amplitude profile contributed by the continuous spectrum current and the discrete spectrum current.

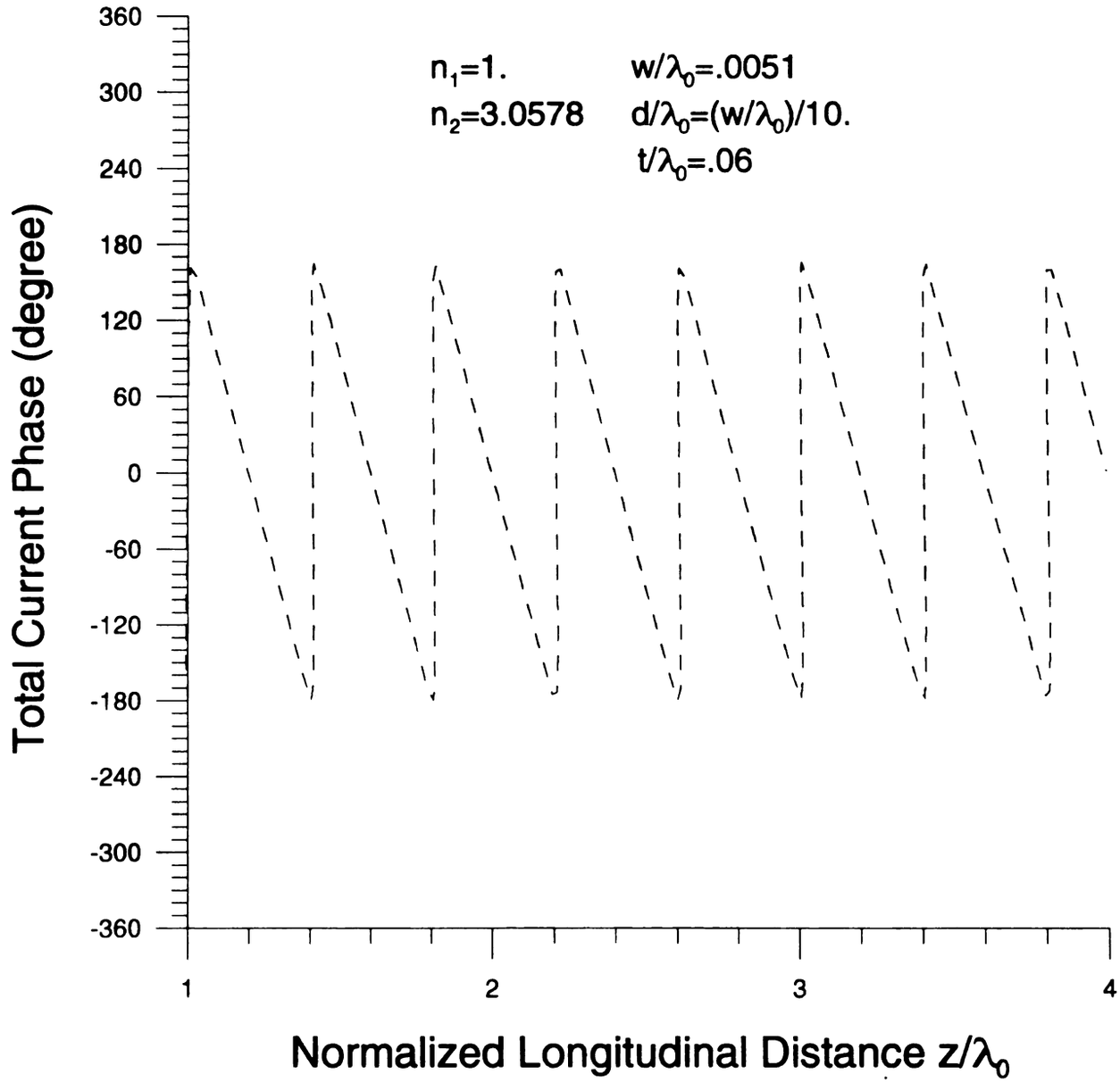

Figure 5.5.2 Total microstrip current phase profile contributed by the continuous spectrum current and the discrete spectrum current.

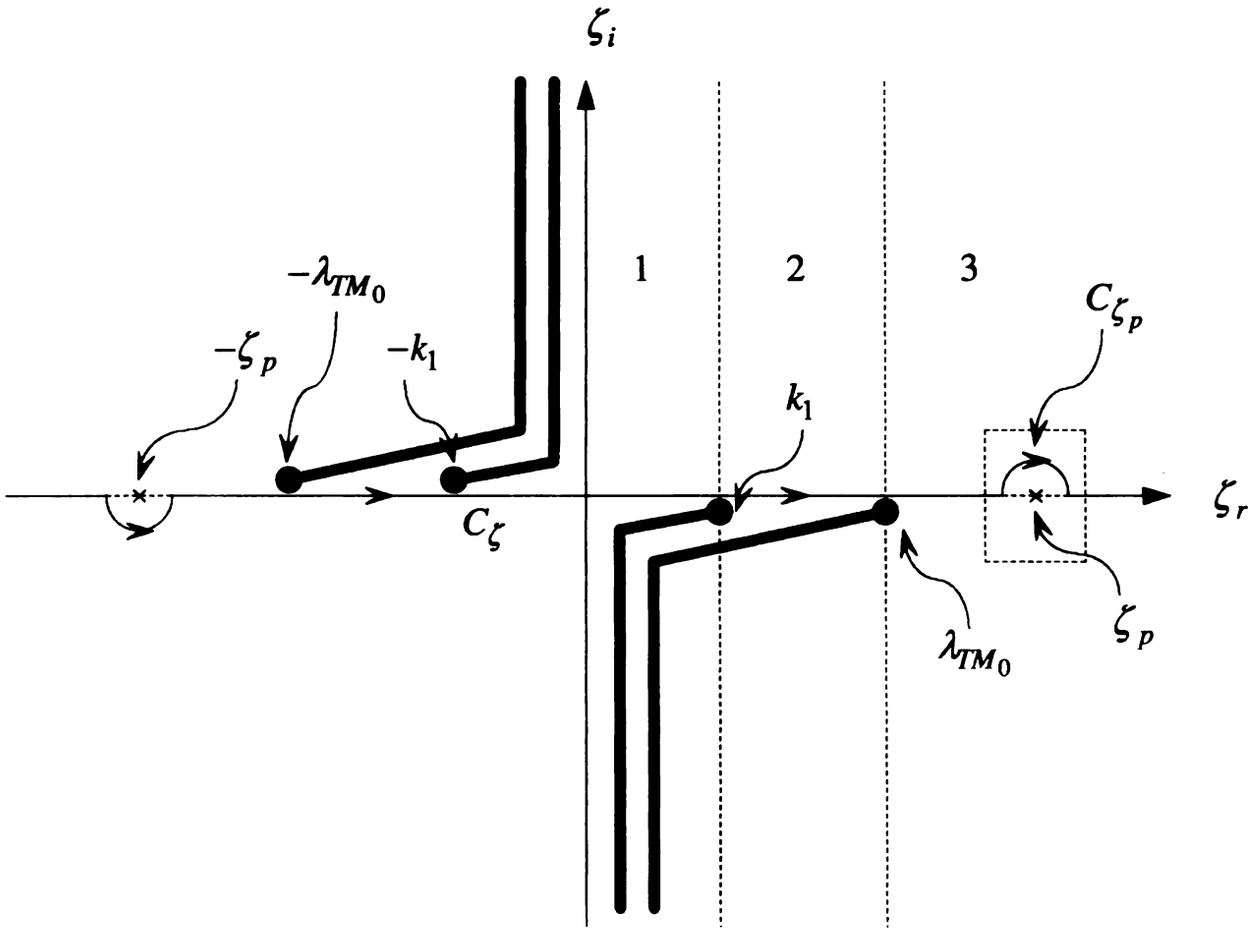

Figure 5.5.3 $\mathrm{Re}\{\zeta\}$**-axis inversion contour** C_ζ **and the half residue contribution about** $\zeta = \zeta_p$.

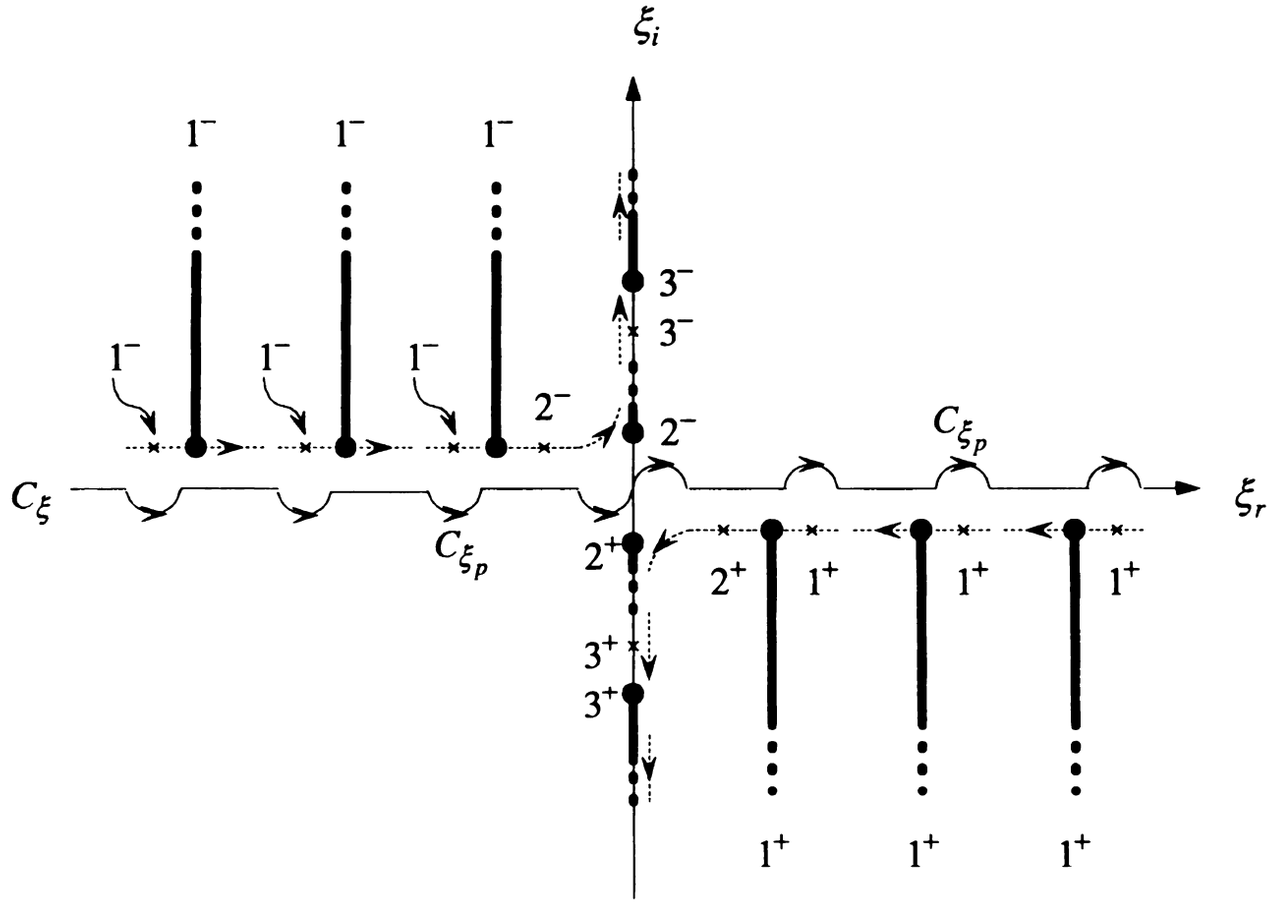

Figure 5.5.4 Migration of complex transverse transform plane (complex ξ-plane) branch-point singularities $\pm\xi_{k_1}$ and surface-wave pole singularities $\pm\xi_{TM_0}$ in conjunction with changing spatial-frequency ζ on $\mathrm{Re}\{\zeta\}$-axis inversion contour in the low-loss limit.

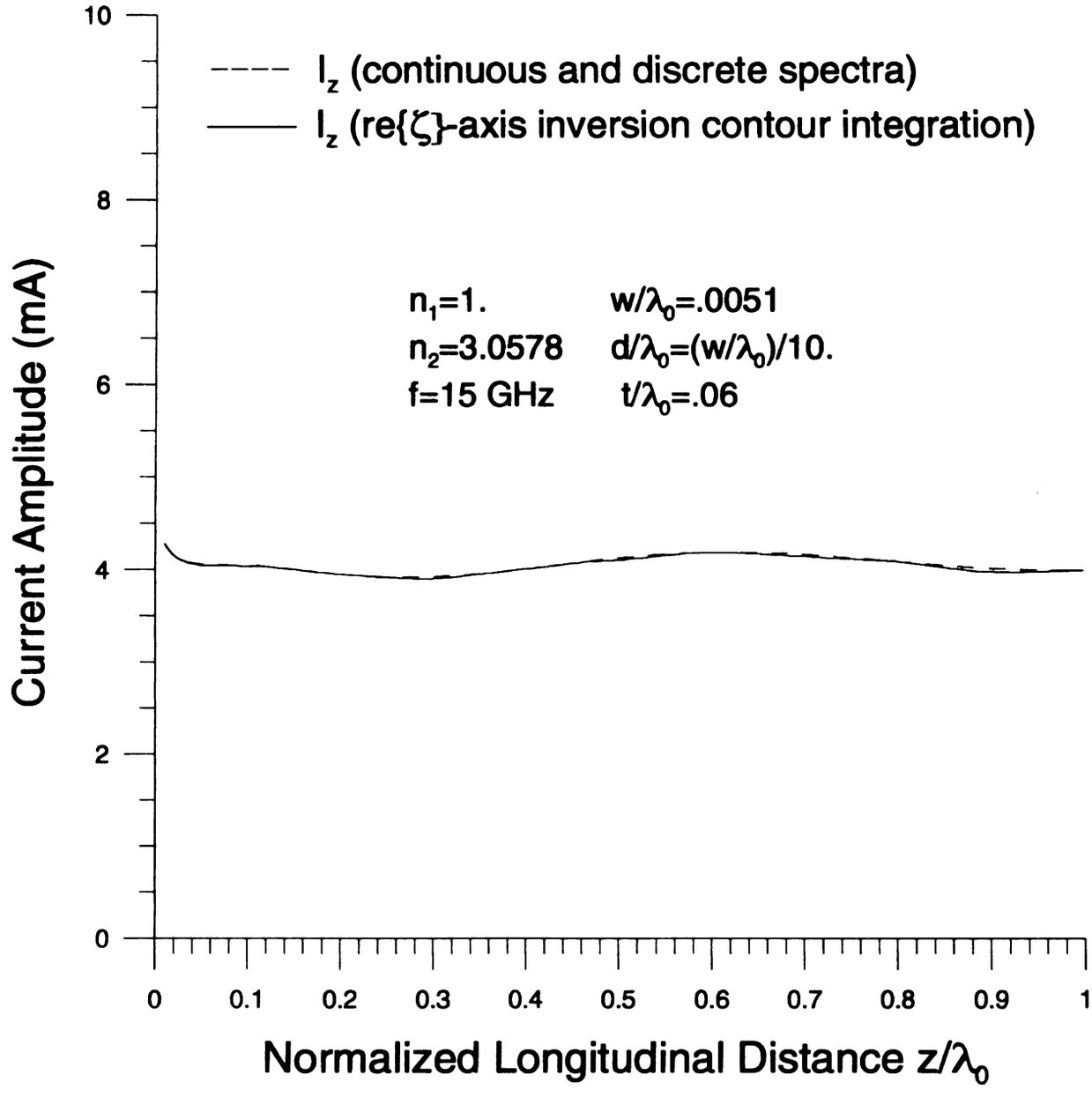

Figure 5.5.5 $\mathrm{Re}\{\zeta\}$**-axis inversion contour validation of microstrip current amplitude profile contributed by the continuous spectrum current and the discrete spectrum current for near zone.**

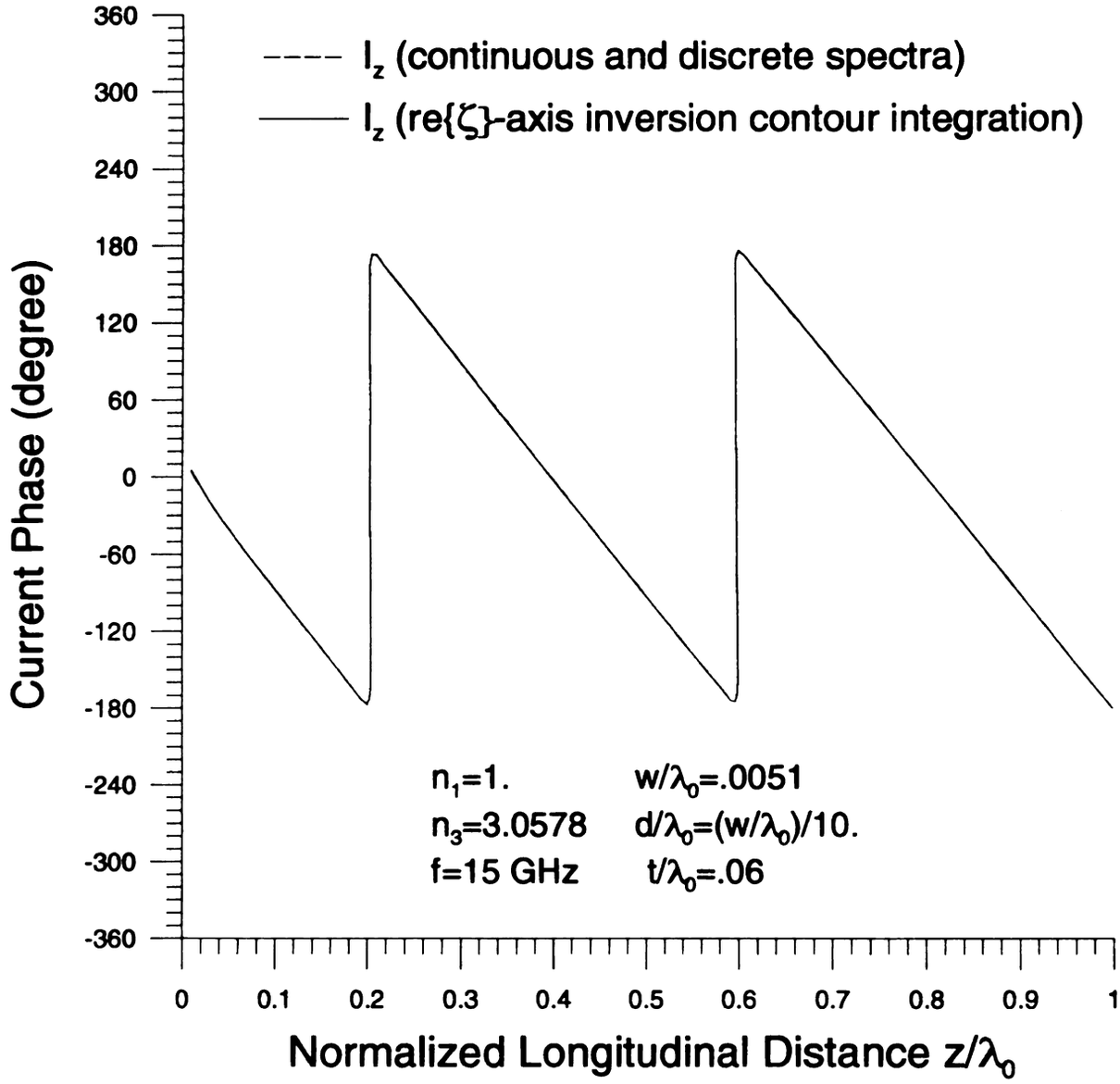

Figure 5.5.6 $\mathrm{Re}\{\zeta\}$**-axis inversion contour validation of microstrip current phase profile contributed by the continuous spectrum current and the discrete spectrum current for near zone.**

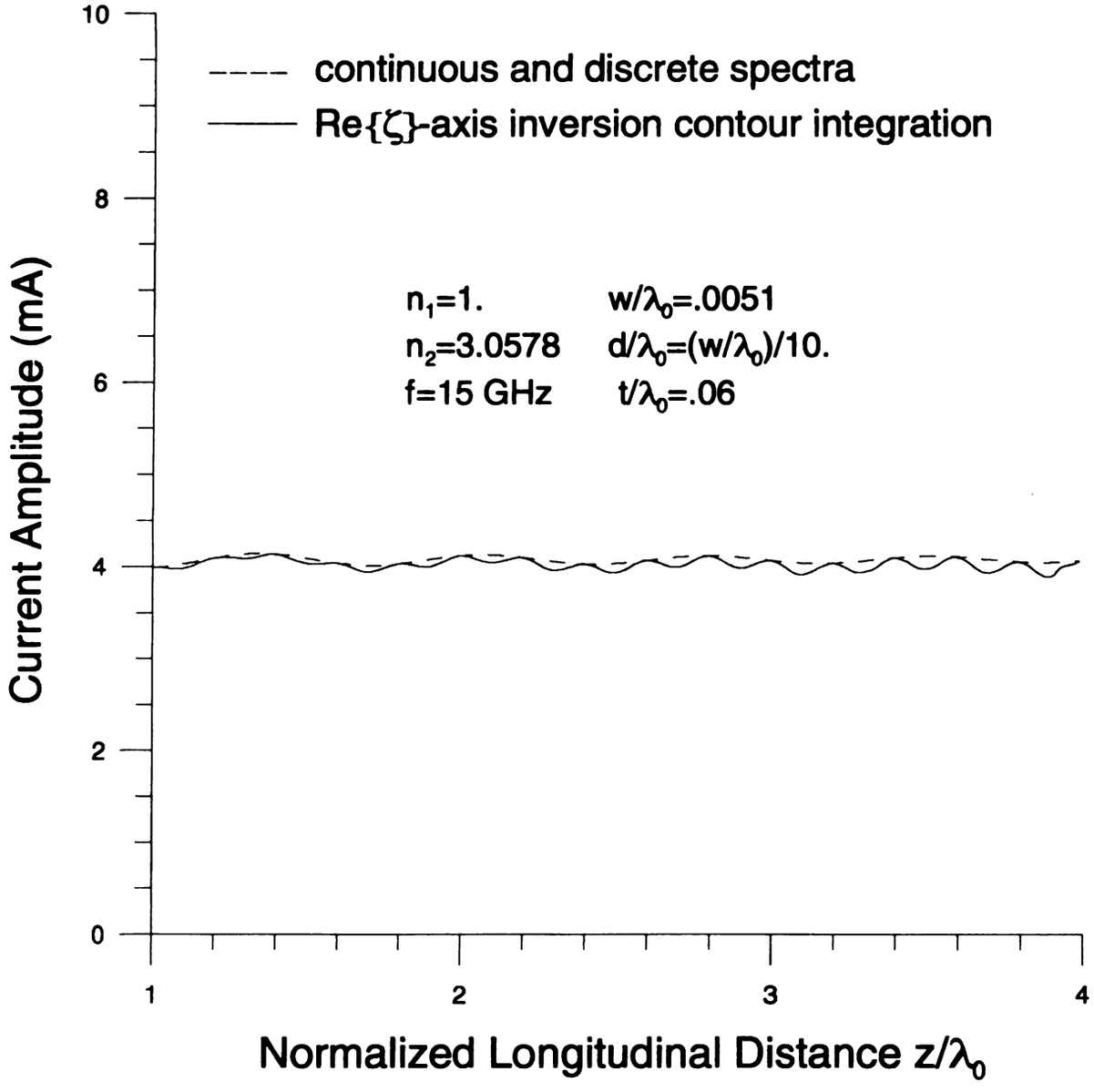

Figure 5.5.7 $\mathrm{Re}\{\zeta\}$**-axis inversion contour validation of microstrip current amplitude profile contributed by the continuous spectrum current and the discrete spectrum current.**

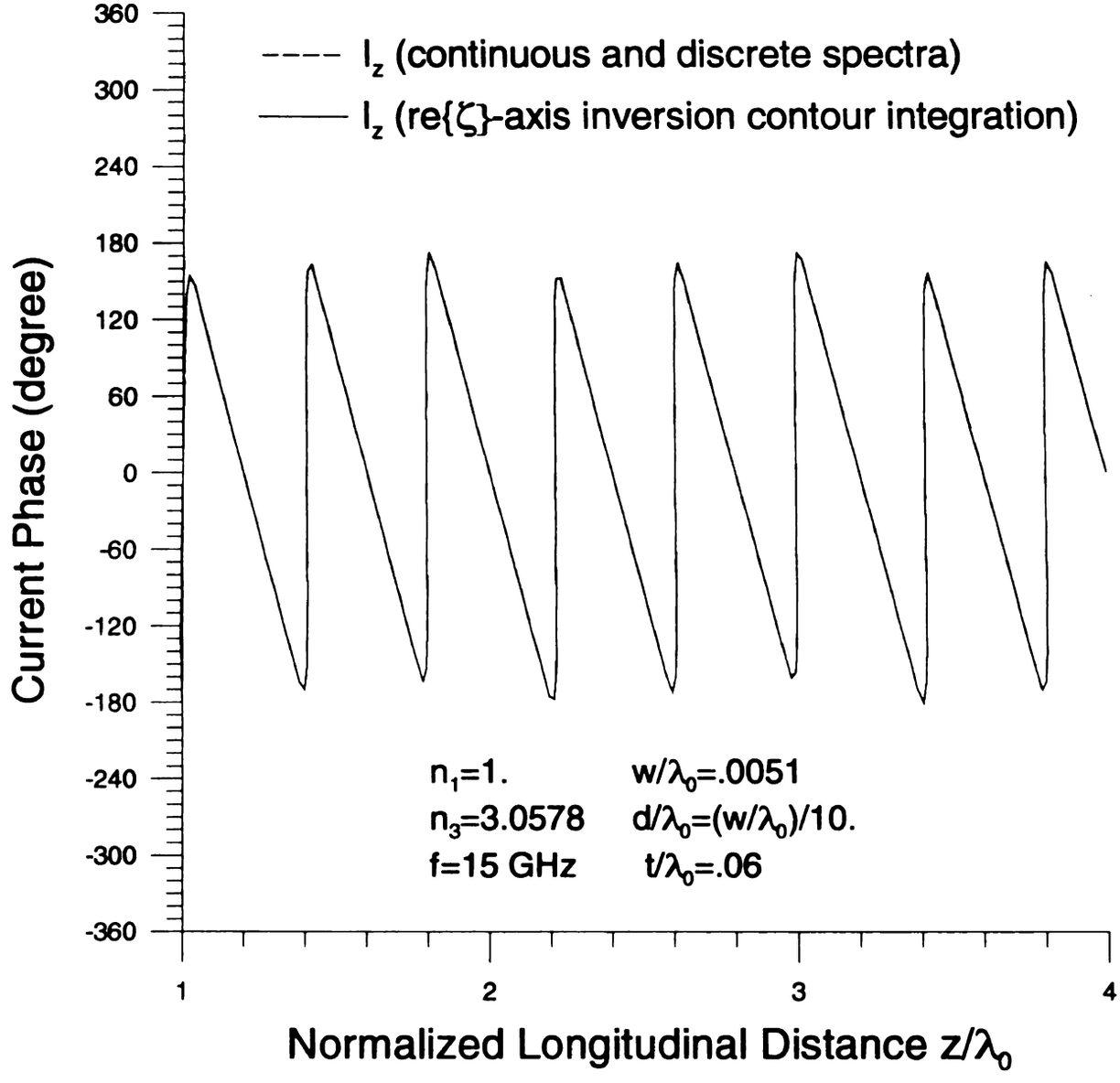

Figure 5.5.8 $\mathrm{Re}\{\zeta\}$**-axis inversion contour validation of microstrip current phase profile contributed by the continuous spectrum current and the discrete spectrum current.**

5.6 NUMERICAL RESULTS

Numerical results are obtained using the integrated microstrip configuration with

$$\begin{aligned}
&\textit{microstrip width}: w = .1016\, mm \Rightarrow w/\lambda_0 = .0051 \\
&\textit{effective gap width}: d = w/10\, mm \Rightarrow d/\lambda_0 = (w/\lambda_0)/10 \\
&\textit{film thickness}: t = 1.27\, mm \Rightarrow t/\lambda_0 = .06 \\
&\textit{operating frequency}: f = 15\, GHz
\end{aligned}$$

Microstrip current contributed by the continuous and the discrete spectrum currents in the near zone with various electrical strip widths are depicted in Fig. 5.6.1. Fig. 5.6.2 depicts the microstrip current amplitude profile with various electrical strip widths. The continuous (I_C) and discrete (I_D) spectrum current amplitude-ratio with various electrical strip widths is depicted in Fig. 5.6.3. Fig. 5.6.4 depicts the continuous (I_C) and discrete (I_D) spectrum current amplitude-ratio versus electrical film thickness with various electrical strip widths. As discussed in Section 5.5, the microstrip current is dominated by the discrete spectrum current rather than the continuous spectrum current. It is noted that physically, the microstrip current is associated with the guiding structure rather than the background layer environment. Therefore, the microstrip current is less dominated by the continuous spectrum current contributed by that background layer. In Fig. 5.6.5, the dependence of continuous spectrum current amplitude upon electrical film thickness with various electrical strip widths is depicted. The dependence of continuous spectrum current amplitude upon electrical strip width is depicted in Fig. 5.6.6. Fig. 5.6.7 depicts the microstrip current amplitude versus electrical film thickness with various electrical strip widths. Finally, the microstrip current amplitude versus electrical strip width is depicted in Fig. 5.6.8.

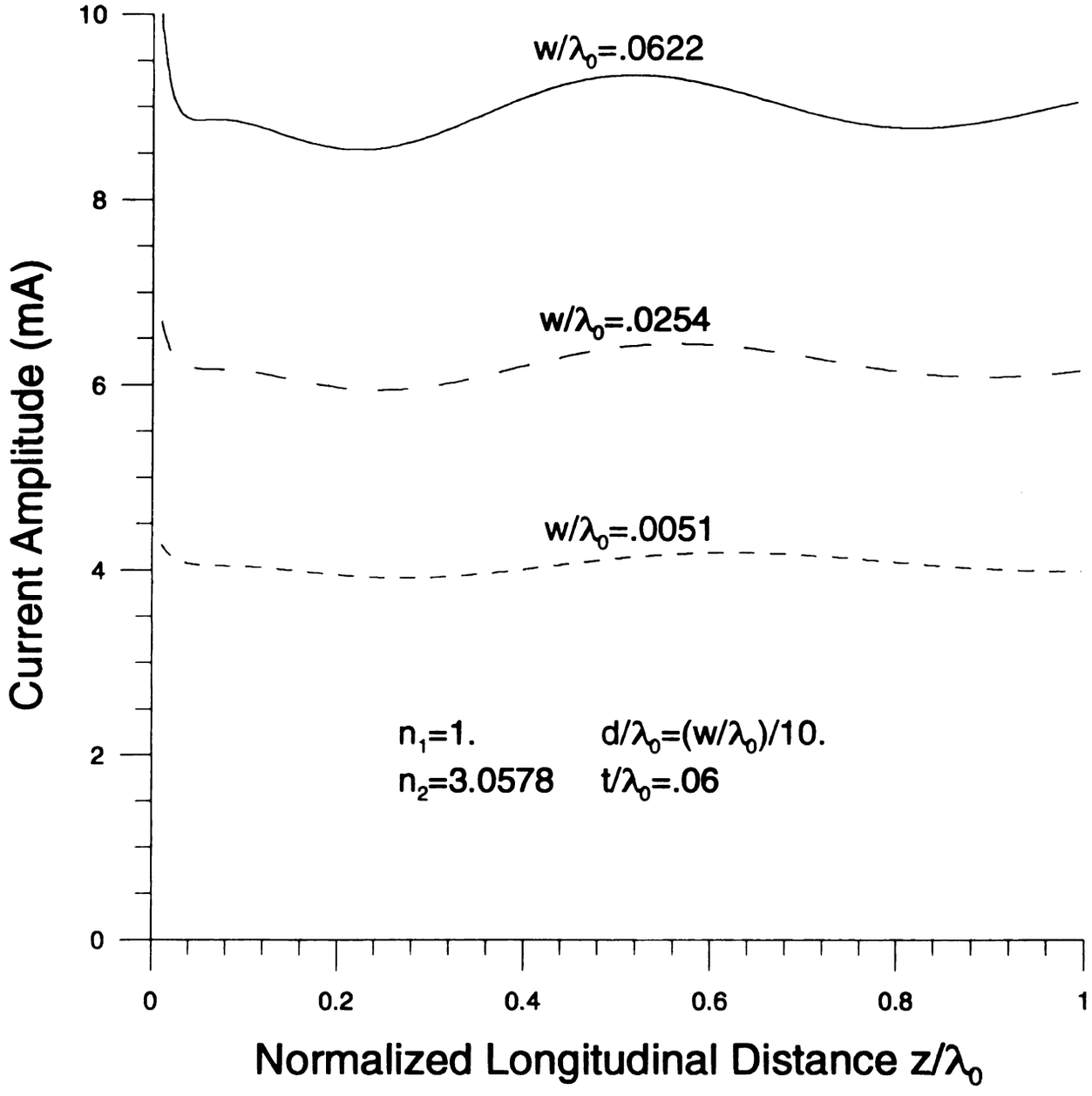

Figure 5.6.1 Near zone microstrip current amplitude profile with various electrical strip widths.

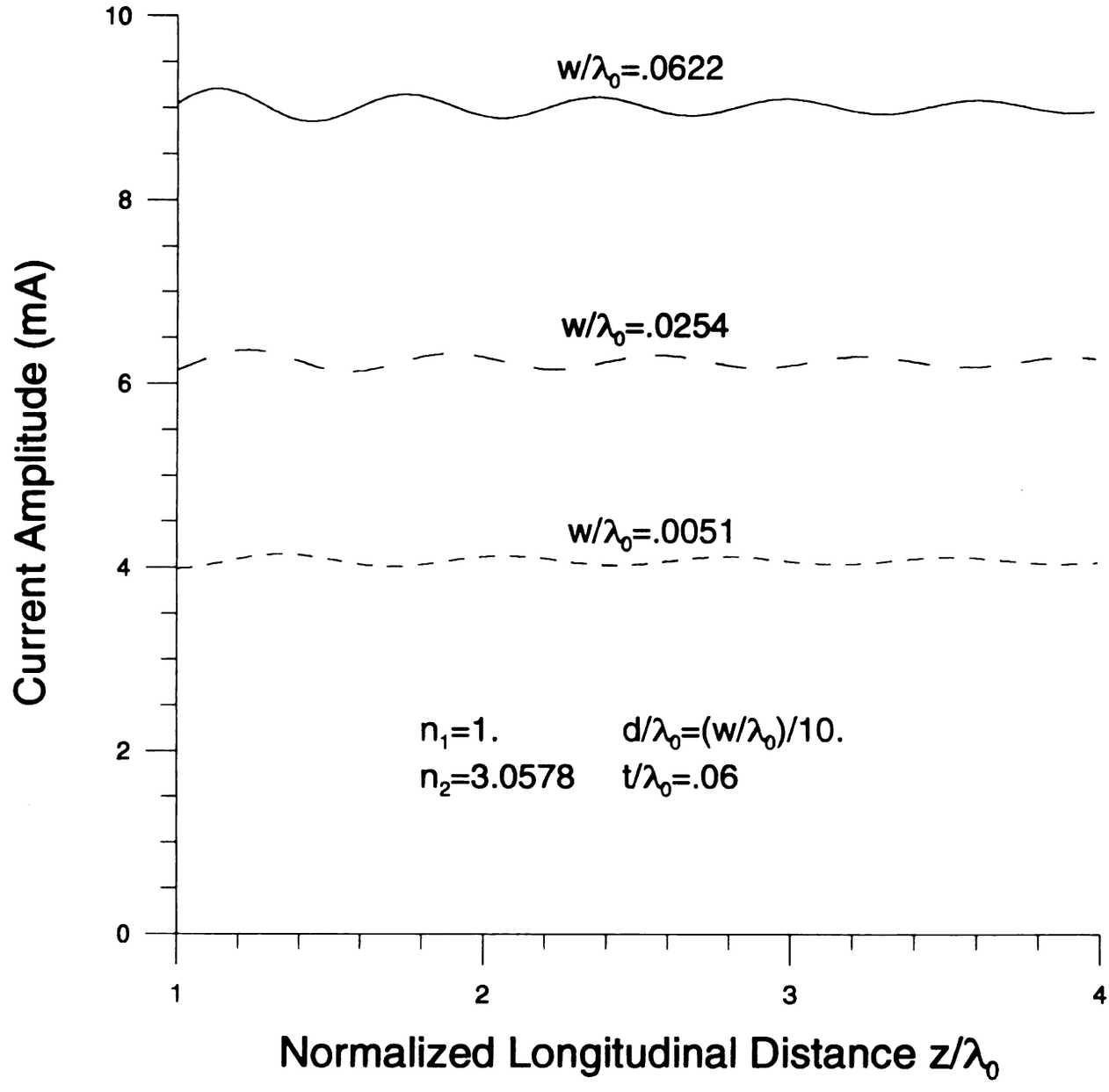

Figure 5.6.2 Microstrip current amplitude profile with various electrical strip widths.

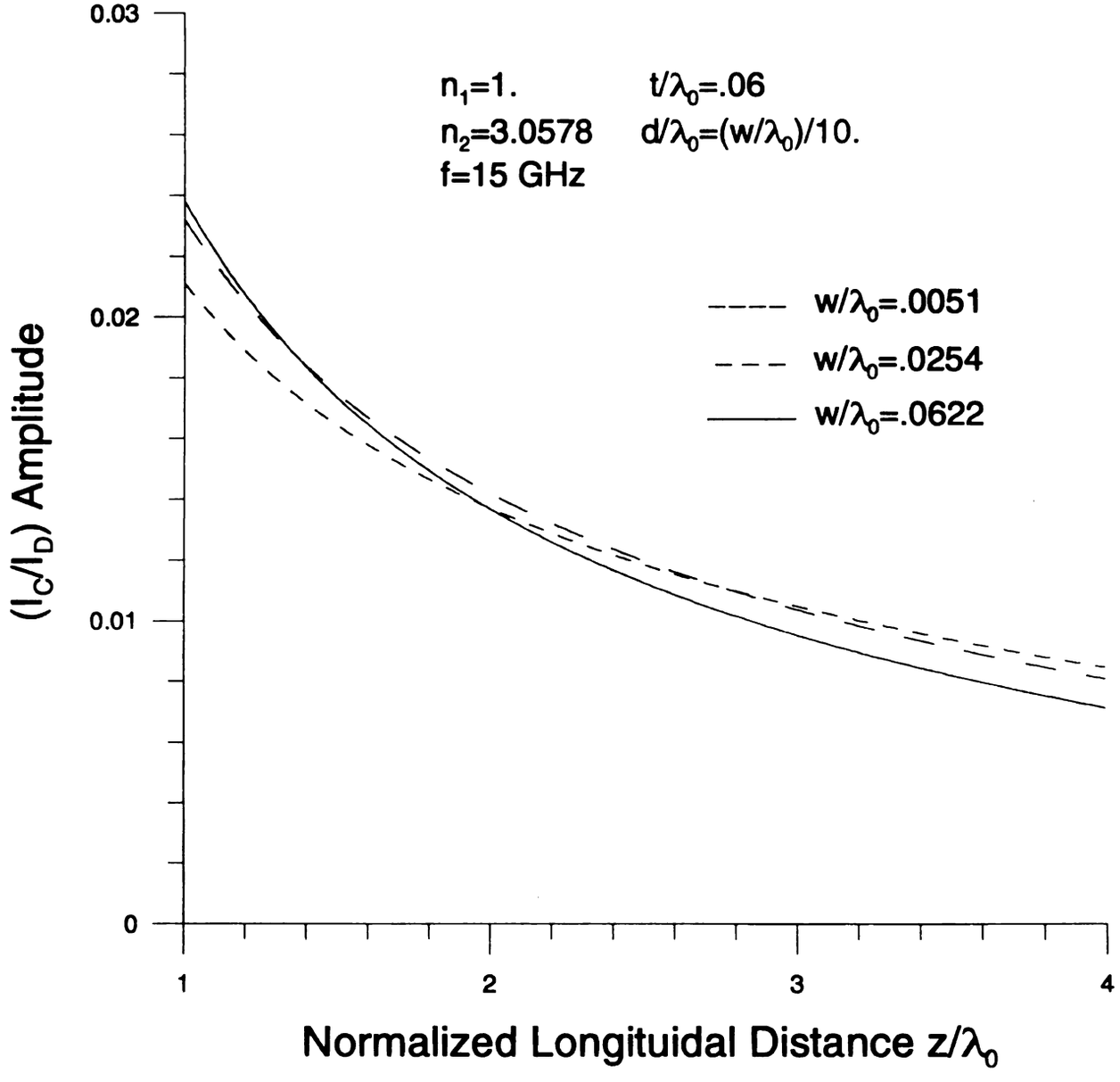

Figure 5.6.3 Microstrip continuous and discrete spectrum current amplitude-ratio with various electrical strip widths.

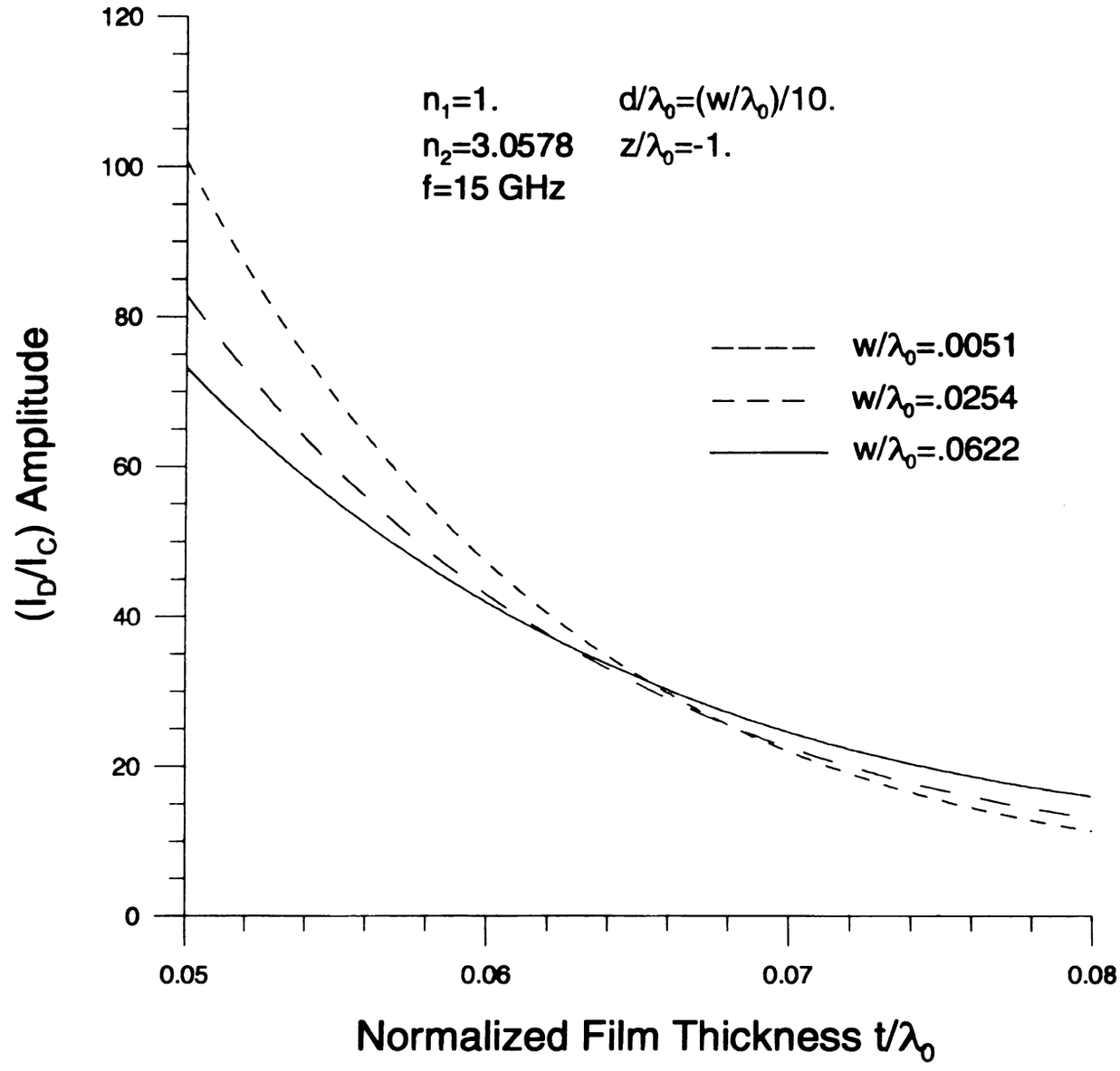

Figure 5.6.4 Microstrip continuous and discrete spectrum current amplitude-ratio versus electrical film thickness with various electrical strip widths.

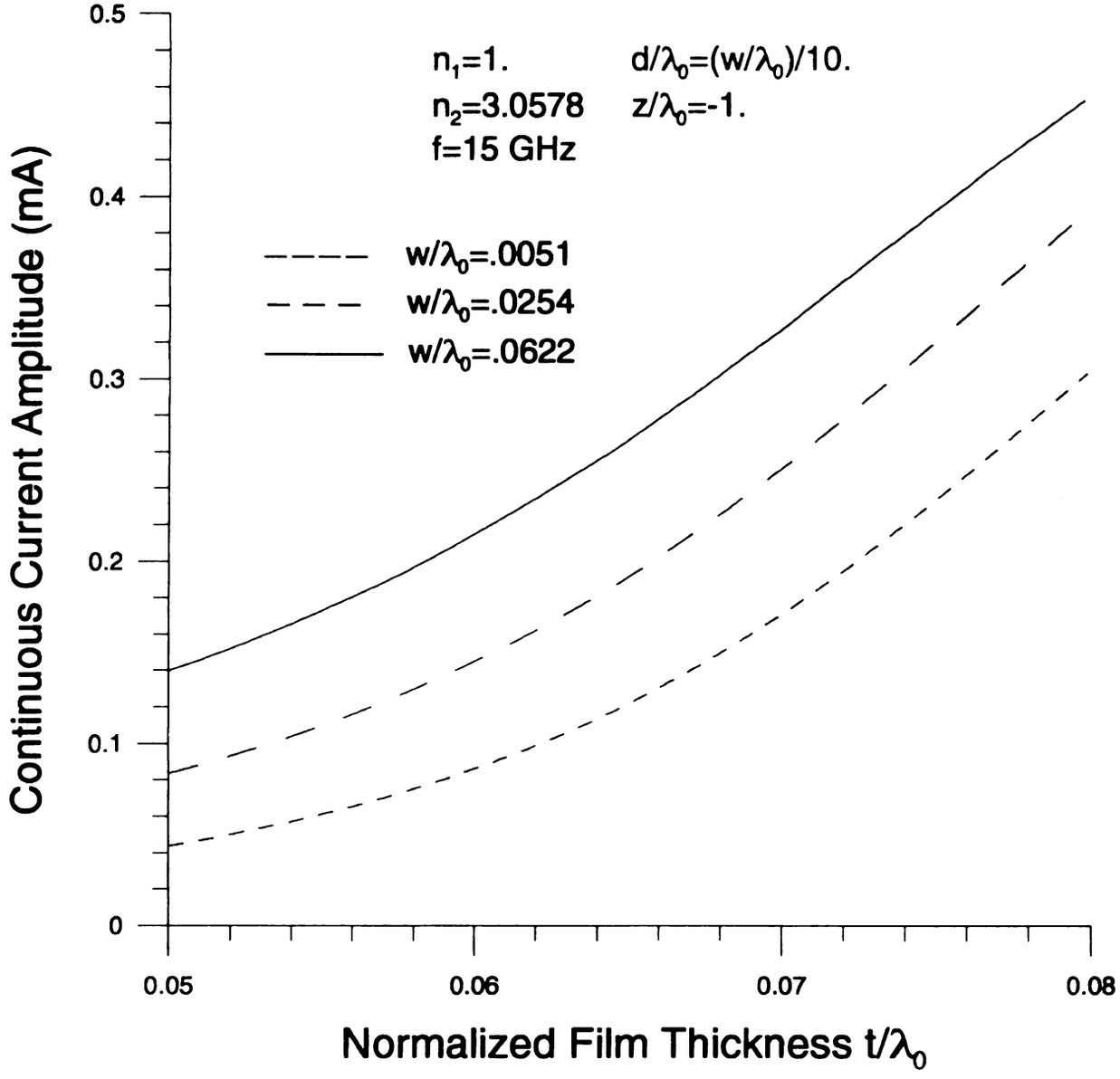

Figure 5.6.5 Microstrip continuous spectrum current amplitude versus electrical film thickness with various electrical strip widths.

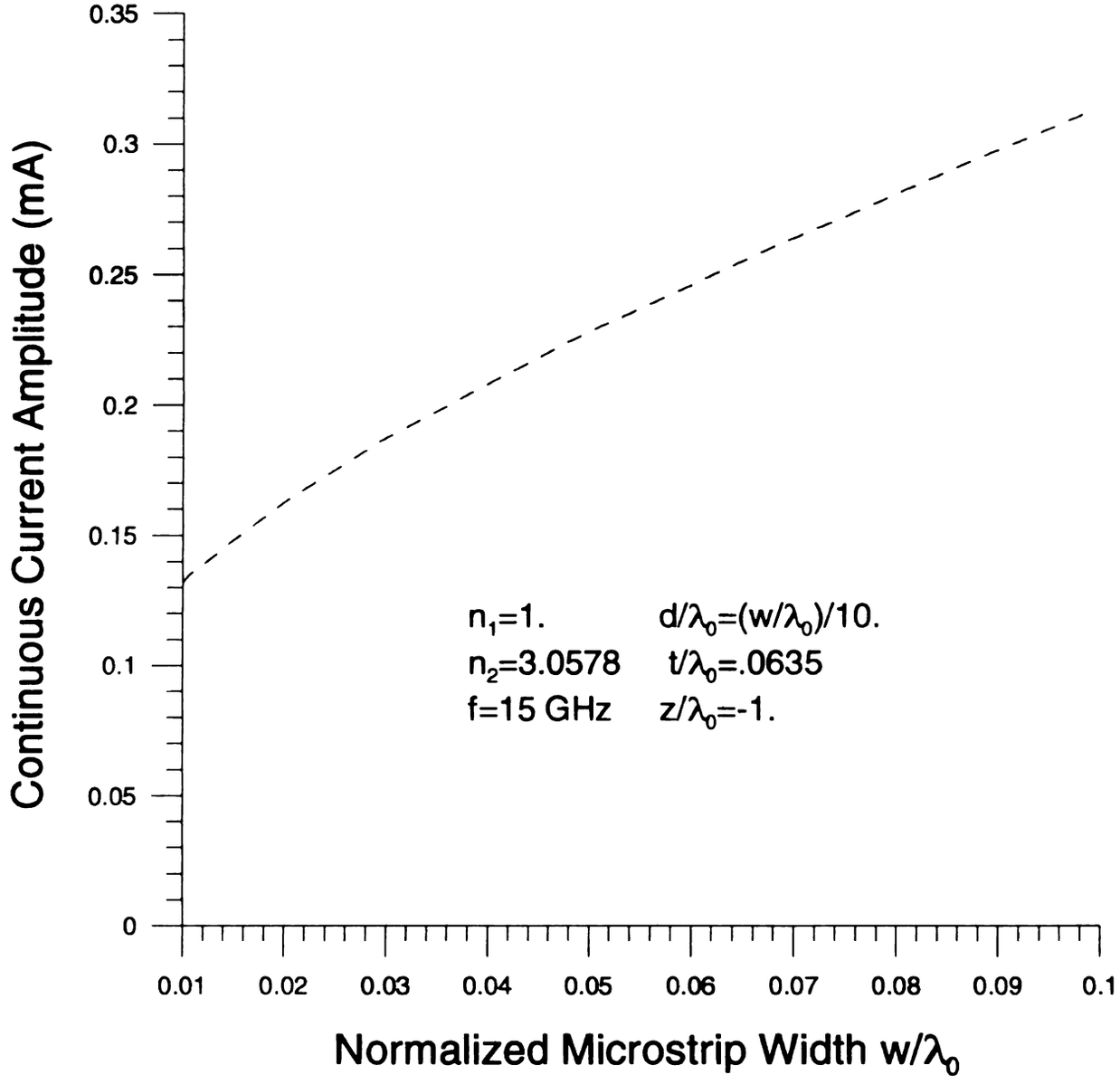

Figure 5.6.6 Microstrip continuous spectrum current amplitude versus electrical strip width.

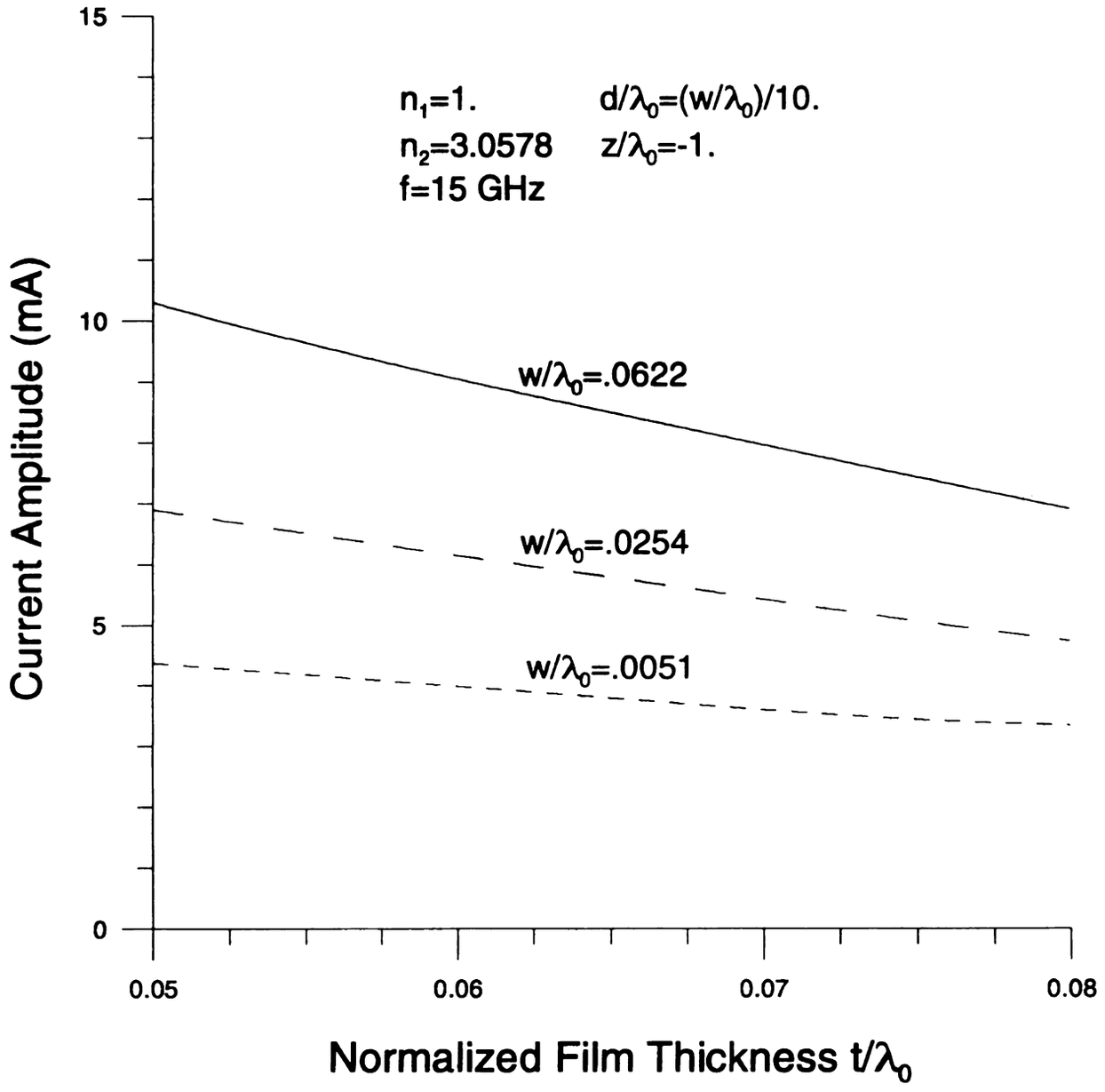

Figure 5.6.7 Microstrip current amplitude versus electrical film thickness with electrical strip widths.

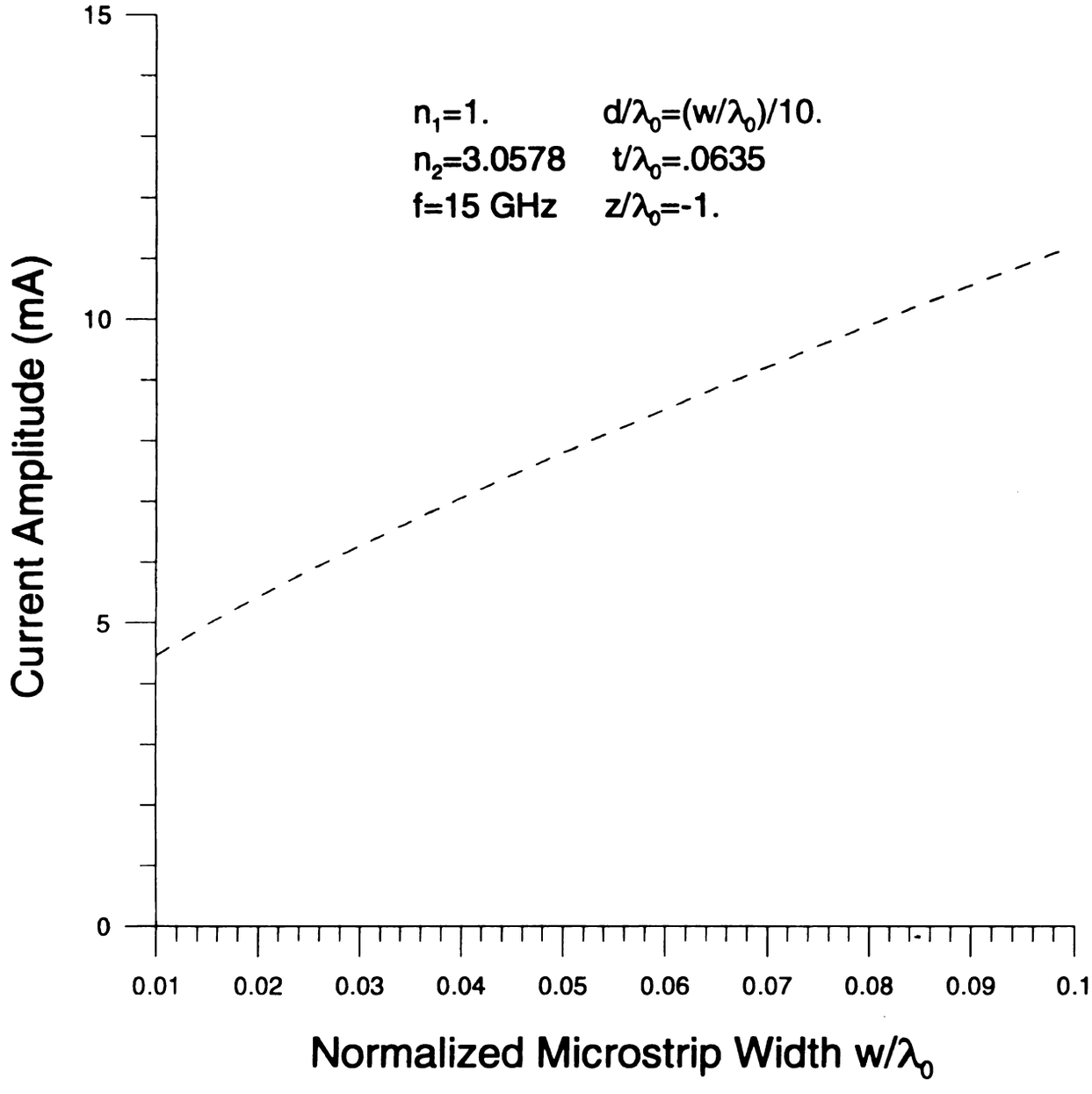

Figure 5.6.8 Microstrip current amplitude versus electrical strip widths.

5.7 CONCLUSION

It is observed that singularities in the complex ζ -plane include poles associated with the guiding structure and branch points contributed by the layered background environment. Singularities associated with the background layer environment manifest themselves as branch points in the complex ζ -plane. The continuous spectrum current is contributed by the integration contour about branch cuts associated with those branch points. The discrete spectrum current is contributed by residues at pole singularities associated with the guiding structure. The characteristic impedance of the microstrip was obtained using the discrete- or bound-mode spectrum current and was validated by comparison with a well-known empirical formula.

Microstrip current is composed of the continuous spectrum current and the discrete spectrum current. Numerically it is observed that the total microstrip current is dominated by the discrete spectrum current rather than that of the continuous spectrum. The microstrip current was validated by comparison with $\mathrm{Re}\{\zeta\}$-axis inversion contour integration. The 3D-EM fields in the background layer environment will be calculated in Chapter 6 based upon the microstrip current found here.

THE ASYMPTOTIC RADIATION FIELD AND PROPER PROPAGATION MODE SPECTRA OF THE OPEN PLANAR WAVEGUIDE

VOLUME II

By

Jeong-Seog Lee

A DISSERTATION

Submitted to
Michigan State University
in partial fulfillment of the requirements
for the degree of

DOCTOR OF PHILOSOPHY

Department of Electrical and Computer Engineering

2002

TH

6.1

L

wave

adequ

expan

in Ch

structu

recalle

themse

As

source

the inte

contour

backgro

spectrum

singulari

branch c

branch c

identicall

CHAPTER 6

THE PROPER EM FIELD SPECTRUM OF AN OPEN INTEGRATED MICROSTRIP WAVEGUIDE

6.1 INTRODUCTION AND GEOMETRICAL CONFIGURATION

Like in Chapter 5 for its current, the continuous spectrum fields of integrated open waveguide structures have been until recently neither conceptualized nor quantified adequately. That spectrum was identified as the branch cut contribution to singularity expansion of those fields in the complex axial transform plane (ζ-plane). As discussed in Chapters 4 and 5, singularities in that plane include poles associated with the guiding structure and branch points contributed by layered background environments. It is also recalled that singularities associated with the background layer environments manifest themselves as branch points in the complex ζ-plane.

As discussed in Chapter 5, a δ-gap field feed model was exploited as an excitatory source [49]-[52]. Using the resulting spectral microstrip current from Chapter 5, fields of the integrated open waveguide are recovered from the spectral domain by integration contour deformation on the top sheet of the complex ζ-plane. As a result, fields in the background layer environments are obtained in terms of the proper propagation mode spectrum. That spectrum consists of bound propagation modes associated with pole singularities and a continuous spectrum [31], [53] associated with integration around branch cuts contributed by layered background environments. During integration around branch cuts, singularities in the transverse complex transform plane (ξ-plane) migrate identically as in Chapter 5. Therefore, the overall procedure leads to a decomposition of

the tot

numer

Ex

continu

recogn

continu

layers

conduc

spectru

The

planar-l

view is

axis tan

assumec

$l = 1, 2,$

guiding

the total fields into bound modes and continuous spectrum contributions. The result is numerically validated by real axis integration in the complex ζ-plane.

Extensive numerical results are obtained, which can compare bound mode and continuous spectrum contributions to fields in the layered background environments. It is recognized, unlike in Chapter 5, that most fields in both layers are dominated by the continuous spectrum. However, physically, it is acceptable since fields in background layers are directly associated with those environments branch points rather than the conducting microstrip poles. The continuous spectrum dominates over the discrete spectrum near the feed point.

The geometrical configuration of integrated microstrip waveguide immersed in a planar-layered background environment is depicted in Fig. 6.1.1 while its cross-sectional view is depicted in Fig. 6.1.2. The waveguiding axis is chosen to be z-axis with the x-axis tangential and y-axis normal to the planar interfaces. Each of the planar layers is assumed to be non-magnetic, isotropic and homogeneous with complex permittivity ε_l, $l = 1, 2, 3$ for the cover, film, and substrate layers with $\varepsilon_3 \to -j\infty$ or $\sigma \to \infty$. The guiding structure is embedded in the cover layer adjacent to the cover/film interface.

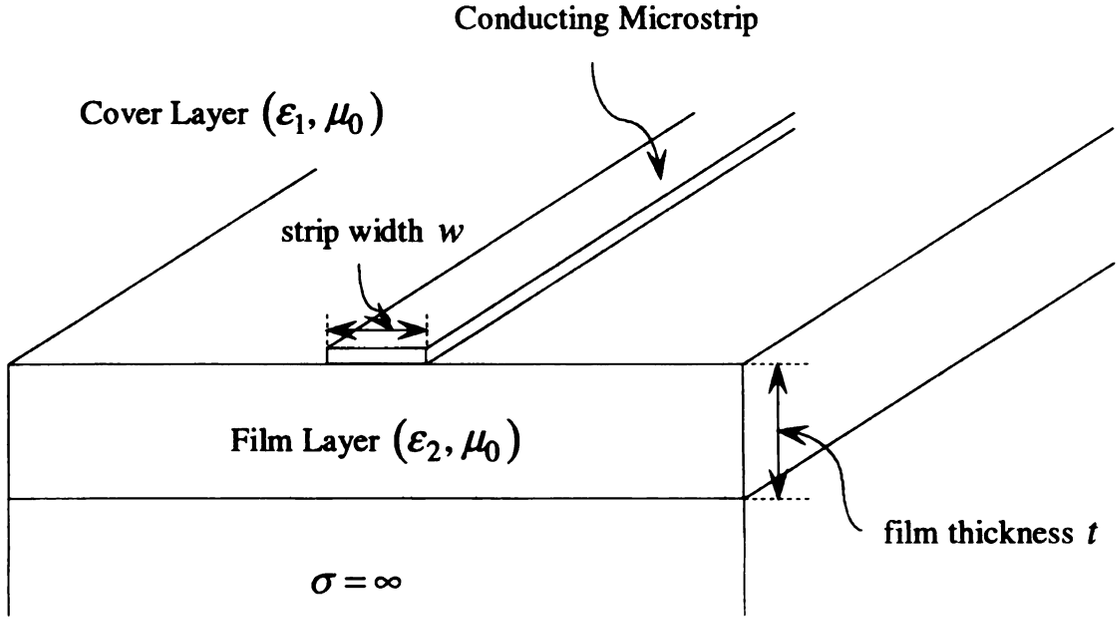

Figure 6.1.1 Geometrical configuration of open microstrip structure immersed in layered background environment.

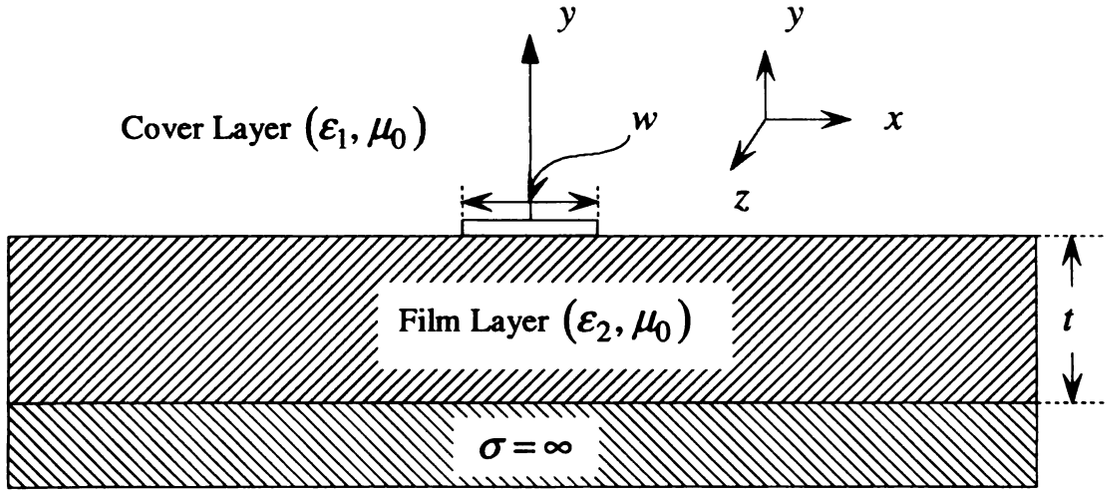

Figure 6.1.2 Cross-sectional view of immersed microstrip structure.

6.2 E

The

induced

where I

where S

$r' = x\hat{x}$

Then, the

Therefor

where r

6.2 EM FIELD FORMULATION

The electric type Hertzian potential in the *l'th (l=1 and 2)* layer maintained by the induced surface current $\boldsymbol{k}(\boldsymbol{r})\big|_{y=0\hat{y}}$ immersed in the cover layer *(l=1)* satisfies

$$\nabla^2\boldsymbol{\Pi}_l(\boldsymbol{r})+k_l^2\boldsymbol{\Pi}_l(\boldsymbol{r})=-\frac{\boldsymbol{P}(\boldsymbol{r})}{\varepsilon_l} \tag{6.2.1}$$

where $\boldsymbol{P}(\boldsymbol{r})=\boldsymbol{k}(\boldsymbol{r})/j\omega$ and $k_l^2=\omega^2\varepsilon_l\mu_0$. Then,

$$\boldsymbol{\Pi}_l(\boldsymbol{r})=\int_S \bar{\boldsymbol{G}}_l(\boldsymbol{r}|\boldsymbol{r}')\cdot\frac{\boldsymbol{k}(\boldsymbol{r}')}{j\omega\varepsilon_1}dS' \tag{6.2.2}$$

where S denotes the conducting surface of the microstrip. Since $\boldsymbol{k}(\boldsymbol{r}')=\hat{z}k_z(\boldsymbol{r}')$ for $\boldsymbol{r}'=x\hat{x}+0\hat{y}+z\hat{z}$ in accordance with Eqn. (5.2.12),

$$\boldsymbol{\Pi}_l(\boldsymbol{r})=\int_{-\infty}^{\infty}\int_{-w/2}^{w/2}\bar{\boldsymbol{G}}_l(\boldsymbol{r}|\boldsymbol{r}')\cdot\frac{\boldsymbol{J}(z')\eta(x')}{j\omega\varepsilon_1}dx'dz' \tag{6.2.3}$$

Then, the EM fields are derived from

$$\begin{aligned}\boldsymbol{E}_l(\boldsymbol{r})&=\left(k_l^2+\nabla\nabla\cdot\right)\boldsymbol{\Pi}_l(\boldsymbol{r})\\ \boldsymbol{H}_l(\boldsymbol{r})&=j\omega\varepsilon_l\nabla\times\boldsymbol{\Pi}_l(\boldsymbol{r})\end{aligned} \tag{6.2.4}$$

Therefore, the electric fields for the *l'th* layer are

$$\begin{aligned}E_{lx}(\boldsymbol{r})&=k_l^2\Pi_{lx}(\boldsymbol{r})+\frac{\partial}{\partial x}\left[\nabla\cdot\boldsymbol{\Pi}_l(\boldsymbol{r})\right]\\ E_{ly}(\boldsymbol{r})&=k_l^2\Pi_{ly}(\boldsymbol{r})+\frac{\partial}{\partial y}\left[\nabla\cdot\boldsymbol{\Pi}_l(\boldsymbol{r})\right]\\ E_{lz}(\boldsymbol{r})&=k_l^2\Pi_{lz}(\boldsymbol{r})+\frac{\partial}{\partial z}\left[\nabla\cdot\boldsymbol{\Pi}_l(\boldsymbol{r})\right]\end{aligned} \tag{6.2.5}$$

where $\boldsymbol{r}=\hat{x}x+\hat{y}y+\hat{z}z$.

For the

6.2.1

Sinc

There f

$\Pi_1($

whe

G_1^P

G_{1t}^r

∂C

Γ_t

For the magnetic fields,

$$H_{lz}(r)=j\omega\varepsilon_l\left[\frac{\partial\Pi_{ly}(r)}{\partial x}-\frac{\partial\Pi_{lx}(r)}{\partial y}\right]$$
$$H_{lx}(r)=j\omega\varepsilon_l\left[\frac{\partial\Pi_{lz}(r)}{\partial y}-\frac{\partial\Pi_{ly}(r)}{\partial z}\right] \qquad (6.2.6)$$
$$H_{ly}(r)=j\omega\varepsilon_l\left[\frac{\partial\Pi_{lx}(r)}{\partial z}-\frac{\partial\Pi_{lz}(r)}{\partial x}\right]$$

6.2.1 COVER FIELD FORMULATION

Since $\boldsymbol{J}(z')=\hat{z}J_z(z')$ (see Appendix E),

$$\bar{G}_1(r|r')\cdot\hat{z}=\hat{y}\frac{\partial G_{1c}^r(r|r')}{\partial z}+\hat{z}\left[G_1^p(r|r')+G_{1t}^r(r|r')\right] \qquad (6.2.7)$$

Therefore, exploiting Eqn. (6.2.3)

$$\boldsymbol{\Pi}_1(r)=\int_{-\infty}^{\infty}\int_{-w/2}^{w/2}\left\{\hat{y}\frac{\partial G_{1c}^r(r|r')}{\partial z}+\hat{z}\left[G_1^p(r|r')+G_{1t}^r(r|r')\right]\right\}\frac{J_z(z')\eta(x')}{j\omega\varepsilon_1}dx'dz'$$

where

$$G_1^p(r|r')=\iint_{\infty}\frac{e^{j\left[\xi(x-x')+\zeta(z-z')\right]}e^{-p_1(\xi,\zeta)y}}{2(2\pi)^2p_1(\xi,\zeta)}d\xi d\zeta$$

$$G_{1t}^r(r|r')=\iint_{\infty}R_{1t}(\xi,\zeta)\frac{e^{j\left[\xi(x-x')+\zeta(z-z')\right]}e^{-p_1(\xi,\zeta)y}}{2(2\pi)^2p_1(\xi,\zeta)}d\xi d\zeta$$

$$\frac{\partial G_{1c}^r(r|r')}{\partial z}=\iint_{\infty}j\zeta C_{1r}(\xi,\zeta)\frac{e^{j\left[\xi(x-x')+\zeta(z-z')\right]}e^{-p_1(\xi,\zeta)y}}{2(2\pi)^2p_1(\xi,\zeta)}d\xi d\zeta \qquad (6.2.8)$$

The coefficients $R_{1t}(\xi,\zeta)$ and $C_{1r}(\xi,\zeta)$ are determined by

$$R_{1t}(\xi,\zeta)=\frac{p_1(\xi,\zeta)-p_2(\xi,\zeta)\coth\left[p_2(\xi,\zeta)t\right]}{Z^h(\xi,\zeta)}$$

$$C_{1r}(\xi,\zeta)=\frac{2\left(N_{21}^2-1\right)p_1(\xi,\zeta)}{Z^h(\xi,\zeta)Z^e(\xi,\zeta)}$$

where

$$Z^h(\xi,\zeta)=p_1(\xi,\zeta)+p_2(\xi,\zeta)\coth\left[p_2(\xi,\zeta)t\right]$$

$$Z^e(\xi,\zeta)=N_{21}^2p_1(\xi,\zeta)+p_2(\xi,\zeta)\tanh\left[p_2(\xi,\zeta)t\right]$$

Then,

$$\Pi_{1y}(r)=\frac{1}{2\pi}\frac{1}{j\omega\epsilon_1}\int_{-\infty}^{\infty}\left\{\int_{-\infty}^{\infty}j\zeta C_{1r}(\xi,\zeta)\frac{e^{j\xi x}e^{-p_1y}}{4\pi p_1}\right.$$
$$\left.\left[\int_{-\infty}^{\infty}J_z(z')e^{-j\zeta z'}dz'\int_{-w/2}^{w/2}\eta(x')e^{-j\xi x'}dx'\right]d\xi\right\}e^{j\zeta z}d\zeta \tag{6.2.9}$$

and

$$\Pi_{1z}(r)=\frac{1}{2\pi}\frac{1}{j\omega\epsilon_1}\int_{-\infty}^{\infty}\left\{\int_{-\infty}^{\infty}\left[1+R_{1t}(\xi,\zeta)\right]\frac{e^{j\xi x}e^{-p_1y}}{4\pi p_1}\right.$$
$$\left.\left[\int_{-\infty}^{\infty}J_z(z')e^{-j\zeta z'}dz'\int_{-w/2}^{w/2}\eta(x')e^{-j\xi x'}dx'\right]d\xi\right\}e^{j\zeta z}d\zeta \tag{6.2.10}$$

In accordance with Eqns. (5.2.8), (5.2.10) and (5.2.11)

$$\int_{-w/2}^{w/2}\eta(x')e^{-j\xi x'}dx'=\tilde{\eta}(\xi)=\begin{cases}J_0(\xi w/2)\cdots w/t<2\\ sinc(\xi w/2)\cdots w/t\geq 2\end{cases} \tag{6.2.11}$$

Rearranging the Fourier transformation leads from Eqn. (6.2.9) to

$$\tilde{\Pi}_{1y}(\boldsymbol{\rho},\zeta)=\frac{1}{j\omega\epsilon_1}\int_{-\infty}^{\infty}j\zeta C_{1r}(\xi,\zeta)\tilde{J}_z(\zeta)\tilde{\eta}(\xi)\frac{e^{j\xi x}e^{-p_1y}}{4\pi p_1}d\xi$$

where (6.2.12)

$$\boldsymbol{\rho}=\hat{x}x+\hat{y}y$$

Similarly, Eqn. (6.2.10) leads to

$$\tilde{\Pi}_{1z}(\boldsymbol{\rho},\zeta)=\frac{1}{j\omega\varepsilon_1}\int_{-\infty}^{\infty}\frac{2}{Z^h(\xi,\zeta)}\tilde{J}_z(\zeta)\tilde{\eta}(\xi)\frac{e^{j\xi x}e^{-p_1 y}}{4\pi}d\xi \qquad (6.2.13)$$

The forward Fourier transformation leads from Eqn. (6.2.5) to

$$\begin{aligned}
e_{lx}(\boldsymbol{\rho},\zeta)&=k_l^2\tilde{\Pi}_{lx}(r)+\frac{\partial}{\partial x}\left[\tilde{\nabla}\bullet\tilde{\boldsymbol{\Pi}}_l(\boldsymbol{\rho},\zeta)\right]\\
e_{ly}(\boldsymbol{\rho},\zeta)&=k_l^2\tilde{\Pi}_{ly}(r)+\frac{\partial}{\partial y}\left[\tilde{\nabla}\bullet\tilde{\boldsymbol{\Pi}}_l(\boldsymbol{\rho},\zeta)\right] \qquad (6.2.14)\\
e_{lz}(\boldsymbol{\rho},\zeta)&=k_l^2\tilde{\Pi}_{lz}(r)+\frac{\partial}{\partial z}\left[\tilde{\nabla}\bullet\tilde{\boldsymbol{\Pi}}_l(\boldsymbol{\rho},\zeta)\right]
\end{aligned}$$

Then, choosing the y-component of the cover field yields

$$\begin{aligned}
e_{1y}(\boldsymbol{\rho},\zeta)&=k_1^2\tilde{\Pi}_{1y}(\boldsymbol{\rho},\zeta)+\frac{\partial}{\partial y}\left[\tilde{\nabla}\bullet\tilde{\boldsymbol{\Pi}}_1(\boldsymbol{\rho},\zeta)\right]\\
&=\left(k_1^2+\frac{\partial^2}{\partial y^2}\right)\tilde{\Pi}_{1y}(\boldsymbol{\rho},\zeta)+j\zeta\frac{\partial}{\partial y}\tilde{\Pi}_{1z}(\boldsymbol{\rho},\zeta) \qquad (6.2.15)\\
&=\left(\xi^2+\zeta^2\right)\tilde{\Pi}_{1y}(\boldsymbol{\rho},\zeta)+j\zeta\frac{\partial}{\partial y}\tilde{\Pi}_{1z}(\boldsymbol{\rho},\zeta)
\end{aligned}$$

Therefore,

$$\begin{aligned}
e_{1y}(\boldsymbol{\rho},\zeta)=&\frac{1}{j\omega\varepsilon_1}\int_{-\infty}^{\infty}j\zeta\left(\xi^2+\zeta^2\right)C_{1r}(\xi,\zeta)\tilde{J}_z(\zeta)\tilde{\eta}(\xi)\frac{e^{j\xi x}e^{-p_1 y}}{4\pi p_1}d\xi\\
&-\frac{1}{j\omega\varepsilon_1}\int_{-\infty}^{\infty}j\zeta\frac{2p_1^2}{Z^h(\xi,\zeta)}\tilde{J}_z(\zeta)\tilde{\eta}(\xi)\frac{e^{j\xi x}e^{-p_1 y}}{4\pi p_1}d\xi
\end{aligned} \qquad (6.2.16)$$

The above becomes

$$e_{1y}(\boldsymbol{\rho},\zeta)=\frac{1}{\omega\varepsilon_1}\int_{-\infty}^{\infty}\zeta\tilde{J}_z\tilde{\eta}(\xi)\left[\left(\xi^2+\zeta^2\right)C_{1r}(\xi,\zeta)-\frac{2p_1^2}{Z^h}\right]\frac{e^{j\xi x}e^{-p_1 y}}{4\pi p_1}d\xi \qquad (6.2.17)$$

In agreement with Eqn. (5.2.19),

The

Finally

and $\tilde{C}_{\ldots}$

$$e_{1y}(\rho,\zeta)=\frac{2\pi}{\omega\varepsilon_1}\frac{\zeta\tilde{L}_g(\zeta)}{\int_{-\infty}^{\infty}\tilde{\eta}^2(\xi')\left[\frac{j\eta_1}{k_1}\tilde{\tilde{C}}_{zz}(\xi',\zeta)\right]d\xi'}$$
$$\int_{-\infty}^{\infty}\tilde{\eta}(\xi)\left[\left(\xi^2+\zeta^2\right)C_{1r}(\xi,\zeta)-\frac{2p_1^2}{Z^h(\xi,\zeta)}\right]\frac{e^{j\xi x}e^{-p_1 y}}{4\pi p_1}d\xi \tag{6.2.18}$$

Then,

$$e_{1y}(\rho,\zeta)=-\frac{j}{2}\frac{\zeta\tilde{L}_g(\zeta)}{\int_{-\infty}^{\infty}\tilde{\eta}^2(\xi')\tilde{\tilde{C}}_{zz}(\xi',\zeta)d\xi'}$$
$$\int_{-\infty}^{\infty}\tilde{\eta}(\xi)\left[\left(\xi^2+\zeta^2\right)C_{1r}(\xi,\zeta)-\frac{2p_1^2}{Z^h(\xi,\zeta)}\right]\frac{e^{j\xi x}e^{-p_1 y}}{p_1}d\xi \tag{6.2.19}$$

where

$$\frac{1}{\omega\varepsilon_1}\frac{k_1}{\eta_1}=\frac{1}{\omega\varepsilon_1}\omega\sqrt{\varepsilon_1\mu_1}\sqrt{\frac{\varepsilon_1}{\mu_1}}=1$$

Finally, the y-component of the cover field is

$$E_{1y}(\boldsymbol{r})=-\frac{j}{4\pi}\int_{-\infty}^{\infty}d\zeta\frac{\zeta\tilde{L}_g(\zeta)}{\int_{-\infty}^{\infty}\tilde{\eta}^2(\xi')\tilde{\tilde{C}}_{zz}(\xi',\zeta)d\xi'}e^{j\zeta z}$$
$$\int_{-\infty}^{\infty}\tilde{\eta}(\xi)\left[\left(\xi^2+\zeta^2\right)C_{1r}(\xi,\zeta)-\frac{2p_1^2}{Z^h(\xi,\zeta)}\right]\frac{e^{j\xi x}e^{-p_1 y}}{p_1}d\xi$$

where (6.2.20)

$$\tilde{\eta}(\xi)=\begin{cases}J_0(\xi w/2)\cdots w/t<2\\ sinc(\xi w/2)\cdots w/t\geq 2\end{cases}$$

$$\tilde{L}_g(\zeta)=e^{-(\zeta d)^2/2}$$

and $\tilde{\tilde{C}}_{zz}(\xi',\zeta)$ is given by (see Chapter 5)

asso

$\lambda =$

plana

poles

simpl

compl

consis

$\lambda^2 =$

denotes

which

$\lambda_p = \lambda$

Bound-

depicte

$$\tilde{\tilde{C}}_{zz}(\xi',\zeta)=\frac{\left(k_1^2-\zeta^2\right)}{Z^h(\xi',\zeta)}+\frac{\zeta^2 p_1(\xi',\zeta)\left(N_{21}^2-1\right)}{Z^h(\xi',\zeta)Z^e(\xi',\zeta)}$$

As discussed in Section 5.3, the cover wavenumber parameter $p_1(\lambda)=\sqrt{\lambda^2-k_1^2}$ associated with the layered background environment yields branch point singularities at $\lambda=\pm k_1$. Pole singularities of $\tilde{\tilde{C}}_{zz}(\xi',\zeta)$ contribute simple-poles associated with the planar-layered background environment. In Section 5.3, $Z^h(\lambda)=0$ leads to simple poles at $\lambda=\pm\lambda_p$ associated with TE-odd surface waves and $Z^e(\lambda)=0$ leads to simple poles associated with TM-even surface waves. Again, as discussed in Section 5.3, complex λ-plane singularities of the integral representation for the microstrip current consist of branch points at $\lambda=\pm k_1$ and poles $\lambda=\pm\lambda_p$. It is observed that since $\lambda^2=\xi^2+\zeta^2$, $\lambda_s^2=\xi_s^2+\zeta^2$ for $\lambda_s=\pm k_1, \pm\lambda_p$. It is noted that conventionally, λ_s denotes λ-plane singularities and ξ_s does ξ-plane singularities. Then,

$$\begin{aligned}\pm\xi_{k_1}&=\mp j\sqrt{\zeta-\lambda_s}\sqrt{\zeta+\lambda_s}=\mp j\sqrt{\zeta-k_1}\sqrt{\zeta+k_1}\\ \pm\xi_{TM_0}&=\mp j\sqrt{\zeta-\lambda_s}\sqrt{\zeta+\lambda_s}=\mp j\sqrt{\zeta-\lambda_{TM_0}}\sqrt{\zeta+\lambda_{TM_0}}\end{aligned}\qquad(6.2.21)$$

which clearly implicates the branch points at $\zeta=\pm\lambda_s$ in the complex ζ-plane with $\lambda_p=\lambda_{TM_0}$ being the fundamental proper surface-wave mode as depicted in Fig. 5.3.1. Bound- or guided-mode pole singularities associated with the waveguiding structure are depicted in Fig. 5.4.1 and determined by

$$\int_{-\infty}^{\infty}\tilde{\eta}^2(\xi)\left[\frac{j\eta_1}{k_1}\tilde{\tilde{C}}_{zz}\left(\xi,\zeta_p\right)\right]d\xi=0\qquad(6.2.22)$$

Thu

the bac

the gui

upper

integral

where

allows

Therefo

Then, a

consist

square-r

mode

bound-

singular

about th

Section

Thus, Fig. 5.3.2 depicts branch-point singularities contributed by pole singularities in the background layer environments and the bound-mode pole singularity contributed by the guiding structure. The $\mathrm{Re}\{\zeta\}$-axis inversion contour can be deformed into the upper $(z>0)$ half and the lower $(z<0)$ half of the complex ζ-plane. Cauchy's integral theorem leads to

$$\int_{-\infty}^{\infty}(\cdots)d\zeta+\int_{C_{\zeta_p}}(\cdots)d\zeta+\int_{C_b}(\cdots)d\zeta+\int_{C_\infty}(\cdots)d\zeta=0 \qquad (6.2.23)$$

where $(\cdots)$ is the integrand of $d\zeta$ in Eqn. (6.2.20). Sommerfeld's radiation condition allows

$$\int_{C_\infty}(\cdots)d\zeta\to 0 \qquad (6.2.24)$$

Therefore,

$$\int_{-\infty}^{\infty}(\cdots)d\zeta=-\int_{C_b}(\cdots)d\zeta-\int_{C_{\zeta_p}}(\cdots)d\zeta \qquad (6.2.25)$$

Then, as like with the microstrip current, fields in the background layer environments consist of the continuous spectrum contributed by detouring about logarithmic and square-root type branch cuts arising from the k_1 branch point and the proper background mode λ_{TM_0} and the discrete spectrum is contributed by the residue evaluated at the bound- or guided-mode pole singularity ζ_p. In agreement with Eqn. (6.2.21), singularities in the complex ξ-plane migrate identically for the corresponding point ζ about the branch cut in the complex ζ-plane in Fig. 5.3.3 as discussed previously in Section 5.3. It is noted that ξ' singularities in the complex ξ'-plane in Eqn. (6.2.20)

also n

singul

As di

from

Re{

where

inversi

implica

pole si

configu

6.2.2.

contribu

singular

branch-

support

respect

as depic

also migrate in an identical fashion. Those ξ-plane singularities consist of branch-point singularities $\pm\xi_{k_1}$ and surface-wave pole singularities $\pm\xi_{TM_0}$ in that complex plane. As discussed before in Section 5.3, throughout the integration detour about branch cuts from a point 1 to 6 as depicted in Fig. 5.3.3, the corresponding overall procedure for $\mathrm{Re}\{\xi\}$-axis inversion contour C_ξ's leads to

$$\int_{\sum_{m=1}^{6} C_\xi(m)} (\cdots) d\xi = \int_{\sum_{m=1}^{3} C_\xi(m)} (\cdots) d\xi - \int_{\sum_{m=4}^{6} C_\xi(m)} (\cdots) d\xi \qquad (6.2.26)$$

where $(\cdots)$ is the integrand of $d\zeta$ in Eqn. (6.2.20) and $C_\xi(m)$ indicates $\mathrm{Re}\{\xi\}$-axis inversion contour for a corresponding point *m* in Fig. 5.3.3. Therefore, Eqn. (6.2.26) implicates $\mathrm{Re}\{\xi\}$-axis inversion contour integral contribution excluding surface-wave pole singularities on $\mathrm{Re}\{\xi\}$-axis defined by Eqn. (6.2.21). Again, using the same configuration of an integrated microstrip waveguide detailed in Chapter 5, Figs. 6.2.1, 6.2.2, 6.2.3 and 6.2.4 depict the field amplitude and phase longitudinal profiles contributed by $\mathrm{Re}\{\xi\}$ -axis inversion contour excluding the surface-wave pole singularities contribution in the complex ξ-plane obtained by integrating ζ about the branch-cut contour in Fig. 5.3.3. In Section 5.3, TE-odd and TM-even surface-waves are supported by pole singularities associated with $Z^h(\xi,\zeta)=0$ and $Z^e(\xi,\zeta)=0$, respectively. As discussed in Section 5.3, the full residue for TM-even modes at $\xi=\xi_p$ as depicted in Fig. 5.3.10 becomes

$$\oint_{C_{\xi_p}} C_{1r}(\xi,\zeta) d\xi = j2\pi \frac{2\left(N_{21}^2-1\right)p_1\left(\xi_p,\zeta\right)}{Z^h\left(\xi_p,\zeta\right)Z^{e'}\left(\xi_p,\zeta\right)} \qquad (6.2.27)$$

and

$$Z^{e'}(\xi_p,\zeta)=\frac{N_{21}^2\xi_p}{p_1(\xi_p,\zeta)}+\frac{\xi_p\tanh\left[p_2(\xi_p,\zeta)t\right]}{p_2(\xi_p,\zeta)}+\xi_p t\,\mathrm{sech}^2\left[p_2(\xi_p,\zeta)t\right]$$

Then, the surface-wave residue at $\xi=\xi_p$ for the corresponding point ζ on the branch-cut contour in Fig. 5.3.3 becomes in accordance with Eqn. (6.2.27)

$$-\int_{C_b}\left\{\oint_{C_{\xi_p}}(\cdots)d\xi\right\}\zeta\tilde{L}_g(\zeta)e^{j\zeta z}d\zeta=$$

$$-\int_{C_b}d\zeta\frac{\zeta\tilde{L}_g(\zeta)}{\int_{-\infty}^{\infty}\tilde{\eta}^2(\xi')\tilde{\tilde{C}}_{zz}(\xi',\zeta)d\xi'}e^{j\zeta z}\tilde{\eta}(\xi)\left(\xi^2+\zeta^2\right)e^{j\xi x}e^{-p_1 y}\Big|_{\xi=\xi_p}$$

$$\frac{\left(N_{21}^2-1\right)}{Z^h(\xi_p,\zeta)Z^{e'}(\xi_p,\zeta)}$$

where

$$(\cdots)=\frac{-j\tilde{\eta}(\xi)\left[\left(\xi^2+\zeta^2\right)C_{1r}(\xi,\zeta)-\dfrac{2p_1^2(\xi,\zeta)}{Z^h(\xi,\zeta)}\right]\dfrac{e^{j\xi x}e^{-p_1 y}}{4\pi p_1}}{\int_{-\infty}^{\infty}\tilde{\eta}^2(\xi')\tilde{\tilde{C}}_{zz}(\xi',\zeta)d\xi'}$$

$$\tilde{\eta}(\xi)=\begin{cases}J_0(\xi w/2)\cdots w/t<2\\ sinc(\xi w/2)\cdots w/t\geq 2\end{cases}$$

$$\tilde{L}_g(\zeta)=e^{-(\zeta d)^2/2}$$

The minus sign remains for agreement with Eqn. (6.2.25). Figs. 6.2.5, 6.2.6, 6.2.7 and 6.2.8 depict the field amplitude and phase longitudinal profiles contributed by the residue evaluated at the surface-wave pole singularity $\xi=\xi_p$ in the complex ξ-plane obtained by integrating ζ about the branch-cut contour in Fig. 5.3.3. The cut-off criterion for the nth surface-wave mode was previously discussed in Appendix F and is also identical.

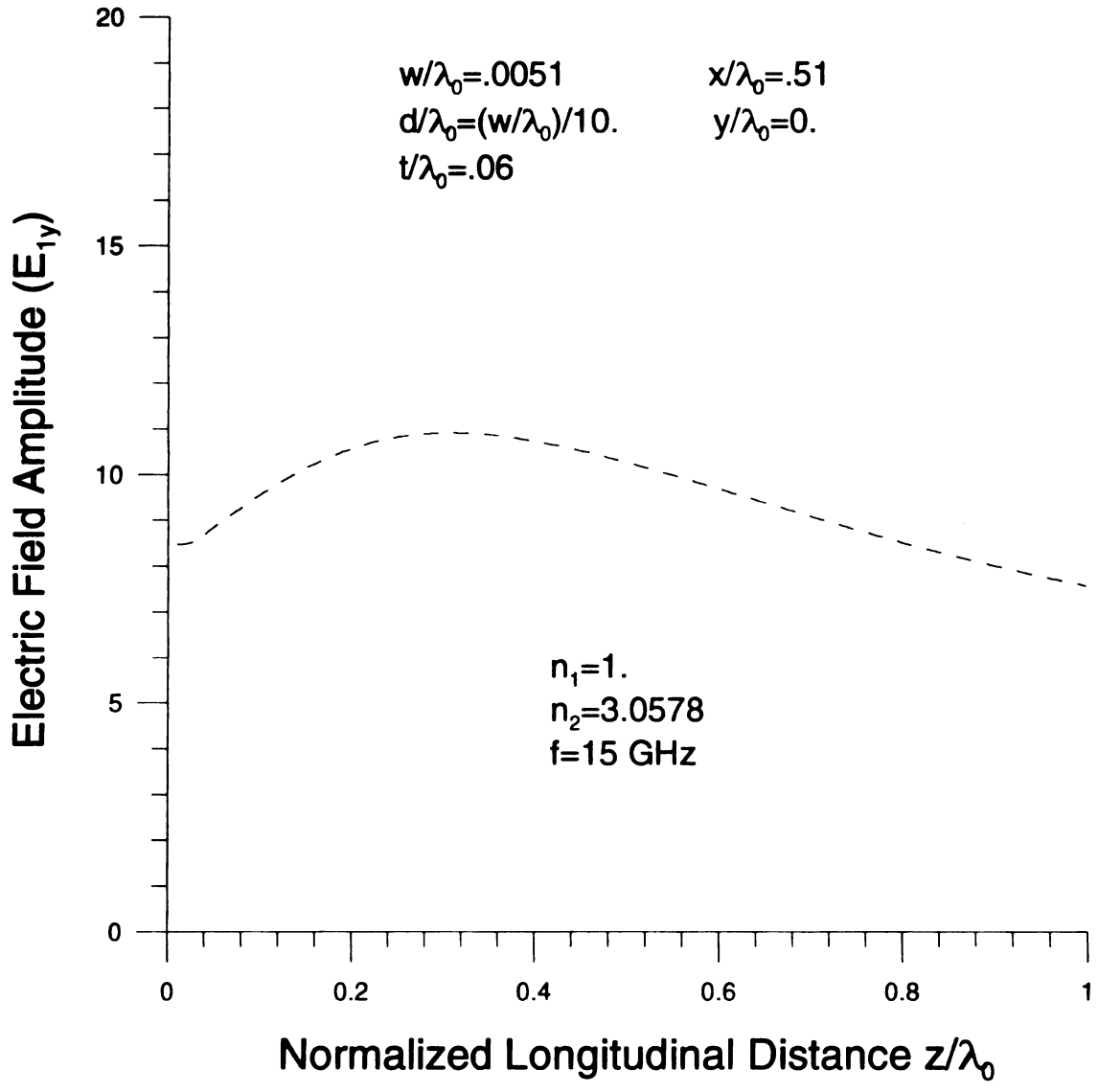

Figure 6.2.1 Field amplitude longitudinal profile contributed by $\mathrm{Re}\{\xi\}$-axis inversion contour excluding surface-wave pole singularities with integrating ζ about the branch-cut contour.

Electric Field Phase (E_{1y})

Figure

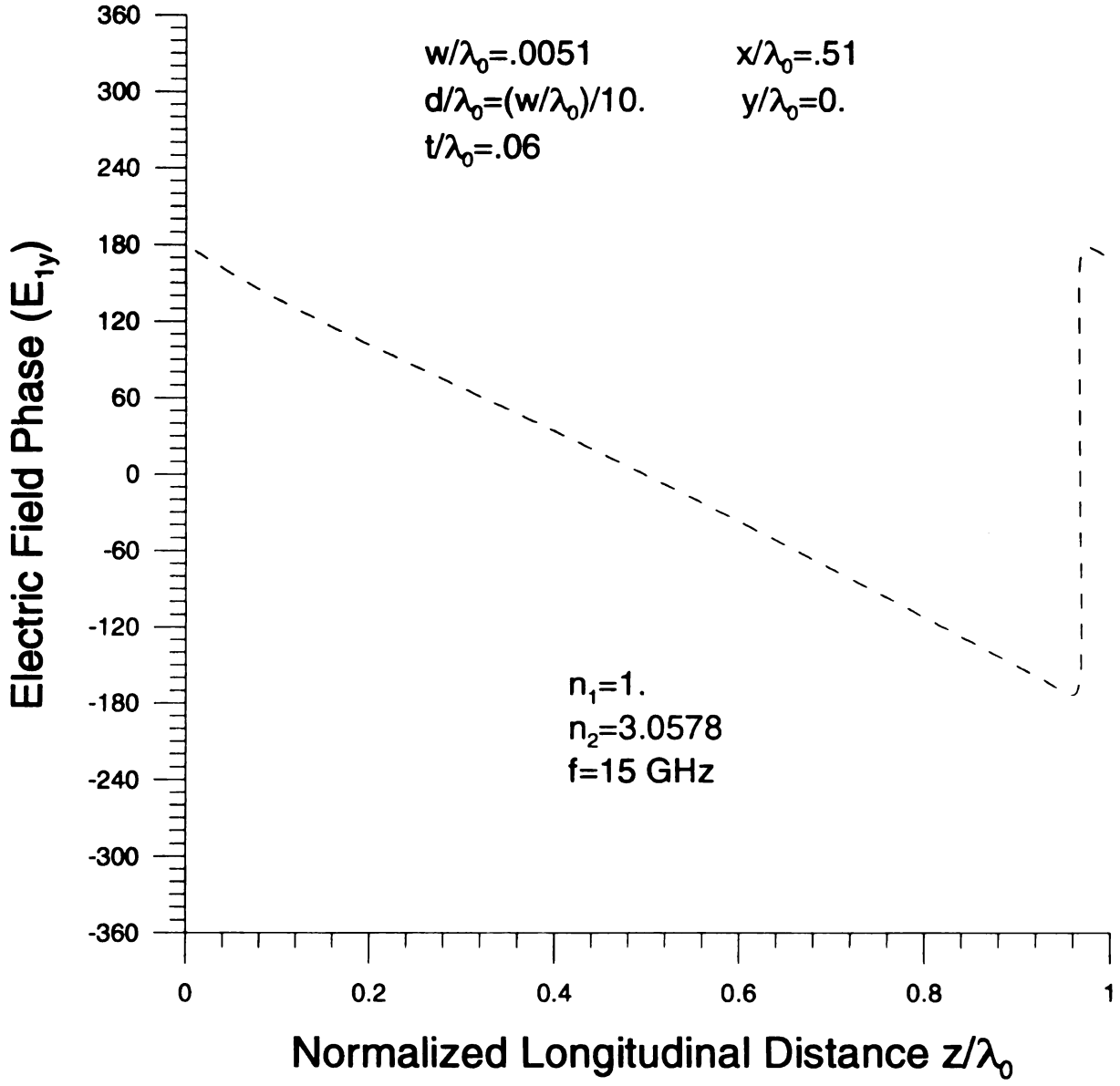

Figure 6.2.2 Field phase longitudinal profile contributed by $\mathrm{Re}\{\xi\}$-axis inversion contour excluding surface-wave pole singularities with integrating ζ about the branch-cut contour.

Electric Field Amplitude (E_{1y})

Figure

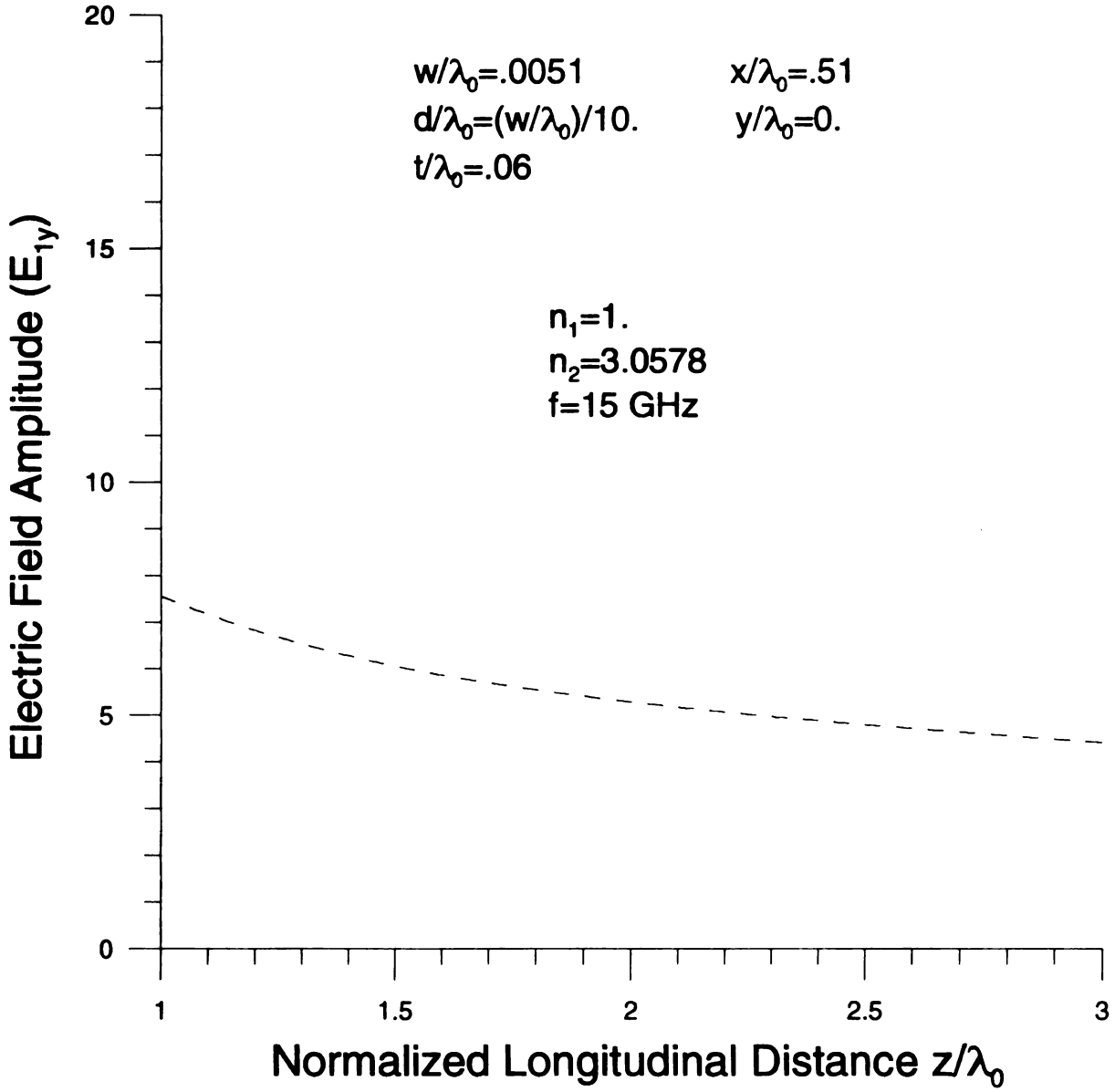

Figure 6.2.3 Field amplitude longitudinal profile contributed by $\mathrm{Re}\{\xi\}$-axis inversion contour excluding surface-wave pole singularities with integrating ζ about the branch-cut contour.

Electric Field Amplitude (E_{1y})

Figure

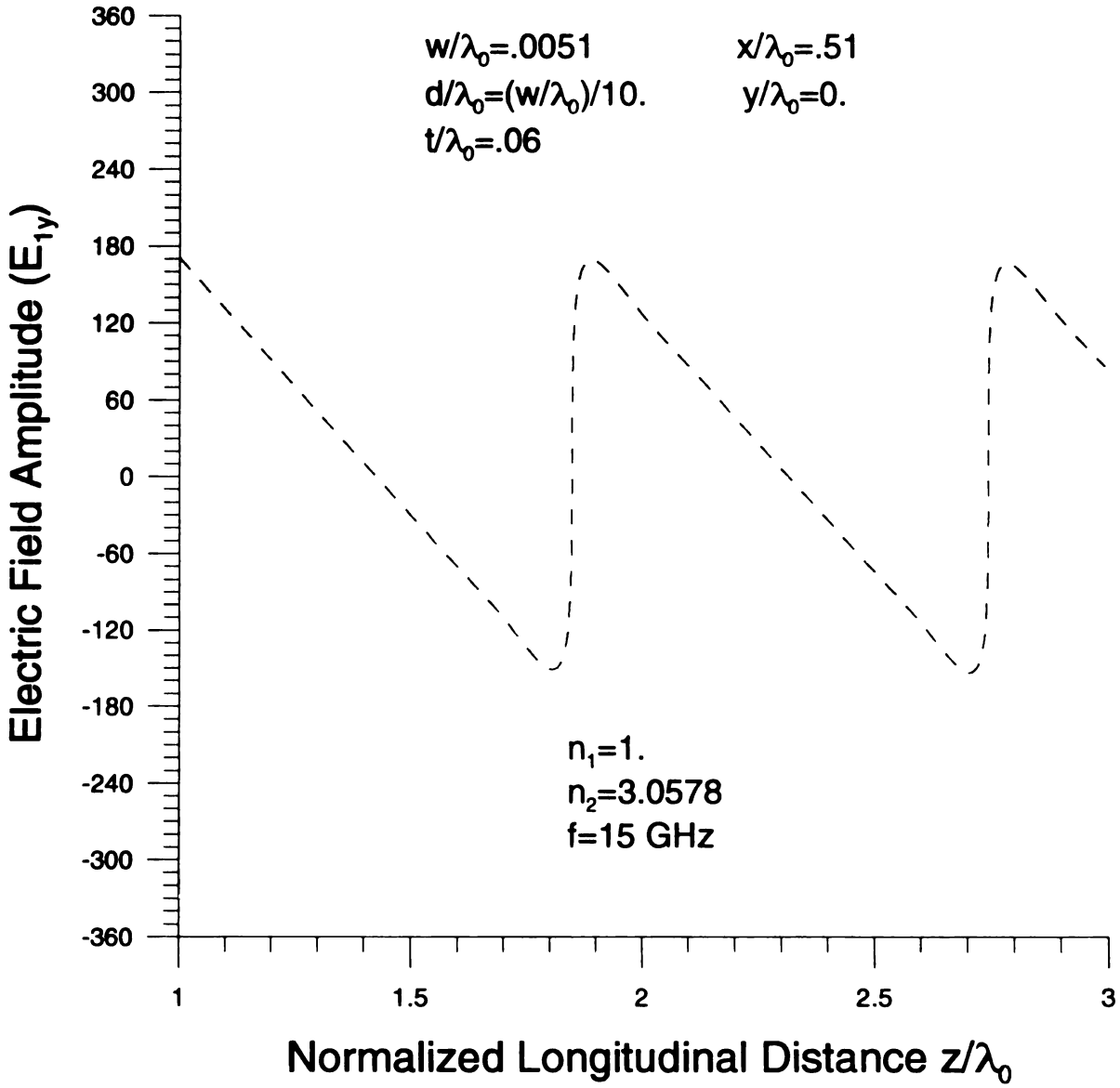

Figure 6.2.4 Field phase longitudinal profile contributed by $\mathrm{Re}\{\xi\}$-axis inversion contour excluding surface-wave pole singularities with integrating ζ about the branch-cut contour.

Electric Field Amplitude (E

Figure

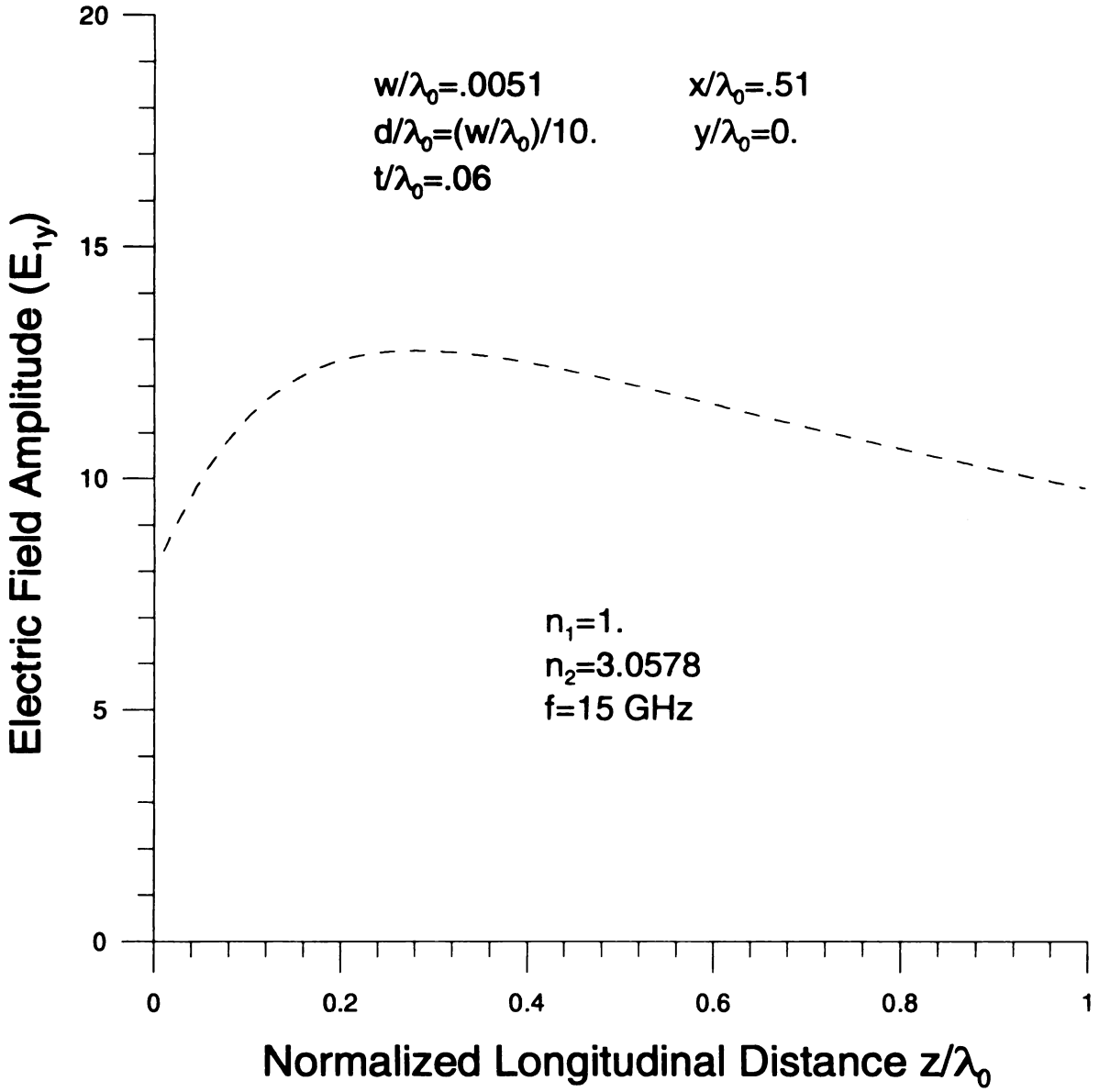

Figure 6.2.5 Field amplitude longitudinal profile contributed by the residue evaluated at the surface-wave pole singularity with integrating ζ about the branch-cut contour.

Figure

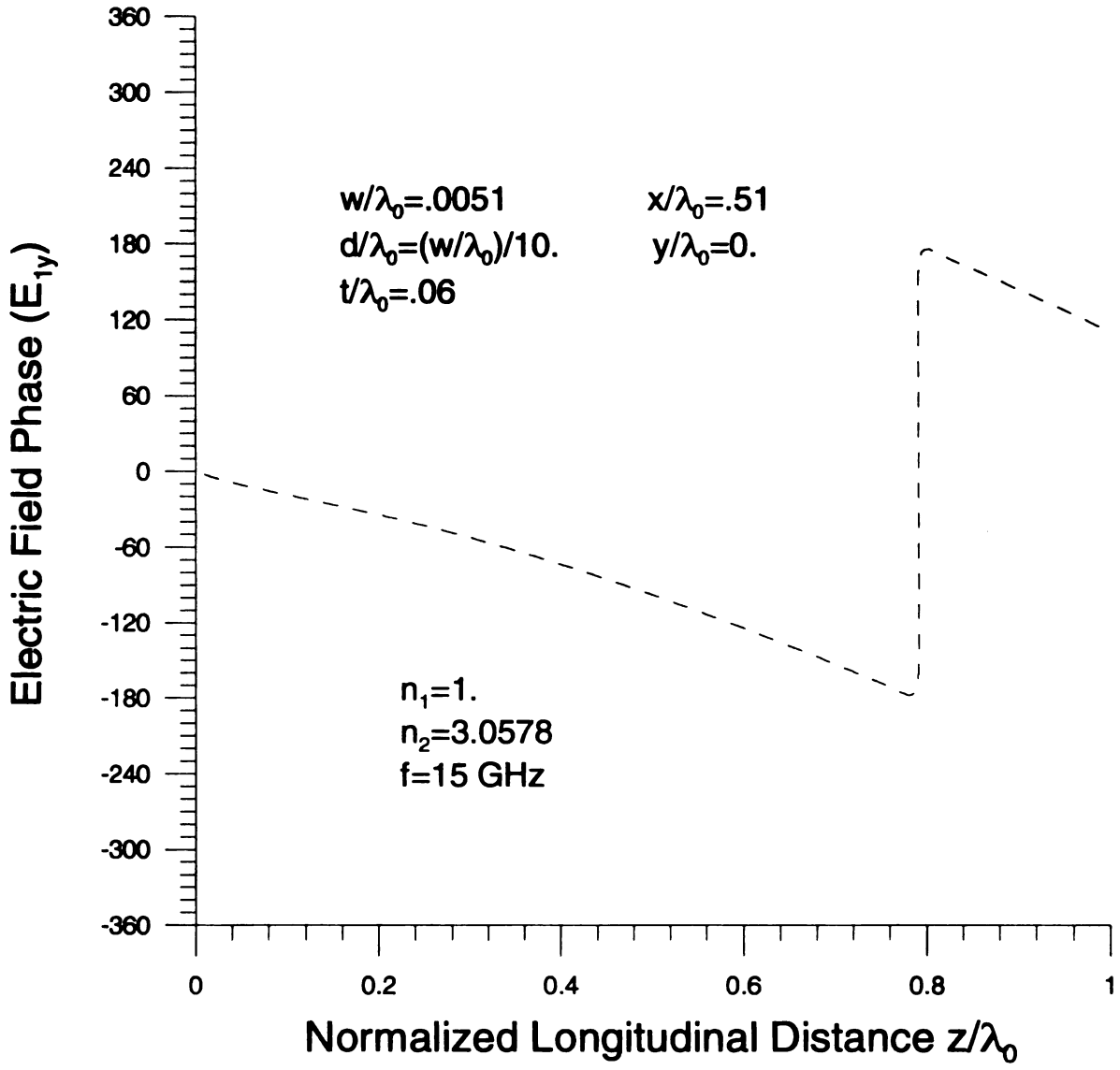

Figure 6.2.6 Field phase longitudinal profile contributed by the residue evaluated at the surface-wave pole singularity with integrating ζ about the branch-cut contour.

Electric Field Amplitude (E

Figure

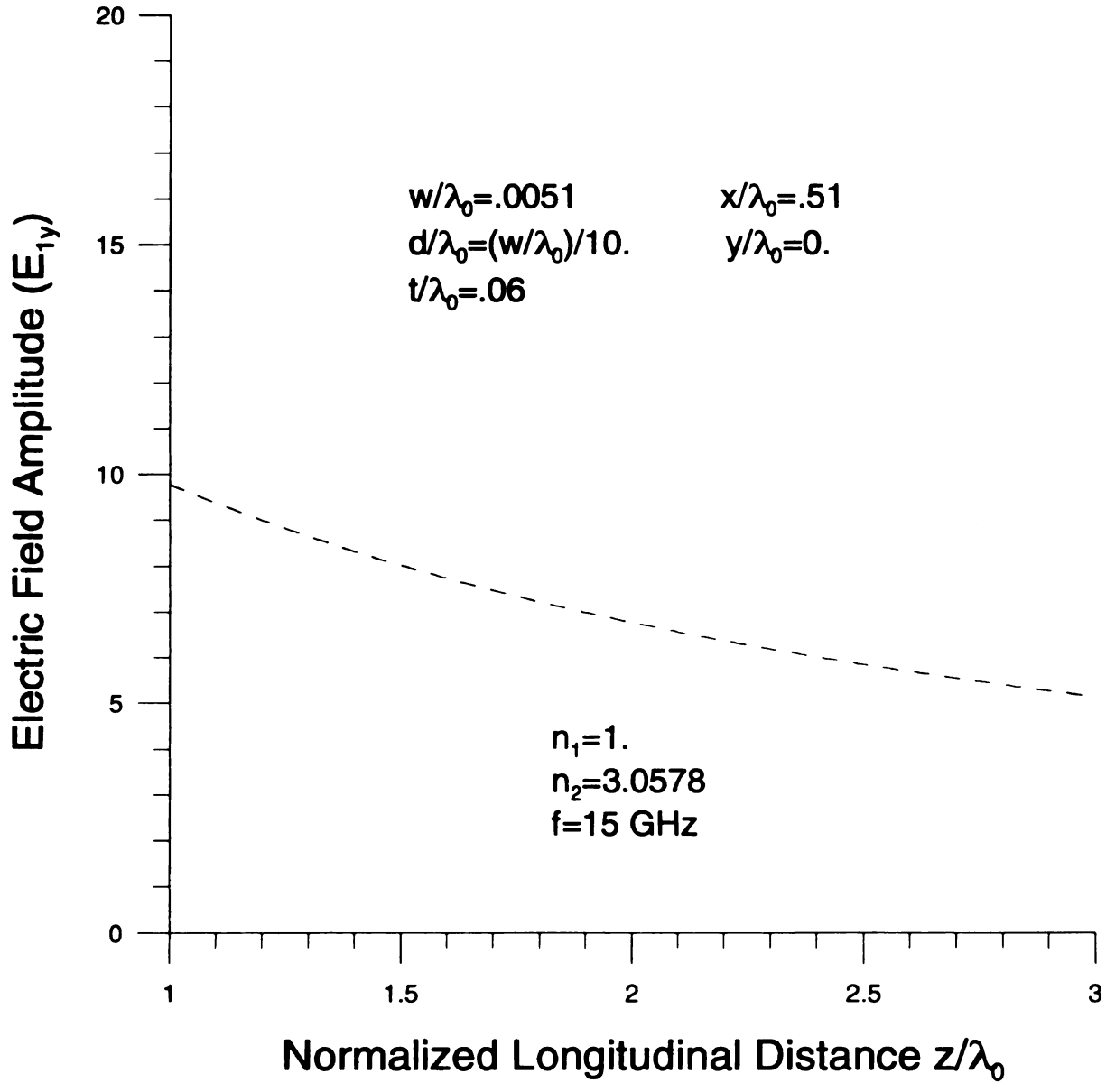

Figure 6.2.7 Field amplitude longitudinal profile contributed by the residue evaluated at the surface-wave pole singularity with integrating ζ about the branch-cut contour.

Figure

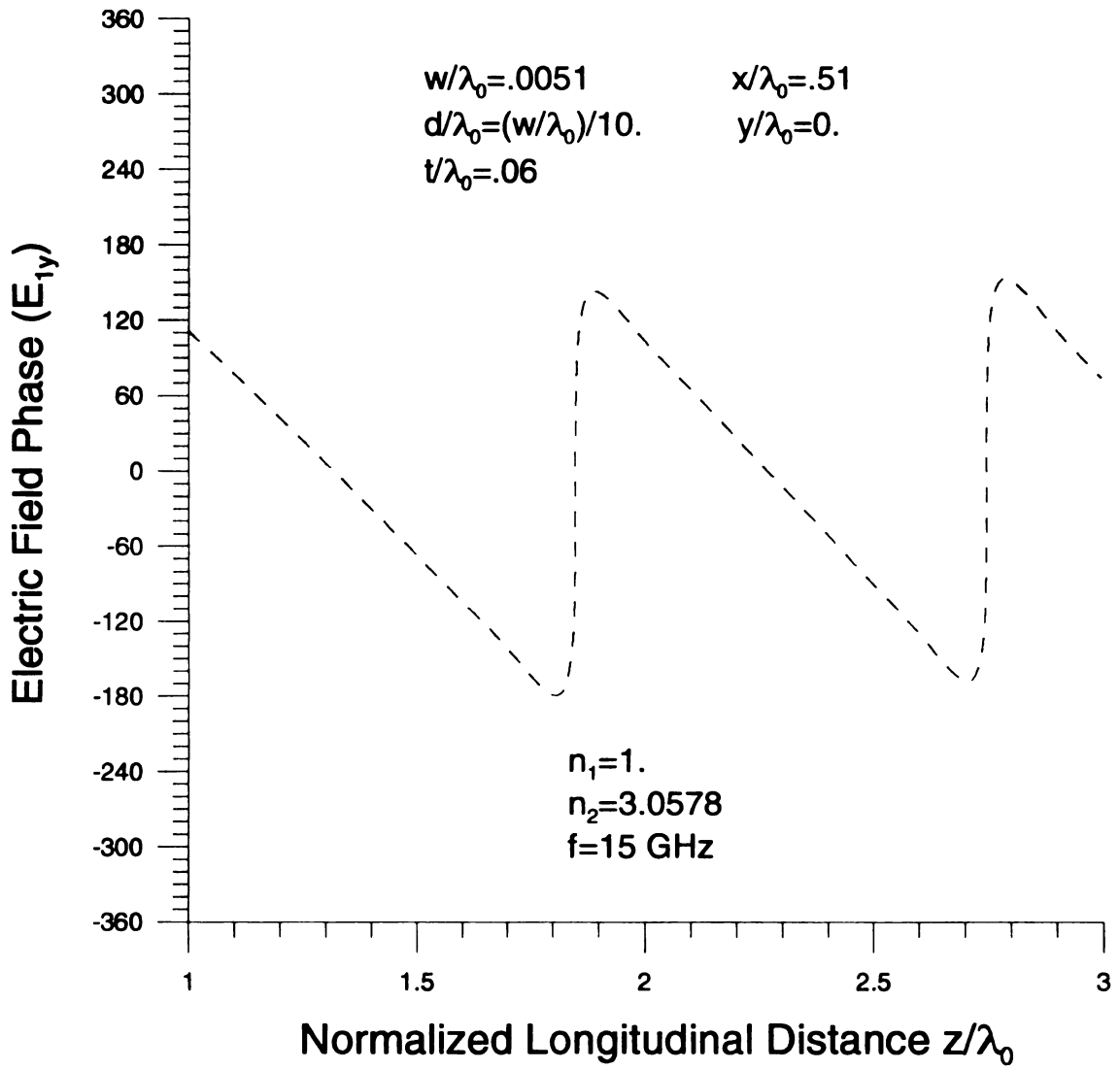

Figure 6.2.8 Field phase longitudinal profile contributed by the residue evaluated at the surface-wave pole singularity with integrating ζ about the branch-cut contour.

Therefore, as discussed in Section 5.3, it is recognized that the continuous spectrum is contributed by an integration about the branch cut and proper if the integration path never violates the branch cut as depicted in Figs 5.3.2 and 5.3.3. The continuous spectrum is then decomposed into that contributed by $\mathrm{Re}\{\xi\}$-axis inversion contour excluding surface-wave pole singularities in the complex ξ-plane and that by surface-wave pole singularities in that plane. Therefore, the continuous spectrum is

$$
\begin{aligned}
&-\int_{C_b} d\zeta \frac{\zeta \tilde{L}_g(\zeta)}{\int_{-\infty}^{\infty} \tilde{\eta}^2(\xi')\tilde{\tilde{C}}_{zz}(\xi',\zeta)d\xi'} e^{j\zeta z} \int_{C_\xi} (\cdots) d\xi \\
&= -\int_{C_b} d\zeta \frac{\zeta \tilde{L}_g(\zeta)}{\int_{-\infty}^{\infty} \tilde{\eta}^2(\xi')\tilde{\tilde{C}}_{zz}(\xi',\zeta)d\xi'} e^{j\zeta z} \int_{C_\xi - C_{\xi_p}} (\cdots) d\xi \qquad (6.2.28) \\
&\quad -\int_{C_b} d\zeta \frac{\zeta \tilde{L}_g(\zeta)}{\int_{-\infty}^{\infty} \tilde{\eta}^2(\xi')\tilde{\tilde{C}}_{zz}(\xi',\zeta)d\xi'} e^{j\zeta z} \oint_{C_{\xi_p}} (\cdots) d\xi
\end{aligned}
$$

where

$$
(\cdots) = -j\tilde{\eta}(\xi)\left[\left(\xi^2+\zeta^2\right)C_{1r}(\xi,\zeta) - \frac{2p_1^2}{Z^h(\xi,\zeta)}\right]\frac{e^{j\xi x}e^{-p_1 y}}{4\pi p_1}
$$

Numerical results for the continuous spectrum will be presented in Section 6.3.

As discussed in Section 5.4, the discrete or bound-mode spectrum is associated with bound- or guided-mode pole singularities ζ_p in the complex ζ-plane as depicted in Fig. 5.4.1. In accordance with Eqn. (6.2.20), a characteristic eigenvalue equation for bound-mode pole singularities ζ_ps is

$$
\int_{-\infty}^{\infty} \tilde{\eta}^2(\xi')\tilde{\tilde{C}}_{zz}(\xi',\zeta_p)d\xi' = 0 \qquad (6.2.29)
$$

In accordance with Eqns. (5.4.2), (5.4.3), (5.4.4), and (5.4.5), the full residue becomes

$$\frac{j}{4\pi}\oint_{C_{\zeta_p}} d\zeta \frac{\zeta \tilde{L}_g(\zeta)}{\int_{-\infty}^{\infty} \tilde{\eta}^2(\xi')\tilde{\tilde{C}}_{zz}(\xi',\zeta)d\xi'} e^{j\zeta z}$$

$$\int_{-\infty}^{\infty} \tilde{\eta}(\xi)\left[\left(\xi^2+\zeta^2\right)C_{1r}(\xi,\zeta)-\frac{2p_1^2}{Z^h(\xi,\zeta)}\right]\frac{e^{j\xi x}e^{-p_1 y}}{p_1}d\xi$$

$$=-\frac{1}{2}\frac{\zeta_p \Delta\zeta \tilde{L}_g(\zeta_p)}{\int_{-\infty}^{\infty} \tilde{\eta}^2(\xi')\tilde{\tilde{C}}_{zz}(\xi',\zeta_p+\Delta\zeta)d\xi'} e^{j\zeta_p z}$$

$$\int_{-\infty}^{\infty} d\xi\tilde{\eta}(\xi)\left[\left(\xi^2+\zeta^2\right)C_{1r}(\xi,\zeta)-\frac{2p_1^2}{Z^h(\xi,\zeta)}\right]\frac{e^{j\xi x}e^{-p_1 y}}{p_1}\Bigg|_{\zeta=\zeta_p}$$

where

$$\tilde{\eta}(\xi)=\begin{cases} J_0(\xi w/2)\cdots w/t<2 \\ sinc(\xi w/2)\cdots w/t\geq 2 \end{cases}$$

$$\tilde{L}_g(\zeta)=e^{-(\zeta d)^2/2}$$

The minus sign remains in agreement with Eqn. (6.2.25) and a differential increment $\Delta\zeta$ for a finite-difference scheme must be reasonably chosen. Numerical results for the discrete spectrum will be presented in Section 6.3.

Hence it is observed that the cover field is composed by the continuous spectrum contributed by the background layer environment and the discrete spectrum contributed by the guiding structure. Numerical results for the cover field will be presented in Section 6.3 where it is observed that the cover field is dominated by the continuous spectrum rather than the discrete spectrum. This is because the cover field is associated with the background layer environment rather than the guiding structure. The cover field in accordance with Eqn. (6.2.25) can be then validated by $\mathrm{Re}\{\zeta\}$-axis inversion contour

integr

The m

positiv

bound

Fig. 5.

integration as in Section 5.5. Since the integrand of $d\zeta$ in Eqn. (6.2.20) is odd in ζ

$$E_{1y}(\boldsymbol{r})=\frac{1}{2\pi}\int_0^\infty d\zeta\frac{\zeta\tilde{L}_g(\zeta)}{\int_{-\infty}^{\infty}\tilde{\eta}^2(\xi')\tilde{\tilde{C}}_{zz}(\xi',\zeta)d\xi'}\sin(\zeta z)$$
$$\int_{-\infty}^{\infty}\tilde{\eta}(\xi)\left[\left(\xi^2+\zeta^2\right)C_{1r}(\xi,\zeta)-\frac{2p_1^2}{Z^h(\xi,\zeta)}\right]\frac{e^{j\xi x}e^{-p_1 y}}{p_1}d\xi$$

where (6.2.30)

$$C_{1r}(\xi,\zeta)=\frac{2\left(N_{21}^2-1\right)p_1(\xi,\zeta)}{Z^h(\xi,\zeta)Z^e(\xi,\zeta)}$$
$$Z^h(\xi,\zeta)=p_1(\xi,\zeta)+p_2(\xi,\zeta)\coth\left[p_2(\xi,\zeta)t\right]$$
$$Z^e(\xi,\zeta)=N_{21}^2p_1(\xi,\zeta)+p_2(\xi,\zeta)\tanh\left[p_2(\xi,\zeta)t\right]$$

The migration of ξ-plane singularities with the corresponding changing of ζ along the positive $\mathrm{Re}\{\zeta\}$-axis inversion contour is identical to that discussed in Section 5.5. The bound- or guided-mode pole singularity ζ_p contributes to the half residue as depicted in Fig. 5.5.3. Therefore, the half residue in a clockwise sense about $\zeta=\zeta_p$ is evaluated by

$$\frac{1}{2\pi}\oint_{C_{\zeta_p}}d\zeta\frac{\zeta\tilde{L}_g(\zeta)}{\int_{-\infty}^{\infty}\tilde{\eta}^2(\xi')\tilde{\tilde{C}}_{zz}(\xi',\zeta)d\xi'}\sin(\zeta z)$$
$$\int_{-\infty}^{\infty}\tilde{\eta}(\xi)\left[\left(\xi^2+\zeta^2\right)C_{1r}(\xi,\zeta)-\frac{2p_1^2}{Z^h(\xi,\zeta)}\right]\frac{e^{j\xi x}e^{-p_1 y}}{p_1}d\xi$$
$$=-\frac{j}{2}\frac{\zeta_p\Delta\zeta\tilde{L}_g(\zeta_p)}{\int_{-\infty}^{\infty}\tilde{\eta}^2(\xi')\tilde{\tilde{C}}_{zz}(\xi',\zeta_p+\Delta\zeta)d\xi'}\sin(\zeta_p z) \tag{6.2.31}$$
$$\int_{-\infty}^{\infty}d\xi\tilde{\eta}(\xi)\left[\left(\xi^2+\zeta^2\right)C_{1r}(\xi,\zeta)-\frac{2p_1^2}{Z^h(\xi,\zeta)}\right]\frac{e^{j\xi x}e^{-p_1 y}}{p_1}\Bigg|_{\zeta=\zeta_p}$$

Then, the cover field contributed by $\mathrm{Re}\{\zeta\}$-axis inversion contour integration in Fig. 5.5.3 becomes

$$E_{1y}(\boldsymbol{r})=\frac{1}{2\pi}\int_0^{\infty}d\zeta\frac{\zeta\tilde{L}_g(\zeta)}{\int_{-\infty}^{\infty}\tilde{\eta}^2(\xi')\tilde{\tilde{C}}_{zz}(\xi',\zeta)d\xi'}\sin(\zeta z)$$
$$\int_{-\infty}^{\infty}\tilde{\eta}(\xi)\left[\left(\xi^2+\zeta^2\right)C_{1r}(\xi,\zeta)-\frac{2p_1^2}{Z^h(\xi,\zeta)}\right]\frac{e^{j\xi x}e^{-p_1 y}}{p_1}d\xi$$
$$-\frac{j}{2}\frac{\zeta_p\Delta\zeta\tilde{L}_g(\zeta_p)}{\int_{-\infty}^{\infty}\tilde{\eta}^2(\xi')\tilde{\tilde{C}}_{zz}(\xi',\zeta_p+\Delta\zeta)d\xi'}\sin(\zeta_p z)$$
$$\int_{-\infty}^{\infty}d\xi\tilde{\eta}(\xi)\left[\left(\xi^2+\zeta^2\right)C_{1r}(\xi,\zeta)-\frac{2p_1^2}{Z^h(\xi,\zeta)}\right]\frac{e^{j\xi x}e^{-p_1 y}}{p_1}\Bigg|_{\zeta=\zeta_p}$$

Numerical results for validating Eqn. (6.2.25) will be presented in Section 6.3.

Alternatively, the cover field can be formulated in the complex λ-plane rather than in the complex ξ- and ζ-planes (see Appendix G).

6.2.2 FILM FIELD FORMULATION

Since $\boldsymbol{J}(z')=\hat{z}J_z(z')$ (see Appendix E),

$$\bar{\boldsymbol{G}}_2(\boldsymbol{r}|\boldsymbol{r}')\cdot\hat{z}=\hat{y}\frac{\partial}{\partial z}\left[G_{2c}^t(\boldsymbol{r}|\boldsymbol{r}')+G_{2c}^r(\boldsymbol{r}|\boldsymbol{r}')\right]+\hat{z}\left[G_{2z}^t(\boldsymbol{r}|\boldsymbol{r}')+G_{2z}^r(\boldsymbol{r}|\boldsymbol{r}')\right] \quad (6.2.32)$$

Therefore, exploiting Eqn. (6.2.3)

$$\boldsymbol{\Pi}_2(\boldsymbol{r})=\int_{-\infty}^{\infty}\int_{-w/2}^{w/2}\left\{\hat{y}\frac{\partial}{\partial z}\left[G_{2c}^t(\boldsymbol{r}|\boldsymbol{r}')+G_{2c}^r(\boldsymbol{r}|\boldsymbol{r}')\right]+\hat{z}\left[G_{2z}^t(\boldsymbol{r}|\boldsymbol{r}')+G_{2z}^r(\boldsymbol{r}|\boldsymbol{r}')\right]\right\}\frac{J_z(z')\eta(x')}{j\omega\varepsilon_1}dx'dz' \quad (6.2.33)$$

Th

by

Then,

where

$$G_{2c}^{t}(\vec{r}|\vec{r}') = \iint_{\infty} C_{2t}(\xi,\zeta)\frac{e^{j[\xi(x-x')+\zeta(z-z')]}e^{[p_2(\xi,\zeta)y-p_1(\xi,\zeta)y']}}{2(2\pi)^2 p_1(\xi,\zeta)}d\xi d\zeta$$

$$G_{2c}^{r}(\vec{r}|\vec{r}') = \iint_{\infty} C_{2r}(\xi,\zeta)\frac{e^{j[\xi(x-x')+\zeta(z-z')]}e^{-[p_2(\xi,\zeta)y+p_1(\xi,\zeta)y']}}{2(2\pi)^2 p_1(\xi,\zeta)}d\xi d\zeta$$

$$G_{2z}^{t}(\vec{r}|\vec{r}') = \iint_{\infty} T_{2z}(\xi,\zeta)\frac{e^{j[\xi(x-x')+\zeta(z-z')]}e^{[p_2(\xi,\zeta)y-p_1(\xi,\zeta)y']}}{2(2\pi)^2 p_1(\xi,\zeta)}d\xi d\zeta$$

$$G_{2z}^{r}(\vec{r}|\vec{r}') = \iint_{\infty} R_{2z}(\xi,\zeta)\frac{e^{j[\xi(x-x')+\zeta(z-z')]}e^{-[p_2(\xi,\zeta)y+p_1(\xi,\zeta)y']}}{2(2\pi)^2 p_1(\xi,\zeta)}d\xi d\zeta$$

The coefficients $C_{2t}(\xi,\zeta)$, $C_{2r}(\xi,\zeta)$, $T_{2z}(\xi,\zeta)$, and $R_{2z}(\xi,\zeta)$ are determined by

$$C_{2t}(\xi,\zeta) = \frac{N_{21}^{-2}\left(N_{21}^2-1\right)}{Z^h(\xi,\zeta)z^e(\xi,\zeta)\cosh\left[p_2(\xi,\zeta)t\right]}\frac{e^{p_2(\xi,\zeta)t}}{}p_1(\xi,\zeta)$$

$$C_{2r}(\xi,\zeta) = \frac{N_{21}^{-2}\left(N_{21}^2-1\right)}{Z^h(\xi,\zeta)Z^e(\xi,\zeta)\cosh\left[p_2(\xi,\zeta)t\right]}\frac{e^{-p_2(\xi,\zeta)t}}{}p_1(\xi,\zeta)$$

$$T_{2z}(\xi,\zeta) = \frac{N_{21}^{-2}}{Z^h(\xi,\zeta)\sinh\left[p_2(\xi,\zeta)t\right]}\frac{e^{p_2(\xi,\zeta)t}}{}p_1(\xi,\zeta)$$

$$R_{2z}(\xi,\zeta) = -\frac{N_{21}^{-2}}{Z^h(\xi,\zeta)\sinh\left[p_2(\xi,\zeta)t\right]}\frac{e^{-p_2(\xi,\zeta)t}}{}p_1(\xi,\zeta)$$

where

$$Z^h(\xi,\zeta) = p_1(\xi,\zeta) + p_2(\xi,\zeta)\coth\left[p_2(\xi,\zeta)t\right]$$

$$Z^e(\xi,\zeta) = N_{21}^2 p_1(\xi,\zeta) + p_2(\xi,\zeta)\tanh\left[p_2(\xi,\zeta)t\right]$$

$$N_{21}^{-2} = (n_2/n_1)^{-2} = (n_1/n_2)^2$$

Then,

and

Γ

In acc

Rearra

$\tilde{\Pi}$

Simila

In acc

$$\Pi_{2y}(r)=\frac{1}{2\pi}\frac{1}{j\omega\varepsilon_1}\frac{N_{21}^{-2}}{2\pi}\int_{-\infty}^{\infty}\left(\int_{-\infty}^{\infty}d\xi\, j\zeta\left\{\frac{\left(N_{21}^2-1\right)}{Z^hZ^e}\frac{\cosh\left[p_2(y+t)\right]}{\cosh\left(p_2t\right)}\right\}\right.$$
$$\left.\left[\int_{-\infty}^{\infty}J_z(z')e^{-j\zeta z'}dz'\int_{-w/2}^{w/2}\eta(x')e^{-j\xi x'}dx'\right]e^{j\xi x}\right)e^{j\zeta z}d\zeta \tag{6.2.34}$$

and

$$\Pi_{2z}(r)=\frac{1}{2\pi}\frac{1}{j\omega\varepsilon_1}\frac{N_{21}^{-2}}{2\pi}\int_{-\infty}^{\infty}\left(\int_{-\infty}^{\infty}d\xi\left\{\frac{1}{Z^h(\xi,\zeta)}\frac{\sinh\left[p_2(\xi,\zeta)(y+t)\right]}{\sinh\left[p_2(\xi,\zeta)t\right]}\right\}\right.$$
$$\left.\left[\int_{-\infty}^{\infty}J_z(z')e^{-j\zeta z'}dz'\int_{-w/2}^{w/2}\eta(x')e^{-j\xi x'}dx'\right]e^{j\xi x}\right)e^{j\zeta z}d\zeta \tag{6.2.35}$$

In accordance with Eqn. (6.2.11),

$$\int_{-w/2}^{w/2}\eta(x')e^{-j\xi x'}dx'=\tilde{\eta}(\xi)=\begin{cases}J_0(\xi w/2)\cdots w/t<2\\ sinc(\xi w/2)\cdots w/t\geq 2\end{cases}$$

Rearranging the Fourier transformation leads from Eqn. (6.2.34) to

$$\tilde{\Pi}_{2y}(\rho,\zeta)=\frac{1}{j\omega\varepsilon_1}\frac{N_{21}^{-2}}{2\pi}\int_{-\infty}^{\infty}j\zeta\left\{\frac{\left(N_{21}^2-1\right)}{Z^h(\xi,\zeta)Z^e(\xi,\zeta)}\frac{\cosh\left[p_2(y+t)\right]}{\cosh\left(p_2t\right)}\right\}$$
$$\tilde{J}_z(\zeta)\tilde{\eta}(\xi)e^{j\xi x}d\xi \tag{6.2.36}$$
$$where$$
$$\rho=\hat{x}x+\hat{y}y$$

Similarly, Eqn. (6.2.35) leads to

$$\tilde{\Pi}_{2z}(\rho,\zeta)=\frac{1}{j\omega\varepsilon_1}\frac{N_{21}^{-2}}{2\pi}\int_{-\infty}^{\infty}\left\{\frac{1}{Z^h(\xi,\zeta)}\frac{\sinh\left[p_2(\xi,\zeta)(y+t)\right]}{\sinh\left[p_2(\xi,\zeta)t\right]}\right\}$$
$$\tilde{J}_z(\zeta)\tilde{\eta}(\xi)e^{j\xi x}d\xi \tag{6.2.37}$$

In accordance with Eqns. (6.2.14) and (6.2.15),

$$e_{2y}(\boldsymbol{\rho},\zeta)=\left(\xi^2+\zeta^2\right)\tilde{\Pi}_{2y}(\boldsymbol{\rho},\zeta)+j\zeta\frac{\partial}{\partial y}\tilde{\Pi}_{2z}(\boldsymbol{\rho},\zeta) \tag{6.2.38}$$

Then,

$$\begin{aligned} e_{2y}(\boldsymbol{\rho},\zeta)=&\frac{1}{j\omega\varepsilon_1}\frac{N_{21}^{-2}}{2\pi}\int_{-\infty}^{\infty}j\zeta\left(\xi^2+\zeta^2\right)\frac{\left(N_{21}^2-1\right)}{Z^h(\xi,\zeta)Z^e(\xi,\zeta)}\frac{\cosh\left[p_2(y+t)\right]}{\cosh(p_2t)}\\ &\tilde{J}_z(\zeta)\tilde{\eta}(\xi)e^{j\xi x}d\xi\\ &+\frac{1}{j\omega\varepsilon_1}\frac{N_{21}^{-2}}{2\pi}\int_{-\infty}^{\infty}j\zeta\frac{p_2}{Z^h(\xi,\zeta)}\frac{\cosh\left[p_2(\xi,\zeta)(y+t)\right]}{\sinh\left[p_2(\xi,\zeta)t\right]}\tilde{J}_z(\zeta)\tilde{\eta}(\xi)\\ &e^{j\xi x}d\xi \end{aligned} \tag{6.2.39}$$

The above becomes

$$\begin{aligned} e_{2y}(\boldsymbol{\rho},\zeta)=&\frac{1}{\omega\varepsilon_1}\frac{N_{21}^{-2}}{2\pi}\int_{-\infty}^{\infty}\zeta\tilde{J}_z(\zeta)\tilde{\eta}(\xi)\left\{\frac{\left(N_{21}^2-1\right)}{Z^h(\xi,\zeta)Z^e(\xi,\zeta)}\frac{\left(\xi^2+\zeta^2\right)}{\cosh(p_2t)}\right.\\ &\left.+\frac{1}{Z^h(\xi,\zeta)}\frac{p_2(\xi,\zeta)}{\sinh\left[p_2(\xi,\zeta)t\right]}\right\}\cosh\left[p_2(y+t)\right]e^{j\xi x}d\xi \end{aligned} \tag{6.2.40}$$

In accordance with Eqn. (5.2.19) and after some manipulation,

$$\begin{aligned} e_{2y}(\boldsymbol{\rho},\zeta)=&-\frac{j}{N_{21}^2}\frac{\zeta\tilde{L}_g(\zeta)}{\int_{-\infty}^{\infty}\tilde{\eta}^2(\xi')\tilde{\tilde{C}}_{zz}(\xi',\zeta)d\xi'}\\ &\int_{-\infty}^{\infty}\tilde{\eta}(\xi)\left\{\frac{\left(N_{21}^2-1\right)}{Z^h(\xi,\zeta)Z^e(\xi,\zeta)}\frac{\left(\xi^2+\zeta^2\right)}{\cosh(p_2t)}+\frac{1}{Z^h(\xi,\zeta)}\frac{p_2(\xi,\zeta)}{\sinh\left[p_2(\xi,\zeta)t\right]}\right\}\\ &\cosh\left[p_2(y+t)\right]e^{j\xi x}d\xi \end{aligned} \tag{6.2.41}$$

Taking the inverse Fourier transformation of Eqn. (6.2.41) yields the y-component of the film field as

$$E_{2y}(\boldsymbol{r}) = -\frac{j}{2\pi N_{21}^2}\int_{-\infty}^{\infty} d\zeta \frac{\zeta \tilde{L}_g(\zeta)}{\int_{-\infty}^{\infty}\tilde{\eta}^2(\xi')\tilde{\tilde{C}}_{zz}(\xi',\zeta)d\xi'} e^{j\zeta z}$$

$$\int_{-\infty}^{\infty}\tilde{\eta}(\xi)\left\{\frac{\left(N_{21}^2-1\right)}{Z^h(\xi,\zeta)Z^e(\xi,\zeta)}\frac{\left(\xi^2+\zeta^2\right)}{\cosh(p_2 t)} + \frac{1}{Z^h(\xi,\zeta)}\frac{p_2(\xi,\zeta)}{\sinh\left[p_2(\xi,\zeta)t\right]}\right\}$$

$$\cosh\left[p_2(y+t)\right]e^{j\xi x}d\xi$$

where

$$\tilde{\tilde{C}}_{zz}(\xi',\zeta) = \frac{\left(k_1^2-\zeta^2\right)}{Z^h(\xi',\zeta)} + \frac{\zeta^2 p_1(\xi',\zeta)\left(N_{21}^2-1\right)}{Z^h(\xi',\zeta)Z^e(\xi',\zeta)}$$

$$\tilde{\eta}(\xi) = \begin{cases} J_0(\xi w/2)\cdots w/t < 2 \\ sinc(\xi w/2)\cdots w/t \geq 2 \end{cases}$$

$$\tilde{L}_g(\zeta) = e^{-(\zeta d)^2/2}$$

(6.2.42)

As discussed in Section 6.2.1, Fig. 5.3.2 depicts branch-point singularities contributed by pole singularities in the background layer environments and a bound-mode pole singularity contributed by the guiding structure. The $\mathrm{Re}\{\zeta\}$-axis inversion contour can be deformed into the upper $(z>0)$ half and the lower $(z<0)$ half of the complex ζ-plane. Cauchy's integral theorem, as in Eqn. (6.2.24), leads to

$$\int_{-\infty}^{\infty}(\cdots)d\zeta = -\int_{C_b}(\cdots)d\zeta - \int_{C_{\zeta_p}}(\cdots)d\zeta \qquad (6.2.43)$$

Then, the field in the background layer consists of the continuous spectrum contributed by detouring about logarithmic and square-root type branch cuts arising from the k_1 branch point and the proper background mode λ_{TM_0} and the discrete spectrum contributed by the residue evaluation at the bound- or guided-mode pole singularity ζ_p.

Aga

com

brar

com

inte

corr

surfa

wher

inver

5.3 t

assoc

5.3, t

becom

$\oint_C$

wh

(..

Z^e

Again as discussed in Section 5.3, in accordance with Eqn. (6.2.21), singularities in the complex ξ-plane migrate identically as before for corresponding points ζ about the branch cut in the complex ζ-plane in Fig. 5.3.3. It is noted that ξ' singularities in the complex ξ'-plane in Eqn. (6.2.42) also migrate in an identical fashion. Throughout the integration detour about branch cuts from a point 1 to 6 as depicted in Fig. 5.3.3, the corresponding overall procedure for $\mathrm{Re}\{\xi\}$-axis inversion contour C_ξ's excluding surface-wave pole singularities on $\mathrm{Re}\{\xi\}$-axis defined by Eqn. (6.2.21) leads to

$$\int_{\sum_{m=1}^{6} C_\xi(m)} (\cdots) d\xi = \int_{\sum_{m=1}^{3} C_\xi(m)} (\cdots) d\xi - \int_{\sum_{m=4}^{6} C_\xi(m)} (\cdots) d\xi \qquad (6.2.44)$$

where $(\cdots)$ is an integrand of $d\zeta$ in Eqn. (6.2.42) and $C_\xi(m)$ indicates $\mathrm{Re}\{\xi\}$-axis inversion contour for a corresponding point *m* in Fig. 5.3.3. Also it is observed in Section 5.3 that TE-odd and TM-even surface-waves are supported by pole singularities associated with $Z^h(\xi,\zeta)=0$ and $Z^e(\xi,\zeta)=0$ respectively. As discussed in Section 5.3, the full residue for TM-even modes (TM_0 is the fundamental mode) at $\xi=\xi_p$ becomes

$$\oint_{C_{\xi_p}} (\cdots) d\xi = j2\pi \frac{\left(N_{21}^2-1\right)}{Z^h(\xi_p,\zeta) Z^{e'}(\xi_p,\zeta)}$$

where

$$(\cdots) = \frac{\left(N_{21}^2-1\right)}{Z^h(\xi,\zeta) Z^e(\xi,\zeta)} \qquad (6.2.45)$$

$$Z^{e'}(\xi_p,\zeta) = \frac{N_{21}^2 \xi_p}{p_1(\xi_p,\zeta)} + \frac{\xi_p \tanh\left[p_2(\xi_p,\zeta)t\right]}{p_2(\xi_p,\zeta)} + \xi_p t \,\mathrm{sech}^2\left[p_2(\xi_p,\zeta)t\right]$$

Then, the surface-wave residue at $\xi = \xi_p$ for the corresponding point ζ on the branch-cut contour in Fig. 5.3.3 becomes in agreement with Eqn. (6.2.45)

$$-\int_{C_b}\left\{\oint_{C_{\xi_p}}(\cdots)d\xi\right\}\zeta\tilde{L}_g(\zeta)e^{j\zeta z}d\zeta =$$

$$-\int_{C_b}d\zeta\frac{\zeta\tilde{L}_g(\zeta)}{\int_{-\infty}^{\infty}\tilde{\eta}^2(\xi')\tilde{\tilde{C}}_{zz}(\xi',\zeta)d\xi'}e^{j\zeta z}\tilde{\eta}(\xi)\left(\xi^2+\zeta^2\right)\frac{\cosh\left[p_2(y+t)\right]e^{j\xi x}}{N_{21}^2\cosh(p_2t)}\Bigg|_{\xi=\xi_p}$$

$$\frac{\left(N_{21}^2-1\right)}{Z^h\left(\xi_p,\zeta\right)Z^{e'}\left(\xi_p,\zeta\right)}$$

where

$$(\cdots)=\frac{-j\tilde{\eta}(\xi)\left\{\dfrac{\left(N_{21}^2-1\right)}{Z^h(\xi,\zeta)Z^e(\xi,\zeta)}\dfrac{\left(\xi^2+\zeta^2\right)}{\cosh(p_2t)}+\dfrac{1}{Z^h(\xi,\zeta)}\dfrac{p_2(\xi,\zeta)}{\sinh\left[p_2(\xi,\zeta)t\right]}\right\}}{\int_{-\infty}^{\infty}\tilde{\eta}^2(\xi')\tilde{\tilde{C}}_{zz}(\xi',\zeta)d\xi'}$$

$$\frac{\cosh\left[p_2(y+t)\right]e^{j\xi x}}{2\pi N_{21}^2}$$

$$\tilde{\eta}(\xi)=\begin{cases}J_0(\xi w/2)\cdots w/t<2\\ sinc(\xi w/2)\cdots w/t\geq 2\end{cases}$$

$$\tilde{L}_g(\zeta)=e^{-(\zeta d)^2/2}$$

The minus sign remains for agreement with Eqn. (6.2.43).

Therefore, as discussed in Section 5.3, it is recognized that the continuous spectrum is contributed by an integration about the branch cut and is proper if the integration path never violates the branch cut as depicted in Figs 5.3.2, and 5.3.3. The continuous spectrum is then decomposed into that contributed by $\mathrm{Re}\{\xi\}$-axis inversion contour excluding surface-wave pole singularities in the complex ξ-plane and that contributed by

surface-wave pole singularities in that plane. Therefore, the continuous spectrum is

$$
\begin{aligned}
&-\int_{C_b} d\zeta \frac{\zeta \tilde{L}_g(\zeta)}{\int_{-\infty}^{\infty} \tilde{\eta}^2(\xi')\tilde{\tilde{C}}_{zz}(\xi',\zeta)d\xi'} e^{j\zeta z} \int_{C_\xi} (\cdots) d\xi \\
&= -\int_{C_b} d\zeta \frac{\zeta \tilde{L}_g(\zeta)}{\int_{-\infty}^{\infty} \tilde{\eta}^2(\xi')\tilde{\tilde{C}}_{zz}(\xi',\zeta)d\xi'} e^{j\zeta z} \int_{C_\xi - C_{\xi_p}} (\cdots) d\xi \qquad (6.2.46) \\
&-\int_{C_b} d\zeta \frac{\zeta \tilde{L}_g(\zeta)}{\int_{-\infty}^{\infty} \tilde{\eta}^2(\xi')\tilde{\tilde{C}}_{zz}(\xi',\zeta)d\xi'} e^{j\zeta z} \oint_{C_{\xi_p}} (\cdots) d\xi
\end{aligned}
$$

where

$$
(\cdots) = -j\tilde{\eta}(\xi)\left\{ \frac{\left(N_{21}^2 - 1\right)}{Z^h(\xi,\zeta)Z^e(\xi,\zeta)} \frac{\left(\xi^2+\zeta^2\right)}{\cosh(p_2 t)} + \frac{1}{Z^h(\xi,\zeta)} \frac{p_2(\xi,\zeta)}{\sinh\left[p_2(\xi,\zeta)t\right]} \right\}
$$

$$
\frac{\cosh\left[p_2(y+t)\right] e^{j\xi x}}{2\pi N_{21}^2}
$$

$$
\tilde{\eta}(\xi) = \begin{cases} J_0(\xi w/2) \cdots w/t < 2 \\ sinc(\xi w/2) \cdots w/t \geq 2 \end{cases}
$$

$$
\tilde{L}_g(\zeta) = e^{-(\zeta d)^2/2}
$$

As discussed in Section 5.4, the discrete or bound-mode spectrum is associated with bound- or guided-mode pole singularities ζ_p in the complex ζ -plane as depicted in Fig. 5.4.1. Also, in agreement with Eqn. (6.2.29), a characteristic eigenvalue equation for bound-mode pole singularities ζ_p is

$$
\int_{-\infty}^{\infty} \tilde{\eta}^2(\xi')\tilde{\tilde{C}}_{zz}(\xi',\zeta_p)d\xi' = 0 \qquad (6.2.47)
$$

In accordance with Eqns. (5.4.2), (5.4.3), (5.4.4), and (5.4.5), the full residue becomes

T

fo

co

by

6.3

spec

film

discre

longit

Eqn.

integr

$$\frac{j}{2\pi N_{21}^2}\oint_{C_{\zeta_p}} d\zeta \frac{\zeta \tilde{L}_g(\zeta)}{\int_{-\infty}^{\infty}\tilde{\eta}^2(\xi')\tilde{\tilde{C}}_{zz}(\xi',\zeta)d\xi'} e^{j\zeta z}$$

$$\int_{-\infty}^{\infty}\tilde{\eta}(\xi)\left\{\frac{\left(N_{21}^2-1\right)}{Z^h(\xi,\zeta)Z^e(\xi,\zeta)}\frac{\left(\xi^2+\zeta^2\right)}{\cosh(p_2 t)}+\frac{1}{Z^h(\xi,\zeta)}\frac{p_2(\xi,\zeta)}{\sinh\left[p_2(\xi,\zeta)t\right]}\right\}$$

$$\cosh\left[p_2(y+t)\right]e^{j\xi x}d\xi$$

$$=-\frac{1}{N_{21}^2}\frac{\zeta_p\Delta\zeta\tilde{L}_g(\zeta_p)}{\int_{-\infty}^{\infty}\tilde{\eta}^2(\xi')\tilde{\tilde{C}}_{zz}(\xi',\zeta_p+\Delta\zeta)d\xi'} e^{j\zeta_p z}$$

$$\int_{-\infty}^{\infty}d\xi\tilde{\eta}(\xi)\left\{\frac{\left(N_{21}^2-1\right)}{Z^h(\xi,\zeta)Z^e(\xi,\zeta)}\frac{\left(\xi^2+\zeta^2\right)}{\cosh(p_2 t)}+\frac{1}{Z^h(\xi,\zeta)}\frac{p_2(\xi,\zeta)}{\sinh\left[p_2(\xi,\zeta)t\right]}\right\}$$

$$\cosh\left[p_2(y+t)\right]e^{j\xi x}\Big|_{\zeta=\zeta_p}$$

The minus sign remains in agreement with Eqn. (6.2.43) and a differential increment $\Delta\zeta$ for a finite-difference scheme must be reasonably chosen.

Then it is observed that the film field is composed by the continuous spectrum contributed by the background layer environment and the discrete spectrum contributed by the guiding structure. Numerical results for the film field will be presented in Section 6.3 and it is observed that the film field is also mostly dominated by the continuous spectrum rather than the discrete spectrum. Meanwhile only the longitudinal profile of film field is dominated by the discrete spectrum away from the near zone since the discrete spectrum is constant while the continuous spectrum is decreasing with longitudinal displacement away from the source. It is also observed, in agreement with Eqn. (6.2.43), that the film field can be validated by $\mathrm{Re}\{\zeta\}$-axis inversion contour integration as discussed previously in Section 5.5. This allows one to confirm the physics

of the film field. Since the integrand of $d\zeta$ in Eqn. (6.2.42) is odd in ζ,

$$E_{2y}(\boldsymbol{r})=\frac{1}{\pi N_{21}^2}\int_0^\infty d\zeta\frac{\zeta\tilde{L}_g(\zeta)}{\int_{-\infty}^{\infty}\tilde{\eta}^2(\xi')\tilde{\tilde{C}}_{zz}(\xi',\zeta)d\xi'}\sin(\zeta z)$$
$$\int_{-\infty}^{\infty}\tilde{\eta}(\xi)\left\{\frac{\left(N_{21}^2-1\right)}{Z^h(\xi,\zeta)Z^e(\xi,\zeta)}\frac{\left(\xi^2+\zeta^2\right)}{\cosh(p_2t)}+\frac{1}{Z^h(\xi,\zeta)}\frac{p_2(\xi,\zeta)}{\sinh\left[p_2(\xi,\zeta)t\right]}\right\}$$
$$\cosh\left[p_2(y+t)\right]e^{j\xi x}d\xi$$

Again, the migration of ξ-plane singularities with the corresponding changing of ζ along the positive $\mathrm{Re}\{\zeta\}$-axis inversion contour is identical to that discussed in Section 5.5. Also the bound- or guided-mode pole singularity ζ_p contributes to the half residue as depicted in Fig. 5.5.3. Therefore, the half residue in a clockwise sense about $\zeta=\zeta_p$ is evaluated by

$$\frac{1}{\pi N_{21}^2}\oint_{C_{\zeta_p}}d\zeta\frac{\zeta\tilde{L}_g(\zeta)}{\int_{-\infty}^{\infty}\tilde{\eta}^2(\xi')\tilde{\tilde{C}}_{zz}(\xi',\zeta)d\xi'}\sin(\zeta z)$$
$$\int_{-\infty}^{\infty}\tilde{\eta}(\xi)\left\{\frac{\left(N_{21}^2-1\right)}{Z^h(\xi,\zeta)Z^e(\xi,\zeta)}\frac{\left(\xi^2+\zeta^2\right)}{\cosh(p_2t)}+\frac{1}{Z^h(\xi,\zeta)}\frac{p_2(\xi,\zeta)}{\sinh\left[p_2(\xi,\zeta)t\right]}\right\}$$
$$\cosh\left[p_2(y+t)\right]e^{j\xi x}d\xi$$
$$=-\frac{j}{N_{21}^2}\frac{\zeta_p\Delta\zeta\tilde{L}_g(\zeta_p)}{\int_{-\infty}^{\infty}\tilde{\eta}^2(\xi')\tilde{\tilde{C}}_{zz}(\xi',\zeta_p+\Delta\zeta)d\xi'}\sin(\zeta_p z)$$
$$\int_{-\infty}^{\infty}d\xi\tilde{\eta}(\xi)\left\{\frac{\left(N_{21}^2-1\right)}{Z^h(\xi,\zeta)Z^e(\xi,\zeta)}\frac{\left(\xi^2+\zeta^2\right)}{\cosh(p_2t)}+\frac{1}{Z^h(\xi,\zeta)}\frac{p_2(\xi,\zeta)}{\sinh\left[p_2(\xi,\zeta)t\right]}\right\}$$
$$\cosh\left[p_2(y+t)\right]e^{j\xi x}\Big|_{\zeta=\zeta_p}$$

Then, the film field contributed by $\mathrm{Re}\{\zeta\}$-axis inversion contour integration becomes

$$E_{2y}(\boldsymbol{r}) = \frac{1}{\pi N_{21}^2}\int_0^\infty d\zeta \frac{\zeta \tilde{L}_g(\zeta)}{\int_{-\infty}^{\infty}\tilde{\eta}^2(\xi')\tilde{\tilde{C}}_{zz}(\xi',\zeta)d\xi'}\sin(\zeta z)$$
$$\int_{-\infty}^{\infty}\tilde{\eta}(\xi)\left\{\frac{\left(N_{21}^2-1\right)}{Z^h(\xi,\zeta)Z^e(\xi,\zeta)}\frac{\left(\xi^2+\zeta^2\right)}{\cosh(p_2 t)}+\frac{1}{Z^h(\xi,\zeta)}\frac{p_2(\xi,\zeta)}{\sinh\left[p_2(\xi,\zeta)t\right]}\right\}$$
$$\cosh\left[p_2(y+t)\right]e^{j\xi x}d\xi$$
$$-\frac{j}{N_{21}^2}\frac{\zeta_p\Delta\zeta\tilde{L}_g(\zeta_p)}{\int_{-\infty}^{\infty}\tilde{\eta}^2(\xi')\tilde{\tilde{C}}_{zz}(\xi',\zeta_p+\Delta\zeta)d\xi'}\sin(\zeta_p z)$$
$$\int_{-\infty}^{\infty}d\xi\tilde{\eta}(\xi)\left\{\frac{\left(N_{21}^2-1\right)}{Z^h(\xi,\zeta)Z^e(\xi,\zeta)}\frac{\left(\xi^2+\zeta^2\right)}{\cosh(p_2 t)}+\frac{1}{Z^h(\xi,\zeta)}\frac{p_2(\xi,\zeta)}{\sinh\left[p_2(\xi,\zeta)t\right]}\right\}$$
$$\cosh\left[p_2(y+t)\right]e^{j\xi x}\Big|_{\zeta=\zeta_p}$$

Numerical results for validating Eqn. (6.2.43) will be presented in Section 6.3.

Alternatively, the film field can also be formulated in the complex λ-plane rather than in the complex ξ- and ζ-planes (see Appendix G).

6.2.3 NORMAL BOUNDARY CONDITION

One of the reasons to choose the y-component electric field is that it is convenient to match the boundary condition for that normal field at the interface $y=0$, i.e., the normal component difference at the interface $y=0$ is proportional to the charge distribution along the interface. The charge distribution is also determined by the current distribution along the interface. Since the Maxwellian transverse current distribution is assumed,

$$\varepsilon_1 E_{1y}(\boldsymbol{r}) - \varepsilon_2 E_{2y}(\boldsymbol{r})\Big|_{y=0} = \varepsilon_0 \left[n_1^2 E_{1y}(\boldsymbol{r}) - n_2^2 E_{2y}(\boldsymbol{r}) \right]\Big|_{y=0}$$

$$= -\frac{j\varepsilon_0 n_1^2}{4\pi} \int_{-\infty}^{\infty} \frac{\zeta \tilde{L}_g(\zeta)}{\int_{-\infty}^{\infty} \tilde{\eta}^2(\xi') \tilde{\tilde{C}}_{zz}(\xi', \zeta) d\xi'} \int_{-\infty}^{\infty} d\xi \Big(\tilde{\eta}(\xi)$$

$$\left(\left\{ \left(\xi^2 + \zeta^2 \right) C_{1r}(\xi, \zeta) - \frac{2 p_1^2(\xi, \zeta)}{Z^h(\xi, \zeta)} \right\} \frac{1}{p_1(\xi, \zeta)} - \right.$$

$$\left. \left\{ \frac{2\left(N_{21}^2 - 1 \right)\left(\xi^2 + \zeta^2 \right)}{Z^h Z^e} \frac{}{\cosh(p_2 t)} + \frac{2}{Z^h} \frac{p_2}{\sinh(p_2 t)} \right\} \cosh(p_2 t) \right)$$

$$e^{j\xi x} \Big) e^{j\zeta z} d\zeta$$

$$= -\frac{j\varepsilon_0 n_1^2}{4\pi} \int_{-\infty}^{\infty} \frac{\zeta \tilde{L}_g(\zeta)}{\int_{-\infty}^{\infty} \tilde{\eta}^2(\xi') \tilde{\tilde{C}}_{zz}(\xi', \zeta) d\xi'} \int_{-\infty}^{\infty} d\xi \Big(\tilde{\eta}(\xi)$$

$$\left\{ -\frac{2 p_1(\xi, \zeta)}{Z^h(\xi, \zeta)} - \frac{2 p_2(\xi, \zeta)}{Z^h(\xi, \zeta)} \coth\left[p_2(\xi, \zeta) t \right] \right\}$$

$$e^{j\xi x} \Big) e^{j\zeta z} d\zeta$$

$$= -\frac{j\varepsilon_0 n_1^2}{4\pi} \int_{-\infty}^{\infty} \frac{\zeta \tilde{L}_g(\zeta)}{\int_{-\infty}^{\infty} \tilde{\eta}^2(\xi') \tilde{\tilde{C}}_{zz}(\xi', \zeta) d\xi'} \int_{-\infty}^{\infty} d\xi \Big(\tilde{\eta}(\xi)$$

$$\left(-2 \frac{\overbrace{p_1(\xi, \zeta) + p_2(\xi, \zeta) \coth\left[p_2(\xi, \zeta) t \right]}^{= Z^h(\xi, \zeta)}}{Z^h(\xi, \zeta)} \right)$$

$$e^{j\xi x} \Big) e^{j\zeta z} d\zeta$$

$$= \frac{j\varepsilon_0 n_1^2}{2\pi} \int_{-\infty}^{\infty} \frac{\zeta \tilde{L}_g(\zeta)}{\int_{-\infty}^{\infty} \tilde{\eta}^2(\xi') \tilde{\tilde{C}}_{zz}(\xi', \zeta) d\xi'} \int_{-\infty}^{\infty} \tilde{\eta}(\xi) e^{j\xi x} d\xi$$

$$e^{j\zeta z} d\zeta$$

Finally this leads [18] to

$$\varepsilon_1 E_{1y}(\boldsymbol{r}) - \varepsilon_2 E_{2y}(\boldsymbol{r})\Big|_{y=0} = \frac{j\varepsilon_0 n_1^2}{2\pi}\int_{-\infty}^{\infty} \frac{\zeta \tilde{L}_g(\zeta)}{\int_{-\infty}^{\infty} \tilde{\eta}^2(\xi')\tilde{\tilde{C}}_{zz}(\xi',\zeta)d\xi'} \int_{-\infty}^{\infty} \tilde{\eta}(\xi) e^{j\xi x} d\xi$$

$$e^{j\zeta z} d\zeta$$

$$= \begin{cases} j\varepsilon_0 n_1^2 \eta(x) \int_{-\infty}^{\infty} \dfrac{\zeta \tilde{L}_g(\zeta)}{\int_{-\infty}^{\infty} \tilde{\eta}^2(\xi')\tilde{\tilde{C}}_{zz}(\xi',\zeta)d\xi'} e^{j\zeta z} d\zeta \cdots |x| < w/2 \\ 0 \cdots |x| > w/2 \end{cases}$$

where

$$\eta(x) = \begin{cases} \dfrac{1}{\pi(w/2)\sqrt{1-\left[x/(w/2)\right]^2}} \cdots w/t < 2 \\ \dfrac{1}{w} \cdots w/t \geq 2 \end{cases}$$

(6.2.48)

It can also be numerically validated as depicted in Fig. 6.2.9. It is noted that $x/w = \pm .5$ locates each transverse edge of the conducting microstrip and the well-known edge condition is observed to be satisfied.

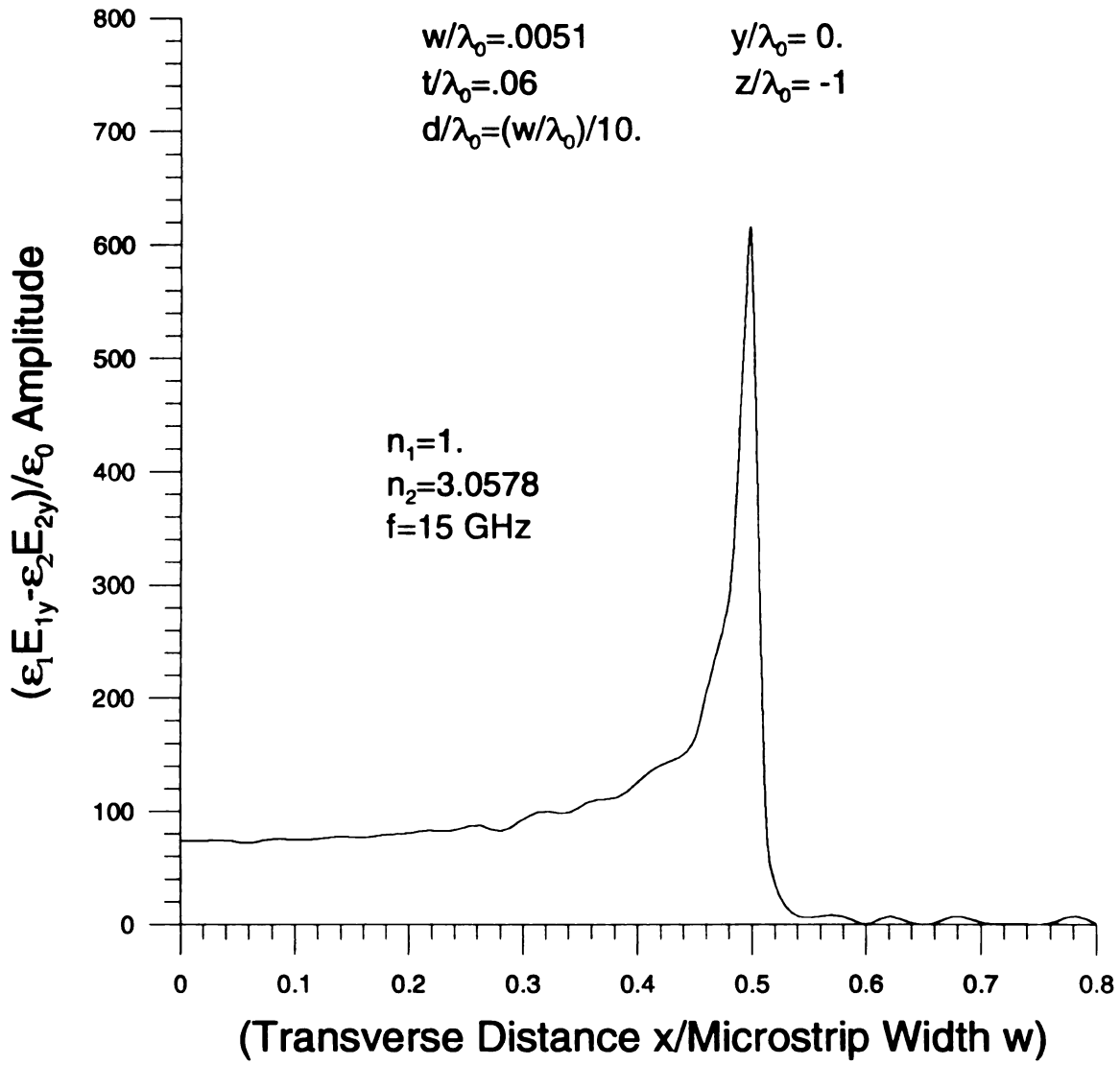

Figure 6.2.9 Maxwellian transverse distribution to be matched with the normal electric field component difference at the interface $y = 0$.

6.3 NUMERICAL RESULTS

Extensive numerical results were obtained. Fig. 6.3.1 depicts the continuous, discrete and total cover field amplitudes, respectively, transversely in the near zone. The total cover field is dominated transversely by the continuous field and decays slowly. The discrete cover field contribution is transversely almost negligible. Figs. 6.3.2, 6.3.3 and 6.3.4 depict the continuous, discrete and total cover field phases, respectively, transversely in the near zone. Similarly, Fig. 6.3.5 depicts the continuous, discrete and total cover field amplitudes, respectively, transversely away from the near zone. The total cover field is still dominated transversely by the continuous cover field and decays slowly. Figs. 6.3.6, 6.3.7 and 6.3.8 depict the continuous, discrete and total cover field phases, respectively, transversely away from the near zone. Fig. 6.3.9 depicts the continuous, discrete and total cover field amplitudes, respectively, vertically in the near zone. The total cover field is dominated vertically by the continuous field and decays exponentially. Figs. 6.3.10, 6.3.11 and 6.3.12 depict the continuous, discrete and total cover field phases, respectively, vertically in the near zone. As depicted in Fig. 6.3.11, the discrete cover field in the near zone ascends vertically up from the conducting microstrip and reverses its direction to descend down to the conducting microstrip. The total field phase is depicted in Fig. 6.3.12. Fig. 6.3.13 depicts the continuous, discrete and total cover field amplitudes vertically away from the near zone. The total cover field is dominated vertically by the continuous field and decays exponentially. Figs. 6.3.14, 6.3.15 and 6.3.16 depict the continuous, discrete and total cover field phases, respectively, vertically away from the near zone. As depicted in Fig. 6.3.14, the continuous cover field is vertically propagating, while the phase of the discrete cover field is vertically constant

in Fig. 6.3.15. The total field phase is depicted in Fig. 6.3.16. Fig. 6.3.17 depicts the continuous, discrete and total cover field amplitudes longitudinally in the near zone. The total cover field is dominated longitudinally by the continuous field and decays exponentially. Figs. 6.3.18, 6.3.19 and 6.3.20 depict the continuous, discrete and total cover field phases, respectively, longitudinally in the near zone. The continuous cover field is slowly longitudinally lagging as depicted in Fig. 6.3.18 and the discrete cover field is longitudinally propagating as depicted in Fig. 6.3.19. The total field phase is depicted in Fig. 6.3.20. Fig. 6.3.21 depicts the continuous, discrete and total cover field amplitudes longitudinally away from the near zone. The total cover field is dominated longitudinally by the continuous cover field and decays oscillatorily due to interference of discrete and continuous spectra and exponentially. Both of the continuous and discrete cover fields are longitudinally propagating as depicted in Figs. 6.3.22 and 6.3.23 and the total field phase is depicted in Fig. 6.3.24. More importantly, the total cover field is validated by the $\mathrm{Re}\{\zeta\}$-axis inversion integration longitudinally in the near zone as depicted in Figs. 6.3.25 and 6.3.26 and by the $\mathrm{Re}\{\zeta\}$-axis inversion integration longitudinally away from the near zone as depicted in Figs. 6.3.27 and 6.3.28.

Fig. 6.3.29 depicts the continuous, discrete and total film field amplitudes, respectively, transversely in the near zone. The total film field is dominated transversely by the continuous field. Figs. 6.3.30, 6.3.31 and 6.3.32 depict the continuous, discrete and total film field phases, respectively, transversely in the near zone. Fig. 6.3.33 depicts the continuous, discrete and total film field amplitudes, respectively, transversely away from the near zone. Even if the continuous and discrete film fields are transversely comparable each other, the total film field is dominated transversely by the continuous

film field. Figs. 6.3.34, 6.3.35 and 6.3.36 depict the continuous, discrete and total film field phases, respectively, transversely away from the near zone. The total field phase is depicted in Fig. 6.3.36. Fig. 6.3.37 depicts the continuous, discrete and total film field amplitudes, respectively, vertically in the near zone. The continuous film field is initially vertically decreasing exponentially but subsequently increasing steadily, while the discrete film field is vertically decreasing. As depicted in Fig. 6.3.37, the total film field is dominated vertically by the continuous field. Figs. 6.3.38, 6.3.39 and 6.3.40 depict the continuous, discrete and total film field phases, respectively, vertically in the near zone. The continuous film field undergoes 180° phase shift at the point where amplitude passes through a minimum as depicted in Figs. 6.3.37 and 6.3.38. The total film field behaves similarly as depicted in Figs 6.3.37 and 6.3.40. Fig. 6.3.41 depicts the continuous, discrete and total film field amplitudes, respectively, vertically away from the near zone. The continuous film field is vertically decreasing followed by a slight increase, while the discrete film field is decreasing vertically. As depicted in Fig. 6.3.41, it is not quite clear within $y/\lambda_0 \approx .03$ that the total film field is dominated vertically by the continuous field but beyond that region the continuous field dominates. Figs. 6.3.42, 6.3.43 and 6.3.44 depict the continuous, discrete and total film field phases, respectively, vertically away from the near zone. The continuous film field phase is vertically smoothly changing where the amplitude begins to increase slightly as depicted in Figs. 6.3.41 and 6.3.42. The total film field behaves similarly as depicted in Figs 6.3.41 and 6.3.44. Again, Fig. 6.3.45 depicts the continuous, discrete and total film field amplitudes, respectively, vertically a little more away from the near zone. The continuous film field is steadily increasing vertically while the discrete field is decreasing. As indicated in Fig.

6

6.

ve

ste

fie

is c

the

Fig.

in tl

field

cont

zone

the d

field

total

cove

the d

oscil

film

longi

const

begin

are lo

6.3.45, the total film field is dominated vertically by the continuous field. Figs. 6.3.46, 6.3.47 and 6.3.48 depict the continuous, discrete and total film field phases, respectively, vertically a little more away from the near zone. Since the continuous film field is steadily increasing vertically (therefore so is the total film field) and the discrete film field is decreasing, the corresponding phases are relatively constant. The total field phase is depicted in Fig. 6.3.48. Additionally, the total film field in Fig. 6.3.45 is validated by the $\mathrm{Re}\{\zeta\}$-axis inversion integration vertically as depicted in Figs. 6.3.49 and 6.3.50. Fig. 6.3.51 depicts the continuous, discrete and total film field amplitudes longitudinally in the near zone. The total film field is dominated longitudinally by the continuous film field and decays rapidly and exponentially. Figs. 6.3.52, 6.3.53 and 6.3.54 depict the continuous, discrete and total film field phases, respectively, longitudinally in the near zone. The continuous film field is lagging longitudinally as depicted in Fig. 6.3.52 and the discrete film field is longitudinally propagating as depicted in Fig. 6.3.53. The total field phase is depicted in Fig. 6.3.54. Fig. 6.3.55 depicts the continuous, discrete and total film field amplitudes longitudinally away from the near zone. Unlike in the total cover field at locations longitudinally, the total film field is dominated longitudinally by the discrete field rather than by the continuous field and propagates longitudinally and oscillatorily due to interference of discrete and continuous spectra. Since the continuous film field amplitude is relatively smaller in the film layer than that in the cover layer and longitudinally decaying exponentially while the discrete film field is longitudinally constant, it is observed that approximately beyond $z/\lambda_0 \approx 1$. the discrete film field begins to dominate the total field longitudinally. The continuous and discrete film fields are longitudinally propagating as depicted in Figs. 6.3.56 and 6.3.57 and the total field

phase is depicted in Fig. 6.3.58. Fig. 6.3.59 depicts the continuous, discrete and total film field amplitudes, respectively, longitudinally approaching the far zone ($z/\lambda_0 = 10.$). The total film field is clearly dominated longitudinally by the discrete film field and propagates a little less oscillatorily. The continuous and discrete film fields are longitudinally propagating as depicted in Figs. 6.3.60 and 6.3.61 and the total film field phase is depicted in Figs. 6.3.62. Importantly, the total film field is validated by the $\mathrm{Re}\{\zeta\}$-axis inversion integration longitudinally in the near zone as depicted in Figs. 6.3.63 and 6.3.64 and by the $\mathrm{Re}\{\zeta\}$-axis inversion contour longitudinally away from the near zone as depicted in Figs. 6.3.65 and 6.3.66.

Fig

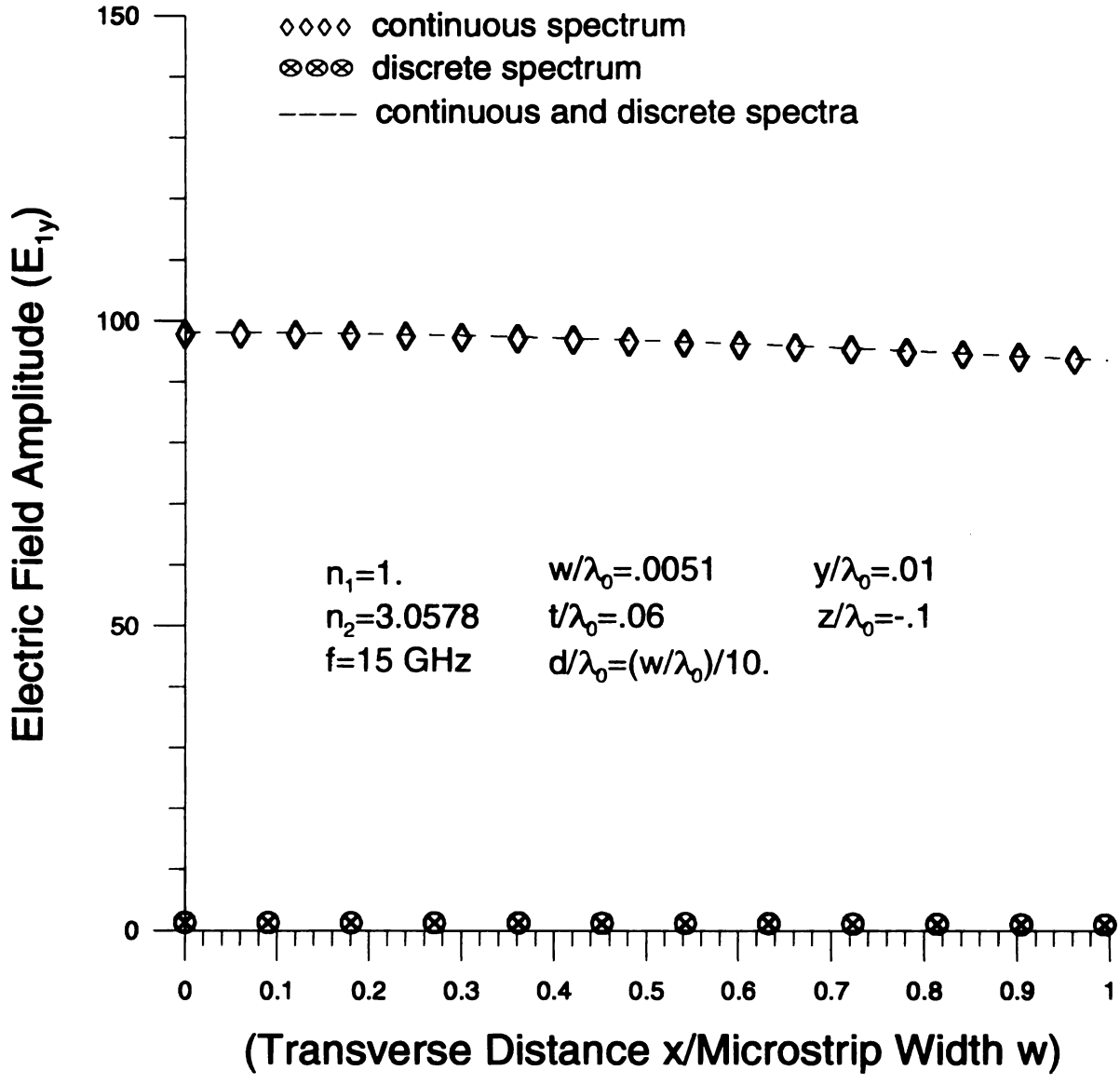

Figure 6.3.1 Transverse continuous and discrete electric cover field spectrum amplitudes profile in the low-loss limit.

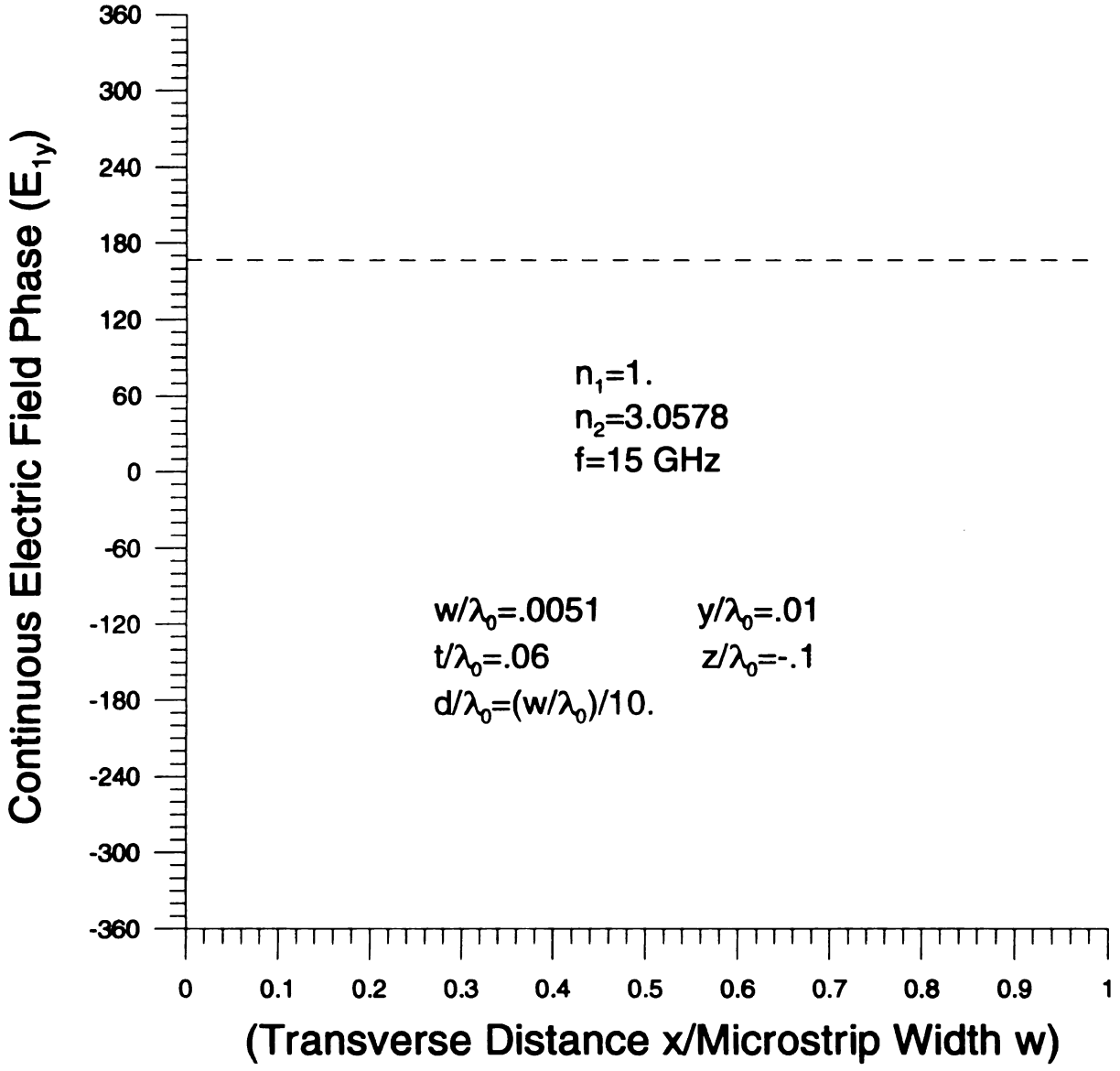

Figure 6.3.2 Transverse continuous electric cover field spectrum phase profile in the low-loss limit.

Discrete Fi

Figu

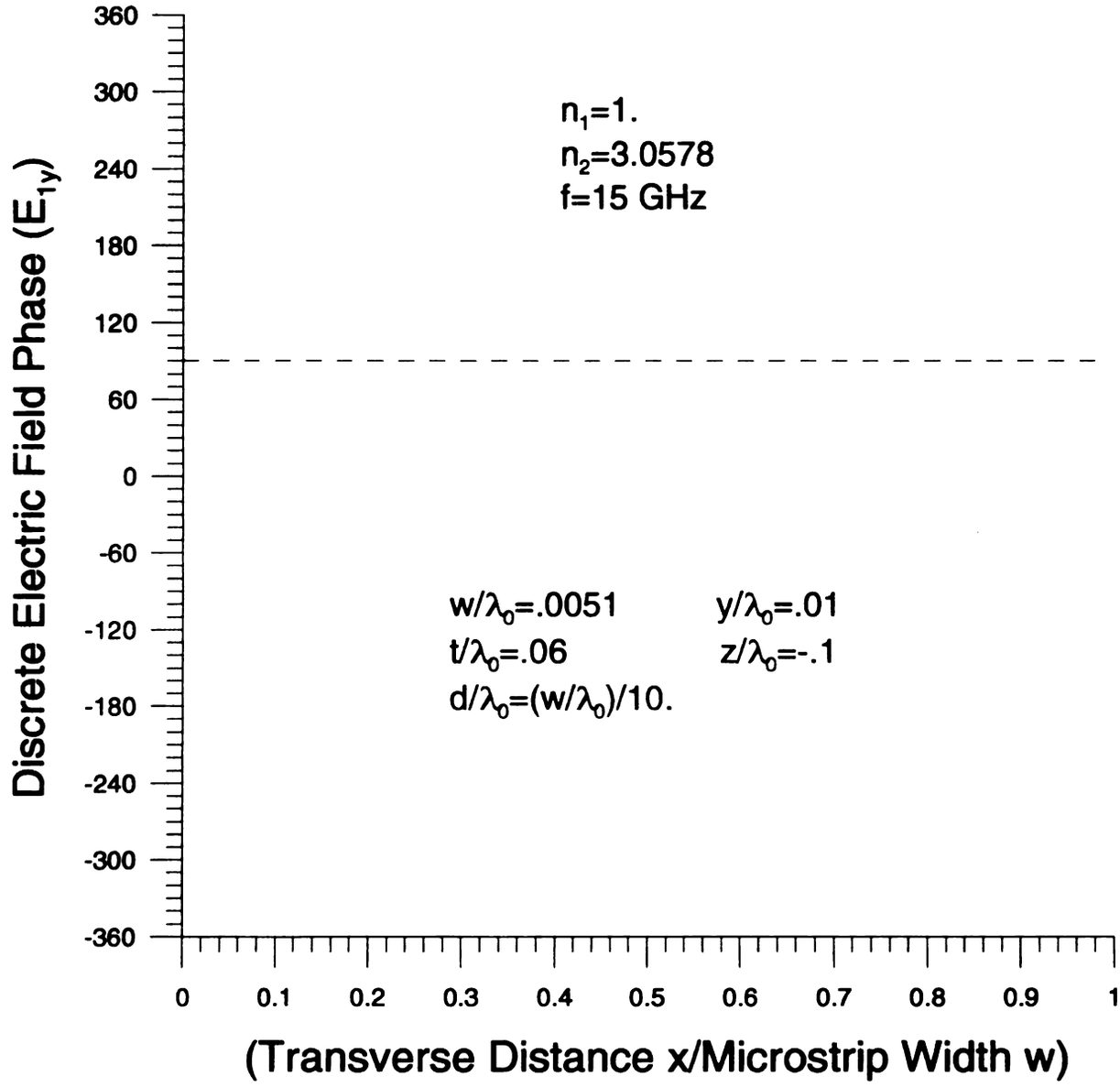

Figure 6.3.3 Transverse discrete electric cover field spectrum phase profile in the low-loss limit.

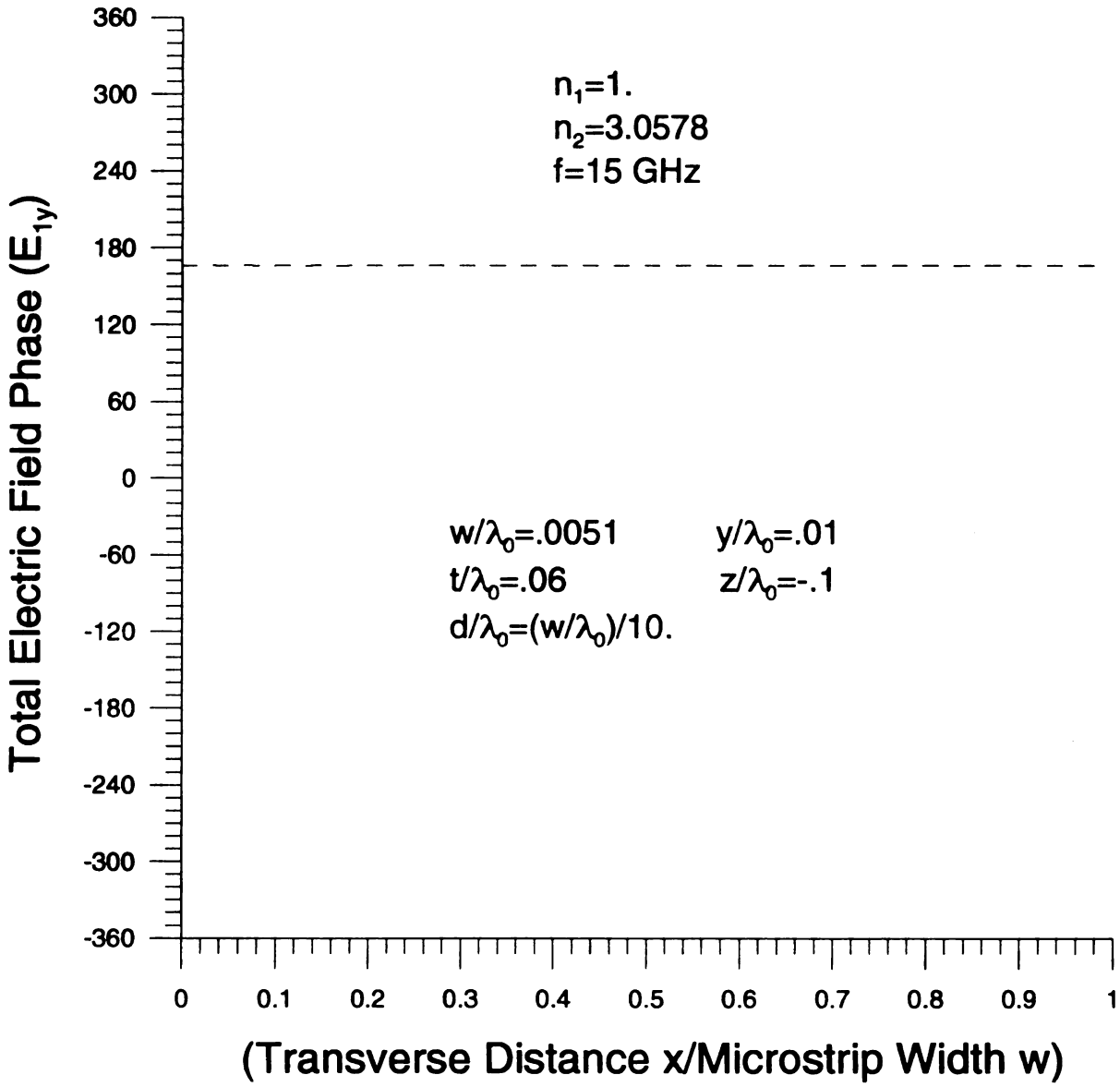

Figure 6.3.4 Transverse total electric cover field spectrum phase profile in the low-loss limit.

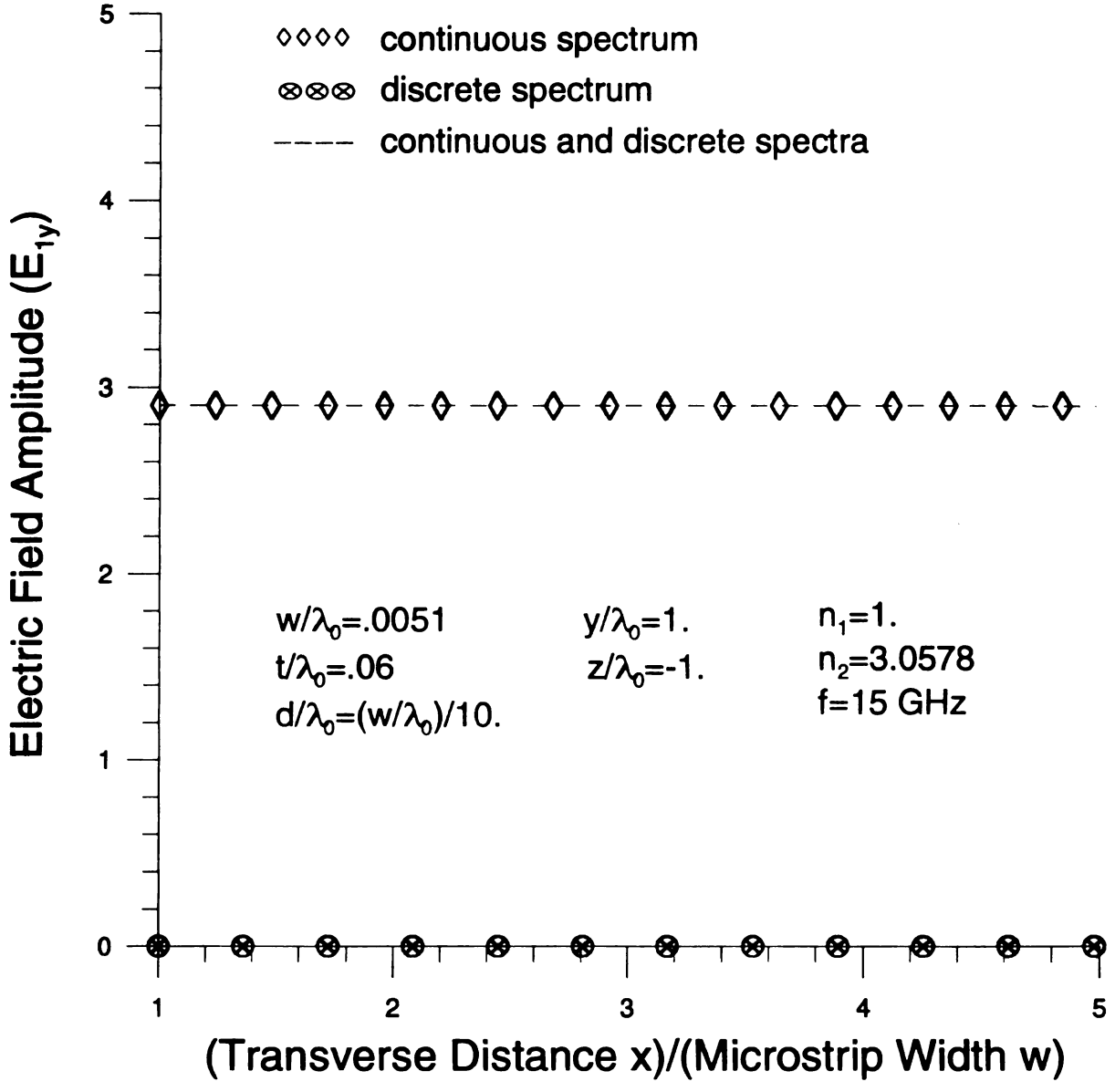

Figure 6.3.5 Transverse continuous and discrete cover electric field spectrum amplitude profiles in the low-loss limit.

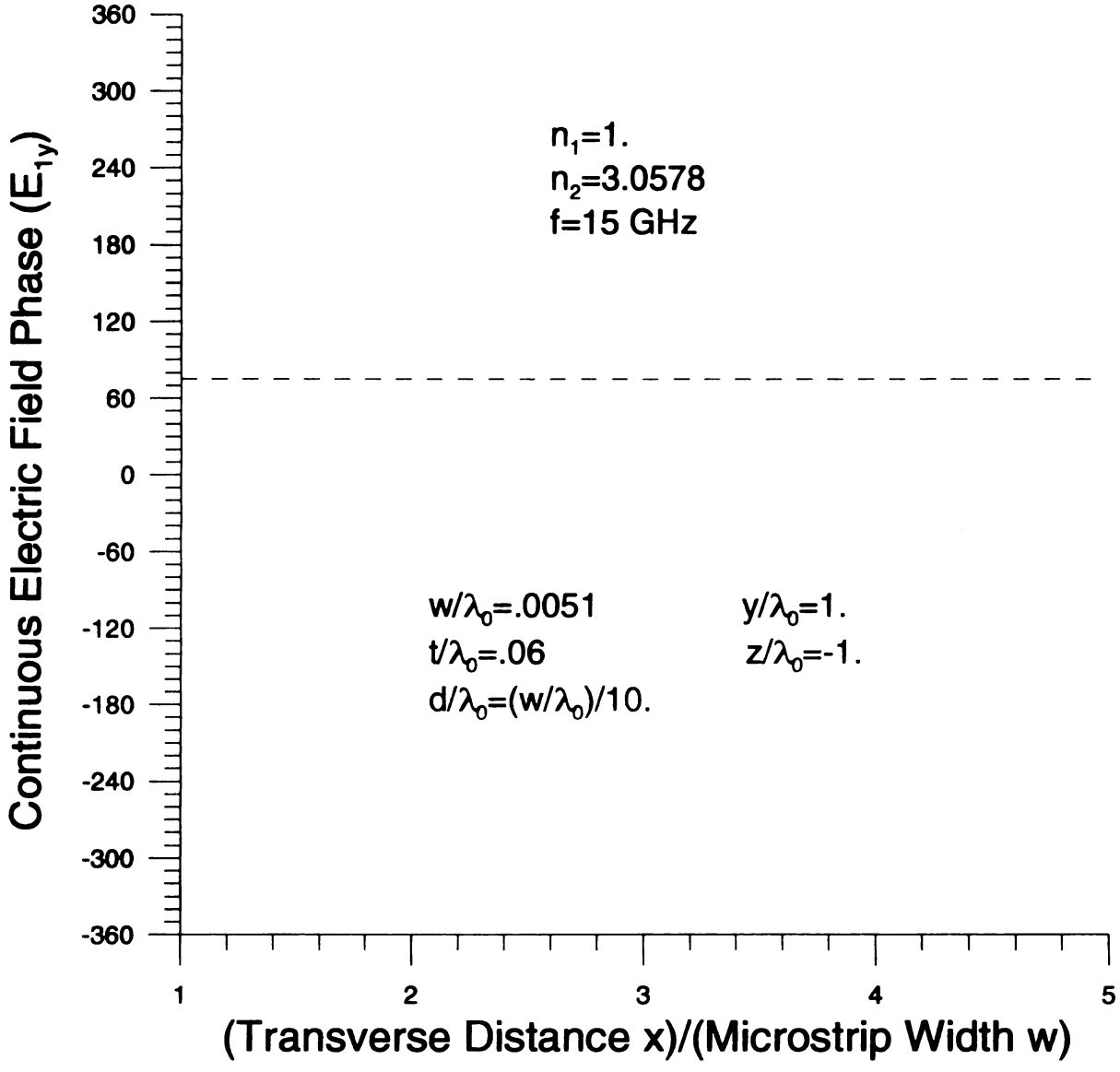

Figure 6.3.6 Transverse continuous electric cover field spectrum phase profile in the low-loss limit.

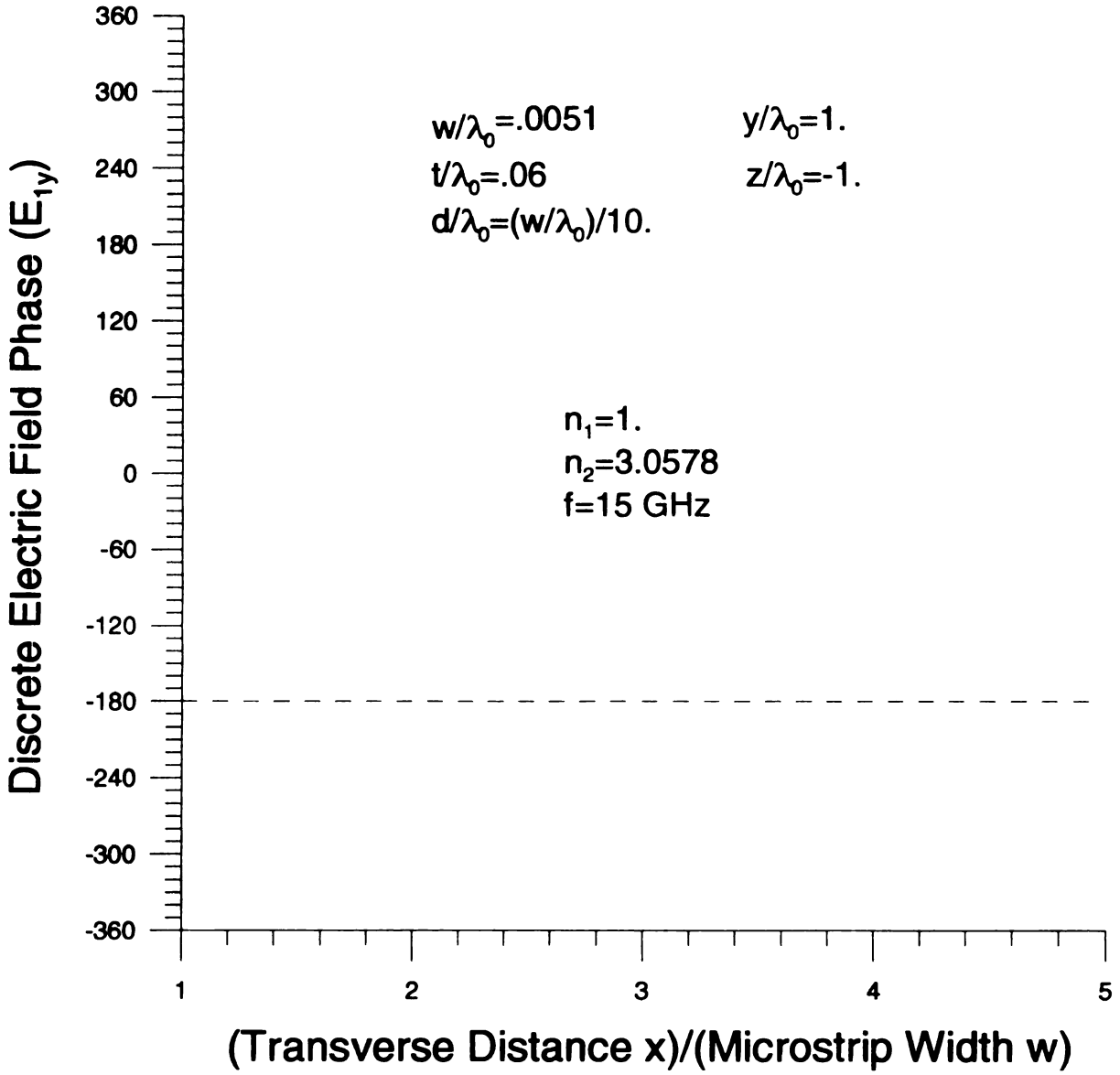

Figure 6.3.7 Transverse discrete electric cover field spectrum phase profile in the low-loss limit.

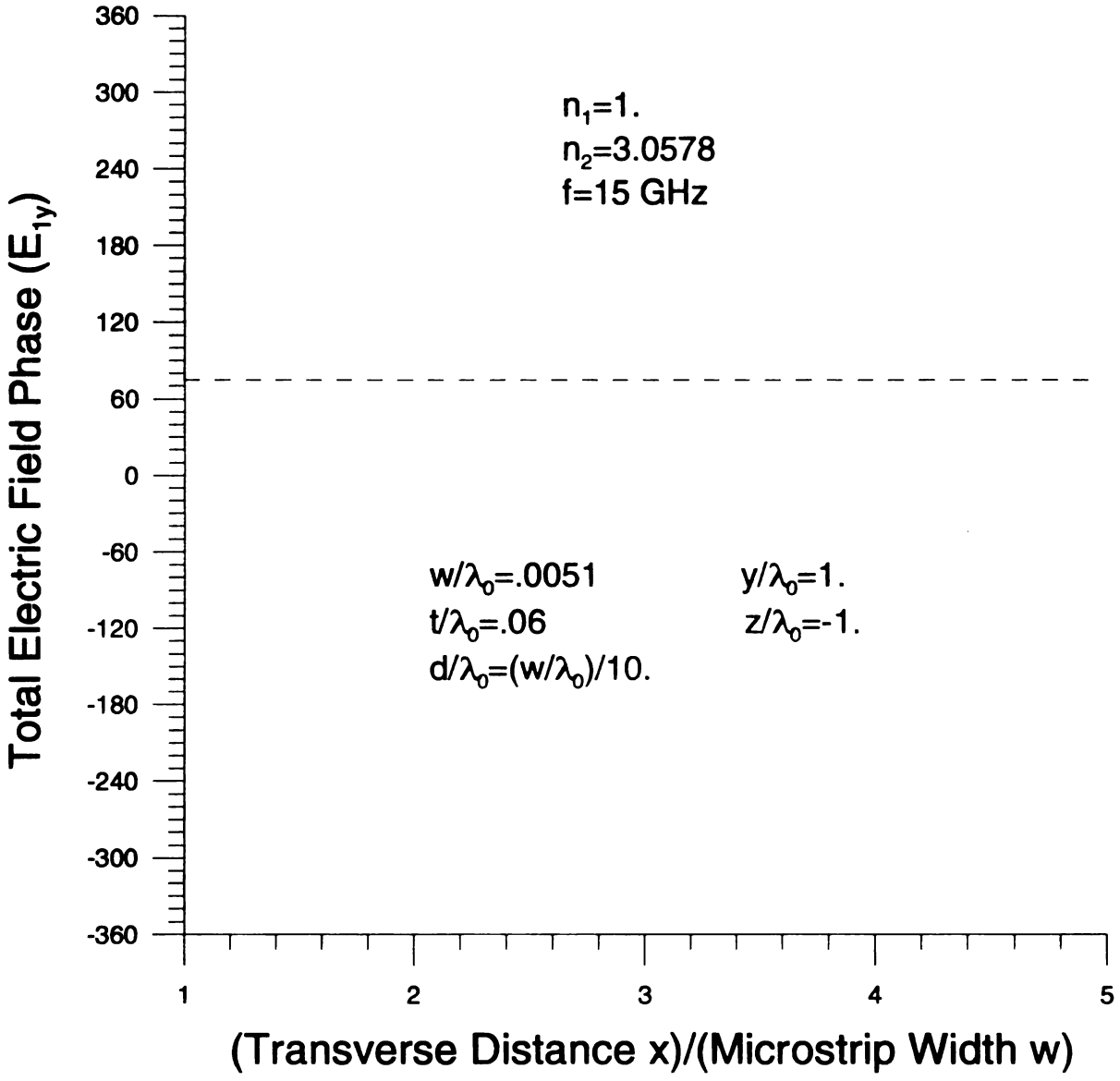

Figure 6.3.8 Transverse total electric cover field spectrum phase profile in the low-loss limit.

Electric Fie

Fig

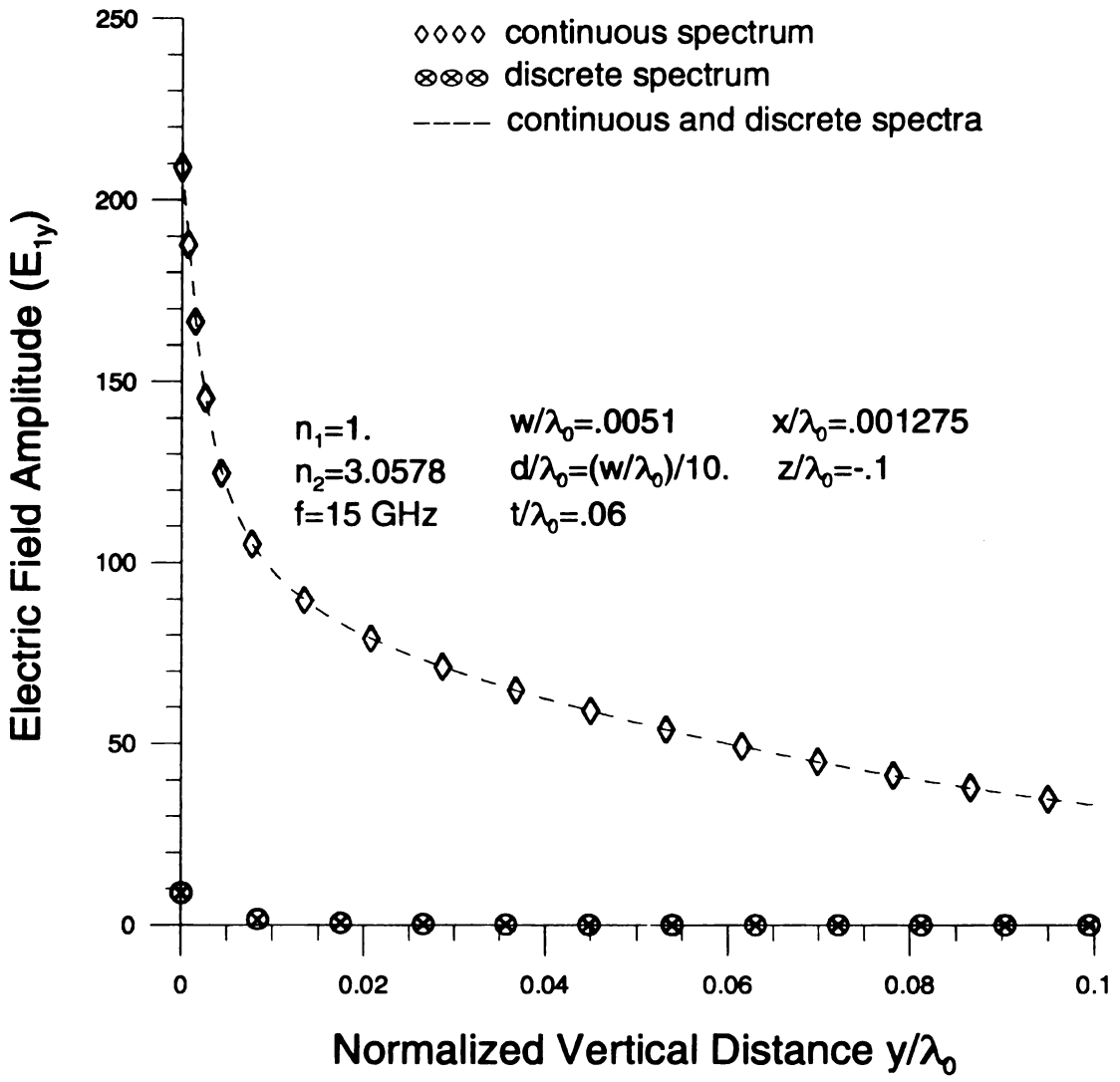

Figure 6.3.9 Vertical continuous and discrete electric cover field spectrum amplitudes profile in the low-loss limit.

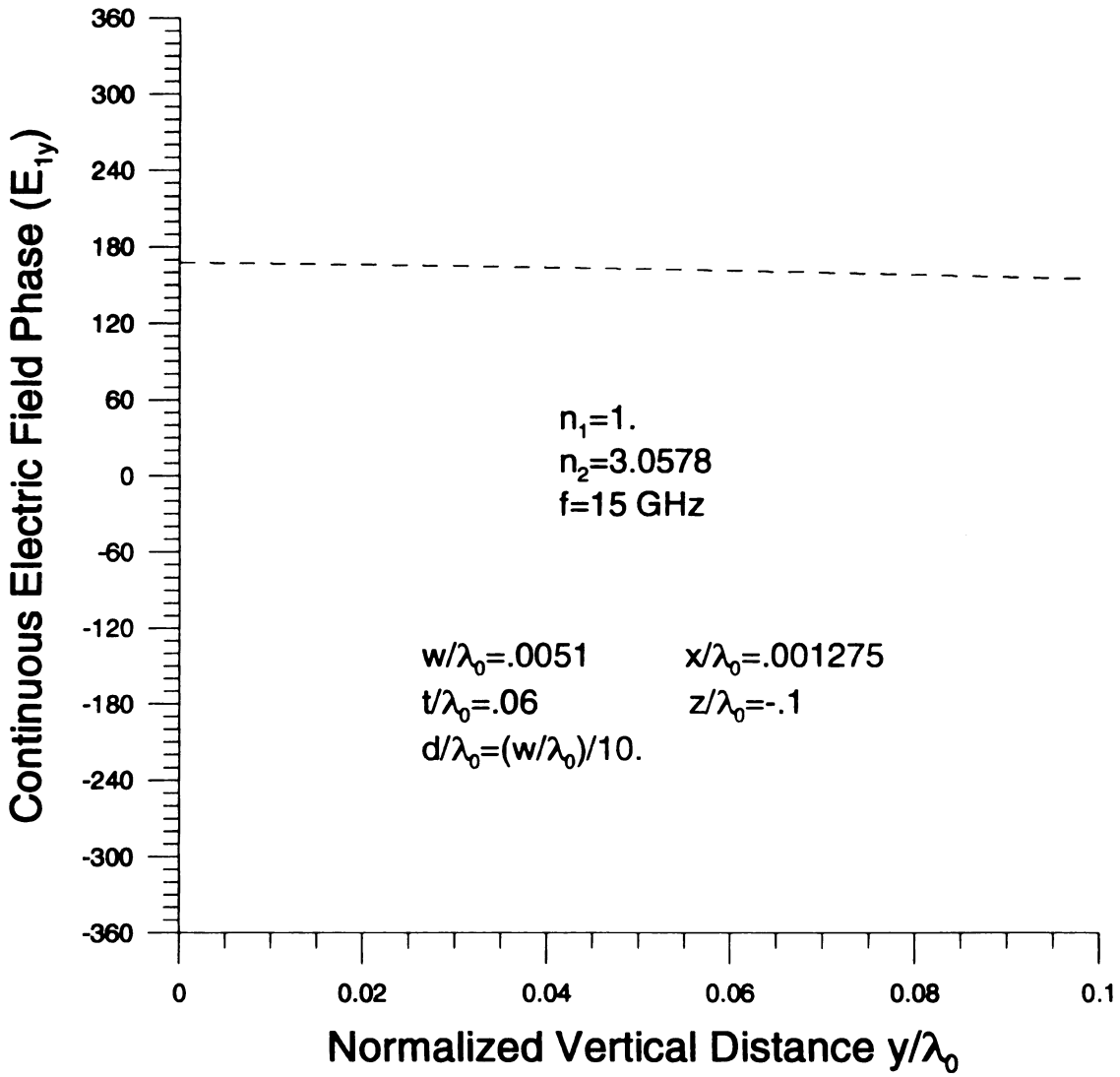

Figure 6.3.10 Vertical continuous electric cover field spectrum phase profile in the low-loss limit.

Discrete Electric Field Phase (E_x)

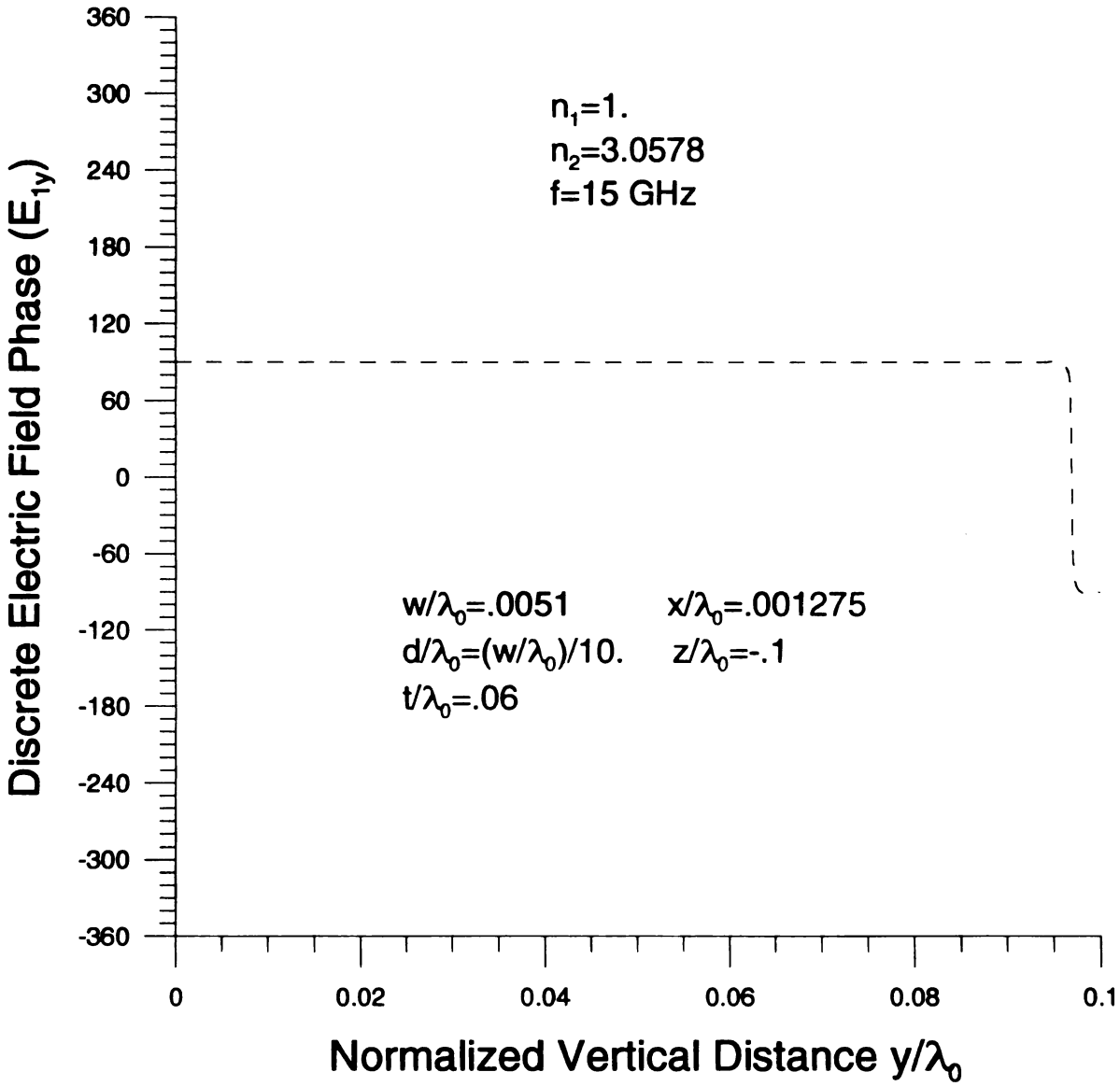

Figure 6.3.11 Vertical discrete electric cover field spectrum phase profile in the low-loss limit.

Total Electric Field Phase (E_x)

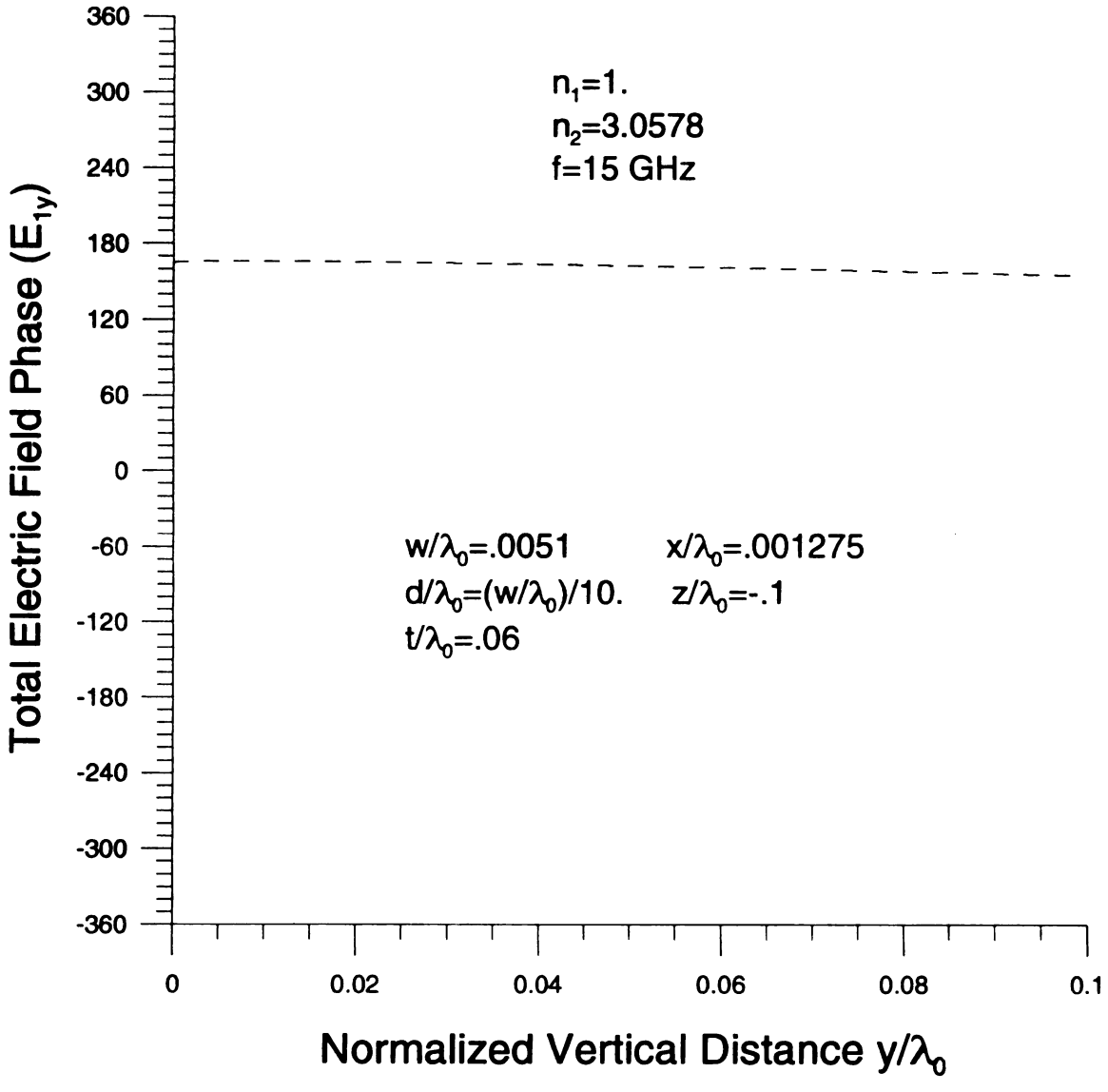

Figure 6.3.12 Vertical total electric cover field spectrum phase profile in the low-loss limit.

Electric Field Amplitude (E_x)

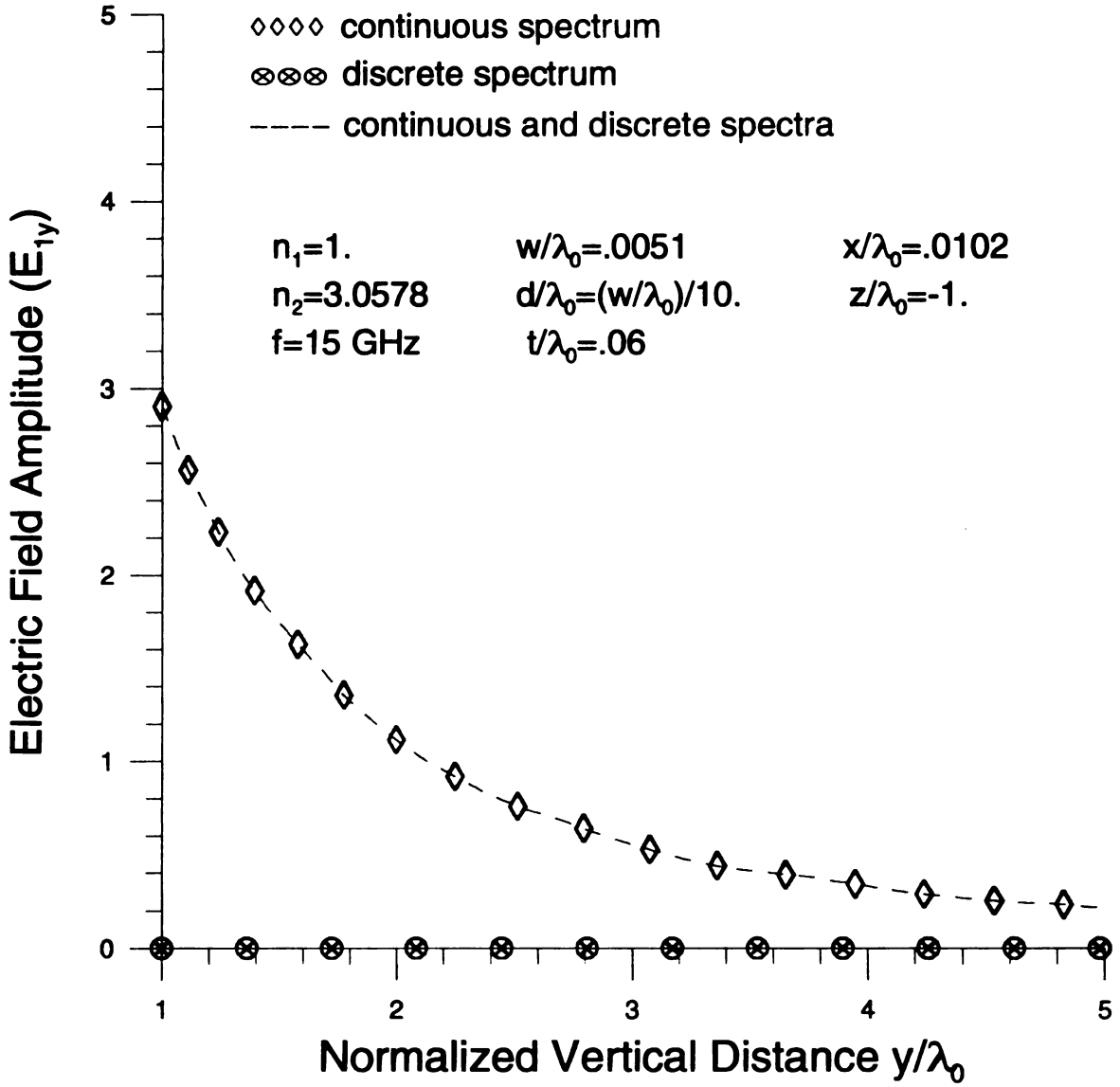

Figure 6.3.13 Vertical continuous and discrete electric cover field spectrum amplitudes profile in the low-loss limit.

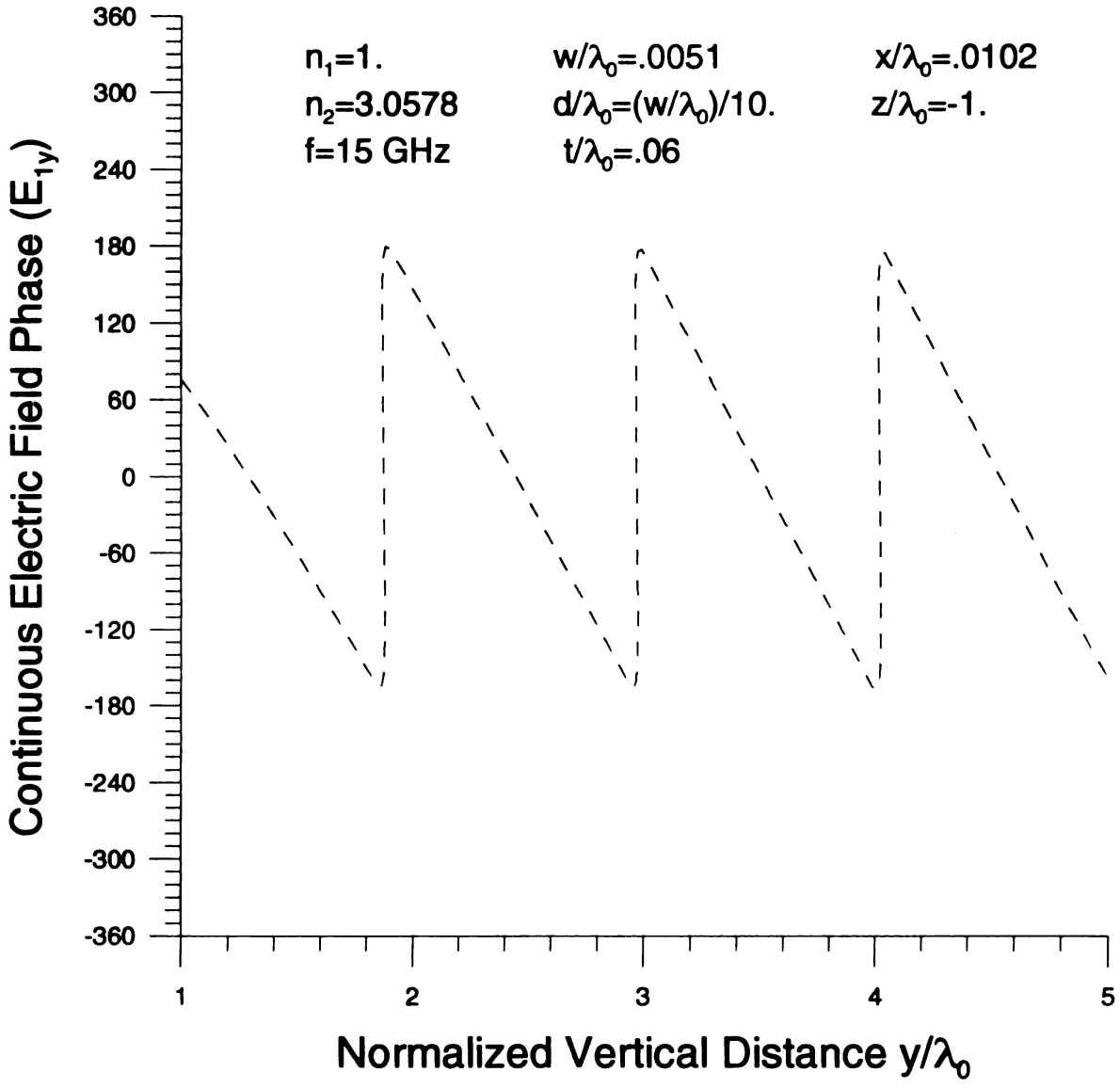

Figure 6.3.14 Vertical continuous electric cover field spectrum phase profile in the low-loss limit.

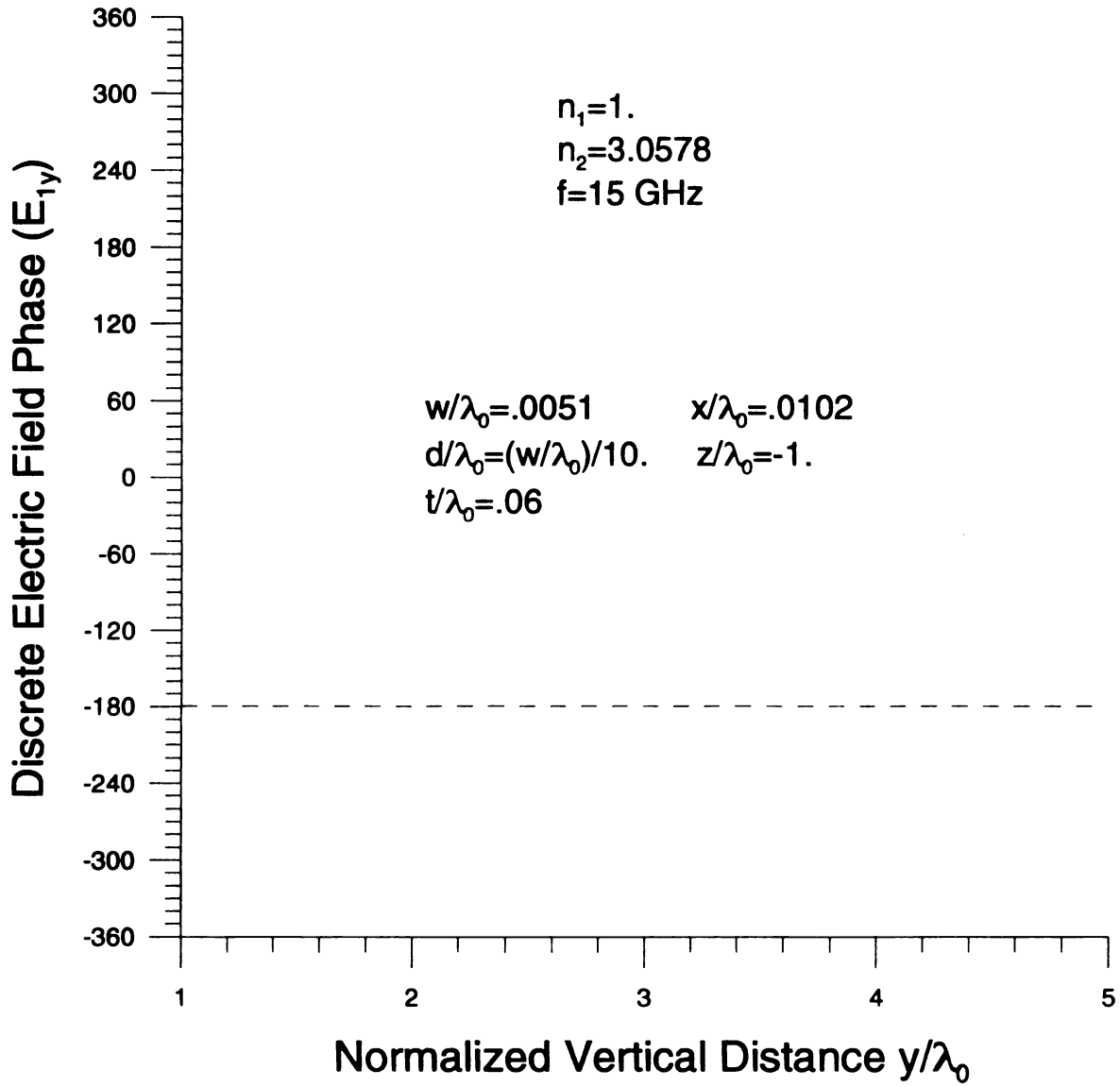

Figure 6.3.15 Vertical discrete electric cover field spectrum phase profile in the low-loss limit.

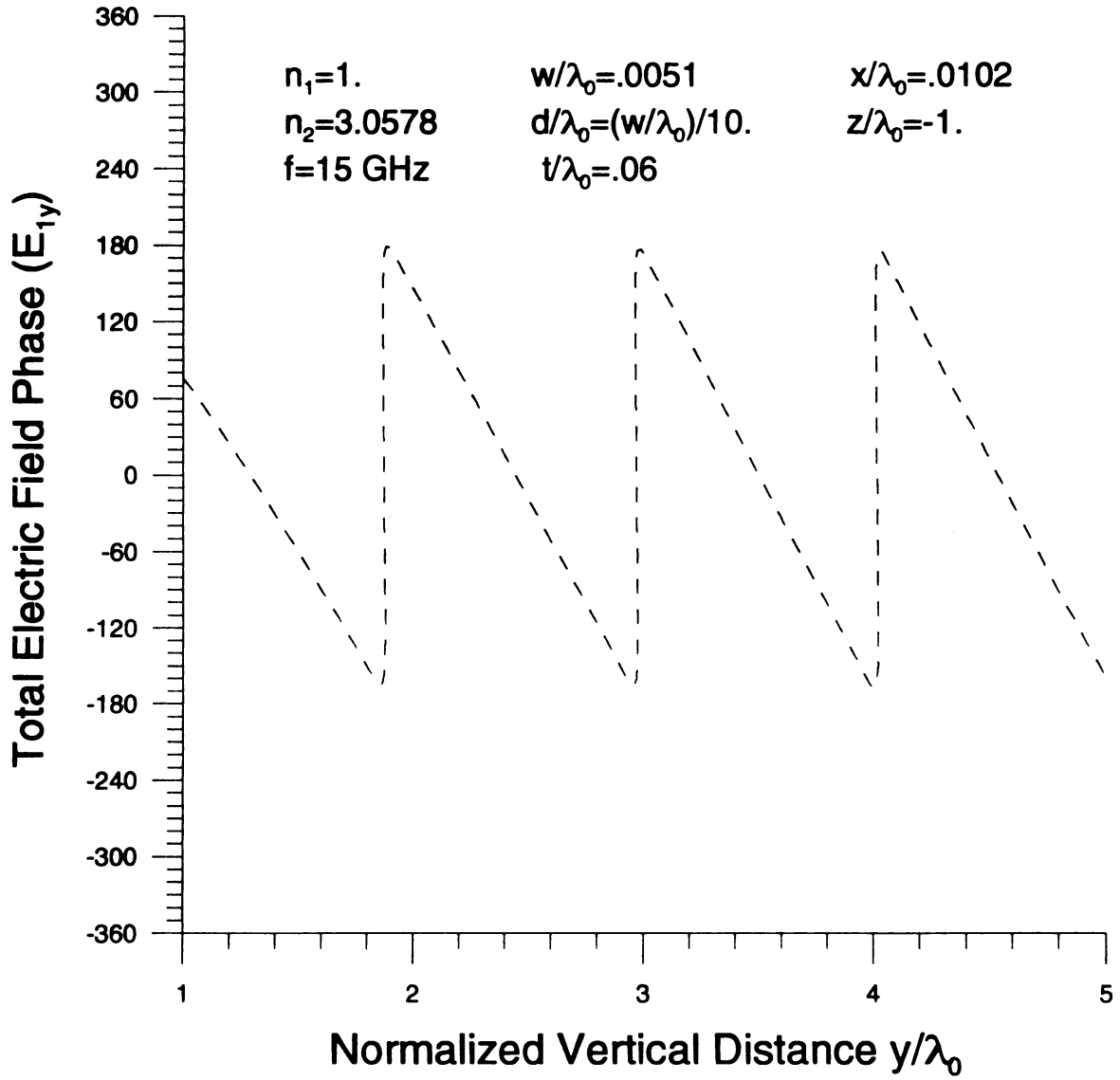

Figure 6.3.16 Vertical total electric cover field spectrum phase profile in the low-loss limit.

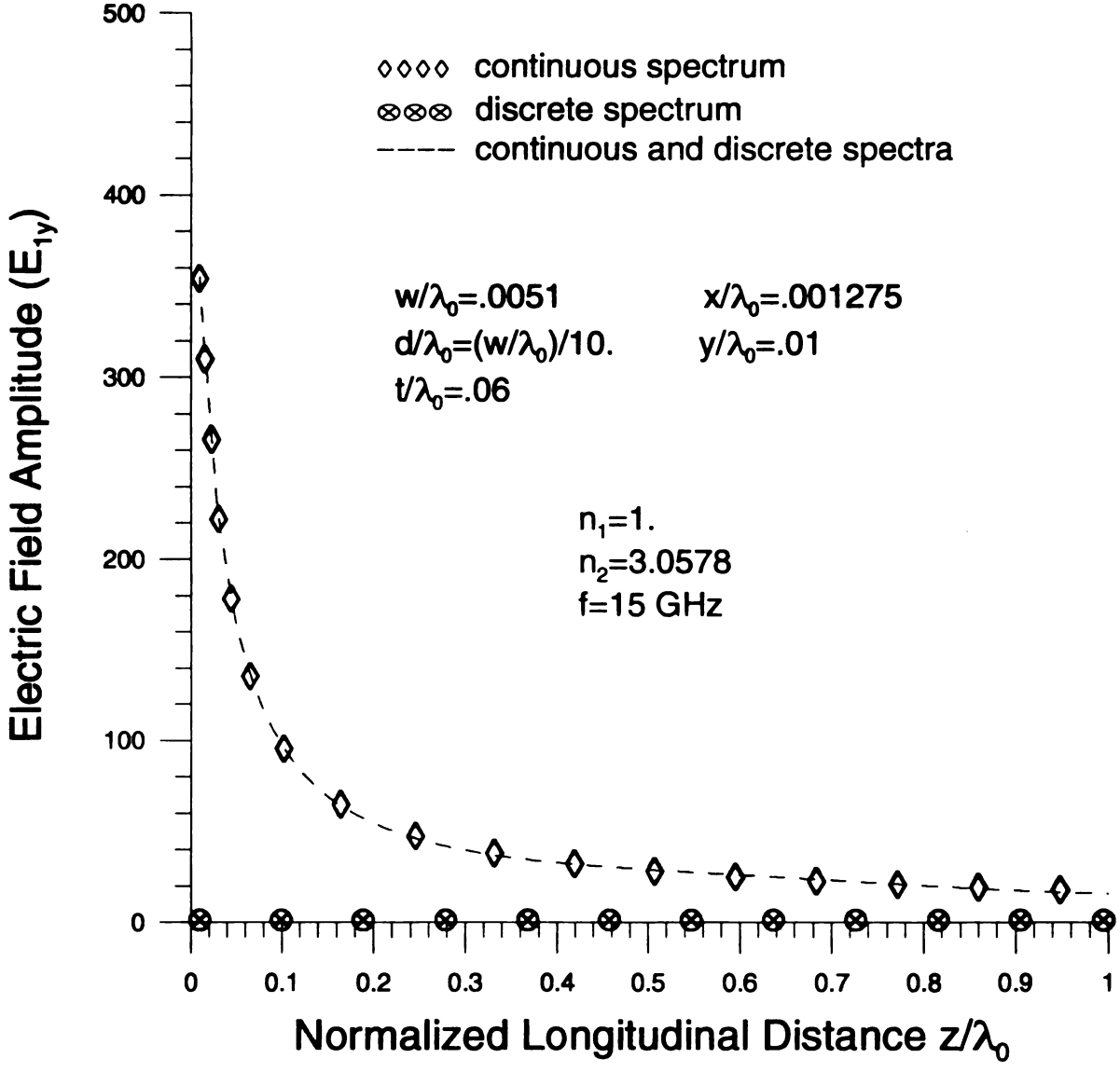

Figure 6.3.17 Longitudinal continuous and discrete electric cover field spectrum amplitudes profile in the low-loss limit.

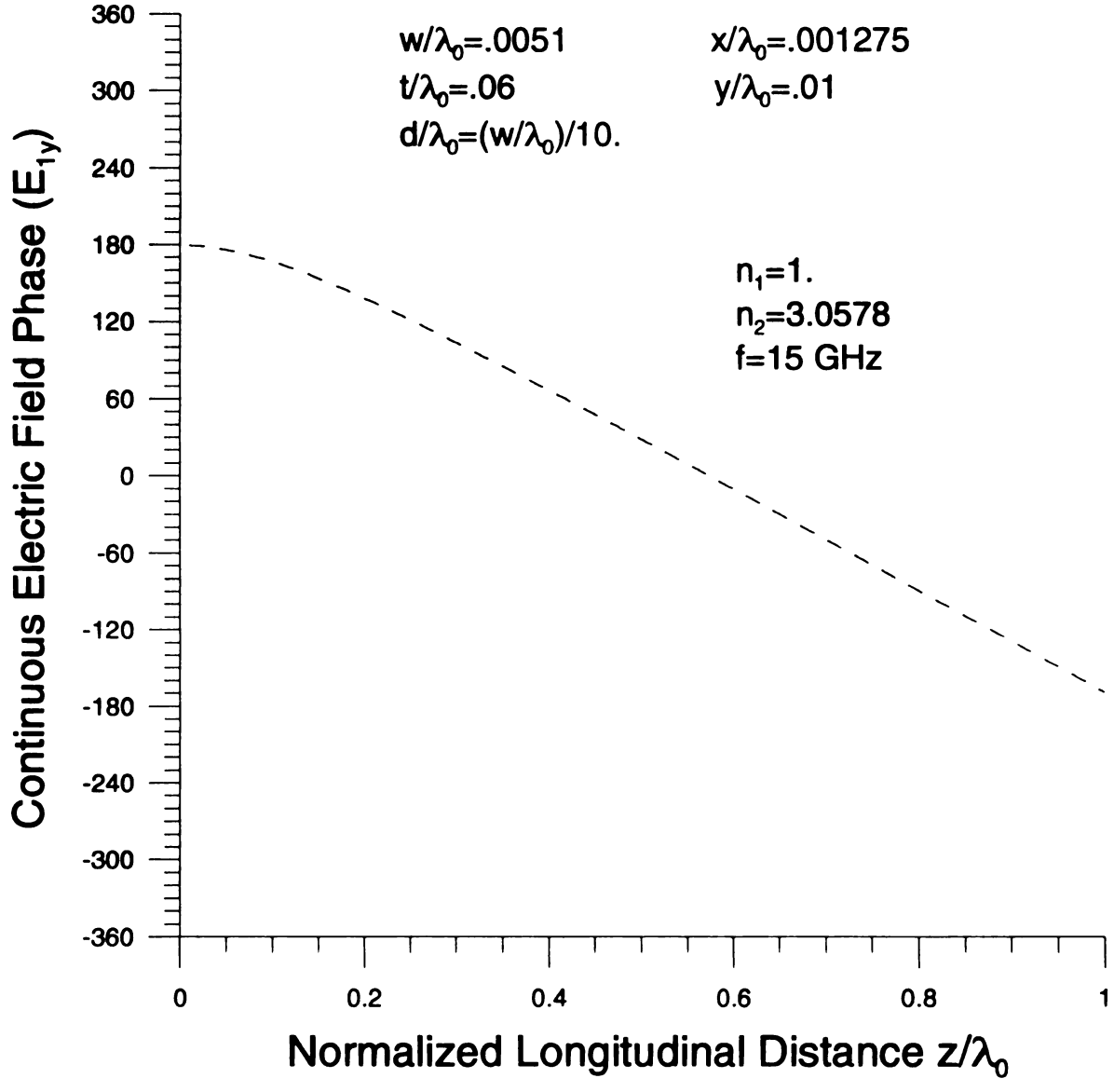

Figure 6.3.18 Longitudinal continuous electric cover field spectrum phase profile in the low-loss limit.

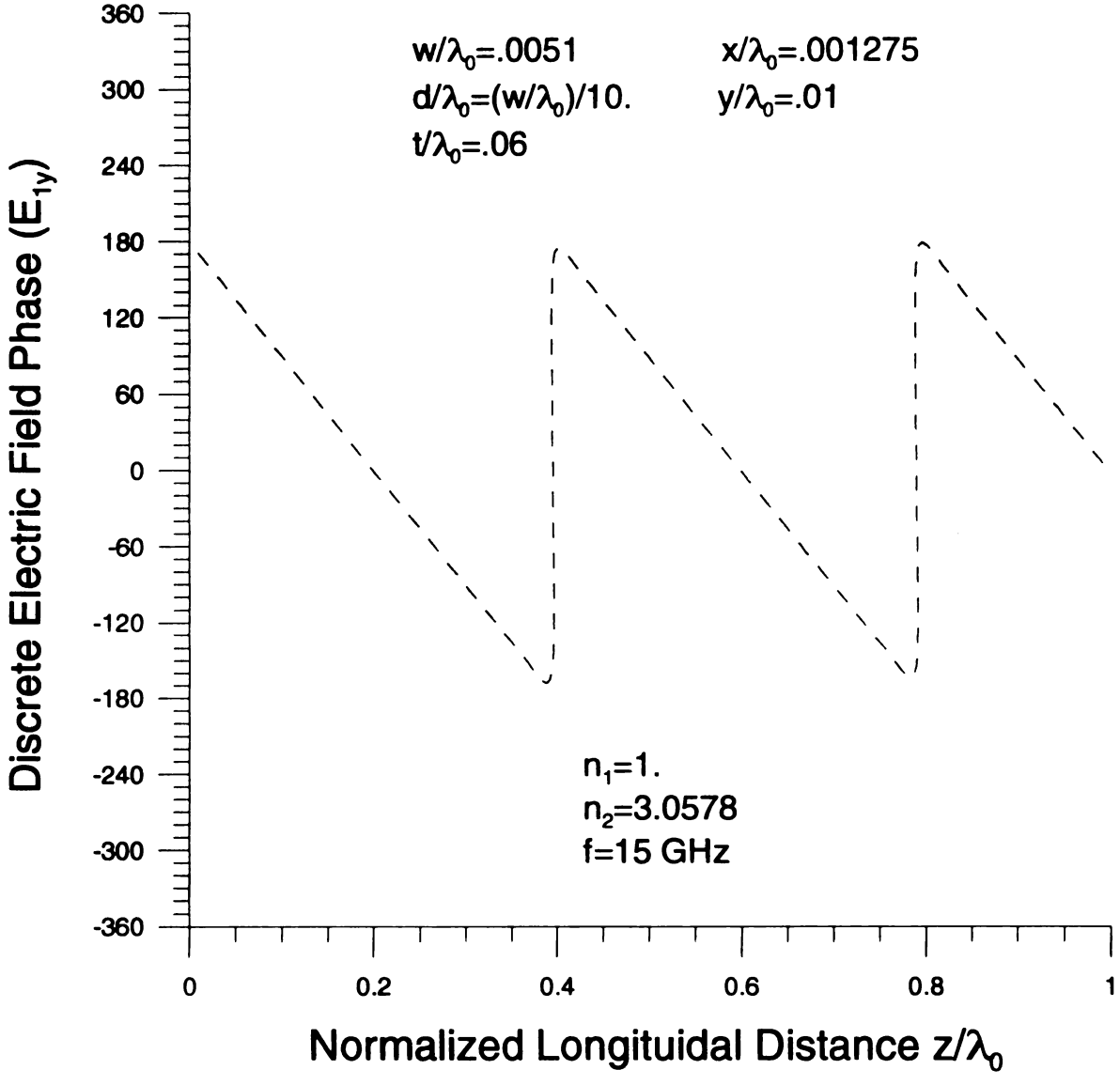

Figure 6.3.19 Longitudinal discrete electric cover field spectrum phase profile in the low-loss limit.

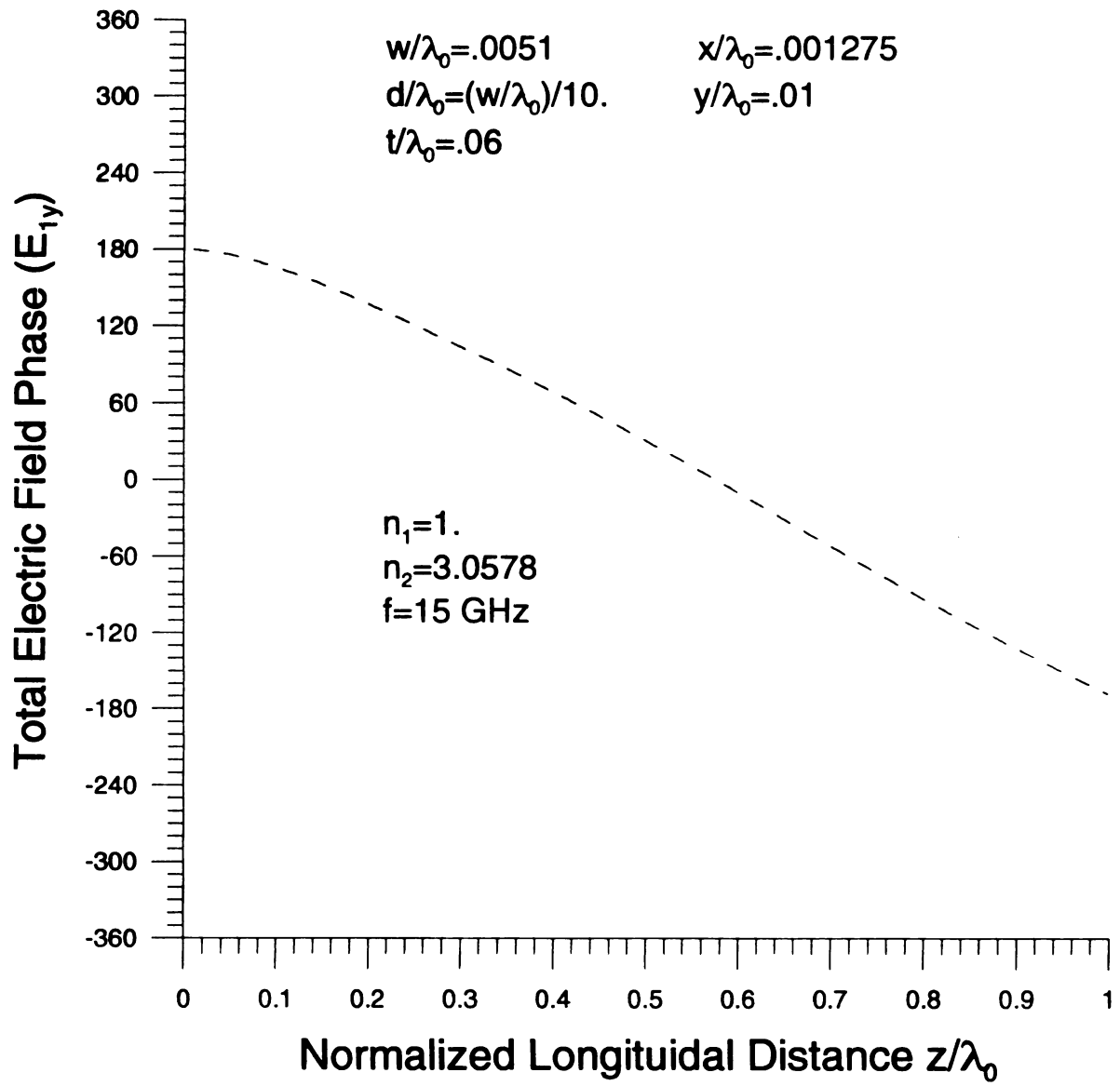

Figure 6.3.20 Longitudinal total electric cover field spectrum phase profile in the low-loss limit.

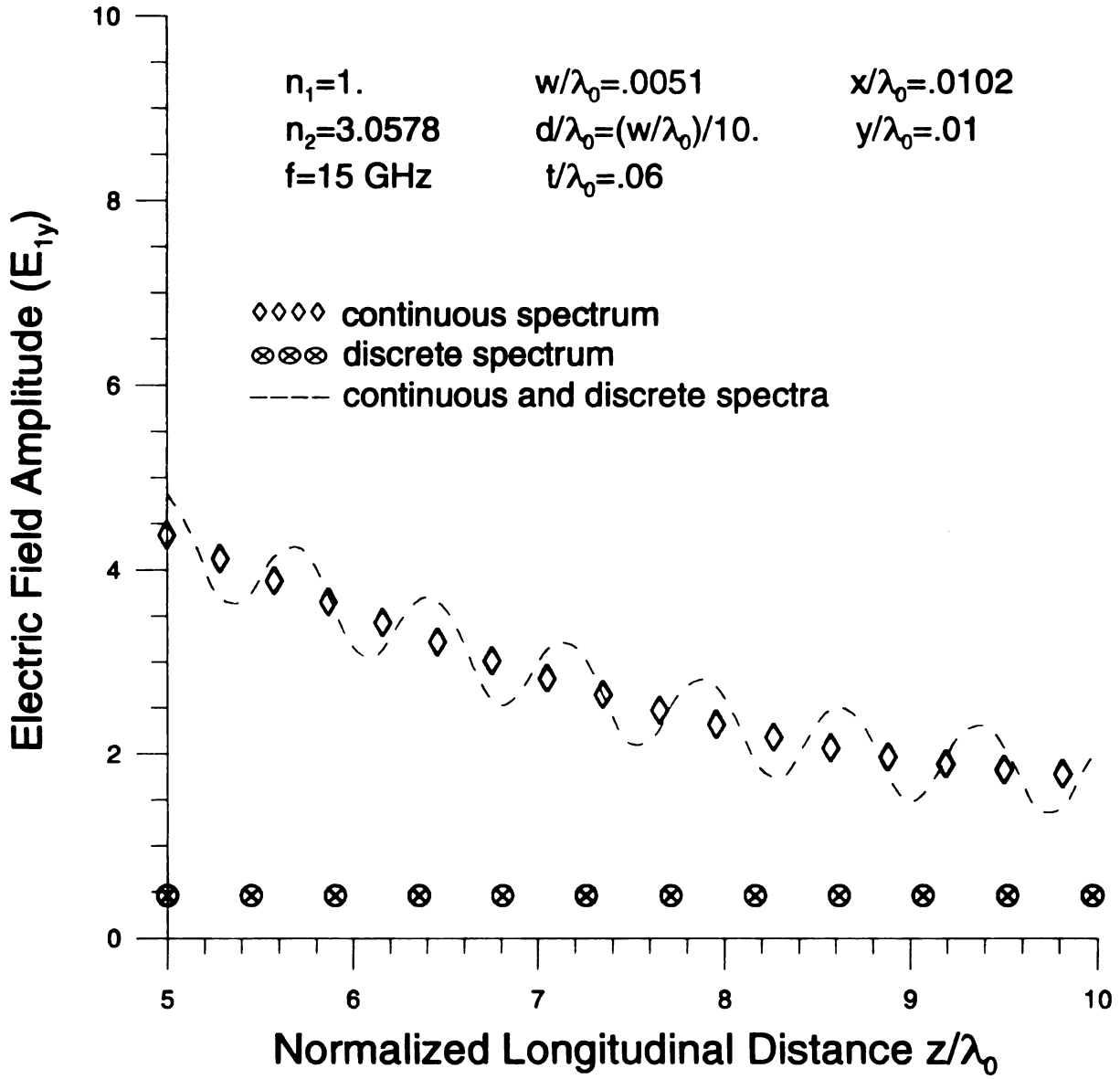

Figure 6.3.21 Longitudinal continuous and discrete electric cover field spectrum amplitudes profile in the low-loss limit.

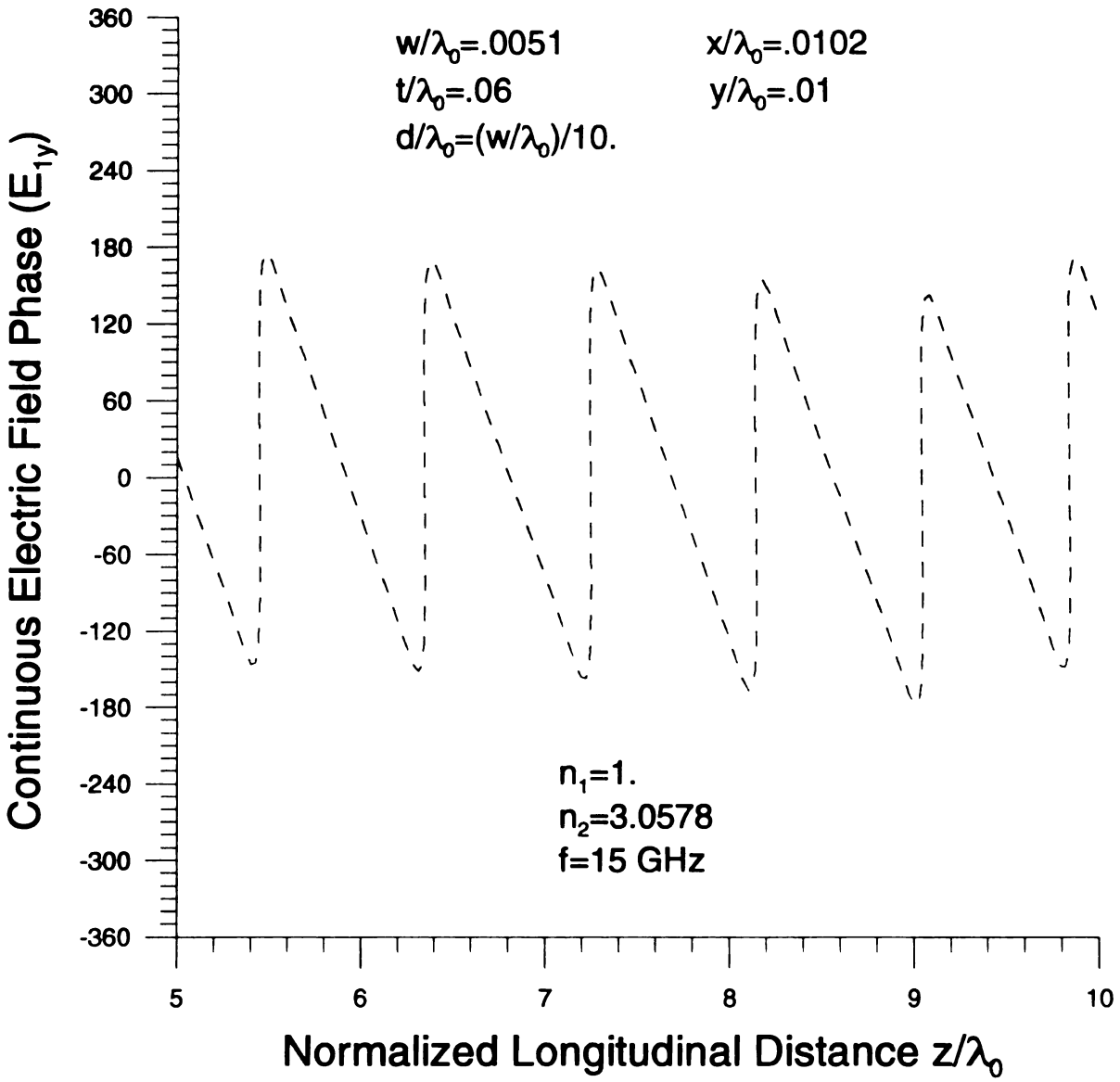

Figure 6.3.22 Longitudinal continuous electric cover field spectrum phase profile in the low-loss limit.

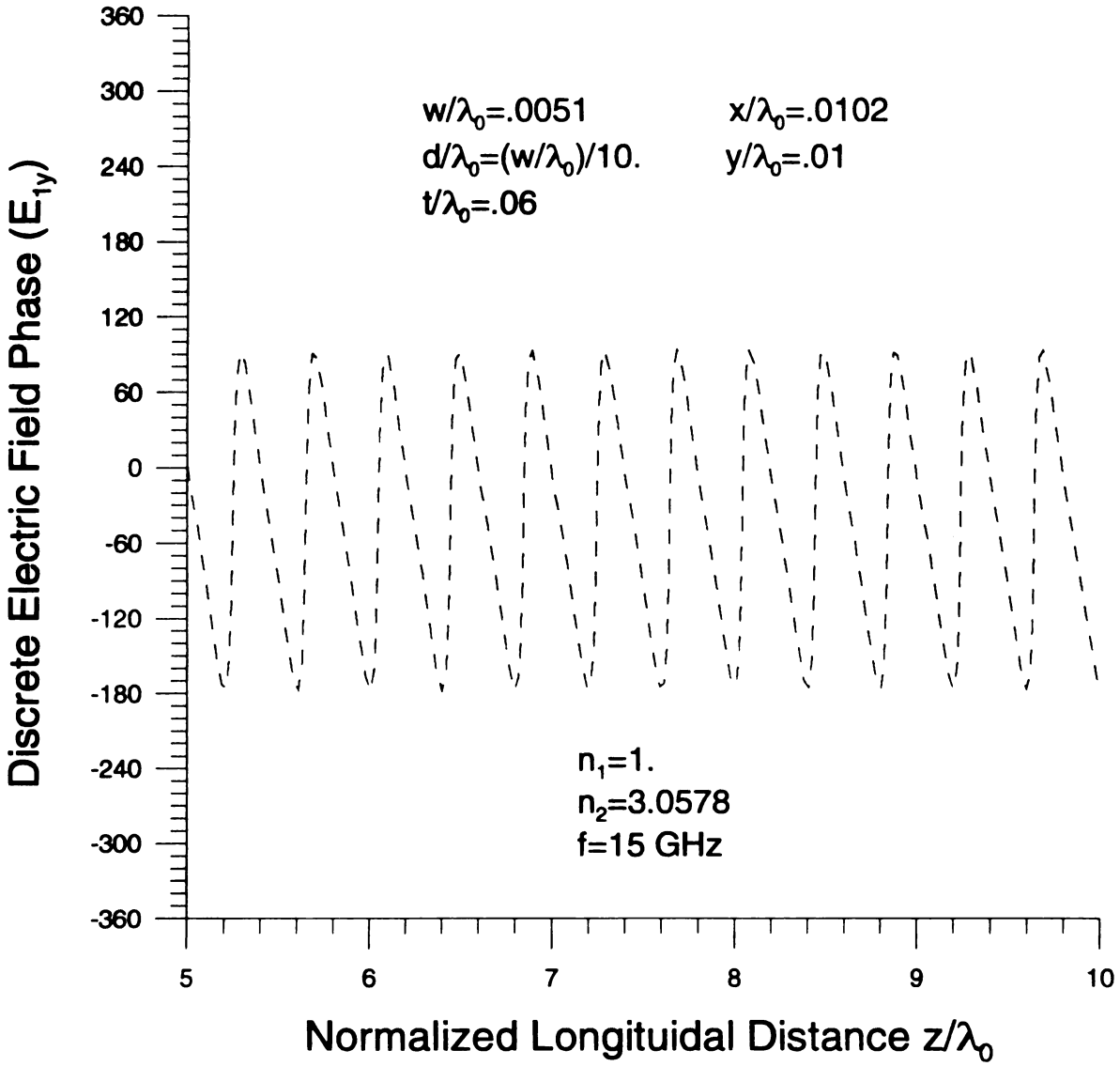

Figure 6.3.23 Longitudinal discrete electric cover field spectrum phase profile in the low-loss limit.

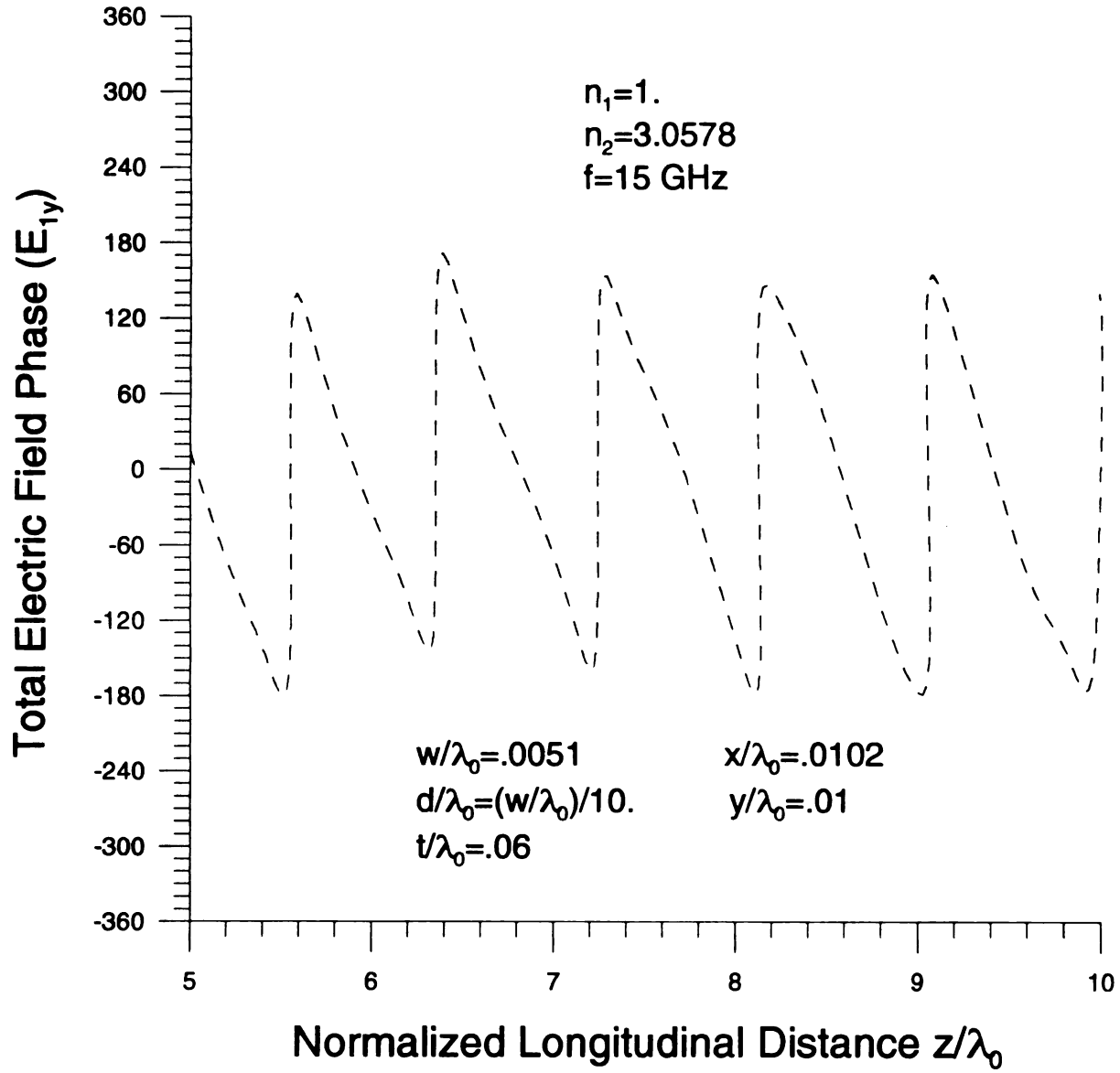

Figure 6.3.24 Longitudinal total electric cover field spectrum phase profile in the low-loss limit.

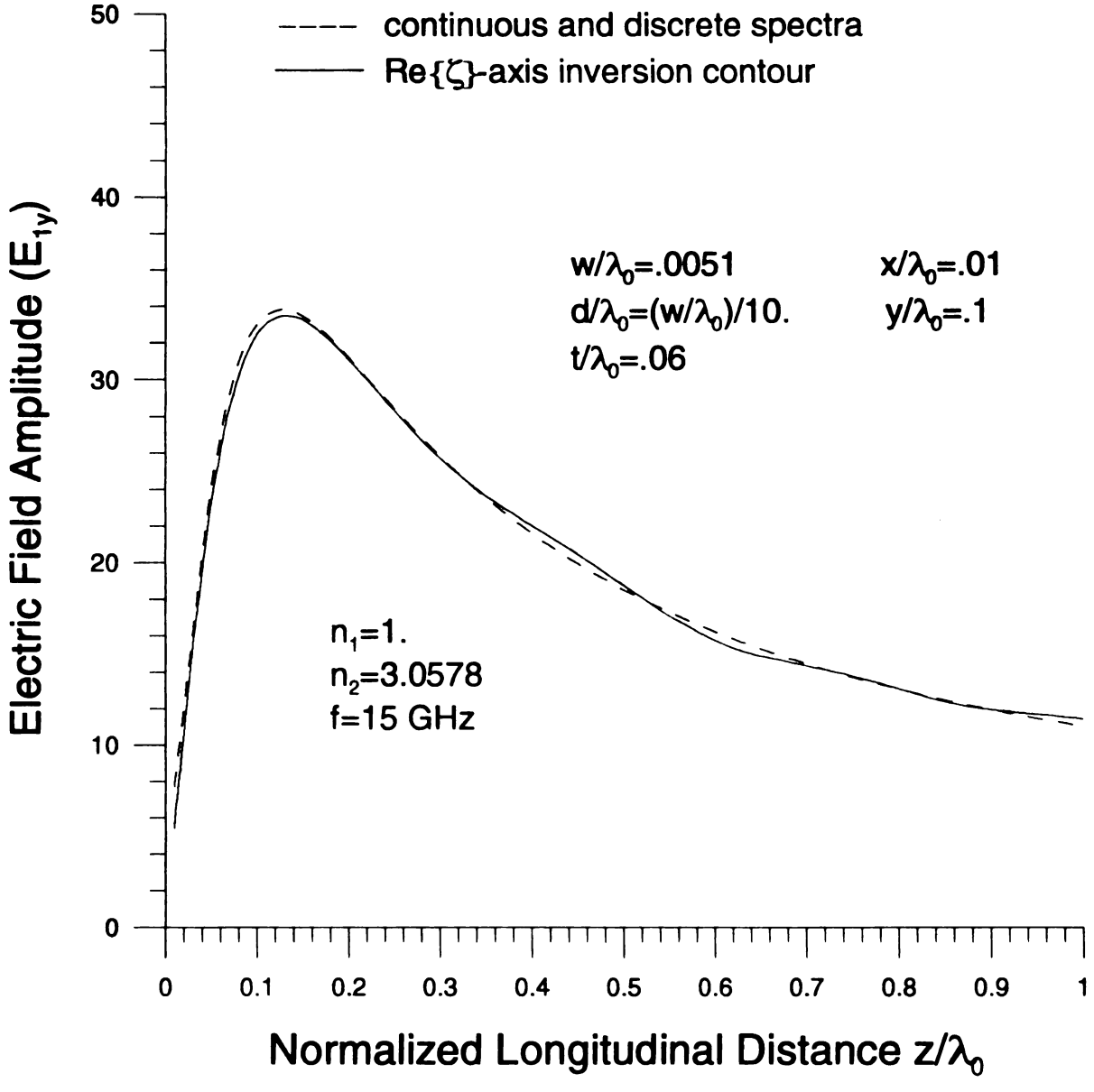

Figure 6.3.25 $\mathrm{Re}\{\zeta\}$**-axis inversion contour validation of microstrip cover field amplitude profile contributed by the continuous spectrum field and the discrete spectrum field in the near zone.**

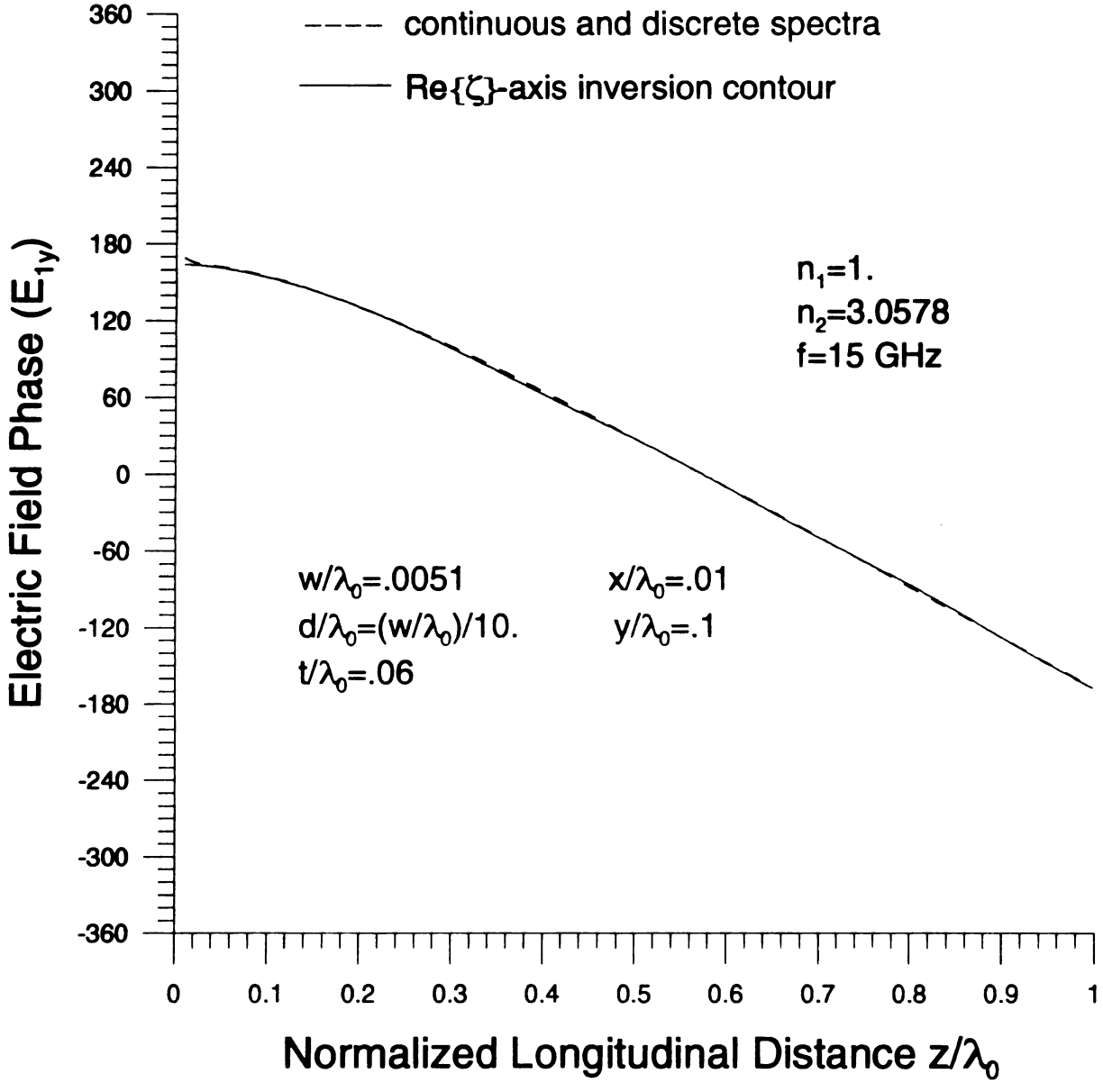

Figure 6.3.26 $\mathrm{Re}\{\zeta\}$**-axis inversion contour validation of microstrip cover field phase profile contributed by the continuous spectrum field and the discrete spectrum field in the near zone.**

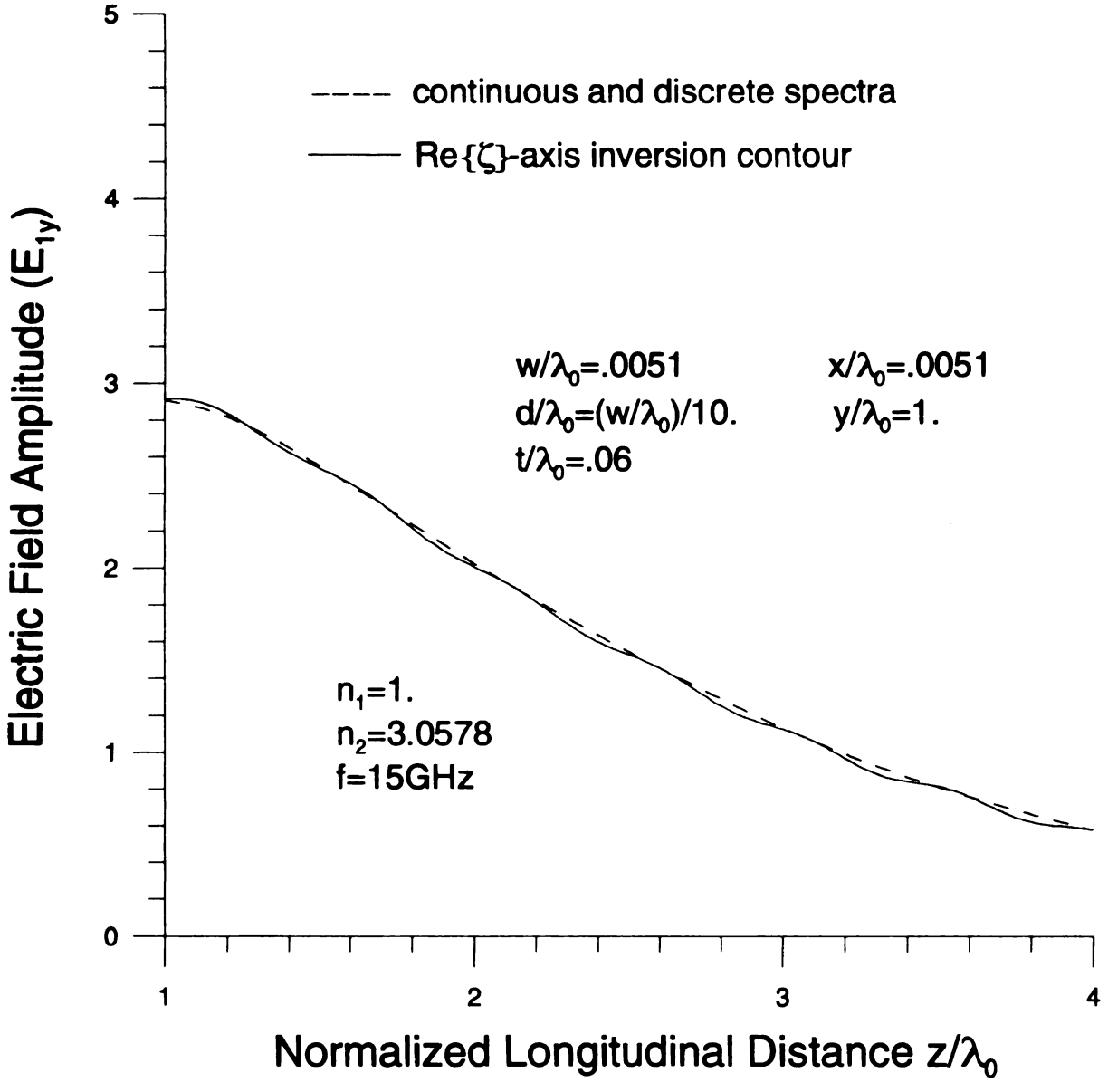

Figure 6.3.27 $\mathrm{Re}\{\zeta\}$**-axis inversion contour validation of microstrip cover field amplitude profile contributed by the continuous spectrum field and the discrete spectrum field.**

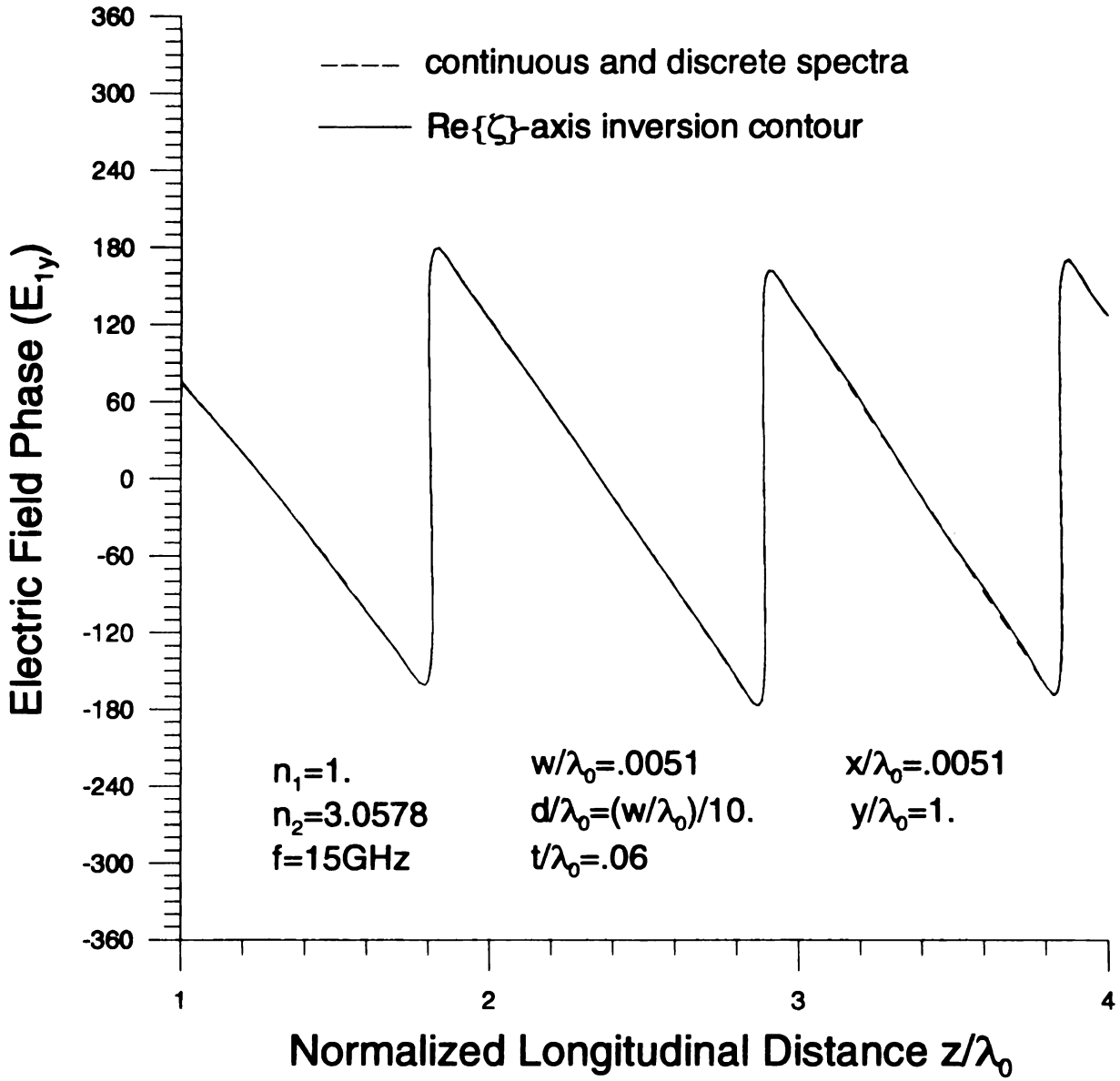

Figure 6.3.28 $\mathrm{Re}\{\zeta\}$**-axis inversion contour validation of microstrip cover field phase profile contributed by the continuous spectrum field and the discrete spectrum field.**

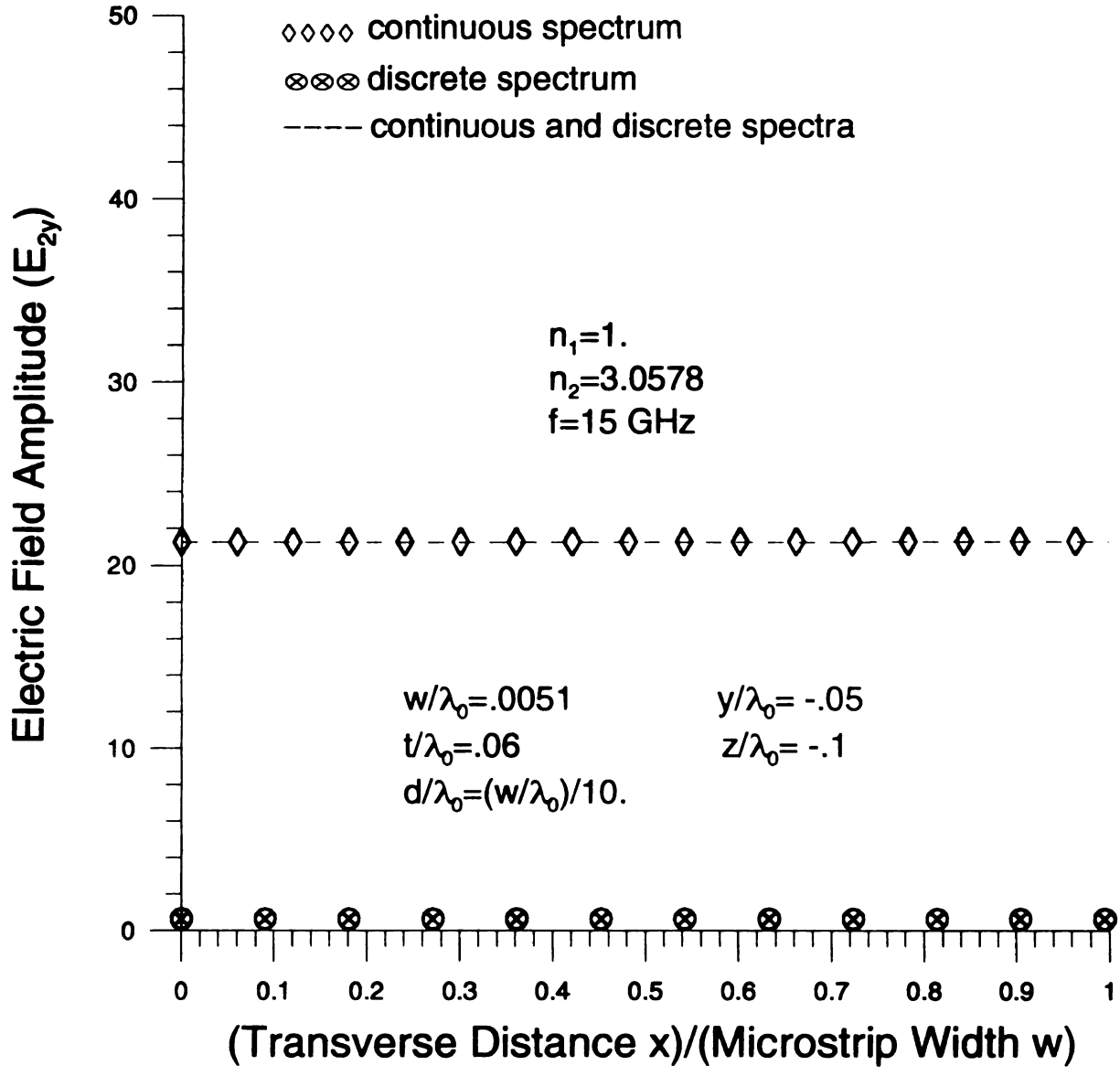

Figure 6.3.29 Transverse continuous and discrete electric film field spectrum amplitudes profile in the low-loss limit.

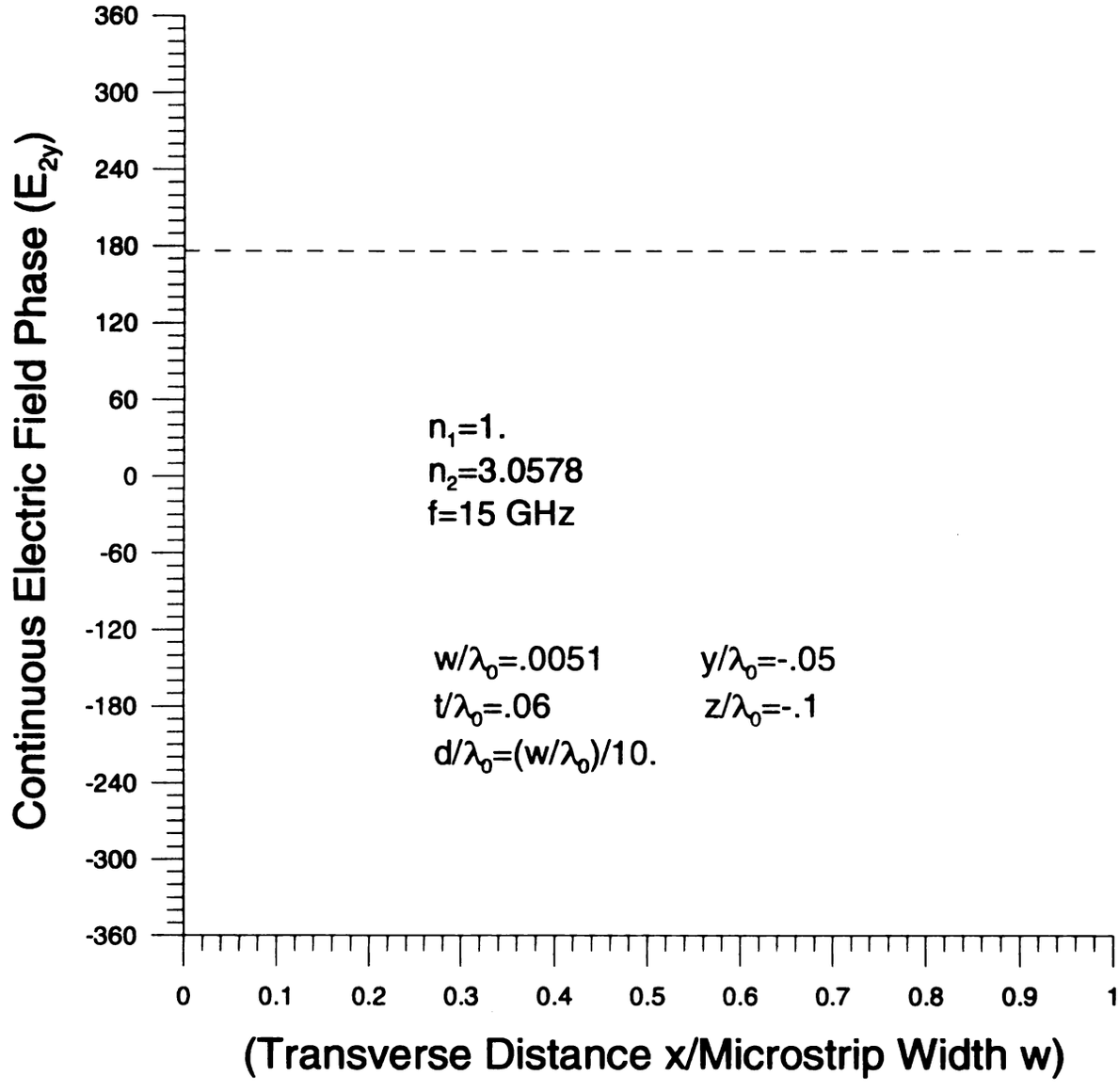

Figure 6.3.30 Transverse continuous electric film field spectrum phase profile in the low-loss limit.

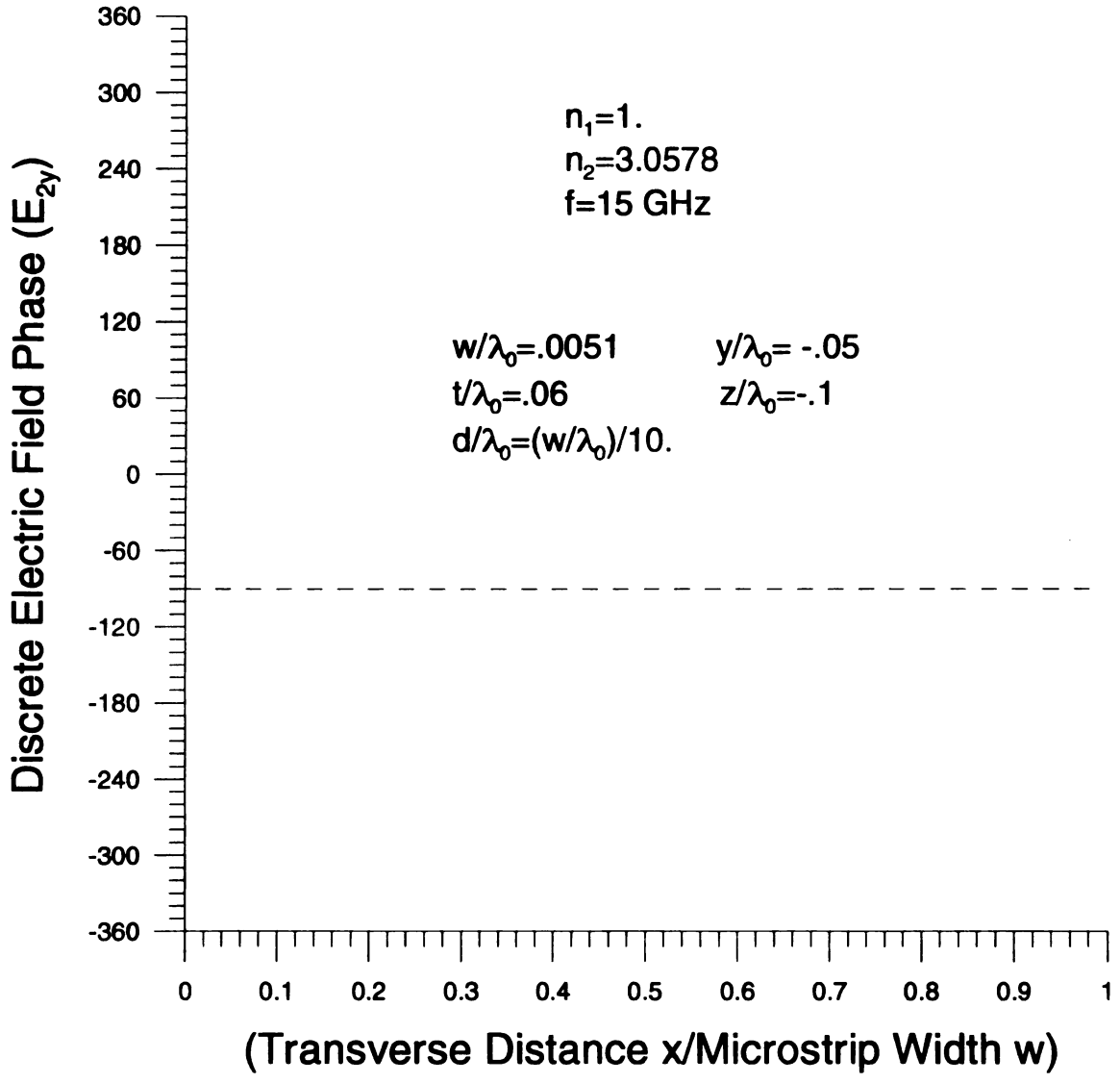

Figure 6.3.31 Transverse discrete electric film field spectrum phase profile in the low-loss limit.

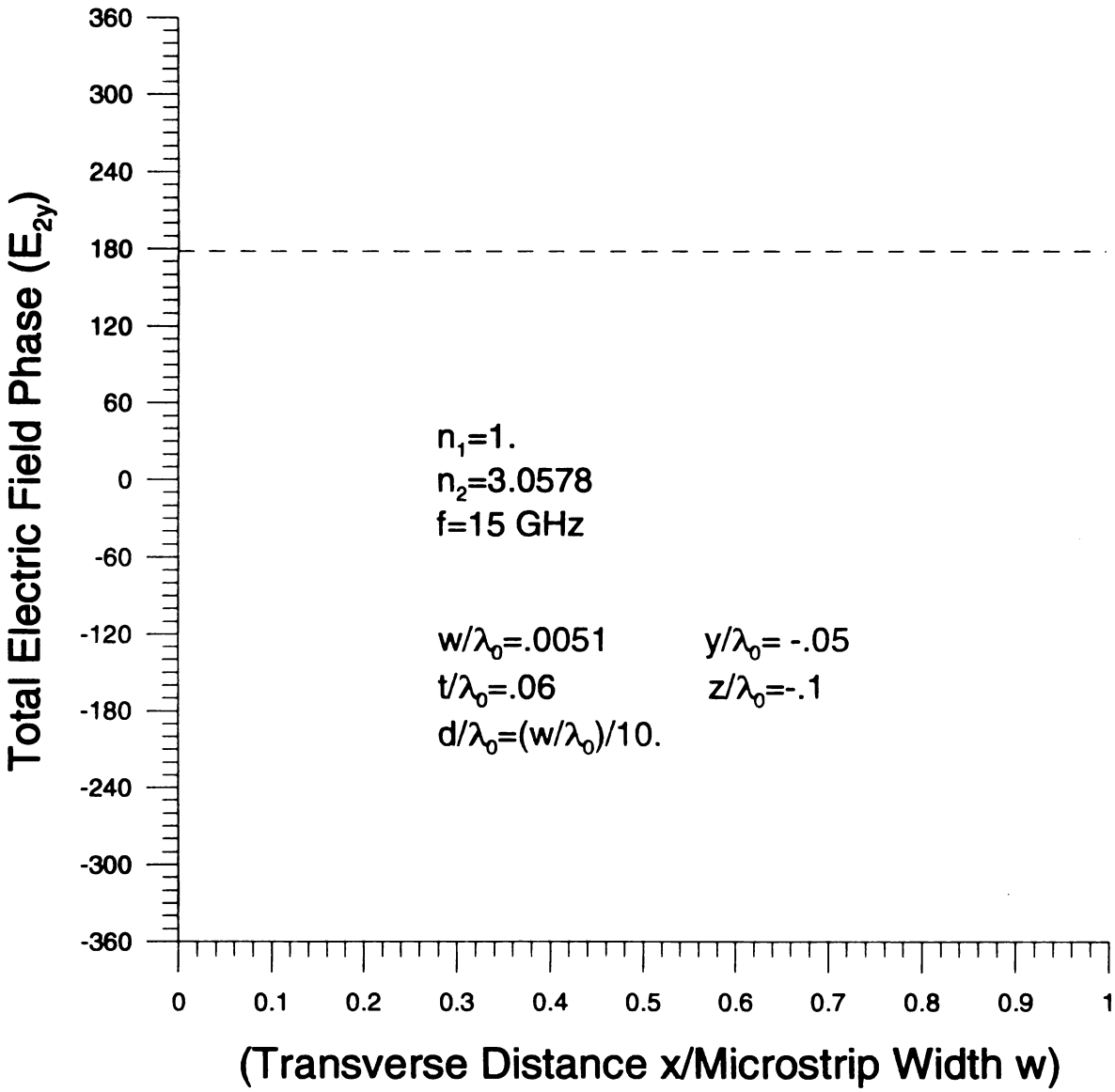

Figure 6.3.32 Transverse total electric film field spectrum phase profile in the low-loss limit.

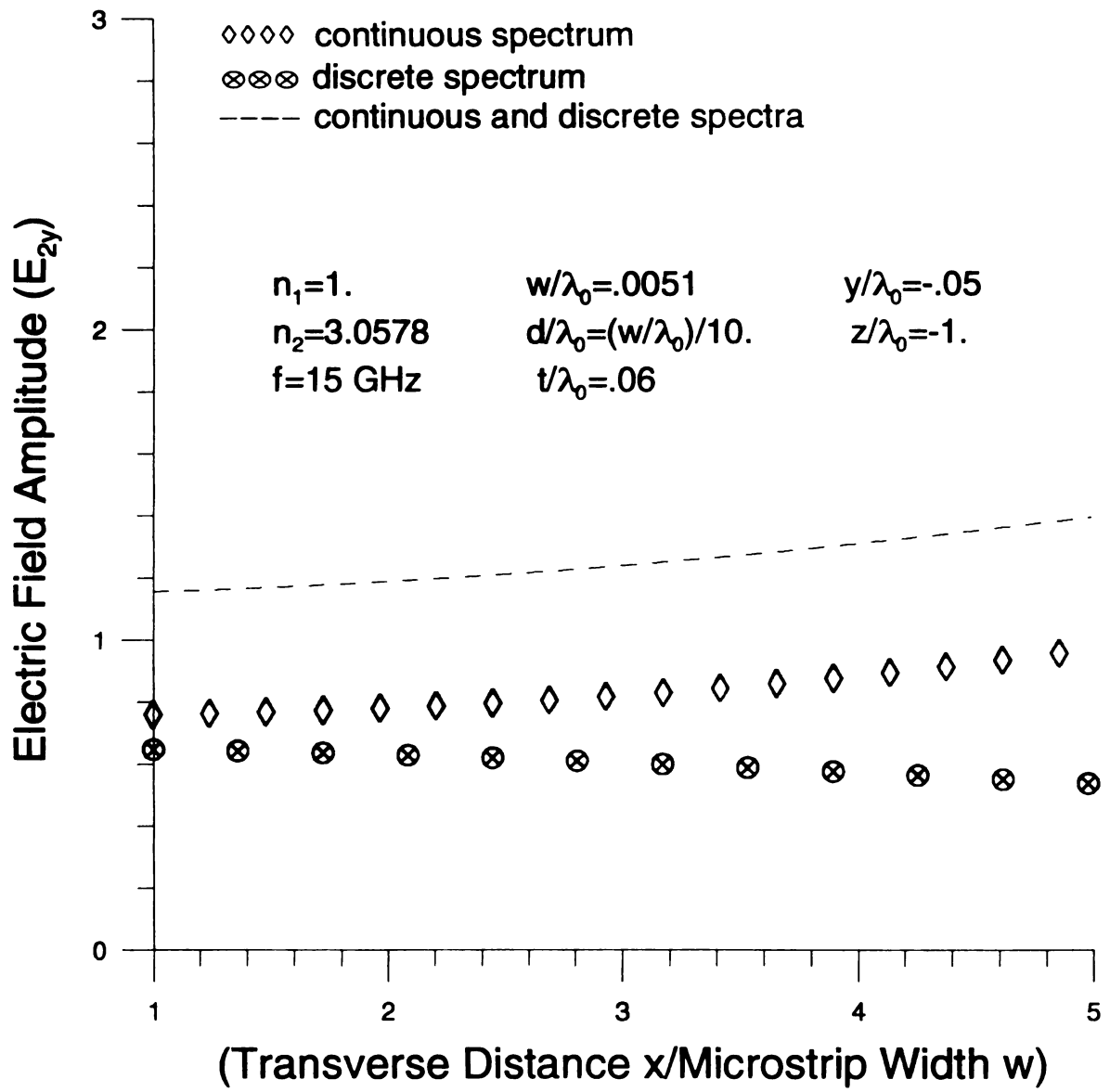

Figure 6.3.33 Transverse continuous and discrete electric film field spectrum amplitudes profile in the low-loss limit.

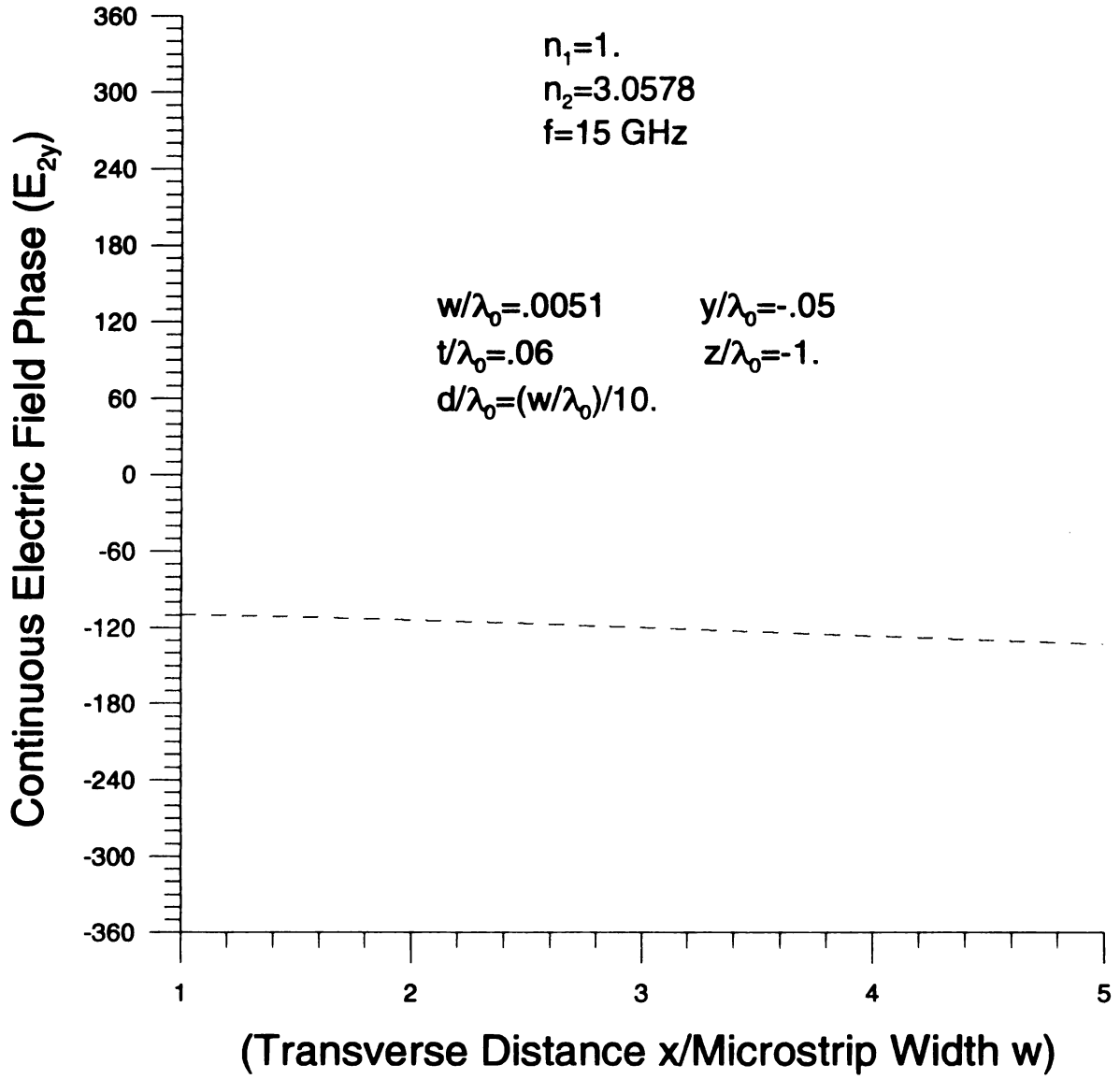

Figure 6.3.34 Transverse continuous electric film field spectrum phase profile in the low-loss limit.

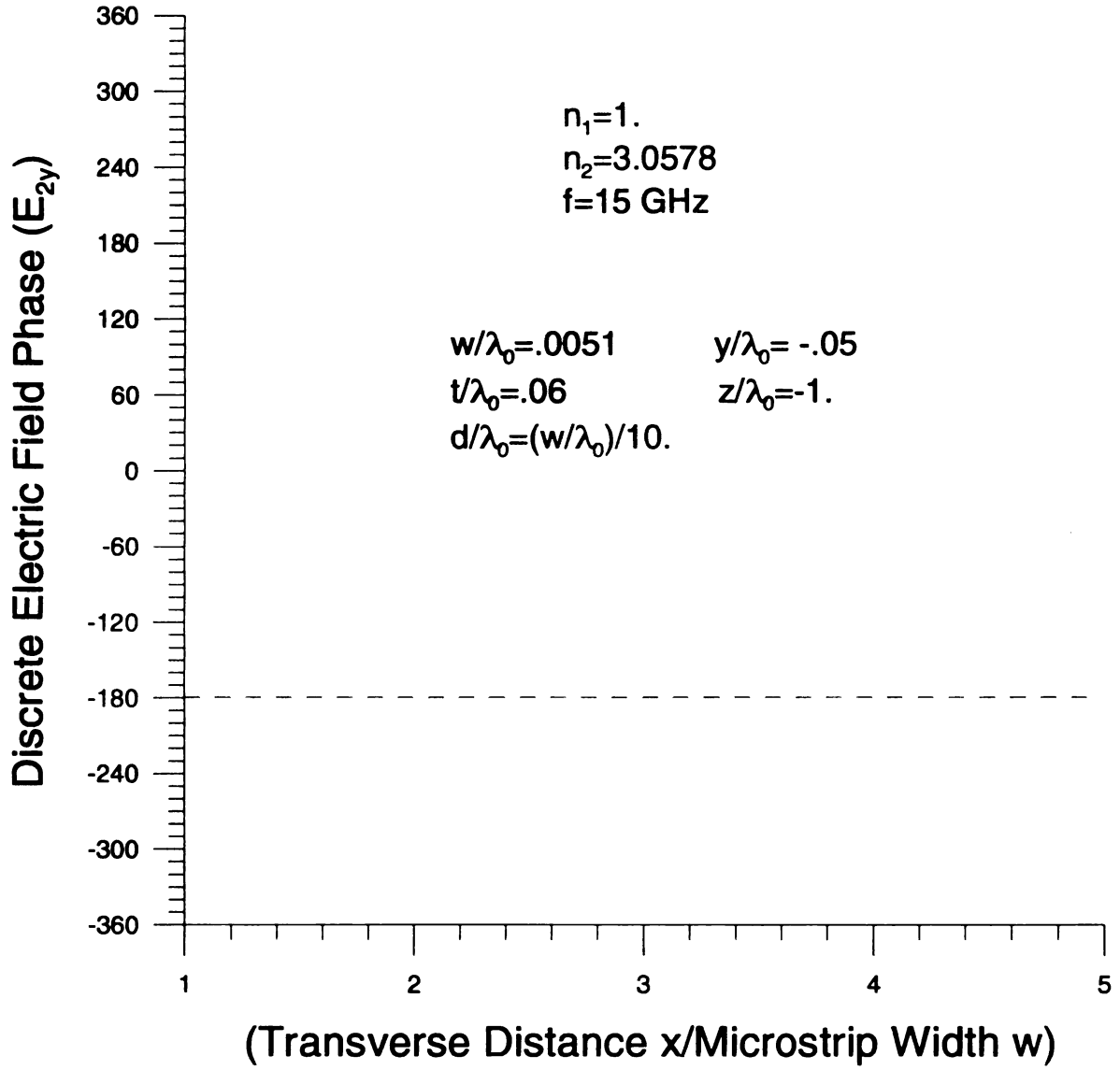

Figure 6.3.35 Transverse discrete electric field spectrum phase profile in the low-loss limit.

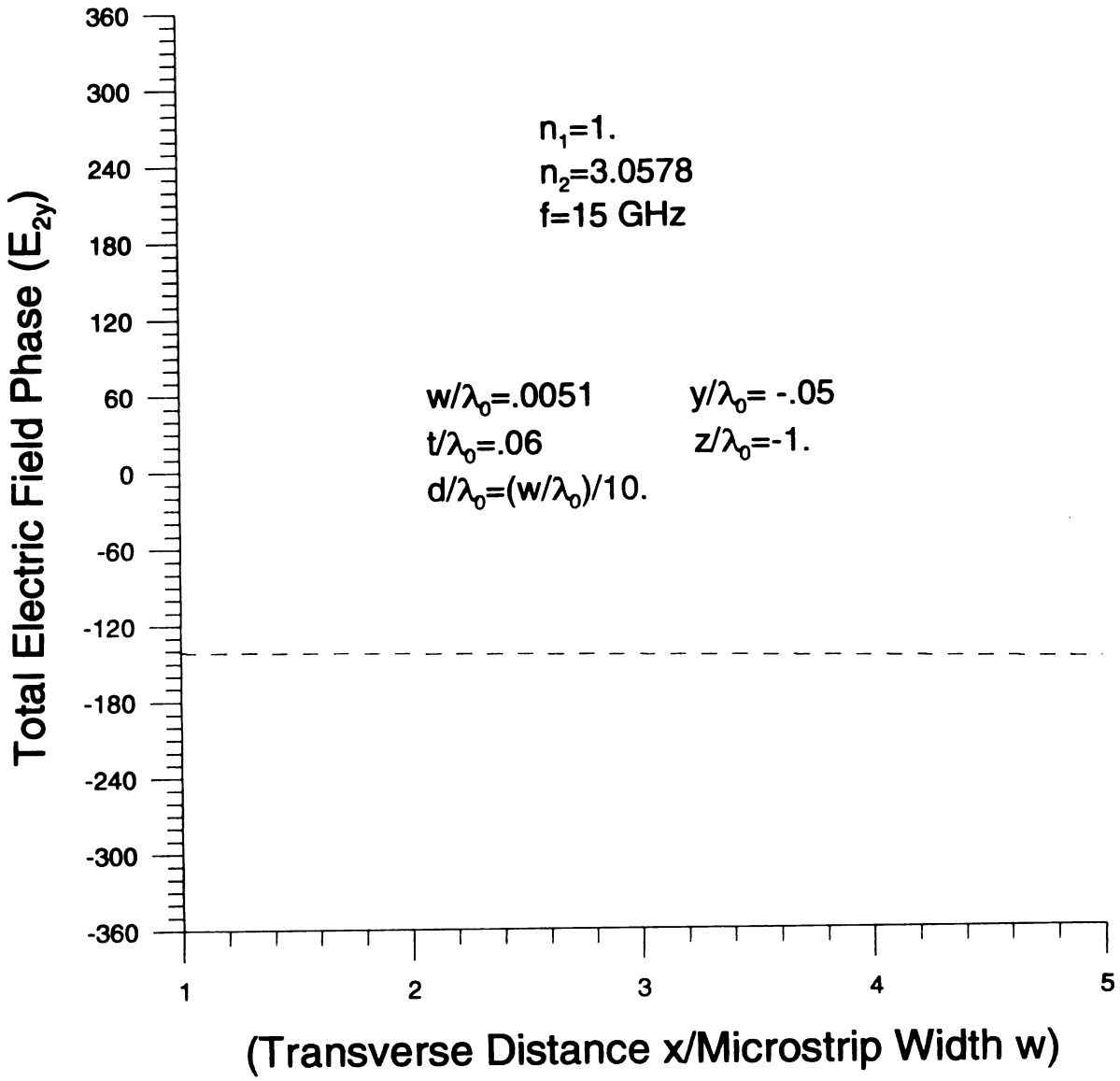

Figure 6.3.36 Transverse total electric film field spectrum phase profile in the low-loss limit.

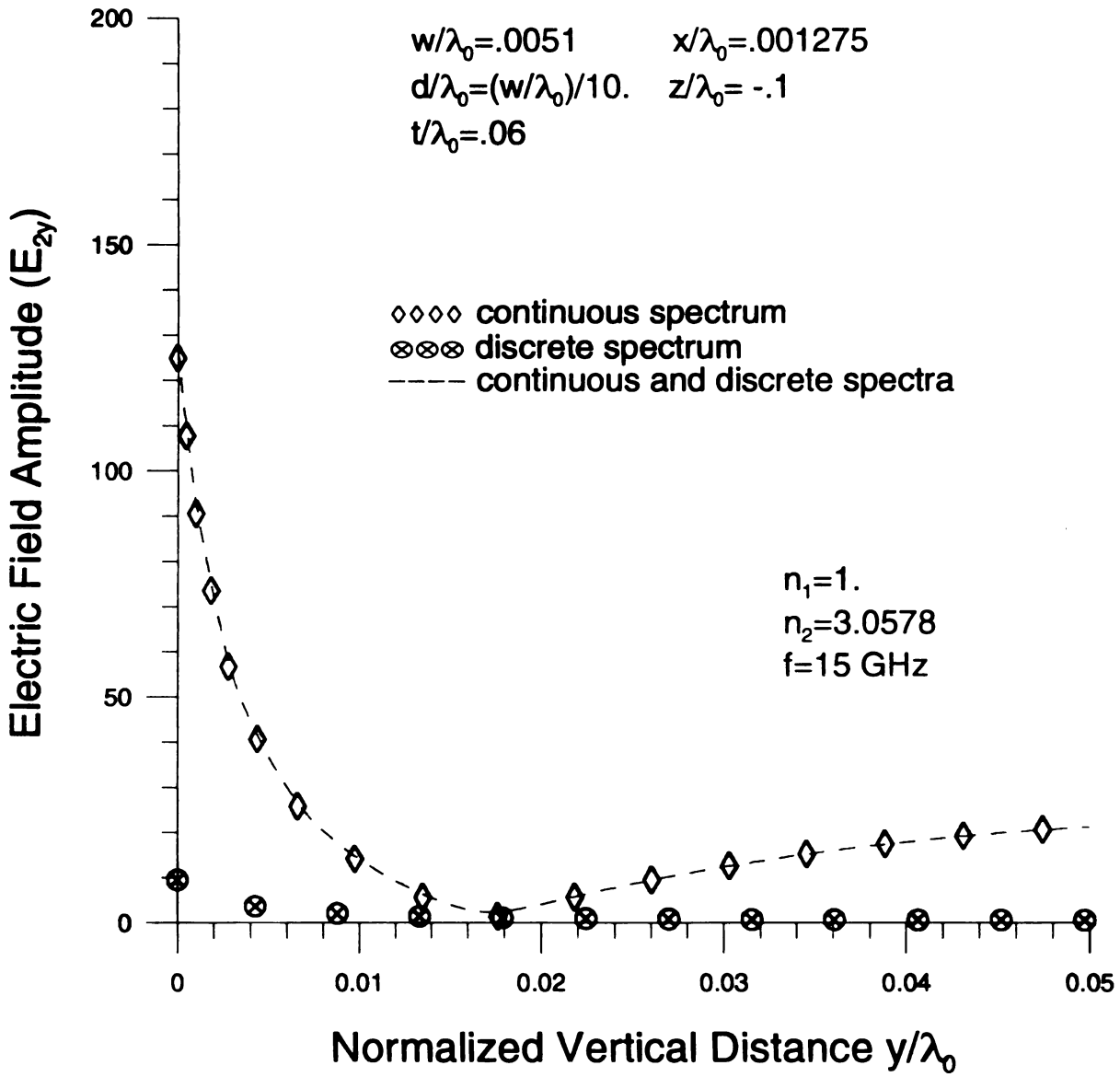

Figure 6.3.37 Vertical continuous and discrete electric film field spectrum amplitudes profile in the low-loss limit.

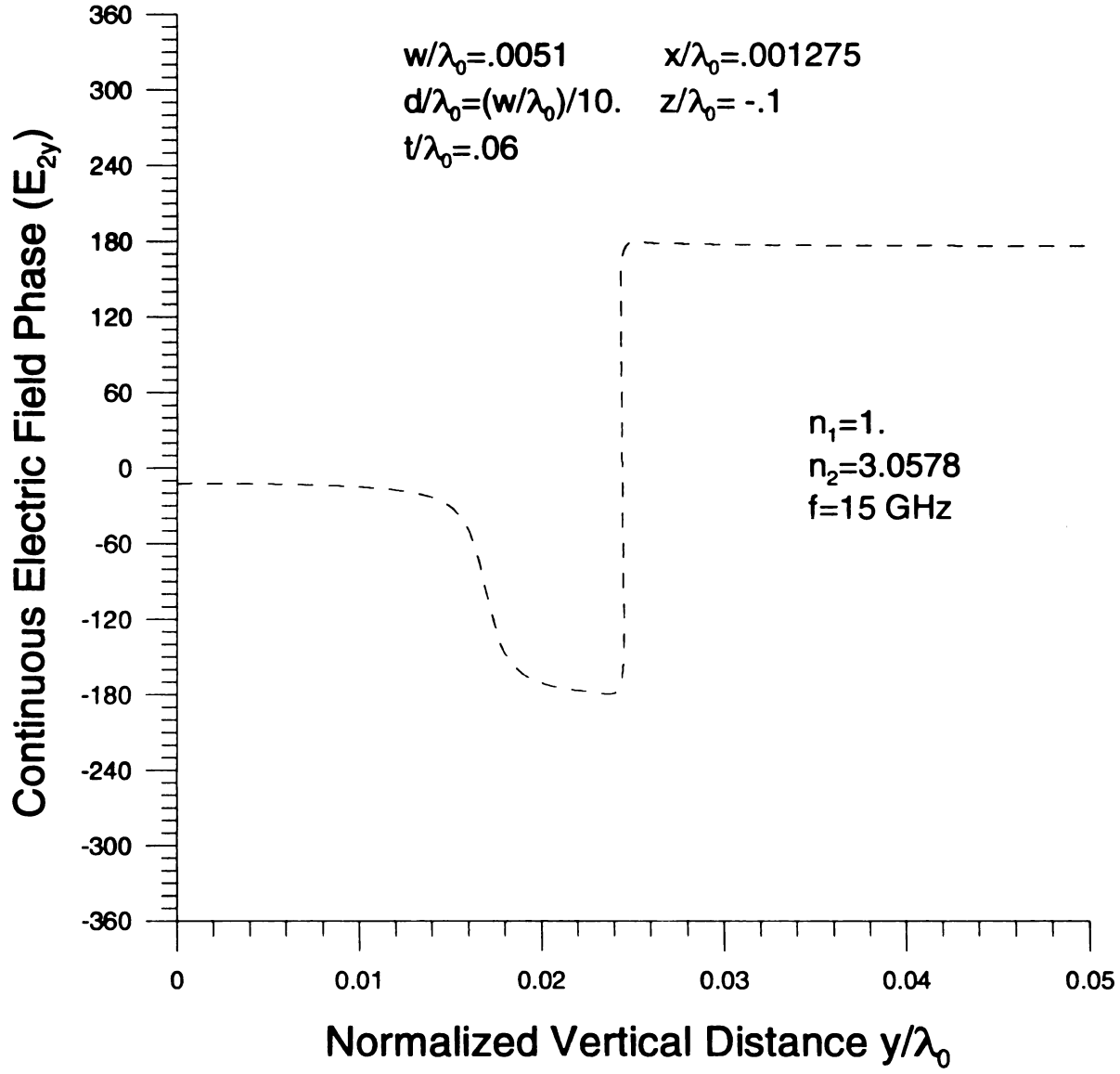

Figure 6.3.38 Vertical continuous electric film field spectrum phase profile in the low-loss limit.

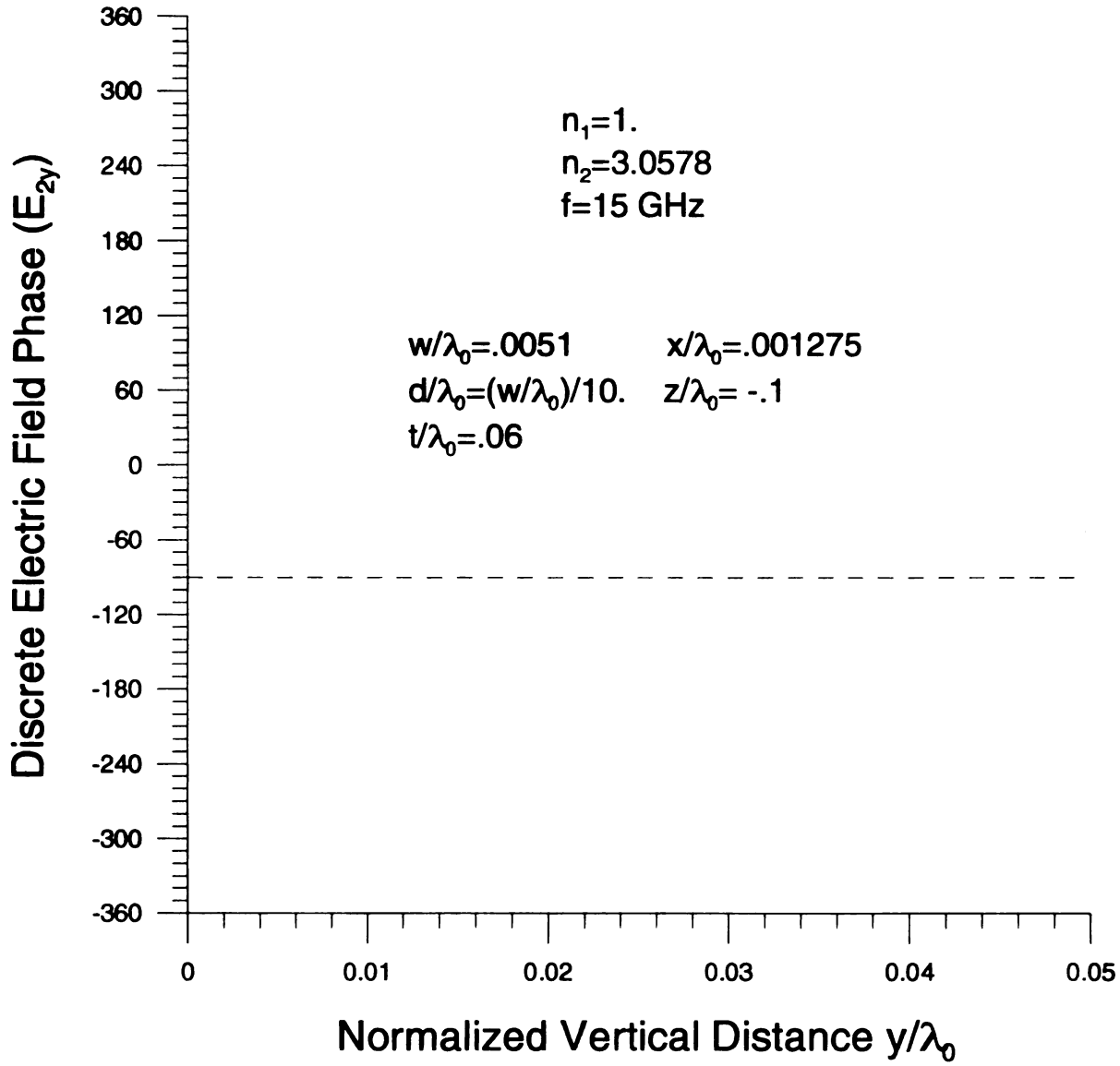

Figure 6.3.39 Vertical discrete electric field spectrum phase profile in the low-loss limit.

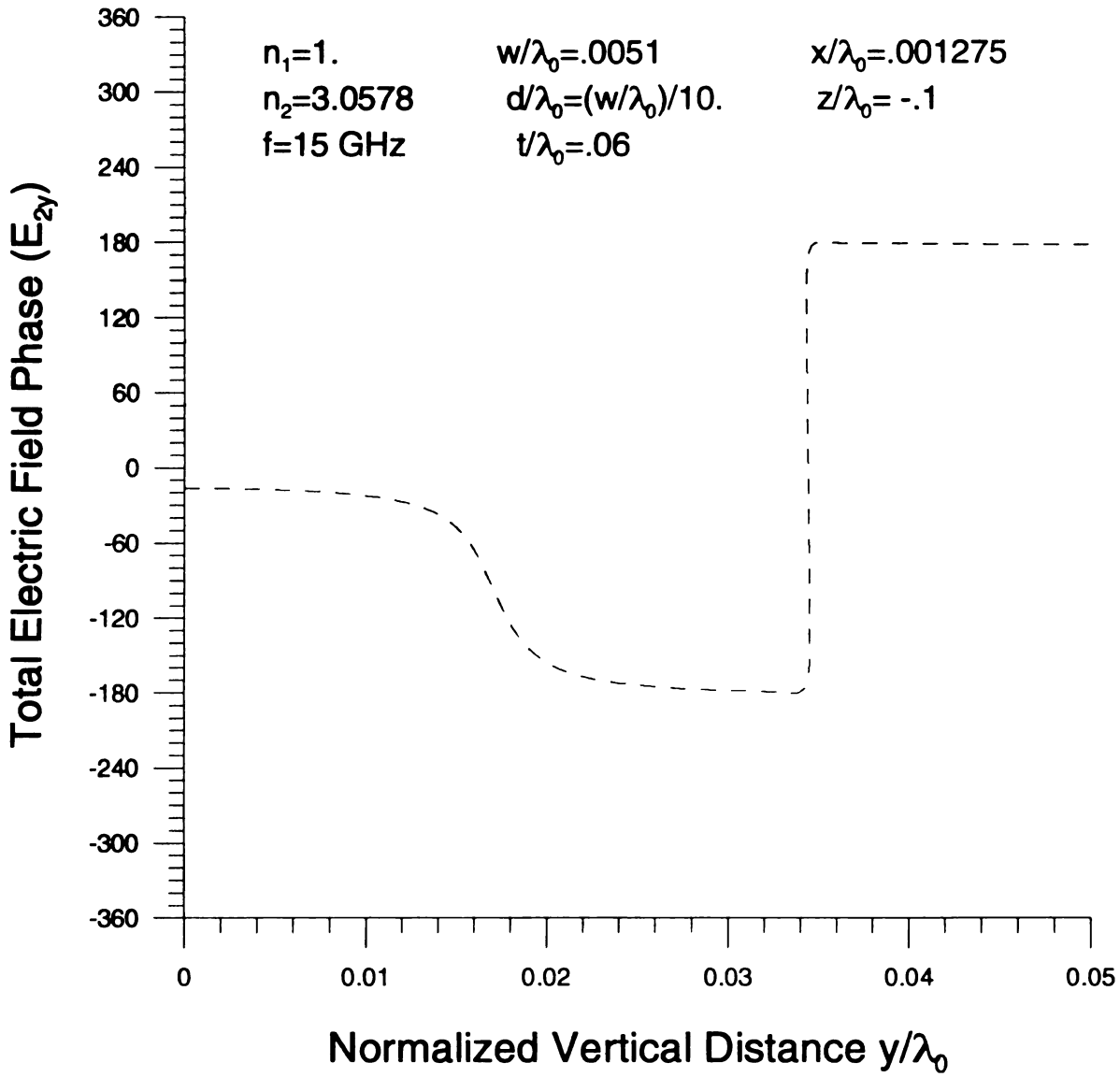

Figure 6.3.40 Vertical total electric film field spectrum phase profile in the low-loss limit.

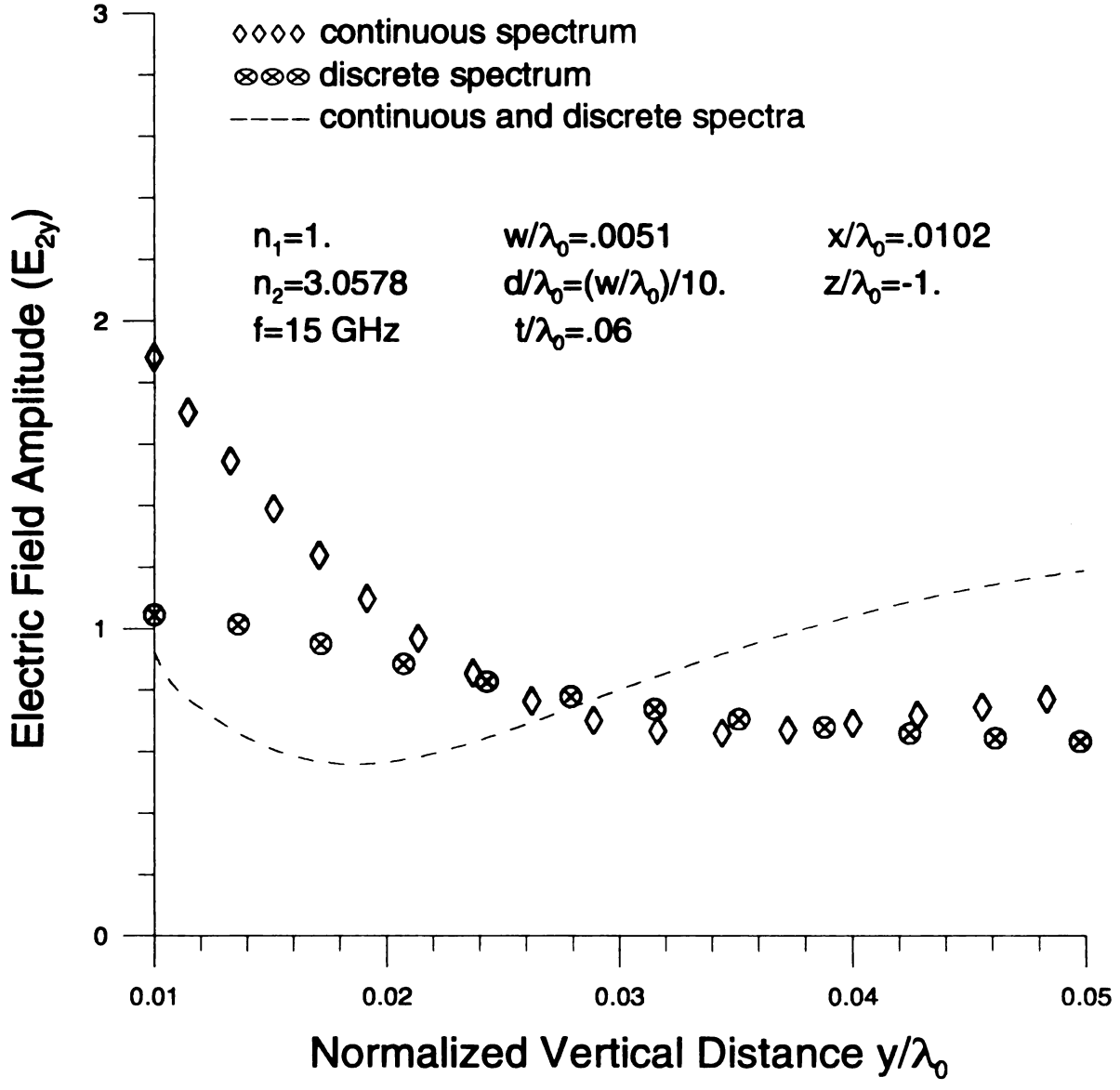

Figure 6.3.41 Vertical continuous and discrete electric field spectrum amplitudes profile in the low-loss limit.

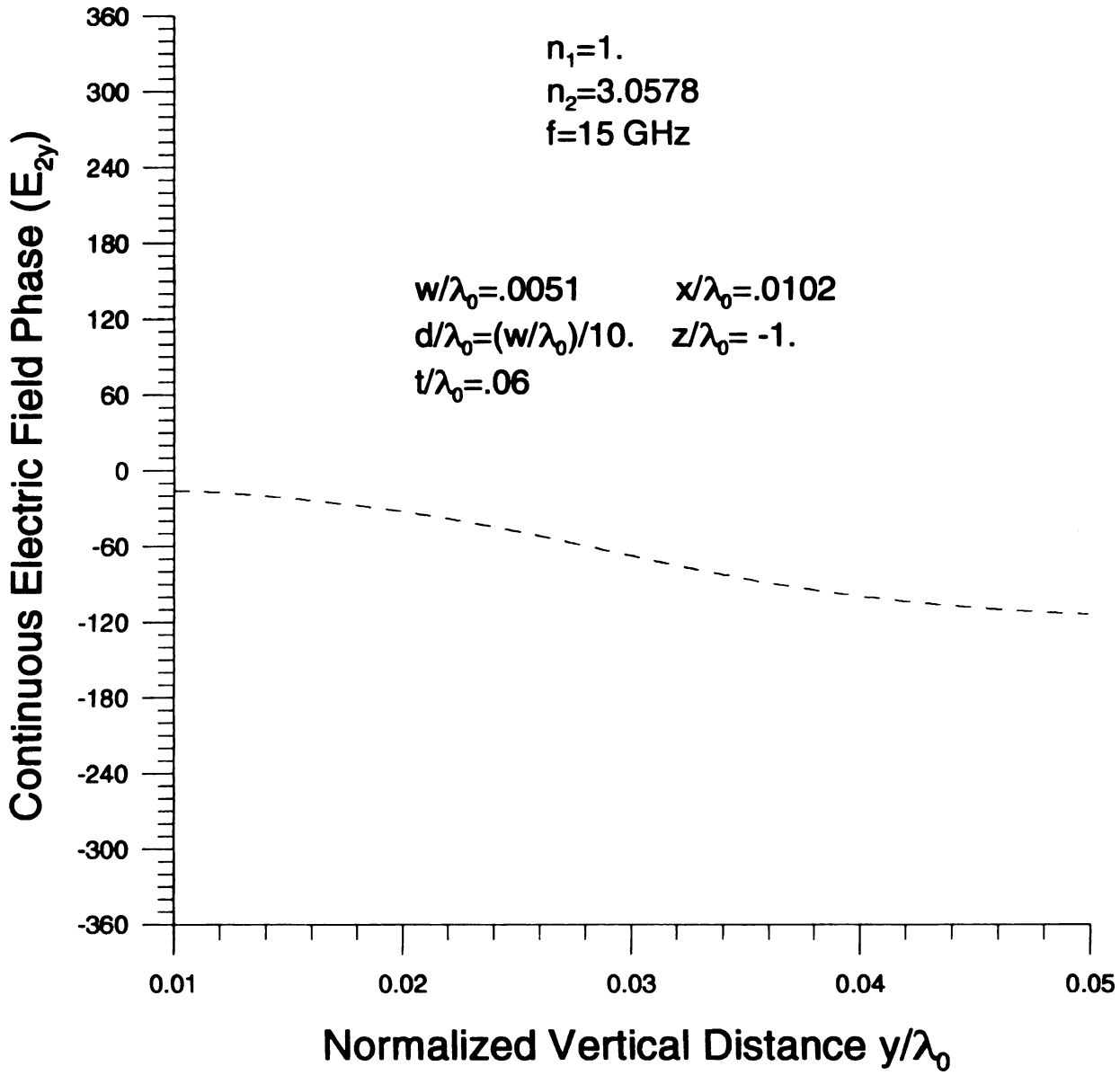

Figure 6.3.42 Vertical continuous electric film field spectrum phase profile in the low-loss limit.

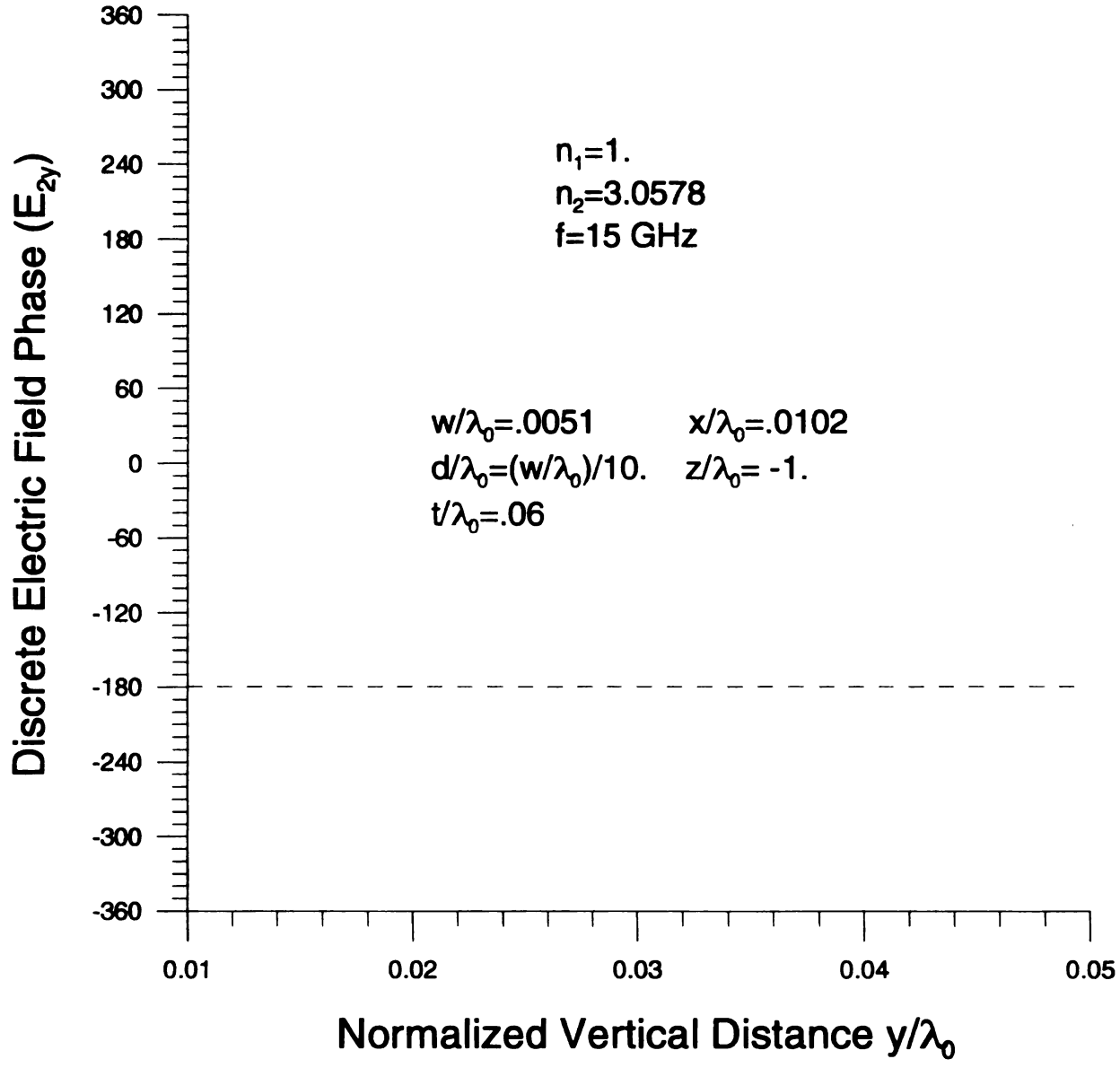

Figure 6.3.43 Vertical discrete electric film field spectrum phase profile in the low-loss limit.

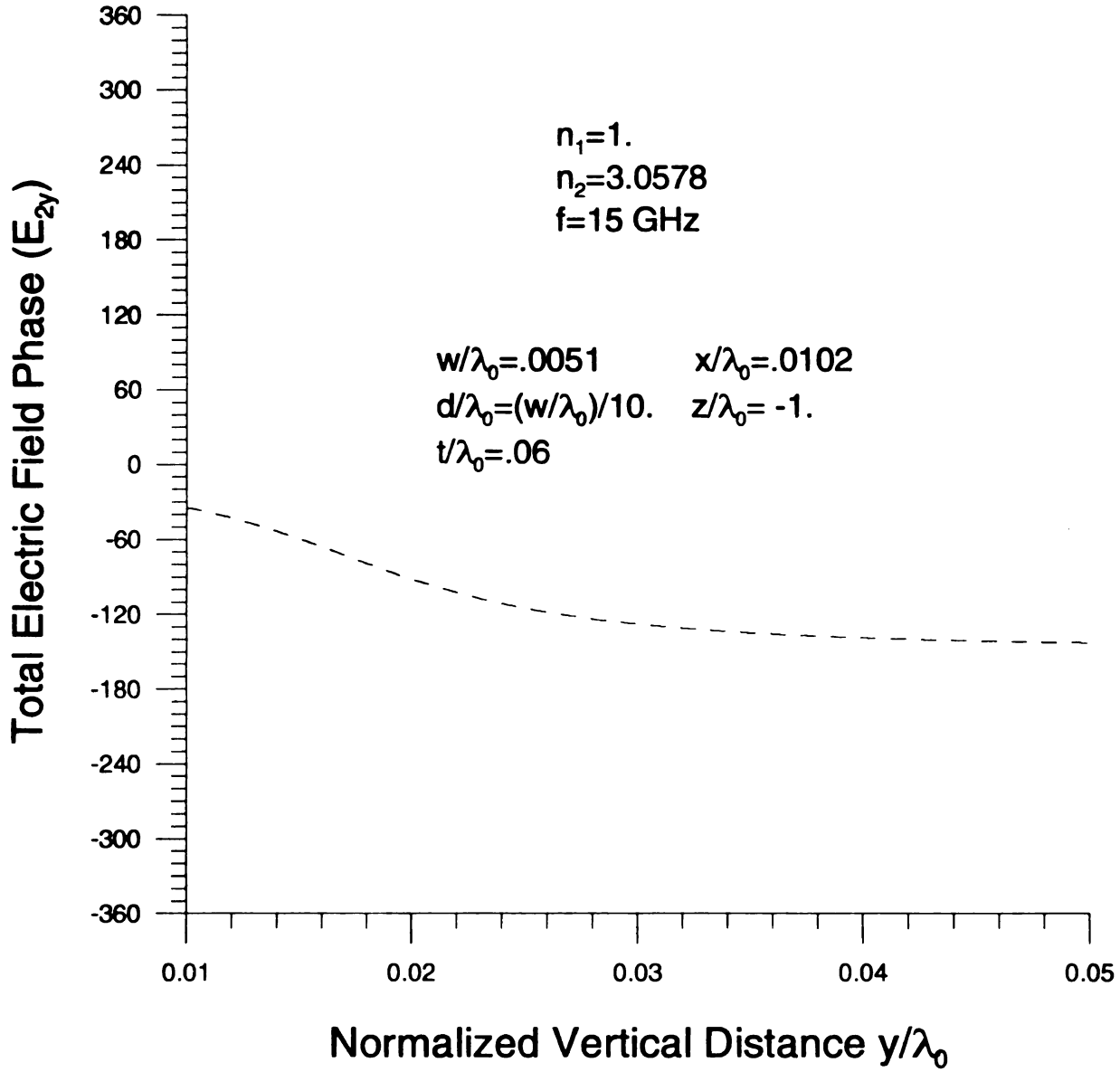

Figure 6.3.44 Vertical total electric film field spectrum phase profile in the low-loss limit.

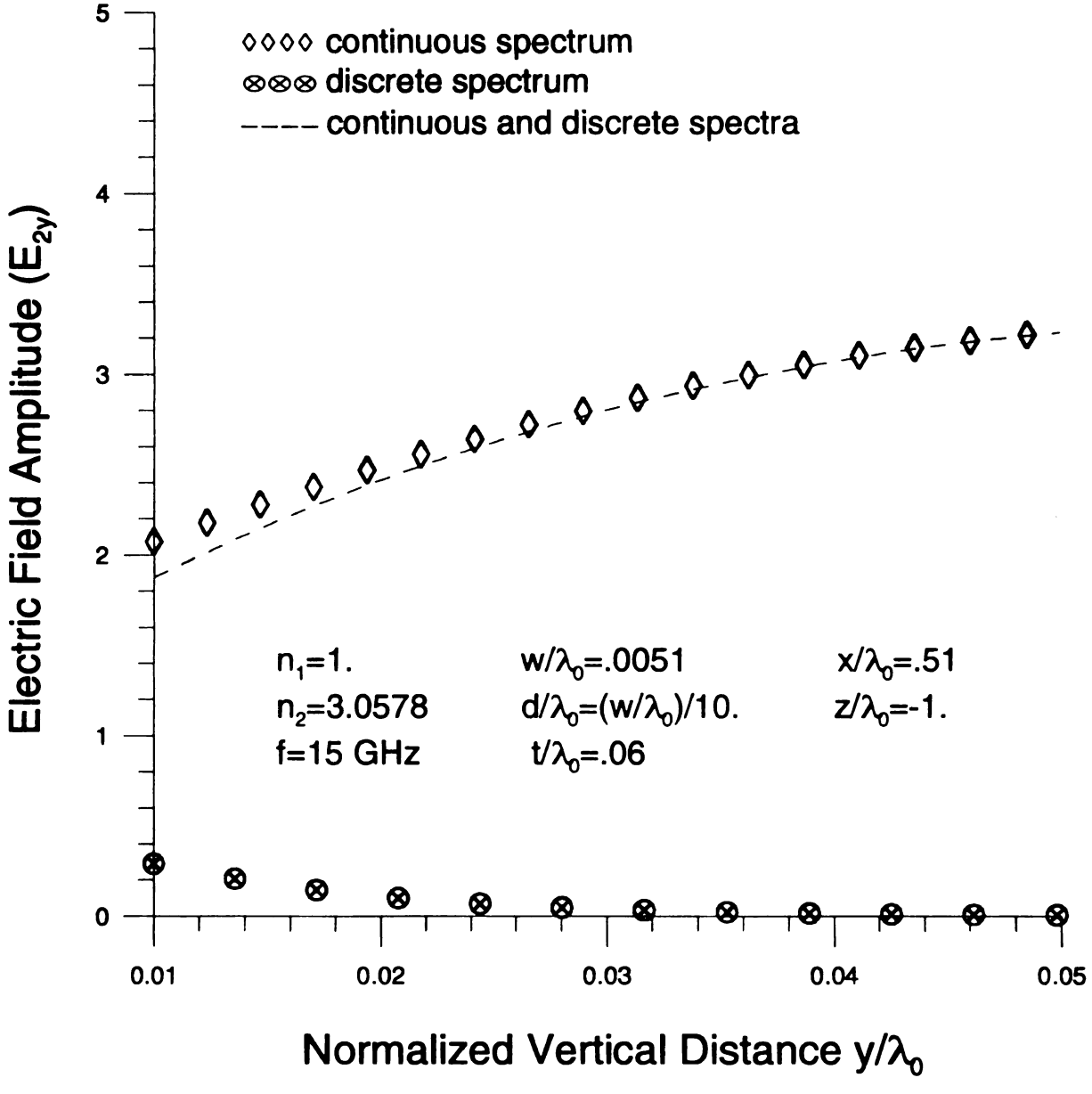

Figure 6.3.45 Vertical continuous and discrete electric field spectrum amplitudes profile in the low-loss limit.

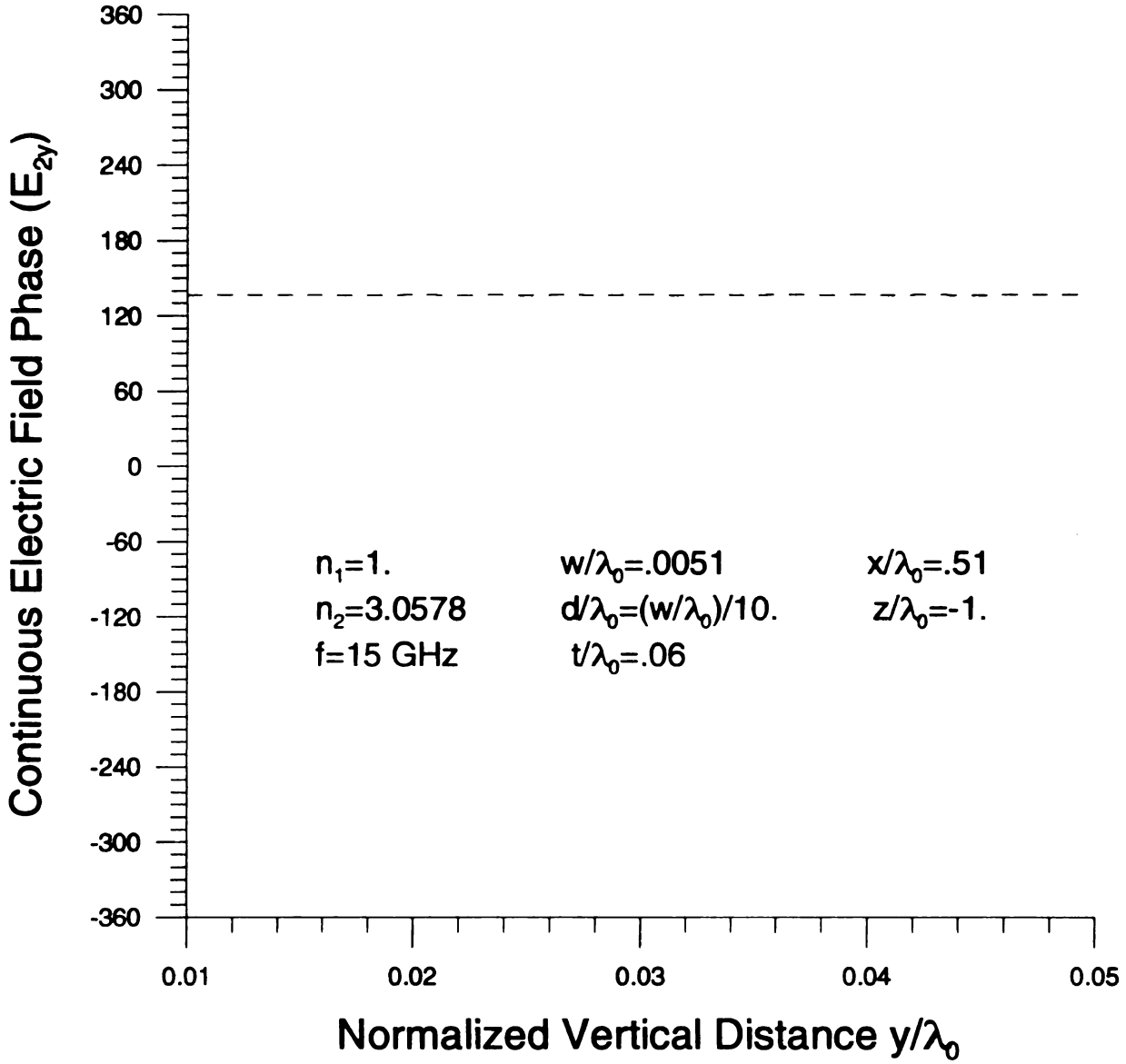

Figure 6.3.46 Vertical continuous electric film field spectrum phase profile in the low-loss limit.

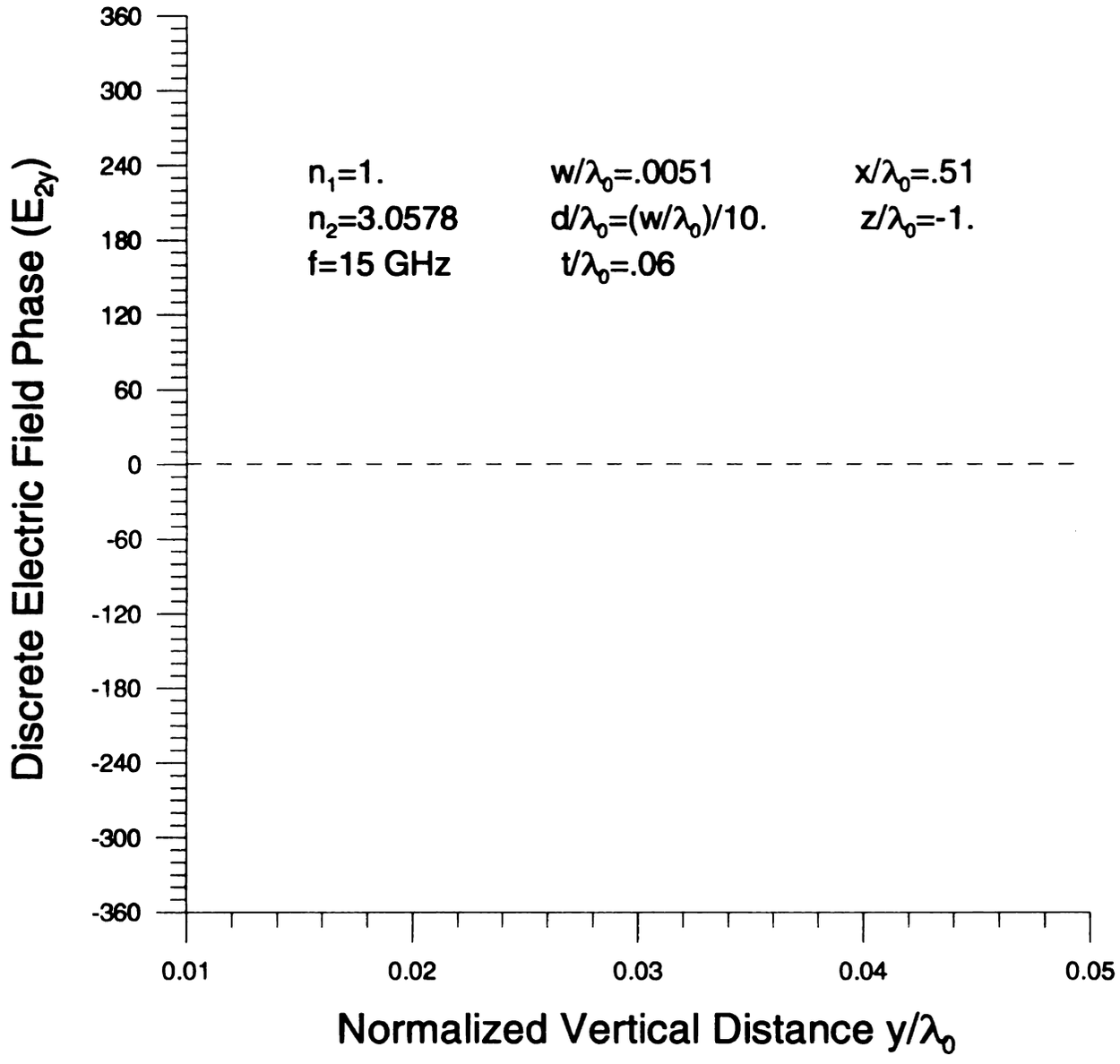

Figure 6.3.47 Vertical discrete electric film field spectrum phase profile in the low-loss limit.

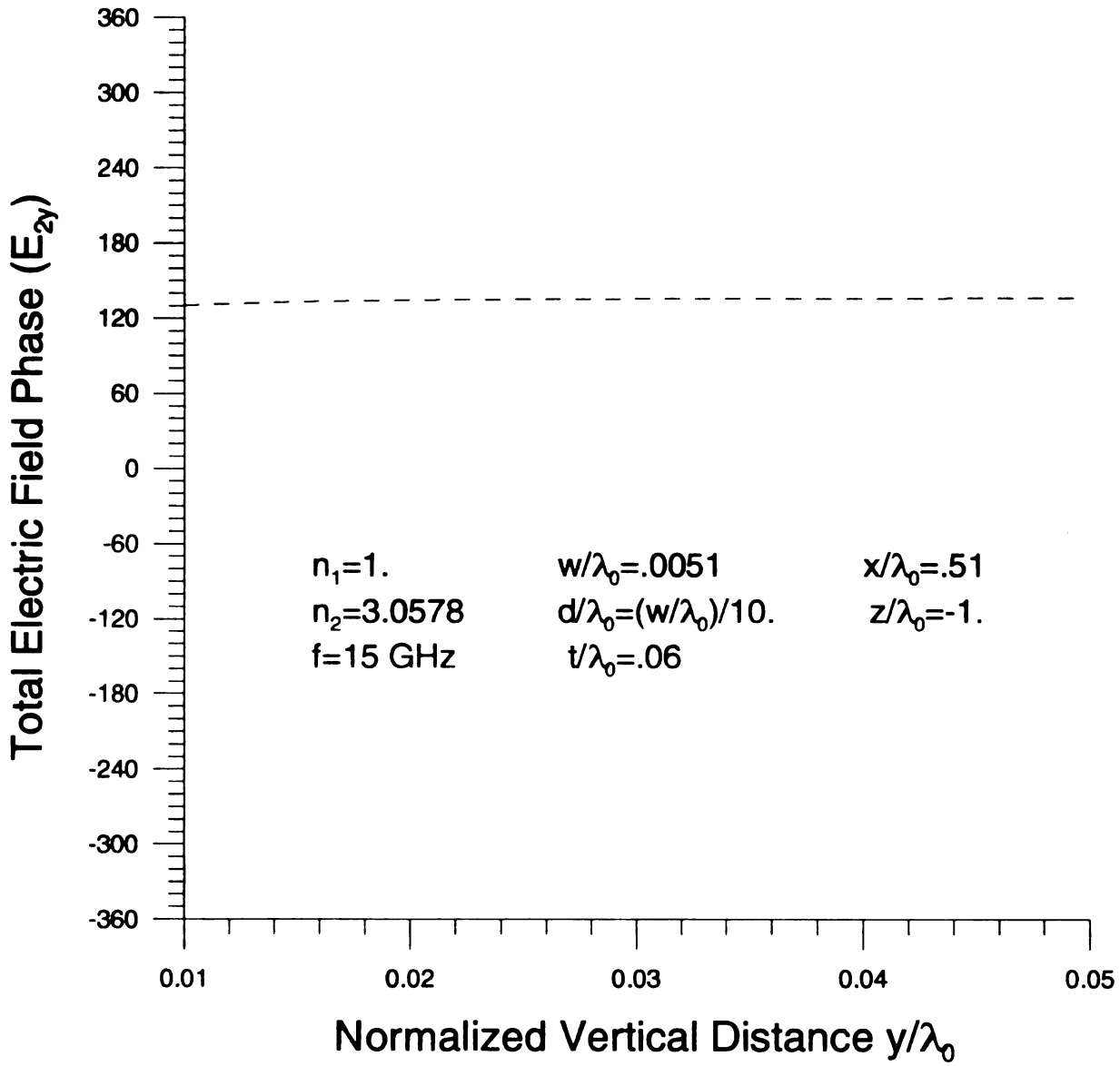

Figure 6.3.48 Vertical total electric film field spectrum phase profile in the low-loss limit.

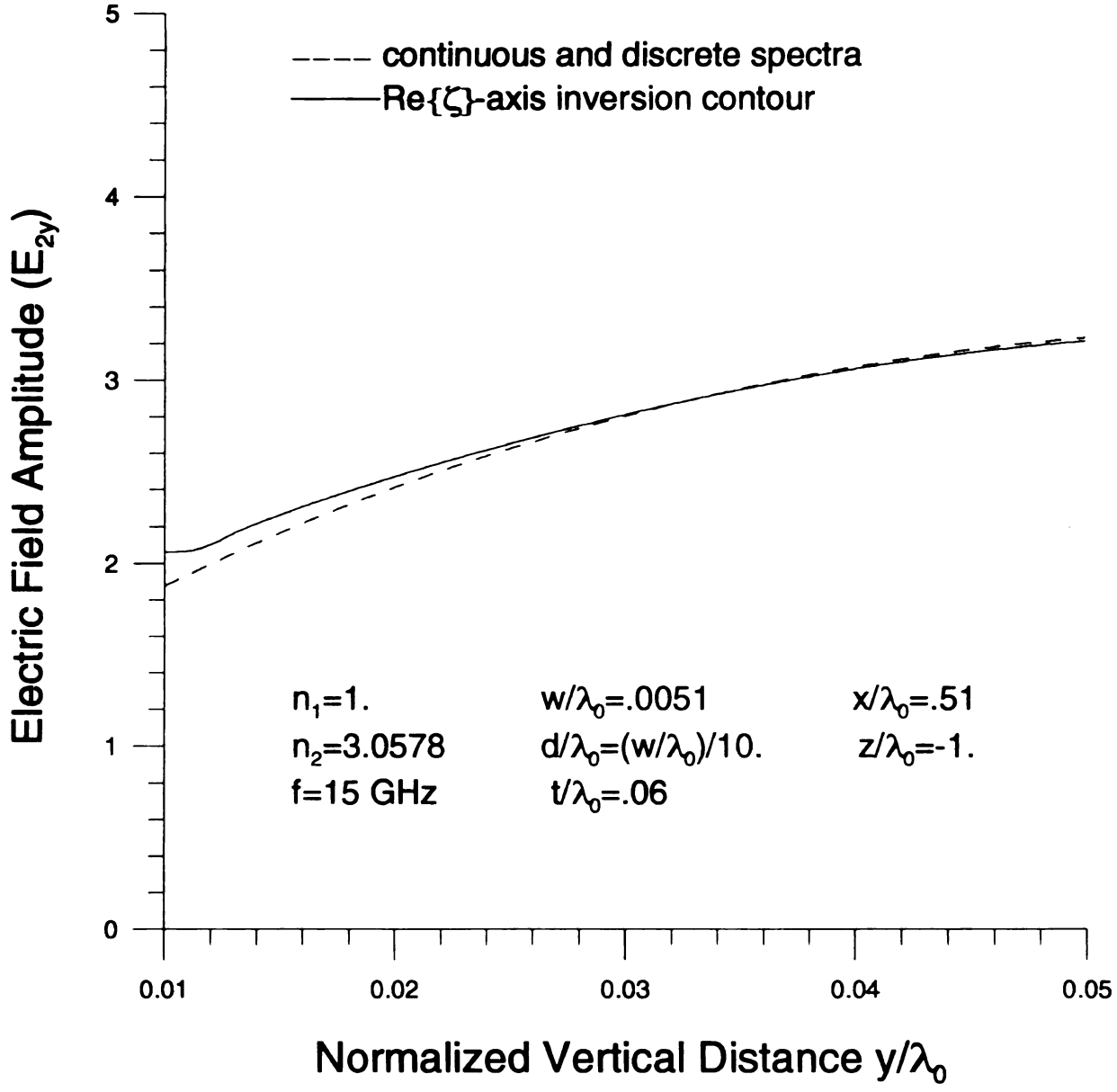

Figure 6.3.49 $\mathrm{Re}\{\zeta\}$**-axis inversion contour validation of microstrip film field amplitude profile contributed by the continuous spectrum field and the discrete spectrum field.**

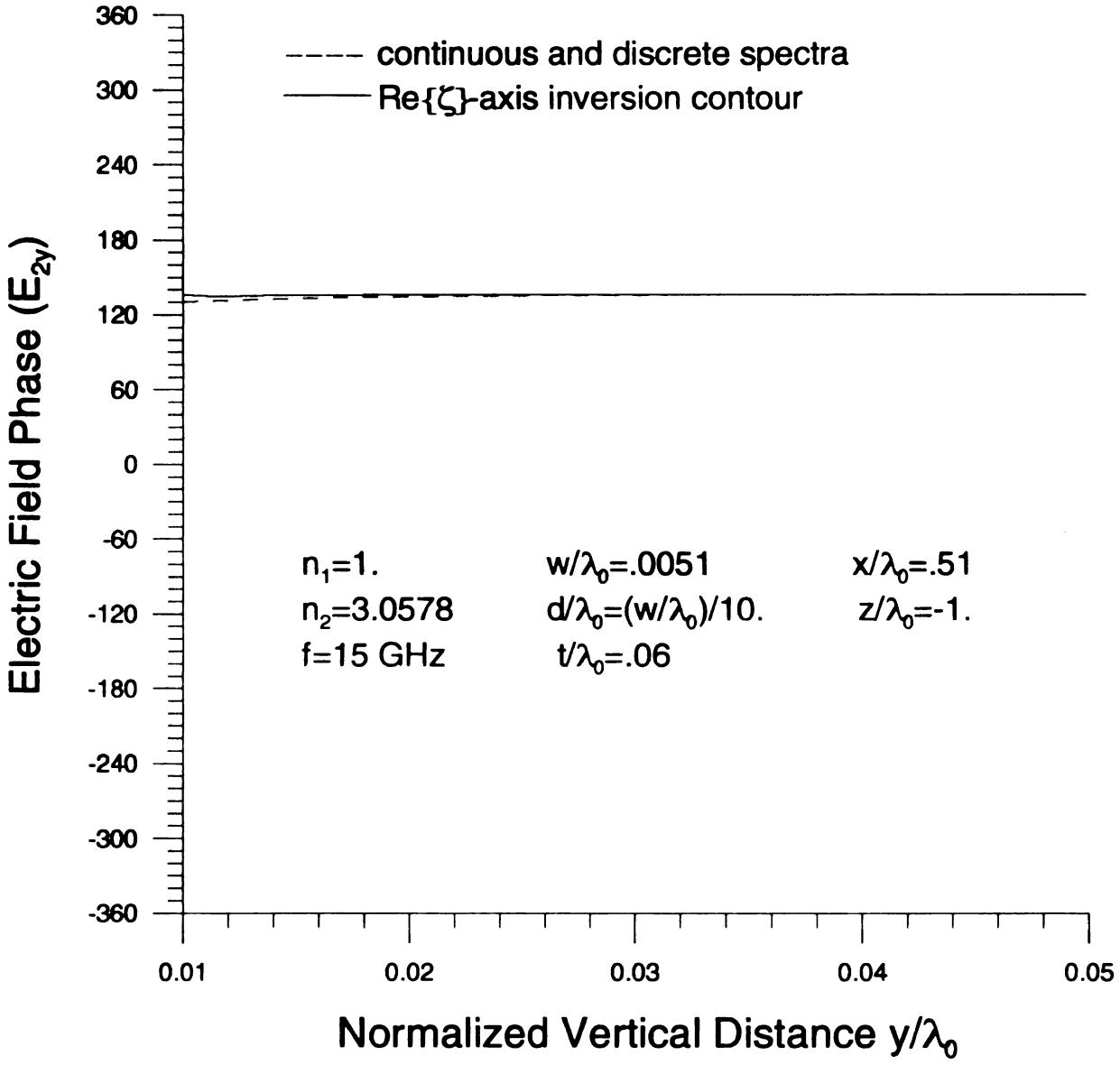

Figure 6.3.50 $\mathrm{Re}\{\zeta\}$**-axis inversion contour validation of microstrip cover field phase profile contributed by the continuous spectrum field and the discrete spectrum field.**

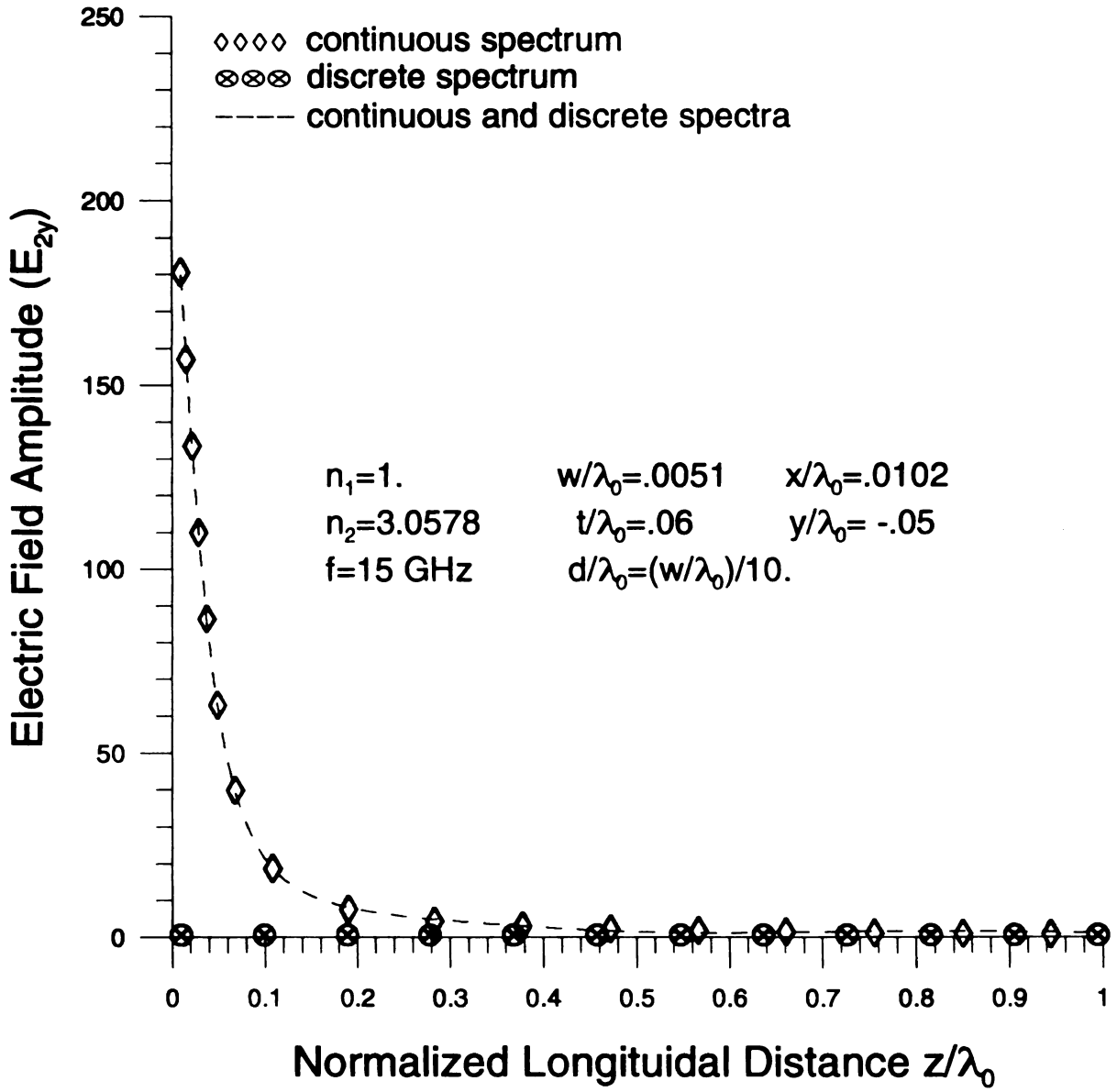

Figure 6.3.51 Longitudinal continuous and discrete electric film field spectrum amplitudes profile in the low-loss limit.

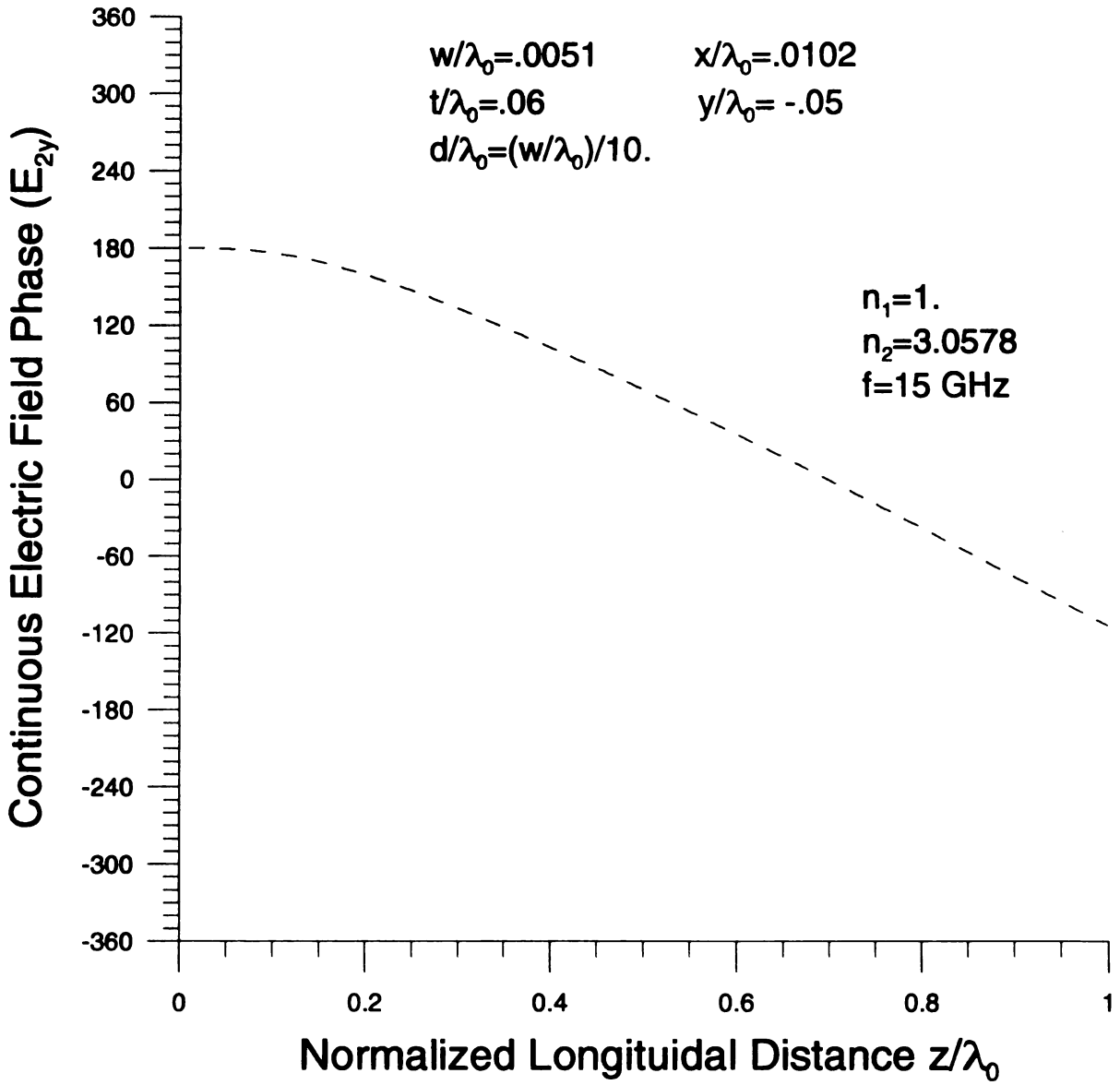

Figure 6.3.52 Longitudinal continuous electric film field spectrum phase profile in the low-loss limit.

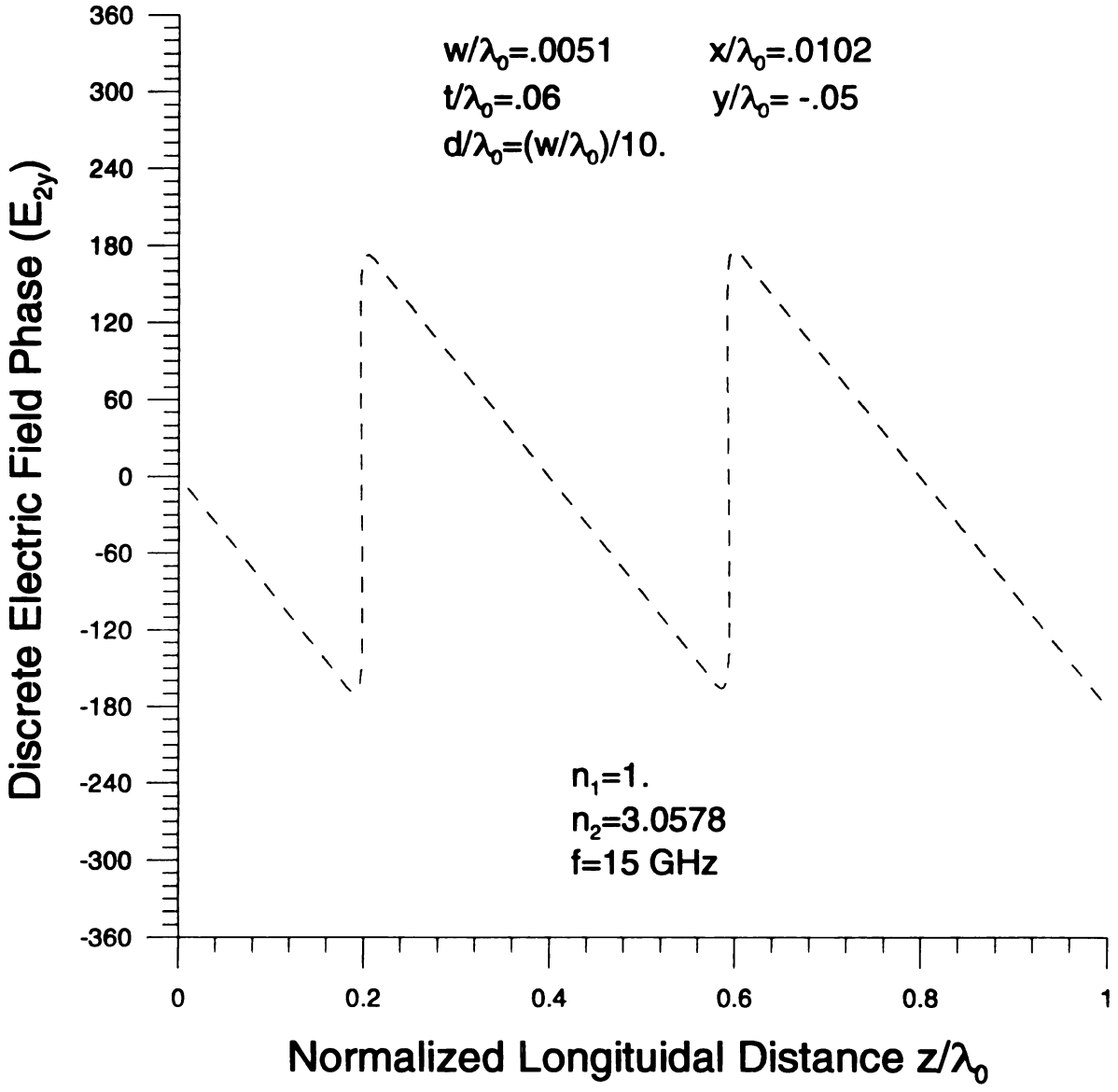

Figure 6.3.53 Longitudinal discrete electric field spectrum phase profile in the low-loss limit.

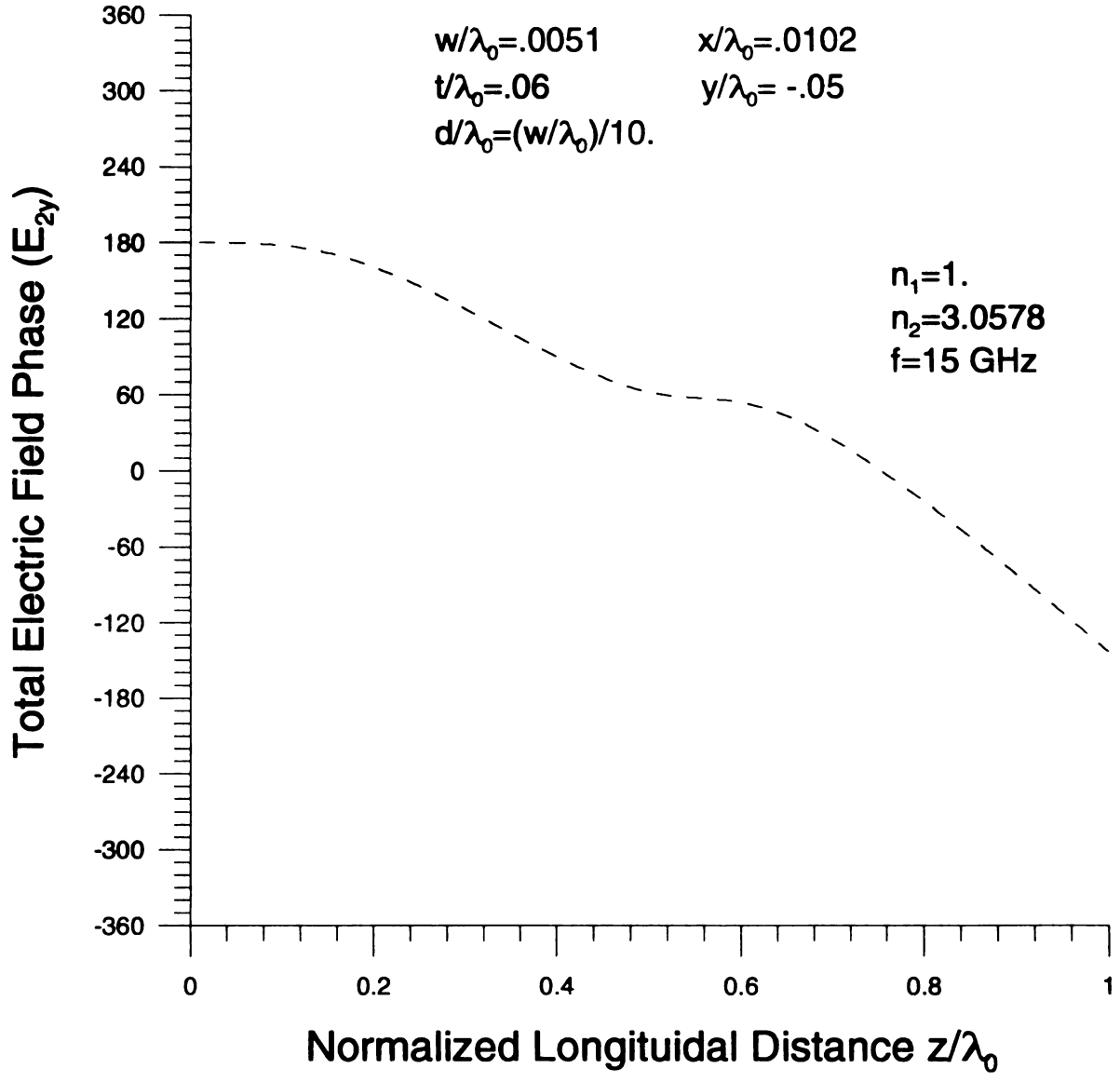

Figure 6.3.54 Longitudinal total electric film field spectrum phase profile in the low-loss limit.

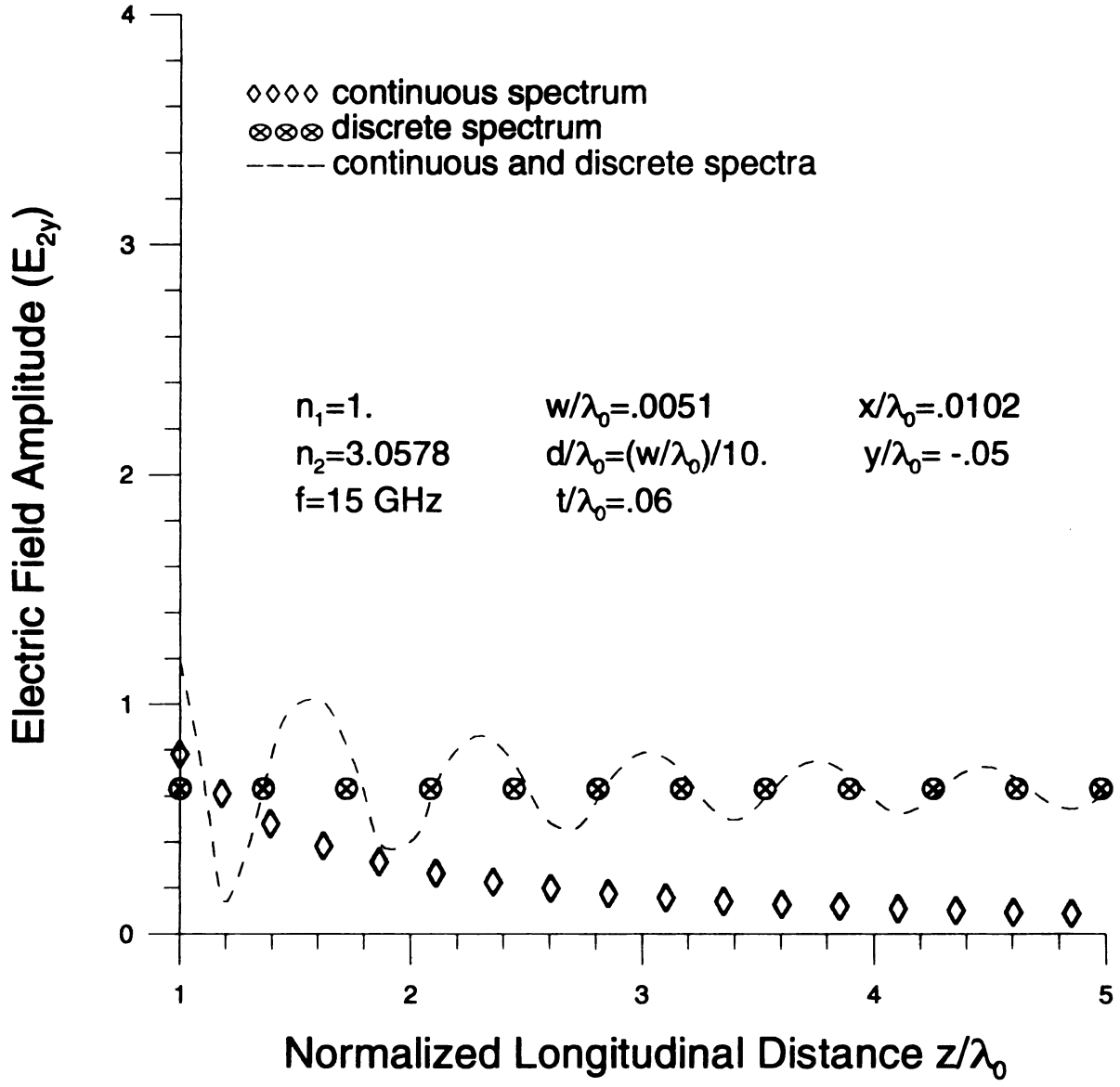

Figure 6.3.55 Longitudinal continuous and discrete electric film field spectrum amplitudes profile in the low-loss limit.

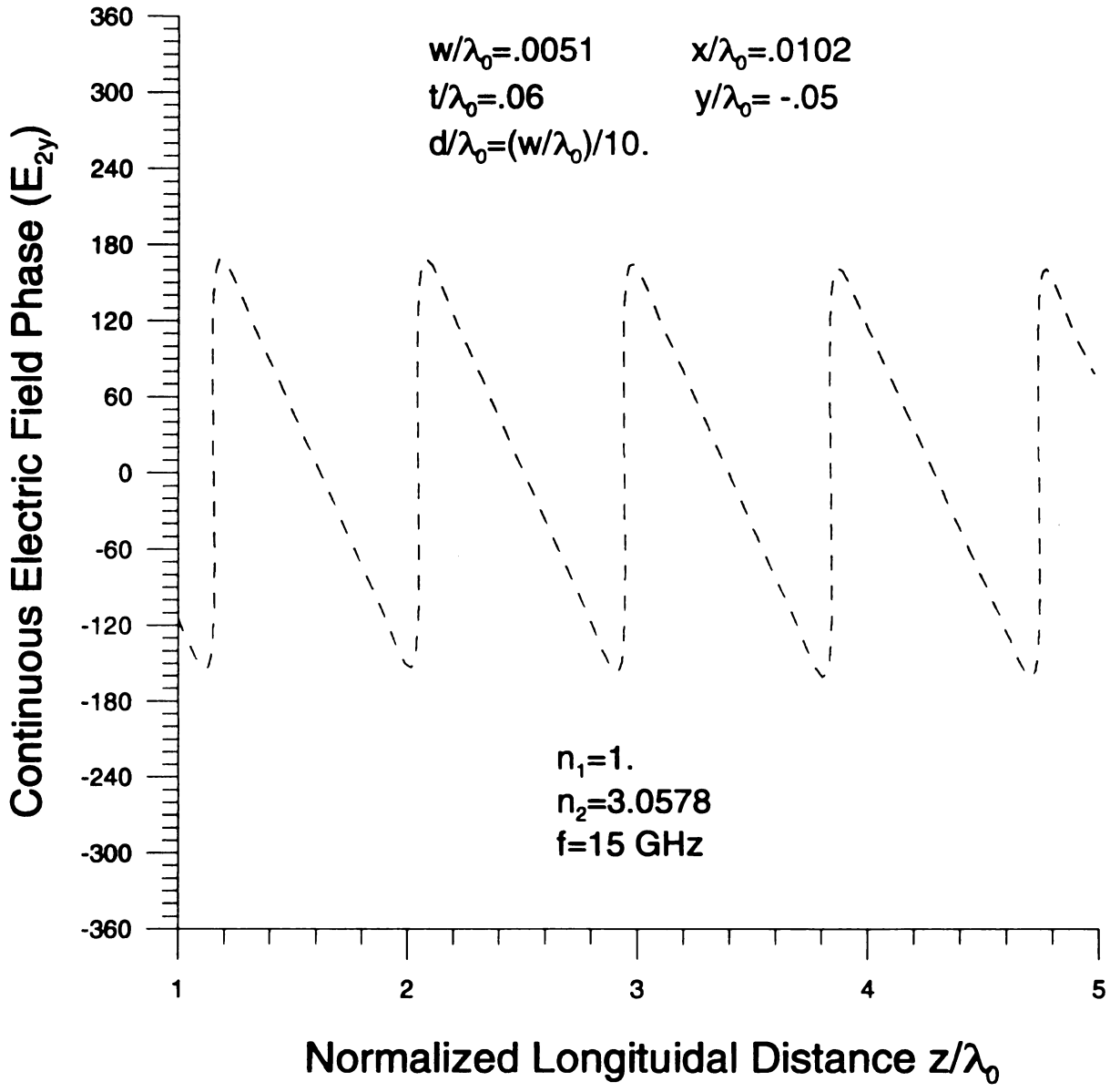

Figure 6.3.56 Longitudinal continuous electric film field spectrum phase profile in the low-loss limit.

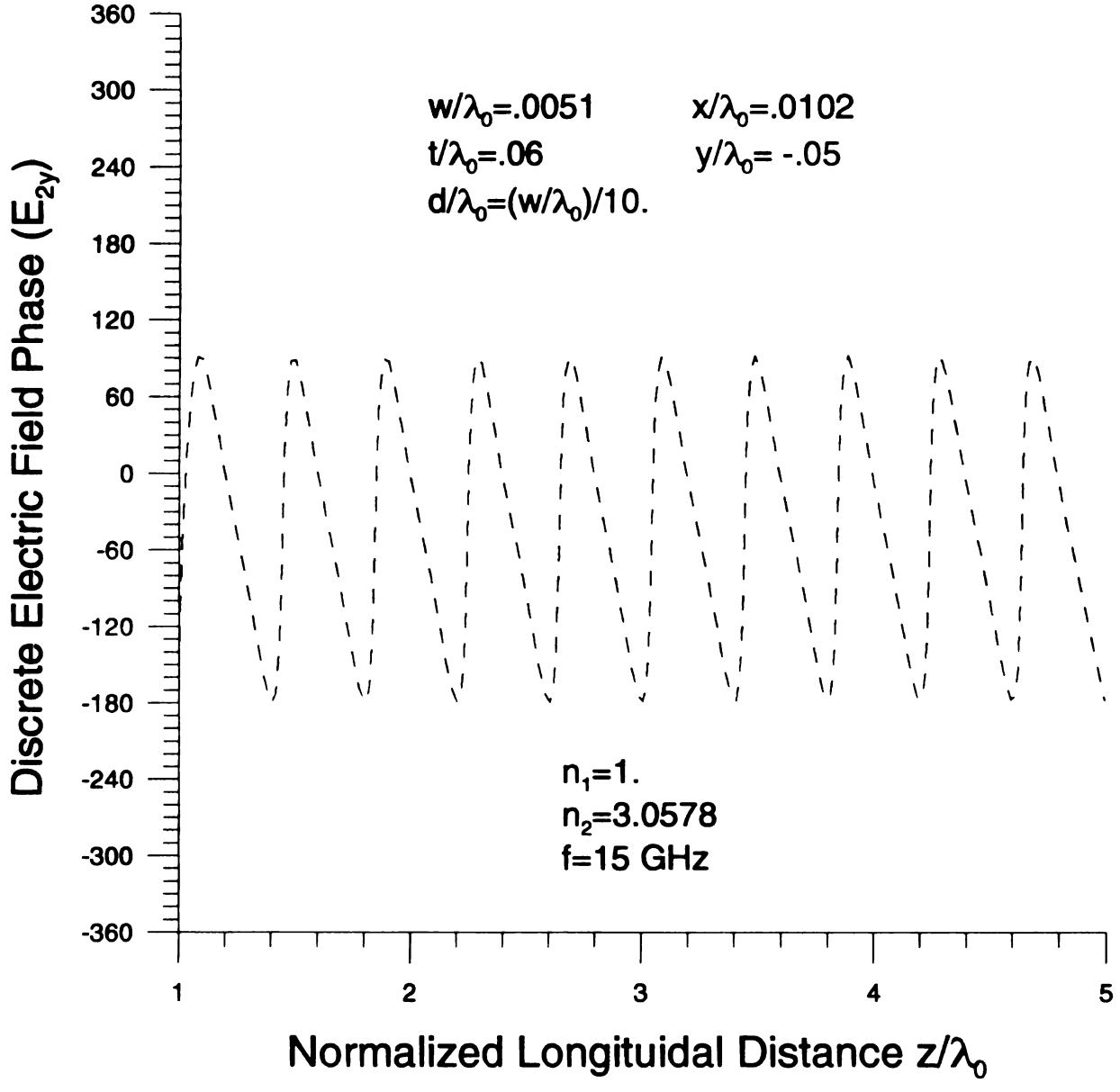

Figure 6.3.57 Longitudinal discrete electric film field spectrum phase profile in the low-loss limit.

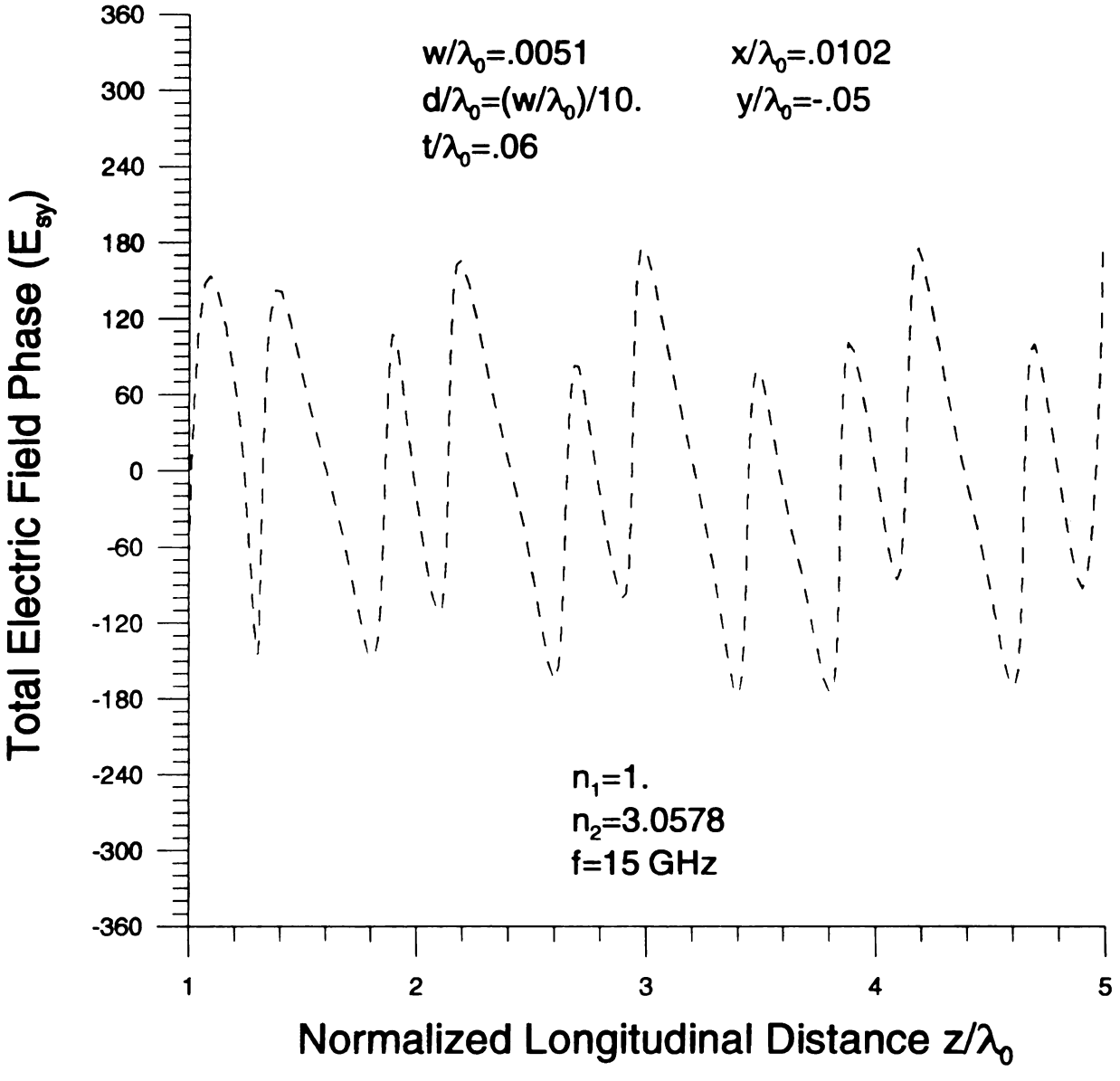

Figure 6.3.58 Longitudinal total electric film field spectrum phase profile in the low-loss limit.

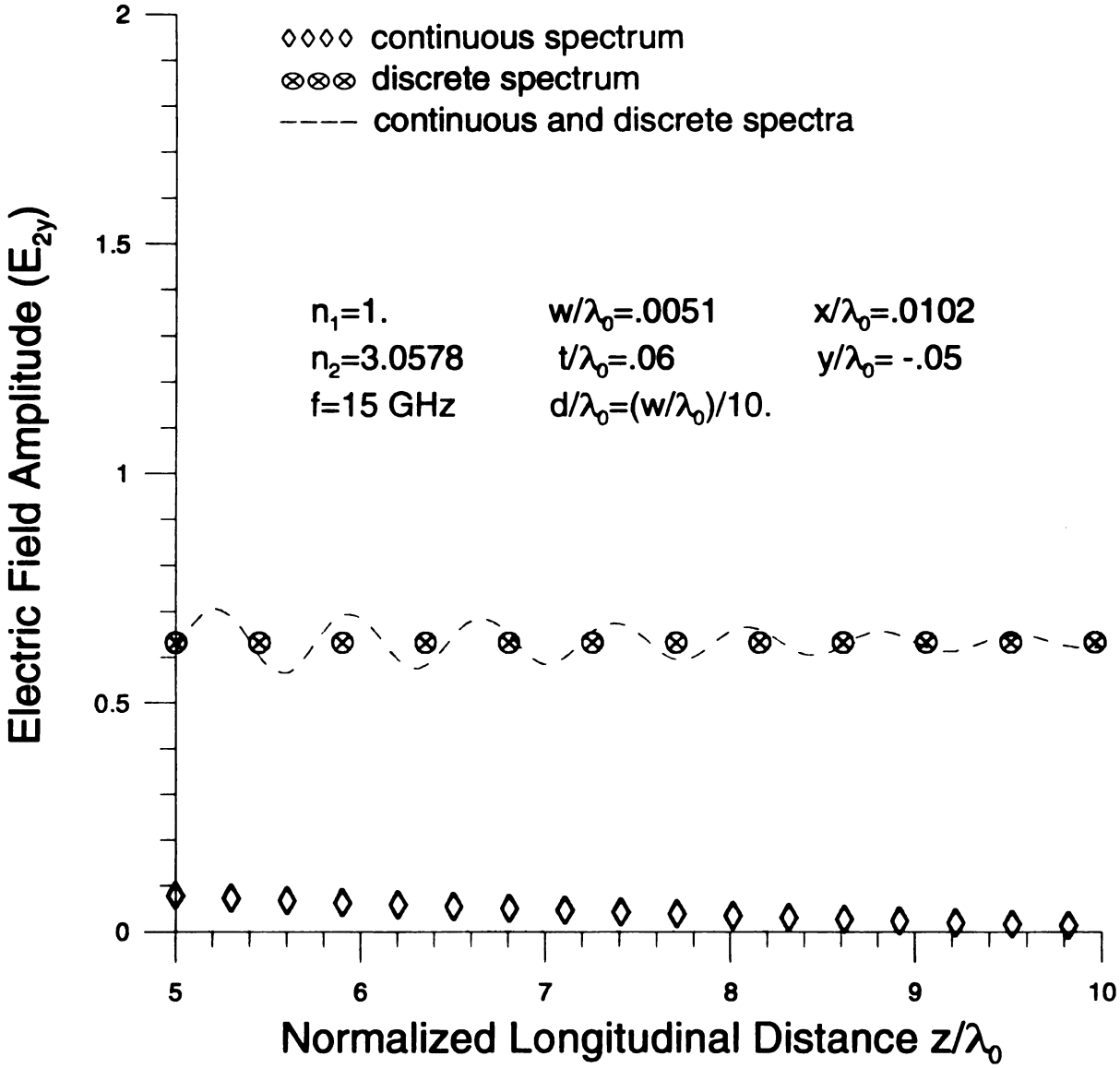

Figure 6.3.59 Longitudinal continuous and discrete electric film field spectrum amplitudes profile in the low-loss limit.

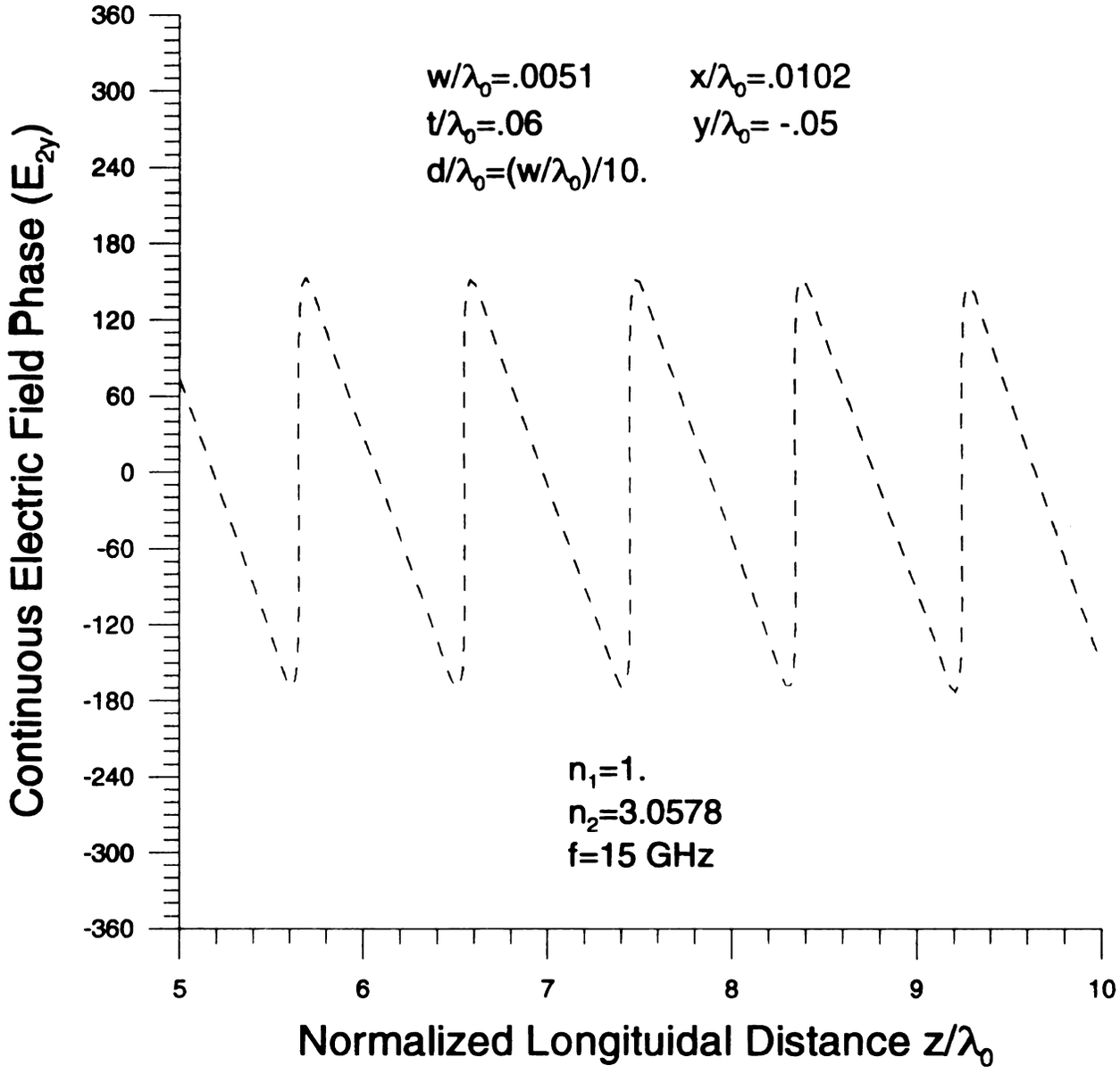

Figure 6.3.60 Longitudinal continuous electric film field spectrum phase profile in the low-loss limit.

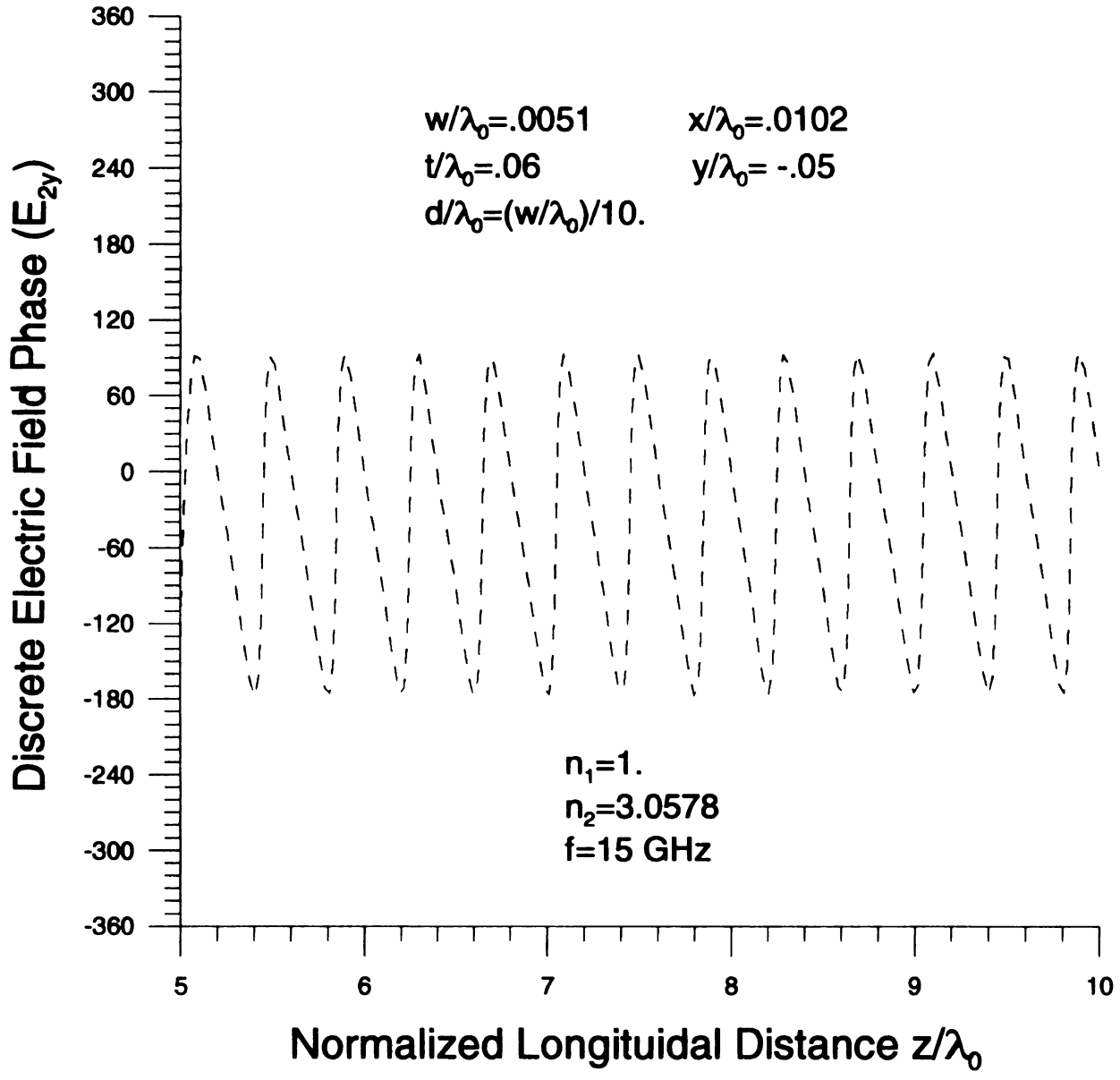

Figure 6.3.61 Longitudinal discrete electric film field spectrum phase profile in the low-loss limit.

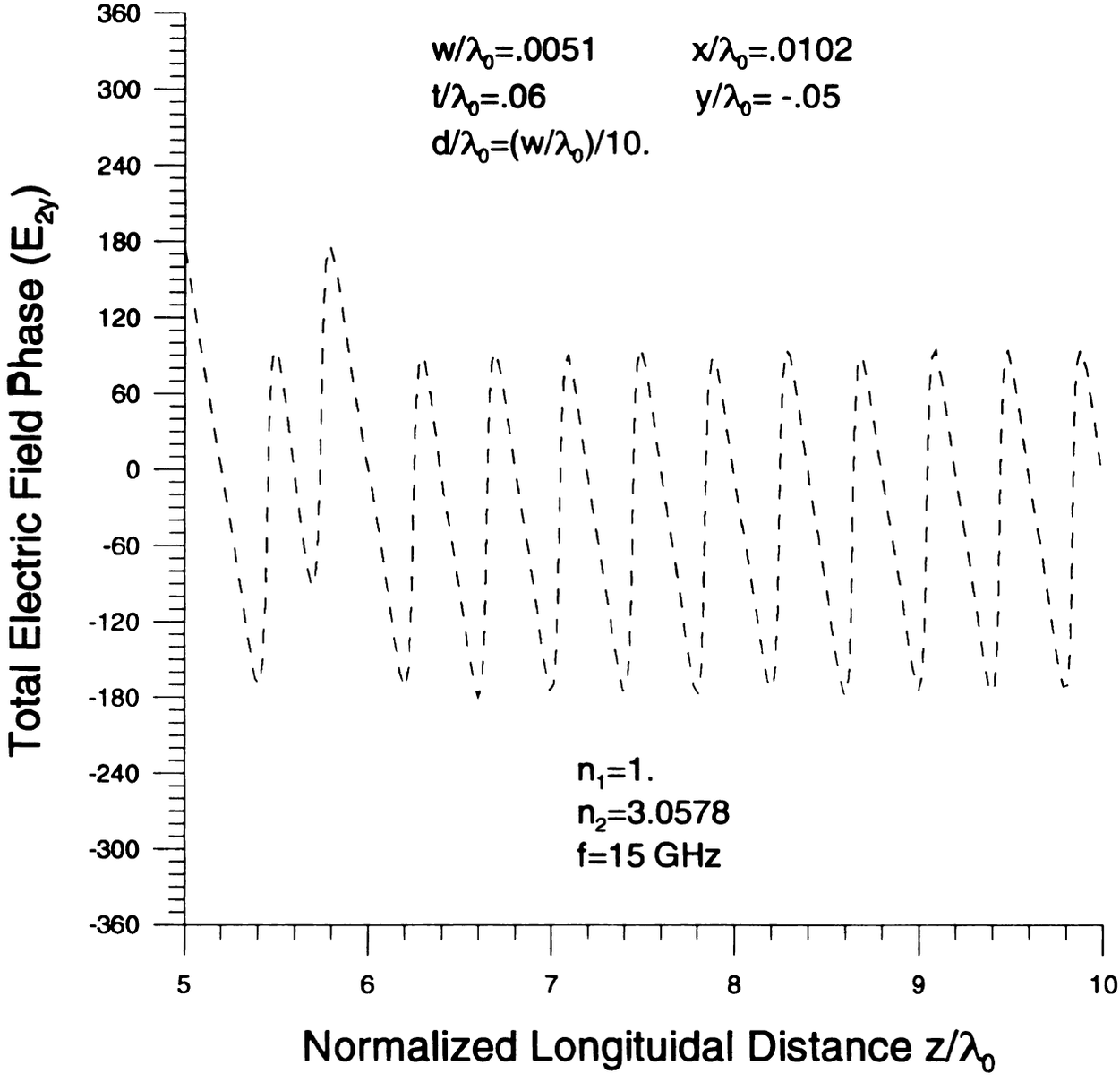

Figure 6.3.62 Longitudinal total electric film field spectrum phase profile in the low-loss limit.

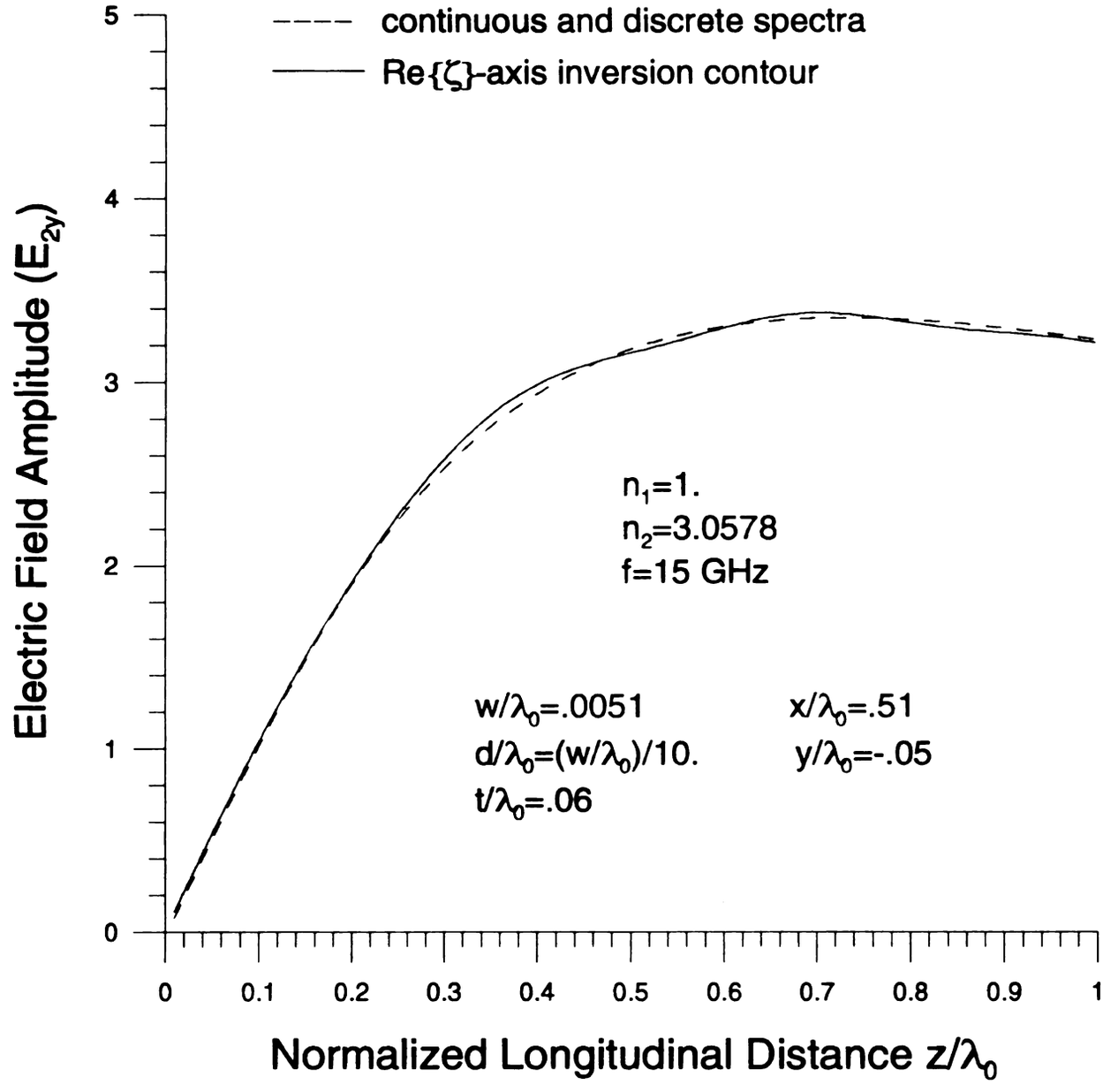

Figure 6.3.63 $\mathrm{Re}\{\zeta\}$**-axis inversion contour validation of microstrip film field amplitude profile contributed by the continuous spectrum field and the discrete spectrum field in the near zone.**

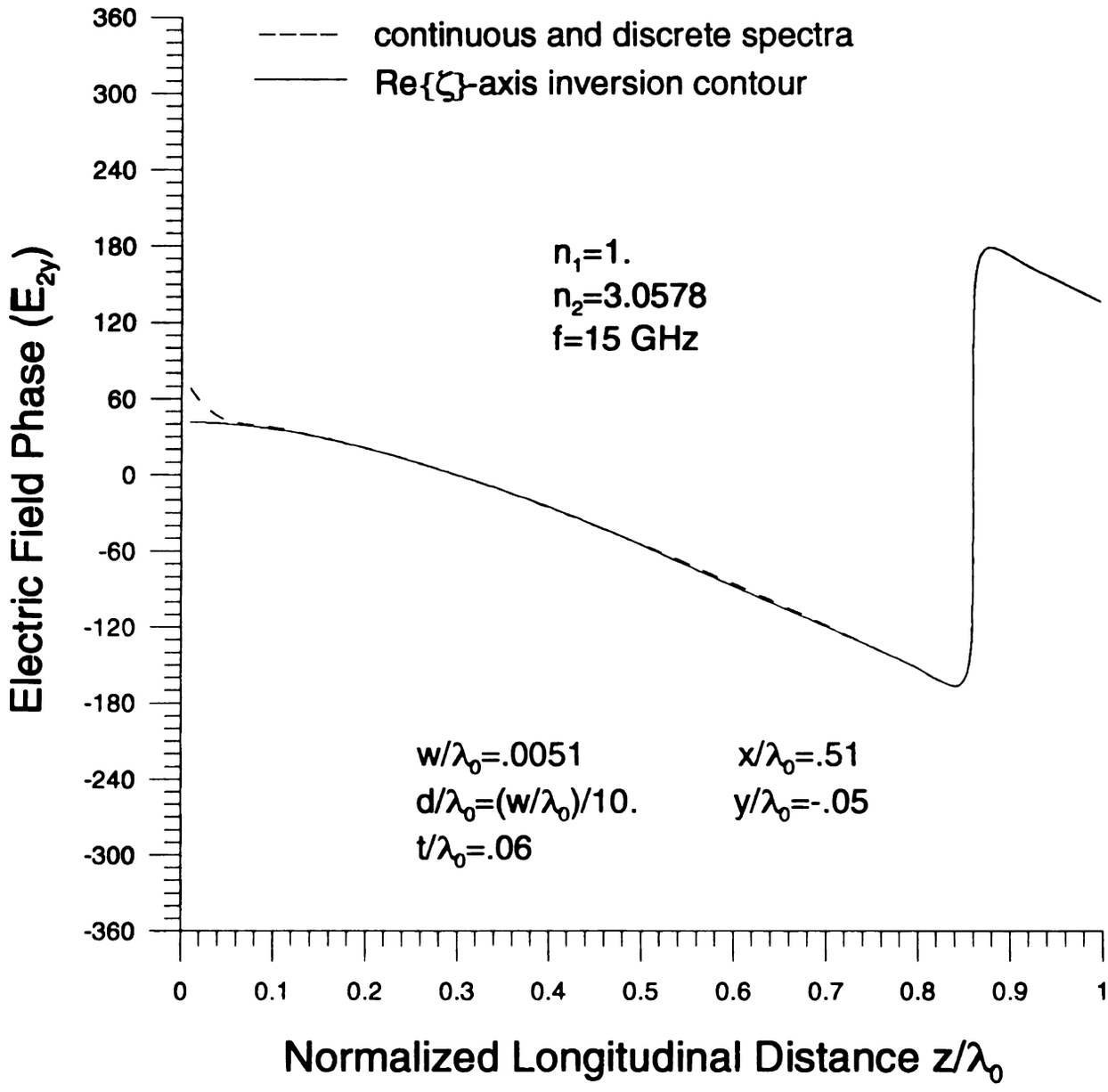

Figure 6.3.64 $\mathrm{Re}\{\zeta\}$**-axis inversion contour validation of microstrip film field phase profile contributed by the continuous spectrum field and the discrete spectrum field in the near zone.**

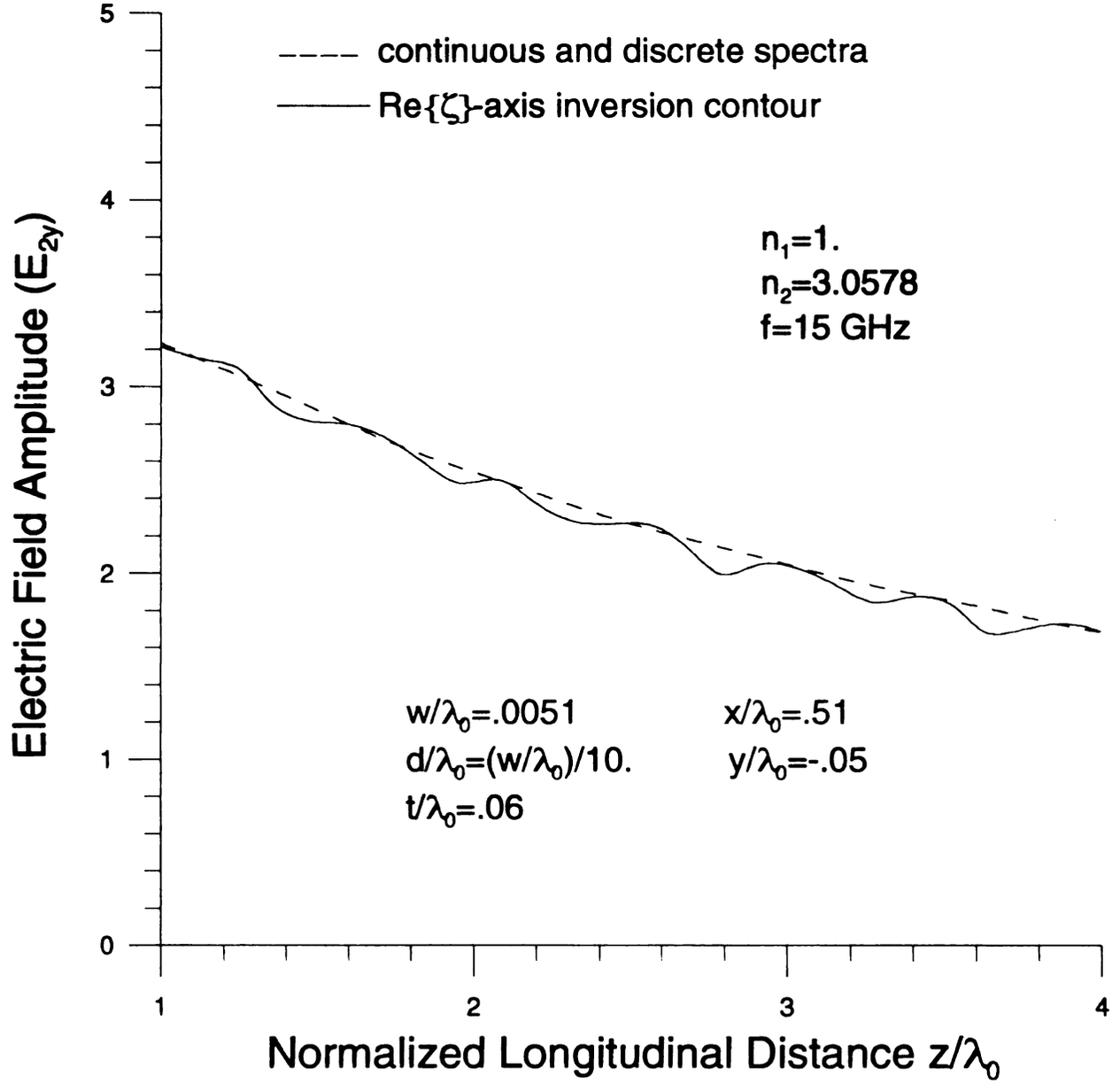

Figure 6.3.65 $\mathrm{Re}\{\zeta\}$**-axis inversion contour validation of microstrip film field amplitude profile contributed by the continuous spectrum field and the discrete spectrum field.**

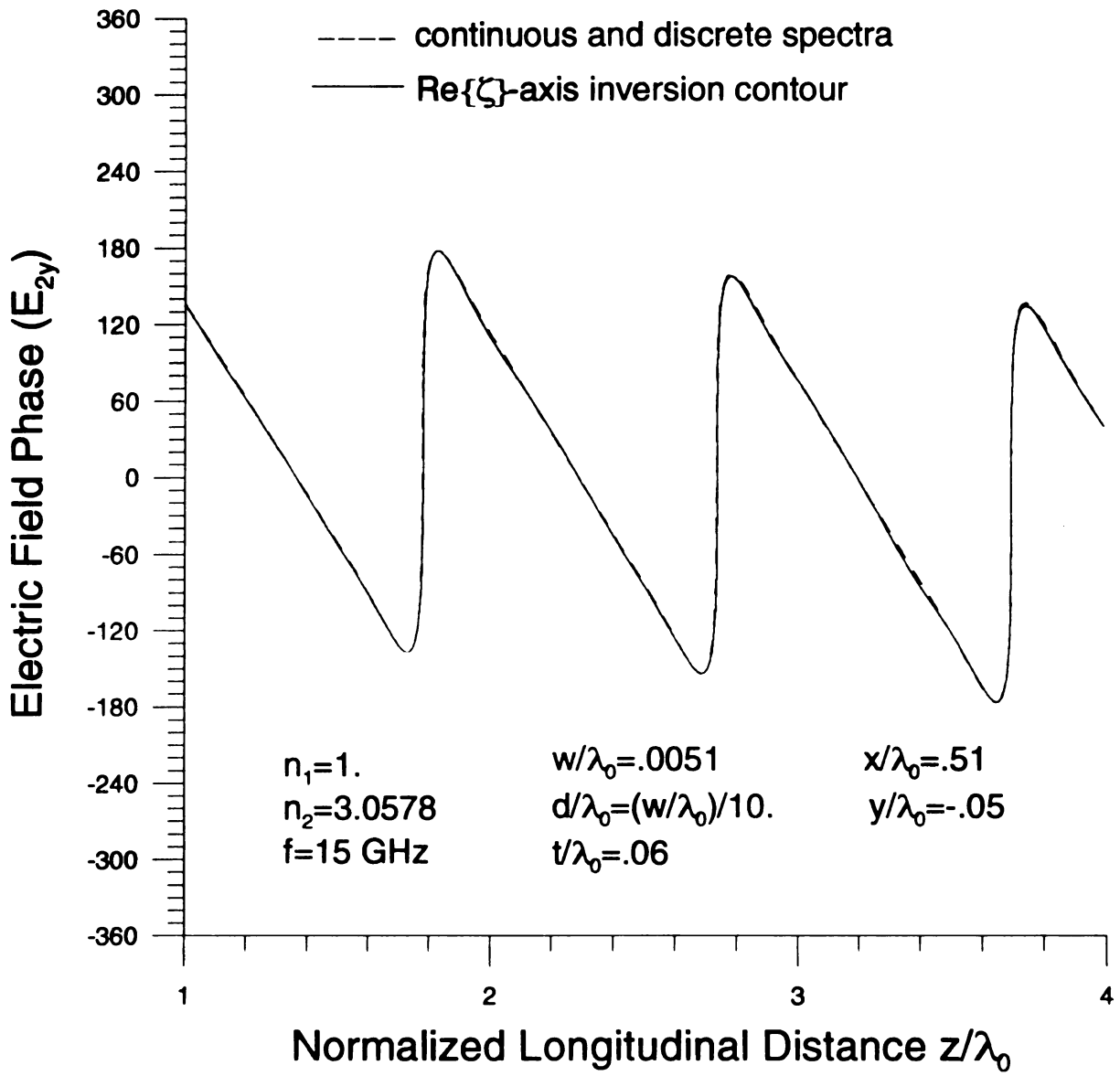

Figure 6.3.66 $\mathrm{Re}\{\zeta\}$**-axis inversion contour validation of microstrip film field phase profile contributed by the continuous spectrum field and the discrete spectrum field.**

6.4 CONCLUSION

The nature of the physics of fields about an open microstrip waveguide are conceptualized and quantified numerically. Since the microstrip fields are represented in proper (continuous and discrete) spectra, therefore no leaky-modes need to be considered. It is recognized that both the cover and film fields of the microstrip waveguide are dominated by the continuous spectrum in the near zone. However, since the continuous film field amplitude is relatively smaller in the film layer than that in the cover layer and the discrete film field is longitudinally constant, approximately beyond $z/\lambda_0 \approx 1.$, the discrete film field begins to dominate the total film field longitudinally.

The total fields are meaningfully validated by $\mathrm{Re}\{\zeta\}$-axis inversion integration in the complex axial transform plane. An asymptotic approximation to far zone EM fields will be discussed in Chapter 7.

CHAPTER 7

ASYMPTOTIC APPROXIMATION TO THE EM FIELD OF AN OPEN INTEGRATED MICROSTRIP WAVEGUIDE

7.1 INTRODUCTION AND GEOMETRICAL CONFIGURATION

The continuous and discrete spectrum fields of an open integrated microstrip have been rigorously discussed in Chapter 6, both theoretically and numerically. It is observed that near fields in the cover and film layers are dominated by the continuous spectrum rather than the discrete spectrum. Only the film field is dominated by the discrete spectrum at locations longitudinally away from the near zone. However, it is extremely difficult to compute the far zone fields due to numerical complexity. It is useful to employ *the method of steepest-descents or saddle-point approximation* to resolve the problem. This method can be applied simultaneously in both the complex transverse (ξ-) and longitudinal (ζ-) planes. Since most contribution to *SDP (Steepest-Descent Path)* arises from the saddle point, only one point in the complex axial transform plane (ζ-plane) needs to be considered instead of all points along *SDP*. Therefore there exist only one pair of branch-point and surface-wave pole singularities in the complex transverse plane (ξ-plane), which allows the complexity of numerical computation for the far zone fields in both the cover and film layers to be significantly reduced. Only the theoretical foundation for the cover field (the approximate film field can be obtained in a similar manner) is presented in this chapter. Therefore, the numerical implementation will be accommodated in future research.

The geometrical configuration of an integrated conducting microstrip waveguide immersed in a planar-layered background environment is depicted in Fig. 7.1.1, which the cross-sectional view is depicted in Fig. 7.1.2. The waveguiding axis is chosen to be z-axis with x-axis tangential and y-axis normal to the planar interfaces. Each of the planar layers is assumed to be non-magnetic, isotropic and homogeneous with complex permittivity ε_l, $l = 1, 2, 3$ for the cover, film, and substrate layers with $\varepsilon_3 \rightarrow -j\infty$ or $\sigma \rightarrow \infty$. The guiding structure is embedded in the cover layer adjacent to the cover/film interface.

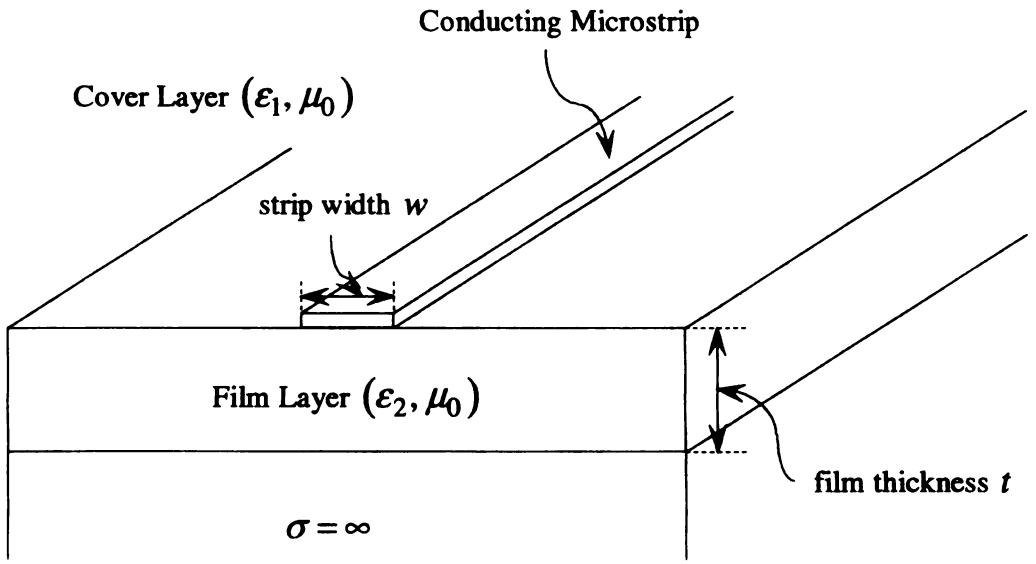

Figure 7.1.1 Geometrical configuration of open microstrip structure immersed in layered background environment.

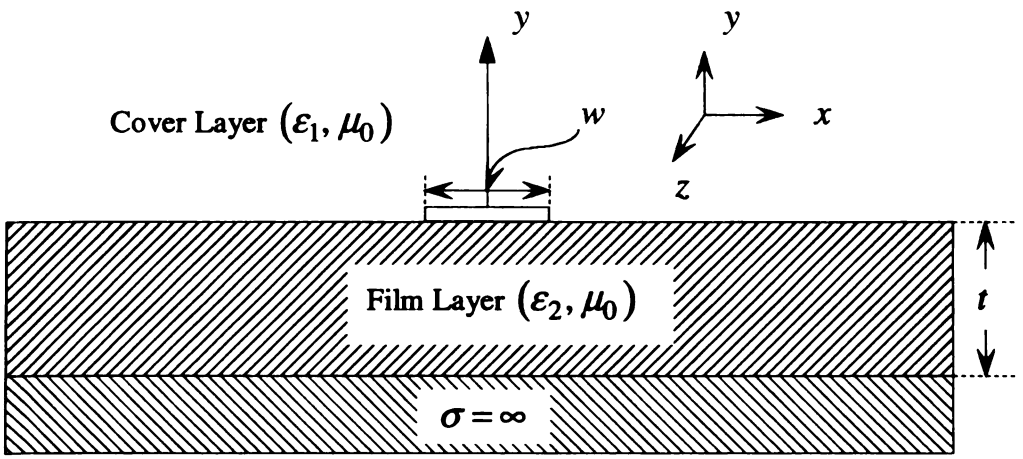

Figure 7.1.2 Cross-sectional view of immersed microstrip structure.

7.2 IDENTIFICATION OF THE STEEPEST-DESCENT PATH

In accordance with Eqn. (6.2.20), the cover field is formulated as

$$E_{1y}(r)=-\frac{j}{4\pi}\int_{-\infty}^{\infty}d\zeta\frac{\zeta\tilde{L}_g(\zeta)}{\int_{-\infty}^{\infty}\tilde{\eta}^2(\xi')\tilde{\tilde{C}}_{zz}(\xi',\zeta)d\xi'}e^{j\zeta z}$$

$$\int_{-\infty}^{\infty}\tilde{\eta}(\xi)\left[\left(\xi^2+\zeta^2\right)C_{1r}(\xi,\zeta)-\frac{2p_1^2}{Z^h(\xi,\zeta)}\right]\frac{e^{j\xi x}e^{-p_1 y}}{p_1}d\xi$$

where

$$\tilde{\tilde{C}}_{zz}(\xi',\zeta)=\frac{\left(k_1^2-\zeta^2\right)}{Z^h(\xi',\zeta)}+\frac{\zeta^2 p_1(\xi',\zeta)\left(N_{21}^2-1\right)}{Z^h(\xi',\zeta)Z^e(\xi',\zeta)}$$

$$C_{1r}(\xi,\zeta)=\frac{2\left(N_{21}^2-1\right)p_1(\xi,\zeta)}{Z^h(\xi,\zeta)Z^e(\xi,\zeta)}$$

$$\tilde{\eta}(\xi)=\begin{cases}J_0(\xi w/2)\cdots w/t<2\\ sinc(\xi w/2)\cdots w/t\geq 2\end{cases}$$

$$\tilde{L}_g(\zeta)=e^{-(\zeta d)^2/2}$$

As discussed in Chapters 5 and 6, for a point on the $\mathrm{Re}\{\zeta\}$-axis inversion contour there exist branch-point singularities $\pm\xi_{k_1}$ and surface-wave pole singularities $\pm\xi_{TM_0}$ in the complex ξ-plane. Fig. 7.2.1 indicates those singularities in the complex ξ-plane for a point in the interval 1 as depicted in Fig. 5.5.3. Since every point on the $\mathrm{Re}\{\zeta\}$-axis inversion contour has those singularities regardless of the quadrant where they occur in the complex ξ-plane, Cauchy's integral theorem in the complex ξ-plane leads to

$$\left(\int_{-\infty}^{\infty}+\int_{C_{\xi_{b1}}}+\int_{C_{\xi_{b2}}}+\oint_{C_{\xi_p}}+\int_{C_\infty}\right)F(\xi,\zeta)e^{j\xi x}d\xi=0 \qquad (7.2.1)$$

where

$$F(\xi,y,\zeta)=\tilde{\eta}(\xi)\left[\left(\xi^2+\zeta^2\right)C_{1r}(\xi,\zeta)-\frac{2p_1^2}{Z^h(\xi,\zeta)}\right]\frac{e^{-p_1 y}}{p_1} \qquad (7.2.2)$$

and the y dependence of F has been suppressed for brevity. Sommerfeld's radiation condition leads to

$$\int_{C_\infty} F(\xi,\zeta)e^{j\xi x}d\xi \to 0$$

$C_{\xi_{b1}}$ indicates one side of the branch cut contour and $C_{\xi_{b2}}$ the other side of the branch cut contour as depicted in Fig. 7.2.1. For $x>0$, the upper half plane (*UHP*) is closed and for $x<0$, the lower half plane (*LHP*) is closed. For points on $C_{\xi_{b1}}$ and $C_{\xi_{b2}}$,

$$\xi=\xi_{k_1}-js \qquad (7.2.3)$$

Then,

$$\int_{C_{\xi_{b1}}} F(\xi,\zeta)e^{j\xi x}d\xi=\int_{\xi_{k_1}-j\infty}^{\xi_{k_1}-j0} F(\xi,\zeta)e^{j\xi x}d\xi=je^{j\xi_{k_1}x}\int_0^\infty f(s,\zeta)e^{sx}ds$$

$$\int_{C_{\xi_{b2}}} F(\xi,\zeta)e^{j\xi x}d\xi=\int_{\xi_{k_1}-j0}^{\xi_{k_1}-j\infty} F(\xi,\zeta)e^{j\xi x}d\xi=-je^{j\xi_{k_1}x}\int_0^\infty f(s,\zeta)e^{sx}ds \qquad (7.2.4)$$

where

$$f(s,\zeta)=F(\xi,\zeta)\big|_{\xi=\xi_{k_1}-js}$$

Since the cover wavenumber $p_1(\xi,\zeta)$ is multi-valued on either side of the branch cut contours ($C_{\xi_{b1}}$ and $C_{\xi_{b2}}$), the branch cut integral contributions will not be annulled.

$$\int_{C_{\xi_{b1}}} F(\xi,\zeta)e^{j\xi x}d\xi+\int_{C_{\xi_{b2}}} F(\xi,\zeta)e^{j\xi x}d\xi=$$
$$je^{j\xi_{k_1}x}\int_0^\infty f(s,\zeta)e^{sx}ds-je^{j\xi_{k_1}x}\int_0^\infty f(s,\zeta)e^{sx}ds\neq 0 \qquad (7.2.5)$$

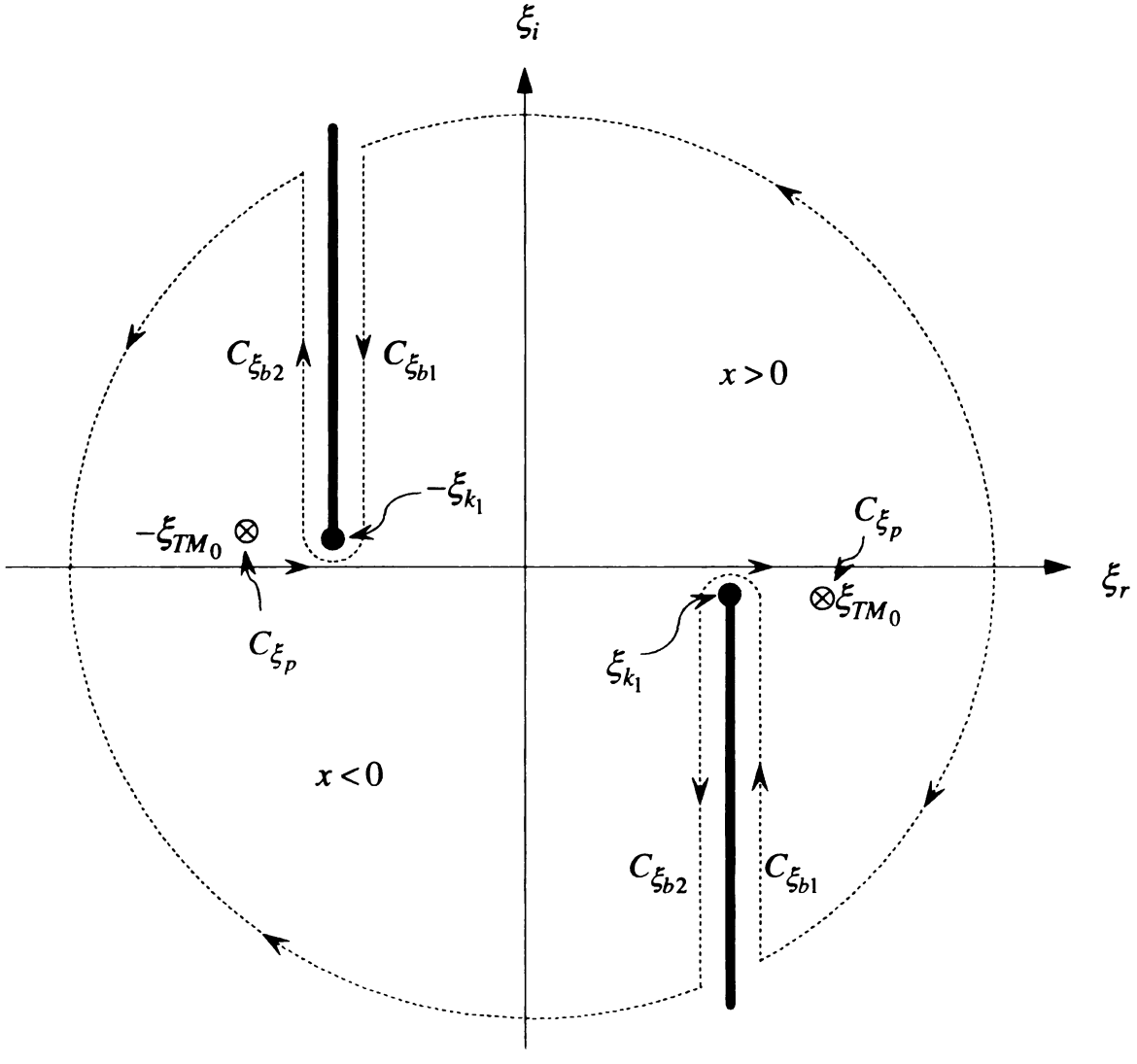

Figure 7.2.1 Branch-point singularities $\pm\xi_{k_1}$ and surface-wave pole singularities $\pm\xi_{TM_0}$ in the complex ξ -plane for a corresponding point on $\mathrm{Re}\{\zeta\}$-axis inversion contour in the complex ζ -plane.

Then,

$$\int_{C_{\xi_{b1}}} F(\xi,\zeta)e^{j\xi x}d\xi + \int_{C_{\xi_{b2}}} F(\xi,\zeta)e^{j\xi x}d\xi = \int_{C_{\xi_b}} F(\xi,\zeta)e^{j\xi x}d\xi$$

where (7.2.6)

$$C_{\xi_b} = C_{\xi_{b1}} + C_{\xi_{b2}}$$

And

$$\int_{C_{\xi_b}} F(\xi,\zeta)e^{j\xi x}d\xi = je^{j\xi_{k_1} x} I_{12}(x,\zeta)$$

where (7.2.7)

$$I_{12}(x,\zeta) = \int_0^\infty \left[f(s,\zeta)\Big|_{s\in C_{\xi_{b1}}} - f(s,\zeta)\Big|_{s\in C_{\xi_{b2}}} \right] e^{sx} ds$$

As discussed previously in Section 6.2.1, the surface-wave contribution is

$$\oint_{C_{\xi_p}} F(\xi,\zeta)e^{j\xi x}d\xi = g_{sw}(\xi_p,\zeta)e^{j\xi_p x}$$

where

$$g_{sw}(\xi_p,\zeta) = j4\pi\tilde{\eta}(\xi_p)\frac{(\xi_p^2+\zeta^2)(N_{21}^2-1)}{Z^h(\xi_p,\zeta)Z^{e'}(\xi_p,\zeta)}e^{-p_1(\xi_p,\zeta)y}$$

$$Z^{e'}(\xi_p,\zeta) = \frac{N_{21}^2\xi_p}{p_1(\xi_p,\zeta)} + \frac{\xi_p \tanh\left[p_2(\xi_p,\zeta)t\right]}{p_2(\xi_p,\zeta)} + \xi_p t \operatorname{sech}^2\left[p_2(\xi_p,\zeta)t\right]$$

$$Z^h(\xi,\zeta) = p_1(\xi,\zeta) + p_2(\xi,\zeta)\coth\left[p_2(\xi,\zeta)t\right]$$

$$\tilde{\eta}(\xi) = \begin{cases} J_0(\xi w/2)\cdots w/t < 2 \\ sinc(\xi w/2)\cdots w/t \geq 2 \end{cases}$$

Therefore,

$$\int_{C_{\xi_b}} F(\xi,\zeta)e^{j\xi x}d\xi + \oint_{C_{\xi_p}} F(\xi,\zeta)e^{j\xi x}d\xi = je^{j\xi_{k_1} x} I_{12}(x,\zeta) + g_{sw}(\xi_p,\zeta)e^{j\xi_p x}$$

Finally, the cover field is reformed as

$$E_{1y}(\boldsymbol{r}) = -\frac{j}{4\pi}\int_{-\infty}^{\infty} \frac{\zeta \tilde{L}_g(\zeta)}{\int_{-\infty}^{\infty} \tilde{\eta}^2(\xi')\tilde{\tilde{C}}_{zz}(\xi',\zeta)d\xi'} \left[\int_{-\infty}^{\infty} F(\xi,\zeta)e^{j\xi x}d\xi\right] e^{j\zeta z}d\zeta$$

$$= -\frac{1}{4\pi}\int_{-\infty}^{\infty} \frac{\zeta \tilde{L}_g(\zeta)}{\int_{-\infty}^{\infty} \tilde{\eta}^2(\xi')\tilde{\tilde{C}}_{zz}(\xi',\zeta)d\xi'} I_{12}(x,\zeta)e^{j\xi_{k_1} x}e^{j\zeta z}d\zeta \qquad (7.2.8)$$

$$+\frac{j}{4\pi}\int_{-\infty}^{\infty} \frac{\zeta \tilde{L}_g(\zeta)}{\int_{-\infty}^{\infty} \tilde{\eta}^2(\xi')\tilde{\tilde{C}}_{zz}(\xi',\zeta)d\xi'} g_{sw}(\xi_p,\zeta)e^{j\xi_p x}e^{j\zeta z}$$

Eqn. (7.2.8) allows one to implement the steepest-descent path in the complex ζ -plane. Since $x<0$ and $z<0$ for *LHP*, using the polar coordinate transformation as depicted in Fig. 7.2.2,

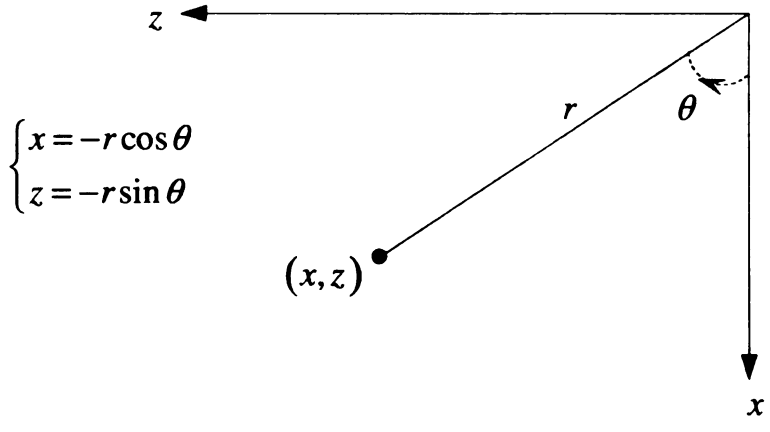

Figure 7.2.2 Polar coordinate transformation.

Then,

$$e^{j\xi_{k_1} x}e^{j\zeta z} = e^{r\left(-j\xi_{k_1}\cos\theta - j\zeta\sin\theta\right)}$$

$$e^{j\xi_{TM_0} x}e^{j\zeta z} = e^{r\left(-j\xi_{TM_0}\cos\theta - j\zeta\sin\theta\right)} \qquad (7.2.9)$$

Since $\xi_{k_1} = -j\sqrt{\zeta^2 - k_1^2}$ and $\xi_{TM_0} = -j\sqrt{\zeta^2 - \lambda_{TM_0}^2}$, the above expressions are

$$\begin{aligned} e^{j\xi_{k_1}x} e^{j\zeta z} &= e^{r\left(-\sqrt{\zeta^2 - k_1^2}\cos\theta - j\zeta\sin\theta\right)} \\ e^{j\xi_{TM_0}x} e^{j\zeta z} &= e^{r\left(-\sqrt{\zeta^2 - \lambda_{TM_0}^2}\cos\theta - j\zeta\sin\theta\right)} \end{aligned} \tag{7.2.10}$$

As discussed in Sections 2.3.1 and 3.2.5, define

$$\begin{aligned} &\delta(\zeta) = -p_s(\zeta)\cos\theta - j\zeta\sin\theta \\ &\textit{where} \\ &p_s(\zeta) = \sqrt{\zeta^2 - \lambda_s^2} \quad (\lambda_s = k_1, \lambda_{TM_0}) \end{aligned} \tag{7.2.11}$$

The stationary point ζ_0 in the complex ζ-plane was shown to be a *saddle point* in that plane. Using Eqn. (2.3.2) yields,

$$\begin{aligned} &\delta'(\zeta_0) = -\frac{\zeta_0}{\sqrt{\zeta_0^2 - \lambda_s^2}}\cos\theta - j\sin\theta = 0 \\ &\therefore \zeta_0 = \lambda_s \sin\theta \end{aligned} \tag{7.2.12}$$

It is noted that since $x < 0$ and $z < 0$ for *LHP*, $\theta = \tan^{-1}(z/x) > 0$. In accordance with Eqn. (2.3.12), the steepest-descent path in the complex ζ-plane is identified as

$$\delta(\zeta) = \delta(\zeta_0) \tag{7.2.13}$$

After some manipulation,

$$\left(\frac{\zeta}{\lambda_s}\right)\sin\theta - j\left[\frac{p_s(\zeta)}{\lambda_s}\right]\cos\theta = 1 \tag{7.2.14}$$

$$\left(\frac{\zeta}{\lambda_s}\right)^*\sin\theta + j\left[\frac{p_s(\zeta)}{\lambda_s}\right]^*\cos\theta = 1 \tag{7.2.15}$$

Consequently, the steepest-descent path in the complex ζ-plane is obtained by adding Eqn. (7.2.14) and Eqn. (7.2.15) as

$$\left[\frac{\zeta}{\lambda_s}+\left(\frac{\zeta}{\lambda_s}\right)^*\right]\frac{\sin\theta}{2}-j\left[\frac{p_s(\zeta)}{\lambda_s}-\left\{\frac{p_s(\zeta)}{\lambda_s}\right\}^*\right]\frac{\cos\theta}{2}=1 \qquad (7.2.16)$$

Therefore, the steepest-descent path on the complex ζ-plane is explicitly derived from Eqn. (7.2.16) and replacing k_l by λ_s in Appendix B such that

$$\zeta=\zeta'+j\zeta''=(\zeta',\zeta'')$$
$$\textit{where} \qquad (7.2.17)$$
$$\zeta''=\pm\frac{|\zeta'-\lambda_s\sin\theta||\lambda_s-\zeta'\sin\theta|}{\cos\theta\sqrt{(\zeta'\cos\theta)^2+(\lambda_s-\zeta'\sin\theta)^2}}$$

Fig. 7.2.3 depicts the steepest-descent path (*SDP*) defined by Eqn. (7.2.17) for an observation aspect angle θ less than the threshold aspect angle θ_t identified in Eqn. (2.6.3) as

$$\theta_t=\frac{\pi}{2}-\cos^{-1}\left(\frac{k_1}{\lambda_{TM_0}}\right) \qquad (7.2.18)$$

Then, the steepest-descent path always violates the cover branch cut C_{bc} and the pole-related branch cut C_{bp} an even number of times for $\theta<\theta_t$ (θ_t = threshold aspect angle). Both ends of the steepest-descent path therefore lie on the top sheet and it does not need to be deformed about any of the branch cuts but can be directly connected to the $\mathrm{Re}\{\zeta\}$-axis inversion contour on the top sheet of the 4-sheeted Riemann surface as depicted in Fig. 7.2.3. For the far zone, generally, $\theta<\theta_t$ as depicted in Fig. 7.2.2.

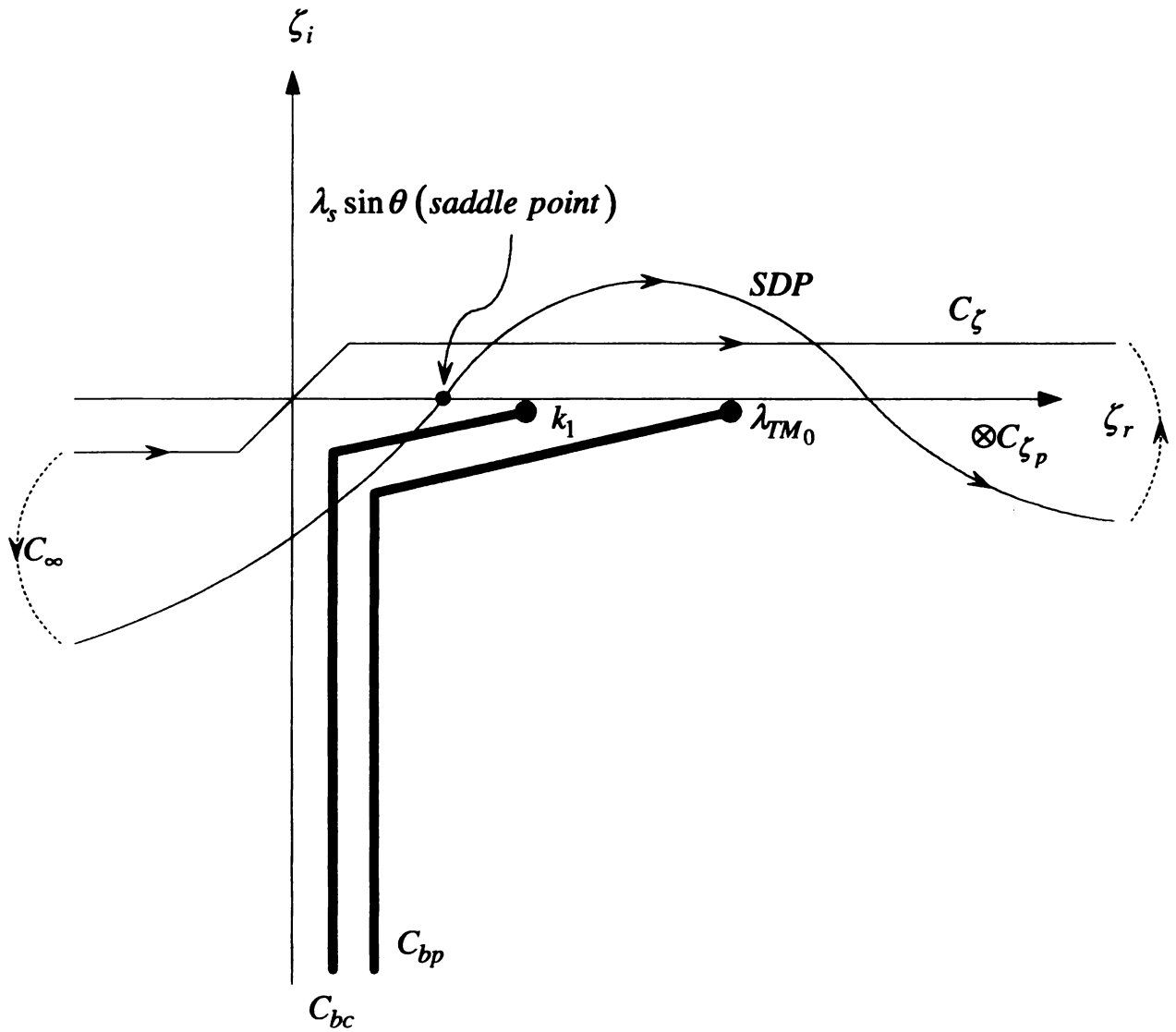

Figure 7.2.3 Identification of the steepest-descent path in the complex ζ -plane for an observation aspect angle θ less than a threshold aspect angle θ_t and branch cuts contributed by the background layer environ-ment in the low-loss limit.

7.3 THE ASYMPTOTIC APPROXIMATION TO THE COVER FIELD

Cauchy's integral theorem leads to

$$-\frac{j}{4\pi}\int_{C_\zeta - SDP - C_{\zeta_p} - C_\infty} \frac{\zeta \tilde{L}_g(\zeta)}{\int_{-\infty}^{\infty} \tilde{\eta}^2(\xi')\tilde{\tilde{C}}_{zz}(\xi',\zeta)d\xi'}\left[\int_{-\infty}^{\infty} F(\xi,\zeta)e^{j\xi x}d\xi\right]e^{j\zeta z}d\zeta = 0$$

Due to Sommerfeld's radiation condition,

$$-\frac{j}{4\pi}\int_{C_\infty} \frac{\zeta \tilde{L}_g(\zeta)}{\int_{-\infty}^{\infty} \tilde{\eta}^2(\xi')\tilde{\tilde{C}}_{zz}(\xi',\zeta)d\xi'}\left[\int_{-\infty}^{\infty} F(\xi,\zeta)e^{j\xi x}d\xi\right]e^{j\zeta z}d\zeta \to 0$$

Therefore, in accordance with Eqn. (7.2.8)

$$\begin{aligned}
&-\frac{j}{4\pi}\int_{C_\zeta} \frac{\zeta \tilde{L}_g(\zeta)}{\int_{-\infty}^{\infty} \tilde{\eta}^2(\xi')\tilde{\tilde{C}}_{zz}(\xi',\zeta)d\xi'}\left[\int_{-\infty}^{\infty} F(\xi,\zeta)e^{j\xi x}d\xi\right]e^{j\zeta z}d\zeta \\
&= \frac{1}{4\pi}\int_{SDP} \frac{\zeta \tilde{L}_g(\zeta)}{\int_{-\infty}^{\infty} \tilde{\eta}^2(\xi')\tilde{\tilde{C}}_{zz}(\xi',\zeta)d\xi'} I_{12}(x,\zeta)e^{j\xi_{k_1} x}e^{j\zeta z}d\zeta \\
&+ \frac{j}{4\pi}\int_{SDP} \frac{\zeta \tilde{L}_g(\zeta)}{\int_{-\infty}^{\infty} \tilde{\eta}^2(\xi')\tilde{\tilde{C}}_{zz}(\xi',\zeta)d\xi'} g_{sw}(\xi_p,\zeta)e^{j\xi_{TM_0} x}e^{j\zeta z}d\zeta \\
&-\frac{j}{4\pi}\oint_{C_{\zeta_p}} \frac{\zeta \tilde{L}_g(\zeta)}{\int_{-\infty}^{\infty} \tilde{\eta}^2(\xi')\tilde{\tilde{C}}_{zz}(\xi',\zeta)d\xi'}\left[\int_{-\infty}^{\infty} F(\xi,\zeta)e^{j\xi x}d\xi\right]e^{j\zeta z}d\zeta
\end{aligned} \tag{7.3.1}$$

Singularities in the complex ξ-plane migrate with varying ζ along the steepest-descent path in the complex ζ-plane. For branch-point singularities in the complex ξ-plane in accordance with Eqn. (5.3.5),

$$\pm\xi_{k_1} = \mp j\sqrt{\zeta - k_1}\sqrt{\zeta + k_1} = \begin{cases} \sqrt{\rho^+\rho^-}\,e^{j\left(-\pi+\theta^+ +\theta^-\right)/2} \\ \sqrt{\rho^+\rho^-}\,e^{j\left(\pi+\theta^+ +\theta^-\right)/2} \end{cases}$$

For the interval I as depicted in Fig. 7.3.1, $\theta^+ \to 3\pi/2$ and $\theta^- \to -\pi$. Then,

$$\xi_{k_1} = \sqrt{\rho^+\rho^-}e^{j(-\pi+3\pi/2-\pi)/2} = \frac{\sqrt{\rho^+\rho^-}}{\sqrt{2}} - j\frac{\sqrt{\rho^+\rho^-}}{\sqrt{2}}$$

At the $\mathrm{Im}\{\zeta\}$-intercept, i.e, on the boundary between I and II, $\theta^+ + \theta^- = \pi$. Then

$$\xi_{k_1} = \sqrt{\rho^+\rho^-}e^{j(-\pi+\pi)/2} = \sqrt{\rho^+\rho^-}$$

For the interval II as depicted in Fig. 7.3.1 , at the first $\mathrm{Re}\{\zeta\}$-intercept, $\theta^+ = \pi$ and $\theta^- = 0$. Therefore,

$$\xi_{k_1} = \sqrt{\rho^+\rho^-}e^{j(-\pi+\pi+0)/2} = \sqrt{\rho^+\rho^-}$$

For the interval III depicted in Fig. 7.3.1, at the second $\mathrm{Re}\{\zeta\}$-intercept, $\theta^+ = \theta^- = 0$. Therefore,

$$\xi_{k_1} = \sqrt{\rho^+\rho^-}e^{j(-\pi+0+0)/2} = -j\sqrt{\rho^+\rho^-}$$

For the interval IV as depicted in Fig. 7.3.1, $\theta^+ \to -\pi/2$ and $\theta^- \to -\pi/2$. Then

$$\xi_{k_1} = \sqrt{\rho^+\rho^-}e^{j(-\pi-\pi/2-\pi/2)/2} = -\sqrt{\rho^+\rho^-}$$

As indicated in Fig. 7.3.2, within interval I, a positive branch point singularity ξ_{k_1} begins to migrate from the fourth quadrant at $\infty - j\infty$ and within interval II, migrate along the positive $\mathrm{Re}\{\xi\}$-axis. At the boundary between the intervals III and IV, it detours about the negative $\mathrm{Im}\{\xi\}$-axis as depicted in Fig. 7.3.2 but not significantly. Finally, within interval IV, it continues to migrate along the negative $\mathrm{Re}\{\xi\}$-axis in Fig. 7.3.2. Within

interval I, a negative branch point singularity $-\xi_{k_1}$ begins to migrate from the second quadrant at $-\infty + j\infty$ and within interval II, migrate along the negative $\mathrm{Re}\{\xi\}$-axis. At the boundary between the intervals III and IV, it detours about the positive $\mathrm{Im}\{\xi\}$-axis as depicted in Fig. 7.3.2 but again not significantly. Finally, within interval IV, it continues to migrate along the positive $\mathrm{Re}\{\xi\}$-axis in Fig. 7.3.2. For surface-wave pole singularities $\pm\xi_{TM_0}$,

$$\pm\xi_{TM_0} = \mp j\sqrt{\zeta - \lambda_{TM_0}}\sqrt{\zeta + \lambda_{TM_0}} = \begin{cases} \sqrt{\rho^+\rho^-}\,e^{j\left(-\pi+\theta^+ +\theta^-\right)/2} \\ \sqrt{\rho^+\rho^-}\,e^{j\left(\pi+\theta^+ +\theta^-\right)/2} \end{cases}$$

Since the steepest-descent path does not cross the square-root type branch cut (λ_{TM_0}-branch cut) a second time in Fig. 7.2.3 for $\theta < \theta_t$, surface-wave pole singularities $\pm\xi_{TM_0}$ migrate identically in Fig. 7.3.3 as branch point singularities $\pm\xi_{k_1}$ do.

It is observed that the primary *SDP* integral contribution comes from the saddle point. In accordance with Eqn. (7.2.12), the saddle point $\lambda_s \sin\theta$ ($\lambda_s = k_1$ for the cover field and $\lambda_s = \lambda_{TM_0}$ for the film field) is located at the boundary between the intervals II and III in Figs. 7.2.3 and 7.3.1. Therefore, corresponding ξ-plane singularities ($\pm\xi_{k_1}$ and $\pm\xi_{TM_0}$) migrate within the fourth quadrant in the complex ξ-plane as depicted in Figs. 7.3.2 and 7.3.3. This situation exactly fits Fig. 7.2.1 for *LHP* $(x<0)$. Therefore, from Eqn. (7.3.1), the steepest-descent integral contribution can be approximated at the saddle point. For the cover field,

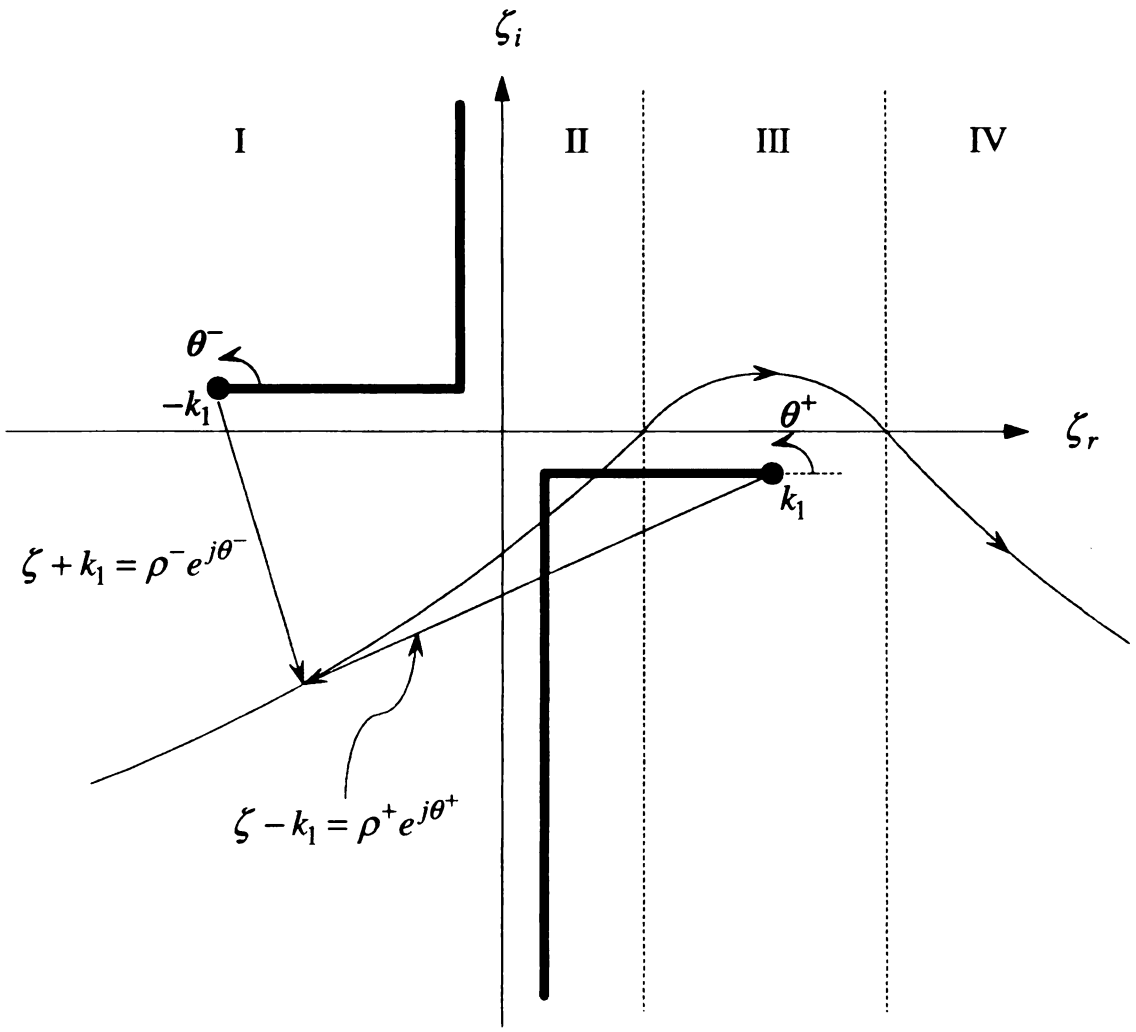

Figure 7.3.1 Complex phasor diagram of the steepest-descent path in the complex ζ -plane with intervals I, II, III, and IV and logarithmic branch cuts in the low-loss limit

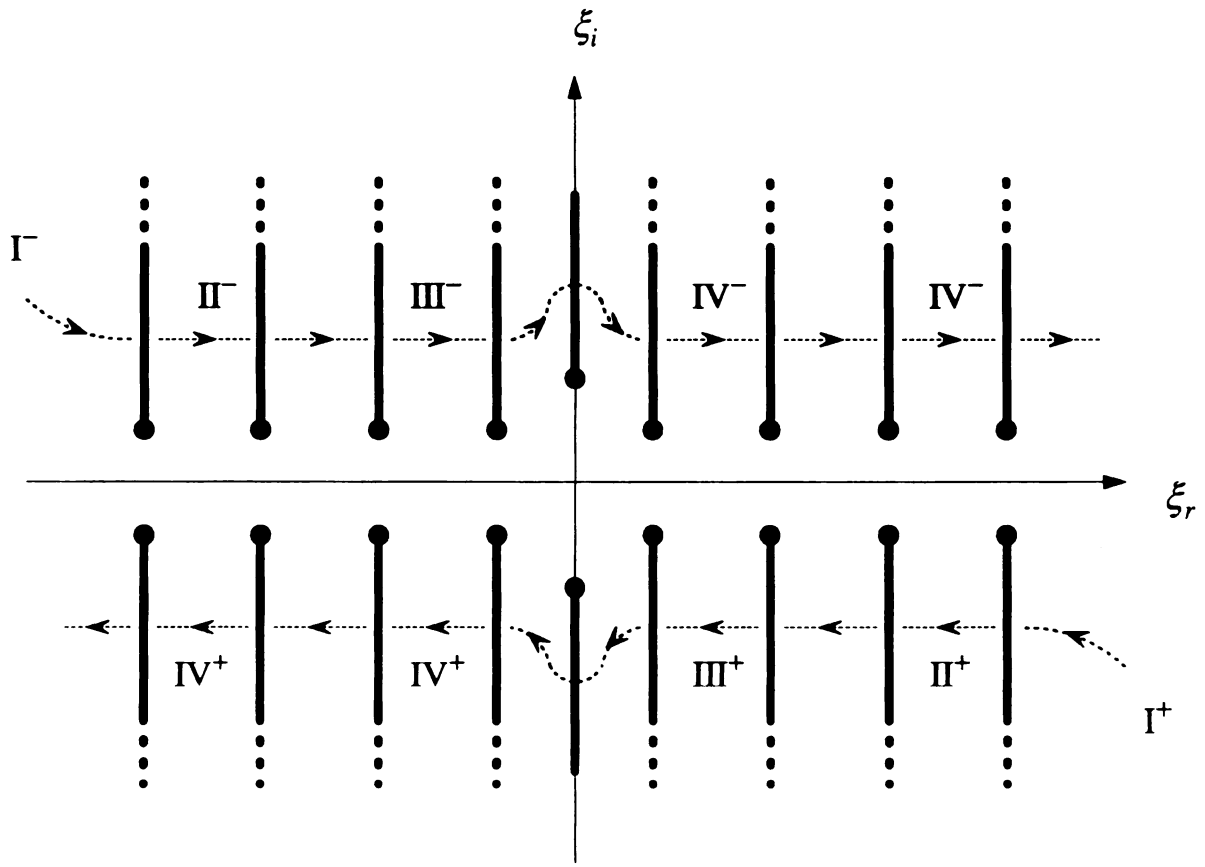

Figure 7.3.2 Migration of complex ξ-plane branch point singularities $\pm\xi_{k_1}$ in the low-loss limit with various ζ contouring along the steepest-descent path in the complex ζ-plane.

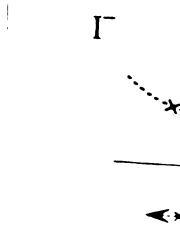

Figure

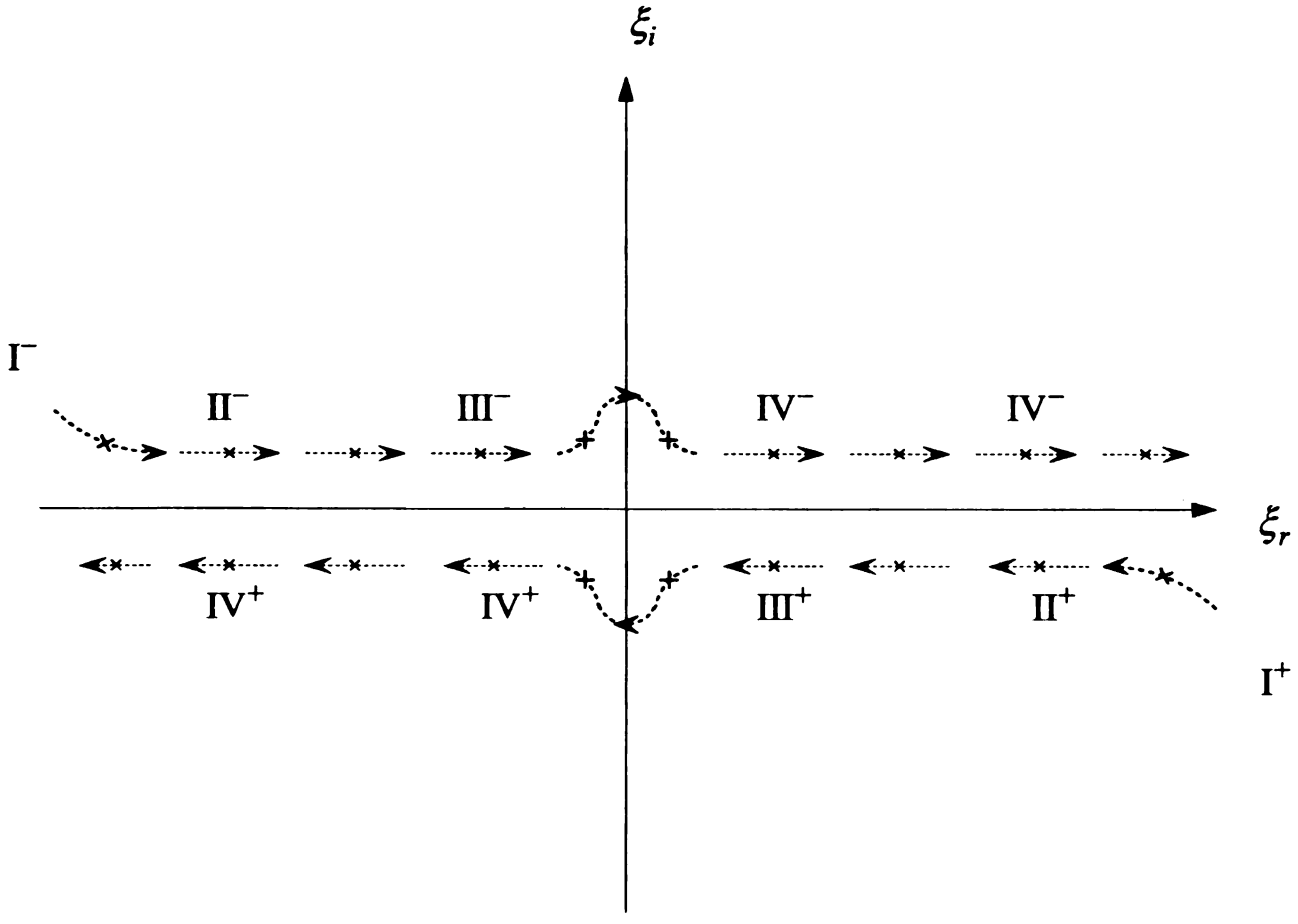

Figure 7.3.3 Migration of complex ξ-plane surface-wave pole singularities $\pm\xi_{TM_0}$ in the low-loss limit with various ζ along the steepest-descent path in the complex ζ-plane.

SDP i

Fig. 2.

Then, I

In accor

As depi

those pa

can be a

in the co

$$\frac{1}{4\pi}\int_{SDP}\frac{\zeta\tilde{L}_g(\zeta)}{\int_{-\infty}^{\infty}\tilde{\eta}^2(\xi')\tilde{\tilde{C}}_{zz}(\xi',\zeta)d\xi'}I_{12}(x,\zeta)e^{j\xi_{k_1}x}e^{j\zeta z}d\zeta$$

$$\approx\frac{1}{4\pi}\frac{\zeta_0\tilde{L}_g(\zeta_0)}{\int_{-\infty}^{\infty}\tilde{\eta}^2(\xi')\tilde{\tilde{C}}_{zz}(\xi',\zeta_0)d\xi'}I_{12}(x,\zeta_0)\int_{SDP}e^{j\xi_{k_1}x}e^{j\zeta z}d\zeta \qquad (7.3.2)$$

where

$$\zeta_0 = k_1\sin\theta$$

SDP in the complex ζ-plane is mapped into *SDP* in the complex ϕ-plane as depicted in Fig. 2.3.4 in Chapter 2. As previously discussed in Section 2.3.2,

$$\int_{SDP}e^{j\xi_{k_1}x}e^{j\zeta z}d\zeta \approx \sqrt{2\pi k_1}\cos\theta\frac{e^{-j(k_1r-\pi/4)}}{\sqrt{r}}$$

Then, Eqn. (7.3.2) becomes

$$\frac{1}{4\pi}\frac{\zeta_0\tilde{L}_g(\zeta_0)}{\int_{-\infty}^{\infty}\tilde{\eta}^2(\xi')\tilde{\tilde{C}}_{zz}(\xi',\zeta_0)d\xi'}I_{12}(x,\zeta_0)\int_{SDP}e^{j\xi_{k_1}x}e^{j\zeta z}d\zeta$$

$$\approx\frac{\sqrt{k_1}}{4}\sqrt{\frac{2}{\pi}}\frac{\zeta_0\tilde{L}_g(\zeta_0)}{\int_{-\infty}^{\infty}\tilde{\eta}^2(\xi')\tilde{\tilde{C}}_{zz}(\xi',\zeta_0)d\xi'}I_{12}(x,\zeta_0)\cos\theta\frac{e^{-j(k_1r-\pi/4)}}{\sqrt{r}} \qquad (7.3.3)$$

In accordance with Eqn. (7.2.7),

$$I_{12}(x,\zeta_0)=\int_0^{\infty}\left[f(s,\zeta_0)\Big|_{s\in C_{\xi_{b1}}}-f(s,\zeta_0)\Big|_{s\in C_{\xi_{b2}}}\right]e^{sx}ds \qquad (7.3.4)$$

As depicted in Fig. 7.2.1, the branch cut contours $C_{\xi_{b1}}$ and $C_{\xi_{b2}}$ are vertical paths and those paths correspond to other *SDP*s in the complex ξ-plane [56]. The same argument can be applied for *SDP*s in the complex ξ'-plane, which means that the complex analysis in the complex ξ'-plane as well as in the complex ξ-plane can be similarly implemented.

As

and

deter

The a

for th

(7.3.4

(7.3.4

As rec

$p_1(\xi_{k_1}$

branch

It is not

[55],

As discussed earlier, the primary *SDP* integral contribution comes from the saddle point and in agreement with Eqn. (7.2.3) the saddle point ξ_0 in the complex ξ-plane is determined by

$$\xi_0 = \xi_{k_1} \tag{7.3.5}$$

The above equation leads to

$$s = 0 \tag{7.3.6}$$

for the saddle point. It is noted that Watson's lemma can be invoked [57] to evaluate Eqn. (7.3.4) asymptotically and to determine the asymptotic behaviour of the integral in Eqn. (7.3.4) for $s \to 0$. Then, if it is known that

$$\begin{aligned} &W(s,\zeta_0) \approx As^{\alpha} \quad \cdots \quad s \to 0 \\ &\textit{where} \\ &W(s,\zeta_0) = f(s,\zeta_0)\big|_{s\in C_{\xi_{b1}}} - f(s,\zeta_0)\big|_{s\in C_{\xi_{b2}}} \end{aligned} \tag{7.3.7}$$

As required by Eqn. (7.3.7), if $\alpha \neq 0$, the function $W(s,\zeta_0) \to 0$ for $s \to 0$ since $p_1(\xi_{k_1},\zeta_0) = 0$. It is noted that $p_1(\xi,\zeta_0)\big|_{\xi=\xi_{k_1}-js}$ is multi-valued on either side of branch cuts $C_{\xi_{b1}}$ and $C_{\xi_{b2}}$. Then, changing the variables $-t = sx$ yields

$$\int_0^{\infty} W(s,\zeta_0)e^{sx}ds \approx \frac{(-1)^{\alpha+1}A}{x^{(\alpha+1)}}\int_0^{\infty} t^{\alpha}e^{-t}dt \tag{7.3.8}$$

It is noted that $x < 0$ for *LHP* in the complex ξ-plane. Therefore, Eqn. (7.3.8) becomes [55],

$$\frac{(-1)^{\alpha+1}A}{x^{(\alpha+1)}}\int_0^{\infty} t^{\alpha}e^{-t}dt \approx \frac{(-1)^{\alpha+1}A}{x^{(\alpha+1)}}\Gamma(\alpha+1) \tag{7.3.9}$$

Finally,

Sim

Fi

E_{1y}

The

α(

disc

of g

pres

Finally,

$$I_{12}(x,\zeta_0)\approx\frac{(-1)^{\alpha+1}A}{x^{(\alpha+1)}}\Gamma(\alpha+1) \tag{7.3.10}$$

Similarly,

$$\begin{aligned}&\frac{j}{4\pi}\int_{SDP}\frac{\zeta\tilde{L}_g(\zeta)}{\int_{-\infty}^{\infty}\tilde{\eta}^2(\xi')\tilde{\tilde{C}}_{zz}(\xi',\zeta)d\xi'}g_{sw}(\xi_p,\zeta)e^{j\xi_{TM_0}x}e^{j\zeta z}d\zeta\\&\approx\frac{j\sqrt{k_1}}{4}\sqrt{\frac{2}{\pi}}\frac{\zeta_0\tilde{L}_g(\zeta_0)}{\int_{-\infty}^{\infty}\tilde{\eta}^2(\xi')\tilde{\tilde{C}}_{zz}(\xi',\zeta_0)d\xi'}g_{sw}(\xi_p,\zeta_0)\cos\theta\frac{e^{-j(k_1r-\pi/4)}}{\sqrt{r}}\end{aligned} \tag{7.3.11}$$

Finally, in accordance with Eqns. (7.2.8) and (7.3.1), Using $x=-r\cos\theta$ yields

$$\begin{aligned}E_{1y}(\boldsymbol{r})\approx&\frac{\sqrt{k_1}}{4}\sqrt{\frac{2}{\pi}}\frac{\zeta_0\tilde{L}_g(\zeta_0)}{\int_{-\infty}^{\infty}\tilde{\eta}^2(\xi')\tilde{\tilde{C}}_{zz}(\xi',\zeta_0)d\xi'}\frac{\Gamma(\alpha+1)A}{\cos^{\alpha}\theta}\frac{e^{-j(k_1r-\pi/4)}}{r^{\alpha+3/2}}\\&+\frac{j\sqrt{k_1}}{4}\sqrt{\frac{2}{\pi}}\frac{\zeta_0\tilde{L}_g(\zeta_0)}{\int_{-\infty}^{\infty}\tilde{\eta}^2(\xi')\tilde{\tilde{C}}_{zz}(\xi',\zeta_0)d\xi'}g_{sw}(\xi_p,\zeta_0)\cos\theta\frac{e^{-j(k_1r-\pi/4)}}{\sqrt{r}}\\&-\frac{j}{4\pi}\oint_{C_{\zeta_p}}\frac{\zeta\tilde{L}_g(\zeta)}{\int_{-\infty}^{\infty}\tilde{\eta}^2(\xi')\tilde{\tilde{C}}_{zz}(\xi',\zeta)d\xi'}\left[\int_{-\infty}^{\infty}F(\xi,\zeta)e^{j\xi x}d\xi\right]e^{j\zeta z}d\zeta\end{aligned}$$

The asymptotic cover field decays algebraically as $r^{-(\alpha+3/2)}$. The algebraic factor $\alpha(\neq 0)$ and the amplitude A will remain to be determined in future research. The discrete field spectrum was previously discussed in Section 6.2.1. Since the cover field is of great concern for the far zone, the asymptotic approximation of the film field is not presented here but it can be achieved in a similar manner.

7.4 C

The

Althoug

can be

of bran

corresp

branch

corresp

observa

Then,

numeri

7.4 CONCLUSION

The asymptotic approximation to the cover field has been discussed in this chapter. Although the asymptotic approximation of the film field has not been discussed here, it can be achieved in a similar manner. One important contribution identifies the migration of branch point and surface-wave pole singularities in the complex ξ-plane for the corresponding points along *SDP* in the complex ζ-plane. This enables one to find the branch point and surface-wave pole singularities in the complex ξ-plane for the corresponding point (*saddle-point*) in the complex ζ-plane. The other important observation indicates that the asymptotic cover field decays algebraically as $r^{-(\alpha+3/2)}$. Then, in order to validate the asymptotic transverse behaviour of the cover field, rigorous numerical implementation is required in future research.

T

micro

conti

spect

insig

obtai

T

mode

cover

nume

H

TM r

There

in bot

future

In

waveg

conce

backg

singu

CHAPTER 8

CONCLUSION

The nature of the physics in electromagnetic currents/fields of an open integrated microstrip waveguide configuration is conceptualized and quantified numerically. The continuous spectrum contributed by the background layer environment and the discrete spectrum contributed by the guiding structure are rigorously revealed, and more physical insight into the EM behaviours of the integrated microstrip waveguide configuration is obtained.

The steepest-descent theoretical and numerical evaluation of the radiation field for TE modes of an asymmetric planar open waveguide was implemented in Chapter 2. Both the cover and substrate field discontinuities near the threshold aspect angle are resolved numerically.

However, only the steepest-descent theoretical evaluation of the radiation field for TM modes of an asymmetric planar open waveguide was implemented in Chapter 3. Therefore, the rigorous numerical implementation for Green's dyad of the radiation field in both the near and far zones and also within the source region will be accommodated in future research.

In Chapter 4, the spectral electric field integral equation (EFIE) for an integrated open waveguide structure in a planar-layered background environment was formulated. The concept of logarithmic and square-root type branch point singularities contributed by the background layer environment [7]-[9] was introduced. The logarithmic type branch point singularities are associated with power loss due to radiation into the cover layer [30].

Meanwh

couplin

of that

In

configu

the mic

Since t

spectra

In

integra

like r

rigoro

EM f

accom

Meanwhile, the square-root type branch point singularities are physically associated with coupling of power into the transversely-propagating principal TM_0 surface-wave mode of that background environment.

In Chapters 5 and 6, currents/fields in an open integrated microstrip waveguide configuration were formulated in the spectral domain. The physics of currents/fields on the microstrip waveguide configuration was conceptualized and quantified numerically. Since the microstrip currents/fields were represented in proper (continuous and discrete) spectra, then no leaky-modes needed to be considered.

In Chapter 7, the asymptotic approximation to electromagnetic fields of an open integrated microstrip waveguide was obtained. The cover field behaved algebraically like $r^{-(\alpha+3/2)}\,(\alpha \neq 0)$ when approaching to the far zone transversely. However, a rigorous numerical implementation is still required in order to understand the asymptotic EM field behaviour in both the cover and film layers more fully; this will be accommodated in future research.

AS

A.1 S

Giv

l'th re

electri

where

l'th re

$x = 0$

$x = -t$

Figure

APPENDIX A

SPECTRAL TE EM FIELD FORMULATION FOR ASYMMETRIC PLANAR DIELECTRIC SLAB WAVEGUIDE USING INTEGRAL TRANSFORM TECHNIQUE

A.1 SPECTRAL HERTZIAN POTENTIAL REPRESENTATION OF EM FIELD

Given the geometry depicted in Fig. A1, consider vector potential $\tilde{\boldsymbol{A}}_l(\boldsymbol{x},\boldsymbol{\zeta})$ for the *l'th region (l=1,2,3 for cover, film and substrate layer)* maintained by y-invariance electric current $\tilde{\boldsymbol{j}}(\boldsymbol{x},\boldsymbol{\zeta}) = \hat{\boldsymbol{y}}\tilde{j}_y(x,\zeta)$ in the transform plane.

$$\tilde{\boldsymbol{A}}(\boldsymbol{x},\boldsymbol{\zeta}) = \hat{\boldsymbol{y}}\tilde{\Pi}_{ly}(x,\zeta) \tag{A1.1}$$

where $\tilde{\boldsymbol{\Pi}}_l(\boldsymbol{x},\boldsymbol{\zeta})$ denotes vector electric Hertzian potential in the transform plane for the *l'th region.*

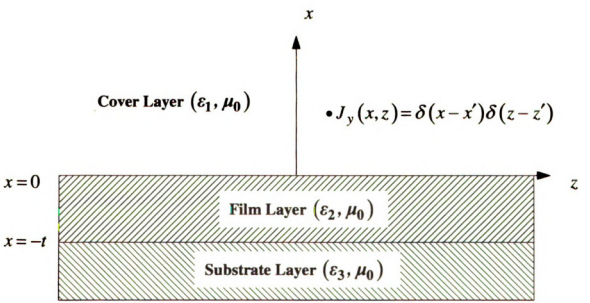

Figure A.1.1 Geometrical configuration of asymmetric planar dielectric slab waveguide.

The subsequent transverse transformation of Eqn. (2.2.3) yields

$$-\xi^2\tilde{\tilde{\Pi}}_{ly}(\xi,\zeta)-p_l^2(\zeta)\tilde{\tilde{\Pi}}(\xi,\zeta)=-\mu_0 e^{-j(\xi x'+\zeta z')} \tag{A1.2}$$

where ξ is the complex transverse transformation variable.

Rearranging Eqn. (A1.2) becomes

$$\left\{\xi^2+p_l^2(\zeta)\right\}\tilde{\tilde{\Pi}}_{ly}(\xi,\zeta)=\mu_0 e^{-j(\xi x'+\zeta z')} \tag{A1.3}$$

A.2 THE SPECTRAL EM FIELD REPRESENTATION IN THE COVER LAYER

Since the complex-wave field decomposes into the principal and the reflected in the cover layer,

$$\tilde{\tilde{\Pi}}_{1y}(\xi,\zeta)=\tilde{\tilde{\Pi}}_{1y}^{p}(\xi,\zeta)+\tilde{\tilde{\Pi}}_{1y}^{r}(\xi,\zeta) \tag{A2.1}$$

where $\tilde{\tilde{\Pi}}_{1y}^{p}(\xi,\zeta)$ and $\tilde{\tilde{\Pi}}_{1y}^{r}(\xi,\zeta)$ indicate the principal and reflected Hertzian potential in the spectral-domain respectively.

For the principal field, in agreement with Eqn. (A1.3)

$$\tilde{\tilde{\Pi}}_{1y}^{p}(\xi,\zeta)=\mu_0\frac{e^{-j(\xi x'+\zeta z')}}{\left[\xi+jp_1(\zeta)\right]\left[\xi-jp_1(\zeta)\right]} \tag{A2.2}$$

Taking inverse Fourier transform of Eqn. (A2.2) yields

$$\tilde{\Pi}_{1y}^{p}(x,\zeta)=\frac{1}{2\pi}\int_{-\infty}^{\infty}\tilde{\tilde{\Pi}}_{1y}^{p}(\xi,\zeta)e^{j\xi x}d\xi \tag{A2.3}$$

Substitution Eqn. (A2.2) into Eqn. (A2.3) leads to

$$\tilde{\Pi}_{1y}^{p}(x,\zeta)=\frac{\mu_0}{2\pi}\int_{-\infty}^{\infty}\frac{e^{j\xi(x-x')}}{\left[\xi+jp_1(\zeta)\right]\left[\xi-jp_1(\zeta)\right]}e^{-j\zeta z'}d\xi \tag{A2.4}$$

ξ

p_1

plan

Figu

App

whi

Fig.

The pole singularities arise from $\xi = \pm jp_1(\zeta)$ and the coordinates in the complex ξ -plane are chosen in order that Sommerfeld radiation condition force $p_1(\zeta) = \sqrt{\zeta^2 - k_1^2}$ to stay on the top Riemann sheet of the 4-sheeted complex ζ -plane, i.e., $\mathrm{Re}\{p_1(\zeta)\} > 0$ and $\mathrm{Im}\{p_1(\zeta)\} < 0$ as depicted in Fig. A2.1.

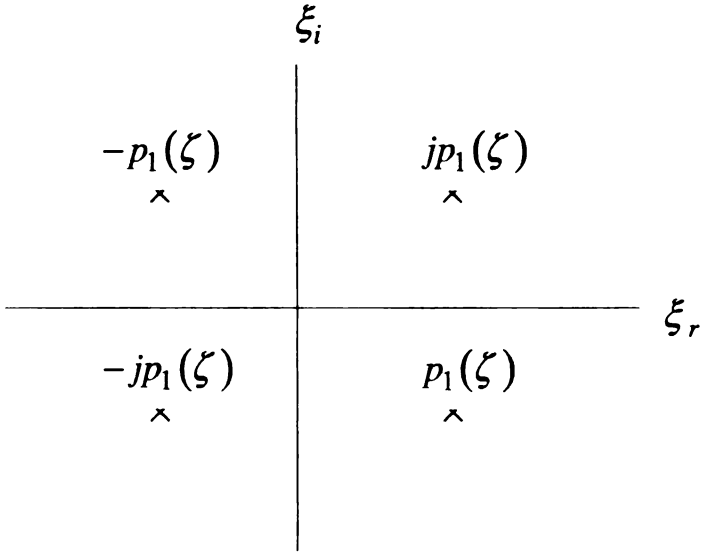

Figure A.2.1 Pole singularities in the complex ξ-plane to be chosen for $p_1(\zeta)$ on the top Riemann sheet of the complex ζ-plane.

Apply Cauchy's integral theorem to the closed *UHP* or *LHP* contours (along and within which the Fourier inversion integrand is analytic) in the complex ξ-plane as depicted in Fig. A2.2.

$$e^{j\xi(x-x')} = e^{-\xi_i(x-x')} e^{j\xi_r(x-x')} \Rightarrow \begin{cases} UHP: x > x' \\ LHP: x < x' \end{cases} \qquad \text{(A2.5)}$$

where *UHP* and *LHP* stand for *Upper* and *Lower Half Plane* closure in the complex ξ-plane respectively.

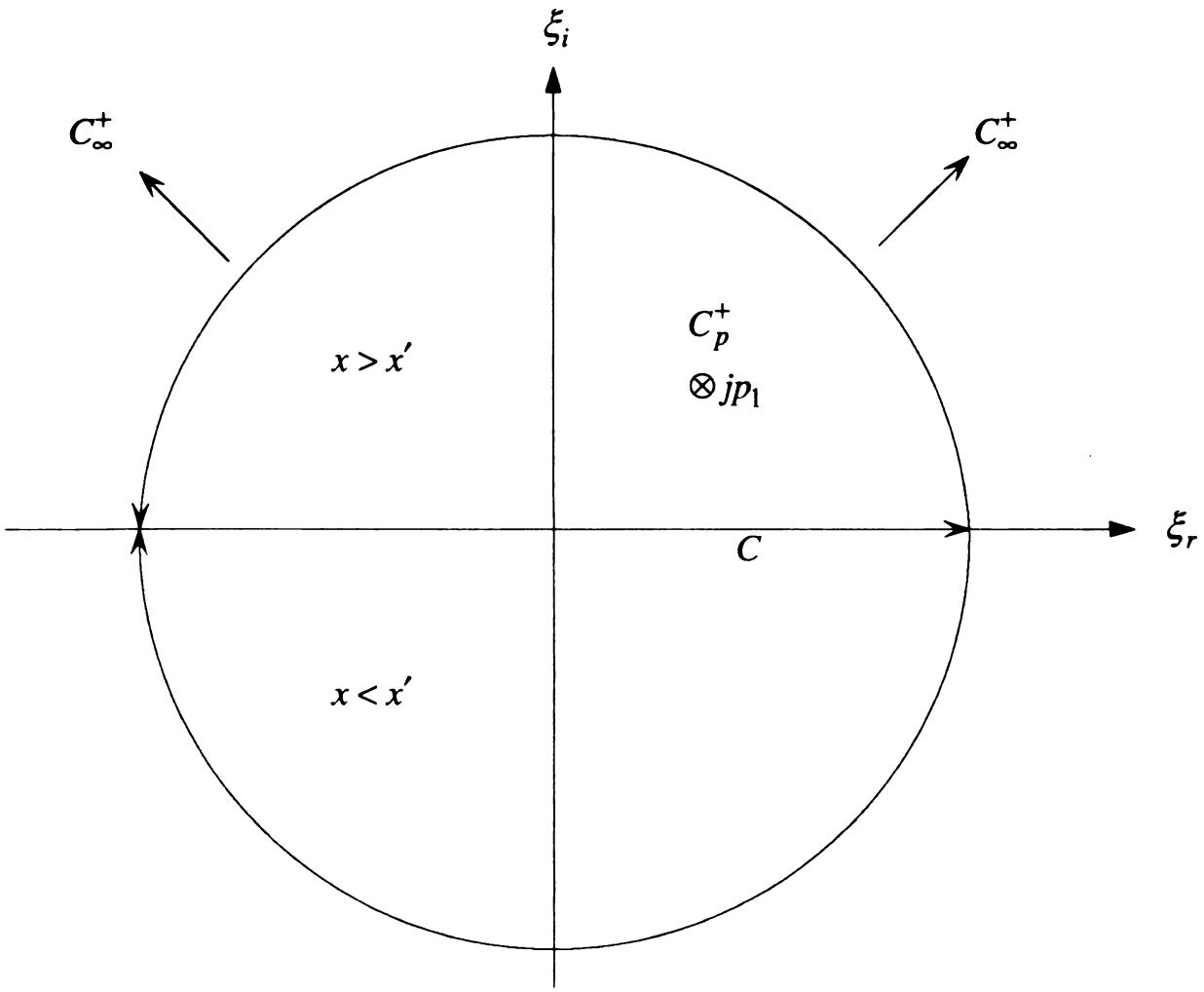

Figure A.2.2 Identification of pole singularities by path deformation of Fourier inversion contour in the complex ξ-plane.

$$\oint_{C^\pm}(\cdots)d\xi = \int_{-\infty}^{\infty}(\cdots)d\xi + \int_{C_p^\pm}(\cdots)d\xi + \int_{C_\infty^\pm}(\cdots)d\xi = 0 \qquad \text{(A2.6)}$$

In ag

Final

Simila

Theref

For

given b

In agreement with $\int_{C_\infty^\pm}(\cdots)d\xi \to 0$,

$$\begin{aligned}
&\frac{\mu_0}{2\pi}\int_{-\infty}^{\infty}\frac{e^{j\xi(x-x')}}{[\xi+jp_1(\zeta)][\xi-jp_1(\zeta)]}e^{-j\zeta z'}d\xi \\
&=-\frac{\mu_0}{2\pi}\int_{C_p^+}\frac{e^{j\xi(x-x')}}{[\xi+jp_1(\zeta)][\xi-jp_1(\zeta)]}e^{-j\zeta z'}d\xi \qquad \text{(A2.7)} \\
&=\frac{\mu_0}{2\pi}(2\pi j)[\xi-jp_1(\zeta)]\frac{e^{j\xi(x-x')}}{[\xi+jp_1(\zeta)][\xi-jp_1(\zeta)]}e^{-j\zeta z'}\Big|_{\xi=jp_1(\zeta)}
\end{aligned}$$

Finally for $x > x'$,

$$\tilde{\Pi}_{1y}^{p}(x,\zeta)=\mu_0\frac{e^{-p_1(\zeta)(x-x')}}{2p_1(\zeta)}e^{-j\zeta z'} \qquad \text{(A2.8)}$$

Similarly for $x < x'$,

$$\tilde{\Pi}_{1y}^{p}(x,\zeta)=\mu_0\frac{e^{-p_1(\zeta)(x'-x)}}{2p_1(\zeta)}e^{-j\zeta z'} \qquad \text{(A2.9)}$$

Therefore for $x > 0$,

$$\tilde{\Pi}_{1y}^{p}(x,\zeta)=\mu_0\frac{e^{-p_1(\zeta)|x-x'|}}{2p_1(\zeta)}e^{-j\zeta z'} \qquad \text{(A2.10)}$$

For the reflected field, the Hertzian potential solutions in *the l'th layer (l=1,2,3)* are given by

$$\begin{aligned}
\tilde{\Pi}_{1y}^{r}(x,\zeta)&=c_1e^{-p_1(\zeta)x} \\
\tilde{\Pi}_{2y}^{r}(x,\zeta)&=c_2e^{-p_2(\zeta)x}+c_3e^{p_2(\zeta)x} \qquad \text{(A2.11)} \\
\tilde{\Pi}_{3y}^{r}(x,\zeta)&=c_4e^{p_3(\zeta)x}
\end{aligned}$$

The bo

The bo

yields

After so

into Eqn

The boundary conditions at $x_l = 0, -t$ implement

$$\begin{aligned}
&\tilde{\Pi}_{ly}^{+}\left(x_l^{+},\zeta\right)=\tilde{\Pi}_{ly}^{-}\left(x_l^{-},\zeta\right)\\
&\frac{\partial\tilde{\Pi}_{ly}^{+}\left(x_l^{+},\zeta\right)}{\partial x}-\frac{\partial\tilde{\Pi}_{ly}^{-}\left(x_l^{-},\zeta\right)}{\partial x}=0
\end{aligned} \tag{A2.12}$$

The boundary condition that $E_y(x,z)$ is continuous at the interface between each layer yields

$$\begin{aligned}
&\tilde{\Pi}_{1y}(x,\zeta)\Big|_{x=0^+}=\tilde{\Pi}_{2y}(x,\zeta)\Big|_{x=0^-}\\
&\frac{\partial\tilde{\Pi}_{1y}(x,\zeta)}{\partial x}\Big|_{x=0^+}-\frac{\partial\tilde{\Pi}_{2y}(x,\zeta)}{\partial x}\Big|_{x=0^-}=0\\
&\tilde{\Pi}_{2y}(x,\zeta)\Big|_{x=-t^+}=\tilde{\Pi}_{3y}(x,\zeta)\Big|_{x=-t^-}\\
&\frac{\partial\tilde{\Pi}_{2y}(x,\zeta)}{\partial x}\Big|_{x=-t^+}-\frac{\partial\tilde{\Pi}_{3y}(x,\zeta)}{\partial x}\Big|_{x=-t^-}=0
\end{aligned} \tag{A2.13}$$

where

$$\tilde{\Pi}_{1y}(x,\zeta)=\tilde{\Pi}_{1y}^{p}(x,\zeta)+\tilde{\Pi}_{1y}^{r}(x,\zeta)$$

After some algebraic manipulation and substitution of Eqn. (A2.10) and Eqn. (A2.11) into Eqn. (A2.13) yields

$$\begin{aligned}
c_1&=\frac{\mu_0}{2p_1(\zeta)}R(\zeta)e^{-p_1(\zeta)x'}e^{-j\zeta z'}\\
c_2&=\frac{\mu_0}{2p_1(\zeta)}C(\zeta)\bar{R}(\zeta)e^{-2p_2(\zeta)t}e^{-p_1(\zeta)x'}e^{-j\zeta z'}\\
c_3&=\frac{\mu_0}{2p_1(\zeta)}C(\zeta)e^{-p_1(\zeta)x'}e^{-j\zeta z'}\\
c_4&=\frac{\mu_0}{2p_1(\zeta)}T(\zeta)e^{-p_1(\zeta)x'}e^{-j\zeta z'}
\end{aligned} \tag{A2.14}$$

where $R(\zeta)$, $C(\zeta)$ and $T(\zeta)$ is reflection, coupling and transmission coefficient respectively and $\bar{R}(\zeta)$ is the interfacial reflection coefficient given by

$$R(\zeta)=\frac{(p_1-p_3)p_2+\left(p_1p_3-p_2^2\right)\tanh(p_2t)}{Z(\zeta)}$$

$$C(\zeta)=\frac{2p_1(p_2+p_3)}{\left(1+e^{-2p_2t}\right)Z(\zeta)}$$

$$T(\zeta)=\frac{2p_1p_2}{\cosh(p_2t)Z(\zeta)} \qquad \text{(A2.15)}$$

$$\bar{R}(\zeta)=\frac{p_2-p_3}{p_2+p_3}$$

where

$$Z(\zeta)=(p_1+p_3)p_2+\left(p_1p_3+p_2^2\right)\tanh(p_2t)$$

The electric Hertzian potential solution for *the l'th layer* can be obtained by

$$\tilde{\Pi}_{1y}(x,\zeta)=\frac{\mu_0}{2p_1(\zeta)}\left\{e^{-p_1(\zeta)|x-x'|}+R(\zeta)e^{-p_1(\zeta)(x+x')}\right\}e^{-j\zeta z'}$$

where

$$\tilde{\Pi}_{1y}^{p}(x,\zeta)=\frac{\mu_0}{2p_1(\zeta)}e^{-p_1(\zeta)|x-x'|}e^{-j\zeta z'}$$

$$\tilde{\Pi}_{1y}^{r}(x,\zeta)=\frac{\mu_0}{2p_1(\zeta)}R(\zeta)e^{-p_1(\zeta)(x+x')}e^{-j\zeta z'} \qquad \text{(A2.16)}$$

$$\tilde{\Pi}_{2y}(x,\zeta)=\frac{\mu_0}{2p_1(\zeta)}C(\zeta)\left[e^{p_2(\zeta)x}+\bar{R}(\zeta)e^{-p_2(\zeta)(x+2t)}\right]e^{-p_1(\zeta)x'}e^{-j\zeta z'}$$

$$\tilde{\Pi}_{3y}(x,\zeta)=\frac{\mu_0}{2p_1(\zeta)}T(\zeta)e^{p_3(\zeta)(x+t)}e^{-p_1(\zeta)x'}e^{-j\zeta z'}$$

II

The e

substrate

Since k_l =

Letting ζ

Eqn. (B2)

Therefore,

The relatio

APPENDIX B

IDENTIFICATION OF THE STEEPEST-DESCENT PATH IN THE COMPLEX AXIAL TRANSFORM PLANE

The equation of the steepest-descent path for the *l'th layer (l=1 and 3 for cover and substrate)* in the complex axial transform plane (ζ -plane) is

$$\left[\frac{\zeta}{k_l}+\left(\frac{\zeta}{k_l}\right)^*\right]\frac{\sin\theta}{2}-j\left[\frac{p_l(\zeta)}{k_l}-\left\{\frac{p_l(\zeta)}{k_l}\right\}^*\right]\frac{\cos\theta}{2}=1 \qquad \text{(AB17)}$$

Since $k_l=(k_l)^*$, Eqn. (B1) can be rewritten as

$$(\zeta+\zeta^*)\frac{\sin\theta}{2}-j\left[p_l(\zeta)-p_l^*(\zeta)\right]\frac{\cos\theta}{2}-k_l=0 \qquad \text{(AB18)}$$

Letting $\zeta=\zeta'+j\zeta''$ and $p_l(\zeta)=\alpha+j\beta=\sqrt{(\zeta'+j\zeta'')^2-k_l^2}$,

Eqn. (B2) becomes

$$\zeta'\sin\theta+\beta\cos\theta-k_l=0 \qquad \text{(AB19)}$$

Therefore,

$$\beta=\frac{k_l-\zeta'\sin\theta}{\cos\theta} \qquad \text{(AB20)}$$

The relation $p_l^2=\alpha^2-\beta^2+j2\alpha\beta=(\zeta')^2-(\zeta'')^2-k_l^2+j2\zeta'\zeta''$ implies that

$$\begin{aligned}(\zeta')^2-(\zeta'')^2-k_l^2&=\alpha^2-\left(\frac{k_l-\zeta'\sin\theta}{\cos\theta}\right)^2\\ \alpha&=\frac{\zeta'\zeta''}{\beta}=\frac{\zeta'\zeta''\cos\theta}{k_l-\zeta'\sin\theta}\end{aligned} \qquad \text{(AB21)}$$

Eqn. (

Some

Rearra

Her

identifi

Eqn. (B5) yields

$$(\zeta')^2-(\zeta'')^2-k_l^2=\left(\frac{\zeta'\zeta''\cos\theta}{k_l-\zeta'\sin\theta}\right)^2-\left(\frac{k_l-\zeta'\sin\theta}{\cos\theta}\right)^2 \qquad \text{(AB22)}$$

Some algebraic manipulation leads to

$$\zeta''=\pm\frac{|\zeta'-k_l\sin\theta|}{\cos\theta\sqrt{\left(\frac{\zeta'\cos\theta}{k_l-\zeta'\sin\theta}\right)^2+1}} \qquad \text{(AB23)}$$

Rearranging Eqn. (B7) gives

$$\zeta''=\pm\frac{|\zeta'-k_l\sin\theta||k_l-\zeta'\sin\theta|}{\cos\theta\sqrt{(\zeta'\cos\theta)^2+(k_l-\zeta'\sin\theta)^2}} \qquad \text{(AB24)}$$

Hence, the steepest-descent path in the complex ζ (axial transform) plane can be identified as

$$\zeta=(\zeta',\zeta'')$$
where (AB25)
$$\zeta''=\pm\frac{|\zeta'-k_l\sin\theta||k_l-\zeta'\sin\theta|}{\cos\theta\sqrt{(\zeta'\cos\theta)^2+(k_l-\zeta'\sin\theta)^2}}$$

C.1

T

$\tilde{j}_x($

agree

$\tilde{e}_{1z}^{r}($

wave

It i

for $\tilde{e}_{1z}^{p}$

APPENDIX C

SPECTRAL GREEN'S DYAD REPRESENTATION OF RADIATION FIELD FOR TM MODES OF THE ASYMMETRIC PLANAR OPEN WAVEGUIDE

C.1 SPECTRAL GREEN'S DYAD FORMULATION WITH UNDETERMINED COEFFICIENTS

The total EM fields in the cover layer are composed of a primary wave excited by $\tilde{j}_x(x,\zeta)$ and $\tilde{j}_z(x,\zeta)$ in an unbounded region and source-free reflected waves. In agreement with Eqn. (3.2.8),

$$\left[\frac{\partial^2}{\partial x^2} - p_1^2(\zeta)\right]\tilde{e}_{1z}^{p}(x,\zeta) = -\frac{\zeta}{\omega\varepsilon_1}\frac{\partial\tilde{j}_x(x,\zeta)}{\partial x} - \frac{jp_1^2(\zeta)}{\omega\varepsilon_1}\tilde{j}_z(x,\zeta)$$

$$\left[\frac{\partial^2}{\partial x^2} - p_1^2(\zeta)\right]\tilde{e}_{1z}^{r}(x,\zeta) = 0 \qquad \text{(C1.1)}$$

where

$$p_1^2(\zeta) = \zeta^2 - k_1^2$$

$\tilde{e}_{1z}^{r}(x,\zeta)$ must satisfy the radiation condition, i.e. it is an outward traveling, decaying wave with $\mathrm{Re}\{p_1(\zeta)\} > 0, \mathrm{Im}\{p_1(\zeta)\} > 0$.

$$\tilde{e}_{1z}^{r}(x,\zeta) = A(\zeta)e^{-p_1(\zeta)x} \qquad \text{(C1.2)}$$

It is necessary to consider the general inhomogeneous second order equation to solve for $\tilde{e}_{1z}^{p}(x,\zeta)$.

$$\left[\frac{\partial^2}{\partial x^2} - p_1^2(\zeta)\right]\tilde{\Pi}(x,\zeta) = -\tilde{s}(x,\zeta) \qquad \text{(C1.3)}$$

Transverse forward and inverse Fourier transformation leads to

$$\begin{aligned}
&\tilde{\Pi}(x,\zeta) \leftrightarrow \tilde{\tilde{\Pi}}(\xi,\zeta) \\
&\tilde{s}(x,\zeta) \leftrightarrow \tilde{\tilde{s}}(\xi,\zeta) \\
&\tilde{\Pi}(x,\zeta) = \frac{1}{2\pi}\int_{-\infty}^{\infty} \tilde{\tilde{\Pi}}(\xi,\zeta) e^{j\xi x} d\xi \\
&\tilde{s}(x,\zeta) = \frac{1}{2\pi}\int_{-\infty}^{\infty} \tilde{\tilde{s}}(\xi,\zeta) e^{j\xi x} d\xi
\end{aligned} \tag{C1.4}$$

Substituting Eqn. (1.14) into Eqn. (1.12) yields

$$\left[\frac{\partial^2}{\partial x^2} - p_1^2(\zeta)\right]\frac{1}{2\pi}\int_{-\infty}^{\infty} \tilde{\tilde{\Pi}}(\xi,\zeta) e^{j\xi x} d\xi = -\frac{1}{2\pi}\int_{-\infty}^{\infty} \tilde{\tilde{s}}(\xi,\zeta) e^{j\xi x} d\xi \tag{C1.5}$$

Rearranging Eqn. (C1.5) becomes

$$\int_{-\infty}^{\infty}\left[-\tilde{\tilde{\Pi}}(\xi,\zeta)\left(\xi^2 + p^2\right) + \tilde{\tilde{s}}(\xi,\zeta)\right] e^{j\xi x} d\xi = 0 \tag{C1.6}$$

By Fourier-Transform theorem,

$$F_{x,z}^{-1}\{\sim\} = 0 \Rightarrow \{\sim\} = 0 \tag{C1.7}$$

Then,

$$\begin{aligned}
\tilde{\tilde{\Pi}}(\xi,\zeta) &= \frac{\tilde{\tilde{s}}(\xi,\zeta)}{\xi^2 + p_1^2(\zeta)} = \frac{\tilde{\tilde{s}}(\xi,\zeta)}{\left[\xi + jp_1(\zeta)\right]\left[\xi - jp_1(\zeta)\right]} \\
\tilde{\Pi}(x,\zeta) &= \frac{1}{2\pi}\int_{-\infty}^{\infty} \frac{\tilde{\tilde{s}}(\xi,\zeta)}{\left[\xi + jp_1(\zeta)\right]\left[\xi - jp_1(\zeta)\right]} e^{j\xi x} d\xi \\
&= \frac{1}{2\pi}\int_{-\infty}^{\infty} \tilde{s}(x',\zeta)\int_{-\infty}^{\infty} \frac{e^{j\xi(x-x')}}{\left[\xi + jp_1(\zeta)\right]\left[\xi - jp_1(\zeta)\right]} d\xi dx' \\
&= \int_{-\infty}^{\infty} \tilde{s}(x',\zeta) g_\zeta^p(x|x') dx'
\end{aligned} \tag{C1.8}$$

Eqn. (C1.8) yields

$$g_{\zeta}^{p}(x|x') = \frac{1}{2\pi}\int_{-\infty}^{\infty} \frac{e^{j\xi(x-x')}}{[\xi + jp_1(\zeta)][\xi - jp_1(\zeta)]} d\xi \tag{C1.9}$$

To perform the inverse transformation, a path deformation of the real axis integration is used and Cauchy's theorem is applied to an upper half plane closure (*UHP*) for $x > x'$ and to a lower half plane closure (*LHP*) for $x < x'$ in agreement with Eqn. (C1.10) as depicted in Fig. A2.2.

$$e^{j\xi(x-x')} = e^{-\xi_i(x-x')} e^{j\xi_r(x-x')} \tag{C1.10}$$

For $x > x'$:

$$\begin{aligned} &\int_{-\infty}^{\infty} \frac{e^{j\xi(x-x')}}{\xi^2 + p_1^2(\zeta)} d\xi + \int_{C_{\infty}^{+}} \frac{e^{j\xi(x-x')}}{\xi^2 + p_1^2(\zeta)} d\xi \\ &= 2\pi j \frac{e^{j\xi(x-x')}}{\xi + jp_1(\zeta)}\bigg|_{\xi = jp_1(\zeta)} \\ &\therefore g_{\zeta}^{p}(x|x') = \frac{e^{-p_1(\zeta)(x-x')}}{2p_1(\zeta)} \end{aligned} \tag{C1.11}$$

For $x < x'$:

$$\begin{aligned} &\int_{-\infty}^{\infty} \frac{e^{j\xi(x-x')}}{\xi^2 + p_1^2(\zeta)} d\xi + \int_{C_{\infty}^{-}} \frac{e^{j\xi(x-x')}}{\xi^2 + p_1^2(\zeta)} d\xi \\ &= -2\pi j \frac{e^{j\xi(x-x')}}{\xi - jp_1(\zeta)}\bigg|_{\xi = -jp_1(\zeta)} \\ &\therefore g_{\zeta}^{p}(x|x') = \frac{e^{p_1(\zeta)(x-x')}}{2p_1(\zeta)} \end{aligned} \tag{C1.12}$$

Therefore, for $|x| < \infty$,

$$g_{\zeta}^{p}(x|x') = \frac{e^{-p_1(\zeta)|x-x'|}}{2p_1(\zeta)} \tag{C1.13}$$

Substituting Eqn. (C1.13) into Eqn. (C1.8) yields,

$$\tilde{e}_{1z}^{p}(x,\zeta) = \int_0^{\infty}\left[\frac{\zeta}{\omega\varepsilon_1}\frac{\partial\tilde{j}_x(x,\zeta)}{\partial x} + \frac{jp_1^2}{\omega\varepsilon_1}\tilde{j}_z(x,\zeta)\right]\frac{e^{-p_1|x-x'|}}{2p_1}dx' \tag{C1.14}$$

Eqn. (C1.14) becomes

$$\tilde{e}_{1z}^{p}(x,\zeta) = -\frac{1}{j\omega\varepsilon_1}\int_0^{\infty}\left[j\zeta p_1\tilde{j}_x\,\mathrm{sgn}(x-x') + p_1^2\tilde{j}_z\right]\frac{e^{-p_1|x-x'|}}{2p_1}dx'$$

where (C1.15)

$$\mathrm{sgn}(x-x') = \begin{cases} 1 \cdots x > x' \\ -1 \cdots x < x' \end{cases}$$

$\tilde{e}_{1x}^{p}(x,\zeta)$ can be obtained as

$$\tilde{e}_{1x}^{p}(x,\zeta) = -\frac{1}{p_1^2}\left[j\zeta\frac{\partial\tilde{e}_{1z}^{p}(x,\zeta)}{\partial x} + j\omega\mu_0\tilde{j}_x(x,\zeta)\right] \tag{C1.16}$$

Eqn. (C1.16) becomes

$$\tilde{e}_{1x}^{p}(x,\zeta) = \frac{1}{j\omega\varepsilon_1}\int_0^{\infty}\left[\zeta^2\tilde{j}_x - j\zeta p_1\tilde{j}_z\,\mathrm{sgn}(x-x')\right]\frac{e^{-p_1|x-x'|}}{2p_1}dx' - \frac{j\omega\mu_0}{p_1^2}\tilde{j}_x \tag{C1.17}$$

$\tilde{e}_{1x}^{r}(x,\zeta)$ can be obtained as

$$\tilde{e}_{1x}^{r}(x,\zeta) = -\frac{1}{p_1^2}\left[j\zeta\frac{\partial\tilde{e}_{1z}^{r}(x,\zeta)}{\partial x} + j\omega\mu_0\tilde{j}_x\right] = \frac{A(\zeta)}{p_1}j\zeta e^{-p_1x} - \frac{j\omega\mu_0}{p_1^2}\tilde{j}_x \tag{C1.18}$$

Similarly, $\tilde{h}_{1y}^{p}(x,\zeta)$ can be obtained as

$$\tilde{h}_{1y}^{p}(x,\zeta)=\frac{1}{p_1^2}\left[j\omega\varepsilon_1\frac{\partial\tilde{e}_{1z}^{p}(x,\zeta)}{\partial x}+j\zeta\tilde{j}_x\right]$$
$$=\int_0^{\infty}\left[j\zeta\tilde{j}_x+p_1\tilde{j}_z\,\mathrm{sgn}(x-x')\right]\frac{e^{-p_1|x-x'|}}{2p_1}dx'+\frac{j\zeta}{p_1^2}\tilde{j}_x \tag{C1.19}$$

$\tilde{h}_{1y}^{r}(x,\zeta)$ can obtained as

$$\tilde{h}_{1y}^{r}(x,\zeta)=\frac{1}{p_1^2}\left[j\omega\varepsilon_1\frac{\partial\tilde{e}_{1z}^{r}(x,\zeta)}{\partial x}+j\zeta\tilde{j}_x\right]$$
$$=-\frac{A(\zeta)}{p_1}j\omega\varepsilon_1e^{-p_1x}+\frac{j\zeta}{p_1^2}\tilde{j}_x \tag{C1.20}$$

In the film layer,

$$\left[\frac{\partial^2}{\partial x^2}-p_2^2(\zeta)\right]\tilde{e}_{2z}(x,\zeta)=0 \tag{C1.21}$$

Therefore,

$$\tilde{e}_{2z}(x,\zeta)=B(\zeta)e^{-p_2(\zeta)x}+C(\zeta)e^{p_2(\zeta)x} \tag{C1.22}$$

Both $\tilde{e}_{2x}(x,\zeta)$ and $\tilde{h}_{2y}(x,\zeta)$ can be obtained as

$$\tilde{e}_{2x}(x,\zeta)=-\frac{1}{p_2^2}\left[j\zeta\frac{\partial\tilde{e}_{2z}(x,\zeta)}{\partial x}\right]$$
$$=\frac{j\zeta}{p_2}\left[B(\zeta)e^{-p_2x}-C(\zeta)e^{p_2x}\right] \tag{C1.23}$$

$$\tilde{h}_{2y}(x,\zeta)=\frac{1}{p_2^2}\left[j\omega\varepsilon_2\frac{\partial\tilde{e}_{2z}(x,\zeta)}{\partial x}\right]$$
$$=-\frac{j\omega\varepsilon_2}{p_2}\left[B(\zeta)e^{-p_2x}-C(\zeta)e^{p_2x}\right] \tag{C1.24}$$

$$\tilde{h}_{1y}^{p}(x,\zeta)=\frac{1}{p_1^2}\left[j\omega\varepsilon_1\frac{\partial\tilde{e}_{1z}^{p}(x,\zeta)}{\partial x}+j\zeta\tilde{j}_x\right]$$
$$=\int_0^{\infty}\left[j\zeta\tilde{j}_x+p_1\tilde{j}_z\,\mathrm{sgn}(x-x')\right]\frac{e^{-p_1|x-x'|}}{2p_1}dx'+\frac{j\zeta}{p_1^2}\tilde{j}_x \tag{C1.19}$$

$\tilde{h}_{1y}^{r}(x,\zeta)$ can obtained as

$$\tilde{h}_{1y}^{r}(x,\zeta)=\frac{1}{p_1^2}\left[j\omega\varepsilon_1\frac{\partial\tilde{e}_{1z}^{r}(x,\zeta)}{\partial x}+j\zeta\tilde{j}_x\right]$$
$$=-\frac{A(\zeta)}{p_1}j\omega\varepsilon_1e^{-p_1x}+\frac{j\zeta}{p_1^2}\tilde{j}_x \tag{C1.20}$$

In the film layer,

$$\left[\frac{\partial^2}{\partial x^2}-p_2^2(\zeta)\right]\tilde{e}_{2z}(x,\zeta)=0 \tag{C1.21}$$

Therefore,

$$\tilde{e}_{2z}(x,\zeta)=B(\zeta)e^{-p_2(\zeta)x}+C(\zeta)e^{p_2(\zeta)x} \tag{C1.22}$$

Both $\tilde{e}_{2x}(x,\zeta)$ and $\tilde{h}_{2y}(x,\zeta)$ can be obtained as

$$\tilde{e}_{2x}(x,\zeta)=-\frac{1}{p_2^2}\left[j\zeta\frac{\partial\tilde{e}_{2z}(x,\zeta)}{\partial x}\right]$$
$$=\frac{j\zeta}{p_2}\left[B(\zeta)e^{-p_2x}-C(\zeta)e^{p_2x}\right] \tag{C1.23}$$

$$\tilde{h}_{2y}(x,\zeta)=\frac{1}{p_2^2}\left[j\omega\varepsilon_2\frac{\partial\tilde{e}_{2z}(x,\zeta)}{\partial x}\right]$$
$$=-\frac{j\omega\varepsilon_2}{p_2}\left[B(\zeta)e^{-p_2x}-C(\zeta)e^{p_2x}\right] \tag{C1.24}$$

In the substrate layer,

$$\left[\frac{\partial^2}{\partial x^2} - p_3^2(\zeta)\right]\tilde{e}_{3z}(x,\zeta) = 0 \tag{C1.25}$$

Therefore, to satisfy the radiation condition at $x \longrightarrow -\infty$

$$\tilde{e}_{3z}(x,\zeta) = D(\zeta)e^{p_3(\zeta)x} \tag{C1.26}$$

$\tilde{e}_{3x}(x,\zeta)$ can be obtained as

$$\tilde{e}_{3x}(x,\zeta) = -\frac{1}{p_3^2}\left[j\zeta\frac{\partial\tilde{e}_{3z}(x,\zeta)}{\partial x}\right] = -\frac{D(\zeta)}{p_3}j\zeta e^{p_3 x} \tag{C1.27}$$

$\tilde{h}_{3y}(x,\zeta)$ can be obtained as

$$\tilde{h}_{3y}(x,\zeta) = \frac{1}{p_3^2}\left[j\omega\varepsilon_3\frac{\partial\tilde{e}_{3z}(x,\zeta)}{\partial x}\right] = \frac{j\omega\varepsilon_3}{p_3}D(\zeta)e^{p_3 x} \tag{C1.28}$$

SUMMARY OF SPECTRAL SOLUTIONS

$$\begin{aligned}
\tilde{e}_{1z}(x,\zeta) &= \tilde{e}_{1z}^{p}(x,\zeta) + \tilde{e}_{1z}^{r}(x,\zeta) \\
&= -\frac{1}{j\omega\varepsilon_1}\int_0^\infty\left[j\zeta p_1\tilde{j}_x\,\mathrm{sgn}(x-x') + p_1^2\tilde{j}_z\right]\frac{e^{-p_1|x-x'|}}{2p_1}dx' + A(\zeta)e^{-p_1 x} \\
\tilde{e}_{1x}(x,\zeta) &= \tilde{e}_{1x}^{p}(x,\zeta) + \tilde{e}_{1x}^{r}(x,\zeta) \\
&= \frac{1}{j\omega\varepsilon_1}\int_0^\infty\left[\zeta^2\tilde{j}_x - j\zeta p_1\tilde{j}_z\,\mathrm{sgn}(x-x')\right]\frac{e^{-p_1|x-x'|}}{2p_1}dx' - \frac{2j\omega\mu_0}{p_1^2}\tilde{j}_x \\
&\quad + \frac{A(\zeta)}{p_1}j\zeta e^{-p_1 x}
\end{aligned}$$

$$\tilde{h}_{1y}(x,\zeta)=\tilde{h}_{1y}^{p}(x,\zeta)+\tilde{h}_{1y}^{r}(x,\zeta)$$

$$=\int_0^\infty\left[j\zeta\tilde{j}_x+p_1\tilde{j}_z\,\mathrm{sgn}(x-x')\right]\frac{e^{-p_1|x-x'|}}{2p_1}dx'+\frac{2j\zeta}{p_1^2}\tilde{j}_x-\frac{A(\zeta)}{p_1}j\omega\epsilon_1 e^{-p_1x}$$

$$\tilde{e}_{2z}(x,\zeta)=B(\zeta)e^{-p_2x}+C(\zeta)e^{p_2x}$$

$$\tilde{e}_{2x}(x,\zeta)=\frac{j\zeta}{p_2}\left[B(\zeta)e^{-p_2x}-C(\zeta)e^{p_2x}\right]$$

$$\tilde{h}_{2y}(x,\zeta)=-\frac{j\omega\epsilon_2}{p_2}\left[B(\zeta)e^{-p_2x}-C(\zeta)e^{p_2x}\right]$$

$$\tilde{e}_{3z}(x,\zeta)=D(\zeta)e^{p_3x}$$

$$\tilde{e}_{3x}(x,\zeta)=-\frac{D(\zeta)}{p_3}j\zeta e^{p_3x}$$

$$\tilde{h}_{3y}(x,\zeta)=\frac{j\omega\epsilon_3}{p_3}D(\zeta)e^{p_3x}$$

C.2 IMPLEMENTATION OF MATCHING BOUNDARY CONDITIONS

Since there are 4 unknown coefficients, 4 boundary conditions must be required to determine them. The 4 boundary conditions at the interfaces, $x=0^{\pm}$ and $x=-t^{\pm}$, are implemented by

$$E_{3z}(x,z)\big|_{x=-t^-}=E_{2z}(x,z)\big|_{x=-t^+} \tag{C2.1}$$

$$H_{3y}(x,z)\big|_{x=-t^-}=H_{2y}(x,z)\big|_{x=-t^+} \tag{C2.2}$$

$$E_{2z}(x,z)\big|_{x=0^-}=E_{1z}(x,z)\big|_{x=0^+} \tag{C2.3}$$

$$H_{2y}(x,z)\big|_{x=0^-}=H_{1y}(x,z)\big|_{x=0^+} \tag{C2.4}$$

Therefore, the 4 spectral boundary conditions are

$$\tilde{e}_{3z}(x,\zeta)\big|_{x=-t^-} = \tilde{e}_{2z}(x,\zeta)\big|_{x=-t^+} \tag{C2.5}$$

$$\tilde{h}_{3y}(x,\zeta)\big|_{x=-t^-} = \tilde{h}_{2y}(x,\zeta)\big|_{x=-t^+} \tag{C2.6}$$

$$\tilde{e}_{2z}(x,\zeta)\big|_{x=0^-} = \tilde{e}_{1z}(x,\zeta)\big|_{x=0^+} \tag{C2.7}$$

$$\tilde{h}_{2y}(x,\zeta)\big|_{x=0^-} = \tilde{h}_{1y}(x,\zeta)\big|_{x=0^+} \tag{C2.8}$$

From Eqn. (C2.5),

$$D(\zeta)e^{-p_3 t} = B(\zeta)e^{p_2 t} + C(\zeta)e^{-p_2 t} \tag{C2.9}$$

From Eqn. (C2.6),

$$\frac{j\omega\varepsilon_3}{p_3}D(\zeta)e^{-p_3 t} = -\frac{j\omega\varepsilon_2}{p_2}\left[B(\zeta)e^{p_2 t} - C(\zeta)e^{-p_2 t}\right] \tag{C2.10}$$

From Eqn. (C2.7),

$$\begin{aligned} &B(\zeta)+C(\zeta) \\ &= -\frac{1}{j\omega\varepsilon_1}\int_0^\infty\left[-j\zeta p_1\tilde{j}_x(0,\zeta)+p_1^2\tilde{j}_z(0,\zeta)\right]\frac{e^{-p_1 x'}}{2p_1}dx' + A(\zeta) \end{aligned} \tag{C2.11}$$

From Eqn. (C2.8),

$$\begin{aligned} -\frac{j\omega\varepsilon_2}{p_2}\left[B(\zeta)-C(\zeta)\right] = \int_0^\infty\left[j\zeta\tilde{j}_x(0,\zeta)-p_1\tilde{j}_z(0,\zeta)\right]\frac{e^{-p_1(\zeta)x'}}{2p_1}dx' \\ +\frac{2j\zeta}{p_1^2}\tilde{j}_x(0,\zeta)-A(\zeta)\frac{j\omega\varepsilon_1}{p_1} \end{aligned} \tag{C2.12}$$

Some algebraic manipulation was implemented to determine the 4 unknown coefficients $A(\zeta)$, $B(\zeta)$, $C(\zeta)$, and $D(\zeta)$ which satisfy Eqns. (C2.9)-(C2.12). Finally, the spectral coefficients are

$$A(\zeta)=\frac{1}{j\omega\varepsilon_1}2\tilde{\Lambda}(\zeta)\varepsilon_1\left[\varepsilon_2 p_3\cosh(p_2 t)+\varepsilon_3 p_2\sinh(p_2 t)\right]$$
$$\left\{\int_0^\infty\left[j\zeta\tilde{j}_x(0,\zeta)-p_1\tilde{j}_z(0,\zeta)\right]\frac{e^{-p_1x'}}{2p_1}dx'+\frac{j\zeta}{p_1^2}\tilde{j}_x(0,\zeta)\right\}$$
$$-\frac{1}{j\omega\varepsilon_1}\int_0^\infty\left[j\zeta p_1\tilde{j}_x(0,\zeta)-p_1^2\tilde{j}_z(0,\zeta)\right]\frac{e^{-p_1x'}}{2p_1}dx'$$

$$B(\zeta)=\frac{1}{j\omega\varepsilon_1}\tilde{\Lambda}(\zeta)\varepsilon_1(\varepsilon_2 p_3-\varepsilon_3 p_2)$$
$$\left\{\int_0^\infty\left[j\zeta\tilde{j}_x(0,\zeta)-p_1\tilde{j}_z(0,\zeta)\right]\frac{e^{-p_1x'}}{2p_1}dx'+\frac{j\zeta}{p_1^2}\tilde{j}_x(0,\zeta)\right\}e^{-p_2t}$$

$$C(\zeta)=\frac{1}{j\omega\varepsilon_1}\tilde{\Lambda}(\zeta)\varepsilon_1(\varepsilon_2 p_3+\varepsilon_3 p_2)$$
$$\left\{\int_0^\infty\left[j\zeta\tilde{j}_x(0,\zeta)-p_1\tilde{j}_z(0,\zeta)\right]\frac{e^{-p_1x'}}{2p_1}dx'+\frac{j\zeta}{p_1^2}\tilde{j}_x(0,\zeta)\right\}e^{p_2t}$$

$$D(\zeta)=\frac{1}{j\omega\varepsilon_1}2\tilde{\Lambda}(\zeta)\varepsilon_1\varepsilon_2 p_3$$
$$\left\{\int_0^\infty\left[j\zeta\tilde{j}_x(0,\zeta)-p_1\tilde{j}_z(0,\zeta)\right]\frac{e^{-p_1x'}}{2p_1}dx'+\frac{j\zeta}{p_1^2}\tilde{j}_x(0,\zeta)\right\}e^{p_3t}$$

where

$$p_l=\sqrt{\zeta^2-k_l^2}\cdots l=1,2,3$$

$$k_l=\omega\sqrt{\mu_0\varepsilon_l}$$

$$\tilde{\Lambda}=\frac{2p_1p_2}{(\varepsilon_2p_3-\varepsilon_3p_2)(\varepsilon_1p_2-\varepsilon_2p_1)e^{-p_2t}+(\varepsilon_2p_3+\varepsilon_3p_2)(\varepsilon_1p_2+\varepsilon_2p_1)e^{p_2t}}$$

APPENDIX D

GREEN'S DYAD INTEGRAL REPRESENTATION OF RADIATION FIELD FOR TM MODES OF THE ASYMMETRIC PLANAR OPEN WAVEGUIDE

The Green's dyad integral representations are recovered from spectral Green's dyads such that

$$G^e_{11xx}(x,z|x',z') = \int_{-\infty}^{\infty} \left\{ \frac{\zeta^2}{4\pi p_1} \left[e^{-p_1|x-x'|} + e^{-p_1(x+x')} \right] + \frac{k_1^2}{\pi p_1^2} \delta(x-x') \right\} \frac{1}{j\omega\varepsilon_1} e^{-j\zeta(z-z')} d\zeta$$

$$G^e_{11xz}(x,z|x',z') = \frac{1}{j\omega\varepsilon_1} \int_{-\infty}^{\infty} \left\{ \frac{j\zeta}{4\pi} \left[\operatorname{sgn}(x-x') e^{-p_1|x-x'|} - e^{-p_1(x+x')} \right] \right\} e^{-j\zeta(z-z')} d\zeta$$

$$G^e_{11zx}(x,z|x',z') = \frac{1}{j\omega\varepsilon_1} \int_{-\infty}^{\infty} \left\{ \frac{j\zeta}{4\pi} \left[\operatorname{sgn}(x-x') e^{-p_1|x-x'|} + e^{-p_1(x+x')} \right] \right\} e^{-j\zeta(z-z')} d\zeta$$

$$G^e_{11zz}(x,z|x',z') = -\frac{1}{j\omega\varepsilon_1} \int_{-\infty}^{\infty} \frac{p_1}{4\pi} \left[e^{-p_1|x-x'|} - e^{-p_1(x+x')} \right] e^{-j\zeta(z-z')} d\zeta$$

$$G^e_{12xx}(x,z|x',z') = -\frac{1}{j\omega\varepsilon_1} \int_{-\infty}^{\infty} \tilde{\Lambda}\varepsilon_1 \left[\varepsilon_2 p_3 \cosh(p_2 t) + \varepsilon_3 p_2 \sinh(p_2 t) \right] \cdot \frac{\zeta^2}{\pi p_1^2} \left[\frac{e^{-p_1 x'}}{2} + \frac{\delta(x-x')}{p_1} \right] e^{-p_1 x} e^{-j\zeta(z-z')} d\zeta$$

$$G^e_{12xz}(x,z|x',z') = \int_{-\infty}^{\infty} j\zeta\tilde{\Lambda}\varepsilon_1\{\varepsilon_2 p_3\cosh(p_2 t)+\varepsilon_3 p_2\sinh(p_2 t)\}$$
$$\cdot\left(\frac{-1}{j\omega\varepsilon_1}\right)\frac{e^{-p_1(x+x')}}{2\pi p_1}e^{-j\zeta(z-z')}d\zeta$$

$$G^e_{12zx}(x,z|x',z') = \int_{-\infty}^{\infty}\tilde{\Lambda}\varepsilon_1\left[\varepsilon_2 p_3\cosh(p_2 t)+\varepsilon_3 p_2\sinh(p_2 t)\right]$$
$$\cdot\left(\frac{-1}{j\omega\varepsilon_1}\right)\frac{j\zeta}{\pi p_1}\left[\frac{e^{-p_1 x'}}{2}+\frac{\delta(x-x')}{p_1}\right]e^{-p_1 x}$$
$$\cdot e^{-j\zeta(z-z')}d\zeta$$

$$G^e_{12zz}(x,z|x',z') = \int_{-\infty}^{\infty}\tilde{\Lambda}\varepsilon_1\left[\varepsilon_2 p_3\cosh(p_2 t)+\varepsilon_3 p_2\sinh(p_2 t)\}\right]$$
$$\cdot\left(\frac{-1}{j\omega\varepsilon_1}\right)\frac{e^{-p_1(x+x')}}{2\pi}e^{-j\zeta(z-z')}d\zeta$$

$$G^e_{21xx}(x,z|x',z') = \int_{-\infty}^{\infty}\tilde{\Lambda}\varepsilon_1\frac{\zeta^2}{\pi p_1 p_2}\left[\frac{e^{-p_1 x'}}{2}+\frac{\delta(x-x')}{p_1}\right]$$
$$\cdot\left\{\varepsilon_2 p_3\sinh\left[p_2(x+t)\right]+\varepsilon_3 p_2\cosh\left[p_2(x+t)\right]\right\}$$
$$\cdot\left(\frac{1}{j\omega\varepsilon_1}\right)e^{-j\zeta(z-z')}d\zeta$$

$$G^e_{21xz}(x,z|x',z')$$
$$= \int_{-\infty}^{\infty}\tilde{\Lambda}\varepsilon_1(j\zeta)\left\{\varepsilon_2 p_3\sinh\left[p_2(x+t)\right]+\varepsilon_3 p_2\cosh\left[p_2(x+t)\right]\right\}$$
$$\cdot\left(\frac{-1}{j\omega\varepsilon_1}\right)\frac{e^{-p_1 x'}}{2\pi p_2}e^{-j\zeta(z-z')}d\zeta$$

$$G^{e}_{21zz}\left(x,z\middle|x',z'\right)$$

$$=\int_{-\infty}^{\infty}\left(-\frac{1}{j\omega\varepsilon_1}\right)\tilde{\Lambda}\varepsilon_1\left\{\varepsilon_2 p_3\cosh\left[p_2(x+t)\right]+\varepsilon_3 p_2\sinh\left[p_2(x+t)\right]\right\}$$

$$\cdot\frac{e^{-p_1x'}}{2\pi}e^{-j\zeta(z-z')}d\zeta$$

$$G^{e}_{31xx}\left(x,z\middle|x',z'\right)=\frac{1}{j\omega\varepsilon_1}\int_{-\infty}^{\infty}\tilde{\Lambda}\varepsilon_1\varepsilon_2\frac{\zeta^2}{\pi p_1}\left[\frac{e^{-p_1x'}}{2}+\frac{\delta(x-x')}{p_1}\right]$$

$$\cdot e^{p_3(x+t)}e^{-j\zeta(z-z')}d\zeta$$

$$G^{e}_{31xz}\left(x,z\middle|x',z'\right)=\frac{-1}{j\omega\varepsilon_1}\int_{-\infty}^{\infty}j\zeta\tilde{\Lambda}\varepsilon_1\varepsilon_2\frac{e^{-p_1x'}e^{p_3(x+t)}}{2\pi}e^{-j\zeta(z-z')}d\zeta$$

$$G^{e}_{31zx}\left(x,z\middle|x',z'\right)=\frac{-1}{j\omega\varepsilon_1}\int_{-\infty}^{\infty}\tilde{\Lambda}\varepsilon_1\varepsilon_2 p_3\frac{j\zeta}{\pi p_1}\left[\frac{e^{-p_1x'}}{2}+\frac{\delta(x-x')}{p_1}\right]$$

$$\cdot e^{p_3(x+t)}e^{-j\zeta(z-z')}d\zeta$$

$$G^{e}_{31zz}\left(x,z\middle|x',z'\right)=-\frac{1}{j\omega\varepsilon_1}\int_{-\infty}^{\infty}\tilde{\Lambda}\varepsilon_1\varepsilon_2 p_3\frac{e^{-p_1x'}e^{p_3(x+t)}}{2\pi}e^{-j\zeta(z-z')}d\zeta$$

$$G^{h}_{11yx}\left(x,z\middle|x',z'\right)=\int_{-\infty}^{\infty}\frac{-j\zeta}{2\pi p_1}\left[\frac{e^{-p_1|x-x'|}}{2}+\frac{e^{-p_1(x+x')}}{2}+\frac{2\delta(x-x')}{p_1}\right]$$

$$\cdot e^{-j\zeta(z-z')}d\zeta$$

$$G^{h}_{11yz}\left(x,z\middle|x',z'\right)=\int_{-\infty}^{\infty}\frac{1}{4\pi}\left[\operatorname{sgn}(x-x')e^{-p_1|x-x'|}-e^{-p_1(x+x')}\right]$$

$$\cdot e^{-j\zeta(z-z')}d\zeta$$

$$G_{12yx}^{h}(x,z|x',z')=\int_{-\infty}^{\infty}\tilde{\Lambda}\varepsilon_1\left[\varepsilon_2 p_3\cosh(p_2 t)+\varepsilon_3 p_2\sinh(p_2 t)\right]$$

$$\cdot\frac{j\zeta}{\pi p_1^2}\left[\frac{e^{-p_1 x'}}{2}+\frac{\delta(x-x')}{jp_1}\right]e^{-p_1 x}e^{-j\zeta(z-z')}d\zeta$$

$$G_{12yz}^{h}(x,z|x',z')$$

$$=\int_{-\infty}^{\infty}\tilde{\Lambda}\varepsilon_1\left[\varepsilon_2 p_3\cosh(p_2 t)+\varepsilon_3 p_2\sinh(p_2 t)\right]\frac{e^{-p_1(x+x')}}{2\pi p_1}e^{-j\zeta(z-z')}d\zeta$$

$$G_{21yx}^{h}(x,z|x',z')=\int_{-\infty}^{\infty}\tilde{\Lambda}\varepsilon_2\frac{-j\zeta}{\pi p_1 p_2}\left[\frac{e^{-p_1 x'}}{2}+\frac{\delta(x-x')}{p_1}\right]$$

$$\cdot\left\{\varepsilon_2 p_3\sinh\left[p_2(x+t)\right]+\varepsilon_3 p_2\cosh\left[p_2(x+t)\right]\right\}e^{-j\zeta(z-z')}d\zeta$$

$$G_{21yz}^{h}(x,z|x',z')=-\int_{-\infty}^{\infty}\left\{\varepsilon_2 p_3\sinh\left[p_2(x+t)\right]+\varepsilon_3 p_2\cosh\left[p_2(x+t)\right]\right\}$$

$$\cdot\tilde{\Lambda}\varepsilon_2\frac{e^{-p_1 x'}}{2\pi p_2}e^{-j\zeta(z-z')}d\zeta$$

$$G_{31yx}^{h}(x,z|x',z')$$

$$=\int_{-\infty}^{\infty}\tilde{\Lambda}\varepsilon_2\varepsilon_3\frac{-j\zeta}{\pi p_1}\left[\frac{e^{-p_1 x'}}{2}+\frac{\delta(x-x')}{p_1}\right]e^{p_3(x+t)}e^{-j\zeta(z-z')}d\zeta$$

$$G_{31yz}^{h}(x,z|x',z')=-\int_{-\infty}^{\infty}\tilde{\Lambda}\varepsilon_2\varepsilon_3\frac{e^{-p_1 x'}e^{p_3(x+t)}}{2\pi}e^{-j\zeta(z-z')}d\zeta$$

where

$$p_l=\sqrt{\zeta^2-k_l^2}\cdots l=1,2,3$$

$$k_l=\omega\sqrt{\mu_0\varepsilon_l}$$

$$\tilde{\Lambda}=\frac{2p_1p_2}{(\varepsilon_2p_3-\varepsilon_3p_2)(\varepsilon_1p_2-\varepsilon_2p_1)e^{-p_2t}+(\varepsilon_2p_3+\varepsilon_3p_2)(\varepsilon_1p_2+\varepsilon_2p_1)e^{p_2t}}$$

APPENDIX E

ELECTRIC HERTZIAN POTENTIAL FORMULATION OF THE ASYMMETRIC TRI PLANAR-LAYERED DIELECTRIC WAVEGUIDE

E.1 GEOMETRICAL CONFIGURATION OF ASYMMETRIC TRI PLANAR-LAYERED DIELECTRIC WAVEGUIDE

Asymmetric tri planar-layered dielectric waveguide consists of cover, film, and substrate layers with complex permittivity ε_l, $l = 1, 2, 3$ for cover, film, and substrate layers in Fig. E1. Each layer is assumed to be non-magnetic, isotropic and homogeneous.

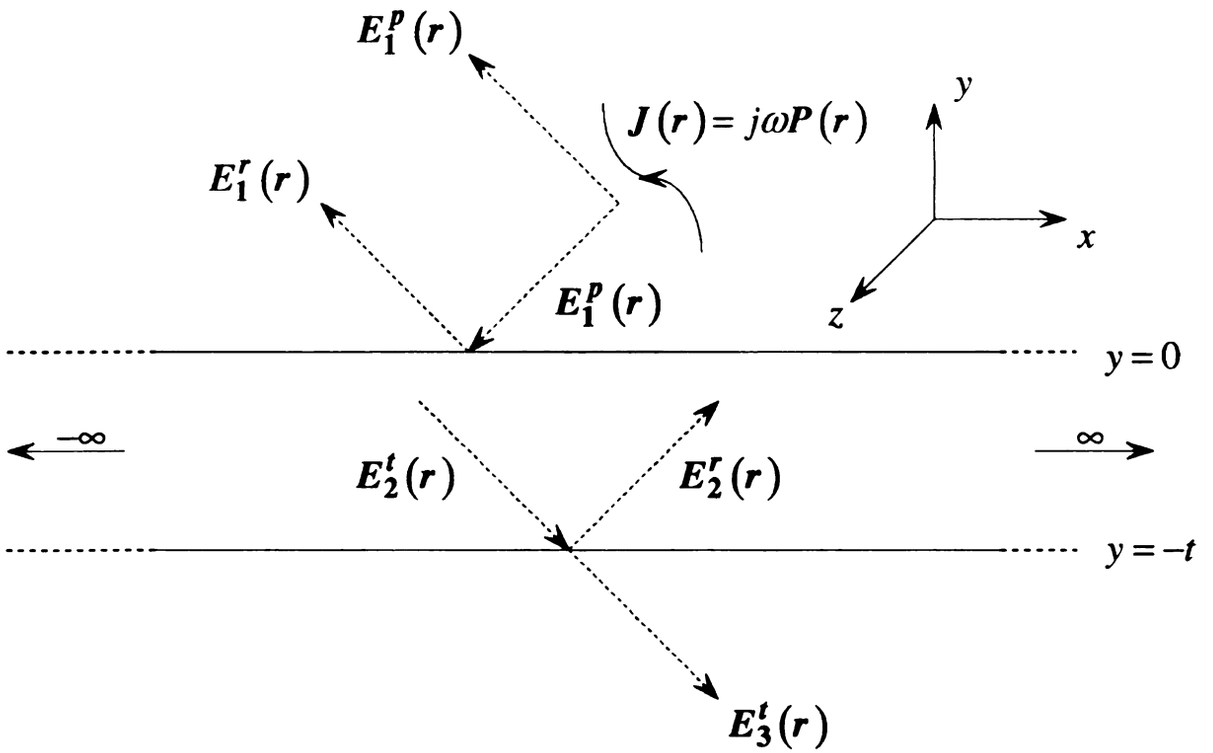

Figure E.1.1 Asymmetric tri planar-layered dielectric waveguide with the z-axis as the waveguiding axis and with the x-axis tangential and the y-axis normal to the planar interfaces.

E.2 BOUNDARY CONDITIONS FOR ELECTRIC HERTZIAN POTENTIALS

Helmholtz equation for $\boldsymbol{\Pi}_l(\boldsymbol{r})$ maintained by polarization $\boldsymbol{P}(\boldsymbol{r})=\boldsymbol{J}(\boldsymbol{r})/j\omega$ in the *l'th* layer is

$$\left(\nabla^2+k_l^2\right)\boldsymbol{\Pi}_l(\boldsymbol{r})=-\frac{\boldsymbol{P}(\boldsymbol{r})}{\varepsilon_l}$$

where (E2.1)

$$k_l^2=\omega^2\mu_0\varepsilon_l\cdots l=1,2,3$$

$$\boldsymbol{r}=x\hat{x}+y\hat{y}+z\hat{z}$$

$\boldsymbol{J}(\boldsymbol{r})$ is the impressed excitatory current immersed in the cover layer.

EM fields in the *l'th* layer in terms of electric Hertzian potential are

$$\begin{aligned}\boldsymbol{E}_l(\boldsymbol{r})&=k_l^2\boldsymbol{\Pi}_l(\boldsymbol{r})+\nabla\left[\nabla\bullet\boldsymbol{\Pi}_l(\boldsymbol{r})\right]\\ \boldsymbol{H}_l(\boldsymbol{r})&=j\omega\varepsilon_l\nabla\times\boldsymbol{\Pi}_l(\boldsymbol{r})\end{aligned} \tag{E2.2}$$

Eqn. (E2.2) yields

$$\begin{aligned}E_{lx}(r)&=k_l^2\Pi_{lx}(r)+\frac{\partial}{\partial x}\left[\nabla\bullet\boldsymbol{\Pi}_l(\boldsymbol{r})\right]\\ E_{ly}(r)&=k_l^2\Pi_{ly}(r)+\frac{\partial}{\partial y}\left[\nabla\bullet\boldsymbol{\Pi}_l(\boldsymbol{r})\right]\\ E_{lz}(r)&=k_l^2\Pi_{lz}(r)+\frac{\partial}{\partial z}\left[\nabla\bullet\boldsymbol{\Pi}_l(\boldsymbol{r})\right]\\ H_{lx}(r)&=j\omega\varepsilon_l\left[\frac{\partial\Pi_{lz}(r)}{\partial y}-\frac{\partial\Pi_{ly}(r)}{\partial z}\right]\\ H_{ly}(r)&=j\omega\varepsilon_l\left[\frac{\partial\Pi_{lx}(r)}{\partial z}-\frac{\partial\Pi_{lz}(r)}{\partial x}\right]\\ H_{lz}(r)&=j\omega\varepsilon_l\left[\frac{\partial\Pi_{ly}(r)}{\partial x}-\frac{\partial\Pi_{lx}(r)}{\partial y}\right]\end{aligned} \tag{E2.3}$$

Boundary conditions at $y = 0$ interface are implemented by

$$E_{1\alpha}(x,y,z)\Big|_{y=0^+} = E_{2\alpha}(x,y,z)\Big|_{y=0^-}$$
$$H_{1\alpha}(x,y,z)\Big|_{y=0^+} = H_{2\alpha}(x,y,z)\Big|_{y=0^-} \qquad \text{(E2.4)}$$
$$\textit{where}$$
$$\alpha = x, z$$

Therefore [28],

$$\Pi_{1\alpha}(x,y,z)\Big|_{y=0^+} = N_{21}^2 \Pi_{2\alpha}(x,y,z)\Big|_{y=0^-} \cdots \alpha = x,\ y,\ z$$
$$\left.\frac{\partial \Pi_{1\alpha}(x,y,z)}{\partial y}\right|_{y=0^+} = N_{21}^2 \left.\frac{\partial \Pi_{2\alpha}(x,y,z)}{\partial y}\right|_{y=0^-}$$
$$\left[\frac{\partial \Pi_{1y}(x,y,z)}{\partial y} - \frac{\partial \Pi_{2y}(x,y,z)}{\partial y}\right]\Bigg|_{y=0} \qquad \text{(E2.5)}$$
$$= -\left(N_{21}^2 - 1\right)\left[\frac{\partial \Pi_{2x}(x,y,z)}{\partial x} + \frac{\partial \Pi_{2z}(x,y,z)}{\partial z}\right]\Bigg|_{y=0}$$
$$\cdots \alpha = x,\ z$$

Boundary conditions at $y = -t$ interface are implemented by

$$\Pi_{1\alpha}(x,y,z)\Big|_{y=-t^+} = N_{21}^2 \Pi_{2\alpha}(x,y,z)\Big|_{y=-t^-} \cdots \alpha = x,\ y,\ z$$
$$\left.\frac{\partial \Pi_{1\alpha}(x,y,z)}{\partial y}\right|_{y=-t^+} = N_{21}^2 \left.\frac{\partial \Pi_{2\alpha}(x,y,z)}{\partial y}\right|_{y=-t^-}$$
$$\left[\frac{\partial \Pi_{1y}(x,y,z)}{\partial y} - \frac{\partial \Pi_{2y}(x,y,z)}{\partial y}\right]\Bigg|_{y=-t} \qquad \text{(E2.6)}$$
$$= -\left(N_{21}^2 - 1\right)\left[\frac{\partial \Pi_{2x}(x,y,z)}{\partial x} + \frac{\partial \Pi_{2z}(x,y,z)}{\partial z}\right]\Bigg|_{y=-t}$$
$$\cdots \alpha = x,\ z$$

where $N_{21}^2 = (n_2/n_1)^2 = \varepsilon_2/\varepsilon_1$ and $N_{32}^2 = (n_3/n_2)^2 = \varepsilon_3/\varepsilon_2$.

E.3 ELECTRIC HERTZIAN POTENTIAL FORMULATION

A prototype homogeneous Helmholtz equation for scattered fields of electric Hertzian potential becomes (exploiting the 3-D Fourier transform pair)

$$\left(\nabla^2 + k_l^2\right)\boldsymbol{\Pi}_l^s(\boldsymbol{r}) = 0 \rightarrow \left(\nabla^2 + k_l^2\right)\Pi_{l\alpha}^s(\boldsymbol{r}) = 0$$

$$\Pi_{l\alpha}^s(\boldsymbol{r}) = \frac{1}{(2\pi)^2}\iint_{\infty} \tilde{\Pi}_{l\alpha}^s(\boldsymbol{\lambda}, y) e^{j\boldsymbol{\lambda}\cdot\boldsymbol{r}} d^2\boldsymbol{\lambda}$$

where (E3.1)

$\boldsymbol{\lambda} = \hat{x}\xi + \hat{z}\zeta$

$l = 1, 2, 3 \quad \alpha = x, y, z$

$\dfrac{d^2\tilde{\Pi}_{l\alpha}^s(\boldsymbol{\lambda}, y)}{dy^2} - p_l^2(\boldsymbol{\lambda})\tilde{\Pi}_{l\alpha}^s(\boldsymbol{\lambda}, y) = 0 \left(p_l = \sqrt{\lambda^2 - k_l^2} = \sqrt{\xi^2 + \zeta^2 - k_l^2}\right)$ leads to

$\tilde{\Pi}_{l\alpha}^s(\boldsymbol{\lambda}, y) = W_{l\alpha}^s(\boldsymbol{\lambda}) e^{\mp p_l(\boldsymbol{\lambda}) y}$ for fields propagating in the $\pm y$ directions yields

$$\Pi_{l\alpha}^s(\boldsymbol{r}) = \frac{1}{(2\pi)^2}\iint_{\infty} W_{l\alpha}^s(\boldsymbol{\lambda}) e^{j\boldsymbol{\lambda}\cdot\boldsymbol{r}} e^{\mp p_l(\boldsymbol{\lambda}) y} d^2\boldsymbol{\lambda} \tag{E3.2}$$

The inhomogeneous Helmholtz equation for principal fields of Hertzian potential in the cover layer is

$$\left(\nabla^2 + k_1^2\right)\boldsymbol{\Pi}_1^p(\boldsymbol{r}) = -\frac{\boldsymbol{P}(\boldsymbol{r})}{\varepsilon_1}$$

$$\rightarrow \left(\nabla^2 + k_1^2\right)\Pi_{1\alpha}^p(\boldsymbol{r}) = -\frac{P_\alpha(\boldsymbol{r})}{\varepsilon_1} \tag{E3.3}$$

where

$\alpha = x, y, z$

Consider Green's function $G_1^p(r|r')$ for unbounded medium defined by

$$\left(\nabla^2 + k_1^2\right) G_1^p(r|r') = -\delta(r - r') \tag{E3.4}$$

Using the relation

$$G_1^p(r|r') = G_1^p(r - r') \tag{E3.5}$$

yields

$$\left(\nabla^2 + k_1^2\right) G_1^p(r - r') = -\delta(r - r') \tag{E3.6}$$

Letting $r' = 0$, while the result can be shifted to $r' \neq 0$,

$$\left(\nabla^2 + k_1^2\right) G_1^p(r) = -\delta(r) \tag{E3.7}$$

The integral representation for $G^p(r)$ through 2-D inverse Fourier transform is

$$G_1^p(r) = \frac{1}{(2\pi)^2} \iint_{\infty} \tilde{G}_1^p(\lambda, y) e^{j\lambda \bullet r} d^2\lambda \tag{E3.8}$$

Then,

$$\tilde{G}_1^p(\lambda, y) = \iint_{\infty} G_1^p(r) e^{-j\lambda \bullet r} dx dz \tag{E3.9}$$

Substitution Eqn. (E3.9) into Eqn. (E3.8) yields

$$\begin{aligned} & G_1^p(x, y, z) \\ &= \frac{1}{(2\pi)^2} \iint_{\infty} \left[\iint_{\infty} G_1^p(x', y, z') e^{-j\lambda \bullet r'} dx' dz' \right] e^{j\lambda \bullet r} d^2\lambda \\ &= \iint_{\infty} G_1^p(x', y, z') \left[\frac{1}{(2\pi)^2} \iint_{\infty} e^{j\lambda \bullet (r - r')} d^2\lambda \right] dx' dz' \end{aligned} \tag{E3.10}$$

Eqn. (E3.10) is true if

$$\frac{1}{(2\pi)^2}\iint_{\infty} e^{j\lambda\cdot(r-r')}d^2\lambda=\delta(x-x')\delta(z-z') \tag{E3.11}$$

Substitution Eqn. (E3.8) and Eqn. (E3.11) into Eqn. (E3.7) yields

$$\left(\nabla^2+k_1^2\right)\frac{1}{(2\pi)^2}\iint_{\infty}\tilde{G}_1^p(\lambda,y)e^{j\lambda\cdot r}d^2\lambda=-\frac{\delta(y)}{(2\pi)^2}\iint_{\infty}e^{j\lambda\cdot r}d^2\lambda \tag{E3.12}$$

Eqn. (E3.12) leads to

$$\iint_{\infty}\left\{\left[\frac{\partial^2}{\partial y^2}-\left(\xi^2+\zeta^2-k_1^2\right)\right]\tilde{G}_1^p(\lambda,y)+\delta(y)\right\}e^{j\lambda\cdot r}d^2\lambda=0 \tag{E3.13}$$

and the Fourier-transform theorem requires

$$\left[\frac{\partial^2}{\partial y^2}-p_1^2(\lambda)\right]\tilde{G}_1^p(\lambda,y)=-\delta(y)$$

$$\textit{where} \tag{E3.14}$$

$$p_1^2(\lambda)=\xi^2+\zeta^2-k_1^2$$

The 1-D ordinary differential equation for $\tilde{G}_1^p(\lambda,y)$ can be solved by exploiting the 1-D transform pair

$$\tilde{\tilde{G}}_1^p(\lambda,\eta)=\int_{-\infty}^{\infty}\tilde{G}_1^p(\lambda,y)e^{-j\eta y}dy$$

$$\tilde{G}_1^p(\lambda,y)=\frac{1}{2\pi}\int_{-\infty}^{\infty}\tilde{\tilde{G}}_1^p(\lambda,\eta)e^{j\eta y}d\eta \tag{E3.15}$$

Substitution Eqn. (E3.15) into Eqn. (E3.14) yields

$$\left[\frac{\partial^2}{\partial y^2}-p_1^2(\lambda)\right]\frac{1}{2\pi}\int_{-\infty}^{\infty}\tilde{\tilde{G}}_1^p(\lambda,\eta)e^{j\eta y}d\eta=-\frac{1}{2\pi}\int_{-\infty}^{\infty}e^{j\eta y}d\eta$$

$$\int_{-\infty}^{\infty}\left\{\left[\eta^2+p_1^2(\lambda)\right]\tilde{\tilde{G}}_1^p(\lambda,\eta)-1\right\}e^{j\eta y}d\eta=0 \tag{E3.16}$$

Therefore, by the Fourier integral theorem

$$\tilde{\tilde{G}}_1^p(\lambda,\eta)=\frac{1}{\eta^2+p_1^2(\lambda)} \tag{E3.17}$$

Substitution Eqn. (E3.17) into Eqn. (E3.15) yields

$$\tilde{G}_1^p(\lambda,y)=\frac{1}{2\pi}\int_{-\infty}^{\infty}\frac{e^{j\eta y}}{[\eta+jp_1(\lambda)][\eta-jp_1(\lambda)]}d\eta \tag{E3.18}$$

As discussed previously in Appendix A, the pole singularities arise from $\eta=\pm jp_1(\lambda)$ and $p_1(\lambda)$ is chosen with $\mathrm{Re}\{p_1(\lambda)\}>0$ and $\mathrm{Im}\{p_1(\lambda)\}<0$ (see Fig. A2.1) to satisfy the radiation condition. Instead of the complex ξ-plane in Fig. A2.2, Cauchy's integral theorem is applied to the closed *UHP* or *LHP* contours (along and within which the Fourier inversion integrand is analytic) in the complex η-plane such that

$$e^{j\eta y}=e^{-\eta_i y}e^{j\eta_r y}\Rightarrow\begin{cases}UHP: y>0\\ LHP: y<0\end{cases} \tag{E3.19}$$

where *UHP* and *LHP* stand for Upper and Lower Half Plane closure in the complex η-plane respectively. Following the same procedure in Appendix A finally yields

$$\tilde{G}_1^p(\lambda,y)=\begin{cases}\dfrac{e^{-p_1(\lambda)y}}{2p_1(\lambda)}\cdots y>0\\ \dfrac{e^{p_1(\lambda)y}}{2p_1(\lambda)}\cdots y<0\end{cases} \tag{E3.20}$$

Therefore, for $|y|<\infty$,

$$\tilde{G}_1^p(\lambda,y)=\frac{e^{-p_1(\lambda)|y|}}{2p_1(\lambda)} \tag{E3.21}$$

Shifting $y' \neq 0$ leads to

$$\tilde{G}_1^p(\lambda, y-y') = \frac{e^{-p_1(\lambda)|y-y'|}}{2p_1(\lambda)} \tag{E3.22}$$

Substitution Eqn. (E3.22) into Eqn. (E3.8) with $r' \neq 0$ yields

$$G_1^p(r|r') = \iint_{\infty} \frac{e^{j\lambda\bullet(r-r')} e^{-p_1(\lambda)|y-y'|}}{2(2\pi)^2 p_1(\lambda)} d^2\lambda \tag{E3.23}$$

Then, the principal wave of potential becomes

$$\begin{aligned} \Pi_{1\alpha}^p(r) &= \int_V \frac{P_\alpha(r')}{\varepsilon_1} G_1^p(r|r') dV' \\ &= \int_V \frac{P_\alpha(r')}{\varepsilon_1} \left[\iint_{\infty} \frac{e^{j\lambda\bullet(r-r')} e^{-p_1(\lambda)|y-y'|}}{2(2\pi)^2 p_1(\lambda)} d^2\lambda \right] dV' \end{aligned} \tag{E3.24}$$

where

$\alpha = x, y, z$

Total electric Hertzian potential in the cover layer becomes

$$\Pi_{1\alpha}(r) = \Pi_{1\alpha}^p(r) + \Pi_{1\alpha}^r(r) \tag{E3.25}$$

where superscript *r* denotes reflected electric Hertzian potential. Again, exploiting Eqn. (E3.2) leads to

$$\Pi_{1\alpha}(r) = \frac{1}{(2\pi)^2} \iint_{\infty} e^{j\lambda\bullet r} \left(\int_V \frac{P_\alpha}{\varepsilon_1} \frac{e^{-j\lambda\bullet r'} e^{-p_1|y-y'|}}{2p_1} dV' + W_{1\alpha}^r e^{-p_1 y} \right) d^2\lambda \tag{E3.26}$$

Total electric Hertzian potential in the film layer becomes

$$\Pi_{2\alpha}(r) = \Pi_{2\alpha}^t(r) + \Pi_{2\alpha}^r(r) \tag{E3.27}$$

This leads to

$$\Pi_{2\alpha}(r)=\frac{1}{(2\pi)^2}\iint_{\infty} e^{j\lambda\bullet r}\left(W_{2\alpha}^{t}e^{p_2 y}+W_{2\alpha}^{r}e^{-p_2 y}\right)d^2\lambda \tag{E3.28}$$

where superscript t denotes transmitted electric Hertzian potential.

Total electric Hertzian potential in the substrate layer becomes

$$\Pi_{3\alpha}(r)=\Pi_{3\alpha}^{t}(r) \tag{E3.29}$$

which leads to

$$\Pi_{3\alpha}(r)=\frac{1}{(2\pi)^2}\iint_{\infty} W_{3\alpha}^{t}e^{j\lambda\bullet r}e^{p_3 y}d^2\lambda \tag{E3.30}$$

E.4 IMPLEMENTATION OF BOUNDARY CONDITIONS

Tangential boundary conditions at the $y=0$ interface become from Eqn. (E2.5),

$$\begin{aligned}
&\Pi_{1\alpha}(x,y,z)\Big|_{y=0^+}=N_{21}^2\Pi_{2\alpha}(x,y,z)\Big|_{y=0^-}\cdots(*)\\
&\left.\frac{\partial\Pi_{1\alpha}(x,y,z)}{\partial y}\right|_{y=0^+}=N_{21}^2\left.\frac{\partial\Pi_{2\alpha}(x,y,z)}{\partial y}\right|_{y=0^-}\cdots(**)\\
&\textit{where}\\
&\alpha=x,z
\end{aligned} \tag{E4.1}$$

$(*)$ in Eqn. (E4.1) yields

$$\begin{aligned}
&\frac{1}{(2\pi)^2}\iint_{\infty} e^{j\lambda\bullet r}\left[\int_V \frac{P_\alpha(r')}{\varepsilon_1}\frac{e^{-j\lambda\bullet r'}e^{-p_1(\lambda)y'}}{2p_1(\lambda)}dV'+W_{1\alpha}^{r}(\lambda)\right]d^2\lambda\\
&=\frac{N_{21}^2}{(2\pi)^2}\iint_{\infty} e^{j\lambda\bullet r}\left[W_{2\alpha}^{t}(\lambda)+W_{2\alpha}^{r}(\lambda)\right]d^2\lambda
\end{aligned} \tag{E4.2}$$

which leads to

$$\iint_{\infty}\left[\int_V \frac{P_\alpha}{\varepsilon_1}\frac{e^{-j\lambda\bullet r'}e^{-p_1 y'}}{2p_1}dV' + W_{1\alpha}^r - N_{21}^2\left(W_{2\alpha}^t + W_{2\alpha}^r\right)\right]e^{j\lambda\bullet r}d^2\lambda = 0$$

Therefore, it is necessary that

$$-W_{1\alpha}^r(\lambda) + N_{21}^2\left[W_{2\alpha}^t(\lambda) + W_{2\alpha}^r(\lambda)\right] = V_\alpha(\lambda)$$

where (E4.3)

$$V_\alpha(\lambda) = \int_V \frac{P_\alpha(r')}{\varepsilon_1}\frac{e^{-j\lambda\bullet r'}e^{-p_1(\lambda)y'}}{2p_1(\lambda)}dV'$$

$(**)$ in Eqn. (E4.1) yields

$$\frac{1}{(2\pi)^2}\iint_{\infty} e^{j\lambda\bullet r}\left[\int_V \frac{P_\alpha(r')}{\varepsilon_1}\frac{e^{-j\lambda\bullet r'}e^{-p_1(\lambda)y'}}{2}dV' - p_1(\lambda)W_{1\alpha}^r(\lambda)\right]d^2\lambda$$
$$= \frac{N_{21}^2}{(2\pi)^2}\iint_{\infty} e^{j\lambda\bullet r}\left[W_{2\alpha}^t(\lambda) - W_{2\alpha}^r(\lambda)\right]p_2(\lambda)d^2\lambda \quad \text{(E4.4)}$$

which leads to

$$\iint_{\infty}\left[\int_V \frac{P_\alpha}{\varepsilon_1}\frac{e^{-j\lambda\bullet r'}e^{-p_1 y'}}{2p_1}dV' - W_{1\alpha}^r - \frac{N_{21}^2 p_2}{p_1}\left(W_{2\alpha}^t - W_{2\alpha}^r\right)\right]p_1 e^{j\lambda\bullet r}d^2\lambda = 0$$

Therefore, it is again necessary that

$$W_{1\alpha}^r(\lambda) + \frac{N_{21}^2 p_2(\lambda)}{p_1(\lambda)}\left[W_{2\alpha}^t(\lambda) - W_{2\alpha}^r(\lambda)\right] = V_\alpha(\lambda)$$

where (E4.5)

$$V_\alpha(\lambda) = \int_V \frac{P_\alpha(r')}{\varepsilon_1}\frac{e^{-j\lambda\bullet r'}e^{-p_1(\lambda)y'}}{2p_1(\lambda)}dV'$$

Then, exploiting Eqn. (E4.3) and Eqn. (E4.5), after some manipulation, the reflected and transmitted coefficients are

$$W_{1\alpha}^{r}(\lambda)=R_{21}^{t}(\lambda)V_{\alpha}(\lambda)+T_{21}^{t}(\lambda)W_{2\alpha}^{r}(\lambda)$$

$$W_{2\alpha}^{t}(\lambda)=T_{12}^{t}(\lambda)V_{\alpha}(\lambda)+R_{12}^{t}(\lambda)W_{2\alpha}^{r}(\lambda)$$

where

$$R_{21}^{t}(\lambda)=\frac{p_1(\lambda)-p_2(\lambda)}{p_1(\lambda)+p_2(\lambda)}$$

$$R_{12}^{t}(\lambda)=\frac{p_2(\lambda)-p_1(\lambda)}{p_2(\lambda)+p_1(\lambda)}$$

$$T_{21}^{t}(\lambda)=\frac{2N_{21}^{2}p_2(\lambda)}{p_1(\lambda)+p_2(\lambda)}$$

$$T_{12}^{t}(\lambda)=\frac{2p_1(\lambda)}{N_{21}^{2}\left[p_1(\lambda)+p_2(\lambda)\right]}$$

Tangential boundary conditions at the $y=-t$ interface become from Eqn. (E2.6),

$$\Pi_{2\alpha}(x,y,z)\Big|_{y=-t^{+}}=N_{32}^{2}\Pi_{3\alpha}(x,y,z)\Big|_{y=-t^{-}}\cdots(*)$$

$$\frac{\partial\Pi_{2\alpha}(x,y,z)}{\partial y}\Big|_{y=-t^{+}}=N_{32}^{2}\frac{\partial\Pi_{3\alpha}(x,y,z)}{\partial y}\Big|_{y=-t^{-}}\cdots(**) \qquad \text{(E4.6)}$$

where

$\alpha=x,z$

$(*)$ in Eqn. (E4.6) yields

$$\frac{1}{(2\pi)^2}\iint_{\infty}e^{j\lambda\cdot r}\left[W_{2\alpha}^{t}(\lambda)e^{-p_2(\lambda)t}+W_{2\alpha}^{r}(\lambda)e^{p_2(\lambda)t}\right]d^2\lambda$$

$$=\frac{N_{32}^{2}}{(2\pi)^2}\iint_{\infty}W_{3\alpha}^{t}(\lambda)e^{j\lambda\cdot r}e^{-p_3(\lambda)t}d^2\lambda \qquad \text{(E4.7)}$$

which leads to

$$\iint_{\infty}\left(W_{2\alpha}^{t}e^{-p_2t}+W_{2\alpha}^{r}e^{p_2t}-N_{32}^{2}W_{3\alpha}^{t}e^{-p_3t}\right)e^{j\lambda\cdot r}d^2\lambda=0$$

Therefore, it is required that

$$W_{2\alpha}^{t}e^{-p_2 t}+W_{2\alpha}^{r}e^{p_2 t}-N_{32}^{2}W_{3\alpha}^{t}e^{-p_3 t}=0 \tag{E4.8}$$

$(**)$ in Eqn. (E4.6) yields

$$\begin{aligned}&\frac{1}{(2\pi)^2}\iint_{\infty} e^{j\lambda\bullet r}\left[W_{2\alpha}^{t}(\lambda)e^{-p_2(\lambda)t}-W_{2\alpha}^{r}(\lambda)e^{p_2(\lambda)t}\right]p_2(\lambda)d^2\lambda\\&=\frac{N_{32}^{2}}{(2\pi)^2}\iint_{\infty} p_3(\lambda)W_{3\alpha}^{t}(\lambda)e^{j\lambda\bullet r}e^{-p_3(\lambda)t}d^2\lambda\end{aligned} \tag{E4.9}$$

which leads to

$$\iint_{\infty}\left(W_{2\alpha}^{t}e^{-p_2 t}-W_{2\alpha}^{r}e^{p_2 t}-\frac{N_{32}^{2}p_3}{p_2}W_{3\alpha}^{t}e^{-p_3 t}\right)p_2 e^{j\lambda\bullet r}d^2\lambda=0$$

Therefore, it is again required that

$$W_{2\alpha}^{t}e^{-p_2 t}-W_{2\alpha}^{r}e^{p_2 t}-\frac{N_{32}^{2}p_3}{p_2}W_{3\alpha}^{t}e^{-p_3 t}=0 \tag{E4.10}$$

Exploiting Eqn. (E4.8) and Eqn. (E4.10), after some manipulation

$$\begin{aligned}&W_{2\alpha}^{r}(\lambda)=R_{32}^{t}(\lambda)e^{-2p_2(\lambda)t}W_{2\alpha}^{t}(\lambda)\\&W_{3\alpha}^{t}(\lambda)=T_{23}^{t}(\lambda)e^{\left[p_3(\lambda)-p_2(\lambda)\right]t}W_{2\alpha}^{t}(\lambda)\\&\textit{where}\\&R_{32}^{t}(\lambda)=\frac{p_2(\lambda)-p_3(\lambda)}{p_2(\lambda)+p_3(\lambda)}\\&T_{23}^{t}(\lambda)=\frac{2p_2(\lambda)}{N_{32}^{2}\left[p_2(\lambda)+p_3(\lambda)\right]}\end{aligned}$$

From the tangential boundary conditions at the $y=0$ interface, it was previously noted that $W_{2\alpha}^{t}(\lambda)=T_{12}^{t}(\lambda)V_{\alpha}(\lambda)+R_{12}^{t}(\lambda)W_{2\alpha}^{r}(\lambda)$. Then, it is concluded that

$$W_{2\alpha}^{t}(\lambda)=T_{12}^{t}(\lambda)V_{\alpha}(\lambda)+R_{12}^{t}(\lambda)R_{32}^{t}(\lambda)e^{-2p_2(\lambda)t}W_{2\alpha}^{t}(\lambda)$$

Finally, for tangential boundary conditions

$$W_{1\alpha}^{r}(\lambda)=\left[R_{21}^{t}(\lambda)+\frac{T_{21}^{t}(\lambda)T_{12}^{t}(\lambda)R_{32}^{t}(\lambda)e^{-2p_2(\lambda)t}}{1-R_{12}^{t}(\lambda)R_{32}^{t}(\lambda)e^{-2p_2(\lambda)t}}\right]V_{\alpha}(\lambda)$$

$$W_{2\alpha}^{t}(\lambda)=\frac{T_{12}^{t}(\lambda)}{1-R_{12}^{t}(\lambda)R_{32}^{t}(\lambda)e^{-2p_2(\lambda)t}}V_{\alpha}(\lambda)$$

$$W_{2\alpha}^{r}(\lambda)=\frac{T_{12}^{t}(\lambda)R_{32}^{t}(\lambda)e^{-2p_2(\lambda)t}}{1-R_{12}^{t}(\lambda)R_{32}^{t}(\lambda)e^{-2p_2(\lambda)t}}V_{\alpha}(\lambda) \qquad \text{(E4.11)}$$

$$W_{3\alpha}^{t}(\lambda)=\frac{T_{12}^{t}(\lambda)T_{23}^{t}(\lambda)e^{\left[p_3(\lambda)-p_2(\lambda)\right]t}}{1-R_{12}^{t}(\lambda)R_{32}^{t}(\lambda)e^{-2p_2(\lambda)t}}V_{\alpha}(\lambda)$$

where

$\alpha = x, z$

Normal boundary conditions at the $y=0$ interface become from Eqn. (E2.5),

$$\Pi_{1y}(x,y,z)\Big|_{y=0^+}=N_{21}^{2}\Pi_{2y}(x,y,z)\Big|_{y=0^-}\cdots(*)$$

$$\left[\frac{\partial\Pi_{1y}(x,y,z)}{\partial y}-\frac{\partial\Pi_{2y}(x,y,z)}{\partial y}\right]\Bigg|_{y=0} \qquad \text{(E4.12)}$$

$$=-\left(N_{21}^{2}-1\right)\left[\frac{\partial\Pi_{2x}(x,y,z)}{\partial x}+\frac{\partial\Pi_{2z}(x,y,z)}{\partial z}\right]\Bigg|_{y=0}\cdots(**)$$

$(*)$ in Eqn. (E4.12) yields

$$\frac{1}{(2\pi)^2}\iint_{\infty}e^{j\lambda\cdot r}\left[\int_{V}\frac{P_y(r')}{\varepsilon_1}\frac{e^{-j\lambda\cdot r'}e^{-p_1(\lambda)y'}}{2p_1(\lambda)}dV'+W_{1y}^{r}(\lambda)\right]d^2\lambda \qquad \text{(E4.13)}$$

$$=\frac{N_{21}^{2}}{(2\pi)^2}\iint_{\infty}e^{j\lambda\cdot r}\left[W_{2y}^{t}(\lambda)+W_{2y}^{r}(\lambda)\right]d^2\lambda$$

which leads to

$$\iint_{\infty}\left[\int_V \frac{P_y}{\varepsilon_1}\frac{e^{-j\lambda\bullet r'}e^{-p_1 y'}}{2p_1}dV' + W_{1y}^r - N_{21}^2\left(W_{2y}^t + W_{2y}^r\right)\right]e^{j\lambda\bullet r}d^2\lambda = 0$$

Therefore, it is necessary that

$$-W_{1y}^r(\lambda) + N_{21}^2\left[W_{2y}^t(\lambda) + W_{2y}^r(\lambda)\right] = V_y(\lambda)$$

where (E4.14)

$$V_y(\lambda) = \int_V \frac{P_y(r')}{\varepsilon_1}\frac{e^{-j\lambda\bullet r'}e^{-p_1(\lambda)y'}}{2p_1(\lambda)}dV'$$

$(**)$ in Eqn. (E4.12) yields

$$\begin{aligned}
&\frac{1}{(2\pi)^2}\iint_{\infty} e^{j\lambda\bullet r}\left[\int_V \frac{P_y(r')}{\varepsilon_1}\frac{e^{-j\lambda\bullet r'}e^{-p_1(\lambda)y'}}{2}dV' - p_1(\lambda)W_{1y}^r(\lambda)\right]d^2\lambda \\
&-\frac{1}{(2\pi)^2}\iint_{\infty} e^{j\lambda\bullet r}\left[W_{2y}^t(\lambda) - W_{2y}^r(\lambda)\right]p_2(\lambda)d^2\lambda \\
&= -\left(N_{21}^2 - 1\right)\left\{\frac{1}{(2\pi)^2}\iint_{\infty} j\xi\left[W_{2x}^t(\lambda) + W_{2x}^r(\lambda)\right]e^{j\lambda\bullet r}d^2\lambda\right. \\
&\left.+\frac{1}{(2\pi)^2}\iint_{\infty} j\zeta\left[W_{2z}^t(\lambda) + W_{2z}^r(\lambda)\right]e^{j\lambda\bullet r}d^2\lambda\right\}
\end{aligned} \tag{E4.15}$$

which leads to

$$\begin{aligned}
&\iint_{\infty}\left(\int_V \frac{P_y(r')}{\varepsilon_1}\frac{e^{-j\lambda\bullet r'}e^{-p_1(\lambda)y'}}{2p_1(\lambda)}dV' - W_{1y}^r(\lambda) - \frac{p_2(\lambda)}{p_1(\lambda)}\left[W_{2y}^t(\lambda) - W_{2y}^r(\lambda)\right] + \left(N_{21}^2 - 1\right)\right. \\
&\left.\left\{\frac{j\xi}{p_1(\lambda)}\left[W_{2x}^t(\lambda) + W_{2x}^r(\lambda)\right] + \frac{j\zeta}{p_1(\lambda)}\left[W_{2z}^t(\lambda) + W_{2z}^r(\lambda)\right]\right\}\right)p_1(\lambda)e^{j\lambda\bullet r}d^2\lambda = 0
\end{aligned}$$

Therefore, it is again necessary that

$$W_{1y}^r + \frac{p_2}{p_1}\left(W_{2y}^t - W_{2y}^r\right) = V_y + \frac{\left(N_{21}^2 - 1\right)}{p_1}\left[j\xi\left(W_{2x}^t + W_{2x}^r\right) + j\zeta\left(W_{2z}^t + W_{2z}^r\right)\right] \quad \text{(E4.16)}$$

Exploiting Eqn. (E4.11),

$$W_{2\alpha}^t(\lambda) + W_{2\alpha}^r(\lambda) = \frac{T_{12}^t(\lambda)\left[1 + R_{32}^t(\lambda)e^{-2p_2(\lambda)t}\right]}{1 - R_{12}^t(\lambda)R_{32}^t(\lambda)e^{-2p_2(\lambda)t}} V_\alpha(\lambda)$$

and defining

$$F(\lambda) = \frac{\left(N_{21}^2 - 1\right)}{p_1(\lambda)}\left[W_{2\alpha}^t(\lambda) + W_{2\alpha}^r(\lambda)\right]V_\alpha^{-1}(\lambda)$$

yields

$$W_{1y}^r + \frac{p_2}{p_1}\left(W_{2y}^t - W_{2y}^r\right) = V_y + F(\lambda)\left(j\xi V_x + j\zeta V_z\right) \quad \text{(E4.17)}$$

Again, solve for $W_{1y}^r(\lambda)$ and $W_{2y}^t(\lambda)$ in terms of $W_{2y}^r(\lambda)$ and $V_\alpha(\lambda)$. Exploiting again Eqn. (E4.14) and Eqn. (E4.17), after some manipulation

$$\left(N_{21}^2 + \frac{p_2}{p_1}\right)W_{2y}^t + \left(N_{21}^2 - \frac{p_2}{p_1}\right)W_{2y}^r = 2V_y + F(\lambda)\left(j\xi V_x + j\zeta V_z\right)$$

$$\therefore W_{2y}^t = -\frac{N_{21}^2 p_1 - p_2}{N_{21}^2 p_1 + p_2} W_{2y}^r + \frac{2p_1}{N_{21}^2 p_1 + p_2} V_y + \frac{p_1 F(\lambda)}{N_{21}^2 p_1 + p_2}\left(j\xi V_x + j\zeta V_z\right)$$

Exploiting Eqn. (E4.14),

$$-W_{1y}^r + N_{21}^2\left(W_{2y}^t + W_{2y}^r\right) = V_y$$

$$\therefore W_{1y}^r = \frac{N_{21}^2 p_1 - p_2}{N_{21}^2 p_1 + p_2} V_y + \frac{2N_{21}^2 p_2}{N_{21}^2 p_1 + p_2} W_{2y}^r + \frac{N_{21}^2 p_1 F(\lambda)}{N_{21}^2 p_1 + p_2}\left(j\xi V_x + j\zeta V_z\right)$$

Then,

$$W_{1y}^{r}(\lambda)=R_{21}^{n}(\lambda)V_y(\lambda)+T_{21}^{n}(\lambda)W_{2y}^{r}(\lambda)+C_1(\lambda)\left[j\xi V_x(\lambda)+j\zeta V_z(\lambda)\right]$$

$$W_{2y}^{t}(\lambda)=T_{12}^{n}(\lambda)V_y(\lambda)-R_{21}^{n}(\lambda)W_{2y}^{r}(\lambda)+N_{21}^{-2}C_1(\lambda)\left[j\xi V_x(\lambda)+j\zeta V_z(\lambda)\right]$$

where

$$R_{21}^{n}(\lambda)=\frac{N_{21}^2p_1(\lambda)-p_2(\lambda)}{N_{21}^2p_1(\lambda)+p_2(\lambda)}$$

$$T_{21}^{n}(\lambda)=\frac{2N_{21}^2p_2(\lambda)}{N_{21}^2p_1(\lambda)+p_2(\lambda)}=\frac{2p_2(\lambda)}{N_{12}^2p_2(\lambda)+p_1(\lambda)}$$

$$T_{12}^{n}(\lambda)=\frac{2p_1(\lambda)}{N_{21}^2p_1(\lambda)+p_2(\lambda)}$$

$$C_1(\lambda)=\frac{N_{21}^2p_1(\lambda)F(\lambda)}{N_{21}^2p_1(\lambda)+p_2(\lambda)}=\frac{N_{21}^2\left(N_{21}^2-1\right)T_{12}^{t}(\lambda)}{N_{21}^2p_1(\lambda)+p_2(\lambda)}\frac{1+R_{32}^{t}(\lambda)e^{-2p_2(\lambda)t}}{1-R_{12}^{t}(\lambda)R_{32}^{t}(\lambda)e^{-2p_2(\lambda)t}}$$

Normal boundary conditions at the $y=-t$ interface become from Eqn. (E2.6),

$$\Pi_{2y}(x,y,z)\Big|_{y=0^+}=N_{32}^2\Pi_{3y}(x,y,z)\Big|_{y=0^-}\cdots(*)$$

$$\left[\frac{\partial\Pi_{2y}(x,y,z)}{\partial y}-\frac{\partial\Pi_{3y}(x,y,z)}{\partial y}\right]\Bigg|_{y=0} \tag{E4.18}$$

$$=-\left(N_{32}^2-1\right)\left[\frac{\partial\Pi_{3x}(x,y,z)}{\partial x}+\frac{\partial\Pi_{3z}(x,y,z)}{\partial z}\right]\Bigg|_{y=0}\cdots(**)$$

$(*)$ in Eqn. (E4.18) yields

$$\frac{1}{(2\pi)^2}\iint_{\infty}e^{j\lambda\cdot r}\left(W_{2y}^{t}e^{-p_2t}+W_{2y}^{r}e^{p_2t}\right)d^2\lambda=\frac{N_{32}^2}{(2\pi)^2}\iint_{\infty}W_{3y}^{t}e^{j\lambda\cdot r}e^{-p_3t}d^2\lambda \tag{E4.19}$$

which leads to

$$\iint_{\infty}\left(W_{2y}^{t}e^{-p_2t}+W_{2y}^{r}e^{p_2t}-N_{32}^2W_{3y}^{t}e^{-p_3t}\right)e^{j\lambda\cdot r}d^2\lambda=0$$

Therefore, it is necessary that

$$W_{2y}^{t}e^{-p_2 t}+W_{2y}^{r}e^{p_2 t}-N_{32}^{2}W_{3y}^{t}e^{-p_3 t}=0 \tag{E4.20}$$

So, $(**)$ in Eqn. (E4.18) yields

$$\begin{aligned}
&\frac{1}{(2\pi)^2}\iint_{\infty} e^{j\lambda\cdot r}\left[W_{2y}^{t}(\lambda)e^{-p_2(\lambda)t}-W_{2y}^{r}(\lambda)e^{p_2(\lambda)t}\right]p_2(\lambda)d^2\lambda \\
&-\frac{1}{(2\pi)^2}\iint_{\infty} W_{3y}^{t}(\lambda)e^{j\lambda\cdot r}e^{-p_3(\lambda)t}p_3(\lambda)d^2\lambda \\
&=-\left(N_{32}^{2}-1\right)\left\{\frac{1}{(2\pi)^2}\iint_{\infty} j\xi W_{3x}^{t}(\lambda)e^{j\lambda\cdot r}e^{-p_3(\lambda)t}d^2\lambda\right. \\
&\left.+\frac{1}{(2\pi)^2}\iint_{\infty} j\zeta W_{3z}^{t}(\lambda)e^{j\lambda\cdot r}e^{-p_3(\lambda)t}d^2\lambda\right\}
\end{aligned} \tag{E4.21}$$

which leads to

$$\begin{aligned}
&\iint_{\infty}\left\{W_{2y}^{t}(\lambda)e^{-p_2(\lambda)t}-W_{2y}^{r}(\lambda)e^{p_2(\lambda)t}-\frac{p_3(\lambda)}{p_2(\lambda)}W_{3y}^{t}(\lambda)e^{-p_3(\lambda)t}+\left(N_{32}^{2}-1\right)\right. \\
&\left.\left[\frac{j\xi}{p_2(\lambda)}W_{3x}^{t}(\lambda)e^{-p_3(\lambda)t}+\frac{j\zeta}{p_2(\lambda)}W_{3z}^{t}(\lambda)e^{-p_3(\lambda)t}\right]\right\}p_2(\lambda)e^{j\lambda\cdot r}d^2\lambda=0
\end{aligned}$$

Therefore, it is again necessary that

$$W_{2y}^{t}e^{-p_2 t}-W_{2y}^{r}e^{p_2 t}-\frac{p_3}{p_2}W_{3y}^{t}e^{-p_3 t}=-\frac{\left(N_{32}^{2}-1\right)}{p_2}\left(j\xi W_{3x}^{t}+j\zeta W_{3z}^{t}\right)e^{-p_3 t} \tag{E4.22}$$

Exploiting Eqn. (E4.11),

$$W_{3\alpha}^{t}(\lambda)=\frac{T_{12}^{t}(\lambda)T_{23}^{t}(\lambda)e^{\left[p_3(\lambda)-p_2(\lambda)\right]t}}{1-R_{12}^{t}(\lambda)R_{32}^{t}(\lambda)e^{-2p_2(\lambda)t}}V_{\alpha}(\lambda)$$

and defining

$$G(\lambda)=\frac{\left(N_{32}^2-1\right)}{p_2(\lambda)}e^{-p_3(\lambda)t}W_{3\alpha}^t(\lambda)V_\alpha^{-1}(\lambda)$$

yields

$$W_{2y}^t e^{-p_2 t}-W_{2y}^r e^{p_2 t}-\frac{p_3}{p_2}W_{3y}^t e^{-p_3 t}=-G(\lambda)(j\xi V_x+j\zeta V_z) \quad \text{(E4.23)}$$

Exploiting Eqn. (E4.20) and Eqn. (E4.23), after some manipulation

$$\left(N_{32}^2+\frac{p_3}{p_2}\right)W_{3y}^t e^{-p_3 t}=2W_{2y}^t e^{-p_2 t}+G(\lambda)(j\xi V_x+j\zeta V_z)$$

$$\therefore W_{3y}^t=\frac{2p_2}{N_{32}^2p_2+p_3}e^{(p_3-p_2)t}W_{2y}^t+\frac{p_2G(\lambda)}{N_{32}^2p_2+p_3}e^{p_3 t}(j\xi V_x+j\zeta V_z)$$

Using Eqn. (E4.20),

$$W_{2y}^r=\frac{N_{32}^2p_2-p_3}{N_{32}^2p_2+p_3}e^{-2p_2 t}W_{2y}^t+C_2(\lambda)(j\xi V_x+j\zeta V_z)e^{-2p_2 t}$$

Then, finally

$$W_{2y}^r(\lambda)=\left\{R_{32}^n(\lambda)W_{2y}^t(\lambda)+C_2(\lambda)\left[j\xi V_x(\lambda)+j\zeta V_z(\lambda)\right]\right\}e^{-2p_2(\lambda)t}$$

$$W_{3y}^t(\lambda)=\left\{T_{23}^n(\lambda)W_{2y}^t(\lambda)+N_{32}^{-2}C_2(\lambda)\left[j\xi V_x(\lambda)+j\zeta V_z(\lambda)\right]\right\}e^{\left[p_3(\lambda)-p_2(\lambda)\right]t}$$

where

$$R_{32}^n(\lambda)=\frac{N_{32}^2p_2(\lambda)-p_3(\lambda)}{N_{32}^2p_2(\lambda)+p_3(\lambda)}$$

$$T_{23}^n(\lambda)=\frac{2p_2(\lambda)}{N_{32}^2p_2(\lambda)+p_3(\lambda)}$$

$$C_2(\lambda)=\frac{N_{32}^2p_2(\lambda)G(\lambda)e^{p_2(\lambda)t}}{N_{32}^2p_2(\lambda)+p_3(\lambda)}=\frac{N_{32}^2\left(N_{32}^2-1\right)}{N_{32}^2p_2(\lambda)+p_3(\lambda)}\frac{T_{12}^t(\lambda)T_{23}^t(\lambda)}{1-R_{12}^t(\lambda)R_{32}^t(\lambda)e^{-2p_2(\lambda)t}}$$

From normal boundary conditions at $y=0$ and $y=-t$ interfaces, it is observed that

$$W_{2y}^{t}(\lambda)=T_{12}^{n}(\lambda)V_{y}(\lambda)-R_{21}^{n}(\lambda)W_{2y}^{r}(\lambda)+N_{21}^{-2}C_{1}(\lambda)\left[j\xi V_{x}(\lambda)+j\zeta V_{z}(\lambda)\right]$$

$$W_{2y}^{r}(\lambda)=\left\{R_{32}^{n}(\lambda)W_{2y}^{t}(\lambda)+C_{2}(\lambda)\left[j\xi V_{x}(\lambda)+j\zeta V_{z}(\lambda)\right]\right\}e^{-2p_{2}(\lambda)t}$$

which leads to

$$W_{2y}^{r}=\left[R_{32}^{n}T_{12}^{n}V_{y}-R_{32}^{n}R_{21}^{n}W_{2y}^{r}+R_{32}^{n}N_{21}^{-2}C_{1}(\lambda)(j\xi V_{x}+j\zeta V_{z})+C_{2}(\lambda)(j\xi V_{x}+j\zeta V_{z})\right]$$
$$e^{-2p_{2}t}$$

Finally, for normal boundary conditions

$$W_{1y}^{r}=\left(R_{21}^{n}+\frac{T_{12}^{n}R_{32}^{n}T_{21}^{n}e^{-2p_{2}t}}{1+R_{21}^{n}R_{32}^{n}e^{-2p_{2}t}}\right)V_{y}+\left[C_{1}+\frac{T_{21}^{n}\left(R_{32}^{n}N_{21}^{-2}C_{1}+C_{2}\right)e^{-2p_{2}t}}{1+R_{21}^{n}R_{32}^{n}e^{-2p_{2}t}}\right]$$
$$(j\xi V_{x}+j\zeta V_{z})$$

$$W_{2y}^{t}=\frac{T_{12}^{n}}{1+R_{21}^{n}R_{32}^{n}e^{-2p_{2}t}}V_{y}+\left(\frac{N_{21}^{-2}C_{1}-R_{21}^{n}C_{2}e^{-2p_{2}t}}{1+R_{21}^{n}R_{32}^{n}e^{-2p_{2}t}}\right)(j\xi V_{x}+j\zeta V_{z})$$

$$W_{2y}^{r}=\frac{T_{12}^{n}R_{32}^{n}e^{-2p_{2}t}}{1+R_{21}^{n}R_{32}^{n}e^{-2p_{2}t}}V_{y}+\frac{\left(R_{32}^{n}N_{21}^{-2}C_{1}+C_{2}\right)e^{-2p_{2}t}}{1+R_{21}^{n}R_{32}^{n}e^{-2p_{2}t}}(j\xi V_{x}+j\zeta V_{z})$$

$$W_{3y}^{t}=\left\{\frac{T_{12}^{n}T_{23}^{n}}{1+R_{21}^{n}R_{32}^{n}e^{-2p_{2}t}}V_{y}+\left[N_{32}^{-2}C_{2}+\frac{T_{23}^{n}\left(N_{21}^{-2}C_{1}-R_{21}^{n}C_{2}e^{-2p_{2}t}\right)}{1+R_{21}^{n}R_{32}^{n}e^{-2p_{2}t}}\right](j\xi V_{x}+j\zeta V_{z})\right\}$$
$$e^{(p_{3}-p_{2})t}$$

(E4.24)

As required by Eqn. (E3.25), total electric Hertzian potential in the cover layer is

$$\Pi_{1\alpha}(r)=\Pi_{1\alpha}^{p}(r)+\Pi_{1\alpha}^{r}(r)$$

$\Pi_{1\alpha}^{p}(r)$ is obtained from Eqn. (E3.23) and Eqn. (E3.24) and $\Pi_{1\alpha}^{r}(r)$ is obtained from

Eqn. (E3.2) such that

$$\Pi_{1\alpha}^{r}(r)=\frac{1}{(2\pi)^2}\iint_{\infty} W_{1\alpha}^{r}(\lambda)e^{j\lambda\bullet r}e^{-p_1(\lambda)y}d^2\lambda \tag{E4.25}$$

As required by Eqn. (E4.11) and Eqn. (E4.24),

$$W_{1\alpha}^{r}(\lambda)=R_{1t}(\lambda)V_{\alpha}(\lambda)\cdots\alpha=x,z$$

$$W_{1y}^{r}=R_{1n}(\lambda)V_y+C_{1r}(\lambda)\left[j\xi V_x(\lambda)+j\zeta V_z(\lambda)\right]$$

where

$$R_{1t}(\lambda)=R_{21}^{t}(\lambda)+\frac{T_{21}^{t}(\lambda)T_{12}^{t}(\lambda)R_{32}^{t}(\lambda)e^{-2p_2(\lambda)t}}{1-R_{12}^{t}(\lambda)R_{32}^{t}(\lambda)e^{-2p_2(\lambda)t}}$$

$$R_{1n}(\lambda)=R_{21}^{n}(\lambda)+\frac{T_{12}^{n}(\lambda)R_{32}^{n}(\lambda)T_{21}^{n}(\lambda)e^{-2p_2(\lambda)t}}{1+R_{21}^{n}(\lambda)R_{32}^{n}(\lambda)e^{-2p_2(\lambda)t}}$$

$$C_{1r}(\lambda)=C_1(\lambda)+\frac{T_{21}^{n}(\lambda)\left[R_{32}^{n}(\lambda)N_{21}^{-2}C_1(\lambda)+C_2(\lambda)\right]e^{-2p_2(\lambda)t}}{1+R_{21}^{n}(\lambda)R_{32}^{n}(\lambda)e^{-2p_2(\lambda)t}}$$

Then, it is concluded that

$$\Pi_{1\alpha}^{r}(r)$$

$$=\iint_{\infty} R_{1t}(\lambda)V_{\alpha}(\lambda)\frac{e^{j\lambda\bullet r}e^{-p_1(\lambda)y}}{(2\pi)^2}d^2\lambda$$

$$=\int_V dV'\frac{P_{\alpha}(r')}{\varepsilon_1}\iint_{\infty} R_{1t}(\lambda)\frac{e^{j\lambda\bullet(r-r')}e^{-p_1(\lambda)(y+y')}}{2(2\pi)^2 p_1(\lambda)}d^2\lambda$$

where

$\alpha=x,z$

and

$$\Pi_{1y}^{r}(r)=\iint_{\infty}\left\{R_{1n}(\lambda)V_y(\lambda)+C_{1r}(\lambda)\left[j\xi V_x(\lambda)+j\zeta V_z(\lambda)\right]\right\}\frac{e^{j\lambda\bullet r}e^{-p_1(\lambda)y}}{(2\pi)^2}d^2\lambda$$

will be rearranged as

$$\Pi_{1y}^{r}(r)=\int_V\left[\frac{P_x(r')}{\varepsilon_1}\iint_{\infty}C_{1r}(\lambda)\frac{\partial}{\partial x}\frac{e^{j\lambda\bullet(r-r')}e^{-p_1(\lambda)(y+y')}}{2(2\pi)^2 p_1(\lambda)}d^2\lambda\right.$$
$$+\frac{P_y(r')}{\varepsilon_1}\iint_{\infty}R_{1n}(\lambda)\frac{e^{j\lambda\bullet(r-r')}e^{-p_1(\lambda)(y+y')}}{2(2\pi)^2 p_1(\lambda)}d^2\lambda$$
$$\left.+\frac{P_z(r')}{\varepsilon_1}\iint_{\infty}C_{1r}(\lambda)\frac{\partial}{\partial z}\frac{e^{j\lambda\bullet(r-r')}e^{-p_1(\lambda)(y+y')}}{2(2\pi)^2 p_1(\lambda)}d^2\lambda\right]dV'$$

Therefore in dyadic notation,

$$\boldsymbol{\Pi}_1(r)=\int_V\bar{\boldsymbol{G}}_1(r|r')\bullet\frac{\boldsymbol{P}(r')}{\varepsilon_1}dV' \qquad \text{(E4.26)}$$

Green's dyads in the cover layer are represented by

$$\bar{\boldsymbol{G}}_1(r|r')=\bar{\boldsymbol{G}}_1^{p}(r|r')+\bar{\boldsymbol{G}}_1^{r}(r|r')$$
where
$$\bar{\boldsymbol{G}}_1^{p}(r|r')=\bar{\mathbf{I}}G_1^{p}(r|r') \qquad \text{(E4.27)}$$
$$\bar{\boldsymbol{G}}_1^{r}(r|r')$$
$$=(\hat{x}\hat{x}+\hat{z}\hat{z})G_{1t}^{r}(r|r')+\hat{y}\left[\frac{\partial G_{1c}^{r}(r|r')}{\partial x}\hat{x}+G_{1n}^{r}(r|r')\hat{y}+\frac{\partial G_{1c}^{r}(r|r')}{\partial z}\hat{z}\right]$$

The principal and reflected Green's dyads in the cover layer are,

$$G_1^{p}(r|r')=\iint_{\infty}\frac{e^{j\lambda\bullet(\mathbf{r}-\mathbf{r}')}e^{-p_1(\lambda)|y-y'|}}{2(2\pi)^2 p_1(\lambda)}d^2\lambda$$

$$\begin{bmatrix}G_{1t}^{r}(r|r')\\G_{1n}^{r}(r|r')\\G_{1c}^{r}(r|r')\end{bmatrix}=\iint_{\infty}\begin{bmatrix}R_{1t}(\lambda)\\R_{1n}(\lambda)\\C_{1r}(\lambda)\end{bmatrix}\frac{e^{j\lambda\bullet(\mathbf{r}-\mathbf{r}')}e^{-p_1(\lambda)(y+y')}}{2(2\pi)^2 p_1(\lambda)}d^2\lambda$$

As required by Eqn. (E3.27), total electric Hertzian potential in the film layer is

$$\Pi_{2\alpha}(r)=\Pi^{t}_{2\alpha}(r)+\Pi^{r}_{2\alpha}(r)$$

leading to

$$\Pi_{2\alpha}(r)=\frac{1}{(2\pi)^2}\iint_{\infty} e^{j\lambda\bullet r}\left(W^{t}_{2\alpha}e^{p_2 y}+W^{r}_{2\alpha}e^{-p_2 y}\right)d^2\lambda \qquad \text{(E4.28)}$$

Exploiting Eqn. (E4.11) and Eqn. (E4.24),

$$W^{t}_{2\alpha}(\lambda)=T_{2t}(\lambda)V_{\alpha}(\lambda)$$

$$W^{t}_{2y}(\lambda)=T_{2n}(\lambda)V_{y}(\lambda)+C_{2t}(\lambda)\left[j\xi V_{x}(\lambda)+j\zeta V_{z}(\lambda)\right]$$

$$W^{r}_{2\alpha}(\lambda)=R_{2t}(\lambda)V_{\alpha}(\lambda)$$

$$W^{r}_{2y}(\lambda)=R_{2n}(\lambda)V_{y}(\lambda)+C_{2r}(\lambda)\left[j\xi V_{x}(\lambda)+j\zeta V_{z}(\lambda)\right]$$

where

$$T_{2t}(\lambda)=\frac{T^{t}_{12}(\lambda)}{1-R^{t}_{12}(\lambda)R^{t}_{32}(\lambda)e^{-2p_2(\lambda)t}}$$

$$T_{2n}(\lambda)=\frac{T^{n}_{12}(\lambda)}{1+R^{n}_{21}(\lambda)R^{n}_{32}(\lambda)e^{-2p_2(\lambda)t}}$$

$$C_{2t}(\lambda)=\frac{N^{-2}_{21}C_1(\lambda)-R^{n}_{21}(\lambda)C_2(\lambda)e^{-2p_2(\lambda)t}}{1+R^{n}_{21}(\lambda)R^{n}_{32}(\lambda)e^{-2p_2(\lambda)t}}$$

$$R_{2t}(\lambda)=\frac{T^{t}_{12}(\lambda)R^{t}_{32}(\lambda)e^{-2p_2(\lambda)t}}{1-R^{t}_{12}(\lambda)R^{t}_{32}(\lambda)e^{-2p_2(\lambda)t}}$$

$$R_{2n}(\lambda)=\frac{T^{n}_{12}(\lambda)R^{n}_{32}(\lambda)e^{-2p_2(\lambda)t}}{1+R^{n}_{21}(\lambda)R^{n}_{32}(\lambda)e^{-2p_2(\lambda)t}}$$

$$C_{2r}(\lambda)=\frac{\left[R^{n}_{32}(\lambda)N^{-2}_{21}C_1(\lambda)+C_2(\lambda)\right]e^{-2p_2(\lambda)t}}{1+R^{n}_{21}(\lambda)R^{n}_{32}(\lambda)e^{-2p_2(\lambda)t}}$$

The transmitted film potential is

$$\Pi_{2\alpha}^{t}(r)$$

$$= \iint_{\infty} T_{2t}(\lambda) V_{\alpha}(\lambda) \frac{e^{j\lambda \bullet r} e^{p_2(\lambda) y}}{(2\pi)^2} d^2\lambda$$

$$= \int_V dV' \frac{P_{\alpha}(r')}{\varepsilon_1} \iint_{\infty} T_{2t}(\lambda) \frac{e^{j\lambda \bullet (r-r')} e^{\left[p_2(\lambda) y - p_1(\lambda) y'\right]}}{2(2\pi)^2 p_1(\lambda)} d^2\lambda$$

where

$\alpha = x, z$

$$\Pi_{2y}^{t}(\lambda) = \iint_{\infty} \left\{ T_{2n}(\lambda) V_y(\lambda) + C_{2t}(\lambda) \left[j\xi V_x(\lambda) + j\zeta V_z(\lambda) \right] \right\} \frac{e^{j\lambda \bullet r} e^{p_2(\lambda) y}}{(2\pi)^2} d^2\lambda$$

(the normal transmitted potential) will be rearranged as

$$\Pi_{2y}^{t}(\lambda) = \int_V \left[\frac{P_x(r')}{\varepsilon_1} \iint_{\infty} C_{2t}(\lambda) \frac{\partial}{\partial x} \frac{e^{j\lambda \bullet (r-r')} e^{\left[p_2(\lambda) y - p_1(\lambda) y'\right]}}{2(2\pi)^2 p_1(\lambda)} d^2\lambda \right.$$

$$+ \frac{P_y(r')}{\varepsilon_1} \iint_{\infty} T_{2n}(\lambda) \frac{e^{j\lambda \bullet (r-r')} e^{\left[p_2(\lambda) y - p_1(\lambda) y'\right]}}{2(2\pi)^2 p_1(\lambda)} d^2\lambda$$

$$\left. + \frac{P_z(r')}{\varepsilon_1} \iint_{\infty} C_{2t}(\lambda) \frac{\partial}{\partial z} \frac{e^{j\lambda \bullet (r-r')} e^{\left[p_2(\lambda) y - p_1(\lambda) y'\right]}}{2(2\pi)^2 p_1(\lambda)} d^2\lambda \right] dV'$$

Similarly, using Eqn. (E4.11) and Eqn. (E4.24),

$$\Pi_{2\alpha}^{r}(r)$$

$$= \iint_{\infty} R_{2t}(\lambda) V_{\alpha}(\lambda) \frac{e^{j\lambda \bullet r} e^{-p_2(\lambda) y}}{(2\pi)^2} d^2\lambda$$

$$= \int_V dV' \frac{P_{\alpha}(r')}{\varepsilon_1} \iint_{\infty} R_{2t}(\lambda) \frac{e^{j\lambda \bullet (r-r')} e^{-\left[p_2(\lambda) y + p_1(\lambda) y'\right]}}{2(2\pi)^2 p_1(\lambda)} d^2\lambda$$

where

$\alpha = x, z$

Similarly

$$\Pi_{2y}^{r}(\lambda)=\iint_{\infty}\left\{R_{2n}(\lambda)V_y(\lambda)+C_{2r}(\lambda)\left[j\xi V_x(\lambda)+j\zeta V_z(\lambda)\right]\right\}\frac{e^{j\lambda\bullet r}e^{-p_2(\lambda)y}}{(2\pi)^2}d^2\lambda$$

will be rearranged as

$$\Pi_{2y}^{r}(\lambda)=\int_V\left[\frac{P_x(r')}{\varepsilon_1}\iint_{\infty}C_{2r}(\lambda)\frac{\partial}{\partial x}\frac{e^{j\lambda\bullet(r-r')}e^{-\left[p_2(\lambda)y+p_1(\lambda)y'\right]}}{2(2\pi)^2p_1(\lambda)}d^2\lambda\right.$$
$$+\frac{P_y(r')}{\varepsilon_1}\iint_{\infty}R_{2n}(\lambda)\frac{e^{j\lambda\bullet(r-r')}e^{-\left[p_2(\lambda)y+p_1(\lambda)y'\right]}}{2(2\pi)^2p_1(\lambda)}d^2\lambda$$
$$\left.+\frac{P_z(r')}{\varepsilon_1}\iint_{\infty}C_{2r}(\lambda)\frac{\partial}{\partial z}\frac{e^{j\lambda\bullet(r-r')}e^{-\left[p_2(\lambda)y+p_1(\lambda)y'\right]}}{2(2\pi)^2p_1(\lambda)}d^2\lambda\right]dV'$$

Therefore in dyadic notation,

$$\boldsymbol{\Pi}_2(r)=\int_V\bar{\boldsymbol{G}}_2(r|r')\bullet\frac{\boldsymbol{P}(r')}{\varepsilon_1}dV' \qquad \text{(E4.29)}$$

Green's dyads in the film layer are represented by

$$\bar{\boldsymbol{G}}_2(r|r')=\bar{\boldsymbol{G}}_2^{t}(r|r')+\bar{\boldsymbol{G}}_2^{r}(r|r')$$

where

$$\bar{\boldsymbol{G}}_2^{t}(r|r')$$
$$=(\hat{x}\hat{x}+\hat{z}\hat{z})G_{2t}^{t}(r|r')+\hat{y}\left[\frac{\partial}{\partial x}G_{2c}^{t}(r|r')\hat{x}+G_{2n}^{t}(r|r')\hat{y}+\frac{\partial}{\partial z}G_{2c}^{t}(r|r')\hat{z}\right] \qquad \text{(E4.30)}$$

$$\bar{\boldsymbol{G}}_2^{r}(r|r')$$
$$=(\hat{x}\hat{x}+\hat{z}\hat{z})G_{2t}^{r}(r|r')+\hat{y}\left[\frac{\partial}{\partial x}G_{2c}^{r}(r|r')\hat{x}+G_{2n}^{r}(r|r')\hat{y}+\frac{\partial}{\partial z}G_{2c}^{r}(r|r')\hat{z}\right]$$

Again, similarly for the principal and reflected Green's dyads in the cover layer, for those transmitted and reflected in the film layer,

Similarly

$$\Pi_{2y}^{r}(\lambda)=\iint_{\infty}\left\{R_{2n}(\lambda)V_y(\lambda)+C_{2r}(\lambda)\left[j\xi V_x(\lambda)+j\zeta V_z(\lambda)\right]\right\}\frac{e^{j\lambda\bullet r}e^{-p_2(\lambda)y}}{(2\pi)^2}d^2\lambda$$

will be rearranged as

$$\Pi_{2y}^{r}(\lambda)=\int_V\left[\frac{P_x(r')}{\varepsilon_1}\iint_{\infty}C_{2r}(\lambda)\frac{\partial}{\partial x}\frac{e^{j\lambda\bullet(r-r')}e^{-\left[p_2(\lambda)y+p_1(\lambda)y'\right]}}{2(2\pi)^2p_1(\lambda)}d^2\lambda\right.$$
$$+\frac{P_y(r')}{\varepsilon_1}\iint_{\infty}R_{2n}(\lambda)\frac{e^{j\lambda\bullet(r-r')}e^{-\left[p_2(\lambda)y+p_1(\lambda)y'\right]}}{2(2\pi)^2p_1(\lambda)}d^2\lambda$$
$$\left.+\frac{P_z(r')}{\varepsilon_1}\iint_{\infty}C_{2r}(\lambda)\frac{\partial}{\partial z}\frac{e^{j\lambda\bullet(r-r')}e^{-\left[p_2(\lambda)y+p_1(\lambda)y'\right]}}{2(2\pi)^2p_1(\lambda)}d^2\lambda\right]dV'$$

Therefore in dyadic notation,

$$\boldsymbol{\Pi}_2(r)=\int_V\bar{\boldsymbol{G}}_2(r|r')\bullet\frac{\boldsymbol{P}(r')}{\varepsilon_1}dV' \qquad \text{(E4.29)}$$

Green's dyads in the film layer are represented by

$$\bar{G}_2(r|r')=\bar{G}_2^{t}(r|r')+\bar{G}_2^{r}(r|r')$$

where

$$\bar{G}_2^{t}(r|r')$$
$$=(\hat{x}\hat{x}+\hat{z}\hat{z})G_{2t}^{t}(r|r')+\hat{y}\left[\frac{\partial}{\partial x}G_{2c}^{t}(r|r')\hat{x}+G_{2n}^{t}(r|r')\hat{y}+\frac{\partial}{\partial z}G_{2c}^{t}(r|r')\hat{z}\right] \qquad \text{(E4.30)}$$

$$\bar{G}_2^{r}(r|r')$$
$$=(\hat{x}\hat{x}+\hat{z}\hat{z})G_{2t}^{r}(r|r')+\hat{y}\left[\frac{\partial}{\partial x}G_{2c}^{r}(r|r')\hat{x}+G_{2n}^{r}(r|r')\hat{y}+\frac{\partial}{\partial z}G_{2c}^{r}(r|r')\hat{z}\right]$$

Again, similarly for the principal and reflected Green's dyads in the cover layer, for those transmitted and reflected in the film layer,

$$\begin{bmatrix} G_{2t}^{t}(\vec{r}|\vec{r}') \\ G_{2n}^{t}(\vec{r}|\vec{r}') \\ G_{2c}^{t}(\vec{r}|\vec{r}') \end{bmatrix} = \iint_{-\infty} \begin{bmatrix} T_{2t}(\lambda) \\ T_{2n}(\lambda) \\ C_{2t}(\lambda) \end{bmatrix} \frac{e^{j\vec{\lambda}\bullet(\vec{r}-\vec{r}')} e^{[p_2(\lambda)y - p_1(\lambda)y']}}{2(2\pi)^2 p_1(\lambda)} d^2\lambda$$

$$\begin{bmatrix} G_{2t}^{r}(\vec{r}|\vec{r}') \\ G_{2n}^{r}(\vec{r}|\vec{r}') \\ G_{2c}^{r}(\vec{r}|\vec{r}') \end{bmatrix} = \iint_{-\infty} \begin{bmatrix} R_{2t}(\lambda) \\ R_{2n}(\lambda) \\ C_{2r}(\lambda) \end{bmatrix} \frac{e^{j\vec{\lambda}\bullet(\vec{r}-\vec{r}')} e^{-[p_2(\lambda)y + p_1(\lambda)y']}}{2(2\pi)^2 p_1(\lambda)} d^2\lambda$$

As given by Eqn. (E3.29), total electric Hertzian potential in the substrate layer is

$$\Pi_{3\alpha}(r) = \Pi_{3\alpha}^{t}(r)$$

which leads to

$$\Pi_{3\alpha}(r) = \frac{1}{(2\pi)^2} \iint_{\infty} W_{3\alpha}^{t}(\lambda) e^{j\lambda\bullet r} e^{p_3(\lambda)y} d^2\lambda \qquad \text{(E4.31)}$$

As required by Eqn. (E4.11) and Eqn. (E4.24),

$$W_{3\alpha}^{t}(\lambda) = T_{3t}(\lambda) V_{\alpha}(\lambda)$$

$$W_{3y}^{t}(\lambda) = \left\{ T_{3n}(\lambda) V_y(\lambda) + C_{3t}(\lambda) \left[j\xi V_x(\lambda) + j\zeta V_z(\lambda) \right] \right\} e^{[p_3(\lambda) - p_2(\lambda)]t}$$

where

$$T_{3t}(\lambda) = \frac{T_{12}^{t}(\lambda) T_{23}^{t}(\lambda) e^{[p_3(\lambda) - p_2(\lambda)]t}}{1 - R_{12}^{t}(\lambda) R_{32}^{t}(\lambda) e^{-2p_2(\lambda)t}}$$

$$T_{3n}(\lambda) = \frac{T_{12}^{n}(\lambda) T_{23}^{n}(\lambda)}{1 + R_{21}^{n}(\lambda) R_{32}^{n}(\lambda) e^{-2p_2(\lambda)t}}$$

$$C_{3t}(\lambda) = N_{32}^{-2} C_2(\lambda) + \frac{T_{23}^{n}(\lambda) \left[N_{21}^{-2} C_1(\lambda) - R_{21}^{n}(\lambda) C_2(\lambda) e^{-2p_2(\lambda)t} \right]}{1 + R_{21}^{n}(\lambda) R_{32}^{n}(\lambda) e^{-2p_2(\lambda)t}}$$

The substrate potential then becomes

$$\Pi_{3\alpha}^{t}(r)$$

$$= \iint_{\infty} T_{3t}(\lambda) V_{\alpha}(\lambda) \frac{e^{j\lambda\bullet r} e^{p_3(\lambda)y}}{(2\pi)^2} d^2\lambda$$

$$= \int_V dV' \frac{P_{\alpha}(r')}{\varepsilon_1} \iint_{\infty} T_{3t}(\lambda) \frac{e^{j\lambda\bullet(r-r')} e^{\left[p_3(\lambda)y - p_1(\lambda)y'\right]}}{2(2\pi)^2 p_1(\lambda)} d^2\lambda$$

where

$\alpha = x, z$

$$\Pi_{3y}^{t}(\lambda) = \iint_{\infty} \left\{ T_{3n}(\lambda) V_y(\lambda) + C_{3t}(\lambda)\left[j\xi V_x(\lambda) + j\zeta V_z(\lambda) \right] \right\} \frac{e^{j\lambda\bullet r} e^{p_3(\lambda)y}}{(2\pi)^2} d^2\lambda$$

will be similarly rearranged as

$$\Pi_{3y}^{t}(\lambda) = \int_V \left[\frac{P_x(r')}{\varepsilon_1} \iint_{\infty} C_{3t}(\lambda) \frac{\partial}{\partial x} \frac{e^{j\lambda\bullet(r-r')} e^{\left[p_3(\lambda)y - p_1(\lambda)y'\right]}}{2(2\pi)^2 p_1(\lambda)} d^2\lambda \right.$$

$$+ \frac{P_y(r')}{\varepsilon_1} \iint_{\infty} T_{3n}(\lambda) \frac{e^{j\lambda\bullet(r-r')} e^{\left[p_3(\lambda)y - p_1(\lambda)y'\right]}}{2(2\pi)^2 p_1(\lambda)} d^2\lambda$$

$$\left. + \frac{P_z(r')}{\varepsilon_1} \iint_{\infty} C_{3t}(\lambda) \frac{\partial}{\partial z} \frac{e^{j\lambda\bullet(r-r')} e^{\left[p_3(\lambda)y - p_1(\lambda)y'\right]}}{2(2\pi)^2 p_1(\lambda)} d^2\lambda \right] dV'$$

Therefore in dyadic notation,

$$\boldsymbol{\Pi}_3(\boldsymbol{r}) = \int_V \bar{\boldsymbol{G}}_3(\boldsymbol{r}|\boldsymbol{r}') \bullet \frac{\boldsymbol{P}(\boldsymbol{r}')}{\varepsilon_1} dV' \qquad \text{(E4.32)}$$

Green's dyads in the substrate layer are represented by

$$\bar{\boldsymbol{G}}_3(\boldsymbol{r}|\boldsymbol{r}')$$

$$= \bar{\boldsymbol{G}}_3^{t}(\boldsymbol{r}|\boldsymbol{r}') \qquad \text{(E4.33)}$$

$$= (\hat{x}\hat{x} + \hat{z}\hat{z}) G_{3t}^{t}(r|r') + \hat{y}\left[\frac{\partial}{\partial x} G_{3c}^{t}(r|r')\hat{x} + G_{3n}^{t}(r|r')\hat{y} + \frac{\partial}{\partial z} G_{3c}^{t}(r|r')\hat{z} \right]$$

For transmitted Green's dyads in the substrate layer are,

$$\begin{bmatrix} G_{3t}^{t}(\vec{r}|\vec{r}') \\ G_{3n}^{t}(\vec{r}|\vec{r}') \\ G_{3c}^{t}(\vec{r}|\vec{r}') \end{bmatrix} = \iint_{-\infty} \begin{bmatrix} T_{3t}(\lambda) \\ T_{3n}(\lambda) \\ C_{3t}(\lambda) \end{bmatrix} \frac{e^{j\vec{\lambda}\bullet(\vec{r}-\vec{r}')} e^{[p_3(\lambda)y - p_1(\lambda)y']}}{2(2\pi)^2 p_1(\lambda)} d^2\lambda$$

Consider a special case when the substrate layer is replaced by a perfect conductor, i.e, $\varepsilon_3 \to -j\infty$. For example,

$$R_{1t}(\lambda) = R_{21}^{t} + \frac{T_{21}^{t} T_{12}^{t} R_{32}^{t} e^{-2p_2 t}}{1 - R_{12}^{t} R_{32}^{t} e^{-2p_2 t}}$$

$$= \frac{p_1 - p_2}{p_1 + p_2} + \frac{\dfrac{2N_{21}^2 p_2}{p_1 + p_2} \dfrac{2p_1}{N_{21}^2(p_1 + p_2)} \dfrac{p_2 - p_3}{p_2 + p_3} e^{-2p_2 t}}{1 - \dfrac{p_2 - p_1}{p_2 + p_1} \dfrac{p_2 - p_3}{p_2 + p_3} e^{-2p_2 t}}$$

leads to

$$R_{1t}(\lambda) = \frac{p_1(\lambda) - p_2(\lambda)\coth[p_2(\lambda)t]}{p_1(\lambda) + p_2(\lambda)\coth[p_2(\lambda)t]}$$

Similarly for $p_3(\lambda) \to \infty$,

$$R_{1n}(\lambda) = \frac{N_{21}^2 p_1(\lambda) - p_2(\lambda)\tanh[p_2(\lambda)t]}{Z^e(\lambda)}$$

$$C_{1r}(\lambda) = \frac{2\left(N_{21}^2 - 1\right)p_1(\lambda)}{Z^h(\lambda)Z^e(\lambda)}$$

$$T_{2t}(\lambda) = \frac{N_{21}^{-2}}{Z^h(\lambda)} \frac{e^{p_2(\lambda)t}}{\sinh[p_2(\lambda)t]} p_1(\lambda)$$

$$T_{2n}(\lambda) = \frac{1}{Z^e(\lambda)} \frac{e^{p_2(\lambda)t}}{\cosh[p_2(\lambda)t]} p_1(\lambda)$$

$$C_{2t}(\lambda)=\frac{N_{21}^{-2}\left(N_{21}^{2}-1\right)}{Z^{h}(\lambda)Z^{e}(\lambda)}\frac{e^{p_2(\lambda)t}}{\cosh\left[p_2(\lambda)t\right]}p_1(\lambda)$$

$$R_{2t}(\lambda)=-\frac{N_{21}^{-2}}{Z^{h}(\lambda)}\frac{e^{-p_2(\lambda)t}}{\sinh\left[p_2(\lambda)t\right]}p_1(\lambda)$$

$$R_{2n}(\lambda)=\frac{1}{Z^{e}(\lambda)}\frac{e^{-p_2(\lambda)t}}{\cosh\left[p_2(\lambda)t\right]}p_1(\lambda)$$

$$C_{2r}(\lambda)=\frac{N_{21}^{-2}\left(N_{21}^{2}-1\right)}{Z^{h}(\lambda)Z^{e}(\lambda)}\frac{e^{-p_2(\lambda)t}}{\cosh\left[p_2(\lambda)t\right]}p_1(\lambda)$$

where

$$Z^{h}(\lambda)=p_1(\lambda)+p_2(\lambda)\coth\left[p_2(\lambda)t\right]$$

$$Z^{e}(\lambda)=N_{21}^{2}p_1(\lambda)+p_2(\lambda)\tanh\left[p_2(\lambda)t\right]$$

SUMMARY FOR THE SPECIAL CASE OF $\varepsilon_3 \to -j\infty$

$$\mathbf{\Pi}_l(r)=\int_V \bar{G}_l(r|r')\bullet\frac{\boldsymbol{P}(r')}{\varepsilon_1}dV'\cdots l=1,2$$

$$\bar{G}_1(r|r')=\bar{G}_1^{p}(r|r')+\bar{G}_1^{r}(r|r')$$

$$\bar{G}_2(r|r')=\bar{G}_2^{t}(r|r')+\bar{G}_2^{r}(r|r')$$

where

$$\bar{G}_1^{p}(r|r')=\bar{\mathbf{I}}G_1^{p}(r|r')$$

$$\bar{G}_1^{r}(r|r')$$

$$=(\hat{x}\hat{x}+\hat{z}\hat{z})G_{1t}^{r}(r|r')+\hat{y}\left[\frac{\partial G_{1c}^{r}(r|r')}{\partial x}\hat{x}+G_{1n}^{r}(r|r')\hat{y}+\frac{\partial G_{1c}^{r}(r|r')}{\partial z}\hat{z}\right]$$

$$\bar{G}_2^{t}(r|r')$$

$$=(\hat{x}\hat{x}+\hat{z}\hat{z})G_{2t}^{t}(r|r')+\hat{y}\left[\frac{\partial}{\partial x}G_{2c}^{t}(r|r')\hat{x}+G_{2n}^{t}(r|r')\hat{y}+\frac{\partial}{\partial z}G_{2c}^{t}(r|r')\hat{z}\right]$$

$$\bar{G}_2^r(r|r')$$

$$=(\hat{x}\hat{x}+\hat{z}\hat{z})G_{2t}^r(r|r')+\hat{y}\left[\frac{\partial}{\partial x}G_{2c}^r(r|r')\hat{x}+G_{2n}^r(r|r')\hat{y}+\frac{\partial}{\partial z}G_{2c}^r(r|r')\hat{z}\right]$$

Green's dyads in the cover and film layers are

$$G_1^p(r|r')=\iint_{\infty}\frac{e^{j\vec{\lambda}\bullet(\mathbf{r}-\mathbf{r}')}e^{-p_1(\lambda)|y-y'|}}{2(2\pi)^2 p_1(\lambda)}d^2\lambda$$

$$\begin{bmatrix}G_{1t}^r(r|r')\\G_{1n}^r(r|r')\\G_{1c}^r(r|r')\end{bmatrix}=\iint_{\infty}\begin{bmatrix}R_{1t}(\lambda)\\R_{1n}(\lambda)\\C_{1r}(\lambda)\end{bmatrix}\frac{e^{j\vec{\lambda}\bullet(\mathbf{r}-\mathbf{r}')}e^{-p_1(\lambda)(y+y')}}{2(2\pi)^2 p_1(\lambda)}d^2\lambda$$

$$\begin{bmatrix}G_{2t}^t(\vec{r}|\vec{r}')\\G_{2n}^t(\vec{r}|\vec{r}')\\G_{2c}^t(\vec{r}|\vec{r}')\end{bmatrix}=\iint_{\infty}\begin{bmatrix}T_{2t}(\lambda)\\T_{2n}(\lambda)\\C_{2t}(\lambda)\end{bmatrix}\frac{e^{j\vec{\lambda}\bullet(\vec{r}-\vec{r}')}e^{[p_2(\lambda)y-p_1(\lambda)y']}}{2(2\pi)^2 p_1(\lambda)}d^2\lambda$$

$$\begin{bmatrix}G_{2t}^r(\vec{r}|\vec{r}')\\G_{2n}^r(\vec{r}|\vec{r}')\\G_{2c}^r(\vec{r}|\vec{r}')\end{bmatrix}=\iint_{\infty}\begin{bmatrix}R_{2t}(\lambda)\\R_{2n}(\lambda)\\C_{2r}(\lambda)\end{bmatrix}\frac{e^{j\vec{\lambda}\bullet(\vec{r}-\vec{r}')}e^{-[p_2(\lambda)y+p_1(\lambda)y']}}{2(2\pi)^2 p_1(\lambda)}d^2\lambda$$

The coefficients for the *l'th* ($l=1, 2$ for the cover and the film layer respectively) layer are determined by

$$R_{1t}(\lambda)=\frac{p_1(\lambda)-p_2(\lambda)\coth[p_2(\lambda)t]}{Z^h(\lambda)}$$

$$R_{1n}(\lambda)=\frac{N_{21}^2 p_1(\lambda)-p_2(\lambda)\tanh[p_2(\lambda)t]}{Z^e(\lambda)}$$

$$C_{1r}(\lambda)=\frac{2(N_{21}^2-1)p_1(\lambda)}{Z^h(\lambda)Z^e(\lambda)}$$

$$C_{2t}(\lambda)=\frac{N_{21}^{-2}\left(N_{21}^{2}-1\right)}{Z^{h}(\lambda)Z^{e}(\lambda)}\frac{e^{p_2(\lambda)t}}{\cosh\left[p_2(\lambda)t\right]}p_1(\lambda)$$

$$R_{2t}(\lambda)=-\frac{N_{21}^{-2}}{Z^{h}(\lambda)}\frac{e^{-p_2(\lambda)t}}{\sinh\left[p_2(\lambda)t\right]}p_1(\lambda)$$

$$R_{2n}(\lambda)=\frac{1}{Z^{e}(\lambda)}\frac{e^{-p_2(\lambda)t}}{\cosh\left[p_2(\lambda)t\right]}p_1(\lambda)$$

$$C_{2r}(\lambda)=\frac{N_{21}^{-2}\left(N_{21}^{2}-1\right)}{Z^{h}(\lambda)Z^{e}(\lambda)}\frac{e^{-p_2(\lambda)t}}{\cosh\left[p_2(\lambda)t\right]}p_1(\lambda)$$

where

$$Z^{h}(\lambda)=p_1(\lambda)+p_2(\lambda)\coth\left[p_2(\lambda)t\right]$$

$$Z^{e}(\lambda)=N_{21}^{2}p_1(\lambda)+p_2(\lambda)\tanh\left[p_2(\lambda)t\right]$$

SUMMARY FOR THE SPECIAL CASE OF $\varepsilon_3 \to -j\infty$

$$\Pi_l(r)=\int_V \bar{G}_l(r|r')\bullet\frac{P(r')}{\varepsilon_1}dV'\cdots l=1,2$$

$$\bar{G}_1(r|r')=\bar{G}_1^{p}(r|r')+\bar{G}_1^{r}(r|r')$$

$$\bar{G}_2(r|r')=\bar{G}_2^{t}(r|r')+\bar{G}_2^{r}(r|r')$$

where

$$\bar{G}_1^{p}(r|r')=\bar{\mathbf{I}}G_1^{p}(r|r')$$

$$\bar{G}_1^{r}(r|r')$$

$$=(\hat{x}\hat{x}+\hat{z}\hat{z})G_{1t}^{r}(r|r')+\hat{y}\left[\frac{\partial G_{1c}^{r}(r|r')}{\partial x}\hat{x}+G_{1n}^{r}(r|r')\hat{y}+\frac{\partial G_{1c}^{r}(r|r')}{\partial z}\hat{z}\right]$$

$$\bar{G}_2^{t}(r|r')$$

$$=(\hat{x}\hat{x}+\hat{z}\hat{z})G_{2t}^{t}(r|r')+\hat{y}\left[\frac{\partial}{\partial x}G_{2c}^{t}(r|r')\hat{x}+G_{2n}^{t}(r|r')\hat{y}+\frac{\partial}{\partial z}G_{2c}^{t}(r|r')\hat{z}\right]$$

$$\bar{G}_2^r(r|r')$$

$$=(\hat{x}\hat{x}+\hat{z}\hat{z})G_{2t}^r(r|r')+\hat{y}\left[\frac{\partial}{\partial x}G_{2c}^r(r|r')\hat{x}+G_{2n}^r(r|r')\hat{y}+\frac{\partial}{\partial z}G_{2c}^r(r|r')\hat{z}\right]$$

Green's dyads in the cover and film layers are

$$G_1^p(r|r')=\iint_{\infty}\frac{e^{j\lambda\bullet(\mathbf{r}-\mathbf{r}')}e^{-p_1(\lambda)|y-y'|}}{2(2\pi)^2 p_1(\lambda)}d^2\lambda$$

$$\begin{bmatrix}G_{1t}^r(r|r')\\G_{1n}^r(r|r')\\G_{1c}^r(r|r')\end{bmatrix}=\iint_{\infty}\begin{bmatrix}R_{1t}(\lambda)\\R_{1n}(\lambda)\\C_{1r}(\lambda)\end{bmatrix}\frac{e^{j\lambda\bullet(\mathbf{r}-\mathbf{r}')}e^{-p_1(\lambda)(y+y')}}{2(2\pi)^2 p_1(\lambda)}d^2\lambda$$

$$\begin{bmatrix}G_{2t}^t(\vec{r}|\vec{r}')\\G_{2n}^t(\vec{r}|\vec{r}')\\G_{2c}^t(\vec{r}|\vec{r}')\end{bmatrix}=\iint_{\infty}\begin{bmatrix}T_{2t}(\lambda)\\T_{2n}(\lambda)\\C_{2t}(\lambda)\end{bmatrix}\frac{e^{j\vec{\lambda}\bullet(\vec{r}-\vec{r}')}e^{[p_2(\lambda)y-p_1(\lambda)y']}}{2(2\pi)^2 p_1(\lambda)}d^2\lambda$$

$$\begin{bmatrix}G_{2t}^r(\vec{r}|\vec{r}')\\G_{2n}^r(\vec{r}|\vec{r}')\\G_{2c}^r(\vec{r}|\vec{r}')\end{bmatrix}=\iint_{\infty}\begin{bmatrix}R_{2t}(\lambda)\\R_{2n}(\lambda)\\C_{2r}(\lambda)\end{bmatrix}\frac{e^{j\vec{\lambda}\bullet(\vec{r}-\vec{r}')}e^{-[p_2(\lambda)y+p_1(\lambda)y']}}{2(2\pi)^2 p_1(\lambda)}d^2\lambda$$

The coefficients for the *l'th* ($l=1, 2$ for the cover and the film layer respectively) layer are determined by

$$R_{1t}(\lambda)=\frac{p_1(\lambda)-p_2(\lambda)\coth[p_2(\lambda)t]}{Z^h(\lambda)}$$

$$R_{1n}(\lambda)=\frac{N_{21}^2 p_1(\lambda)-p_2(\lambda)\tanh[p_2(\lambda)t]}{Z^e(\lambda)}$$

$$C_{1r}(\lambda)=\frac{2(N_{21}^2-1)p_1(\lambda)}{Z^h(\lambda)Z^e(\lambda)}$$

$$T_{2t}(\lambda)=\frac{N_{21}^{-2}}{Z^h(\lambda)\sinh\left[p_2(\lambda)t\right]}\frac{e^{p_2(\lambda)t}}{}p_1(\lambda)$$

$$T_{2n}(\lambda)=\frac{1}{Z^e(\lambda)\cosh\left[p_2(\lambda)t\right]}\frac{e^{p_2(\lambda)t}}{}p_1(\lambda)$$

$$C_{2t}(\lambda)=\frac{N_{21}^{-2}\left(N_{21}^2-1\right)}{Z^h(\lambda)z^e(\lambda)\cosh\left[p_2(\lambda)t\right]}\frac{e^{p_2(\lambda)t}}{}p_1(\lambda)$$

$$R_{2t}(\lambda)=-\frac{N_{21}^{-2}}{Z^h(\lambda)\sinh\left[p_2(\lambda)t\right]}\frac{e^{-p_2(\lambda)t}}{}p_1(\lambda)$$

$$R_{2n}(\lambda)=\frac{1}{Z^e(\lambda)\cosh\left[p_2(\lambda)t\right]}\frac{e^{-p_2(\lambda)t}}{}p_1(\lambda)$$

$$C_{2r}(\lambda)=\frac{N_{21}^{-2}\left(N_{21}^2-1\right)}{Z^h(\lambda)Z^e(\lambda)\cosh\left[p_2(\lambda)t\right]}\frac{e^{-p_2(\lambda)t}}{}p_1(\lambda)$$

where

$$Z^h(\lambda)=p_1(\lambda)+p_2(\lambda)\coth\left[p_2(\lambda)t\right]$$

$$Z^e(\lambda)=N_{21}^2p_1(\lambda)+p_2(\lambda)\tanh\left[p_2(\lambda)t\right]$$

APPENDIX F

CUT-OFF CRITERION FOR THE SURFACE-WAVE OF AN OPEN INTEGRATED MICROSTRIP WAVEGUIDE

It is necessary to observe the cut-off criterion for the nth surface-wave mode. It is recognized that TE-odd and TM-even surface-waves are contributed by pole singularities associated with $Z^h(\xi,\zeta)=0$ and $Z^e(\xi,\zeta)=0$ respectively. Defining

$$\gamma^2=\lambda^2-k_1^2 \quad \kappa^2=k_2^2-\lambda^2 \quad \left(\lambda^2=\xi^2+\zeta^2\right)$$

yields

$$p_1(\xi,\zeta)=\gamma$$
$$p_2(\xi,\zeta)=j\kappa$$

Then, the TE-odd characteristic eigenvalue equation becomes

$$\gamma+j\kappa\coth(j\kappa t)=0\rightarrow\gamma t=-\kappa t\cot(\kappa t) \tag{F1}$$

while the TM-even characteristic eigenvalue equation becomes

$$N_{21}^2\gamma+j\kappa\tanh(j\kappa t)=0\rightarrow\gamma t=\frac{\kappa t}{N_{21}^2}\tan(\kappa t) \tag{F2}$$

Since $\gamma^2+\kappa^2=k_2^2-k_1^2$,

$$(\gamma t)^2+(\kappa t)^2=\left(k_2^2-k_1^2\right)t^2 \tag{F3}$$

To determine the cut-off criterion for the nth surface-wave mode, a graphical solution in of Eqn. (F1), Eqn. (F2), and Eqn. (F3) needs to be exploited as depicted in Fig. F1. As illustrated in Fig. F1, the surface-wave modes are captured in the order of TM_0,

$TE_1, TM_2, TE_3, TM_4, TE_5, \cdots$. It is observed that $\gamma > 0$ is required for a confined surface-wave mode, thus, the allowed range of κt is for $\gamma > 0$ along that axis. The $TM_n\ (n = even)$ modes have one principal mode, the TM_0 mode, with no low-frequency cut-off. Cut-off criterion for the surface-wave mode occurs when those intersection points fall along the κt-axis or when $\kappa t = n\pi/2$ with $n = even$ for TM_n modes and $n = odd$ for TE_n modes or when $\kappa t = n\pi/2$. At those intersection points, $\gamma = 0$ such that

$$(\kappa t)_{co} = \sqrt{k_2^2 - k_1^2}\, t = \frac{n\pi}{2} \tag{F4}$$

Since $k_l = n_l k_0$ with $k_0 = 2\pi/\lambda_0$ (λ_0 is a free-space wavelength),

$$\left(\frac{t}{\lambda_0}\right)_{co} = \frac{n}{4\sqrt{n_2^2 - n_1^2}} \tag{F5}$$

Therefore, Eqn. (F5) defines the cut-off criterion for the surface-wave mode.

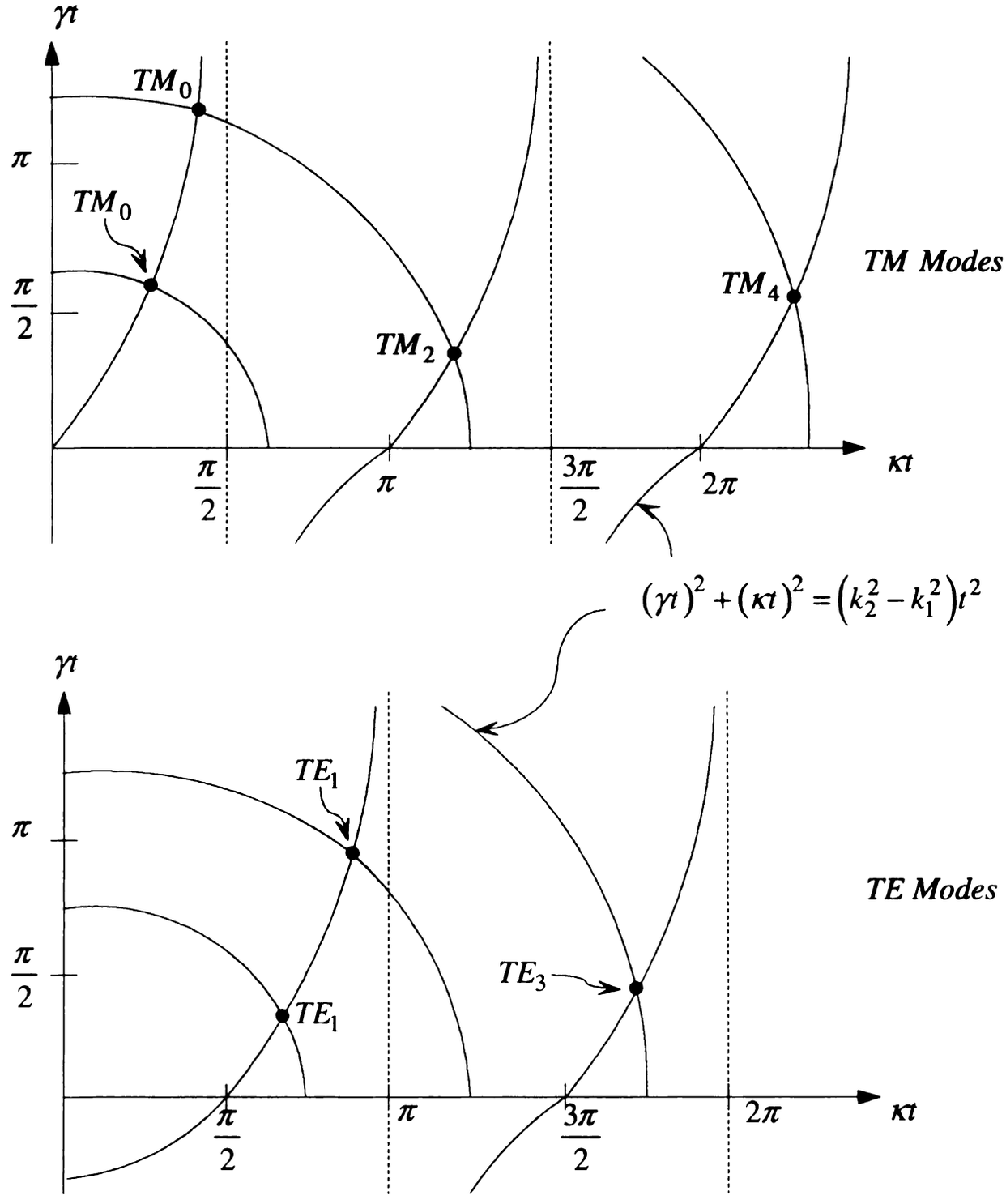

Figure E.4.1 Graphical solution to determine the cut-off criterion for the $n'th$ even or odd surface-wave modes of the microstrip waveguide.

Alternatively, an image theorem can be exploited to determine the cut-off criterion of the integrated background environment. Since the substrate layer is perfectly conducting, the film layer polarization currents can be imaged. The perpendicular current distribution $\boldsymbol{J}_{\perp}(\boldsymbol{r})$ is identically mirrored with an amplitude and a phase but the parallel current distribution $\boldsymbol{J}_{\parallel}(\boldsymbol{r})$ is also identically mirrored with an amplitude except an opposite phase with respect to the $y=-t$ interface as depicted in Fig. F2. Then, it is noted that the well-known cut-off criterion for the nth surface-wave mode of a dielectric waveguide is

$$\left(\frac{t}{\lambda_0}\right)_{\text{co}} = \frac{n}{2\sqrt{n_2^2 - n_1^2}} \tag{F6}$$

However, as depicted in Fig. F2, it is observed that $t \rightarrow 2t$ due to the image current. Therefore,

$$\left(\frac{t}{\lambda_0}\right)_{\text{co}} = \frac{n}{4\sqrt{n_2^2 - n_1^2}} \cdots \textit{as required} \tag{F7}$$

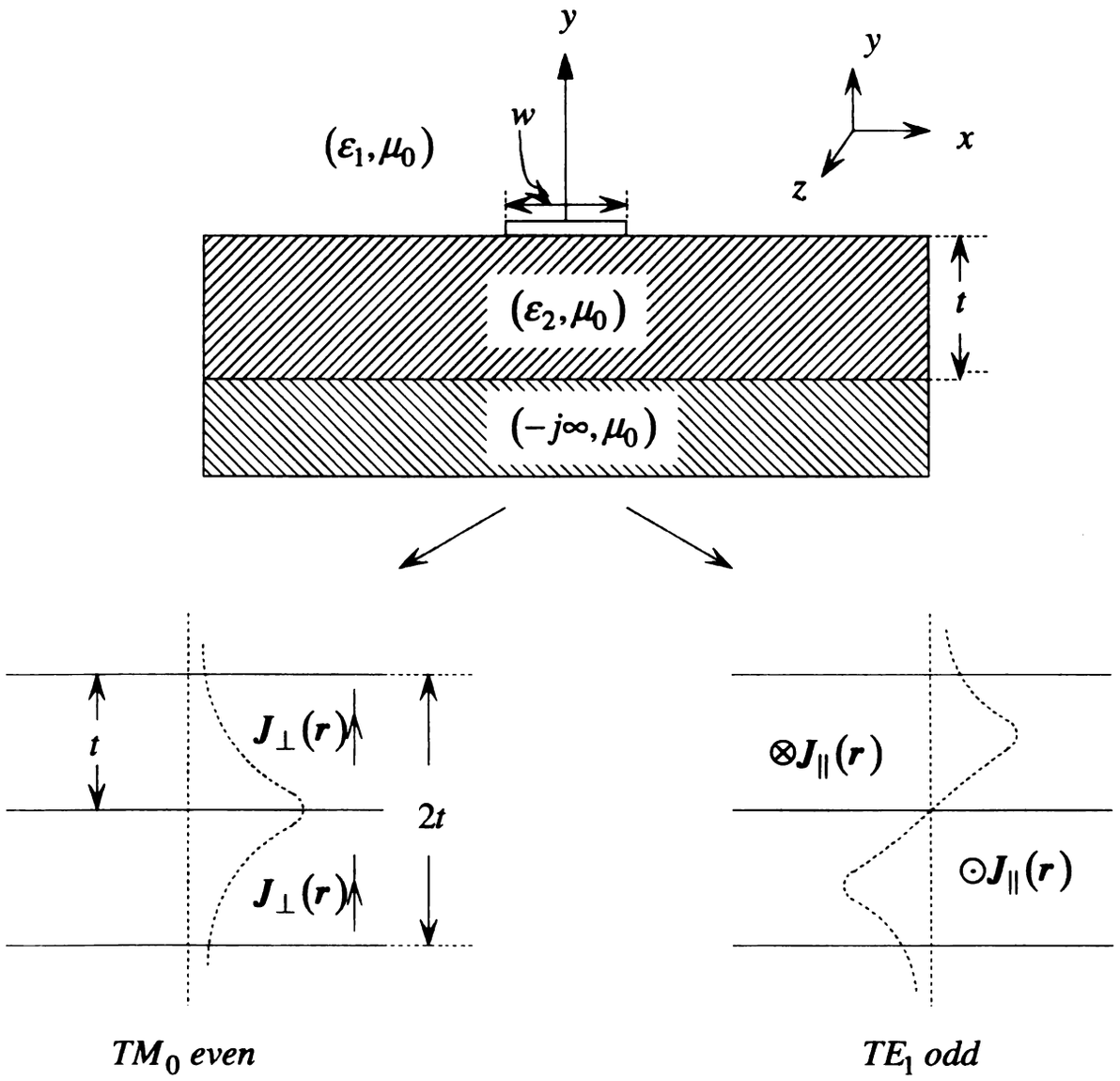

Figure E.4.2 Cross-sectional view of the integrated microstrip waveguide with $\varepsilon_3 \rightarrow -j\infty$. Perpendicular TM_0 even- and parallel TE_1 odd-mode currents and their images are mirrored with respect to the $y = -t$ interface.

APPENDIX G

ELECTROMAGNETIC FIELDS FORMULATION OF AN OPEN INTEGRTED MICROSTRIP WAVEGUIDE IN THE COMPLEX λ-PLANE

G.1 COVER FIELD FORMULATION

$\lambda = \hat{x}\xi + \hat{z}\zeta$ leads from Eqn. (6.2.9) to

$$\Pi_{1y}(r) = \int_{-\infty}^{\infty} dz' J_z(z') \iint_{\infty} j\zeta \mathrm{K}_{1y}(\lambda, y)\tilde{\eta}(\xi) e^{j\xi x} e^{j\zeta(z-z')} d^2\lambda$$

where

$$\mathrm{K}_{1y}(\lambda, y) = \frac{1}{j\omega\varepsilon_1} \frac{1}{2(2\pi)^2} C_{1r}(\lambda) \frac{e^{-p_1 y}}{p_1} \tag{G1.1}$$

$$\tilde{\eta}(\xi) = \begin{cases} J_0(\xi w/2) \cdots w/t < 2 \\ sinc(\xi w/2) \cdots w/t \geq 2 \end{cases}$$

Similarly Eqn. (6.2.10) becomes

$$\Pi_{1z}(r) = \int_{-\infty}^{\infty} dz' J_z(z') \iint_{\infty} \mathrm{K}_{1z}(\lambda, y)\tilde{\eta}(\xi) e^{j\xi x} e^{j\zeta(z-z')} d^2\lambda$$

where (G1.2)

$$\mathrm{K}_{1z}(\lambda, y) = \frac{1}{j\omega\varepsilon_1} \frac{1}{2(2\pi)^2} \frac{2P_1}{Z^h(\lambda)} \frac{e^{-p_1 y}}{p_1}$$

Since $x < 0$ and $z - z' < 0$ for *LHP* in the complex λ-plane as depicted in Fig. (G1.1),

$$\begin{aligned} x &= -r\sin\theta & \xi &= \lambda\sin\phi \\ z - z' &= -r\cos\theta & \zeta &= \lambda\cos\phi \end{aligned} \tag{G1.3}$$

Then,

$$\Pi_{1y}(r) = \int_{-\infty}^{\infty} dz' J_z(z') \int_0^{\infty} d\lambda\lambda^2 \mathrm{K}_{1y} \int_{-\pi}^{\pi} \tilde{\eta}(\lambda\sin\phi)\, j\cos\phi\, e^{-j\lambda r\cos(\phi-\theta)} d\phi \tag{G1.4}$$

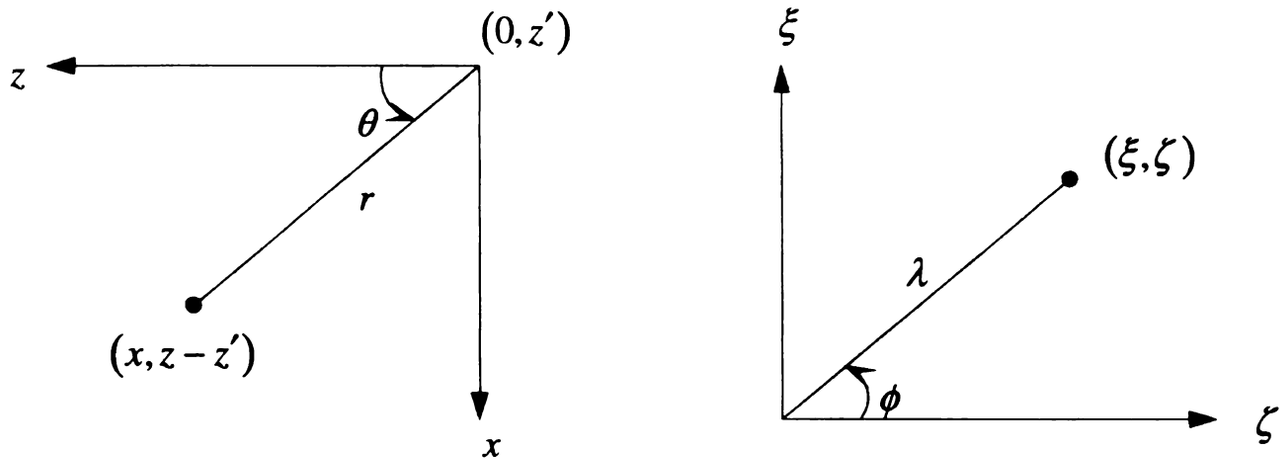

Figure G.1.1 Transformation of $(x, z-z')$ into (r,θ) and (ξ,ζ) into (λ,ϕ).

and

$$\Pi_{1z}(r)=\int_{-\infty}^{\infty}dz'J_z(z')\int_0^{\infty}d\lambda\lambda \mathrm{K}_{1z}\int_{-\pi}^{\pi}\tilde{\eta}(\lambda\sin\phi)e^{-j\lambda r\cos(\phi-\theta)}d\phi \quad \text{(G1.5)}$$

Restricting the microstrip dimension such that $w/t < 2$ leads to

$$\tilde{\eta}(\lambda\sin\phi)=J_0\left(\frac{\lambda w\sin\phi}{2}\right) \quad \text{(G1.6)}$$

It is observed [55] that

$$J_0\left(\frac{\lambda w\sin\phi}{2}\right)\approx 1-\frac{\frac{1}{4}\left(\frac{\lambda w\sin\phi}{2}\right)^2}{(1!)^2}+\frac{\left[\frac{1}{4}\left(\frac{\lambda w\sin\phi}{2}\right)^2\right]^2}{(2!)^2}-\cdots \quad \text{(G1.7)}$$

Since the width of the microstrip is already assumed to be narrow in agreement with Eqn. (G1.6), it is assumed, regardless of λ, that approximately

$$J_0\left(\frac{\lambda w \sin\phi}{2}\right) \approx 1 \tag{G1.8}$$

and letting $\psi = \theta - \phi$ leads to

$$\begin{aligned}
\Pi_{1y}(r) &= \int_{-\infty}^{\infty} dz' J_z(z') \int_0^{\infty} d\lambda \lambda^2 \mathrm{K}_{1y}(\lambda, y) \int_{-\pi+\theta}^{\pi+\theta} j\cos(\psi-\theta) e^{j\lambda r\cos\psi} d\psi \\
&= \int_{-\infty}^{\infty} dz' J_z(z') \int_0^{\infty} d\lambda \lambda^2 \mathrm{K}_{1y}(\lambda, y) j\cos\theta \underbrace{\int_{-\pi+\theta}^{\pi+\theta} \cos\psi\, e^{j\lambda r\cos\psi} d\psi}_{=j2\pi J_1(\lambda r)} \\
&= -2\pi \int_{-\infty}^{\infty} dz' J_z(z') \cos\theta \int_0^{\infty} \mathrm{K}_{1y}(\lambda, y) J_1(\lambda r) \lambda^2 d\lambda \\
&= -\pi \int_{-\infty}^{\infty} dz' J_z(z') \cos\theta \int_{-\infty}^{\infty} \mathrm{K}_{1y}(\lambda, y) H_1^{(2)}(\lambda r) \lambda^2 d\lambda
\end{aligned} \tag{G1.9}$$

where

$$\theta = \tan^{-1}\left(\frac{x}{z-z'}\right)$$

Therefore, even for $\lambda \to \infty$, $H_1^{(2)}(\lambda r)$ decays rapidly to annul the integrand of $d\lambda$ in Eqn. (G1.9). Then, without loss of any generality, it is noted for all λ and $w/t < 2$ that

$$J_0\left(\frac{\lambda w \sin\phi}{2}\right) \approx 1$$

Similarly,

$$\Pi_{1z}(r) = 2\pi \int_{-\infty}^{\infty} dz' J_z(z') \int_0^{\infty} \mathrm{K}_{1z}(\lambda, y) J_0(\lambda r) \lambda d\lambda \tag{G1.10}$$

In accordance with Eqn. (6.2.5),

$$\begin{aligned}
E_{1y}(r) &= \left(k_1^2 + \frac{\partial^2}{\partial y^2}\right)\Pi_{1y}(r) + \frac{\partial^2}{\partial y \partial z}\Pi_{1z}(r) \\
&= \lambda^2 \Pi_{1y}(r) + \frac{\partial^2}{\partial y \partial z}\Pi_{1z}(r)
\end{aligned} \tag{G1.11}$$

and

$$\frac{\partial}{\partial z}\Pi_{1z}(r)=-2\pi\int_{-\infty}^{\infty}dz'J_z(z')\cos\theta\int_0^{\infty}\mathrm{K}_{1z}(\lambda,y)J_1(\lambda r)\lambda^2 d\lambda$$

$$=-\pi\int_{-\infty}^{\infty}dz'J_z(z')\cos\theta\int_{-\infty}^{\infty}\mathrm{K}_{1z}(\lambda,y)H_1^{(2)}(\lambda r)\lambda^2 d\lambda \quad \text{(G1.12)}$$

where

$$\cos\theta=\cos\left[\tan^{-1}\left(\frac{x}{z-z'}\right)\right]$$

Therefore,

$$E_{1y}(r)=-\frac{1}{j\omega\varepsilon_1}\frac{\pi}{2(2\pi)^2}\int_{-\infty}^{\infty}dz'J_z(z')\cos\theta\int_{-\infty}^{\infty}\left[\lambda^2 C_{1r}(\lambda)-\frac{2p_1^2(\lambda)}{Z^h(\lambda)}\right]\frac{e^{-p_1(\lambda)y}}{p_1(\lambda)}H_1^{(2)}(\lambda r)\lambda^2 d\lambda \quad \text{(G1.13)}$$

As depicted in Fig. G1.2, Cauchy's integral theorem leads to

$$\begin{aligned}
&\int_{C_\lambda}\left[\lambda^2 C_{1r}(\lambda)-\frac{2p_1^2(\lambda)}{Z^h(\lambda)}\right]\frac{e^{-p_1(\lambda)y}}{p_1(\lambda)}H_1^{(2)}(\lambda r)\lambda^2 d\lambda+\\
&\oint_{C_{\lambda_p}}\left[\lambda^2 C_{1r}(\lambda)-\frac{2p_1^2(\lambda)}{Z^h(\lambda)}\right]\frac{e^{-p_1(\lambda)y}}{p_1(\lambda)}H_1^{(2)}(\lambda r)\lambda^2 d\lambda+\\
&\int_{C_b}\left[\lambda^2 C_{1r}(\lambda)-\frac{2p_1^2(\lambda)}{Z^h(\lambda)}\right]\frac{e^{-p_1(\lambda)y}}{p_1(\lambda)}H_1^{(2)}(\lambda r)\lambda^2 d\lambda+\\
&\int_{C_\infty}\left[\lambda^2 C_{1r}(\lambda)-\frac{2p_1^2(\lambda)}{Z^h(\lambda)}\right]\frac{e^{-p_1(\lambda)y}}{p_1(\lambda)}H_1^{(2)}(\lambda r)\lambda^2 d\lambda=0
\end{aligned} \quad \text{(G1.14)}$$

Sommerfeld's radiation condition requires

$$\int_{C_\infty}\left[\lambda^2 C_{1r}(\lambda)-\frac{2p_1^2(\lambda)}{Z^h(\lambda)}\right]\frac{e^{-p_1(\lambda)y}}{p_1(\lambda)}H_1^{(2)}(\lambda r)\lambda^2 d\lambda\to 0 \quad \text{(G1.15)}$$

The discrete or bound-mode spectrum becomes

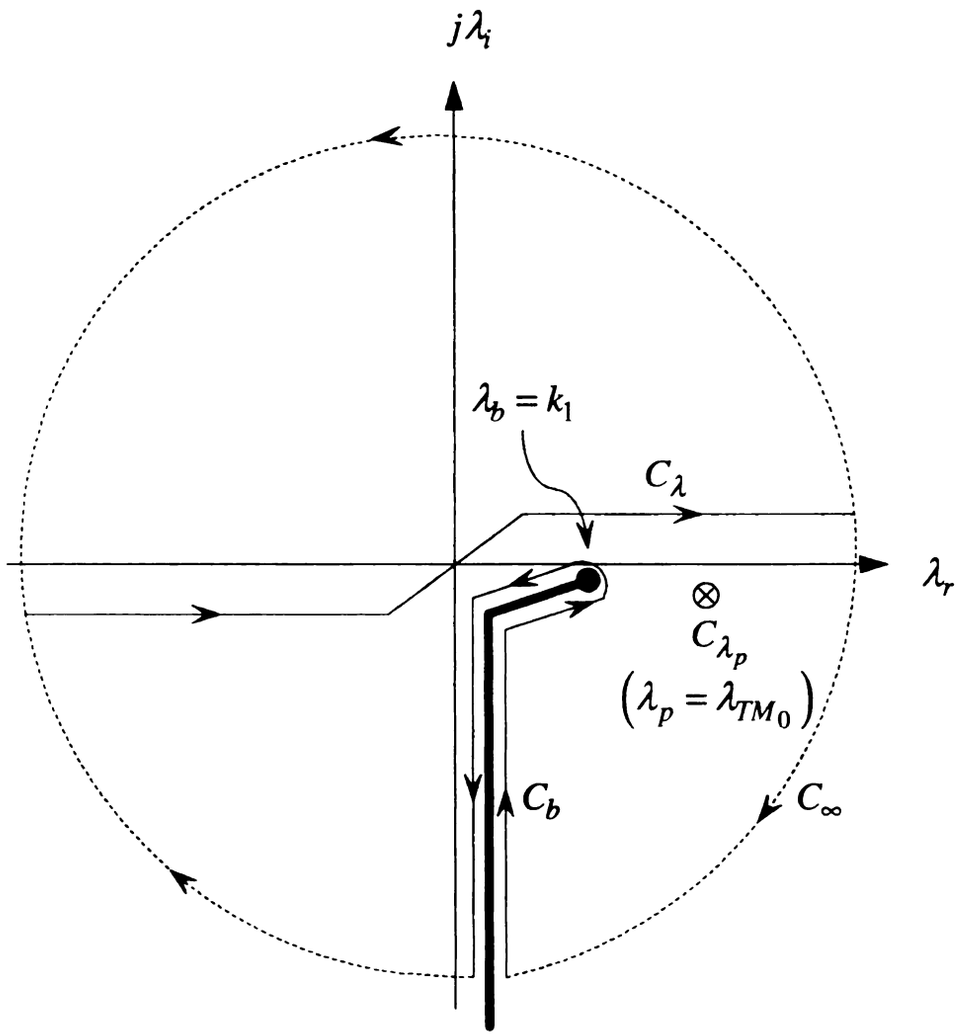

Figure G.1.2 Proper spectrum in the complex λ-plane with the branch-point and the bound-mode pole singularities in the low-loss limit.

$$\oint_{C_{\lambda_p}}\left[\lambda^2 C_{1r}(\lambda)-\frac{2p_1^2(\lambda)}{Z^h(\lambda)}\right]\frac{e^{-p_1(\lambda)y}}{p_1(\lambda)}H_1^{(2)}(\lambda r)\lambda^2 d\lambda$$

$$=j2\pi\frac{2\left(N_{21}^2-1\right)\lambda^4}{Z^h(\lambda)Z^{e'}(\lambda)}e^{-p_1(\lambda)y}H_1^{(2)}(\lambda r)\Big|_{\lambda=\lambda_p} \tag{G1.16}$$

where

$$Z^{e'}(\lambda)=\frac{N_{21}^2\lambda}{p_1(\lambda)}+\frac{\lambda\tanh\left[p_2(\lambda)t\right]}{p_2(\lambda)}+\lambda t\,\mathrm{sech}^2\left[p_2(\lambda)t\right]$$

Then,

$$\int_{C_\lambda}\left[\lambda^2 C_{1r}(\lambda)-\frac{2p_1^2(\lambda)}{Z^h(\lambda)}\right]\frac{e^{-p_1(\lambda)y}}{p_1(\lambda)}H_1^{(2)}(\lambda r)\lambda^2 d\lambda$$

$$=-j2\pi\frac{2\left(N_{21}^2-1\right)\lambda^4}{Z^h(\lambda)Z^{e'}(\lambda)}e^{-p_1(\lambda)y}H_1^{(2)}(\lambda r)\Big|_{\lambda=\lambda_p} \tag{G1.17}$$

$$-\int_{C_b}\left[\lambda^2 C_{1r}(\lambda)-\frac{2p_1^2(\lambda)}{Z^h(\lambda)}\right]\frac{e^{-p_1(\lambda)y}}{p_1(\lambda)}H_1^{(2)}(\lambda r)\lambda^2 d\lambda$$

Finally, the cover field in the complex λ-plane becomes

$$E_{1y}(r)=\frac{1}{2\omega\varepsilon_1}\frac{\left(N_{21}^2-1\right)\lambda^4}{Z^h(\lambda)Z^{e'}(\lambda)}e^{-p_1(\lambda)y}\int_{-\infty}^{\infty}J_z(z')H_1^{(2)}(\lambda r)\cos\theta dz'\Big|_{\lambda=\lambda_p}$$

$$+\frac{1}{2\omega\varepsilon_1}\frac{1}{j4\pi}\int_{-\infty}^{\infty}dz'J_z(z')\cos\theta\int_{C_b}\left[\lambda^2 C_{1r}(\lambda)-\frac{2p_1^2(\lambda)}{Z^h(\lambda)}\right] \tag{G1.18}$$

$$\frac{e^{-p_1(\lambda)y}}{p_1(\lambda)}H_1^{(2)}(\lambda r)\lambda^2 d\lambda$$

where $r=\sqrt{x^2+(z-z')^2}$ and $\theta=\tan^{-1}\left[x/(z-z')\right]$.

G.2 FILM FIELD FORMULATION

$\lambda = \hat{x}\xi + \hat{z}\zeta$ leads from Eqn. (6.2.34) to

$$\Pi_{2y}(r) = \int_{-\infty}^{\infty} dz' J_z(z') \iint_{\infty} j\zeta \mathrm{K}_{2y}(\lambda, y)\tilde{\eta}(\xi) e^{j\xi x} e^{j\zeta(z-z')} d^2\lambda$$

where

$$\mathrm{K}_{2y}(\lambda, y) = \frac{1}{j\omega\varepsilon_1} \frac{1}{(2\pi)^2} \frac{N_{21}^{-2}\left(N_{21}^2 - 1\right)}{Z^h(\lambda) Z^e(\lambda)} \frac{\cosh\left[p_2(y+t)\right]}{\cosh(p_2 t)} \tag{G2.1}$$

$$\tilde{\eta}(\xi) = \begin{cases} J_0(\xi w/2) \cdots w/t < 2 \\ sinc(\xi w/2) \cdots w/t \geq 2 \end{cases}$$

Similarly Eqn. (6.2.35) becomes

$$\Pi_{2z}(r) = \int_{-\infty}^{\infty} dz' J_z(z') \iint_{\infty} \mathrm{K}_{2z}(\lambda, y)\tilde{\eta}(\xi) e^{j\xi x} e^{j\zeta(z-z')} d^2\lambda$$

where (G2.2)

$$\mathrm{K}_{2z}(\lambda, y) = \frac{1}{j\omega\varepsilon_1} \frac{1}{(2\pi)^2} \frac{N_{21}^{-2}}{Z^h(\lambda)} \frac{\sinh\left[p_2(y+t)\right]}{\sinh(p_2 t)}$$

After the transformation,

$$\Pi_{2y}(r) = \int_{-\infty}^{\infty} dz' J_z(z') \int_0^{\infty} d\lambda \lambda^2 \mathrm{K}_{2y} \int_{-\pi}^{\pi} \tilde{\eta}(\lambda \sin\phi)\, j\cos\phi\, e^{-j\lambda r\cos(\phi-\theta)} d\phi$$
$$\Pi_{2z}(r) = \int_{-\infty}^{\infty} dz' J_z(z') \int_0^{\infty} d\lambda \lambda \mathrm{K}_{2z} \int_{-\pi}^{\pi} \tilde{\eta}(\lambda \sin\phi) e^{-j\lambda r\cos(\phi-\theta)} d\phi \tag{G2.3}$$

Restricting the microstrip dimension such that $w/t < 2$ and applying the argument that

$J_0(\lambda w \sin\phi/2) \approx 1$ for all λ due to $H_1^{(2)}(\lambda r)$ leads to

$$\Pi_{2y}(r) = -\pi \int_{-\infty}^{\infty} dz' J_z(z') \cos\theta \int_{-\infty}^{\infty} \mathrm{K}_{2y}(\lambda, y) H_1^{(2)}(\lambda r) \lambda^2 d\lambda \tag{G2.4}$$

Similarly,

$$\Pi_{2z}(r)=2\pi\int_{-\infty}^{\infty}dz'J_z(z')\int_0^{\infty}\mathrm{K}_{2z}(\lambda,y)J_0(\lambda r)\lambda d\lambda \tag{G2.5}$$

In accordance with Eqn. (6.2.5),

$$\begin{aligned}E_{2y}(r)&=\left(k_2^2+\frac{\partial^2}{\partial y^2}\right)\Pi_{2y}(r)+\frac{\partial^2}{\partial y\partial z}\Pi_{2z}(r)\\&=\lambda^2\Pi_{2y}(r)+\frac{\partial^2}{\partial y\partial z}\Pi_{2z}(r)\end{aligned} \tag{G2.6}$$

and

$$\begin{aligned}\frac{\partial}{\partial z}\Pi_{2z}(r)&=-2\pi\int_{-\infty}^{\infty}dz'J_z(z')\cos\theta\int_0^{\infty}\mathrm{K}_{2z}(\lambda,y)J_1(\lambda r)\lambda^2 d\lambda\\&=-\pi\int_{-\infty}^{\infty}dz'J_z(z')\cos\theta\int_{-\infty}^{\infty}\mathrm{K}_{2z}(\lambda,y)H_1^{(2)}(\lambda r)\lambda^2 d\lambda\end{aligned} \tag{G2.7}$$

where

$$\theta=\tan^{-1}\left(\frac{x}{z-z'}\right)$$

Therefore,

$$E_{2y}(r)=-\frac{1}{j\omega\varepsilon_1}\frac{N_{21}^{-2}}{4\pi}\int_{-\infty}^{\infty}dz'J_z(z')\cos\theta\int_{-\infty}^{\infty}(\cdots)d\lambda$$

where (G2.8)

$$(\cdots)=\left[\frac{\left(N_{21}^2-1\right)}{Z^hZ^e}\frac{\lambda^2}{\cosh(p_2t)}+\frac{1}{Z^h}\frac{p_2}{\sinh(p_2t)}\right]\cosh\left[p_2(y+t)\right]H_1^{(2)}(\lambda r)\lambda^2$$

As depicted in Fig. G1.2, Cauchy's integral theorem leads to

$$\int_{C_\lambda}(\cdots)d\lambda+\oint_{C_{\lambda_p}}(\cdots)d\lambda+\int_{C_b}(\cdots)d\lambda+\int_{C_\infty}(\cdots)d\lambda=0$$

where $(\cdots)$ is the integrand of $d\lambda$ in Eqn. (G2.8) and Sommerfeld's radiation condition must be satisfied. The discrete or bound-mode spectrum becomes

$$\oint_{C_{\lambda_p}}(\cdots)d\lambda = j2\pi\frac{\left(N_{21}^2-1\right)\lambda^4}{Z^h(\lambda)Z^{e'}(\lambda)}\frac{\cosh\left[p_2(y+t)\right]}{\cosh(p_2 t)}H_1^{(2)}(\lambda r)\Big|_{\lambda=\lambda_p} \tag{G2.9}$$

Then,

$$\int_{C_\lambda}(\cdots)d\lambda = -j2\pi\frac{\left(N_{21}^2-1\right)\lambda^4}{Z^h(\lambda)Z^{e'}(\lambda)}\frac{\cosh\left[p_2(y+t)\right]}{\cosh(p_2 t)}H_1^{(2)}(\lambda r)\Big|_{\lambda=\lambda_p} - \int_{C_b}(\cdots)d\lambda \tag{G2.10}$$

Finally, the film field in the complex λ-plane becomes

$$E_{2y}(r) = \frac{N_{21}^{-2}}{2\omega\varepsilon_1}\frac{\left(N_{21}^2-1\right)\lambda_p^4}{Z^h(\lambda_p)Z^{e'}(\lambda_p)}\frac{\cosh\left[p_2(\lambda_p)(y+t)\right]}{\cosh\left[p_2(\lambda_p)t\right]}$$
$$\int_{-\infty}^{\infty}J_z(z')H_1^{(2)}(\lambda_p r)\cos\theta dz' +$$
$$\frac{1}{j\omega\varepsilon_1}\frac{N_{21}^{-2}}{4\pi}\int_{-\infty}^{\infty}dz'J_z(z')\cos\theta\int_{C_b}(\cdots)d\lambda$$
where (G2.11)
$$(\cdots) = \left[\frac{\left(N_{21}^2-1\right)}{Z^h(\lambda)Z^e(\lambda)\cosh(p_2 t)}\frac{\lambda^2}{}+\frac{1}{Z^h(\lambda)\sinh(p_2 t)}\frac{p_2}{}\right]$$
$$\cosh\left[p_2(y+t)\right]H_1^{(2)}(\lambda r)\lambda^2$$
$$r=\sqrt{x^2+(z-z')^2} \qquad \theta=\tan^{-1}\left[x/(z-z')\right]$$

BIBLIOGRAPHY

[1] L. M. Brekhovskikh, *Waves in layered Media*, Academic Press, New York, 1960.

[2] D. Marcuse, *Theory of Dielectric Optical Waveguides*, Academic Press, New York, 1960.

[3] C. T. Tai, *Dyadic Green's Function in Electromagnetic Theory*, Intext Publishers, New York, 1971.

[4] J. A. Kong, *Theory of Electromagnetic Waves*, John Wiley & Sons, New York, 1975.

[5] J. K. Lee and J. A. Kong, "Dyadic Green's functions for layered anisotropic medium," *Electromagnetics*, vol. 3, pp. 111-130, 1983.

[6] J. A. Kong, *Electromagnetic Wave Theory*, John Wiley & Sons, New York, 1986.

[7] F. Mesa and R. Marques, "Integral Representation of Spatial Green's function and Spectral Domain Analysis of Leaky Covered Strip-Like Lines," *IEEE Trans. Microwave Theory and Techniques*, MTT-43, pp. 828-837, 1995.

[8] D. P. Nyquist and D. J. Infante, "Discrete Higher-Order Leaky-Wave Modes and the Continuous Spectrum of Stripline," *IEICE Trans.*, vol. E78-C, pp. 1331-1338, 1995.

[9] F. Mesa, C. D. Nallo, and D. R. Jackson, "The Theory of Surface-Wave and Space-Wave Leaky-Mode Excitation on Microstrip Lines," *IEEE Trans. Microwave Theory and Techniques*, MTT-47, pp. 207-215, 1999.

[10] J. A. Stratton, *Electromagnetic Theory*, McGraw-Hill, New York, 1941.

[11] C. T. Tai, "Effect of a Grounded Slab on Radiation from a Line Source," J. Appl. Phys., vol. 22, 1951.

[12] T. Tamir and A.A. Oliner, "Guided Complex Waves. I. Fields at an Interface. II. Relation to Radiation Patterns.," Proc. IEE (London), vol. 110, 1963.

[13] L. B. Felsen and N. Marcuvitz, *Radiation and Scattering of Waves*, Prentice-Hall, Englewood Cliffs, N.J., Chapter 5, 1973.

[14] D. P. Nyquist, "Leaky-Wave and Radiation Modes of the Planar Dielectric Waveguide-A Review of their Origin and Significance," International Symposium on Electromagnetic Theory, Thessaloniki, Greece, 1998.

[15] D. P. Nyquist, "Asymptotic Radiation Field of Asymmetric Planar Dielectric Waveguide," Mathematical Methods in Electromagnetic Theory, Kharkov, Ukraine, 1998.

[16] A. Erdelyi, Asymptotic Expansions, Dover Publication, Inc., pp. 39-41, 1956.

[17] W. C. Chew, *Waves and Fields in Inhomogeneous Media*, Van Nostrand Reinhold, New York, 1990.

[18] I.S. Gradshteyn, I.M. Ryzbik, Table of Integrals, Series, and Products, Academic Press, San Diego, CA, 2000.

[19] J. Song, S. Ohnuki, D. P. Nyquist, K. M. Chen, and E. J. Rothwell, "Scattering of TE polarized EM wave by discontinuity in grounded dielectric layer," *IEEE Trans. Microwave Theory and Techniques*, MTT-42, pp. 481-488, Mar. 1994.

[20] N. Marcuvitz, "On Field Representation in Terms of Leaky Modes," IRE Trans., vol. AP-4, 1956.

[21] E. S. Cassedy and M. Cohn, "On the Existence of Leaky Waves Due to a Line Source Above a Grounded Dielectric Slab," IRE Trans., vol. MTT-9, 1961.

[22] D. P. Nyquist, *Advanced Topics in Electromagnetics Planar Waveguides and Circuits (Class Notes)*, Aug. 1994.

[23] C. T. Tai, "On the eigenfunction expansion of dyadic Green's functions," *Proc. IEEE*, vol. 61, 1973.

[24] M. S. Viola and D. P. Nyquist, "An observation on the Sommerfeld-integral representation of the electric dyadic Green's function for layered media," *IEEE Trans. Microwave Theory and Techniques*, MTT-36, pp. 1289-1292, 1988.

[25] W. C. Chew, "Some observations on the spatial and eigenfunction representations of dyadic Green's functions," *IEEE Trans. Microwave Theory and Techniques*, MTT-37, pp. 1322-1327, 1989.

[26] Y. Rahmat-Samii, "On the question of computation of dyadic Green's function at the source region in waveguides and cavities," *IEEE Trans. Microwave Theory and Technique*, MTT-23, 1975.

[27] A. D. Yaghjian, "Electric dyadic Green's functions in the source region," *Proc. IEEE*, vol. 68, 1980.

[28] J. S. Bagby, D. P. Nyquist, and B. C. Drachman, "Integral Formulation for analysis of integrated dielectric waveguides," *IEEE Trans. Microwave Theory and Techniques*, MTT-33, pp. 906-915, 1985.

[29] J. M. Grimm and D. P. Nyquist, "Spectral Analysis Considerations relevant to Radiation and Leaky Modes of Microstrip Transmission Line," *IEEE Trans. Microwave Theory and Techniques*, MTT-41, pp. 150-153, 1993.

[30] D. P. Nyquist, J. M. Grimm, D. J. Infante, and H. Braunisch, "Classification of the Proper Propagation-Mode Spectrum and Leaky-Wave Modes on Open Planar Waveguides," *Electromagnetics*, vol. 17, pp. 105-130, 1997.

[31] R. E. Collin, *Field Theory of Guided Waves*, 2nd ed., New York, IEEE Press, 1991.

[32] A. A. Oliner, "Leakage from higher modes on microstrip line with application to antennas," *Radio Sci.*, vol. 22, pp. 907-912, Nov. 1987.

[33] H. Shigesawa, M. Tsuji, and A. A. Oliner, "Conductor-backed slot line and coplanar waveguide: Dangers and full-wave analysis," in *Proc. IEEE Int. Microwave Symp. Dig.*, pp. 199-202, June 1988.

[34] K. A. Michalski and D. Zheng, "Rigorous analysis of open microstrip lines of arbitrary cross section in bound and leaky regimes," *IEEE Trans. Microwave Theory and Techniques*, MTT-37, pp. 2005-2010, Dec. 1989.

[35] N. K. Das and D. M. Pozar, "Full-wave spectral-domain computation of material, radiation, and guided wave losses in infinite multilayered printed transmission lines," *IEEE Trans. Microwave Theory and Techniques*, MTT-39, pp. 54-63, Jan. 1991.

[36] H. Shigesawa, M. Tsuji, and A. A. Oliner,, "Dominant mode power leakage from printed-circuit waveguide" *Radio sci.*, vol. 26, pp. 559-564, Mar.-Apr. 1991.

[37] J. M. Grimm and D. P. Nyquist, "Spectral analysis considerations relevant to radiation and leaky modes of open-boundary microstrip transmission line," *IEEE Trans. Microwave Theory and Techniques*, MTT-41, pp. 150-153, Jan. 1993.

[38] D. Nghiem, J. T. Williams, D. R. Jackson, and A. A. Oliner, "Proper and improper dominant mode solutions for stripline with an air gap," *Radio Sci.*, vol. 28, no. 6, pp. 1163-1180, Nov.-Dec. 1993.

[39] F. Mesa and R. Marques,, "Integral representation of spatial Green's function and spectral domain analysis of leaky covered strip-like lines," *IEEE Trans. Microwave Theory and Techniques*, MTT-43, pp. 828-837, Apr. 1995.

[40] D. Nghiem, J. T. Williams, D. R. Jackson, and A. A. Oliner, "Leakage of the dominant mode on stripline with a small air gap," *IEEE Trans. Microwave Theory and Techniques*, MTT-43, pp. 2549-2556, Nov. 1995.

[41] H. Shigesawa, M. Tsuji, and A. A. Oliner,, "A simultaneous propagation of bound and leaky dominant modes on printed-circuit lines: A new general effect," *IEEE Trans. Microwave Theory and Techniques*, MTT-43, pp. 3007-3019, Dec. 1995.

[42] F. Mesa and R. Marques,, "Power based considerations on the spectral domain analysis of leaky waves in covered strip-like transmission lines," *Proc. Inst. Elec. Eng.*, vol. 143, pp. 25-30, Jan. 1996.

[43] N. K. Das, "Methods of suppression or avoidance of parallel-plate power leakage from conductor-backed transmission lines," *IEEE Trans. Microwave Theory and Techniques*, MTT-44, pp. 169-181, Feb. 1996.

[44] D. Nghiem, J. T. Williams, D. R. Jackson, and A. A. Oliner, "Existence of a leaky dominant mode on microstrip line with an isotropic substrate: Theory and measurement," *IEEE Trans. Microwave Theory and Techniques*, MTT-44, pp. 1710-1715, Oct. 1996.

[45] F. Mesa, D. R. Jackson, and M. J. Freire, "Evolution of Leaky Modes on Printed-Circuit Lines," *IEEE Trans. Microwave Theory and Techniques*, MTT-50, pp. 94-104, Jan. 2002.

[46] J. Boukamp and R. H. Jansen, "Spectral domain investigation of surface wave excitation and radiation by microstrip lines and microstrip disk resonator," in *Proc 13rd European Microwave Conf.*, pp. 721-726, Sept. 1983.

[47] J. S. Bagby, C. -H. Lee, D. P. Nyquist, and Y. Yuan, "Identification of propagation regimes on integrated microstrip transmission lines," *IEEE Trans. Microwave Theory and Techniques*, MTT-41, pp. 1887-1893, Nov. 1993.

[48] H. Shigesawa, M. Tsuji, and A. A. Oliner, "The nature of the spectral-gap between bound and leaky solution when dielectric loss is present in printed-circuit lines," *Radio sci.*, vol. 28, no. 6, pp. 1235-1243, Nov.-Dec. 1993.

[49] J. L. Cina and L. Carin, "Mode Conversion and Leaky-Wave Excitation at Open-End Coupled-Microstrip Discontinuities," *IEEE Trans. Microwave Theory and Techniques*, MTT-43, pp. 2066-2071, Sept. 1995.

[50] N. K. Das, "Power Leakage, Characteristic Impedance and Leakage-Transition Behaviour of Finite-Length Stub Section of Leaky Printed Transmission Lines," *IEEE Trans. Microwave Theory and Techniques*, MTT-44, pp. 526-536, Apr. 1996.

[51] G. –J. Chou and C. –K. C. Tzuang, "Oscillator-Type Active-Integrated Antenna: The Leaky Mode Approach," *IEEE Trans. Microwave Theory and Techniques*, MTT-44, pp. 2265-2272, Dec. 1996.

[52] C. D. Nallo, F. Mesa, D. R. Jackson, "Excitation of Leaky Modes on Multilayer Stripline Structures," *IEEE Trans. Microwave Theory and Techniques*, MTT-46, pp. 1062-1071, Aug. 1998.

[53] L. B. Felsen and N. Marcuvitz, *Radiation and Scattering of Waves*, Prentice-Hall, Englewood Cliffs, N.J., Chapter 5, 1973.

[54] Pozar, Microwave Engineering, Addison-Wesley Publishing Company, Inc, pp. 185, 1990.

[55] M. Abramowitz and I. A. Stegun, Handbook of Mathematical Functions With Formulas, Graphs, and Mathematical Tables, U.S. Government Printing Office, Washington, D.C., June 1964.

[56] D. R. Jackson, F. Mesa, M. J. Freire, D. P. Nyquist, and C. D. Nallo, "An excitation theory for bound modes, leaky modes, and residual-wave currents on stripline structures," *Radio Sci.*, vol. 35, pp. 495-510, Mar.-Apr. 2000.

[57] N. Bleistein and R. A. Handelsman, *Asymptotic Expansions of Integrals*, Holt Rinehart and Winston, New York, 1975.